CYTOSKELETAL DYNAMICS AND MECHANICS IN CELL GROWTH, DIVISION, DIFFERENTIATION AND AGING

EDITED BY: Ting Gang Chew, Anne Straube, Ana Xavier De Carvalho, Marin Barisic and Yi Zhang

PUBLISHED IN: Frontiers in Cell and Developmental Biology

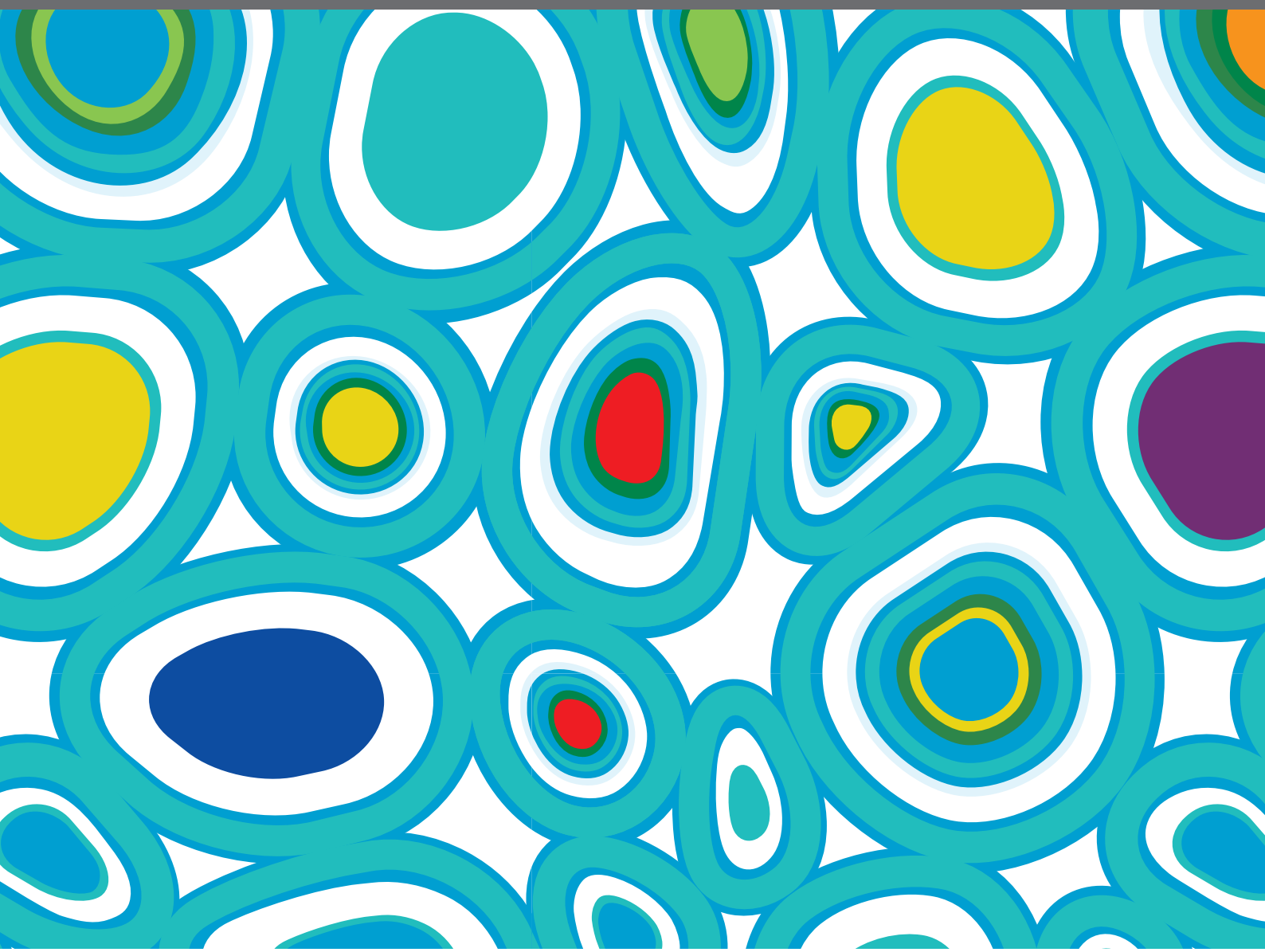

frontiers Research Topics

frontiers

ISSN 1664-8714
ISBN 978-2-88974-160-1
DOI 10.3389/978-2-88974-160-1

About Frontiers

Frontiers is more than just an open-access publisher of scholarly articles: it is a pioneering approach to the world of academia, radically improving the way scholarly research is managed. The grand vision of Frontiers is a world where all people have an equal opportunity to seek, share and generate knowledge. Frontiers provides immediate and permanent online open access to all its publications, but this alone is not enough to realize our grand goals.

Frontiers Journal Series

The Frontiers Journal Series is a multi-tier and interdisciplinary set of open-access, online journals, promising a paradigm shift from the current review, selection and dissemination processes in academic publishing. All Frontiers journals are driven by researchers for researchers; therefore, they constitute a service to the scholarly community. At the same time, the Frontiers Journal Series operates on a revolutionary invention, the tiered publishing system, initially addressing specific communities of scholars, and gradually climbing up to broader public understanding, thus serving the interests of the lay society, too.

Dedication to Quality

Each Frontiers article is a landmark of the highest quality, thanks to genuinely collaborative interactions between authors and review editors, who include some of the world's best academicians. Research must be certified by peers before entering a stream of knowledge that may eventually reach the public - and shape society; therefore, Frontiers only applies the most rigorous and unbiased reviews.
Frontiers revolutionizes research publishing by freely delivering the most outstanding research, evaluated with no bias from both the academic and social point of view. By applying the most advanced information technologies, Frontiers is catapulting scholarly publishing into a new generation.

What are Frontiers Research Topics?

Frontiers Research Topics are very popular trademarks of the Frontiers Journals Series: they are collections of at least ten articles, all centered on a particular subject. With their unique mix of varied contributions from Original Research to Review Articles, Frontiers Research Topics unify the most influential researchers, the latest key findings and historical advances in a hot research area! Find out more on how to host your own Frontiers Research Topic or contribute to one as an author by contacting the Frontiers Editorial Office: frontiersin.org/about/contact

CYTOSKELETAL DYNAMICS AND MECHANICS IN CELL GROWTH, DIVISION, DIFFERENTIATION AND AGING

Topic Editors:
Ting Gang Chew, Zhejiang University-University of Edinburgh Institute, China
Anne Straube, University of Warwick, United Kingdom
Ana Xavier De Carvalho, Universidade do Porto, Portugal
Marin Barisic, Danish Cancer Society Research Center (DCRC), Denmark
Yi Zhang, Beijing Normal University, China

Citation: Chew, T. G., Straube, A., De Carvalho, A. X., Barisic, M., Zhang, Y., eds. (2022). Cytoskeletal Dynamics and Mechanics in Cell Growth, Division, Differentiation and Aging. Lausanne: Frontiers Media SA.
doi: 10.3389/978-2-88974-160-1

Table of Contents

04 ***Control of the Actin Cytoskeleton Within Apical and Subapical Regions of Pollen Tubes***
Yanan Xu and Shanjin Huang

16 ***Arabidopsis ADF5 Acts as a Downstream Target Gene of CBFs in Response to Low-Temperature Stress***
Pan Zhang, Dong Qian, Changxin Luo, Yingzhi Niu, Tian Li, Chengying Li, Yun Xiang, Xinyu Wang and Yue Niu

28 ***Bil2 Is a Novel Inhibitor of the Yeast Formin Bnr1 Required for Proper Actin Cable Organization and Polarized Secretion***
Thomas J. Rands and Bruce L. Goode

44 ***Dynamic Microtubule Arrays in Leukocytes and Their Role in Cell Migration and Immune Synapse Formation***
Aglaja Kopf and Eva Kiermaier

62 **Arabidopsis *QWRF1 and QWRF2 Redundantly Modulate Cortical Microtubule Arrangement in Floral Organ Growth and Fertility***
Huifang Ma, Liyuan Xu, Ying Fu and Lei Zhu

74 ***Multifaceted Function of Myosin-18, an Unconventional Class of the Myosin Superfamily***
Zhaohui Ouyang, Shuangshuang Zhao, Su Yao, Jing Wang, Yanqin Cui, Ke Wei and Yaming Jiu

83 ***Nucleus-Cytoskeleton Crosstalk During Mitotic Entry***
Margarida Dantas, Joana T. Lima and Jorge G. Ferreira

92 ***The Morphological Diversity of Plant Organs: Manipulating the Organization of Microtubules May Do the Trick***
Zhiru Bao, Zhijing Xu, Jingze Zang, Katharina Bürstenbinder and Pengwei Wang

98 ***The Nuclear Mitotic Apparatus (NuMA) Protein: A Key Player for Nuclear Formation, Spindle Assembly, and Spindle Positioning***
Tomomi Kiyomitsu and Susan Boerner

110 ***Feedback-Driven Mechanisms Between Phosphorylated Caveolin-1 and Contractile Actin Assemblies Instruct Persistent Cell Migration***
Xuemeng Shi, Zeyu Wen, Yajun Wang, Yan-Jun Liu, Kun Shi and Yaming Jiu

126 ***The Role of Cell Adhesion and Cytoskeleton Dynamics in the Pathogenesis of the Ehlers-Danlos Syndromes and Hypermobility Spectrum Disorders***
Sabeeha Malek and Darius V. Köster

139 ***Wnt Signaling Induces Asymmetric Dynamics in the Actomyosin Cortex of the* C. elegans *Endomesodermal Precursor Cell***
Francesca Caroti, Wim Thiels, Michiel Vanslambrouck and Rob Jelier

frontiers in Cell and Developmental Biology

REVIEW
published: 03 December 2020
doi: 10.3389/fcell.2020.614821

Control of the Actin Cytoskeleton Within Apical and Subapical Regions of Pollen Tubes

*Yanan Xu and Shanjin Huang**

Center for Plant Biology, School of Life Sciences, Tsinghua University, Beijing, China

In flowering plants, sexual reproduction involves a double fertilization event, which is facilitated by the delivery of two non-motile sperm cells to the ovule by the pollen tube. Pollen tube growth occurs exclusively at the tip and is extremely rapid. It strictly depends on an intact actin cytoskeleton, and is therefore an excellent model for uncovering the molecular mechanisms underlying dynamic actin cytoskeleton remodeling. There has been a long-term debate about the organization and dynamics of actin filaments within the apical and subapical regions of pollen tube tips. By combining state-of-the-art live-cell imaging with the usage of mutants which lack different actin-binding proteins, our understanding of the origin, spatial organization, dynamics and regulation of actin filaments within the pollen tube tip has greatly improved. In this review article, we will summarize the progress made in this area.

Keywords: pollen tube growth, cytoplasmic streaming, actin dynamics, apical actin structure, actin-binding proteins, formin, ADF, villin

OPEN ACCESS

Edited by:
Yi Zhang,
Beijing Normal University, China

Reviewed by:
Yun Xiang,
Lanzhou University, China
Hui Su,
Northwest University, China

***Correspondence:**
Shanjin Huang
sjhuang@mail.tsinghua.edu.cn

Specialty section:
This article was submitted to Cell Growth and Division, a section of the journal Frontiers in Cell and Developmental Biology

Received: *07 October 2020*
Accepted: *13 November 2020*
Published: *03 December 2020*

Citation:
Xu Y and Huang S (2020) Control of the Actin Cytoskeleton Within Apical and Subapical Regions of Pollen Tubes. Front. Cell Dev. Biol. 8:614821. doi: 10.3389/fcell.2020.614821

INTRODUCTON

In flowering plants (angiosperms), seed formation requires two fertilization events. The male germ unit, called the male gametophyte, is contained within pollen grains and comprises a vegetative cell and two sperm cells that have already lost their motility (Kaul et al., 2000; Dresselhaus et al., 2016; Higashiyama, 2018). The process of double fertilization begins when pollen grains land on and adhere to the surface of the stigma. Following hydration of the pollen grain, the vegetative cell generates a pollen tube (Chapman and Goring, 2010). Pollen tubes then grow through the transmitting tissue of the style and serve as an active vehicle to transport the two immotile sperm cells into the ovule under the attraction of various female molecules (Higashiyama and Takeuchi, 2015; Zhang et al., 2017; Johnson et al., 2019). Therefore, pollen tube growth represents a critical stage during the extended journey that is required for double fertilization in flowering plants.

Similar to the filamentous protonemata of mosses and the root hairs of high plants, pollen tubes are tip-growing cells, with growth strictly occurring within the apical region (Rounds and Bezanilla, 2013). Pollen tubes grow rapidly both *in vivo* and *in vitro*. For instance, the growth rate of lily (*Lilium longiflorum* and *Lilium formosanum*) pollen tubes can reach up to 12–18 μm min^{-1} (Hepler et al., 2001). Although *Arabidopsis thaliana* pollen tubes and *Nicotiana tabacum* pollen tubes grow comparatively slowly when compared to lily pollen tubes, their growth rate can reach

up to 2 and 1.5–6 μm min^{-1}, respectively (Cheung and Wu, 2008). The rapidity of pollen tube growth greatly shortens the time required for the delivery of sperm cells to the ovules, thus favoring fertilization. Plant biologists have been fascinated by this remarkable growth phenomenon. The rapid growth of pollen tubes requires the availability of a huge amount of materials for plasma membrane expansion and cell wall synthesis within the pollen tube growth region. In line with this, pollen tubes harbor an active intracellular transport system to enable the efficient delivery of materials to the growth region, which subsequently coordinate with tightly regulated endocytotic and exocytotic events to support pollen tube tip growth (Rounds and Bezanilla, 2013). The actin cytoskeleton plays an essential role in driving the growth and morphogenesis of pollen tubes by choreographing endo- and exocytotic vesicle traffic (Taylor and Hepler, 1997; Cole and Fowler, 2006; Cheung and Wu, 2008; Yang, 2008; Qin and Yang, 2011; Guan et al., 2013). As such, the role and mechanism of action of the actin cytoskeleton in the regulation of polarized pollen tube growth have been subjected to intensive scrutiny in the past few decades. Careful examination of the organization of actin filaments in living and fixed pollen tubes has provided significant insights into the spatial organization of actin filaments in pollen tubes (for reviews see Hepler et al., 2001; Vidali and Hepler, 2001; Samaj et al., 2006; Ren and Xiang, 2007; Chen et al., 2009; Staiger et al., 2010; Cai et al., 2015; Fu, 2015; Qu et al., 2015; Stephan, 2017). In this review, we will describe our current understanding of the organization, dynamics and regulation of the actin cytoskeleton in pollen tubes, with the focus on the apical and subapical regions.

THE ACTIN CYTOSKELETON IN POLLEN TUBES

Experimental treatments with actin-based pharmacological agents showed that the actin cytoskeleton is absolutely required for pollen germination and pollen tube growth (Franke et al., 1972; Herth et al., 1972; Mascarenhas and Lafountain, 1972; Speranza and Calzoni, 1989; Heslopharrison and Heslopharrison, 1991; Mascarenhas, 1993; Gibbon et al., 1999; Vidali et al., 2001). As the building block of the actin cytoskeleton, actin is a very abundant protein in pollen, accounting for about 2–20% of the total soluble protein in pollen grains (Liu and Yen, 1992; Ren et al., 1997; Vidali and Hepler, 1997; Gibbon et al., 1999; Snowman et al., 2002). Therefore, plant scientists have used pollen as the starting material to isolate polymerization-competent plant actin (Liu and Yen, 1992; Ren et al., 1997). Different methods have been used to determine the cellular concentration of actin monomers in pollen from maize (Gibbon et al., 1999), poppy (Snowman et al., 2002), lily (Vidali and Hepler, 1997), and *Arabidopsis* (Jiang et al., 2019). These investigations showed that the total actin concentration can reach up to about 200 μM in pollen. In fact, there are five reproductive actin isovariants (*ACT1*, *ACT3*, *ACT4*, *ACT11,* and *ACT12*) expressed in *Arabidopsis* pollen, and simultaneous silence of *ACT1*, *ACT3*, *ACT4,* and *ACT12* by RNA interference (RNAi) causes obvious reproductive defects (Pawloski et al., 2006). The direct evidence for the involvement of actin in regulating pollen germination and pollen tube growth came from the analysis of the mutant lacking *ACT11*, showing that pollen germination was inhibited (Chang and Huang, 2015). Surprisingly, loss of function of *ACT11* upregulates pollen tube growth (Chang and Huang, 2015), which is presumably due to the increase in actin dynamics in pollen tubes. Given that the local concentration of actin monomers directly impacts their assembly and disassembly, researchers in this field have tried to reveal the intracellular localization of actin monomers in pollen tubes. They showed that there exists a tip-focused gradient of monomeric G-actin in pollen tubes (Li et al., 2001; Cardenas et al., 2005). One interesting study showed that actin monomers actually distribute uniformly within the cytoplasm of *Arabidopsis* pollen tubes and are rapidly redistributed via cytoplasmic streaming (Chang et al., 2017), which suggests that actin monomers are readily available to assemble within the pollen tube. Given that most actin-based functions are carried out by the filamentous form (F-actin), plant scientists have tried different methods to uncover the organization of actin filaments in pollen tubes. These approaches include labeling actin filaments with fluorescently-tagged phalloidin or immunostaining with an anti-actin antibody in fixed pollen tubes (Tang et al., 1989; Gibbon et al., 1999; Geitmann et al., 2000; Lovy-Wheeler et al., 2005; Thomas et al., 2006; Wilsen et al., 2006; Ye et al., 2009; Wu et al., 2010; Zhang et al., 2010; Qu et al., 2020), or using actin markers including GFP-mTalin or YFP-mTalin, GFP-ABD2, GFP-ADF, GFP-LIM, and Lifeact-GFP or YFP-Lifeact (Kost et al., 1998; Fu et al., 2001; Wilsen et al., 2006; Cheung et al., 2008; Vidali et al., 2009; Zhang et al., 2009; Zhang et al., 2010; Qu et al., 2013; Stephan et al., 2014) to decorate actin filaments in living pollen tubes. These investigations have resulted in a consensus view that actin filaments are arranged into longitudinally aligned bundles in the shank region of pollen tubes (**Figure 1A**). Shank actin filaments are important for a transport mechanism in angiosperm pollen tubes called reverse-fountain cytoplasmic streaming. The flow of cytoplasm is generated by the movement of barbed-end directed myosin motors along the shank-localized actin filaments. In the cortex of the pollen tube, cytoplasm flows toward the tip, while in the middle of the pollen tube, it flows back toward the bottom. Based on the determination of the polarity of shank-localized actin bundles in root hairs (Tominaga et al., 2000), which also generate reverse-fountain cytoplasmic streaming, cortical actin bundles and inner actin bundles likely have their barbed ends facing toward the tip and base of pollen tubes, respectively. Indeed, this has been verified by visualizing actin filaments decorated with myosin II subfragment 1 in pollen tubes by electron microscopy (Lenartowska and Michalska, 2008). Both cortical and inner actin bundles terminate at the subapex of pollen tubes. By comparison, determining the organization of the actin cytoskeleton within the apical and subapical regions has been problematic, as different configurations have been reported in pollen tubes from different species using different methods. In the following sections, we will focus on describing our understanding of the organization, dynamics and regulation

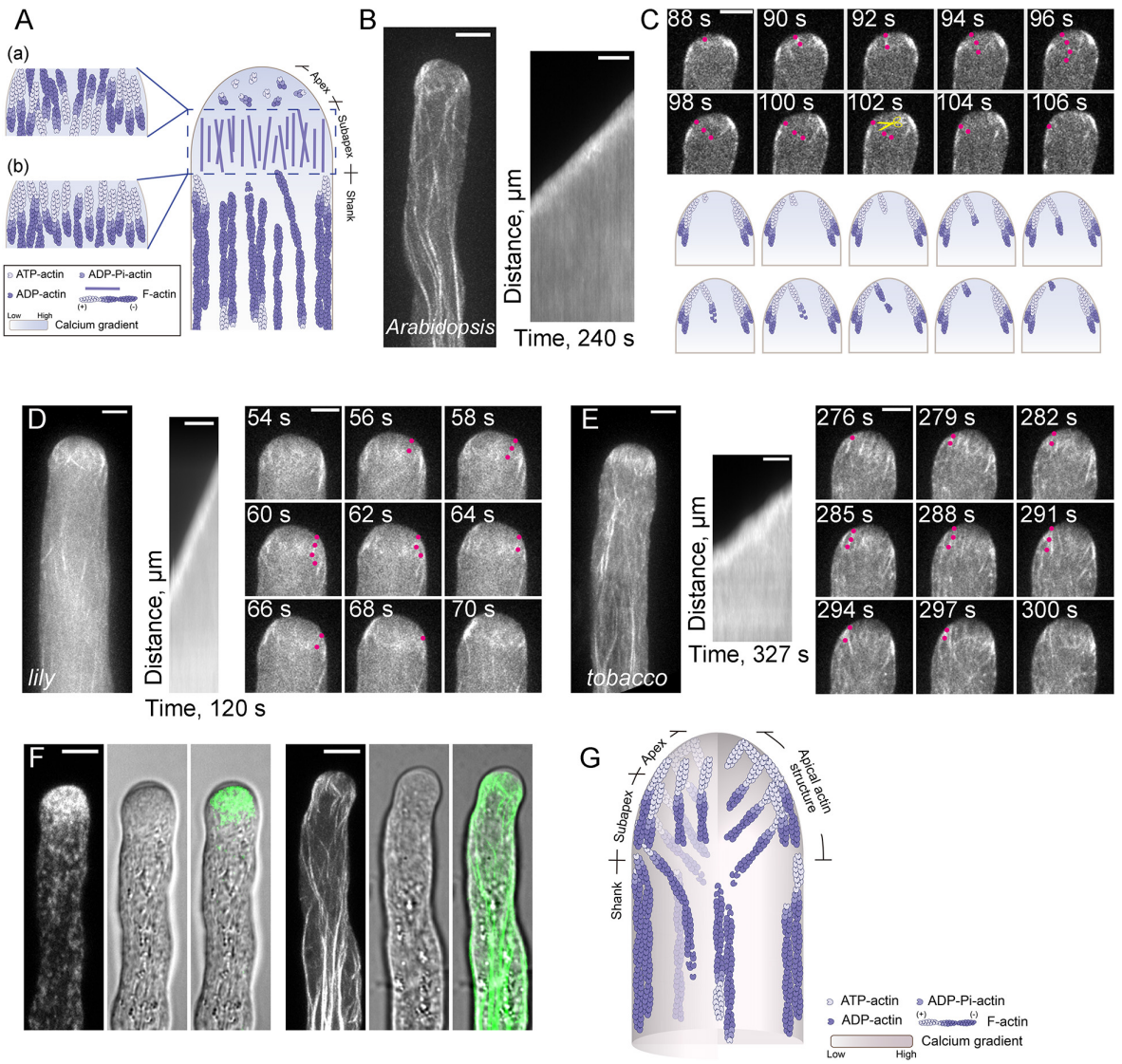

FIGURE 1 | Actin Filaments are Continuously Polymerized from the Plasma Membrane within the Apical and Subapical Regions of the Pollen Tube. **(A)** Schematic diagram depicting our previous understanding of the spatial distribution of actin filaments in the pollen tube. This model refers to the models shown in previous review articles with slight modifications (Vidali and Hepler, 2001; Lovy-Wheeler et al., 2005; Ren and Xiang, 2007; Cheung and Wu, 2008; Yang, 2008; Cai and Cresti, 2009; Qin and Yang, 2011; Guan et al., 2013; Rounds and Bezanilla, 2013; Cai et al., 2015; Fu, 2015; Bascom et al., 2018). Specifically, actin filaments are arrayed into longitudinally oriented actin bundles in the shank and in the actin fringe structure at the subapex. In terms of the polarity of actin filaments within the actin fringe, the models in (a,b) were drawn with reference to Ren and Xiang (2007); Cheung and Wu (2008), and Qin and Yang (2011), respectively. By comparison, actin filaments at the apex are short, less abundant and disorganized. **(B)** Actin filaments are polymerized from the plasma membrane in an *Arabidopsis* pollen tube tip. The right panel shows the kymograph analysis of apical actin filaments decorated with Lifeact-eGFP in the growing wild-type (WT) *Arabidopsis* pollen tube shown in the left panel. Scale bar = 5 μm. **(C)** Time-lapse images of apical actin filaments in the pollen tube shown in **(B)**. Red dots indicate an actin filament that is polymerized from the plasma membrane, then grows into the inner region of the pollen tube. The yellow scissors indicate a severing event of the same actin filament. Scale bar = 5 μm. The lower panel shows a schematic depiction of the events in the upper panel. **(D,E)** Actin filaments polymerized from the plasma membrane at the tip of a growing lily **(D)** and tobacco **(E)** pollen tube. In each figure, the left panel shows the Z-projection image of actin filaments in the pollen tube. The middle panel shows kymograph analysis of actin filaments growing from the plasma membrane at the pollen tube tip, and the right panel shows some time-lapse images of actin filaments in the growing pollen tube shown in the left panel. Red dots indicate an actin filament that was polymerized from the plasma membrane, then grew into the inner region of the pollen tube. Scale bar = 5 μm. **(F)** Visualization of RabA4b-positive transport vesicles (left panel) and actin filaments (right panel) in WT *Arabidopsis* pollen tubes. Transport vesicles accumulate within the region corresponding to the clear zone at the pollen tube tip (left panel). Actin filaments at the base of the clear zone, which polymerize from the plasma membrane, correspond to the actin fringe at the subapex shown in **(A)**. Scale bar = 5 μm. **(G)** Schematic depiction of our current view of the organization of actin filaments in the *Arabidopsis* pollen tube. Similar to the model shown in **(A)**, actin filaments are organized into actin bundles oriented longitudinally in the shank region. Within the apical and subapical regions of the pollen tube, actin filaments are polymerized from the plasma membrane. These filaments can be viewed as a whole and defined as the "apical actin structure." Membrane-originated actin filaments within this "apical actin structure" assume a distinct spatial distribution, with some cortical actin filaments forming thick actin bundles, while some inner actin filaments are comparatively fine and extend toward the inner region of the cytoplasm.

of the actin cytoskeleton within the apical and subapical regions of pollen tubes.

THE ORIGIN AND SPATIAL ORGANIZATION OF ACTIN FILAMENTS WITHIN THE APICAL AND SUBAPICAL REGIONS OF POLLEN TUBES

Previous studies suggested that pollen tube growth is more sensitive to the treatment of actin destabilizing reagents than cytoplasmic streaming (Gibbon et al., 1999; Vidali et al., 2001), which suggests that the actin cytoskeleton within the pollen tube growth region is highly dynamic. This is also the reason why the actin cytoskeleton within the apical and subapical regions cannot be fixed instantly, thus preventing us from reaching a consensus view about the organization of the actin cytoskeleton within the pollen tube growth region. In the past, efforts have been made to describe the organization of the actin cytoskeleton within the apical and subapical regions separately. Although there is some argument about whether actin filaments exist within the apical region of pollen tubes, researchers in the field believe that the apical region does contain actin filaments, but they are short, less abundant and randomly distributed (Yang, 2008; Staiger et al., 2010). Different organizational patterns of subapical actin filaments within pollen tubes have been revealed by different actin labeling approaches and, as such, different names have been provided to describe the organization of subapical actin filaments in pollen tubes from different species. These names include actin collar (Gibbon et al., 1999; Qu et al., 2013), actin fringe (Lovy-Wheeler et al., 2005; Dong et al., 2012; Rounds et al., 2014), actin ring or actin mesh (Kost et al., 1998; Chen et al., 2002). The variation in the subapical actin structure might be due to the employment of different actin labeling approaches or to true differences among pollen tubes from different species. Different schematic models had been generated to describe the organization of actin filaments within the apical and subapical regions of pollen tubes. One typical schematic model, presented in **Figure 1A**, shows that actin filaments are arranged into an actin fringe structure at the subapex, and are shorter, less abundant and more disorganized at the extreme apex. However, the polarity of actin filaments within the actin fringe remains the subject of debate. Different models are presented in the literature in terms of the polarity of actin filaments within the actin fringe structure. One model showed that actin filaments at the cortex and in the inner region within the actin fringe have their barbed ends facing toward the tip and base of the pollen tube, respectively (**Figure 1Aa**; Ren and Xiang, 2007; Cheung and Wu, 2008). Another model showed that actin filaments within the actin fringe have their barbed ends facing toward the tip of the pollen tube (**Figure 1Ab**; Qin and Yang, 2011). Therefore, the origin and exact organization of subapical and apical actin filaments are unclear.

In this regard, live-cell imaging of Lifeact-GFP-decorated actin filaments in growing wild-type pollen tubes and in mutant *Arabidopsis* pollen tubes with loss of function of specific actin-binding proteins (ABPs) has revolutionized our view about the origin, polymerization and organization of actin filaments within the apical and subapical regions of pollen tubes. Specifically, this approach has shown that actin filaments are continuously polymerized from the plasma membrane at the growing *Arabidopsis* pollen tube tips (**Figures 1B,C**; Qu et al., 2013). A similar phenomenon was also noticed in lily and tobacco pollen tubes (**Figures 1D,E**; Vidali et al., 2009; Rounds et al., 2014), which suggests that the polymerization of actin filaments from the apical plasma membrane is a common design in angiosperm pollen tubes. In support of this notion, loss of function of class I formins, which are important actin nucleating factors in pollen tubes, impairs the polymerization of actin filaments from the plasma membrane at pollen tube tips (Cheung et al., 2010; Lan et al., 2018). In line with this finding, loss of function of profilins, the functional partners of formins, impaired the polymerization of actin filaments from the plasma membrane at the extreme apex of pollen tubes (Liu et al., 2015). Simultaneous visualization of actin filaments, the clear zone (which corresponds to the previously defined actin fringe) and transport vesicles showed that the actin structure at the base of the clear zone (Lovy-Wheeler et al., 2005, 2006) is made up of actin filaments polymerized from the plasma membrane (**Figure 1F**; Qu et al., 2017). These findings allow us to propose a schematic model describing the spatial organization of apical and subapical actin filaments in the pollen tube (**Figure 1G**). In this model, actin filaments within both the apical and subapical regions of pollen tubes are generated from the plasma membrane, and the actin filaments within the two regions can be viewed as a whole, which is defined as the "apical actin structure" (**Figure 1G**; Qu et al., 2017). Consequently, actin filaments can be viewed as forming two notable structures in pollen tubes: the shank-localized longitudinal actin bundles and the "apical actin structure" (Qu et al., 2017).

MOLECULAR MECHANISM UNDERLYING THE REGULATION OF ACTIN POLYMERIZATION FROM THE PLASMA MEMBRANE IN POLLEN TUBES

Live-cell imaging of the dynamics of actin filaments revealed that actin polymerization continuously occurs from the plasma membrane at pollen tube tips, and this polymerization is required for and concurrent with pollen tube growth (Qu et al., 2017). How apical actin polymerization is regulated during pollen tube growth is an interesting question. Actin polymerization is dictated by specific actin nucleation factors, and Arp2/3 complex and formins are two major types of actin nucleation factors that have been characterized in plants (Blanchoin and Staiger, 2010). Both Arp2/3 complex and formins have received widespread attention in the context of plasma membrane-originated actin polymerization. The role of Arp2/3 complex in regulating the

morphogenesis of trichome and epidermal pavement cells has been studied extensively (Le et al., 2003; Li et al., 2003; Mathur et al., 2003a,b; El-Din El-Assal et al., 2004), but the role of Arp2/3 complex in regulating actin polymerization in pollen is not clear. The tips of wild-type pollen tubes do not contain dense branched F-actin networks (Qu et al., 2015), and loss of function of Arp2/3 complex does not affect fertility in *Arabidopsis* (Szymanski, 2005), which indicates that the Arp2/3 complex is not essential for pollen tube growth. Therefore, there is no direct evidence that Arp2/3 complex is involved in the regulation of actin polymerization in pollen tubes. Formin proteins contain the characteristic formin homology (FH) domains, FH1 and FH2, and are able to nucleate actin assembly from actin monomers or actin-profilin complexes (Kovar, 2006; Goode and Eck, 2007). Based on the sequence of their FH2 domains, plant formins are divided into three classes, class I, class II, and class III (Cvrckova et al., 2004). Only two class III formins have been identified, and they are found in land plants that contain flagellate sperm (Grunt et al., 2008; van Gisbergen and Bezanilla, 2013). Class I and class II formins are common in plants. Most of the class I formins contain a transmembrane (TM) domain at their N-terminus, which enables them to target to the plasma membrane or endomembrane systems. The N-terminus of class II formins is quite variable. Some of them have a phosphatase and tensin homolog (PTEN)-like domain at their N-terminus (Blanchoin and Staiger, 2010). Considering that actin is buffered by an almost equimolar amount of profilin (Vidali and Hepler, 1997; Gibbon et al., 1999; Snowman et al., 2002; Jiang et al., 2019), and actin-profilin complexes are favored by formins rather than the Arp2/3 complex (Rotty et al., 2015; Suarez et al., 2015), it is easy to imagine the important role of formins in controlling actin polymerization in pollen. Accordingly, it was shown that treatment with the formin inhibitor SMIFH2 (Rizvi et al., 2009), which inhibits plant formins *in vitro* (Cao et al., 2016), impairs actin polymerization from the plasma membrane at pollen tube tips (Qu et al., 2017). As actin polymerization continuously occurs from the plasma membrane at the pollen tube tip (Qu et al., 2013), the TM-containing class I formins are particularly relevant. Indeed, two class I formins, *Arabidopsis* formin 3 (AtFH3), and AtFH5, have been shown to nucleate actin assembly from actin monomers or actin bound to profilin (Ingouff et al., 2005; Ye et al., 2009), and are redundantly required for actin polymerization from the plasma membrane in pollen tubes (Lan et al., 2018). Accordingly, reducing the expression of *Nicotiana tabacum* homolog of *AtFH5*, *NtFH5*, in tobacco pollen impairs the actin polymerization from the plasma membrane (Cheung et al., 2010). In line with this finding, overexpression of *Arabidopsis* formin 1 induces the formation of supernumerary actin cables from the plasma membrane and causes membrane deformation (Cheung and Wu, 2004). The importance of class I formins in regulating actin polymerization at pollen tube tips is also supported by the finding that the pollen-specific *Lilium longiflorum Formin 1* (*LlFH1*) controls the construction of the actin fringe in pollen tubes (Li et al., 2017). These findings together suggest that class I formins play important roles in controlling actin polymerization within the apical and subapical regions of pollen tubes.

Functional characterization of *Arabidopsis* profilins in pollen also provides evidence that formin is a major player in controlling actin polymerization at the tip of pollen tubes. Profilin is a low molecular weight protein, ranging from 12 to 15 kDa, and it can bind to G-actin to form high affinity 1:1 profilin-actin complexes (Carlsson et al., 1977; Vidali and Hepler, 1997). It was shown that profilin has a dual role in regulating actin dynamics. When the barbed ends of actin filaments are capped, profilin acts as a simple actin monomer sequestering protein to promote actin depolymerization (Huang et al., 2004). In support of this notion, it was shown that microinjection of profilin into *Tradescantia blossfeldiana* stamen hair cells causes the disappearance of transvacuole strands and displacement of nuclei (Staiger et al., 1994). However, when the barbed ends of actin filaments are free, actin-profilin complexes can add onto the barbed ends to elongate actin filaments and thus promote actin polymerization (Pantaloni and Carlier, 1993). Evidence for such a functional role of profilin was strengthened by the finding that the presence of formin can facilitate the addition of actin-profilin complexes onto the barbed ends of actin filaments to accelerate their elongation (Romero et al., 2004; Kovar et al., 2006). Within this framework, formin facilitates the addition of actin-profilin complexes onto the barbed end of actin filaments through its proline-rich FH1 domain. Consistent with this, it was shown that the function of profilin depends on its interaction with proline-rich motifs (Gibbon et al., 1998). Based on the fact that actin binds to profilin with high affinity (Gibbon et al., 1997; Kovar et al., 2000) and they exist in roughly equimolar amounts in pollen (Vidali and Hepler, 1997; Gibbon et al., 1999; Snowman et al., 2002; Jiang et al., 2019), it was predicted that actin mainly exists in the form of actin-profilin complexes in pollen (Staiger and Blanchoin, 2006; Chen et al., 2009). In support of the role of profilin in promoting actin polymerization, it was shown that loss of function of profilins impairs actin polymerization from the plasma membrane at the tip of *Arabidopsis* pollen tubes (Liu et al., 2015). Importantly, it was shown that the mutant $PRF5_{Y6A}$, which is defective in binding to PLP but retains normal G-actin binding activity, has impaired function in actin polymerization at pollen tube tips (Liu et al., 2015). This strongly suggests that formin and profilin work as a module in controlling actin polymerization from the plasma membrane at the tip of pollen tubes.

To support continuous actin polymerization during pollen tube growth, a pool of polymerizable actin monomers must be available within pollen tubes. Given that actin is assumed to be buffered by equimolar profilin in pollen, and plant profilins lack or have weak actin nucleotide exchange activity (Kovar et al., 2001; Chaudhry et al., 2007; Liu et al., 2015), a mechanism is required to recharge the dissociated ADP-G-actin before the formation of actin-profilin complexes. Adenylyl cyclase-associated protein 1 (CAP1), also known as Srv2p in budding yeast, is a protein shown to have actin nucleotide exchange activity in *Arabidopsis* (Chaudhry et al., 2007). It is assumed to take on the role of recharging ADP-G-actin in plants. CAP1 is an abundant protein and its cellular concentration falls between that of ADF and profilin in *Arabidopsis* pollen (Jiang et al., 2019). It can coordinate with

ADF and profilin to promote actin turnover and enhance actin nucleotide exchange *in vitro* (Chaudhry et al., 2007; Jiang et al., 2019). CAP1 distributes uniformly in pollen tubes and depletion of CAP1 impairs membrane-originated actin polymerization at pollen tube tips. Furthermore, CAP1 protein that is defective in actin nucleotide exchange activity cannot fully rescue the apical actin polymerization defects in *cap1* mutant pollen tubes (Jiang et al., 2019), which suggests that the actin nucleotide exchange activity of CAP1 is biologically significant. These findings together allow us to propose a model for the regulation of actin polymerization from the plasma membrane at pollen tube tips (**Figure 2**; Jiang et al., 2019). Specifically, the membrane-anchored class I formins initiate actin polymerization from the pool of actin-profilin complexes within the cytoplasm, and ADF drives the turnover of membrane-originated actin filaments and controls their length via its actin severing and depolymerizing activity (see the detailed description below). CAP1 works as the shuttle molecule between ADF and profilin to promote actin turnover and maintain the pool of polymerizable actin monomers to drive formin-mediated actin polymerization from the plasma membrane (**Figure 2**). These findings provide significant insights into the molecular mechanism that controls actin polymerization from the plasma membrane at the pollen tube tip.

REGULATION OF THE TURNOVER AND ORGANIZATION OF MEMBRANE-ORIGINATED APICAL AND SUBAPICAL ACTIN FILAMENTS IN POLLEN TUBES

The mechanisms that regulate the turnover of apical and subapical actin filaments have been the subject of intensive studies in the past. Given that actin filaments are mainly generated from the membrane-anchored class I formins (Cheung et al., 2010; Lan et al., 2018), the ends of actin filaments facing toward the cytoplasm are pointed ends that should be favored by actin-depolymerizing factors (ADFs). ADFs are extremely relevant players in trimming actin filaments to control their length and drive their turnover. Indeed, ADFs have been implicated in the regulation of actin dynamics in pollen grains and pollen tubes (Smertenko et al., 2001; Chen et al., 2002), but the precise mechanism underlying their action remains largely unknown. With the employment of the *Arabidopsis* genetic approach, our understanding of the role and mechanism of action of ADFs in pollen has improved substantially. Besides *Arabidopsis* ADF5, which regulates the actin cytoskeleton via stabilizing and bundling actin filaments in pollen tubes (Zhu et al., 2017), ADF7 and ADF10, which are expressed specifically in *Arabidopsis* pollen (Bou Daher et al., 2011; Daher and Geitmann, 2012), are two major typical actin depolymerizing factors that promote the turnover of the actin cytoskeleton in pollen via severing and depolymerizing actin filaments (Zheng et al., 2013; Jiang et al., 2017). The role of ADF7 in promoting the turnover of shank-localized actin bundles was demonstrated several years ago (Zheng et al., 2013), but its role in regulating the dynamics of apical and subapical actin filaments remains to be characterized. ADF10 was demonstrated to sever and depolymerize subapical actin filaments to promote their turnover and ordering (Jiang et al., 2017). In line with these findings, loss of function of actin-interacting protein 1 (AIP1), the cofactor of ADF (Allwood et al., 2002; Shi et al., 2013; Diao et al., 2020), reduces the rate of actin turnover and induces disorganization of subapical actin filaments in *Arabidopsis* pollen tubes (Diao et al., 2020). In addition, it was shown that depletion of CAP1 decreases ADF-mediated actin depolymerization and severing, which reduces the rate of actin turnover in pollen tubes (Jiang et al., 2019). These data together identify ADF as an essential player in promoting the turnover of actin filaments in pollen tubes.

In addition, as pollen tubes harbor a tip-high Ca^{2+} gradient (HoldawayClarke et al., 1997; Diao et al., 2018), several Ca^{2+}-responsive actin severing proteins are involved in regulating the turnover of apical and subapical actin filaments. In this regard, the Ca^{2+}-responsive villin/gelsolin/fragmin members are extremely relevant (Yamashiro et al., 2001; Huang et al., 2004; Xiang et al., 2007; Wang et al., 2008; Khurana et al., 2010; Zhang et al., 2010; Zhang et al., 2011; Bao et al., 2012; Wu et al., 2015). Most of the *in vivo* functional data about villin/gelsolin/fragmin family members have come from the analysis of villins using the reverse genetic approach, as the plant genome only encodes genes for full-length villins (Klahre et al., 2000; Huang et al., 2015). The villin homologs were originally identified from pollen by biochemical means and demonstrated to be *bona fide* actin bundlers (Yokota et al., 1998, 2003). Although it was subsequently confirmed that villin can bind to G-actin and promote actin depolymerization in the presence of Ca^{2+}/Calmodulin (Yokota et al., 2005), the direct evidence supporting the role of villins in severing actin filaments came from biochemical analyses of villins from *Arabidopsis* and rice (Khurana et al., 2010; Zhang et al., 2010; Zhang et al., 2011; Bao et al., 2012; Wu et al., 2015). In support of the role of villins in promoting actin turnover in pollen tubes, it was shown that loss of function of *Arabidopsis villin2* (*VLN2*) and *VLN5* causes accumulation of filamentous actin at pollen tube tips (Qu et al., 2013). The reduction in the frequency of actin filament severing in *vln2 vln5* double mutant pollen tubes suggests that the severing activity of villins likely contributes to their role in promoting actin turnover (Qu et al., 2013). In line with this finding, it was shown that the severing activity of villin is involved in the formation of actin foci triggered by elevation of the cytosolic Ca^{2+} concentration in pollen tubes (Zhao et al., 2020). Within this framework, several other Ca^{2+}-responsive actin severing proteins were also shown to be involved in the regulation of actin turnover at pollen tube tips, such as MAP18, MDP25, and ROP-interactive CRIB motif-containing protein 1 (RIC1) (Zhu et al., 2013; Qin et al., 2014; Zhou et al., 2015). In addition, although there is no evidence showing the direct interaction of RIC3 with the actin cytoskeleton, it was shown that RIC3 promotes the release of free Ca^{2+}, which induces actin depolymerization in pollen tubes (Gu et al., 2005). How exactly RIC3 promotes actin turnover in pollen tubes remains to be determined. Nonetheless, these data suggest that the Ca^{2+}-responsive actin severing

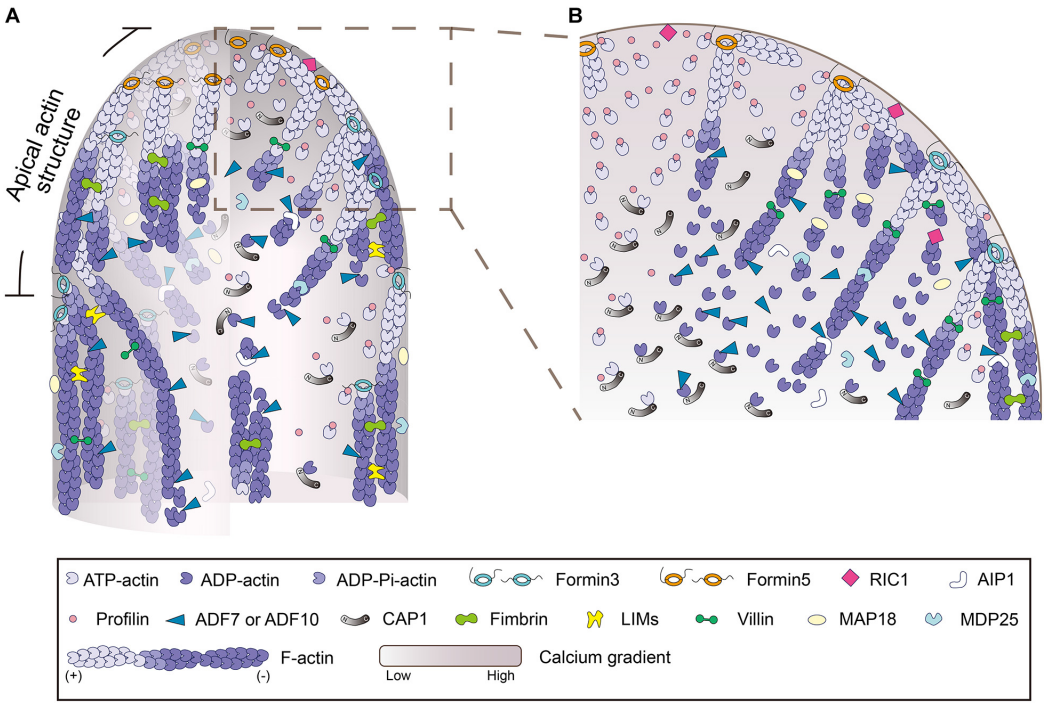

FIGURE 2 | Schematic depiction of the regulation of actin polymerization and dynamics in the pollen tube. **(A)** Schematic depiction of the intracellular localization pattern and function of various ABPs in pollen tube growth domain. The model is mainly based on data from *Arabidopsis*. **(B)** An enlarged picture of the boxed region in **(A)** is presented in order to show more details about the regulation of actin polymerization and dynamics in the tip of pollen tube. In brief, within the pollen tube, actin predominantly exists in the monomeric form. It is buffered by an equimolar amount of profilin to form actin-profilin complexes. Actin polymerization is initiated by membrane-anchored formins, which utilize actin-profilin complexes within the cytoplasm. The membrane-originated actin filaments assume distinct distributions in space as described in **Figure 1G**, and they are turned over by ADF and its cofactors, including AIP1 and CAP1, and several Ca^{2+}-responsive actin severing proteins, which promote the dynamics and control the length of actin filaments. Under the action of various actin bundling/crosslinking proteins, including villins (Qu et al., 2013), LIMs (Wang et al., 2008; Papuga et al., 2010; Zhang et al., 2019), and fimbrins (Su et al., 2012; Zhang et al., 2016), membrane-originated actin filaments are organized into distinct structures and assume distinct distributions in the cortical and inner regions of the pollen tube.

proteins act in concert with the Ca^{2+} gradient to promote actin turnover in pollen tubes.

THE ROLE OF APICAL AND SUBAPICAL ACTIN FILAMENTS IN REGULATING VESICLE TRAFFIC IN POLLEN TUBES

It remains largely unknown how actin functions within the apical and subapical regions of pollen tubes. This is partly because we lack a unified view about the organization of actin filaments within that region. As discussed above, one common view is that actin filaments are arrayed into an actin fringe structure at the subapex (**Figure 1A**; Lovy-Wheeler et al., 2005, 2006). Different hypotheses were raised to explain the function of the actin fringe. The proposed functions include: organizing endomembranes and controlling the location of endo- and exocytotic events; acting as a physical barrier to exclude large organelles; structurally supporting the plasma membrane to facilitate turgor driven extension; and generating the force to drive cell growth (Stephan, 2017). Among the different functions, the actin cytoskeleton plays an obvious role in regulating tip-directed vesicle traffic, which leads to the accumulation of vesicles at the pollen tube tip to support pollen tube growth. Different hypotheses were proposed to explain the role of apical and subapical actin filaments in regulating vesicle traffic in pollen tubes (Geitmann and Emons, 2000). These include spatially constraining the distribution of vesicles (Kroeger et al., 2009), acting as a filter for small vesicles (Kost et al., 1998; Cheung et al., 2008), and acting as the tracks for myosin motors to transport vesicles to the tip (Lovy-Wheeler et al., 2005; Daher and Geitmann, 2011; Chebli et al., 2013). As described above, studies in *Arabidopsis* pollen tubes have revealed more details about the spatial organization and dynamics of the actin cytoskeleton within the apical and subapical regions, which provides an opportunity to understand how actin regulates vesicle traffic in pollen tubes. Within the apical and subapical regions, membrane-originated actin filaments assume distinct spatial distributions, including thick actin bundles in the cortex and relatively fine actin filaments in the middle (**Figure 1G**; Qu et al., 2017). Further analysis revealed that the cortical actin bundles act as tracks for myosin motors, allowing the transportation of vesicles to the pollen tube tip, while the inner fine actin filaments act as the physical barrier to prevent the backward movement of vesicles from the tip (Qu et al., 2017). This leads to the generation of a "V" shape of vesicle distribution (**Figures 3A,C**). The apical actin structure as a whole also acts

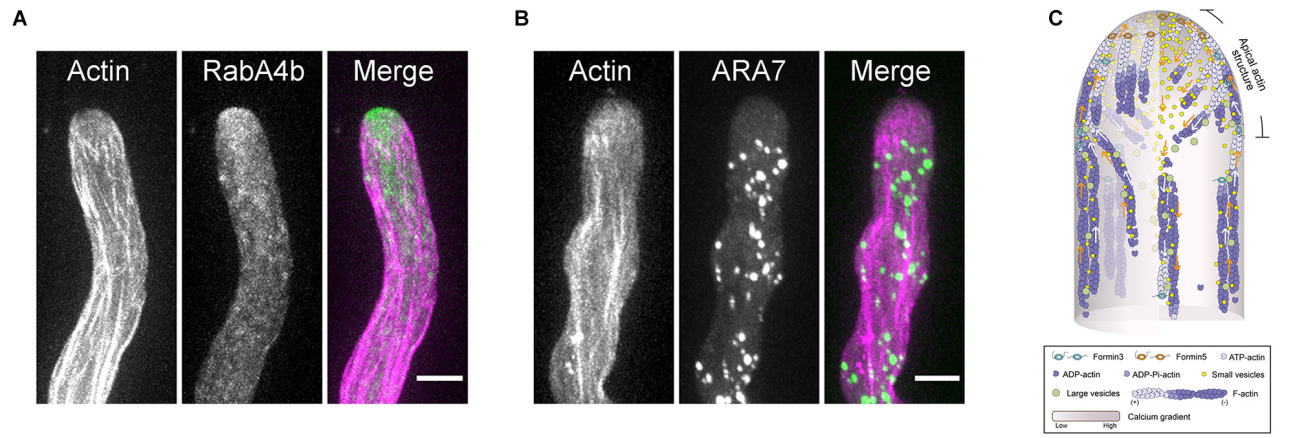

FIGURE 3 | The Role of the Actin Cytoskeleton in Regulating Vesicle Traffic in the Pollen Tube. **(A)** Dual visualization of RabA4b-positive transport vesicles (green) and actin filaments (pink) in a WT *Arabidopsis* pollen tube. The small RabA4b-positive transport vesicles accumulate at the pollen tube tip. Scale bar = 5 μm. **(B)** Dual visualization of ARA7-positive endosomes (green) and actin filaments (pink) in a WT *Arabidopsis* pollen tube. The large ARA7-positive endosomes are absent at the pollen tube tip. Scale bar = 5 μm. **(C)** Schematic depiction of the function of the actin cytoskeleton in regulating vesicle traffic in the pollen tube. Both ARA7-positive large endosomes and RabA4b-positive small vesicles are transported along cortical actin bundles in the shank region. Upon reaching the subapex, ARA7-positive large endosomes reverse their direction of movement and return to the base along the inner actin bundles. This is the basis for the generation of reverse fountain cytoplasmic streaming. However, after reaching the subapex, RabA4b-positive small vesicles run straight to the tip along cortical actin bundles within the "apical actin structure," which leads to the accumulation of vesicles at the pollen tube tip. After reaching the extreme tip, some RabA4b-positive small vesicles will start to move toward the base of the pollen tube. The inner actin filaments within the "apical actin structure" function as physical barrier to prevent their return, which leads to the formation of the "V"-shaped distribution pattern of small vesicles.

as a physical barrier to prevent the invasion of large organelles into the pollen tube tip (**Figures 3B,C**). Therefore, cooperation between the apical actin structure and the shank-localized actin bundles leads to the generation of reverse-fountain cytoplasmic streaming and the "V"-shaped vesicle distribution in the pollen tube (**Figure 3**; Qu et al., 2017). These studies provide significant insights into the functional role of actin in regulating vesicle traffic in pollen tubes.

CONCLUSION AND PERSPECTIVES

Although the essential role of actin in regulating pollen tube growth is well-recognized, the cellular mechanisms underlying the function of actin during pollen tube growth remain to be uncovered. Our understanding of how actin performs its function has been hindered by the lack of a unified view about the origin, spatial organization and dynamics of actin filaments within the growth domain of pollen tubes. Recently, with the introduction of appropriate actin markers and state-of-the-art live cell imaging technologies, along with the usage of mutants lacking different ABPs, our understanding of the origin, polymerization, dynamics, and spatial organization of actin filaments within the growth domain of pollen tubes has improved substantially. Specifically, it is clear that actin filaments are continuously polymerized from the plasma membrane at the extreme apex of pollen tubes during their extension, which answers the long-standing question about whether actin filaments exist at the extreme apex. In addition, actin filaments are polymerized from the plasma membrane at the subapex, where they generate the actin fringe structure reported in pollen tubes (Lovy-Wheeler et al., 2005, 2006). This work provides insights into the origin, polarity and organization of actin filaments within the actin fringe. Together, these findings allow us to conclude that actin filaments within the apical and subapical regions of pollen tubes can be viewed as a whole in terms of their origin, and can be collectively defined as the "apical actin structure" (Qu et al., 2017). Consequently, the pollen tube actin cytoskeleton can be viewed as consisting of two structures: the shank-localized actin bundles and the "apical actin structure" (**Figure 1G**; Qu et al., 2017). The polymerization of actin filaments from the plasma membrane also occurs in lily and tobacco pollen tubes (**Figures 1D,E**; Rounds et al., 2014; Qu et al., 2017). This implies that the polymerization of actin filaments from the plasma membrane and formation of the distinct "apical actin structure" might represent a common design for angiosperm pollen tubes.

Careful observations revealed that membrane-originated actin filaments within the pollen tube growth domain assume distinct spatial distributions: they form comparatively thick actin bundles at the cortex and fine actin filaments extending toward the inner region of the cytoplasm (**Figure 1G**; Qu et al., 2017). The functional coordination of those spatially distinct apical and subapical actin filaments leads to the formation of a "V"-shaped vesicle distribution pattern (**Figure 3C**; Qu et al., 2017). In addition, the apical actin structure acts as a physical barrier to prevent the apical invasion of large organelles, which facilitates the generation of reverse fountain cytoplasmic streaming (**Figure 3C**; Qu et al., 2017). However, it remains to be resolved how subapical actin filaments coordinate spatially and functionally with shank-localized actin bundles. Furthermore, given that actin filaments are continuously generated from the plasma membrane at the extreme apex during pollen tube growth,

it will definitely be worth exploring how those actin filaments might be involved in the control of exo- and endocytotic events.

As actin polymerization is concurrent with and required for pollen tube growth (Qu et al., 2017), a key area for future research is how growing pollen tubes perceive the upstream signals to control the polymerization and dynamics of actin filaments. Within this framework, another outstanding question is how the activity of membrane-anchored class I formins is precisely regulated. In particular, it will be interesting to investigate how the signaling mediated by ROPs (Li et al., 1999; Gu et al., 2005), phospholipids (Zhang and McCormick, 2010; Zonia, 2010) and the receptor-like kinases (RLKs) (Muschietti and Wengier, 2018) might influence the activity of formins. In particular, as ROPs and RLKs have been implicated in pollen tube guidance (Takeuchi and Higashiyama, 2016; Wang et al., 2016; Luo et al., 2017), it remains to be documented how actin reorganization is involved in the turning of pollen tubes in response to female-derived signals. Establishment of a semi-*in vivo* pollen tube growth system that enables the imaging of actin dynamics at high spatiotemporal resolution might allow us to understand how actin undergoes reorganization during pollen tube turning in response to female-derived attractants. Furthermore, pollen tubes have distinct distributions of ions, such as Ca^{2+} and H^{+} (HoldawayClarke et al., 1997; Messerli and Robinson, 1997; Feijo et al., 1999; Diao et al., 2018), which will influence the activity of ABPs and will in turn impact the dynamics and organization of actin filaments. How actin structures adapt to the cytosolic microenvironment at the pollen tube tip is another interesting question. In summary, plant biologists have made great progress in understanding the dynamics, organization and function of the actin cytoskeleton in pollen tube tips, but many questions still remain to be answered. This promises to be an exciting area of research for many years to come.

AUTHOR CONTRIBUTIONS

YX drafted this manuscript. SH conceived this manuscript and revised the writing of this manuscript. Both authors contributed to the article and approved the submitted version.

FUNDING

This work was supported by grants from the National Natural Science Foundation of China (31671390 and 31970180). The research in the Huang Lab was also supported by funding from Tsinghua-Peking Joint Center for Life Sciences.

ACKNOWLEDGMENTS

We thank the members of the Huang lab for constructive comments.

REFERENCES

Allwood, E. G., Anthony, R. G., Smertenko, A. P., Reichelt, S., Drobak, B. K., Doonan, J. H., et al. (2002). Regulation of the pollen-specific actin-depolymerizing factor LlADF1. *Plant Cell* 14, 2915–2927. doi: 10.1105/tpc.005363

Bao, C., Wang, J., Zhang, R., Zhang, B., Zhang, H., Zhou, Y., et al. (2012). Arabidopsis *VILLIN2* and *VILLIN3* act redundantly in sclerenchyma development via bundling of actin filaments. *Plant J.* 71, 962–975. doi: 10.1111/j.1365-313X.2012.05044.x

Bascom, C. S. Jr., Hepler, P. K., and Bezanilla, M. (2018). Interplay between ions, the cytoskeleton, and cell wall properties during tip growth. *Plant Physiol.* 176, 28–40. doi: 10.1104/pp.17.01466

Blanchoin, L., and Staiger, C. J. (2010). Plant formins: diverse isoforms and unique molecular mechanism. *Biochim. Biophys. Acta* 1803, 201–206. doi: 10.1016/j.bbamcr.2008.09.015

Bou Daher, F., van Oostende, C., and Geitmann, A. (2011). Spatial and temporal expression of actin depolymerizing factors ADF7 and ADF10 during male gametophyte development in *Arabidopsis thaliana*. *Plant Cell Physiol.* 52, 1177–1192. doi: 10.1093/pcp/pcr068

Cai, G., and Cresti, M. (2009). Organelle motility in the pollen tube: a tale of 20 years. *J. Exp. Bot.* 60, 495–508. doi: 10.1093/jxb/ern321

Cai, G., Parrotta, L., and Cresti, M. (2015). Organelle trafficking, the cytoskeleton, and pollen tube growth. *J. Integr. Plant Biol.* 57, 63–78. doi: 10.1111/jipb.12289

Cao, L., Henty-Ridilla, J. L., Blanchoin, L., and Staiger, C. J. (2016). Profilin-dependent nucleation and assembly of actin filaments controls cell elongation in Arabidopsis. *Plant Physiol.* 170, 220–233. doi: 10.1104/pp.15.01321

Cardenas, L., Lovy-Wheeler, A., Wilsen, K. L., and Hepler, P. K. (2005). Actin polymerization promotes the reversal of streaming in the apex of pollen tubes. *Cell Motil. Cytoskeleton* 61, 112–127. doi: 10.1002/cm.20068

Carlsson, L., Nystrom, L. E., Sundkvist, I., Markey, F., and Lindberg, U. (1977). Actin polymerizability is influenced by PROFILIN, a low-molecular weight protein in non-muscle cells. *J. Mol. Biol.* 115, 465–483. doi: 10.1016/0022-2836(77)90166-8

Chang, M., and Huang, S. (2015). *Arabidopsis* ACT11 modifies actin turnover to promote pollen germination and maintain the normal rate of tube growth. *Plant J.* 83, 515–527. doi: 10.1111/tpj.12910

Chang, M., Li, Z., and Huang, S. (2017). Monomeric G-actin is uniformly distributed in pollen tubes and is rapidly redistributed via cytoplasmic streaming during pollen tube growth. *Plant J.* 92, 509–519. doi: 10.1111/tpj.13668

Chapman, L. A., and Goring, D. R. (2010). Pollen-pistil interactions regulating successful fertilization in the Brassicaceae. *J. Exp. Bot.* 61, 1987–1999. doi: 10.1093/jxb/erq021

Chaudhry, F., Guerin, C., von Witsch, M., Blanchoin, L., and Staiger, C. J. (2007). Identification of *Arabidopsis* cyclase-associated protein 1 as the first nucleotide exchange factor for plant actin. *Mol. Biol. Cell* 18, 3002–3014. doi: 10.1091/mbc.e06-11-1041

Chebli, Y., Kroeger, J., and Geitmann, A. (2013). Transport logistics in pollen tubes. *Mol. Plant* 6, 1037–1052. doi: 10.1093/mp/sst073

Chen, C. Y., Wong, E. I., Vidali, L., Estavillo, A., Hepler, P. K., Wu, H. M., et al. (2002). The regulation of actin organization by actin-depolymerizing factor in elongating pollen tubes. *Plant Cell* 14, 2175–2190. doi: 10.1105/tpc.003038

Chen, N., Qu, X., Wu, Y., and Huang, S. (2009). Regulation of actin dynamics in pollen tubes: control of actin polymer level. *J. Integr. Plant Biol.* 51, 740–750. doi: 10.1111/j.1744-7909.2009.00850.x

Cheung, A. Y., Duan, Q. H., Costa, S. S., de Graaf, B. H., Di Stilio, V. S., Feijo, J., et al. (2008). The dynamic pollen tube cytoskeleton: live cell studies using actin-binding and microtubule-binding reporter proteins. *Mol. Plant* 1, 686–702. doi: 10.1093/mp/ssn026

Cheung, A. Y., Niroomand, S., Zou, Y., and Wu, H. M. (2010). A transmembrane formin nucleates subapical actin assembly and controls tip-focused growth in pollen tubes. *Proc. Natl. Acad. Sci. U.S.A.* 107, 16390–16395. doi: 10.1073/pnas.1008527107

Cheung, A. Y., and Wu, H. M. (2004). Overexpression of an *Arabidopsis* formin stimulates supernumerary actin cable formation from pollen tube cell membrane. *Plant Cell* 16, 257–269. doi: 10.1105/tpc.016550

Cheung, A. Y., and Wu, H.-M. (2008). Structural and signaling networks for the polar cell growth machinery in pollen tubes. *Annu. Rev. Plant Biol.* 59, 547–572. doi: 10.1146/annurev.arplant.59.032607.092921

Cole, R. A., and Fowler, J. E. (2006). Polarized growth: maintaining focus on the tip. *Curr. Opin. Plant Biol.* 9, 579–588. doi: 10.1016/j.pbi.2006.09.014

Cvrckova, F., Novotny, M., Pickova, D., and Zarsky, V. (2004). Formin homology 2 domains occur in multiple contexts in angiosperms. *BMC Genomics* 5:44. doi: 10.1186/1471-2164-5-44

Daher, F. B., and Geitmann, A. (2011). Actin is involved in pollen tube tropism through redefining the spatial targeting of secretory vesicles. *Traffic* 12, 1537–1551. doi: 10.1111/j.1600-0854.2011.01256.x

Daher, F. B., and Geitmann, A. (2012). Actin depolymerizing factors ADF7 and ADF10 play distinct roles during pollen development and pollen tube growth. *Plant Signal. Behav.* 7, 879–881. doi: 10.4161/psb.20436

Diao, M., Li, X., and Huang, S. J. (2020). *Arabidopsis* AIP1-1 regulates the organization of apical actin filaments by promoting their turnover in pollen tubes. *Sci. China Life Sci.* 63, 239–250. doi: 10.1007/s11427-019-9532-0

Diao, M., Qu, X., and Huang, S. (2018). Calcium imaging in *Arabidopsis* pollen cells using G-CaMP5. *J. Integr. Plant Biol.* 60, 897–906. doi: 10.1111/jipb.12642

Dong, H., Pei, W., and Ren, H. (2012). Actin fringe is correlated with tip growth velocity of pollen tubes. *Mol. Plant* 5, 1160–1162. doi: 10.1093/mp/sss073

Dresselhaus, T., Sprunck, S., and Wessel, G. M. (2016). Fertilization mechanisms in flowering plants. *Curr. Biol.* 26, R125–R139. doi: 10.1016/j.cub.2015.12.032

El-Din El-Assal, S., Le, J., Basu, D., Mallery, E. L., and Szymanski, D. B. (2004). *DISTORTED2* encodes an ARPC2 subunit of the putative *Arabidopsis* ARP2/3 complex. *Plant J.* 38, 526–538. doi: 10.1111/j.1365-313X.2004.02065.x

Feijo, J. A., Sainhas, J., Hackett, G. R., Kunkel, J. G., and Hepler, P. K. (1999). Growing pollen tubes possess a constitutive alkaline band in the clear zone and a growth-dependent acidic tip. *J. Cell Biol.* 144, 483–496. doi: 10.1083/jcb.144.3.483

Franke, W. W., Herth, W., Vanderwoude, W. J., and Morre, D. J. (1972). Tubular and filamentous structures in pollen tubes: possible involvement as guide elements in protoplasmic streaming and vectorial migration of secretory vesicles. *Planta* 105, 317–341. doi: 10.1007/BF00386769

Fu, Y. (2015). The cytoskeleton in the pollen tube. *Curr. Opin. Plant Biol.* 28, 111–119. doi: 10.1016/j.pbi.2015.10.004

Fu, Y., Wu, G., and Yang, Z. B. (2001). Rop GTPase-dependent dynamics of tip-localized F-actin controls tip growth in pollen tubes. *J. Cell Biol.* 152, 1019–1032. doi: 10.1083/jcb.152.5.1019

Geitmann, A., and Emons, A. M. C. (2000). The cytoskeleton in plant and fungal cell tip growth. *J. Microsc.* 198, 218–245. doi: 10.1046/j.1365-2818.2000.00702.x

Geitmann, A., Snowman, B. N., Emons, A. M. C., and Franklin-Tong, V. E. (2000). Alterations in the actin cytoskeleton of pollen tubes are induced by the self-incompatibility reaction in *Papaver rhoeas*. *Plant Cell* 12, 1239–1251. doi: 10.1105/tpc.12.7.1239

Gibbon, B. C., Kovar, D. R., and Staiger, C. J. (1999). Latrunculin B has different effects on pollen germination and tube growth. *Plant Cell* 11, 2349–2363. doi: 10.1105/tpc.11.12.2349

Gibbon, B. C., Ren, H., and Staiger, C. J. (1997). Characterization of maize (*Zea mays*) pollen profilin function in vitro and in live cells. *Biochem. J.* 327(Pt 3), 909–915. doi: 10.1042/bj3270909

Gibbon, B. C., Zonia, L. E., Kovar, D. R., Hussey, P. J., and Staiger, C. J. (1998). Pollen profilin function depends on interaction with proline-rich motifs. *Plant Cell* 10, 981–993. doi: 10.1105/tpc.10.6.981

Goode, B. L., and Eck, M. J. (2007). Mechanism and function of formins in the control of actin assembly. *Annu. Rev. Biochem.* 76, 593–627. doi: 10.1146/annurev.biochem.75.103004.142647

Grunt, M., Zarsky, V., and Cvrckova, F. (2008). Roots of angiosperm formins: the evolutionary history of plant FH2 domain-containing proteins. *BMC Evol. Biol.* 8:115. doi: 10.1186/1471-2148-8-115

Gu, Y., Fu, Y., Dowd, P., Li, S. D., Vernoud, V., Gilroy, S., et al. (2005). A Rho family GTPase controls actin dynamics and tip growth via two counteracting downstream pathways in pollen tubes. *J. Cell Biol.* 169, 127–138. doi: 10.1083/jcb.200409140

Guan, Y., Guo, J., Li, H., and Yang, Z. (2013). Signaling in pollen tube growth: crosstalk, feedback, and missing links. *Mol. Plant* 6, 1053–1064. doi: 10.1093/mp/sst070

Hepler, P. K., Vidali, L., and Cheung, A. Y. (2001). Polarized cell growth in higher plants. *Annu. Rev. Cell Dev. Biol.* 17, 159–187. doi: 10.1146/annurev.cellbio.17.1.159

Herth, W., Franke, W. W., and Vanderwoude, W. J. (1972). Cytochalasin stops tip growth in plants. *Naturwissenschaften* 59, 38–39. doi: 10.1007/bf00594629

Heslopharrison, J., and Heslopharrison, Y. (1991). Restoration of movement and apical growth in the angiosperm pollen-tube following cytochalasin-induced paralysis. *Philos. Trans. R. Soc. Lond. Ser. B Biol. Sci.* 331, 225–235. doi: 10.1098/rstb.1991.0011

Higashiyama, T. (2018). Plant reproduction: autocrine machinery for the long journey of the pollen tube. *Curr. Biol.* 28, R266–R269. doi: 10.1016/j.cub.2018.01.067

Higashiyama, T., and Takeuchi, H. (2015). The mechanism and key molecules involved in pollen tube guidance. *Annu. Rev. Plant Biol.* 66, 393–413. doi: 10.1146/annurev-arplant-043014-115635

HoldawayClarke, T. L., Feijo, J. A., Hackett, G. R., Kunkel, J. G., and Hepler, P. K. (1997). Pollen tube growth and the intracellular cytosolic calcium gradient oscillate in phase while extracellular calcium influx is delayed. *Plant Cell* 9, 1999–2010. doi: 10.1105/tpc.9.11.1999

Huang, S., Blanchoin, L., Chaudhry, F., Franklin-Tong, V. E., and Staiger, C. J. (2004). A gelsolin-like protein from *Papaver rhoeas* pollen (PrABP80) stimulates calcium-regulated severing and depolymerization of actin filaments. *J. Biol. Chem.* 279, 23364–23375. doi: 10.1074/jbc.M312973200

Huang, S., Qu, X., and Zhang, R. (2015). Plant villins: versatile actin regulatory proteins. *J. Integr. Plant Biol.* 57, 40–49. doi: 10.1111/jipb.12293

Ingouff, M., Fitz Gerald, J. N., Guerin, C., Robert, H., Sorensen, M. B., Van Damme, D., et al. (2005). Plant formin AtFH5 is an evolutionarily conserved actin nucleator involved in cytokinesis. *Nat. Cell Biol.* 7, 374–380. doi: 10.1038/ncb1238

Jiang, Y., Chang, M., Lan, Y., and Huang, S. (2019). Mechanism of CAP1-mediated apical actin polymerization in pollen tubes. *Proc. Natl. Acad. Sci. U.S.A.* 116, 12084–12093. doi: 10.1073/pnas.1821639116

Jiang, Y., Wang, J., Xie, Y., Chen, N., and Huang, S. (2017). ADF10 shapes the overall organization of apical actin filaments by promoting their turnover and ordering in pollen tubes. *J. Cell Sci.* 130, 3988–4001. doi: 10.1242/jcs.207738

Johnson, M. A., Harper, J. F., and Palanivelu, R. (2019). A fruitful journey: pollen tube navigation from germination to fertilization. *Annu. Rev. Plant Biol.* 70, 809–837. doi: 10.1146/annurev-arplant-050718-100133

Kaul, S., Koo, H. L., Jenkins, J., Rizzo, M., Rooney, T., Tallon, L. J., et al. (2000). Analysis of the genome sequence of the flowering plant *Arabidopsis thaliana*. *Nature* 408, 796–815. doi: 10.1038/35048692

Khurana, P., Henty, J. L., Huang, S., Staiger, A. M., Blanchoin, L., and Staiger, C. J. (2010). *Arabidopsis* VILLIN1 and VILLIN3 have overlapping and distinct activities in actin bundle formation and turnover. *Plant Cell* 22, 2727–2748. doi: 10.1105/tpc.110.076240

Klahre, U., Friederich, E., Kost, B., Louvard, D., and Chua, N. H. (2000). Villin-like actin-binding proteins are expressed ubiquitously in Arabidopsis. *Plant Physiol.* 122, 35–47. doi: 10.1104/pp.122.1.35

Kost, B., Spielhofer, P., and Chua, N. H. (1998). A GFP-mouse talin fusion protein labels plant actin filaments in vivo and visualizes the actin cytoskeleton in growing pollen tubes. *Plant J.* 16, 393–401. doi: 10.1046/j.1365-313x.1998.00304.x

Kovar, D. R. (2006). Molecular details of formin-mediated actin assembly. *Curr. Opin. Cell Biol.* 18, 11–17. doi: 10.1016/j.ceb.2005.12.011

Kovar, D. R., Drobak, B. K., and Staiger, C. J. (2000). Maize profilin isoforms are functionally distinct. *Plant Cell* 12, 583–598. doi: 10.1105/tpc.12.4.583

Kovar, D. R., Harris, E. S., Mahaffy, R., Higgs, H. N., and Pollard, T. D. (2006). Control of the assembly of ATP- and ADP-actin by formins and profilin. *Cell* 124, 423–435. doi: 10.1016/j.cell.2005.11.038

Kovar, D. R., Yang, P., Sale, W. S., Drobak, B. K., and Staiger, C. J. (2001). *Chlamydomonas reinhardtii* produces a profilin with unusual biochemical properties. *J. Cell Sci.* 114(Pt 23), 4293–4305.

Kroeger, J. H., Daher, F. B., Grant, M., and Gieitmann, A. (2009). Microfilament orientation constrains vesicle flow and spatial distribution in growing pollen tubes. *Biophys. J.* 97, 1822–1831. doi: 10.1016/j.bpj.2009.07.038

Lan, Y., Liu, X., Fu, Y., and Huang, S. (2018). *Arabidopsis* class I formins control membrane-originated actin polymerization at pollen tube tips. *PLoS Genet.* 14:e1007789. doi: 10.1371/journal.pgen.1007789

Le, J., El-Assal Sel, D., Basu, D., Saad, M. E., and Szymanski, D. B. (2003). Requirements for *Arabidopsis ATARP2* and *ATARP3* during epidermal development. *Curr. Biol.* 13, 1341–1347. doi: 10.1016/s0960-9822(03)00493-7

Lenartowska, M., and Michalska, A. (2008). Actin filament organization and polarity in pollen tubes revealed by myosin II subfragment 1 decoration. *Planta* 228, 891–896. doi: 10.1007/s00425-008-0802-5

Li, H., Lin, Y. K., Heath, R. M., Zhu, M. X., and Yang, Z. B. (1999). Control of pollen tube tip growth by a pop GTPase-dependent pathway that leads to tip-localized calcium influx. *Plant Cell* 11, 1731–1742. doi: 10.1105/tpc.11.9.1731

Li, S., Blanchoin, L., Yang, Z., and Lord, E. M. (2003). The putative Arabidopsis arp2/3 complex controls leaf cell morphogenesis. *Plant Physiol.* 132, 2034–2044. doi: 10.1104/pp.103.028563

Li, S., Dong, H., Pei, W., Liu, C., Zhang, S., Sun, T., et al. (2017). LlFH1-mediated interaction between actin fringe and exocytic vesicles is involved in pollen tube tip growth. *New Phytol.* 214, 745–761. doi: 10.1111/nph.14395

Li, Y., Zee, S. Y., Liu, Y. M., Huang, B. Q., and Yen, L. F. (2001). Circular F-actin bundles and a G-actin gradient in pollen and pollen tubes of *Lilium davidii*. *Planta* 213, 722–730. doi: 10.1007/s004250100543

Liu, X., Qu, X., Jiang, Y., Chang, M., Zhang, R., Wu, Y., et al. (2015). Profilin regulates apical actin polymerization to control polarized pollen tube growth. *Mol. Plant* 8, 1694–1709. doi: 10.1016/j.molp.2015.09.013

Liu, X., and Yen, L. F. (1992). Purification and characterization of actin from maize pollen. *Plant Physiol.* 99, 1151–1155. doi: 10.1104/pp.99.3.1151

Lovy-Wheeler, A., Kunkel, J. G., Allwood, E. G., Hussey, P. J., and Hepler, P. K. (2006). Oscillatory increases in alkalinity anticipate growth and may regulate actin dynamics in pollen tubes of lily. *Plant Cell* 18, 2182–2193. doi: 10.1105/tpc.106.044867

Lovy-Wheeler, A., Wilsen, K. L., Baskin, T. I., and Hepler, P. K. (2005). Enhanced fixation reveals the apical cortical fringe of actin filaments as a consistent feature of the pollen tube. *Planta* 221, 95–104. doi: 10.1007/s00425-004-1423-2

Luo, N., Yan, A., Liu, G., Guo, J., Rong, D., Kanaoka, M. M., et al. (2017). Exocytosis-coordinated mechanisms for tip growth underlie pollen tube growth guidance. *Nat. Commun.* 8:1687.

Mascarenhas, J. P. (1993). Molecular mechanism of pollen-tube growth and differentiation. *Plant Cell* 5, 1303–1314. doi: 10.1105/tpc.5.10.1303

Mascarenhas, J. P., and Lafountain, J. (1972). Protoplasmic streaming, cytochalasin B, and growth of the pollen tube. *Tissue Cell* 4, 11–14. doi: 10.1016/s0040-8166(72)80002-8

Mathur, J., Mathur, N., Kernebeck, B., and Hulskamp, M. (2003a). Mutations in actin-related proteins 2 and 3 affect cell shape development in Arabidopsis. *Plant Cell* 15, 1632–1645. doi: 10.1105/tpc.011676

Mathur, J., Mathur, N., Kirik, V., Kernebeck, B., Srinivas, B. P., and Hulskamp, M. (2003b). Arabidopsis CROOKED encodes for the smallest subunit of the ARP2/3 complex and controls cell shape by region specific fine F-actin formation. *Development* 130, 3137–3146. doi: 10.1242/dev.00549

Messerli, M., and Robinson, K. R. (1997). Tip localized Ca2+ pulses are coincident with peak pulsatile growth rates in pollen tubes of *Lilium longiflorum*. *J. Cell Sci.* 110(Pt 11), 1269–1278.

Muschietti, J. P., and Wengier, D. L. (2018). How many receptor-like kinases are required to operate a pollen tube. *Curr. Opin. Plant Biol.* 41, 73–82. doi: 10.1016/j.pbi.2017.09.008

Pantaloni, D., and Carlier, M. F. (1993). How profilin promotes actin filament assembly in the presence of thymosin beta 4. *Cell* 75, 1007–1014. doi: 10.1016/0092-8674(93)90544-z

Papuga, J., Hoffmann, C., Dieterle, M., Moes, D., Moreau, F., Tholl, S., et al. (2010). *Arabidopsis* LIM proteins: a family of actin bundlers with distinct expression patterns and modes of regulation. *Plant Cell* 22, 3034–3052. doi: 10.1105/tpc.110.075960

Pawloski, L. C., Kandasamy, M. K., and Meagher, R. B. (2006). The late pollen actins are essential for normal male and female development in *Arabidopsis*. *Plant Mol. Biol.* 62, 881–896. doi: 10.1007/s11103-006-9063-5

Qin, T., Liu, X., Li, J., Sun, J., Song, L., and Mao, T. (2014). *Arabidopsis* microtubule-destabilizing protein 25 functions in pollen tube growth by severing actin filaments. *Plant Cell* 26, 325–339. doi: 10.1105/tpc.113.119768

Qin, Y., and Yang, Z. (2011). Rapid tip growth: insights from pollen tubes. *Semin. Cell Dev. Biol.* 22, 816–824. doi: 10.1016/j.semcdb.2011.06.004

Qu, X., Jiang, Y., Chang, M., Liu, X., Zhang, R., and Huang, S. (2015). Organization and regulation of the actin cytoskeleton in the pollen tube. *Front. Plant Sci.* 5:786. doi: 10.3389/fpls.2014.00786

Qu, X., Wang, Q., Wang, H., and Huang, S. (2020). Visualization of actin organization and quantification in fixed *Arabidopsis* pollen grains and tubes. *Bio Protoc.* 10:e3509. doi: 10.21769/BioProtoc.3509

Qu, X., Zhang, H., Xie, Y., Wang, J., Chen, N., and Huang, S. (2013). *Arabidopsis* villins promote actin turnover at pollen tube tips and facilitate the construction of actin collars. *Plant Cell* 25, 1803–1817. doi: 10.1105/tpc.113.110940

Qu, X., Zhang, R., Zhang, M., Diao, M., Xue, Y., and Huang, S. (2017). Organizational innovation of apical actin filaments drives rapid pollen tube growth and turning. *Mol. Plant* 10, 930–947. doi: 10.1016/j.molp.2017.05.002

Ren, H., and Xiang, Y. (2007). The function of actin-binding proteins in pollen tube growth. *Protoplasma* 230, 171–182. doi: 10.1007/s00709-006-0231-x

Ren, H. Y., Gibbon, B. C., Ashworth, S. L., Sherman, D. M., Yuan, M., and Staiger, C. J. (1997). Actin purified from maize pollen functions in living plant cells. *Plant Cell* 9, 1445–1457. doi: 10.1105/tpc.9.8.1445

Rizvi, S. A., Neidt, E. M., Cui, J., Feiger, Z., Skau, C. T., Gardel, M. L., et al. (2009). Identification and characterization of a small molecule inhibitor of formin-mediated actin assembly. *Chem. Biol.* 16, 1158–1168. doi: 10.1016/j.chembiol.2009.10.006

Romero, S., Le Clainche, C., Didry, D., Egile, C., Pantaloni, D., and Carlier, M. F. (2004). Formin is a processive motor that requires profilin to accelerate actin assembly and associated ATP hydrolysis. *Cell* 119, 419–429. doi: 10.1016/j.cell.2004.09.039

Rotty, J. D., Wu, C., Haynes, E. M., Suarez, C., Winkelman, J. D., Johnson, H. E., et al. (2015). Profilin-1 serves as a gatekeeper for actin assembly by Arp2/3-dependent and -independent pathways. *Dev. Cell* 32, 54–67. doi: 10.1016/j.devcel.2014.10.026

Rounds, C. M., and Bezanilla, M. (2013). "Growth mechanisms in tip-growing plant cells," in *Annual Review of Plant Biology*, Vol. 64, ed. S. S. Merchant (Palo Alto, CA: Annual Reviews), 243–265. doi: 10.1146/annurev-arplant-050312-120150

Rounds, C. M., Hepler, P. K., and Winship, L. J. (2014). The apical actin fringe contributes to localized cell wall deposition and polarized growth in the Lily pollen tube. *Plant Physiol.* 166, 139–151. doi: 10.1104/pp.114.242974

Samaj, J., Muller, J., Beck, M., Bohm, N., and Menzel, D. (2006). Vesicular trafficking, cytoskeleton and signalling in root hairs and pollen tubes. *Trends Plant Sci.* 11, 594–600. doi: 10.1016/j.tplants.2006.10.002

Shi, M., Xie, Y., Zheng, Y., Wang, J., Su, Y., Yang, Q., et al. (2013). *Oryza sativa* actin-interacting protein 1 is required for rice growth by promoting actin turnover. *Plant J.* 73, 747–760. doi: 10.1111/tpj.12065

Smertenko, A. P., Allwood, E. G., Khan, S., Jiang, C. J., Maciver, S. K., Weeds, A. G., et al. (2001). Interaction of pollen-specific actin-depolymerizing factor with actin. *Plant J.* 25, 203–212. doi: 10.1046/j.1365-313x.2001.00954.x

Snowman, B. N., Kovar, D. R., Shevchenko, G., Franklin-Tong, V. E., and Staiger, C. J. (2002). Signal-mediated depolymerization of actin in pollen during the self-incompatibility response. *Plant Cell* 14, 2613–2626. doi: 10.1105/tpc.002998

Speranza, A., and Calzoni, G. L. (1989). Cytochalasin-B affects protein secretion in germinating pollen of malus-domestica borkh. *J. Plant Physiol.* 133, 719–726. doi: 10.1016/s0176-1617(89)80079-3

Staiger, C. J., and Blanchoin, L. (2006). Actin dynamics: old friends with new stories. *Curr. Opin. Plant Biol.* 9, 554–562. doi: 10.1016/j.pbi.2006.09.013

Staiger, C. J., Poulter, N. S., Henty, J. L., Franklin-Tong, V. E., and Blanchoin, L. (2010). Regulation of actin dynamics by actin-binding proteins in pollen. *J. Exp. Bot.* 61, 1969–1986. doi: 10.1093/jxb/erq012

Staiger, C. J., Yuan, M., Valenta, R., Shaw, P. J., Warn, R. M., and Lloyd, C. W. (1994). Microinjected profilin affects cytoplasmic streaming in plant cells by rapidly depolymerizing actin microfilaments. *Curr. Biol.* 4, 215–219. doi: 10.1016/s0960-9822(00)00050-6

Stephan, O., Cottier, S., Fahlen, S., Montes-Rodriguez, A., Sun, J., Eklund, D. M., et al. (2014). RISAP is a TGN-associated RAC5 effector regulating membrane traffic during polar cell growth in Tobacco. *Plant Cell* 26, 4426–4447. doi: 10.1105/tpc.114.131078

Stephan, O. O. H. (2017). Actin fringes of polar cell growth. *J. Exp. Bot.* 68, 3303–3320. doi: 10.1093/jxb/erx195

Su, H., Zhu, J., Cai, C., Pei, W., Wang, J., Dong, H., et al. (2012). FIMBRIN1 is involved in lily pollen tube growth by stabilizing the actin fringe. *Plant Cell* 24, 4539–4554. doi: 10.1105/tpc.112.099358

Suarez, C., Carroll, R. T., Burke, T. A., Christensen, J. R., Bestul, A. J., Sees, J. A., et al. (2015). Profilin regulates F-actin network homeostasis by favoring formin over Arp2/3 complex. *Dev. Cell* 32, 43–53. doi: 10.1016/j.devcel.2014.10.027

Szymanski, D. B. (2005). Breaking the WAVE complex: the point of *Arabidopsis* trichomes. *Curr. Opin. Plant Biol.* 8, 103–112. doi: 10.1016/j.pbi.2004.11.004

Takeuchi, H., and Higashiyama, T. (2016). Tip-localized receptors control pollen tube growth and LURE sensing in *Arabidopsis*. *Nature* 531, 245–248. doi: 10.1038/nature17413

Tang, X. J., Lancelle, S. A., and Hepler, P. K. (1989). Fluorescence microscopic localization of actin in pollen tubes: comparison of actin antibody and phalloidin staining. *Cell Motil. Cytoskeleton* 12, 216–224. doi: 10.1002/cm.970120404

Taylor, L. P., and Hepler, P. K. (1997). Pollen germination and tube growth. *Annu. Rev. Plant Physiol. Plant Mol. Biol.* 48, 461–491.

Thomas, S. G., Huang, S., Li, S., Staiger, C. J., and Franklin-Tong, V. E. (2006). Actin depolymerization is sufficient to induce programmed cell death in self-incompatible pollen. *J. Cell Biol.* 174, 221–229. doi: 10.1083/jcb.200604011

Tominaga, M., Yokota, E., Vidali, L., Sonobe, S., Hepler, P. K., and Shimmen, T. (2000). The role of plant villin in the organization of the actin cytoskeleton, cytoplasmic streaming and the architecture of the transvacuolar strand in root hair cells of *Hydrocharis*. *Planta* 210, 836–843. doi: 10.1007/s004250050687

van Gisbergen, P. A. C., and Bezanilla, M. (2013). Plant formins: membrane anchors for actin polymerization. *Trends Cell Biol.* 23, 227–233. doi: 10.1016/j.tcb.2012.12.001

Vidali, L., and Hepler, P. K. (1997). Characterization and localization of profilin in pollen grains and tubes of *Lilium longiflorum*. *Cell Motil. Cytoskeleton* 36, 323–338. doi: 10.1002/(sici)1097-0169(1997)36:4<323::aid-cm3>3.0.co;2-6

Vidali, L., and Hepler, P. K. (2001). Actin and pollen tube growth. *Protoplasma* 215, 64–76. doi: 10.1007/bf01280304

Vidali, L., McKenna, S. T., and Hepler, P. K. (2001). Actin polymerization is essential for pollen tube growth. *Mol. Biol. Cell* 12, 2534–2545. doi: 10.1091/mbc.12.8.2534

Vidali, L., Rounds, C. M., Hepler, P. K., and Bezanilla, M. (2009). Lifeact-mEGFP reveals a dynamic apical F-actin network in tip growing plant cells. *PLoS One* 4:e5744. doi: 10.1371/journal.pone.0005744

Wang, H. J., Wan, A. R., and Jauh, G. Y. (2008). An actin-binding protein, LlLIM1, mediates calcium and hydrogen regulation of actin dynamics in pollen tubes. *Plant Physiol.* 147, 1619–1636. doi: 10.1104/pp.108.118604

Wang, T., Liang, L., Xue, Y., Jia, P.-F., Chen, W., Zhang, M.-X., et al. (2016). A receptor heteromer mediates the male perception of female attractants in plants. *Nature* 531, 241–244. doi: 10.1038/nature16975

Wang, T., Xiang, Y., Hou, J., and Ren, H. Y. (2008). ABP41 is involved in the pollen tube development via fragmenting actin filaments. *Mol. Plant* 1, 1048–1055. doi: 10.1093/mp/ssn073

Wilsen, K. L., Lovy-Wheeler, A., Voigt, B., Menzel, D., Kunkel, J. G., and Hepler, P. K. (2006). Imaging the actin cytoskeleton in growing pollen tubes. *Sex. Plant Reprod.* 19, 51–62. doi: 10.1007/s00497-006-0021-9

Wu, S., Xie, Y., Zhang, J., Ren, Y., Zhang, X., Wang, J., et al. (2015). VLN2 regulates plant architecture by affecting microfilament dynamics and polar auxin transport in Rice. *Plant Cell* 27, 2829–2845. doi: 10.1105/tpc.15.00581

Wu, Y., Yan, J., Zhang, R., Qu, X., Ren, S., Chen, N., et al. (2010). *Arabidopsis* FIMBRIN5, an actin bundling factor, is required for pollen germination and pollen tube growth. *Plant Cell* 22, 3745–3763. doi: 10.1105/tpc.110.080283

Xiang, Y., Huang, X., Wang, T., Zhang, Y., Liu, Q., Hussey, P. J., et al. (2007). ACTIN BINDING PROTEIN 29 from Lilium pollen plays an important role in dynamic actin remodeling. *Plant Cell* 19, 1930–1946. doi: 10.1105/tpc.106.048413

Yamashiro, S., Kameyama, K., Kanzawa, N., Tamiya, T., Mabuchi, I., and Tsuchiya, T. (2001). The gelsolin/fragmin family protein identified in the higher plant *Mimosa pudica*. *J. Biochem.* 130, 243–249. doi: 10.1093/oxfordjournals.jbchem.a002978

Yang, Z. (2008). Cell polarity signaling in *Arabidopsis*. *Annu. Rev. Cell Dev. Biol.* 24, 551–575. doi: 10.1146/annurev.cellbio.23.090506.123233

Ye, J., Zheng, Y., Yan, A., Chen, N., Wang, Z., Huang, S., et al. (2009). *Arabidopsis* formin3 directs the formation of actin cables and polarized growth in pollen tubes. *Plant Cell* 21, 3868–3884. doi: 10.1105/tpc.109.068700

Yokota, E., Takahara, K., and Shimmen, T. (1998). Actin-bundling protein isolated from pollen tubes of lily - biochemical and immunocytochemical characterization. *Plant Physiol.* 116, 1421–1429. doi: 10.1104/pp.116.4.1421

Yokota, E., Tominaga, M., Mabuchi, I., Tsuji, Y., Staiger, C. J., Oiwa, K., et al. (2005). Plant villin, lily P-135-ABP, possesses G-actin binding activity and accelerates the polymerization and depolymerization of actin in a Ca2+-sensitive manner. *Plant Cell Physiol.* 46, 1690–1703. doi: 10.1093/pcp/pci185

Yokota, E., Vidali, L., Tominaga, M., Tahara, H., Orii, H., Morizane, Y., et al. (2003). Plant 115-kDa actin-filament bundling protein, P-115-ABP, is a homologue of plant villin and is widely distributed in cells. *Plant Cell Physiol.* 44, 1088–1099. doi: 10.1093/pcp/pcg132

Zhang, H., Qu, X., Bao, C., Khurana, P., Wang, Q., Xie, Y., et al. (2010). *Arabidopsis* VILLIN5, an actin filament bundling and severing protein, is necessary for normal pollen tube growth. *Plant Cell* 22, 2749–2767. doi: 10.1105/tpc.110.076257

Zhang, J., Huang, Q., Zhong, S., Bleckmann, A., Huang, J., Guo, X., et al. (2017). Sperm cells are passive cargo of the pollen tube in plant fertilization. *Nat. Plants* 3:17079. doi: 10.1038/nplants.2017.79

Zhang, M., Zhang, R., Qu, X., and Huang, S. (2016). Arabidopsis FIM5 decorates apical actin filaments and regulates their organization in the pollen tube. *J. Exp. Bot.* 67, 3407–3417. doi: 10.1093/jxb/erw160

Zhang, R., Qu, X., Zhang, M., Jiang, Y., Dai, A., Zhao, W., et al. (2019). The balance between actin-bundling factors controls actin architecture in pollen tubes. *iScience* 16, 162–176. doi: 10.1016/j.isci.2019.05.026

Zhang, Y., He, J., Lee, D., and McCormick, S. (2010). Interdependence of endomembrane trafficking and actin dynamics during polarized growth of Arabidopsis pollen tubes. *Plant Physiol.* 152, 2200–2210. doi: 10.1104/pp.109.142349

Zhang, Y., He, J., and McCormick, S. (2009). Two Arabidopsis AGC kinases are critical for the polarized growth of pollen tubes. *Plant J.* 58, 474–484. doi: 10.1111/j.1365-313X.2009.03792.x

Zhang, Y., and McCormick, S. (2010). The regulation of vesicle trafficking by small GTPases and phospholipids during pollen tube growth. *Sex. Plant Reprod.* 23, 87–93. doi: 10.1007/s00497-009-0118-z

Zhang, Y., Xiao, Y., Du, F., Cao, L., Dong, H., and Ren, H. (2011). *Arabidopsis* VILLIN4 is involved in root hair growth through regulating actin organization in a Ca2+-dependent manner. *New Phytol.* 190, 667–682. doi: 10.1111/j.1469-8137.2010.03632.x

Zhao, W., Qu, X., Zhuang, Y., Wang, L., Bosch, M., Franklin-Tong, V. E., et al. (2020). Villin controls the formation and enlargement of punctate actin foci in pollen tubes. *J. Cell Sci.* 133:jcs237404. doi: 10.1242/jcs.237404

Zheng, Y., Xie, Y., Jiang, Y., Qu, X., and Huang, S. (2013). *Arabidopsis* actin-depolymerizing factor7 severs actin filaments and regulates actin cable turnover to promote normal pollen tube growth. *Plant Cell* 25, 3405–3423. doi: 10.1105/tpc.113.117820

Zhou, Z., Shi, H., Chen, B., Zhang, R., Huang, S., and Fu, Y. (2015). Arabidopsis RIC1 severs actin filaments at the apex to regulate pollen tube growth. *Plant Cell* 27, 1140–1161. doi: 10.1105/tpc.114.135400

Zhu, J., Nan, Q., Qin, T., Qian, D., Mao, T., Yuan, S., et al. (2017). Higher-ordered actin structures remodeled by *Arabidopsis* ACTIN-DEPOLYMERIZING FACTOR5 are important for pollen germination and pollen tube growth. *Mol. Plant* 10, 1065–1081. doi: 10.1016/j.molp.2017.06.001

Zhu, L., Zhang, Y., Kang, E., Xu, Q., Wang, M., Rui, Y., et al. (2013). MAP18 regulates the direction of pollen tube growth in *Arabidopsis* by modulating F-actin organization. *Plant Cell* 25, 851–867. doi: 10.1105/tpc.113.110528

Zonia, L. (2010). Spatial and temporal integration of signalling networks regulating pollen tube growth. *J. Exp. Bot.* 61, 1939–1957. doi: 10.1093/jxb/erq073

Conflict of Interest: The authors declare that the research was conducted in the absence of any commercial or financial relationships that could be construed as a potential conflict of interest.

frontiers in Cell and Developmental Biology

ORIGINAL RESEARCH
published: 28 January 2021
doi: 10.3389/fcell.2021.635533

Arabidopsis ADF5 Acts as a Downstream Target Gene of CBFs in Response to Low-Temperature Stress

*Pan Zhang, Dong Qian, Changxin Luo, Yingzhi Niu, Tian Li, Chengying Li, Yun Xiang, Xinyu Wang and Yue Niu**

Ministry of Education Key Laboratory of Cell Activities and Stress Adaptations, School of Life Sciences, Lanzhou University, Lanzhou, China

Low temperature is a major adverse environment that affects normal plant growth. Previous reports showed that the actin cytoskeleton plays an important role in the plant response to low-temperature stress, but the regulatory mechanism of the actin cytoskeleton in this process is not clear. C-repeat binding factors (CBFs) are the key molecular switches for plants to adapt to cold stress. However, whether CBFs are involved in the regulation of the actin cytoskeleton has not been reported. We found that *Arabidopsis actin depolymerizing factor 5* (*ADF5*), an ADF that evolved F-actin bundling function, was up-regulated at low temperatures. We also demonstrated that CBFs bound to the *ADF5* promoter directly *in vivo* and *in vitro*. The cold-induced expression of *ADF5* was significantly inhibited in the *cbfs* triple mutant. The freezing resistance of the *adf5* knockout mutant was weaker than that of wild type (WT) with or without cold acclimation. After low-temperature treatment, the actin cytoskeleton of WT was relatively stable, but the actin cytoskeletons of *adf5*, *cbfs*, and *adf5 cbfs* were disturbed to varying degrees. Compared to WT, the endocytosis rate of the amphiphilic styryl dye FM4-64 in *adf5*, *cbfs*, and *adf5 cbfs* at low temperature was significantly reduced. In conclusion, CBFs directly combine with the CRT/DRE DNA regulatory element of the *ADF5* promoter after low-temperature stress to transcriptionally activate the expression of *ADF5*; ADF5 further regulates the actin cytoskeleton dynamics to participate in the regulation of plant adaptation to a low-temperature environment.

Keywords: actin depolymerizing factor, cold stress, C-repeat binding factors genes, actin cytoskeleton, regulatory mechanism

OPEN ACCESS

Edited by:
Yi Zhang,
Beijing Normal University, China

Reviewed by:
Xiangfeng Wang,
China Agricultural University, China
Zhaosheng Kong,
Chinese Academy of Sciences, China

****Correspondence:***
Yue Niu
niuy@lzu.edu.cn

Specialty section:
This article was submitted to Cell Growth and Division, a section of the journal Frontiers in Cell and Developmental Biology

Received: *30 November 2020*
Accepted: *08 January 2021*
Published: *28 January 2021*

Citation:
Zhang P, Qian D, Luo C, Niu Y, Li T, Li C, Xiang Y, Wang X and Niu Y (2021) Arabidopsis ADF5 Acts as a Downstream Target Gene of CBFs in Response to Low-Temperature Stress. Front. Cell Dev. Biol. 9:635533. doi: 10.3389/fcell.2021.635533

INTRODUCTION

Low temperature is a major plant stress factor that causes plant growth delay, stagnation, and retrogression and reduces grain yield (Dolferus, 2014; Zhang et al., 2019). Over long evolutionary process, plants have created a series of complex mechanisms to adapt to low-temperature stress. Cold acclimation is one of these mechanisms. When plants are exposed to non-freezing low temperatures for a period of time, their tolerance to lower temperatures improves (Thomashow, 1999; Shi et al., 2018). C-repeat binding factors (CBFs) are the key molecular switches in this process (Liu J. et al., 2018). *CBF1*, *CBF2*, and *CBF3*, also known as *DREB1B*, *DREB1C*, and *DREB1A*, belong to the AP2/ERF transcription factor family, which recognizes the C-repeat

(CRT)/dehydration responsive element (DRE) DNA regulatory element (CCGAC) (Stockinger et al., 1997; Gilmour et al., 1998; Liu et al., 1998; Medina et al., 1999; Thomashow, 1999). Low temperature rapidly induces the expression of *CBFs*. CBFs further activate the expression of a set of *COLD-REGULATED* (*COR*) genes (Chinnusamy et al., 2007; Ding et al., 2019). These genes generally encode some cryoprotective proteins, reactive oxygen species scavenging proteins, enzymes for osmolyte biosynthesis and photosynthetic membrane protective proteins, which enhance the freezing resistance of plants (Lin and Thomashow, 1992; Jaglo-Ottosen et al., 1998; Liu et al., 1998; Janmohammadi et al., 2015; Bremer et al., 2017).

The maintenance and establishment of specific structures and highly dynamic changes in the plant actin cytoskeleton are necessary for plant cellular processes, such as cell division, cytoplasmic streaming, and vesicular transport (Staiger, 2000). The rapid remodeling of actin cytoskeleton is directly regulated by diverse actin-binding proteins (ABPs), such as profilin, ADF/cofilin, capping protein, villin/gelsolin, formin, and actin-related protein2/3 (Arp2/3) complex (Staiger and Blanchoin, 2006; Qian and Xiang, 2019). Actin depolymerizing factors (ADFs) are conserved actin binding proteins in eukaryotes that regulate the actin cytoskeleton by forming more pointed ends and monomer actins via their severing/depolymerizing activity (Staiger et al., 1997; Hussey et al., 2002; Andrianantoandro and Pollard, 2006). The *Arabidopsis* genome encodes 11 ADF genes, which are divided into 4 subfamilies (Ruzicka et al., 2007). Our laboratory reported that the third subfamily of *Arabidopsis thaliana* (ADF5, ADF9) have developed new functionalization during the process of evolution. They lost the conservative severing/depolymerizing activity of the family and evolved F-actin bundling function (Nan et al., 2017). The other three subfamilies retain the conserved function of severing/depolymerizing activities (Tholl et al., 2011; Nan et al., 2017). The physiological functions of plant ADFs were reported in recent years, such as pollen germination, pollen tube polar growth (Chen et al., 2002, 2003; Bou Daher et al., 2011; Zheng et al., 2013; Jiang et al., 2017; Zhu et al., 2017), hypocotyl elongation (Dong et al., 2001; Henty et al., 2011), stomatal movement (Zhao S. et al., 2016; Qian et al., 2019), innate immunity (Tian et al., 2009; Porter et al., 2012; Fu et al., 2014; Inada et al., 2016), and nematode and aphid infection (Clément et al., 2009; Mondal et al., 2018). The new function of ADF5 plays an important role in regulating the actin bundling process during certain plant-specific physiological activities, such as pollen germination, pollen tube polar growth and ABA-induced stomatal closure (Zhu et al., 2017; Qian et al., 2019). ADF9 is primarily involved in plant growth and development. Under long-day light cycles, the *adf9* mutant showed an early flowering phenotype. Compared to the WT, *adf9* had delayed growth, a reduced number of lateral branches and a weakened callus formation ability (Burgos-Rivera et al., 2008). Previous studies showed that wheat *ADF* (*TaADF*) was rapidly and strongly up-regulated under low temperature (Danyluk et al., 1996). Bioinformatics analysis and previous reports showed that the expression of *ADFs* in *Arabidopsis thaliana* changed under low temperature stress (Fan et al., 2015), which suggests that members of this family also participate in the plant response and adaptation to low-temperature stress. However, the physiological function and molecular mechanisms of ADF members after low-temperature stress are not clear.

We found that CBFs directly bound to the CRT/DRE DNA regulatory element of *the ADF5* promoter to induce the up-regulation of *ADF5* expression and finely regulated actin cytoskeleton dynamics at low temperature and affected the endocytosis rate of the FM4-64-labeled plasma membrane. The present study identified the molecular module of the CBF pathway regulating the actin cytoskeleton at low temperature, which enriched the physiological function of ADF5 and revealed the potential mechanism of the actin cytoskeleton response to cold stress.

RESULTS

ADF5 Promotes Basic and Acquired Freezing Resistance in *Arabidopsis thaliana*

The bioinformatics data showed that low temperature treatment up-regulated the expression of *ADF5* and inhibited *ADF9* expression (Nan et al., 2017), which suggests that this subfamily is involved in the plant response to low-temperature stress. To reveal the physiological function of *Arabidopsis ADF5* under low-temperature stress, we used three *adf5* knockout/gene editing mutants: *adf5-1*, *adf5-2*, and *adf5-3*. Our laboratory previously reported *adf5-1* (Zhu et al., 2017). The *adf5-2* is a T-DNA insertion mutant (SALK_030145) from ABRC. PCR and sequencing showed that two T-DNAs were inserted after the first G of the second intron (**Figure 1A**). RT-PCR showed that the full-length *ADF5* gene in *adf5-2* was not expressed (**Figure 1B**). The *adf5-3* was generated by CRISPR/Cas9 technology in which the 236 bp of *ADF5* genome was deleted (221 to 455 bp after ATG) and only 21 amino acids were correctly translated (**Figure 1A**).

To verify the phenotype of these mutants under low temperature stress, we first used 12 to 15-day-old seedlings grown on 1/2 MS plates for freezing analyses. The results showed that the three *adf5* knockout mutants had lower freezing resistance and lower survival rate than WT with or without cold acclimation, and the difference was statistically significant (**Figures 1C–E**). Ion leakage generally represents damage to the cell membrane under stress, and it negatively correlates with the survival rate of plants after freezing (Ye et al., 2019). Second, we used seedlings that grew in soil for 21 days to perform independent freezing treatment experiments and obtained the ion leakage of WT and *adf5* with or without cold acclimation. The ion leakage of *adf5* was higher than WT under both treatment conditions, and the difference was statistically significant (**Figures 1F,G**). In conclusion, the results of freezing experiments and physiological data indicate that ADF5 promotes basic and acquired freezing resistance in *Arabidopsis thaliana*.

Low Temperature Can Induce the Expression of *ADF5* Through a Partial CBFs Dependent Pathway

To verify whether the bioinformatics analysis is correct, we used qRT-PCR to detect the expression of *ADF5* in the

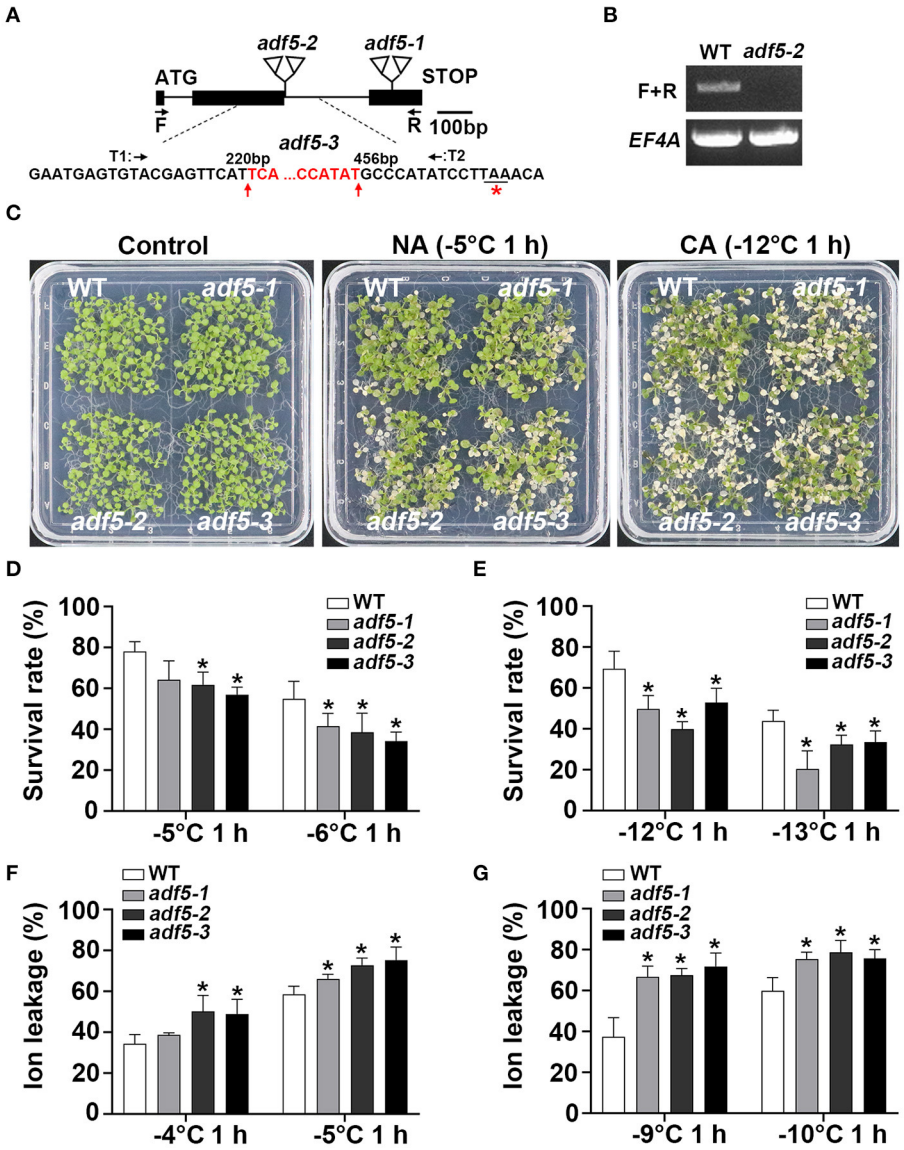

FIGURE 1 | Mutation of *ADF5* results in increased freezing sensitivity. **(A)** Sketch map of *adf5* mutants. The black square represents the exon, and the black line represents the intron. The positions of *adf5-1* and *adf5-2* T-DNA are shown in the triangle. F and R are amplification sites of *ADF5* for RT-PCR or identification of *adf5-3*. T1 and T2 are specific Cas9-splicing sites. The red base is deleted in *adf5-3*, and the red asterisk is the edited termination site. **(B)** Expression of full length *ADF5* in WT and *adf5-2*. *EF4A* is used as an internal control gene. **(C)** Freezing phenotypes of WT and *adf5s*, each material contains ∼40 seedlings, which were directly used for freezing treatments (non-cold-acclimated, NA), or treated at 4°C for 3 days (cold-acclimated, CA) before freezing treatment. **(D,E)** Survival rate of WT and *adf5s*. After 3–5 days of recovery under normal growth conditions, the survival rate was calculated. The data are the means of three biological replicates ± SD ($n = 40$ for each replicate). Asterisks indicate statistically significant differences ($P < 0.05$, one-way ANOVA with a Dunnett's multiple comparisons test). **(F,G)** Ion leakage of WT and *adf5s*. After 3 weeks of normal growth in soil, the fully developed rosettes of seedlings were used for freezing treatment to obtain ion leakage under NA and CA conditions. The data are the means of three biological replicates ± SD ($n = 5$ for each replicate). Asterisks indicate statistically significant differences ($P < 0.05$, one-way ANOVA with a Dunnett's multiple comparisons test).

WT at low temperature. *ADF5* was up-regulated nearly 10-fold after 12 h at 4°C, which indicates that *ADF5* is a cold-induced gene (**Figure 2**). To examine the transcriptional regulatory factors upstream of *ADF5*, we analyzed its promoter sequence and found a CCGAC element at −231 to −227 bp and −472 to −468 bp sites, which could be recognized by CBFs (**Figure 3A**). To demonstrate that CBFs are the upstream transcription activator of *ADF5*, we used the *cbf3* single mutant, *cbf1 cbf3* double mutant and *cbf1 cbf2 cbf3* triple mutant (*cbfs-1*) to detect the induction of *ADF5* at 4°C for different durations. The induction amount of *ADF5* in the single mutant was lower than that in WT, and the double mutant was further reduced. *ADF5* induction was significantly inhibited in the triple mutant (**Figure 2**). Together,

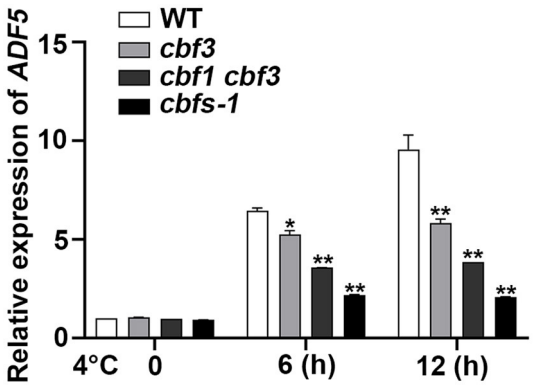

FIGURE 2 | *ADF5* expression is induced by cold in *WT, cbf3, cbf1/3*, and *cbfs*. Ten-day-old *Arabidopsis* seedlings were treated at 4°C for different durations, and the leaves were detached for RNA extraction. *UBQ10* was used as an internal standard. Data presented are the means ± SD of three independent biological replicates (*$P < 0.05$; **$P < 0.01$; Student's two-tailed *t*-test).

these results indicate that ADF5 may participate in the CBFs signaling pathway.

ADF5 Is a Downstream Target Gene of CBFs

To further confirm that CBFs bind to the corresponding region of the *ADF5* promoter, we performed yeast one-hybrid (Y1H) experiment. The results show that CBF1, CBF2, and CBF3 bind to the *ADF5* promoter (**Figures 3B,C**). We further mutated the CBF recognition sites on the *ADF5* promoter to determine the key binding sites (Stockinger et al., 1997) (**Figure 3A**). We found the mutation of the two binding sites recognized by CBFs or the binding sites at −231 to −227 bp, CBFs no longer bound to the *ADF5* promoter in yeast, but the sites at −472 to −468 bp remained functional (**Figures 3B,C**). These results indicate that CBFs bind to the *ADF5* promoter via the CRT/DRE DNA regulatory element at −231 to −227 bp sites.

To determine the effect of CBFs on *ADF5* activation, we performed transient transcriptional activation experiments in tobacco leaves. Because Y1H analysis found that CBF1, CBF2, and CBF3 bound to the *ADF5* promoter, and their function had a certain redundancy (Park et al., 2015), we selected the CBF3 with the strongest binding ability in the Y1H experiments for follow-up experiments (**Figures 3B,C**). Transcriptional activation analysis showed that CBF3 directly transcriptionally activated the expression of *ADF5* in tobacco mesophyll cells (**Figures 3D,E**). Subsequent mutation analysis showed that the recognition sites at −472 to −468 bp did not affect the transcriptional activation efficiency of CBF3 to *ADF5* and the mutation at −231 to −227 bp sites or both significantly reduced the transcriptional activation efficiency (**Figure 3E**). The results indicate that CBF3 activates the expression of *ADF5* via binding to the CBF recognition sites of the *ADF5* promoter at −231 to −227 bp.

To further confirm that CBFs bound to the *ADF5* promoter *in vivo*, ChIP experiments were performed. Col/*pSuper::CBF3-Myc* was treated at 4°C for different times. Chromatin was precipitated using anti-c-myc antibody magnetic beads. P1 primers containing −472 to −468 bp sites and P2 primers containing −231 to −227 bp sites were used to analyze the enrichment by qRT-PCR (**Figure 3A**). The results showed no significant difference between the *CBF3* overexpression line and the WT at the −472 to −468 bp sites at 0 h, but the *CBF3* overexpression line was 1.3 times more enriched than the WT at the −231 to −227 bp sites. After 6 h of low-temperature treatment, the enrichment of WT at the two recognition sites did not change significantly, and *CBF3* overexpression line showed a significant increase that was nearly three times the enrichment at the −231 to −227 bp sites (**Figure 3F**). These results suggest that CBF3 binds to the CBF recognition element of the *ADF5* promoter *in vivo*, and this binding activity is regulated by low temperature. In conclusion, CBFs primarily bind to the CBF recognition sites at the −231 to −227 bp of the *ADF5* promoter *in vivo*, and *ADF5* is a downstream target gene of CBFs.

The Effect of ADF5 on Freezing Resistance in *Arabidopsis thaliana* Partially Depends on the CBF Pathway

To further investigate the genetic relationship between ADF5 and CBFs, *adf5 cbfs* quadruple mutant was obtained by crossing *adf5-1* with the triple mutant *cbfs-1*. Freezing experiments showed that *adf5-1*, *cbfs-1*, and *adf5 cbfs* were more sensitive than WT under non-cold-acclimated (NA) conditions, and the survival rate was significantly different. The freezing resistance of *adf5 cbfs* was closer to *adf5-1* with decreasing temperature and there was no significant difference between the two groups (**Figures 4A,B**). Under cold-acclimated (CA) conditions, *adf5-1*, *cbfs-1*, and *adf5 cbfs* were more sensitive to freezing than WT, and their survival rate was significantly different. The freezing resistance of the *adf5 cbfs* showed the freezing resistance of *cbfs-1* and there was no significant difference between the two groups (**Figures 4A,C**). Seedlings grown in soil for 21 days were used for freezing treatment to obtain ion leakage. Under NA conditions, the ion leakage of WT and *cbfs-1* treated at −4°C was similar, and there was no significant difference. *adf5-1* and *adf5 cbfs* had higher ion leakage than WT and were significantly different. At −5°C, the ion leakage of *cbfs-1* increased significantly relative to WT. The *adf5-1* and *adf5 cbfs* had significantly higher ion leakage than WT, and the *adf5 cbfs* had significantly higher ion leakage than *adf5-1* (**Figure 4D**). Under CA conditions, the ion leakage of *adf5-1, cbfs-1,* and *adf5 cbfs* was significantly higher than WT. The ion leakage of *adf5 cbfs* resembled *cbfs-1*, and there was no significant difference (**Figure 4E**). In conclusion, ADF5 positively regulates the freezing tolerance ability of *Arabidopsis thaliana* by partially relying on the CBF pathway.

The Actin Cytoskeleton of the Mutant Was Disordered During Cold Acclimation

To determine whether the phenotypes of the *adf5* and *cbfs* mutants are directly related to the actin cytoskeleton, we

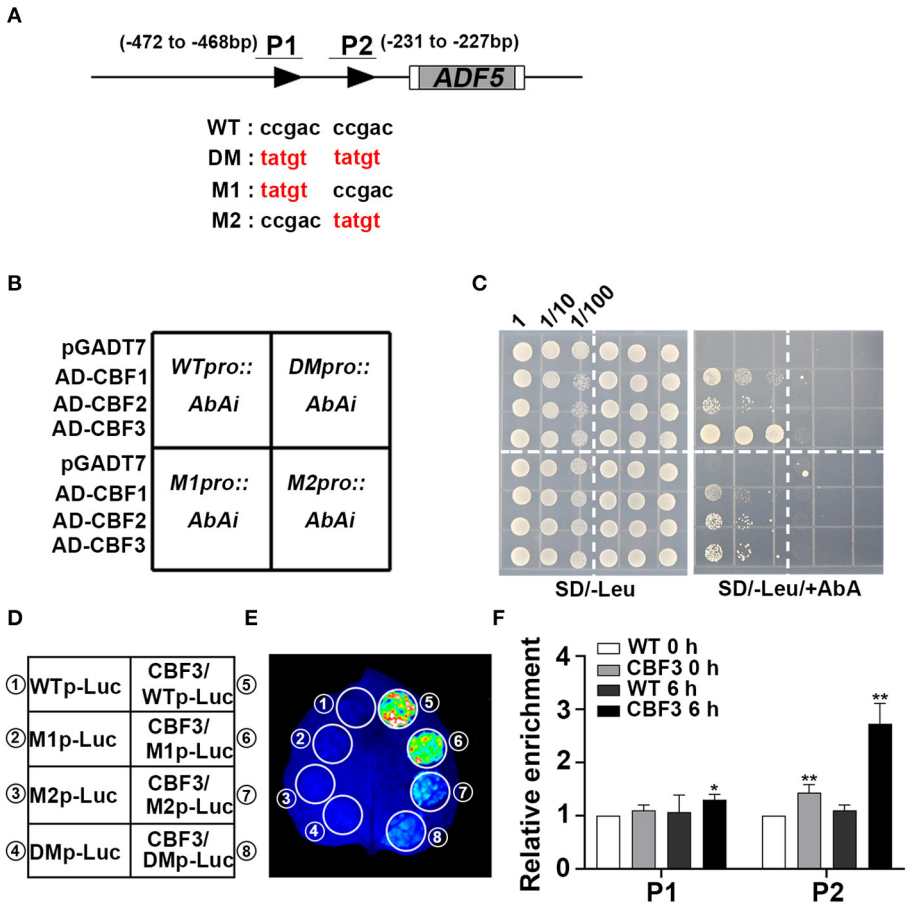

FIGURE 3 | CBFs activate *ADF5* expression via direct binding to the *ADF5* promoter. **(A)** Schematic diagram of the CRT/DRE DNA regulatory element of the *ADF5* promoter. The black triangle represents the CRT/DRE DNA regulatory element. M1 is a mutation at the −472 to −468 bp sites. M2 is a mutation at the −231 to −227 bp sites. DM is a simultaneous mutation of M1 and M2. P1 and P2 are specific primers for ChIP assay. **(B)** Diagram of Y1H colony. **(C)** Y1H assay of the interaction between CBFs and the *ADF5* promoter showing the growth of yeast cells on SD/-Leu medium containing 850 ng/mL Aureobasidin A (AbA). The numbers above the images indicate the dilutions. **(D)** Schematic diagram of the transcriptional activation experiment. **(E)** CBF3 activates the expression of *ADF5* in tobacco leaves via transient expression. **(F)** ChIP analysis of the interaction between CBFs and the *ADF5* promoter under normal conditions or 4°C for 6 h. P1 contains −472 to −468 bp sites of the CRT/DRE DNA regulatory element. P2 contains −231 to −227 bp sites of the CRT/DRE DNA regulatory element. Data presented are the means ± SD of three independent biological replicates (*$P < 0.05$; **$P < 0.01$; Student's two-tailed *t*-test).

observed the actin cytoskeleton morphology in epidermal cells from root transition and elongation zone of WT and mutants under normal growth and different durations of 4°C treatment (**Figure 5A**). ABD2-GFP was expressed in all mutants after crossing Col/*pUBQ10::ABD2-GFP*. The average fluorescence intensity was measured directly. Similar to previous reports, the fluorescence intensity of *adf5-1* under normal growth conditions was significantly lower than the WT (Zhu et al., 2017; Qian et al., 2019). The fluorescence intensity of *cbfs-1* was slightly higher than WT, but *adf5 cbfs* had the highest fluorescence intensity compared to WT, with a significant difference. After 6 h of low temperature treatment, the fluorescence intensity of WT and *cbfs-1* decreased, and *adf5 cbfs* obviously decreased, but the fluorescence intensity of *adf5-1* was not changed. There was no significant difference among the materials at this time. After 12 h of low-temperature treatment, the fluorescence values of all materials recovered, and there was no significant difference among WT, *adf5-1*, and *cbfs-1*. The fluorescence value of the *adf5 cbfs* quadruple mutant increased less, and there was a significant difference between WT and *adf5 cbfs* (**Figure 5B**).

We analyzed the actin cytoskeleton density and skewness after different time points of low-temperature treatment (**Figures 5C,D**). Consistent with a previous report, the structure of the actin cytoskeleton in WT was relatively stable (Shibasaki et al., 2009), and its density and degree of filament bundling (skewness) were not changed. Compared to WT, the mutants had lower actin cytoskeleton density and a higher degree of bundled actin filament at 0 h, which corresponded to the function of ADF5 in forming a more stable actin cytoskeleton network (Zhu et al., 2017; Qian et al., 2019). After 6 hours of low-temperature treatment, the actin cytoskeleton density in the *adf5-1*, *cbfs-1*, and *adf5 cbfs* mutants was relatively changed. However, there was no significant difference between WT and mutants. The degree of bundled actin filament was reduced, there was no significant

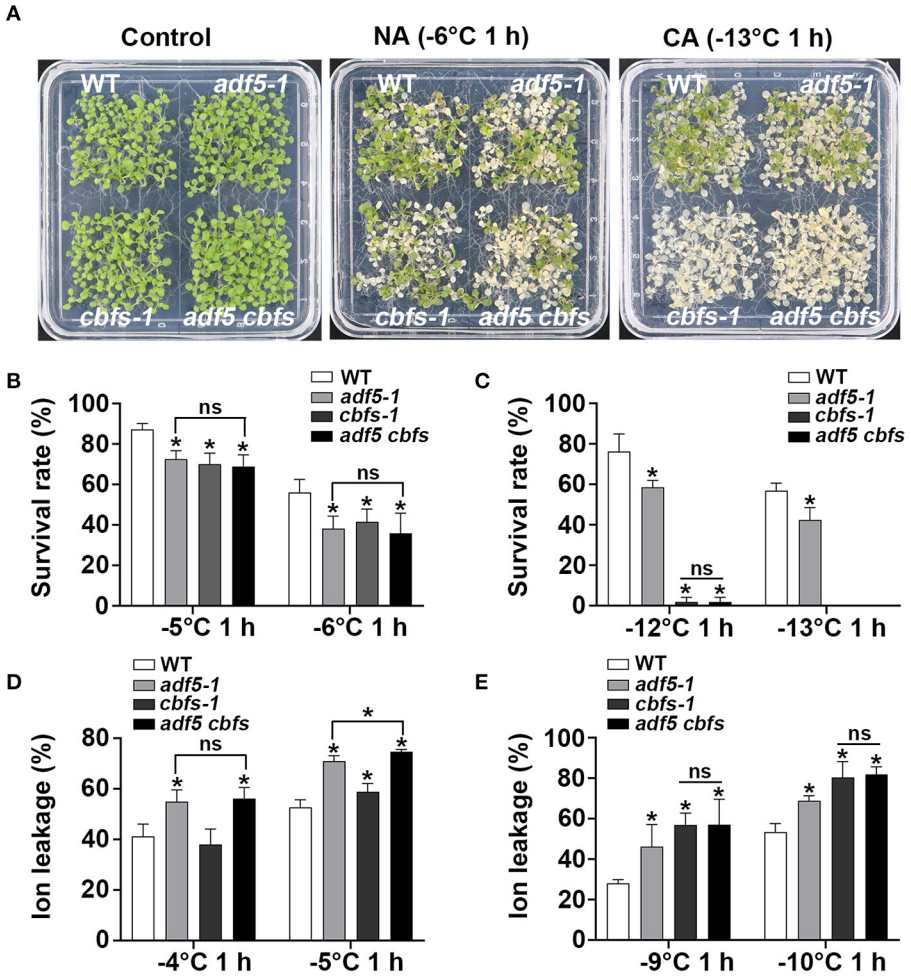

FIGURE 4 | ADF5 is the genetic downstream of CBFs. **(A)** Freezing phenotypes of WT, *adf5-1*, *cbfs-1,* and *adf5 cbfs* under NA or CA conditions. **(B,C)** Survival rate of WT, *adf5-1*, *cbfs-1*, and *adf5 cbfs*. After 3–5 days of recovery under normal growth conditions, the survival rate was calculated. The data are the means of three biological replicates ± SD ($n = 40$ for each replicate). Asterisks indicate statistically significant differences and ns is not significant ($P < 0.05$, one-way ANOVA with a Tukey's multiple comparisons test). **(D,E)** Ion leakage of WT, *adf5-1*, *cbfs-1,* and *adf5 cbfs*. After 3 weeks of normal growth in soil, the fully developed rosettes of seedlings were used for freezing treatment to obtain ion leakage under NA or CA conditions. The data are the means of three biological replicates ±SD ($n = 5$ for each replicate). Asterisks indicate statistically significant differences and ns is not significant ($P < 0.05$, one-way ANOVA with a Tukey's multiple comparisons test).

differences among the *adf5-1*, *cbfs-1*, and WT, but significant differences between *adf5 cbfs* and WT. After 12 h of treatment, the density of *adf5-1* decreased slightly and *cbfs-1* increased, but there was no significant difference compared to WT. The quadruple mutant also increased and was significantly different than WT. The skewness value of *adf5-1* increased, and the values of *cbfs-1* and *adf5 cbfs* decreased. Only the quadruple mutant was significantly different from WT (**Figures 5C,D**). In conclusion, the actin cytoskeleton structure of WT is relatively stable, but the mutants change significantly compared to WT under low temperature treatment, and actin cytoskeleton dynamic process in mutants is affected.

The Endocytosis Rate of the Mutants Decreased During Cold Acclimation

The dynamics of the plasma membrane are very important for the plant response to stress, and the actin cytoskeleton is important for plant endocytosis (Baluška et al., 2002; Wang et al., 2020). Considering the effect of low temperature on actin cytoskeleton dynamics, then to track the endocytosis process, we used amphiphilic styryl dye FM4-64 to label epidermal cells from root transition zone and quantified the cytosol/PM FM4-64 signal intensity ratio to represent the endocytosis rate (**Figures 6A,B**). The results showed that the endocytosis rate of *adf5-1*, *cbfs-1*, and *adf5 cbfs* mutants was faster than WT, and there was significant differences between *adf5-1*, *adf5 cbfs*, and WT, respectively, but there was no significant difference in *cbfs-1*. The endocytosis rate of WT, *adf5-1*, *cbfs-1*, and *adf5 cbfs* decreased after 6 h of low-temperature treatment, and the difference between WT and mutants was reduced. There was a significant difference between *adf5 cbfs* and WT. After 12 h of low-temperature treatment, the endocytosis rate of WT and *adf5-1* increased slightly, and there was no significant difference between *adf5* and WT. The endocytosis rate of *cbfs-1* and *adf5 cbfs* was further reduced, and

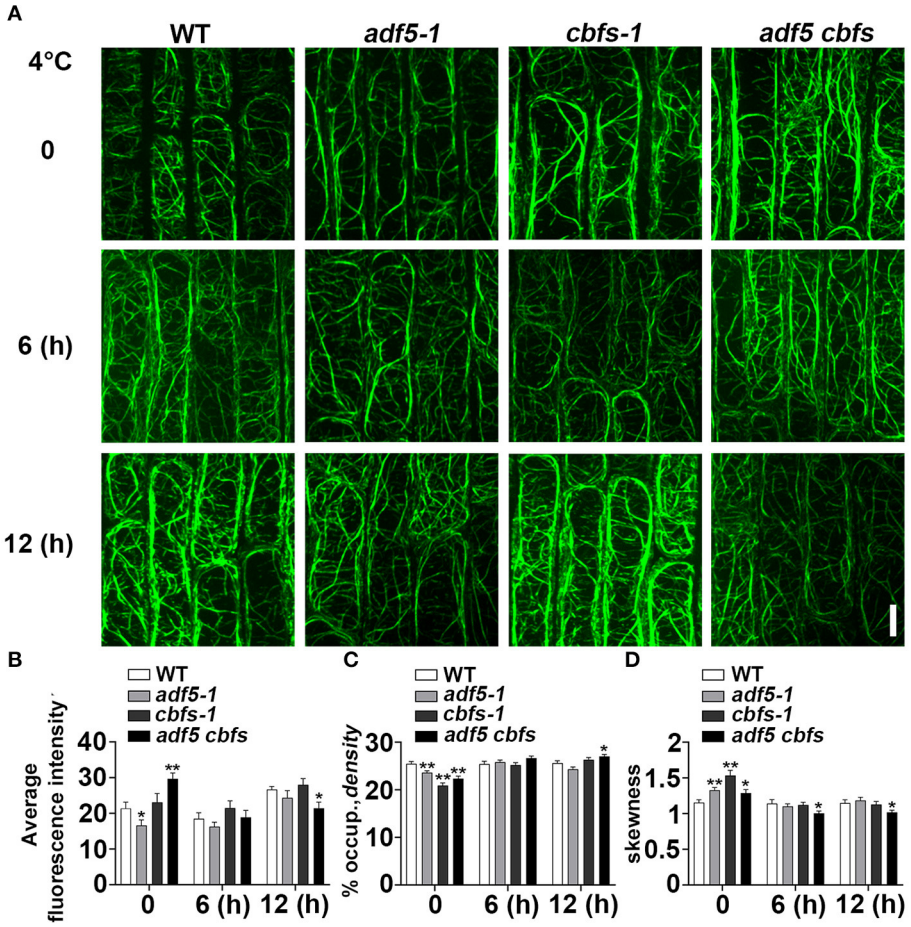

FIGURE 5 | Actin cytoskeleton array rearranges in response to cold treatment. **(A)** Five-day-old seedlings expressing ABD2-GFP were used for fluorescence collection. Images of the cortical actin cytoskeleton array in epidermal cells from the root elongation transition zone of WT, *adf5-1*, *cbfs-1*, and *adf5 cbfs* treated at 4°C for different durations. Scale bar = 10 μm. **(B)** The average intensity of fluorescence of the GFP signal in WT, *adf5-1*, *cbfs-1*, and *adf5 cbfs* root elongation transition zone cells. **(C)** Average actin cytoskeleton density of WT, *adf5-1*, *cbfs-1*, and *adf5 cbfs* root elongation transition zone cells. **(D)** The extent of actin cytoskeleton bundling (skewness) of WT, *adf5-1*, *cbfs-1*, and *adf5 cbfs* root elongation transition zone cells. The values represent the means ± SEM ($n = 60$ cells per genotype. $^*P < 0.05$; $^{**}P < 0.01$; Student's two-tailed *t*-test).

there was a significant difference between *cbfs-1* and WT, but not in the quadruple mutant (**Figure 6B**). The results indicate that the abnormal endocytosis rate of *adf5-1*, *cbfs-1*, and *adf5 cbfs* under normal growth conditions may be the reason for their freezing sensitivity. During the cold training process, the endocytosis rate of non-synchronous change in mutants may cause disorders of cold signals and cryoprotective substance transport, which may affect the freezing resistance of the mutants.

DISCUSSION

Previous reports showed that low temperature disturbed the actin cytoskeleton of plant cells and reduced all cell processes (Das et al., 1966; Pokorná et al., 2004; Fan et al., 2015). The present study provided molecular genetic and physiological evidences for ADF5, which is an ABP that evolved F-actin-bundling function, regulation of actin cytoskeleton dynamics at low temperature partially via a CBF-dependent pathway. The molecular components of fine regulation of the actin cytoskeleton at low temperature were demonstrated.

Cold acclimation reshapes the physiological and biochemical status of cells (Janmohammadi et al., 2015; Ding et al., 2019). CBFs are the core regulatory factor in this process and activate many downstream *COR* genes during cold acclimation (Shi et al., 2018). Published transcriptome data revealed that CBFs regulated a number of potential actin cytoskeleton regulatory genes including *ADF5* (Jia et al., 2016). Previous evidence also showed that TaADF accumulated more in freezing-resistant seedlings (Ouellet et al., 2001). Our qRT-PCR data also directly indicated that *ADF5* was partially up-regulated by CBFs at low temperature treatment (**Figure 2**). Genetic analyses also showed

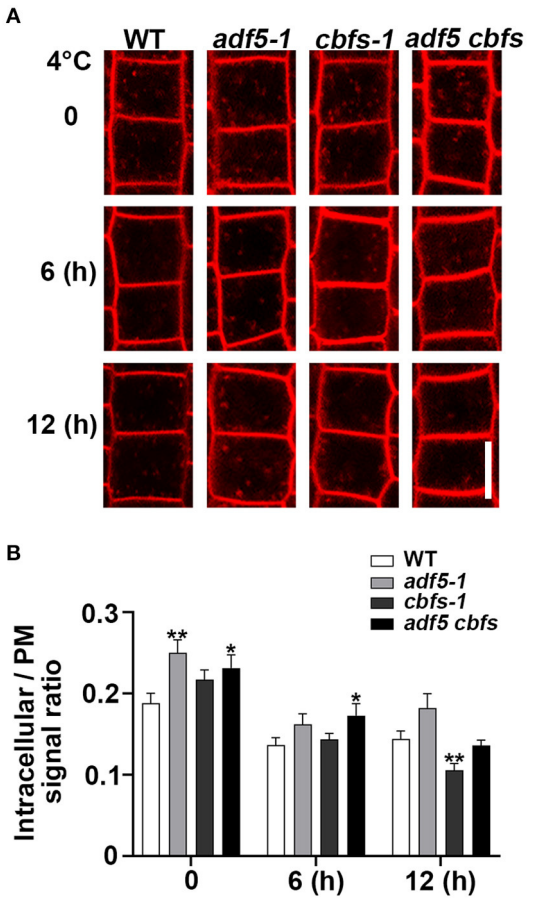

FIGURE 6 | Low temperature reduced the rate of endocytosis in mutants compared to WT. **(A)** Five-day-old seedlings were used for amphiphilic styryl dye FM4-64 signal intensity collection. Seedling roots of WT, *adf5-1, cbfs-1,* and *adf5 cbfs* treated at 4°C for different durations were labeled with FM4-64 to measure internalization. Scale bar = 10 μm. **(B)** The rate of cytosol average fluorescence intensity to plasma membrane average fluorescence intensity. The values represent the means ± SEM ($n = 60$ cells per genotype. $^*P < 0.05$; $^{**}P < 0.01$; Student's two-tailed *t*-test).

that the freezing sensitivity of *adf5 cbfs* was closer to *adf5-1* under NA conditions (**Figure 4A**). Under this condition, the ion leakage of *adf5 cbfs* was higher than *adf5-1*, and the difference was statistically significant (**Figure 4D**). These results suggested that ADF5 promotes the freezing resistance of *Arabidopsis thaliana* via a non-CBF pathway. Under CA conditions, CBFs are the core transcription factors of the cold response pathway, and there are many downstream induced genes. The *adf5 cbfs* primarily showed the freezing sensitivity and physiological characteristics of *cbfs-1* (**Figures 4A,E**). In summary, ADF5 promotes freezing resistance in *Arabidopsis thaliana* partially via the CBF signaling pathway. Moreover, transcriptome data clearly showed that some non-CBF-dependent ABPs were cold regulated (Jia et al., 2016; Zhao C. et al., 2016). For example, *AtFH16* was downregulated, and *FIM4* and *CROLIN* were up-regulated (Jia et al., 2013; Wang J. et al., 2013; Ding et al., 2018). Therefore, coordination of actin cytoskeleton dynamics is an important plant cell process under low-temperature stress.

Membrane vesicle transport is a conserved basic cell process in eukaryotes, and it plays an important role in the plant response to stress. Under stress, it is responsible for the correct sorting and positioning of specific proteins and the stress response (Rosquete and Drakakaki, 2018; Wang et al., 2020). For example, low temperature reduces the intracellular transport of auxin transporters PIN2 and PIN3, which affects auxin transport and changes the gravitropism of roots (Shibasaki et al., 2009). Recent studies also showed that stable GNOM ARF-GEF-mediated endosomal trafficking helped *Arabidopsis* adapt to low temperature (Ashraf and Rahman, 2019). The cryoprotective protein RCl2A also depends on clathrin-mediated endocytosis (Wang C. et al., 2013), and the transport of its homologous protein RCI2B at low temperature is selectively regulated to maintain a normal transport rate (Shibasaki et al., 2009). The actin cytoskeleton plays an important role in endocytosis and intracellular transport (Šamaj et al., 2004; Kim et al., 2005). Previous studies showed that BRI1 and CRPK1 were essential for the regulation of plant freezing resistance (Liu et al., 2017; Unterholzner et al., 2017). BRI1 is internalized by clathrin and sorted by the SYP61/VHA-a1 endosomal compartment, which also sorts the auxin transporters PIN2 and AUX1(Robert et al., 2008). This process requires coordination of the actin cytoskeleton (Lanza et al., 2012; Arieti and Staiger, 2020). The number of actin cytoskeletons decreased in the rice *vln2* mutant, and the polarity distribution and cycle of PIN2 changed (Wu et al., 2015). FH5-regulated actin cytoskeleton polymerization and elongation processes are necessary for the movement of FH5-labeled vesicles in *Arabidopsis* pollen tubes (Liu C. et al., 2018). Therefore, the actin cytoskeleton is very important for the integrity of the endocytosis and sorting processes, which ultimately affects the correct positioning and distribution of endocytic cargos and the plant response to stress. However, the processes of vesicle transport and sorting controlled by the actin cytoskeleton under low temperature are rarely reported.

The present study showed that the morphology of the actin cytoskeleton in WT was relatively stable consistent with previous reports (Shibasaki et al., 2009; **Figure 5**), and its endocytosis rate was reduced during low-temperature treatment (**Figure 6**), which may be related to the slowing of molecular thermal movement at low temperature. However, the endocytosis rate in *adf5-1* had a greater reduction than WT at 6 h, which may be related to the disorder of the *adf5-1* actin cytoskeleton (**Figures 5, 6**). The endocytosis rate of *cbfs-1* and *adf5 cbfs* continuously decreased significantly compared to WT at low temperature (**Figure 6**), which may be due to the influence of their disturbed actin cytoskeleton and additional regulatory pathways regulated downstream of CBFs. In summary, the damaged actin cytoskeleton of mutants changes the endocytosis rate during cold acclimation and the change in the endocytosis rate is not consistent with WT, in which the distribution, recovery and sorting of receptors and cryoprotective substances on the plasma membrane are directly changed. Therefore, the cold acclimation process of mutants is affected, and the freezing resistance of mutants is reduced.

METHODS

Plant Materials and Growth Conditions

Arabidopsis seeds were vernalized for 3 days at 4°C with 2% PPM-Preservative (Plant Cell Technology) and grown on half-strength Murashige and Skoog medium (MS, PhytoTech M519) containing 0.8% agar and 1.5% sucrose for 12–15 days at 22°C with an optical density of 80–100 μmol m^{-2} s^{-1} under a 16 h light/8 h dark LD photoperiod. *Arabidopsis thaliana* Col-0 and *Nicotiana benthamiana* were used in this experiment. Mutants *adf5-1* (Salk_018325) and *adf5-2* (SALK_030145) were obtained from the *Arabidopsis* Biological Resource Center. *adf5-3* was obtained using two specific Cas9-cleaved targets of *ADF5* to mutate Col-0, and this method was obtained from the report (Xing et al., 2014). The *cbf3*, *cbf1 cbf3, cbfs-1*, and Col/*pSuper::CBF3-Myc* were obtained from the Prof. Shuhua Yang Laboratory (China Agricultural University) (Jia et al., 2016; Liu et al., 2017). The *adf5 cbfs* was obtained by crossing *adf5-1* with *cbfs-1*. The primers used to identify homozygous lines and for CRISPR are listed in **Supplementary Table 1**. The materials for ion leakage measurements were grown on MS plates containing 1% agar for 5–7 days, transferred to soil, then grown at 23°C, 16 h light/8 h dark LD photoperiod to an optical density of ∼100 μmol m^{-2} s^{-1} and relative humidity of 60% for 3 weeks. *Nicotiana benthamiana* had similar growth conditions.

Freezing Tolerance and Ion Leakage Assays

This experiment was performed according to the protocol described previously (Shi et al., 2012). Briefly, 12 to 15-day-old seedlings were used to obtain phenotypes by freezing treatment. For cold acclimation (CA) treatment, the normally growing seedlings were grown at 4°C for an additional 3 days at a light density of ∼25 μmol m^{-2} s^{-1}, 16 h light/8 h dark LD photoperiod and transferred to the freezing incubator (PERCIVAL, LT-36VLC8) for treatment according to the following procedure. The seedlings were kept at 0°C for 1 h, then decreased by 1°C per hour until the temperature shown in the figure was maintained for the corresponding times. Non-cold-acclimation (NA) processing was directly performed according to a program. After freezing treatment, the seedlings were shifted to 4°C, kept in darkness for 12 h, and transferred to a normal growth environment for growth recovery for 3–5 days. The survival rate was obtained by calculating the proportion of seedlings that grew new leaves.

Ion leakage assays was performed as described (Guo et al., 2002). Briefly, seedlings grown for 3 weeks in soil were treated for ion leakage analyses with or without cold acclimation (4°C for 3 d). A fully and well-developed rosette leaf was washed with deionized water, and placed in the bottom of a 15-mL sterile centrifuge tube containing 100 μL deionized water, then placed in a low-temperature circulator (SCIENTZ, DC-2030). After holding at 0°C for 30 min, a small amount of tiny and pure ice crystal was added to the centrifuge tube, and the temperature was reduced by 1°C per 30 min until the temperature shown in the figure and maintained for 1 h. The centrifuge tube was removed and kept in darkness at 4°C for 12 h. Then, 10 mL of deionized water was added to the sterile tube, and the tubes were shaken at normal temperature for 2 h. The electrical conductivity S1 was measured. After sterilization at 121°C for 15 min, S2 conductivity was measured after shaking for 2 h. The S0 conductivity of deionized water used in the experiment, and the conductivity $S0'$ after sterilization was measured. The ratio of S1–S0 to S2–$S0'$ was used as the ion leakage.

RNA Extraction and Real-Time Quantitative PCR Analysis

Seedlings grown in a normal environment for 10 days on MS plates containing 1% agar were used for gene expression analyses with or without treatment at 4°C. Total RNA was extracted using a MiniBEST Plant RNA Extraction kit (TaKaRa), and total RNA was reverse transcribed into cDNA using M-MLV reverse transcriptase (TaKaRa). qRT-PCR was performed using SYBR Premix Ex Taq (TaKaRa), and *UBQ10* was used as an internal reference gene. The primers used for qRT-PCR are listed in **Supplementary Table 1**.

Yeast One-Hybrid Assays

Yeast one-hybrid (Y1H) assays were performed as described previously (Qian et al., 2019). Briefly, the *ADF5* promoter containing the CRT/DRE DNA regulatory element was amplified using PCR and cloned into the pAbAi vector. The CRT/DRE mutation sequence was obtained using specific primers and cloned into the pAbAi vector. The vector was linearized and transformed into the Y1H GOLD (Clontech) strain. The full-length *CBF* coding sequence was amplified using PCR, cloned into the pGADT7 vector, and transformed into the constructed Y1H strain. Aureobasidin A (AbA, 850 ng/mL, Clontech) was used for the reporter gene activation test. The primers used to clone are listed in **Supplementary Table 1**.

Transcriptional Activation Assays

This experiment was performed as described previously (Qian et al., 2019). PCR amplified and cloned the *ADF5* promoter sequence into pGWB235-LUC to construct the reporter vector. The full-length *CBF3* coding sequence was amplified using PCR, and it was cloned into the pBIB-35s-GWR-flag vector as the effect vector. The reporter and effector vectors were co-transformed into *N. benthamiana* leaves for transcriptional activation analyses. A reporting vector alone was used as a negative control. Fluorescence of the luciferase and luciferin (Promega) reaction was obtained using a Lumazone CA1300B camera (Photometrics). The primers used to clone are listed in **Supplementary Table 1**.

Chromatin Immunoprecipitation Assays

Under normal growth conditions, seedlings grown on 1% agar MS plates for 12 days were used in this experiment. The seedlings of Col/*pSuper::CBF3-Myc* and Col-0 (without Myc-tag, as negative control) were treated at 4°C or not, and a ChIP experiment was performed according to a previously described method (Ni et al., 2009). The relative enrichment of the *ADF5* promoter region was detected by qRT-PCR

using specific primers. The specific primers are listed in **Supplementary Table 1**.

Visualization of Actin Filaments by Confocal Laser Scanning Microscopy and Quantitative Analyses of Actin Filament

To visualize the actin cytoskeleton, we crossed Col-0/*pUBQ10::ABD2-GFP* (Tian et al., 2015) with *adf5-1*, *cbfs-1*, and *adf5 cbfs* and expressed ABD2-GFP in mutants for GFP fluorescence collection. Under normal growth conditions, seedlings grown on 1% agar MS plates for 5 days were treated with or without 4°C for the duration shown in the figure for fluorescence acquisition. Images of epidermal cells from root transition and elongation zone were acquired using a spinning disk microscope (Andor) equipped with a 63× NA oil immersion lens, and the Z-series images were captured with the step size set at 0.5 μm (Zhou et al., 2020). GFP was excited with a 488-nm laser and observed using a 514-nm emission filter. Images were processed and analyzed using ImageJ. To measure the extra actin cytoskeleton structure, the percentage of occupancy (density) and skewness were measured using ImageJ software as previously described (Higaki et al., 2010; Henty et al., 2011).

FM4-64 Labeling and Endocytosis Measurements

Under normal growth conditions, the seedlings growing on 1% agar MS plates for 5 days were treated with or without 4°C for different times then used in this experiment. Seedlings were held on ice for 2 min with 2 μM FM4-64 and stained at 22 or 4°C for an additional 5 min. After FM4-64 washout, dye internalization was imaged using a Zeiss LSM880 confocal microscope equipped with 40 × 1.3 NA oil immersion lens. FM4-64 signals were excited with a 488-nm laser and observed using a 600 to 630-nm emission filter. The endocytosis rate was measured and calculated in ImageJ software as previously described (Zhang et al., 2020).

DATA AVAILABILITY STATEMENT

The raw data supporting the conclusions of this article will be made available by the authors, without undue reservation.

AUTHOR CONTRIBUTIONS

YuN conceived the study and designed the research. PZ, DQ, CL, YiN, TL, and CL performed the research. PZ, DQ, CL, YX, XW, and YiN analyzed the data. PZ, YuN, YX, and DQ wrote the manuscript.

FUNDING

This work was supported by grants from the National Natural Science Foundation of China (31722005 and 31670180).

ACKNOWLEDGMENTS

We thank Professor Qijun Chen (China Agricultural University) for sharing CRISPR/Cas9 vector. We thank Professor Shuhua Yang (China Agricultural University) for sharing the *cbf* related mutants. We thank the Core Facility of the School of Life Sciences, Lanzhou University for technical assistance.

SUPPLEMENTARY MATERIAL

The Supplementary Material for this article can be found online at: https://www.frontiersin.org/articles/10.3389/fcell.2021.635533/full#supplementary-material

REFERENCES

Andrianantoandro, E., and Pollard, T. D. (2006). Mechanism of actin filament turnover by severing and nucleation at different concentrations of ADF/Cofilin. *Mol. Cell* 24, 13–23. doi: 10.1016/j.molcel.2006.08.006

Arieti, R. S., and Staiger, C. J. (2020). Auxin-induced actin cytoskeleton rearrangements require AUX1. *New Phytol.* 226, 441–459. doi: 10.1111/nph.16382

Ashraf, M. A., and Rahman, A. (2019). Cold stress response in *Arabidopsis thaliana* is mediated by GNOM ARF-GEF. *Plant J.* 97, 500–516. doi: 10.1111/tpj.14137

Baluška, F., Hlavacka, A., Šamaj, J., Palme, K., Robinson, D. G., Matoh, T., et al. (2002). F-actin-dependent endocytosis of cell wall pectins in meristematic root cells. Insights from brefeldin A-induced compartments. *Plant Physiol.* 130, 422–431. doi: 10.1104/pp.007526

Bou Daher, F., Van Oostende, C., and Geitmann, A. (2011). Spatial and temporal expression of actin depolymerizing factors ADF7 and ADF10 during male gametophyte development in *Arabidopsis thaliana*. *Plant Cell Physiol.* 52, 1177–1192. doi: 10.1093/pcp/pcr068

Bremer, A., Wolff, M., Thalhammer, A., and Hincha, D. K. (2017). Folding of intrinsically disordered plant LEA proteins is driven by glycerol-induced crowding and the presence of membranes. *FEBS J.* 284, 919–936. doi: 10.1111/febs.14023

Burgos-Rivera, B., Ruzicka, D. R., Deal, R. B., McKinney, E. C., King-Reid, L., and Meagher, R. B. (2008). Actin depolymerizing factor9 controls development and gene expression in *Arabidopsis*. *Plant Mol. Biol.* 68, 619–632. doi: 10.1007/s11103-008-9398-1

Chen, C. Y., Wong, E. I., Vidali, L., Estavillo, A., Hepler, P. K., Wu, H. M., et al. (2002). The regulation of actin organization by actin-depolymerizing factor in elongating pollen tubes. *Plant Cell* 14, 2175–2190. doi: 10.1105/tpc.003038

Chen, C. Y. H., Cheung, A. Y., and Wu, H. M. (2003). Actin-depolymerizing factor mediates Rac/Rop GTPase-regulated pollen tube growth. *Plant Cell* 15, 237–249. doi: 10.1105/tpc.007153

Chinnusamy, V., Zhu, J., and Zhu, J. K. (2007). Cold stress regulation of gene expression in plants. *Trends Plant Sci.* 12, 444–451. doi: 10.1016/j.tplants.2007.07.002

Clément, M., Ketelaar, T., Rodiuc, N., Banora, M. Y., Smertenko, A., Engler, G., et al. (2009). Actin-depolymerizing factor2-mediated actin dynamics are essential for root-knot nematode infection of *Arabidopsis*. *Plant Cell* 21, 2963–2979. doi: 10.1105/tpc.109.069104

Danyluk, J., Carpentier, E., and Sarhan, F. (1996). Identification and characterization of a low temperature regulated gene encoding an actin-binding protein from wheat. *FEBS Lett.* 389, 324–327. doi: 10.1016/0014-5793(96)00599-6

Das, T. M., Hildebrandt, A. C., and Riker, A. J. (1966). Cine-photomicrography of low temperature effects on cytoplasmic streaming, nucleolar activity and mitosis in single tobacco cells in microculture. *Am. J. Bot.* 53, 253–259. doi: 10.1002/j.1537-2197.1966.tb07331.x

Ding, X., Zhang, S., Liu, J., Liu, S., and Su, H. (2018). *Arabidopsis* FIM4 and FIM5 regulates the growth of root hairs in an auxin-insensitive way. *Plant Signal. Behav.* 13:e1473667. doi: 10.1080/15592324.2018.1473667

Ding, Y., Shi, Y., and Yang, S. (2019). Advances and challenges in uncovering cold tolerance regulatory mechanisms in plants. *New Phytol.* 222, 1690–1704. doi: 10.1111/nph.15696

Dolferus, R. (2014). To grow or not to grow: a stressful decision for plants. *Plant Sci.* 229, 247–261. doi: 10.1016/j.plantsci.2014.10.002

Dong, C. H., Xia, G. X., Hong, Y., Ramachandran, S., Kost, B., and Chua, N. H. (2001). ADF proteins are involved in the control of flowering and regulate F-actin organization, cell expansion, and organ growth in *Arabidopsis*. *Plant Cell* 13, 1333–1346. doi: 10.1105/TPC.010051

Fan, T. T., Ni, J. J., Dong, W. C., An, L. Z., Xiang, Y., and Cao, S. Q. (2015). Effect of low temperature on *profilins* and *ADFs* transcription and actin cytoskeleton reorganization in *Arabidopsis*. *Biol. Plant* 59, 793–796. doi: 10.1007/s10535-015-0546-6

Fu, Y., Duan, X., Tang, C., Li, X., Voegele, R. T., Wang, X., et al. (2014). TaADF7, an actin-depolymerizing factor, contributes to wheat resistance against *Puccinia striiformis* f. *sp. tritici*. *Plant J.* 78, 16–30. doi: 10.1111/tpj.12457

Gilmour, S. J., Zarka, D. G., Stockinger, E. J., Salazar, M. P., Houghton, J. M., and Thomashow, M. F. (1998). Low temperature regulation of the *Arabidopsis* CBF family of AP2 transcriptional activators as an early step in cold-induced *COR* gene expression. *Plant J.* 16, 433–442. doi: 10.1046/j.1365-313x.1998.00310.x

Guo, Y., Xiong, L., Ishitani, M., and Zhu, J. K. (2002). An *Arabidopsis* mutation in translation elongation factor 2 causes superinduction of *CBF/DREB1* transcription factor genes but blocks the induction of their downstream targets under low temperatures. *Proc. Natl. Acad. Sci. U.S.A.* 99, 7786–7791. doi: 10.1073/pnas.112040099

Henty, J. L., Bledsoe, S. W., Khurana, P., Meagher, R. B., Day, B., Blanchoin, L., et al. (2011). *Arabidopsis* actin depolymerizing factor4 modulates the stochastic dynamic behavior of actin filaments in the cortical array of epidermal cells. *Plant Cell* 23, 3711–3726. doi: 10.1105/tpc.111.090670

Higaki, T., Kutsuna, N., Sano, T., Kondo, N., and Hasezawa, S. (2010). Quantification and cluster analysis of actin cytoskeletal structures in plant cells: role of actin bundling in stomatal movement during diurnal cycles in *Arabidopsis* guard cells. *Plant J.* 61, 156–165. doi: 10.1111/j.1365-313X.2009.04032.x

Hussey, P. J., Allwood, E. G., and Smertenko, A. P. (2002). Actin-binding proteins in the *Arabidopsis* genome database: properties of functionally distinct plant actin-depolymerizing factors/cofilins. *Philos. Trans. R. Soc. B Biol. Sci.* 357, 791–798. doi: 10.1098/rstb.2002.1086

Inada, N., Higaki, T., and Hasezawa, S. (2016). Nuclear function of subclass I actin-depolymerizing factor contributes to susceptibility in *Arabidopsis* to an adapted powdery mildew fungus. *Plant Physiol.* 170, 1420–1434. doi: 10.1104/pp.15.01265

Jaglo-Ottosen, K. R., Gilmour, S. J., Zarka, D. G., Schabenberger, O., and Thomashow, M. F. (1998). *Arabidopsis CBF1* overexpression induces *COR* genes and enhances freezing tolerance. *Science* 280, 104–106. doi: 10.1126/science.280.5360.104

Janmohammadi, M., Zolla, L., and Rinalducci, S. (2015). Low temperature tolerance in plants: changes at the protein level. *Phytochemistry* 117, 76–89. doi: 10.1016/j.phytochem.2015.06.003

Jia, H., Li, J., Zhu, J., Fan, T., Qian, D., Zhou, Y., et al. (2013). *Arabidopsis* CROLIN1, a novel plant actin-binding protein, functions in cross-linking and stabilizing actin filaments. *J. Biol. Chem.* 288, 32277–32288. doi: 10.1074/jbc.M113.483594

Jia, Y., Ding, Y., Shi, Y., Zhang, X., Gong, Z., and Yang, S. (2016). The *cbfs* triple mutants reveal the essential functions of *CBFs* in cold acclimation and allow the definition of CBF regulons in *Arabidopsis*. *New Phytol.* 212, 345–353. doi: 10.1111/nph.14088

Jiang, Y., Wang, J., Xie, Y., Chen, N., and Huang, S. (2017). ADF10 shapes the overall organization of apical actin filaments by promoting their turnover and ordering in pollen tubes. *J. Cell Sci.* 130, 3988–4001. doi: 10.1242/jcs.207738

Kim, H., Park, M., Kim, S. J., and Hwang, I. (2005). Actin filaments play a critical role in vacuolar trafficking at the Golgi complex in plant cells. *Plant Cell* 17, 888–902. doi: 10.1105/tpc.104.028829

Lanza, M., Garcia-Ponce, B., Castrillo, G., Catarecha, P., Sauer, M., Rodriguez-Serrano, M., et al. (2012). Role of actin cytoskeleton in brassinosteroid signaling and in its integration with the auxin response in plants. *Dev. Cell* 22, 1275–1285. doi: 10.1016/j.devcel.2012.04.008

Lin, C., and Thomashow, M. F. (1992). DNA sequence analysis of a complementary DNA for cold-regulated *Arabidopsis* Gene *cor15* and characterization of the COR15 polypeptide. *Plant Physiol.* 99, 519–525. doi: 10.1104/pp.99.2.519

Liu, C., Zhang, Y., and Ren, H. (2018). Actin polymerization mediated by AtFH5 directs the polarity establishment and vesicle trafficking for pollen germination in *Arabidopsis*. *Mol. Plant* 11, 1389–1399. doi: 10.1016/j.molp.2018.09.004

Liu, J., Shi, Y., and Yang, S. (2018). Insights into the regulation of C-repeat binding factors in plant cold signaling. *J. Integr. Plant Biol.* 60, 780–795. doi: 10.1111/jipb.12657

Liu, Q., Kasuga, M., Sakuma, Y., Abe, H., Miura, S., Yamaguchi-Shinozaki, K., et al. (1998). Two transcription factors, DREB1 and DREB2, with an EREBP/AP2 DNA binding domain separate two cellular signal transduction pathways in drought- and low-temperature-responsive gene expression, respectively, in *Arabidopsis*. *Plant Cell* 10, 1391–1406. doi: 10.1105/tpc.10.8.1391

Liu, Z., Jia, Y., Ding, Y., Shi, Y., Li, Z., Guo, Y., et al. (2017). Plasma membrane CRPK1-mediated phosphorylation of 14-3-3 proteins induces their nuclear import to fine-tune CBF signaling during cold response. *Mol. Cell* 66, 117–128.e5. doi: 10.1016/j.molcel.2017.02.016

Medina, J., Bargues, M., Terol, J., Pérez-Alonso, M., and Salinas, J. (1999). The *Arabidopsis CBF* gene family is composed of three genes encoding AP2 domain-containing proteins whose expression is regulated by low temperature but not by abscisic acid or dehydration. *Plant Physiol.* 119, 463–469. doi: 10.1104/pp.119.2.463

Mondal, H. A., Louis, J., Archer, L., Patel, M., Nalam, V. J., Sarowar, S., et al. (2018). *Arabidopsis ACTIN-DEPOLYMERIZING FACTOR*$_3$ is required for controlling aphid feeding from the phloem. *Plant Physiol.* 176, 879–890. doi: 10.1104/pp.17.01438

Nan, Q., Qian, D., Niu, Y., He, Y., Tong, S., Niu, Z., et al. (2017). Plant actin-depolymerizing factors possess opposing biochemical properties arising from key amino acid changes throughout evolution. *Plant Cell* 29, 395–408. doi: 10.1105/tpc.16.00690

Ni, Z., Kim, E.-D., Ha, M., Lackey, E., Liu, J., Zhang, Y., et al. (2009). Altered circadian rhythms regulate growth vigour in hybrids and allopolyploids. *Nature* 457, 327–331. doi: 10.1038/nature07523

Ouellet, F., Carpentier, E., Cope, M. J. T. V., Monroy, A. F., and Sarhan, F. (2001). Regulation of a wheat actin-depolymerizing factor during cold acclimation. *Plant Physiol.* 125, 360–368. doi: 10.1104/pp.125.1.360

Park, S., Lee, C. M., Doherty, C. J., Gilmour, S. J., Kim, Y., and Thomashow, M. F. (2015). Regulation of the *Arabidopsis* CBF regulon by a complex low-temperature regulatory network. *Plant J.* 82, 193–207. doi: 10.1111/tpj.12796

Pokorná, J., Schwarzerová, K., Zelenková, S., Petrášek, J., Janotová, I., Capková, V., et al. (2004). Sites of actin filament initiation and reorganization in cold-treated tobacco cells. *Plant Cell Environ.* 27, 641–653. doi: 10.1111/j.1365-3040.2004.01186.x

Porter, K., Shimono, M., Tian, M., and Day, B. (2012). *Arabidopsis* actin-depolymerizing factor-4 links pathogen perception, defense activation and transcription to cytoskeletal dynamics. *PLoS Pathog.* 8:e1003006. doi: 10.1371/journal.ppat.1003006

Qian, D., and Xiang, Y. (2019). Actin cytoskeleton as actor in upstream and downstream of calcium signaling in plant cells. *Int. J. Mol. Sci.* 20:1403. doi: 10.3390/ijms20061403

Qian, D., Zhang, Z., He, J., Zhang, P., Ou, X., Li, T., et al. (2019). *Arabidopsis* ADF5 promotes stomatal closure by regulating actin cytoskeleton remodeling in response to ABA and drought stress. *J. Exp. Bot.* 70, 435–446. doi: 10.1093/jxb/ery385

Robert, S., Chary, S. N., Drakakaki, G., Li, S., Yang, Z., Raikhel, N. V., et al. (2008). Endosidin1 defines a compartment involved in endocytosis of the brassinosteroid receptor BRI1 and the auxin transporters PIN2 and AUX1. *Proc. Natl. Acad. Sci. U.S.A.* 105, 8464–8469. doi: 10.1073/pnas.0711650105

Rosquete, M. R., and Drakakaki, G. (2018). Plant TGN in the stress response: a compartmentalized overview. *Curr. Opin. Plant Biol.* 46, 122–129. doi: 10.1016/j.pbi.2018.09.003

Ruzicka, D. R., Kandasamy, M. K., McKinney, E. C., Burgos-Rivera, B., and Meagher, R. B. (2007). The ancient subclasses of *Arabidopsis ACTIN DEPOLYMERIZING FACTOR* genes exhibit novel and differential expression. *Plant J.* 52, 460–472. doi: 10.1111/j.1365-313X.2007.03257.x

Šamaj, J., Baluška, F., Voigt, B., Schlicht, M., Volkmann, D., and Menzel, D. (2004). Endocytosis, actin cytoskeleton, and signaling. *Plant Physiol.* 135, 1150–1161. doi: 10.1104/pp.104.040683

Shi, Y., Ding, Y., and Yang, S. (2018). Molecular regulation of CBF signaling in cold acclimation. *Trends Plant Sci.* 23, 623–637. doi: 10.1016/j.tplants.2018.04.002

Shi, Y., Tian, S., Hou, L., Huang, X., Zhang, X., Guo, H., et al. (2012). Ethylene signaling negatively regulates freezing tolerance by repressing expression of *CBF* and type-A *ARR* genes in *Arabidopsis*. *Plant Cell* 24, 2578–2595. doi: 10.1105/tpc.112.098640

Shibasaki, K., Uemura, M., Tsurumi, S., and Rahman, A. (2009). Auxin response in *Arabidopsis* under cold stress: underlying molecular mechanisms. *Plant Cell* 21, 3823–3838. doi: 10.1105/tpc.109.069906

Staiger, C. J. (2000). Signaling to the actin cytoskeleton in plants. *Annu. Rev. Plant Biol.* 51, 257–288. doi: 10.1146/annurev.arplant.51.1.257

Staiger, C. J., and Blanchoin, L. (2006). Actin dynamics: old friends with new stories. *Curr. Opin. Plant Biol.* 9, 554–562. doi: 10.1016/j.pbi.2006.09.013

Staiger, C. J., Gibbon, B. C., Kovar, D. R., and Zonia, L. E. (1997). Profilin and actin-depolymerizing factor: modulators of actin organization in plants. *Trends Plant Sci.* 2, 275–281. doi: 10.1016/S1360-1385(97)86350-9

Stockinger, E. J., Gilmour, S. J., and Thomashow, M. F. (1997). *Arabidopsis thaliana CBF1* encodes an AP2 domain-containing transcriptional activator that binds to the C-repeat/DRE, a cis-acting DNA regulatory element that stimulates transcription in response to low temperature and water deficit. *Proc. Natl. Acad. Sci. U.S.A.* 94, 1035–1040. doi: 10.1073/pnas.94.3.1035

Tholl, S., Moreau, F., Hoffmann, C., Arumugam, K., Dieterle, M., Moes, D., et al. (2011). *Arabidopsis* actin-depolymerizing factors (ADFs) 1 and 9 display antagonist activities. *FEBS Lett.* 585, 1821–1827. doi: 10.1016/j.febslet.2011.05.019

Thomashow, M. F. (1999). Plant cold acclimation: freezing tolerance genes and regulatory mechanisms. *Annu. Rev. Plant Biol.* 50, 571–599. doi: 10.1146/annurev.arplant.50.1.571

Tian, J., Han, L., Feng, Z., Wang, G., Liu, W., Ma, Y., et al. (2015). Orchestration of microtubules and the actin cytoskeleton in trichome cell shape determination by a plant-unique kinesin. *Elife* 4:e09351. doi: 10.7554/eLife.09351

Tian, M., Chaudhry, F., Ruzicka, D. R., Meagher, R. B., Staiger, C. J., and Day, B. (2009). *Arabidopsis* actin-depolymerizing factor AtADF4 mediates defense signal transduction triggered by the *Pseudomonas syringae* effector AvrPphB1. *Plant Physiol.* 150, 815–824. doi: 10.1104/pp.109.137604

Unterholzner, S. J., Rathnayake, A. I., Khan, M., Kugler, K. G., May, S. T., Mayer, K. F. X., et al. (2017). Brassinosteroids participate in the control of basal and acquired freezing tolerance of plants. *Proc. Natl. Acad. Sci. U.S.A.* 114, E1038–E1089. doi: 10.1073/pnas.1700593114

Wang, C., Yan, X., Chen, Q., Jiang, N., Fu, W., Ma, B., et al. (2013). Clathrin light chains regulate clathrin-mediated trafficking, auxin signaling, and development in *Arabidopsis*. *Plant Cell* 25, 499–516. doi: 10.1105/tpc.112.108373

Wang, J., Zhang, Y., Wu, J., Meng, L., and Ren, H. (2013). At FH16, an *Arabidopsis* type II formin, binds and bundles both microfilaments and microtubules, and preferentially binds to microtubules. *J. Integr. Plant Biol.* 55, 1002–1015. doi: 10.1111/jipb.12089

Wang, X., Xu, M., Gao, C., Zeng, Y., Cui, Y., Shen, W., et al. (2020). The roles of endomembrane trafficking in plant abiotic stress responses. *J. Integr. Plant Biol.* 62, 55–69. doi: 10.1111/jipb.12895

Wu, S., Xie, Y., Zhang, J., Ren, Y., Zhang, X., Wang, J., et al. (2015). VLN2 regulates plant architecture by affecting microfilament dynamics and polar auxin transport in rice. *Plant Cell.* 27, 2829–2845. doi: 10.1105/tpc.15.00581

Xing, H. L., Dong, L., Wang, Z. P., Zhang, H. Y., Han, C. Y., Liu, B., et al. (2014). A CRISPR/Cas9 toolkit for multiplex genome editing in plants. *BMC Plant Biol.* 14:327. doi: 10.1186/s12870-014-0327-y

Ye, K., Li, H., Ding, Y., Shi, Y., Song, C., Gong, Z., et al. (2019). BRASSINOSTEROID-INSENSITIVE2 negatively regulates the stability of transcription factor ICE1 in response to cold stress in *Arabidopsis*. *Plant Cell* 31, 2682–2696. doi: 10.1105/tpc.19.00058

Zhang, J., Li, X. M., Lin, H. X., and Chong, K. (2019). Crop improvement through temperature resilience. *Annu. Rev. Plant Biol.* 70, 753–780. doi: 10.1146/annurev-arplant-050718-100016

Zhang, X., Adamowski, M., Marhava, P., Tan, S., Zhang, Y., Rodriguez, L., et al. (2020). *Arabidopsis* flippases cooperate with ARF GTPase exchange factors to regulate the trafficking and polarity of PIN auxin transporters. *Plant Cell* 32, 1644–1664. doi: 10.1105/tpc.19.00869

Zhao, C., Zhang, Z., Xie, S., Si, T., Li, Y., and Zhu, J. K. (2016). Mutational evidence for the critical role of CBF transcription factors in cold acclimation in *Arabidopsis*. *Plant Physiol.* 171, 2744–2759. doi: 10.1104/pp.16.00533

Zhao, S., Jiang, Y., Zhao, Y., Huang, S., Yuan, M., Zhao, Y., et al. (2016). CASEIN KINASE1-LIKE PROTEIN2 regulates actin filament stability and stomatal closure via phosphorylation of actin depolymerizing factor. *Plant Cell* 28, 1422–1439. doi: 10.1105/tpc.16.00078

Zheng, Y., Xie, Y., Jiang, Y., Qu, X., and Huang, S. (2013). *Arabidopsis* ACTIN-DEPOLYMERIZING FACTOR7 severs actin filaments and regulates actin cable turnover to promote normal pollen tube growth. *Plant Cell* 25, 3405–3423. doi: 10.1105/tpc.113.117820

Zhou, Y., Yang, Y., Niu, Y., Fan, T., Qian, D., Luo, C., et al. (2020). The tip-localized phosphatidylserine established by *Arabidopsis* ALA3 is crucial for Rab GTPase-mediated vesicle trafficking and pollen tube growth. *Plant Cell* 32, 3170–3187. doi: 10.1105/tpc.19.00844

Zhu, J., Nan, Q., Qin, T., Qian, D., Mao, T., Yuan, S., et al. (2017). Higher-ordered actin structures remodeled by *Arabidopsis* ACTIN-DEPOLYMERIZING FACTOR5 are important for pollen germination and pollen tube growth. *Mol. Plant* 10, 1065–1081. doi: 10.1016/j.molp.2017.06.001

Conflict of Interest: The authors declare that the research was conducted in the absence of any commercial or financial relationships that could be construed as a potential conflict of interest.

frontiers in Cell and Developmental Biology

ORIGINAL RESEARCH
published: 09 February 2021
doi: 10.3389/fcell.2021.634587

Bil2 Is a Novel Inhibitor of the Yeast Formin Bnr1 Required for Proper Actin Cable Organization and Polarized Secretion

*Thomas J. Rands and Bruce L. Goode**

Department of Biology, Rosenstiel Basic Medical Sciences Research Center, Brandeis University, Waltham, MA, United States

Cell growth in budding yeast depends on rapid and on-going assembly and turnover of polarized actin cables, which direct intracellular transport of post-Golgi vesicles to the bud tip. *Saccharomyces cerevisiae* actin cables are polymerized by two formins, Bni1 and Bnr1. Bni1 assembles cables in the bud, while Bnr1 is anchored to the bud neck and assembles cables that specifically extend filling the mother cell. Here, we report a formin regulatory role for YGL015c, a previously uncharacterized open reading frame, which we have named *Bud6 Interacting Ligand 2* (*BIL2*). *bil2*Δ cells display defects in actin cable architecture and partially-impaired secretory vesicle transport. Bil2 inhibits Bnr1-mediated actin filament nucleation *in vitro*, yet has no effect on the rate of Bnr1-mediated filament elongation. This activity profile for Bil2 resembles that of another yeast formin regulator, the F-BAR protein Hof1, and we find that *bil2*Δ with *hof1*Δ are synthetic lethal. Unlike Hof1, which localizes exclusively to the bud neck, GFP-Bil2 localizes to the cytosol, secretory vesicles, and sites of polarized cell growth. Further, we provide evidence that Hof1 and Bil2 inhibitory effects on Bnr1 are overcome by distinct mechanisms. Together, our results suggest that Bil2 and Hof1 perform distinct yet genetically complementary roles in inhibiting the actin nucleation activity of Bnr1 to control actin cable assembly and polarized secretion.

Keywords: actin, cable, formin, secretion, Bud6, Bni1, Bnr1, Bil2

OPEN ACCESS

Edited by:
Ting Gang Chew, Zhejiang University-University of Edinburgh Institute, China

Reviewed by:
Naomi Courtemanche, University of Minnesota Twin Cities, United States
Saravanan Palani, Indian Institute of Science (IISc), India

***Correspondence:**
Bruce L. Goode
goode@brandeis.edu

Specialty section:
This article was submitted to Cell Growth and Division, a section of the journal Frontiers in Cell and Developmental Biology

Received: *28 November 2020*
Accepted: *20 January 2021*
Published: *09 February 2021*

Citation:
Rands TJ and Goode BL (2021) Bil2 Is a Novel Inhibitor of the Yeast Formin Bnr1 Required for Proper Actin Cable Organization and Polarized Secretion. Front. Cell Dev. Biol. 9:634587. doi: 10.3389/fcell.2021.634587

INTRODUCTION

Formins are a conserved family of actin assembly-promoting proteins that perform essential roles in numerous actin-based cellular and physiological processes (Kovar, 2006; Chhabra and Higgs, 2007; Chesarone et al., 2010). Formins nucleate the assembly of new actin filaments and accelerate actin filament elongation while protecting growing barbed ends from capping proteins (Goode and Eck, 2007; Breitsprecher and Goode, 2013). Studies in yeast have led to important advances in our understanding of formin activities, mechanism, and regulation (Breitsprecher and Goode, 2013). Mammalian genomes encode 15 different formins (Higgs and Peterson, 2005), which are used to assemble a wide variety of cellular actin structures, including filopodia, stress fibers, stereocilia, and lamellipodia (Faix and Grosse, 2006). In contrast, the budding yeast *Saccharomyces cerevisiae* has just two formin genes, *BNI1* and *BNR1*, and during most stages of the cell cycle they assemble only a single actin structure, the actin cable network. The relative simplicity of the yeast system, combined with its genetic tractability, have made it a powerful model for elucidating formin regulatory mechanisms.

Bni1 and Bnr1 assemble actin cables from distinct locations in cells, the bud cortex and bud neck, respectively (Moseley and Goode, 2006). However, together they share one essential function in actin cable network assembly, which is crucial for secretory vesicle transport and polarized cell growth (Imamura et al., 1997; Evangelista et al., 2002; Sagot et al., 2002a; Gao and Bretscher, 2008). Bni1 is transiently recruited from the cytosol to the bud cortex, where it assembles cables that fill the bud compartment and extend into the mother cell. In contrast, Bnr1 is stably anchored to the bud neck, where it assembles cables that specifically extend into the mother cell (Ozaki-Kuroda et al., 2001; Pruyne et al., 2004; Buttery et al., 2007, 2012; Gao et al., 2010). Actin cables extend toward the back of the mother cell at a rate of ∼0.3–0.7 μm/sec, and are turned over at the same rate, which means that Bni1 and Bnr1 continuously nucleating and elongating cables (Yang and Pon, 2002; Yu et al., 2011). Post-Golgi secretory vesicles are transported along the cables toward the bud tip by the essential myosin V protein (Myo2) (Govindan et al., 1995; Pruyne et al., 1998). It is believed that the dynamic and constant assembly of the actin cable networks enables them to be rapidly rearranged, and for cells to reorient polarized secretion and cell growth during different stages of the cell cycle (Bi and Park, 2012) and in response to external stimuli, e.g., during the mating response (Ghose and Lew, 2020) and wound healing (Kono et al., 2012). In addition, the rearward (or 'retrograde') treadmilling of the cables provides a quality control mechanism to help keep damaged organelles and proteins, accumulated during cellular aging, out of the bud and increase the fitness of daughter cells (Higuchi et al., 2013). However, these rapid dynamics also put a constant and high demand on the system for controlling actin cable extension rates and lengths. How this regulation is achieved it not fully understood, but appears to involve actin turnover-promoting factors such as cofilin and Aip1 (Okada et al., 2006) and formin-binding proteins that modulate formin actin assembly activity.

Factors that promote yeast formin-mediated actin assembly include profilin, Bud6, Bil1, and Aip5 (Evangelista et al., 1997; Moseley et al., 2004; Graziano et al., 2013; Glomb et al., 2019; Xie et al., 2019). Bud6 directly interacts with G-actin and the C-terminal tail regions of Bni1 and Bnr1, positioning actin monomers near their actin-nucleating formin homology 2 (FH2) domains (Graziano et al., 2011). Interestingly, the Bud6-binding site (BBS) is positioned differently in Bni1 compared to Bnr1, leading to a key difference in their regulation. The BBS on Bni1 is adjacent to its C-terminal diaphanous autoregulatory domain (DAD), which is some distance from the FH2 domain (Moseley and Goode, 2005). As a result, Bud6 alone enhances Bni1-mediated actin nucleation. In contrast, the putative BBS on Bnr1 is much closer to its FH2 domain, and as a result, Bud6 alone obstructs actin nucleation by Bnr1 (Graziano et al., 2013). However, addition of Bil1, a small Bud6-binding protein, unmasks Bud6's nucleation-promoting effects on Bnr1 (Graziano et al., 2013). Thus, Bil1 is required specifically for productive interactions of Bud6 with Bnr1, but not Bni1. In addition to factors that enhance nucleation, there are a number of yeast formin-binding partners that inhibit its nucleation and/or elongation activities, including Bud14, Smy1, and Hof1 (Chesarone et al., 2009; Chesarone-Cataldo et al., 2011; Graziano et al., 2013; Eskin et al., 2016; Garabedian et al., 2018). How these different stimulatory and inhibitory inputs work in concert to tune actin cable extension rate and length *in vivo* is only beginning to be understood.

All three known formin inhibitors in yeast (Hof1, Bud14, and Smy1) regulate Bnr1, but not Bni1. Whereas Bud14 and Smy1 inhibit Bnr1-mediated actin filament elongation (Chesarone et al., 2009; Chesarone-Cataldo et al., 2011; Eskin et al., 2016), Hof1 specifically inhibits Bnr1-mediated actin nucleation and has no effects on filament elongation (Graziano et al., 2014; Garabedian et al., 2018). Hof1 is stably anchored to the septin collar at the bud neck (Kamei et al., 1998; Vallen et al., 2000), similar to Bnr1, and deletion of *HOF1* results in excessive actin assembly, leading to defects in cable orientation and vesicle transport (Graziano et al., 2014; Garabedian et al., 2018, 2020). Hof1 inhibition of Bnr1 is overcome by the nucleation-promoting factor (NPF) Bud6, which is delivered on secretory vesicles to the bud neck (Garabedian et al., 2018). This regulatory scheme of combining a stationary inhibitor (Hof1) with a mobile activator (Bud6) is thought to establish a positive feedback loop for promoting Bnr1-mediated actin cable nucleation. Biochemical experiments have elucidated parts of the underlying mechanism. A C-terminal fragment of Bud6 (489–788), called 'Bud6(L),' enhances Bnr1-mediated actin nucleation when accompanied by its *in vivo* binding partner *Bud6 Interacting Ligand 1* (Bil1) (Graziano et al., 2013). These observations, supported by additional *in vivo* evidence, suggest that Bud6 and Bil1 work together to promote Bnr1-dependent actin cable nucleation.

In the present study, we identify YGL015c, a previously uncharacterized gene product, as a novel regulator of Bnr1 activity and cellular function. YGL015c encodes a 15 kDa protein, and in earlier proteomic studies was shown to interact with Bud6 and actin (Ito et al., 2001; Yu et al., 2008). This prompted us to investigate the potential role(s) of YGL015c in regulating formins and actin cable assembly. Based on its association with Bud6, and our own observations here of YGL015c co-localization with Bud6 on secretory vesicles, we named this gene *Bud6 Interacting Ligand 2* (*BIL2*). Our biochemical and genetic results suggest that Bil2/YGL015c functions as a novel inhibitor of Bnr1-mediated actin nucleation, but not elongation, and that it shares an essential *in vivo* function with the formin regulator Hof1.

MATERIALS AND METHODS

Plasmids and Yeast Strains

A low-copy (CEN) plasmid was used to express GFP-*SEC4* in *S. cerevisiae* (Calero et al., 2003). A CEN plasmid for expressing GFP^{Envy}-*SEC4* in *S. cerevisiae* was constructed by amplification of the GFP^{Envy} sequence from plasmid pFA6a-link-Envy-spHis5 (Slubowski et al., 2015) using primers (forward 5- CAT GCT GTC GAC ATG TCT AAA GGC GAG GAA TT-3; reverse 5- CAT TAG TCT AGA TTT GTA CAA TTC GTC CAT TC-3). The GFP^{Envy} sequence was then stitched in frame with *SEC4* using SalI and XbaI sites into the above-mentioned GFP-*SEC4* plasmid.

A GFP^{Envy}-*BIL2* plasmid was constructed by PCR amplification of the *YGL015c* open reading frame using primers (forward 5-CAT TAG TCT AGA ATG GAA GAC ACG ATA CGT CC-3; reverse 5- TAC GAT CCG CGG CTA ATC ATC AGA AGT GCA GC-3). This PCR product was cloned in frame with GFP^{Envy} using XbaI and SacII sites in the GFP^{Envy}-*SEC4* plasmid above. Importantly, the sequence of the *YGL015c* open reading frame we amplified matched the sequence at the *Saccharomyces* Genome Database (SGD). A mCherry-*SEC4* plasmid was constructed by PCR amplification of the mCherry sequence using primers (forward 5-TAG TCA GTC GAC ATG GTG AGC AAG GGC GAG GA-3; reverse 5- TGC TAC TCT AGA TTA CTT GTA CAG CTC GTC CA-3). This product was cloned in frame with *SEC4*, as above, using SalI and XbaI sites. The plasmids used for galactose-inducible expression in *S. cerevisiae* of 6His-fusions of Bnr1 FH1-FH2-C (residues 757–1375) and Bnr1 FH2 (868–1291) have been described (Moseley and Goode, 2005; Okada et al., 2010; Jaiswal et al., 2013). A plasmid used for *Escherichia coli* expression of full-length 6His-Bil2 was constructed by PCR amplification of the *YGL015c* open reading frame using primers (forward 5-GAC TAG GGA TCC ATG GAA GAC ACG ATA CGT CC-3; reverse 5- TAG GAC AAG CTT CTA ATC ATC AGA AGT GCA GC-3). This PCR product was cloned in frame into the pET-28a vector using BamHI and HindIII sites. For expression of C-Bud6 in E. coli, the sequence encoding amino acids 489–788 of Bud6 was PCR amplified from genomic DNA and subcloned into pET-GST-TEV as previously described (Graziano et al., 2013).

All yeast strains used in this study are in the W303 background, with the exception of **Figure 2E**, which was in the ResGen background (see **Supplementary Table 1**). A *bil2*Δ strain (BGY4248) was generated by integration of a selectable marker into the *BIL2* locus as described (Longtine et al., 1998). To track secretory vesicles in live-imaging experiments, wildtype (BGY10) and *bil2*Δ (BGY4248) cells were transformed with pGFP^{Envy}-*SEC4*. For analyzing Bnr1-GFP levels and neck localization, we crossed a Bnr1-GFP strain (BGY962) to a *bil2*Δ strain (BGY4248). For genetic analyses, we crossed a *bil2*Δ strain (BGY4248) to *hof1*Δ (BGY4253), *bud14*Δ (BGY4259), and *bud6*Δ (BGY1249). To localizing Bud6 and Bil2 *in vivo*, we used a Bud6-mCherry strain (BGY3913) (Garabedian et al., 2018) transformed with pGFP^{Envy}-*BIL2*. For biochemical isolation of secretory vesicles, we used two different strains, one with differential tags on Bud6 and Bil2, and one with differential tags on Bil2 and Sec4, generated as follows. We crossed a *sec6-4* strain (a kind gift from Dr. Erfei Bi) to our *BUD6*-mCherry strain (BGY3913), producing *BUD6*-mCherry *sec6-4* (BGY4258), which was then transformed with pGFP^{Envy}-*BIL2*. We transformed the same *sec6-4* strain with both pGFP^{Envy}-*BIL2* and mCherry-*SEC4* plasmids.

Protein Purification

Rabbit skeletal muscle actin was purified from acetone powder (Spudich and Watt, 1971) generated from frozen ground hind leg muscle tissue of young rabbits (Pel-Freez, United States). Lyophilized acetone powder stored at −80°C was mechanically sheared in a coffee grinder, resuspended in G-buffer [5 mM Tris-HCl pH 7.5, 0.5 mM Dithiothreitol (DTT), 0.2 mM ATP and 0.1 mM $CaCl_2$], and then cleared by centrifugation for 20 min at 50,000 × *g*. Supernatant was collected and further filtered with Whatman paper. Actin was polymerized by addition of 2 mM $MgCl_2$ and 50 mM NaCl to the filtrate and overnight incubation at 4°C with slow stirring. The next morning, NaCl powder was added to a final concentration of 0.6 M, and the mixture was stirred for another 30 min at 4°C. The F-actin was pelleted by centrifugation for 150 min at 120,000 × *g*, and the pellet was solubilized by dounce homogenization and dialyzed against G-buffer for 48 h at 4°C. Monomeric actin was then precleared by centrifugation at 435,000 × *g*, and loaded onto a S200 (16/60) gel-filtration column (GE Healthcare, United States) equilibrated in G-Buffer. Peak fractions were stored at 4°C.

To biotinylate actin on cysteine 374, an F-actin pellet as above was dounced and dialyzed against G-buffer lacking DTT. Monomeric actin was then polymerized by addition of an equal volume of 2× labeling buffer (50 mM imidazole pH 7.5, 200 mM KCl, 0.3 mM ATP, and 4 mM $MgCl_2$). After 5 min, the actin was mixed with a fivefold molar excess of NHS-XX-Biotin (Merck KGaA, Germany) and incubated in the dark for 15 h at 4°C. The F-actin was pelleted as above, and the pellet was rinsed with G-buffer, then homogenized with a dounce, and dialyzed against G-buffer for 48 h at 4°C. Biotinylated monomeric actin was purified further on an S200 (16/60) gel-filtration column as above. Aliquots of biotin-actin were snap frozen in liquid N_2 and stored at −80°C.

To label actin with Oregon Green (OG) on cysteine 374, an F-actin pellet as above was dounced and dialyzed against G-buffer lacking DTT. Monomeric actin was then polymerized by addition of an equal volume of 2× labeling buffer. After 5 min, the actin was mixed with a fivefold molar excess of OG-488 iodoacetamide (Invitrogen), resuspended in anhydrous dimethylformamide, and then incubated in the dark for 15 h at 4°C. The labeled F-actin was pelleted as above, and the pellet was rinsed with G-buffer, depolymerized by Dounce homogenization, dialyzed against G-buffer for 60 h at 4°C, and applied to an S200 (16/60) gel filtration column. Peak fractions were dialyzed for 15 h against G-buffer with 50% glycerol and stored at −20°C.

To label actin with pyrenyl-iodoacetamide on cysteine 374 (Cooper et al., 1984; Graziano et al., 2013), an F-actin pellet prepared as above was dialyzed against pyrene buffer (25 mM Tris-HCl, pH 7.5, 100 mM KCl, 0.3 mM ATP, and 2 mM $MgSO_4$) for 4 h and then diluted with pyrene buffer to 1 mg/mL (23.8 μM). A 10-fold molar excess of pyrenyl-iodoacetamide was added, and the actin solution was incubated overnight at 4°C. The reaction was then centrifuged for 3 h at 4°C 150,000 × *g* in a Ti60 rotor (Beckman Coulter, Indianapolis, IN, United States) to pellet the F-actin. F-actin pellets were dounced, and dialyzed against G-buffer for 48 h to depolymerize the actin, then loaded on a S200 (16/60) column equilibrated in G-buffer. Peak fractions were pooled, aliquoted, snap frozen in liquid N_2, and stored at −80°C.

C-Bnr1 (FH1-FH2-C; 758-1375) and Bnr1-FH2 polypeptides (869–1,289) were expressed as N-terminal 6His-fusions in *S. cerevisiae* strain BJ2168 from high copy plasmids under the control of a galactose-inducible promoter (Moseley and Goode, 2006). For each purification, 2 L of yeast cells were

grown in synthetic medium lacking uracil with 2% raffinose to OD_{600} = 0.6–0.9. Then expression was induced by addition of dry ingredients: 10 g yeast extract, 20 g peptone, and galactose (2% wt/vol). Cells were grown for 12–16 h at 30°C, then pelleted, washed in H_2O, frozen dropwise in liquid N_2, and stored at −80°C. To initiate a protein preparation, frozen yeast pellets were lysed mechanically in a coffee grinder cooled with liquid N_2. Then, 20 g of lysed yeast powder was resuspended in 20 mL of buffer A (20 mM $NaPO_4$, pH 7.4, 150 mM NaCl, 30 mM imidazole, 0.5 mM DTT, 1% NP-40) supplemented with protease inhibitor cocktail as above, and cleared by ultracentrifugation at 200,000 × *g* for 20 min in a TLA100.3 rotor (Beckman Coulter). Cleared lysates were then passed through a 0.45 μm syringe filter (Millex, MilliporeSigma; Darmstadt, Germany) and the 6His-tagged Bnr1 polypeptides were incubated for 1 h at 4°C with 2 mL of Ni-NTA beads (New England Biolabs; Ipswich, MA, United States) with gentle agitation. Beads were washed three times with 10 mL wash buffer (20 mM Tris pH 8.0, 500 mM NaCl, 0.5 mM DTT, and 30 mM Imidazole), and Bnr1 polypeptides were eluted with 4 mL of elution buffer (20 mM Tris pH 8.0, 500 mM NaCl, 0.5 mM DTT, and 300 mM Imidazole). Peak fractions were pooled and loaded on a PD10 desalting column (GE Life Sciences; Marlborough, MA, United States) equilibrated with $HEKG_{10}D$ buffer (20 mM HEPES, pH 7.5, 1 mM EDTA, 50 mM KCl, 10% [vol/vol] glycerol, and 1 mM DTT), then concentrated to ∼200 μL, aliquoted, snap frozen in liquid N_2, and stored at −80°C.

S. cerevisiae profilin was expressed in BL21(DE3) *E. coli* and purified as described (Graziano et al., 2013). Bacterial cells were grown in terrific broth to log phase and induced with 0.4 mM IPTG for 3–4 h at 37°C. Cells were pelleted and stored at −80°C. Frozen pellets were thawed, resuspended in lysis buffer (20 mM Tris-HCl, pH 8.0) supplemented with a protease inhibitor cocktail (1 mM PMSF, 0.5 μM each of pepstatin A, antipain, leupeptin, aprotinin, and chymostatin), and lysed by incubation with lysozyme and sonication. Lysates were cleared by centrifugation at 200,000 × *g* at 4°C for 20 min in a TLA-100.3 rotor (Beckman Coulter). The supernatant was then loaded on a 5 ml HiTrap Q fast flow column (GE Healthcare), and profilin was eluted using a 75 mL salt gradient (0–400 mM NaCl) in 20 mM Tris-HCl, pH 8.0. Peak fractions were pooled, concentrated to 5 mL, and loaded on a Superdex (26/60) gel filtration column (GE Healthcare) equilibrated in G-buffer. Peak fractions were pooled, aliquoted, snap frozen in liquid N_2, and stored at −80°C.

6His-Bil2 protein was expressed in Rosetta 2 BL21(DE3) *E. coli* cells carrying a plasmid for expression of rare codons (MilliporeSigma; Darmstadt, Germany). Cells were grown to OD_{600} = 0.7–0.9 in terrific broth supplemented with kanamycin and chloramphenicol to maintain selection of the expression plasmid and the pRARE plasmid, respectively. Expression was induced with 0.4 mM IPTG overnight at 18°C, and then cells were pelleted and stored at −80°C. To initiate a preparation, a cell pellet was thawed, resuspended in lysis buffer (20 mM Tris pH 8.0, 500 mM NaCl, 0.5 mM DTT, and 30 mM Imidazole) with the same protease inhibitor cocktail as above, and lysed by treatment with 1 mg/mL lysozyme, 0.1 mg/mL DNAse I, and sonication. Lysates were cleared by centrifugation at 10,000 × *g* for 20 min in an F21S-8 × 50y rotor (Thermo Fisher Scientific; Waltham, MA, United States), and the supernatant was mixed with 1 mL of Ni-NTA beads (New England Biolabs) and rotated at 4°C for 1 h. The beads were then washed 3 times with 10 ml wash buffer (20 mM Tris pH 8.0, 500 mM NaCl, 0.5 mM DTT, and 30 mM Imidazole) in a gravity column at 4°C. 6His-Bil2 was eluted from the beads using elution buffer (20 mM Tris pH 8.0, 500 mM NaCl, 0.5 mM DTT, and 300 mM Imidazole), exchanged into $HEKG_{10}D$ on a PD10 desalting column (GE Life Sciences), concentrated to ∼200 μL, aliquoted, snap frozen in liquid N_2 and stored at −80°C.

Bud6(L) was expressed in BL21(DE3) *E. coli* and purified as previously described (Graziano et al., 2011). Bacterial cells were grown in terrific broth to late log phase and induced using 0.4 mM IPTG for 3–4 h at 37°C. Cells were pelleted and frozen at −80°C. Frozen pellets were thawed, resuspended in lysis buffer (50 mM Tris, pH 8.5, 150 mM NaCl, 5 mM EDTA, 1.5% sarkosyl, 5 mM DTT, and standard protease inhibitors), treated with lysozyme, and sonicated. Cell lysates were cleared by centrifugation at 12,000 rpm for 10 min in a Sorvall S600 rotor (Thermo Fisher Scientific). Triton X-100 (final concentration 3.3% [vol/vol]) was added to the supernatant, and the mixture was mixed with 1 ml of preswollen glutathione agarose in PBS (137 mM NaCl, 2.7 mM KCl, 4.3 mM Na2HPO4, and 1.47 mM KH2PO4, pH 7.4). After incubation at 4°C for 3–4 h, beads were washed four times with PBS, and then twice with HEKD (20 mM Hepes, pH 7.5, 1 mM EDTA, 50 mM KCl, and 1 mM DTT). Bud6(L) was cleaved from GST and released from beads by digestion with TEV protease for 2 h at room temperature and snap frozen.

Fixed Cell Imaging

To analyze actin cable organization in cells, yeast were grown to OD_{600} = 0.4–0.6 in YEPD media, fixed in 5% formaldehyde for 45 min at room temperature, and then washed three times with PBS buffer. Cells were stained 1–3 days with Alexa Fluor 488 phalloidin (Life Technologies; Grand Island, NY, United States), and then washed three times with PBS buffer. For experiments in which actin cables were analyzed using SOAX, an open source program for biopolymer networks (Xu et al., 2015), cells were treated with 100 μM CK666 (Sigma-Aldrich; St. Louis, MO, United States) for 20 min before fixation to inhibit the Arp2/3 complex and remove cortical actin patches. Fixed and stained cells then were imaged by structured illumination microscopy (SIM) on a Nikon Ti-2 SIM-E inverted microscope with a Hamamatsu Orca Flash 4.0 camera controlled by NIS-Elements software (Nikon Instruments), using an exposure time of 200 ms at 488 nm excitation and 40% laser power. From the SIM images, individual cells were cropped and background was subtracted, then actin cables were analyzed using SOAX. To optimize detection of cables in the SOAX analysis, default settings were used, with two exceptions: R-threshold value was set to 0.008, and k-stretch factor was set to 0.5. This automated analysis quantifies number of cable segments in cells.

For coefficient of variation (CoV) analysis of cable distribution, samples of the cell preparations made above

(fixed and phalloidin stained) were imaged by SIM, using the same settings as above. CoV measurements are made by first tracing the outline of the mother cell compartment in ImageJ, and then measuring the mean fluorescence of actin cable staining and the standard deviation. The CoV is a ratio of the standard deviation over the mean. Wildtype cells typically have brightly stained cables against a dark background, yielding a high standard deviation, and therefore a higher CoV. Mutants with disorganized and dispersed actin cable networks have lower stand deviation values and consequently lower CoVs.

Live Cell Imaging

For imaging secretory vesicle traffic, wildtype and mutant yeast strains were transformed with a CEN plasmid expressing GFP^{Envy}-Sec4. Cells were grown at 25°C to OD_{600} = 0.4–0.8 in synthetic selective media, then mounted on slides and imaged on an i-E upright confocal microscope (Nikon Instruments) with a CSU-W1 spinning disk head (Yokogawa), 100× oil objective (NA 1.4; Nikon Instruments), and an Ixon 897 Ultra-CCD camera (Andor Technology) controlled by NIS-Elements software (Nikon Instruments). Exposure times of 50 ms at 50% intensity (excitation 488 nm) were used to image cells for 2 min. Movies were analyzed in ImageJ as follows. Secretory vesicle movements were monitored within the mother cells ($n > 25$) of each strain by manually tracking the positions over time for 3–8 puncta (GFP^{Envy}-Sec4) per cell. Tortuosity measurements were made by dividing the length of the path (from the initial point of movement to the bud neck) by the distance between the point of origin and the bud neck. In addition, for each strain, we calculated the fraction of GFP^{Envy}-Sec4 puncta in the mother cell that were successfully transported to the bud during a 30 s observation window ($n > 20$ cells per condition).

To compare Bnr1-GFP (endogenously tagged) levels at the bud neck of wildtype and *bil2*Δ cells, yeast were grown at 25°C in synthetic media to OD_{600} = 0.4–0.8, then mounted on slides, and immediately imaged on an i-E upright confocal microscope (Nikon Instruments) with a CSU-W1 spinning disk head (Yokogawa), 100× oil objective (NA 1.4; Nikon Instruments), and an Ixon 897 Ultra-CCD camera (Andor Technology) controlled by NIS-Elements software (Nikon Instruments). Each image was acquired using an exposure time of 100 ms at 488 nm excitation with 20% laser power. Z-stacks (15 images) were obtained by capturing images every 0.2 μm, and were analyzed in ImageJ as follows; *Z*-stacks were combined using the "sum projection" function, then a box of fixed dimensions was drawn to encompass the bud neck and measure the Bnr1-GFP integrated fluorescence density.

For the Pearson's correlation analysis of Bud6-mCherry and GFP^{Envy}-Bil2 colocalization, yeast cells were grown in synthetic selective media to mid-log phase, mounted on slides, and immediately imaged as above. Images were acquired using exposure times of 200 ms for Bud6-mCherry (561 nm excitation; 40% laser power) and 500 ms for GFP^{Envy}-Bil2 (488 nm excitation; 80% laser power). Individual cells from the images were cropped, background was subtracted, and colocalization was analyzed using the Coloc2 plugin in ImageJ.

To quantify the ratio of GFP-Sec4 signal in the bud versus the entire cell, yeast transformed with the low copy GFP-Sec4 plasmid were grown in synthetic selective media to mid-log phase, mounted on slides, and immediately imaged as above. Images were acquired using exposure times of 50 ms (488 nm excitation; 40% laser power). Integrated density values were determined by selecting the bud and the whole cell using the ROI tool in ImageJ. The ratio of the signal in these two compartments was calculated by dividing the amount of signal in the bud by the amount of signal in the whole cell.

Secretory Vesicle Isolation

Secretory vesicles were isolated from yeast cells using methods adapted from those previously described (Harsay and Bretscher, 1995). Cells were grown at 25°C to OD_{600} = 0.7 in 1 L cultures of selective media, then shifted to 37°C for 2 h. Cells were then harvested by centrifugation for 20 min at 3,000 × *g*, washed with ice-cold 10 mM NaN_3, and incubated for 15 min on ice in softening buffer [0.1 M Tris-H_2SO_4 (pH 9.4), 50 mM 1,3-mercaptoethanol, and 10 mM NaN_3]. Next, cells were washed in ice-cold spheroplast wash buffer (1.4 M sorbitol, 50 mM KPi, pH 7.5, and 10 mM NaN_3), resuspended in the same buffer supplemented with 0.15 mg/mL Zymolyase-100T (US Biological; Salem, MA, United States), and incubated at 37°C for 2 h with gentle agitation. Spheroplasted cells were harvested by gentle centrifugation at 2,000 × *g*, and then gently washed two times with ice-cold spheroplast wash buffer (no zymolase), resting the samples on ice for 10 min between each wash to allow pellets to loosen. Next, using a plastic transfer pipette, the pellets were gently resuspended (to minimize lysis) in 30 mL of lysis buffer (0.8 M sorbitol, 10 mM triethanolamine, 1 mM EDTA, adjusted to pH 7.2 using acetic acid, 1 mM PMSF, and 0.5 μM each of pepstatin A, antipain, leupeptin, aprotinin, and chymostatin). The spheroplasts were transferred to a tight-fitting glass Dounce homogenizer, lysed with 20 strokes of the pestle, and then centrifuged at 700 × *g* for 10 min, generating the P1 (pellet) and S1 (supernatant) fractions. Then, the S1 fraction was centrifuged at 13,000 × *g* for 20 min to generate the P2 fraction (containing large organelles) and the S2 fraction (containing secretory vesicles and soluble proteins). The S2 fraction was then centrifuged for 1 h at 100,000 × *g* to generate the P3 fraction (secretory vesicles) and S3 fraction (soluble proteins). The P3 fraction was resuspended in lysis buffer and mounted on slides, and imaged on an i-E upright confocal microscope (Nikon Instruments) with a CSU-W1 spinning disk head (Yokogawa), 100× oil objective (NA 1.4; Nikon Instruments), and an Ixon 897 Ultra-CCD camera (Andor Technology) controlled by NIS-Elements software (Nikon Instruments). Images were acquired using exposure times of 200 ms for GFP-Bil2 (488 nm excitation; 50% laser power) and 100 ms for mCherry-Sec4 and Bud6-mCherry (561 nm excitation; 50% laser power).

Pyrene-Actin Assembly Assays

Gel-filtered monomeric actin (5% pyrene-labeled) in G-buffer (5 mM Tris-HCl pH 8.0, 0.2 mM ATP, 0.2 mM CaCl2, and 0.2 mM DTT) was converted to Mg-ATP-actin immediately before each reaction (Moseley and Goode, 2005). Final reactions

were 60 μL containing 2 μM G-actin. To initiate a reaction, 42 μL of the ATP-G-actin stock was mixed with 15 μL of proteins and/or control $HEKG_5$ buffer, then mixed with 3 μL of 20× initiation mix (40 mM $MgCl_2$, 10 mM ATP, and 1 M KCl) to initiate polymerization. Fluorescence was monitored at excitation 365 nm and emission 407 nm at 25°C in a fluorimeter (Photon Technology International, Lawrenceville, NJ, United States).

Total Internal Reflection Fluorescence (TIRF) Microscopy

Glass coverslips (60 mm × 3 mm × 24 mm; Thermo Fisher Scientific) were cleaned by sonication for 30 min in detergent, followed by 1 M KOH, and 1 M HCl, and then stored in 100% ethanol. Coverslips were coated with a mixture of 4 mg/mL polyethylene glycol (PEG)-silane and 80 mg/mL biotin-PEG in 80% ethanol pH 1.0, then washed with water and dried with compressed N2. PEG-coated coverslips were stored for 1–3 days at 70°C prior to use. Flow chambers were constructed by sandwiching glass coverslips on top of plastic flow chambers (Ibidi, Fitchburg, WI, United States) using double-sided tape (2.5 cm 3 mm × 2 mm × 3 mm × 120 mm) and 5-min epoxy resin (Devcon, Riviera Beach, FL, United States). To anchor actin filaments in TIRF reactions, 4 mg/mL streptavidin in HEK buffer (20 mM HEPES pH 7.4, 1 mM EDTA, and 50 mM KCl) was flowed into the TIRF chamber for 15 s using a syringe pump (Harvard Apparatus, Holliston, MA, United States). Then the chamber was washed with HEK buffer + 1% BSA. The chamber was then equilibrated with TIRF buffer [10 mM HEPES pH 7.4, 50 mM KCl, 1 mM MgCl2, 1 mM EGTA, 0.2 mM ATP, 10 mM DTT, 15 mM glucose, 20 mg/mL catalase, 100 mg/mL glucose oxidase, 10 mM Imidazole, and 0.5% methylcellulose (4000 cP)]. Prior to experiments, the proteins used in TIRF reactions [His6-Bil2, Bud6(L), C-Bnr1, profilin, and Bnr1-FH2] were diluted into TIRF buffer. A fixed volume of proteins (different combinations) was rapidly mixed with a final concentration of 1 μM G-actin (10% OG-labeled, 0.2% biotinylated, as indicated) and flowed into the TIRF chamber. The TIRF chamber was then immediately mounted on the microscope for imaging. The delay between mixing proteins and initial imaging was 60 s. Time-lapse TIRF imaging was performed on a Ti200 inverted microscope (Nikon Instruments, New York, NY, United States) equipped with 100 mW solid-state lasers (Agilent Technologies, Santa Clara, CA, United States), a CFI Apo 60× 1.49 N.A. oil-immersion TIRF objective (Nikon Instruments), a iXon EMCCD camera with a pixel size of 0.267 mm (Andor Technology), and an additional 1.5× zoom module (Nikon Instruments). Focus was maintained using the Perfect Focus System (Nikon Instruments), and frames were captured every 10 s for a total of 600 s (10 ms at 488 nm excitation, 15% laser power) using NIS Elements software (Nikon Instruments). Image analysis was performed in FIJI, where background fluorescence was removed from each time series using the background subtraction tool in Fiji (rolling ball radius, 50 pixels). For measuring the number of actin filaments nucleated in TIRF reactions, fields of view were analyzed 200 s after the initiation of TIRF imaging. For each TIRF reaction, four separate fields of view were monitored and analyzed. To measure elongation rates, filament lengths were measured at different time points (using the freehand line tool in ImageJ). This analysis was limited to filaments that could be tracked for at least 60 s without growing out of the field of view. To measure filament elongation rates, plots of filament length versus time were generated, and the rates of elongation were determined from the slopes of the lines. To express rates in actin subunits s^{-1}, we used the conversion factor of 374 subunits per μm length of F-actin (Huxley and Brown, 1967).

RESULTS

Bil2 Is Required for Proper Transport of Post-Golgi Secretory Vesicles From the Mother Cell to the Bud

There are no known defects in cell growth or morphology caused by a deletion of YGL015c (henceforth referred to as *BIL2*), and we confirmed this here. However, a genome-wide study reported that *bil2*Δ cells abnormally accumulate a cargo protein in the *trans*-Golgi, suggesting a defect late in the secretory pathway (Proszynski et al., 2005). We considered the possibility that this defect might arise from altered actin organization, given that post-Golgi vesicles are transported on actin cables to the bud. Therefore, we used live imaging to compare the spatial distribution and movements of secretory vesicles (marked with GFP-Sec4) in wildtype and *bil2*Δ cells (**Figure 1A**). Overall, vesicles were polarized to the bud to a similar degree in wildtype and *bil2*Δ cells (**Supplementary Figures 1A,B**). However, our analysis of vesicle movements revealed differences in *bil2*Δ cells. To analyze the vesicle movements, we traced their paths of transport over time (example traces in **Figure 1B**), and then quantified path lengths and tortuosity (ratio of path length to distance traveled). Vesicle paths in *bil2*Δ cells were not significantly longer compared to wildtype cells (**Figure 1C**), but changed direction more often, making them circuitous (**Figure 1D**). We also assessed the overall efficiency of vesicle traffic, by quantifying the fraction of vesicles in mother cells that successfully translocated to the bud compartment during a 30 s window, and observed a modest yet significant decrease in transport efficiency in *bil2*Δ cells (**Figure 1E**). Together, these observations show that *bil2*Δ cells are partially defective in transporting post-Golgi vesicles to the bud, which may explain the previously observed cargo buildup in the *trans*-Golgi of *bil2*Δ cells (Proszynski et al., 2005).

Loss of BIL2 Leads to Disorganized Actin Cable Networks Assembled by Bnr1

Previously, we showed that mutants in *smy1* and *hof1* that have defective actin cable organization also show altered vesicle path lengths and tortuosity (Eskin et al., 2016; Garabedian et al., 2018). Therefore, the circuitous nature of the vesicle paths in *bil2*Δ cells prompted us to carefully compare cable organization between wildtype and *bil2*Δ cells using super-resolution structured illumination microscopy (SIM). Loss of *BIL2* led to a visible disorganization of cable networks, with

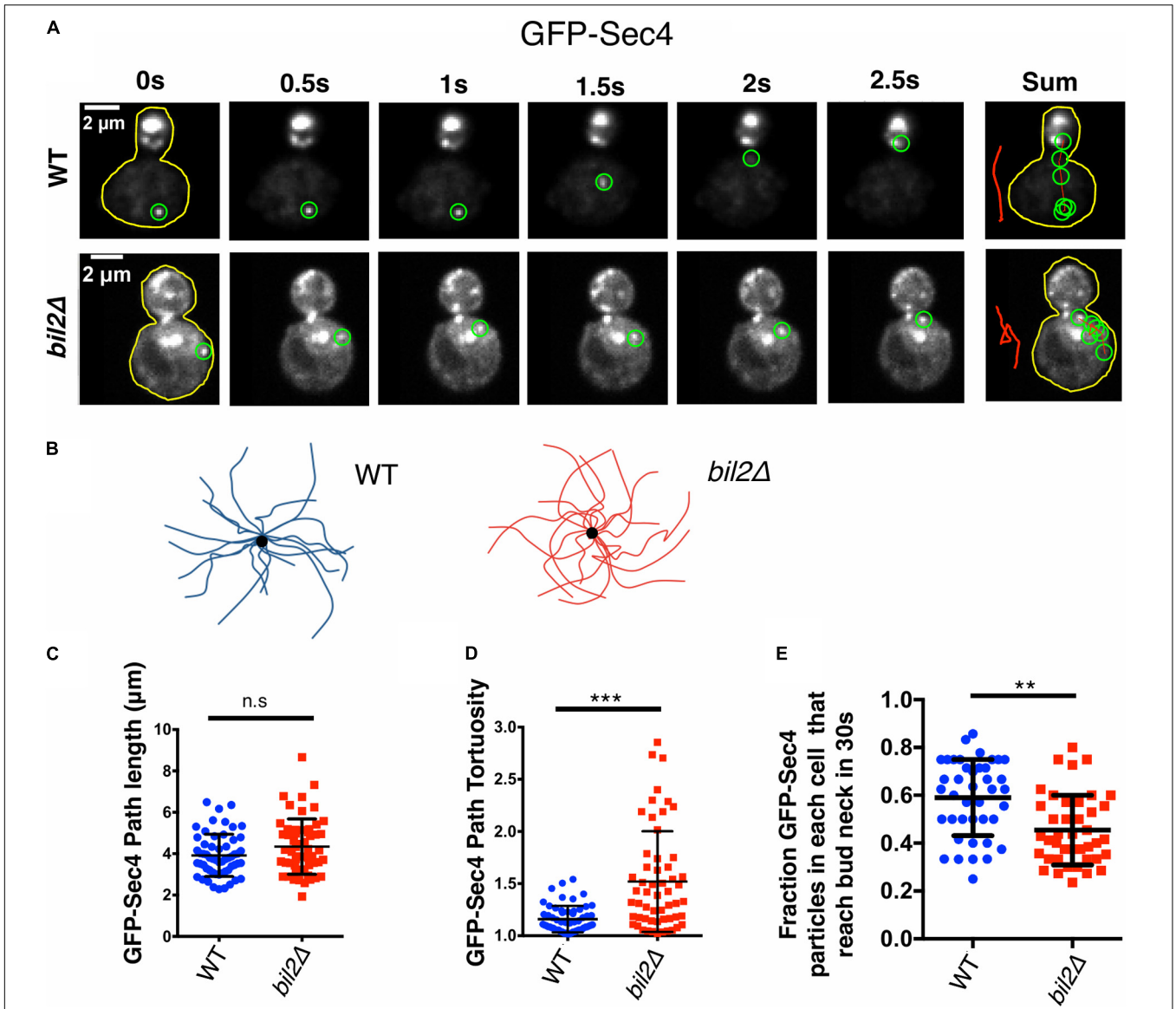

FIGURE 1 | *BIL2* is required for efficient polarized delivery of secretory vesicles. **(A)** Representative time-lapse images showing the transport path of a secretory vesicle (GFP^{Envy}-Sec4) moving from the mother to the bud. At each time point shown, the vesicle being tracked is highlighted by a green circle. To the right is a sum of vesicle positions over time, with a line (red) marking the transport path. The sum of the transport paths are isolated and expanded on the right. **(B)** Bouquets of representative transport paths for secretory vesicles (15 each) in wildtype and *bil2*Δ cells. Vesicle traces are organized such that they start at the periphery of the bouquets and terminate at the central dot (corresponding to the bud neck). **(C)** Quantification of GFP^{Envy}-Sec4 path lengths from traces as in **(B)** (n = 25 vesicles per experiment, 2 independent experiments. Number of cells: experiment 1: 17 for each strain; experiment 2: 18 for each strain). **(D)** Tortuosity of transport paths (ratio of path length to distance traveled) for the same vesicles in **(C)**. **(E)** Fraction of vesicles successfully transported from the mother compartment to the bud during a 30 s observation window (n = 20 cells per condition per experiment, 2 independent experiments). Each dot represents the fraction of vesicles successfully transported to the bud in one cell. In all panels, bars show mean and SD. Statistical significance calculated by 2-way student T-test in all panels (n.s., no significance, $^{*}p \leq 0.05$, $^{**}p \leq 0.01$, $^{***}p \leq 0.001$).

minimal effect on polarized distribution of cortical actin patches (**Figure 2A**). To analyze actin cable organization defects in a more quantitative and unbiased manner, we also employed an open source program (SOAX), which skeletalizes the cable networks from cell images (Xu et al., 2015). Cells were pretreated with the Arp2/3 complex inhibitor CK666 to remove actin patches before this analysis to provide a less obstructed view of the cable networks and increase the accuracy of the SOAX analysis (**Figure 2B**). We focused our analysis on the cable networks in the mother cells, and found that *bil2*Δ cells have an increased number of cable segments compared to wildtype cells (**Figure 2C**). Additionally, we performed coefficient of variation (CoV) analysis on the same mother cells, measuring the mean fluorescence of cable staining and dividing by the standard

deviation of the fluorescence (**Figure 2D**). Since wildtype cells have a well-defined and brightly stained set of actin cables against a dark background, they have a relatively high standard deviation, and a higher CoV. In contrast, mutants with disorganized cable networks, e.g., *hof1*Δ cells (Garabedian et al., 2020), have a lower standard deviation, and a lower CoV. Our data show that *bil2*Δ cells have a lower CoV compared to wildtype cells, which agrees with our SOAX analysis, and together these results indicate that Bil2 is required for the formation of properly organized actin cable networks.

We next asked whether *BIL2* contributes to the organization of actin cables assembled by Bni1 and/or Bnr1, which grow from the bud tip and bud neck, respectively. A comparison of cable organization in *bni1*Δ and *bni1*Δ*bil2*Δ cells, and in *bnr1*Δ and *bnr1*Δ*bil2*Δ revealed that the loss of *BIL2* significantly impaired actin cable organization in the *bni1*Δ background, but no the *bnr1*Δ background. These results suggest that *BIL2* functions to regulate *BNR1*-nediated actin assembly to govern proper cable organization in the mother cell (**Figures 2C,D**). Further, the loss of *BIL2* showed no effect on Bnr1-GFP levels at the bud neck (**Figure 2E**), indicating that Bil2 does not influence cable architecture by changing Bnr1 protein levels or localization.

Bil2 Inhibits Bnr1-Mediated Actin Nucleation *in vitro*

Our *in vivo* observations above inspired us to test *in vitro* whether Bil2 has any effects on Bnr1-mediated actin assembly activity. To address this, we purified 6His-Bil2 from *E. coli* and first tested its effects in bulk actin assembly assays. As expected, C-Bnr1 (FH1-FH2-C) rapidly nucleated actin polymerization (**Figure 3A**), and was enhanced by its nucleation-promoting factors Bud6(L) and Bil1 (Graziano et al., 2013). The addition of Bil2 strongly inhibited C-Bnr1 effects, both in the presence and absence of Bud6(L), but had no effect on the assembly of actin alone in the absence of C-Bnr1. Interestingly, however, the further addition of Bil1 to reactions containing Bil2, Bud6(L), and C-Bnr1 led to rapid actin assembly. On the other hand, Bil1 failed to release C-Bnr1 from Bil2 inhibition in the absence of Bud6(L) (**Supplementary Figure 2**). Thus, Bil1 and Bud6(L) together are required to overcome Bil2 inhibition of C-Bnr1.

To gain additional insights into Bil2 inhibitory effects on C-Bnr1, we used TIRF microscopy assays, and directly visualized individual actin filaments being assembled in real time, where we could distinguish effects on nucleation from effects on filament elongation. In these assays, C-Bnr1 alone increased the number of new filaments formed compared to control reactions, and Bil2 inhibited the nucleation effects (**Figures 3B,C**). To assess whether Bil2 also affects the rate of filament elongation, we pre-assembled filaments in the presence or absence of C-Bnr1, and then flowed in Bil2 or control buffer, and monitored change in filament length over time. As expected, C-Bnr1 markedly increased the rate of filament elongation in the presence of profilin (Chesarone-Cataldo et al., 2011). Flowing in Bil2 did not significantly alter the rate of filament elongation by C-Bnr1 (**Figure 3D**), suggesting that Bil2 acts on C-Bnr1 primarily to inhibit actin nucleation and not elongation.

To better understand how Bil2 blocks Bnr1-mediated actin nucleation, we asked whether it can inhibit an FH2 domain-only (Bnr1-FH2) construct. These nucleation assays were performed in the absence of profilin, since FH2 domains (without FH1 domains) nucleate actin assembly only in the absence of profilin (Sagot et al., 2002b). Bil2 strongly inhibited Bnr1-FH2 nucleation activity (**Figure 3E**), suggesting that it may interact with the FH2 domain to block nucleation.

Finally, in our TIRF experiments, we noticed that all Bil2-containing reactions had a number of small puncta (marked by labeled actin), regardless of whether or not those reactions contained C-Bnr1 (**Figure 3B**). Therefore, we asked whether the puncta were comprised of F-actin or G-actin by pre-incubating reactions with Latrunculin B to block actin polymerization (Coué et al., 1987). While Latrunculin B blocked actin filament formation, as expected, it did not block formation of the actin puncta induced by the presence of Bil2 (**Figure 3F**). These observations suggest that Bil2 may bind to actin monomers, consistent with its reported two-hybrid interaction with actin (Yu et al., 2008).

BIL2 and HOF1 Genetically Interact and Share an Essential *in vivo* Function

The activity profile of Bil2, as an inhibitor of Bnr1-mediated actin nucleation without affecting elongation, is similar to only one other known yeast formin regulator, Hof1. This prompted us test genetic interactions between *BIL2* and *HOF1*. We therefore crossed *bil2*Δ and *hof1*Δ haploid strains, and as controls crossed *bil2*Δ to mutants in two other yeast formin regulators, *bud6*Δ and *bud14*Δ. The resulting diploids were sporulated, tetrads were dissected, and haploid progeny were assessed for growth. This analysis revealed that the majority of *bil2*Δ*hof1*Δ double mutants were inviable, as compared to control crosses where the majority of double mutants were viable (**Figure 4A**). These observations demonstrate that *BIL2* and *HOF1* share an essential function *in vivo*. To gain additional insights into this function, we analyzed the viable *bil2*Δ*hof1*Δ double mutants. Compared to single mutants, the viable double mutants were severely compromised for cell growth (**Figure 4B**) and had enlarged cell sizes (**Figure 4C**) and disorganized actin cable networks (**Figures 4C,D**). Together, these *in vivo* observations suggest that Bil2 and Hof1 may perform related, complementary roles in controlling Bnr1-mediated actin cable nucleation and polarized cell growth.

Bil2 Localizes to Polarity Sites and Associates With Secretory Vesicles

To gain additional insights into Bil2 *in vivo* function, we investigated the localization of Bil2 endogenously tagged at its C-terminus with GFP or 3GFP. Unfortunately, we could not detect the expression of endogenously tagged Bil2-GFP or Bil2-3GFP. It is not clear whether Bil2 expression is very low to begin with, or the C-terminal tags reduced the level of expression. However, we were able to detect N-terminally tagged GFP-Bil2 expressed from a low copy plasmid under the control of the strong constitutive *ACT1* promoter (**Figure 5A**).

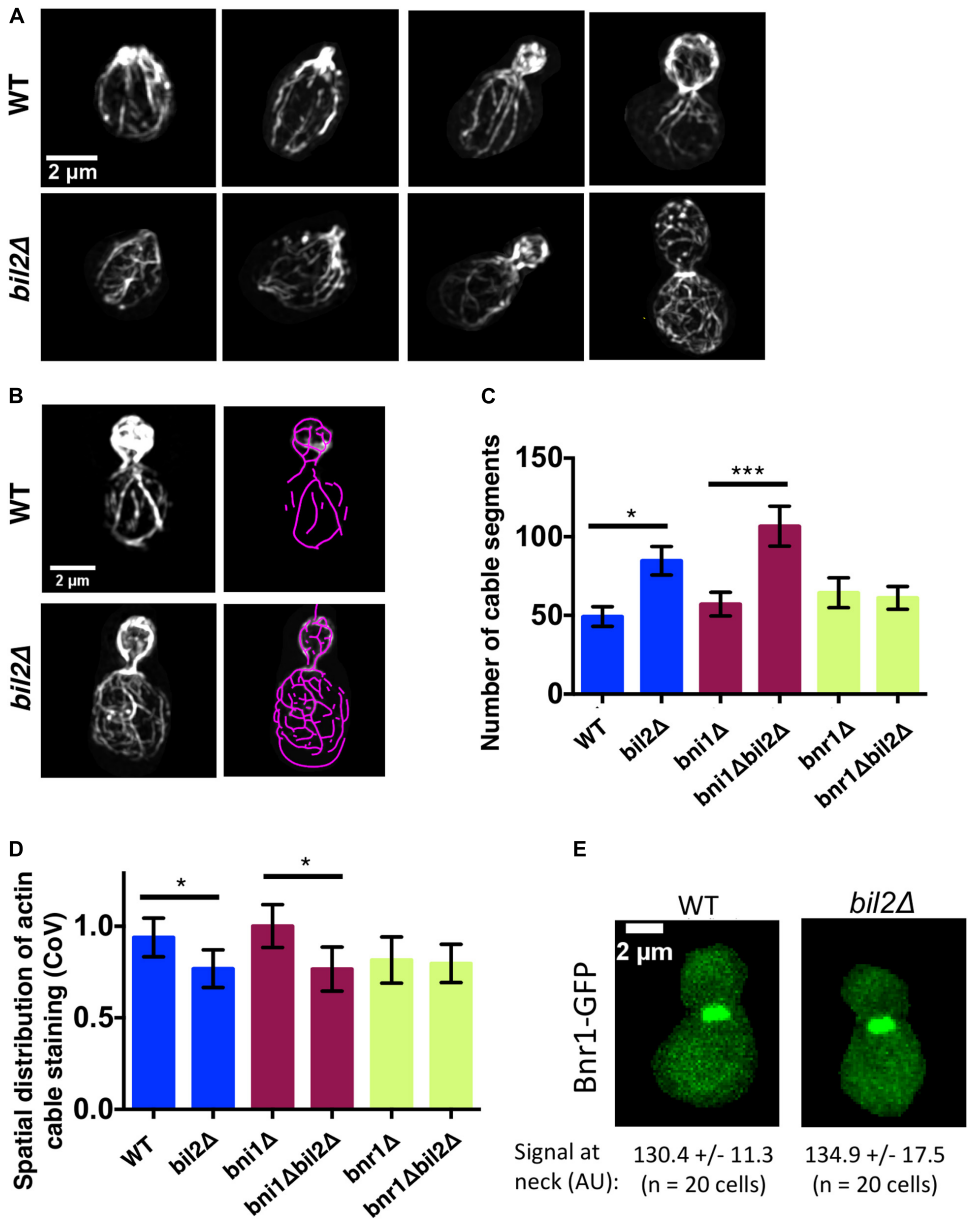

FIGURE 2 | Loss of *BIL2* disrupts the spatial organization of Bnr1-polymerized actin cable networks. **(A)** Representative structured illumination microscopy (SIM) images of F-actin organization in CK666 treated, phalloidin stained wildtype and *bil2*Δ cells at different stages of bud growth. **(B)** Automated traces of actin cables from SIM images as in **(A)**, created using SOAX. Left, phalloidin stained cell. Right, purple cable segments generated by SOAX. **(C)** Average number of actin cable segments per cell analyzed by SOAX (n = 20 cells per condition from two independent experiments). **(D)** Coefficient of variation (CoV) of phalloidin staining within the mother compartment of cells treated with CK666 (n = 20 cells per condition from two independent experiments). **(E)** Representative images of endogenously-expressed Bnr1-GFP in wildtype (WT) and *bil2*Δ cells, with quantification of signals at the bud neck (mean and SD) below each image. In all panels, statistical significance calculated by 2-way student T-test (n.s., no significance, $^{*}p \leq 0.05$, $^{**}p \leq 0.01$, $^{***}p \leq 0.001$).

Importantly, this plasmid complemented *bil2*Δ defects in secretory vesicle transport (**Figure 5B**), suggesting that although the protein is likely to be expressed at higher levels than endogenous Bil2, it is nonetheless capable of performing Bil2's normal functions. GFP-Bil2 localized to the cytosol, to the bud neck and bud tip (sites of polarized growth), and to faint mobile puncta (suggestive of secretory vesicles). However, we acknowledge that addition of the GFP tag and/or the overexpression of Bil2 may alter its normal localization pattern. Interestingly, Bud6-GFP localizes to similar sites, although it shows more pronounced localization to polarity sites and secretory vesicles compared to Bil2 (Jin and Amberg, 2000; Segal et al., 2000). Deletion of *BUD6* did not noticeably change GFP-Bil2 localization (**Supplementary Figure 3A**),

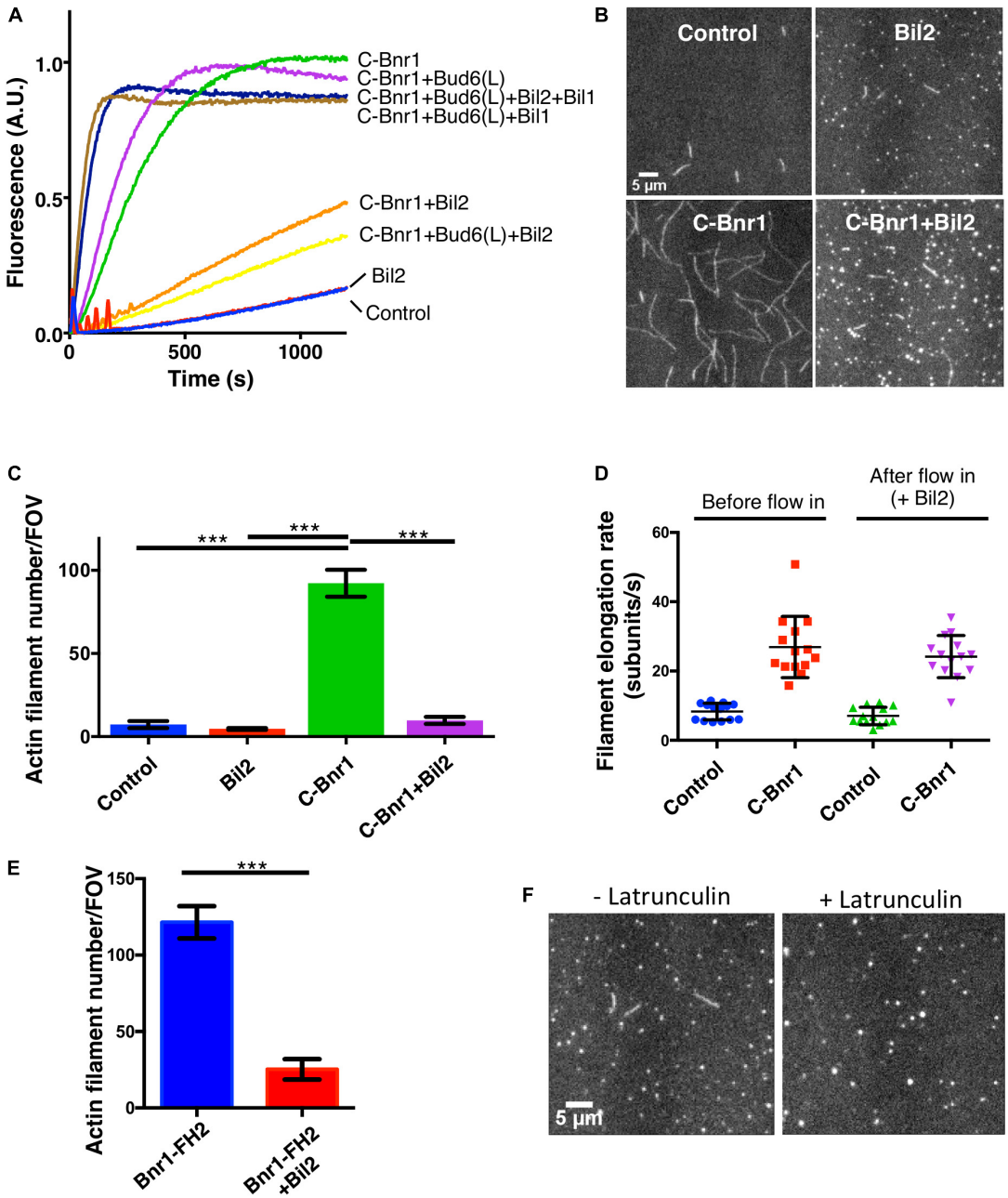

FIGURE 3 | Purified Bil2 inhibits Bnr1-mediated actin nucleation but not elongation. **(A)** Bulk pyrene-actin assembly assays showing that Bil2 inhibits Bnr1-dependent actin nucleation, both in the presence and absence of Bud6. Bil2 with Bud6 and Bil1 present did not inhibit Bnr1. Reactions contain 2 μM actin monomers (5% pyrene labeled) and 5 μM profilin, with 2 nM C-Bnr1 (FH1-FH2-C; 758–1,375), 100 nM Bud6(L) (489–788), 100 nM Bil1, and/or 100 nM Bil2, as indicated. **(B)** Representative images from TIRF microscopy experiments showing the effects of Bil2 on Bnr1-mediated actin assembly. Reactions contain 1 μM actin monomers (10% Oregon green labeled) and 3 μM profilin, with 0.1 nM C-Bnr1 and/or 100 nM Bil2, as indicated. Images shown are from 200 s after the initiation of actin assembly. **(C)** Quantification of the number of actin filaments nucleated per field of view (FOV) at 200 s into TIRF reactions as in **(B)** (four FOVs per condition). Shown are the mean and SEMs. **(D)** Quantification of filament elongation rates for TIRF reactions as in **(B)**, except that 100 nM Bil2 was flowed into reactions 5 min after initiation of actin assembly (n = 20 filaments per condition). **(E)** Bil2 inhibits Bnr1 (FH2)-mediated actin filament assembly. Quantification of number of filaments nucleated per field of view (FOV) at 200 s into TIRF reactions as in B (four FOVs per condition). Reactions contain 1 μM actin monomers (10% Oregon green labeled) and 0.1 nM Bnr1 (FH2), with and without 100 nM Bil2. **(F)** TIRF fields showing that Bil2 produces latrunculin-resistant actin puncta. Reactions contain 1 μM actin monomers (10% Oregon green labeled), 3 μM profilin, and 100 nM Bil2, with or without 100 nM Latrunculin B. Images shown are from 200 s after the initiation of actin assembly. Shown are the mean and SEMs. Statistical significance calculated by 2-way student T-test in all panels (n.s., no significance, $^{*}p \leq 0.05$, $^{**}p \leq 0.01$, $^{***}p \leq 0.001$).

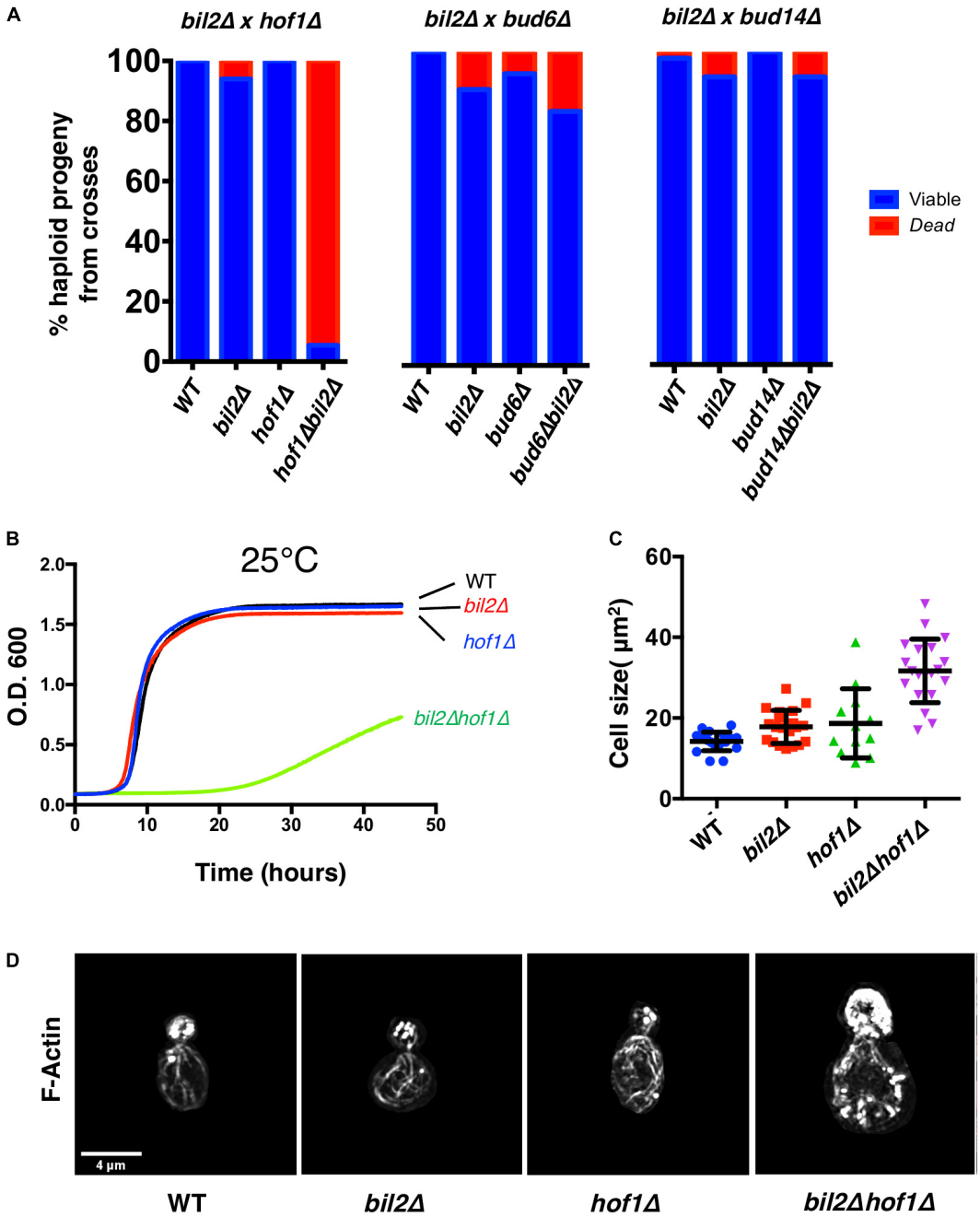

FIGURE 4 | Synthetic genetic interactions between *BIL2* and *HOF1*. **(A)** *bil2*Δ haploids were crossed to haploids carrying deletions in other Bnr1 regulatory genes, including *HOF1*, *BUD6*, and *BUD14*. Diploids were sporulated, and tetrads dissected and genotyped (n = 144, 64, and 104 tetrads from crosses with *hof1*Δ, *bud6*Δ, and *bud14*Δ, respectively). Resulting wildtype, single mutant, and double mutant haploids were analyzed for viability at 25°C. **(B)** The indicated haploid strains were compared for growth in synthetic complete media at 25°C in a shaking microplate reader for 50 h, monitoring growth (OD_{600}) every 5 min. Lines represent the average of three independent cultures per strain. **(C)** Cell size was determined from DIC images in ImageJ by outlining each cell and calculating its area (n = 20 cells per condition). Shown are the mean and SD. **(D)** Representative max projection Z-stacks of phalloidin stained cells imaged by structured illumination microscopy (SIM). Note cell size is to scale, i.e., *hof1*Δ bil2Δ cells are enlarged compared to wildtype, *hof1*Δ, and *bil2*Δ cells, as indicated in **(C)**.

and deletion of *BIL2* did not noticeably change Bud6-GFP localization (**Supplementary Figure 3B**). Thus, despite their ability to interact, Bud6 and Bil2 appear to localize independently to polarity sites.

Localization of GFP-Bil2 in live cells overlapped significantly with Bud6-mCherry and with mCherry-Sec4 (**Figure 5C**). Bud6 has been localized to secretory vesicles (Garabedian et al., 2018), which have a similar appearance to the faint mobile puncta we

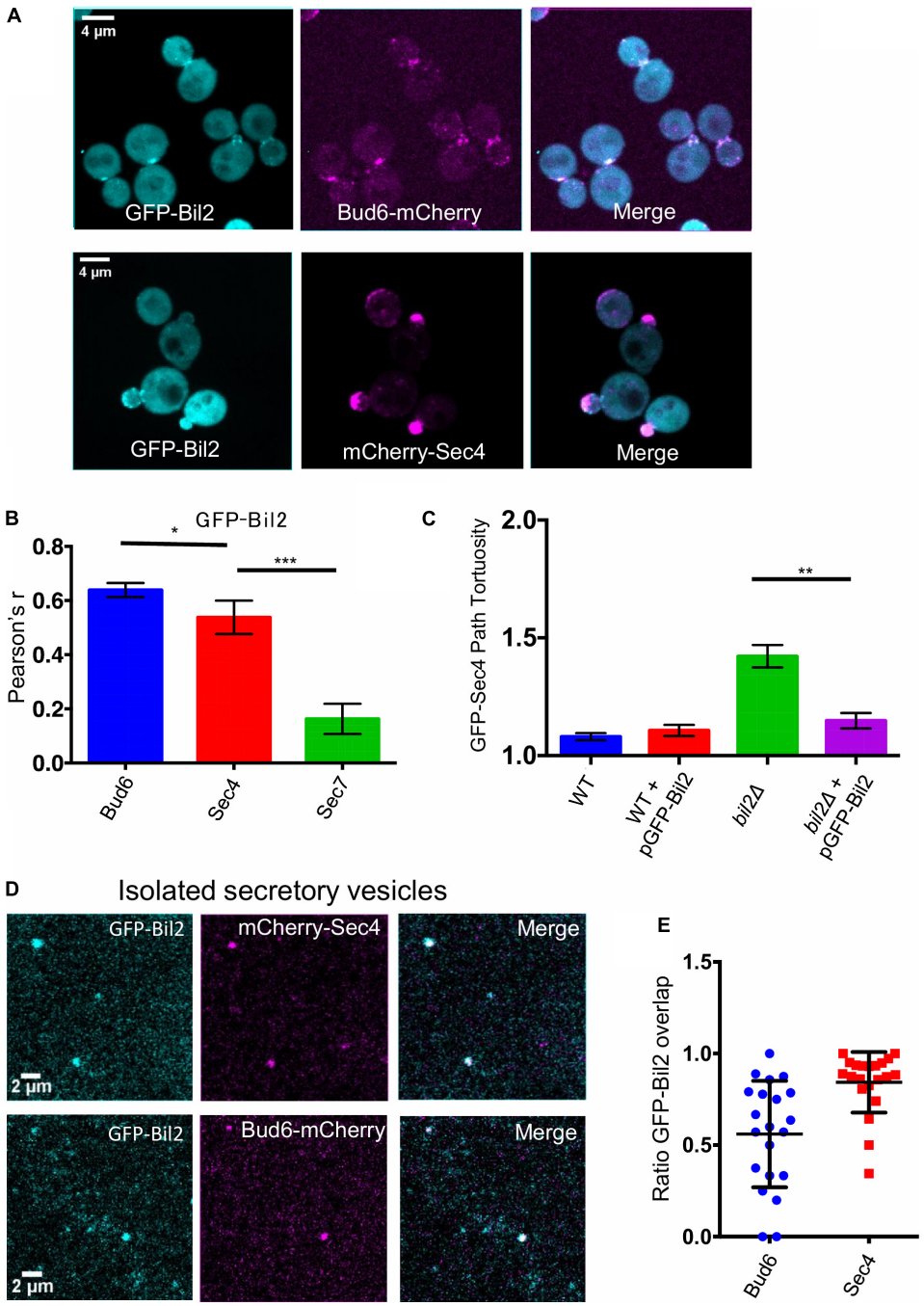

FIGURE 5 | GFP-Bil2 localization to polarity sites and association with secretory vesicles. **(A)** Representative images of live cells expressing GFP-Bil2 (from a low copy plasmid under the control of the *ACT1* promoter) and either integrated Bud6-mCherry or mCherry-Sec4 (expressed from a low copy plasmid under the control of its own promoter). **(B)** GFP-Bil2 colocalization in live cells with mCherry-Sec4 (secretory vesicle marker) or Sec7-mCherry (*trans*-Golgi marker) quantified by Pearson correlation. **(C)** Comparison of GFP-Sec4 vesicle transport paths (ratio of path length to distance traveled) in wildtype (WT) and *bil2*Δ cells with or without the pACT1-GFP-Bil2 plasmid (n = 25 vesicles per condition). **(D)** Representative fields of view of secretory vesicles isolated from cells expressing GFP-Bil2 (plasmid, as in **A**) along with Bud6-mCherry (integrated) or mCherry-Sec4 (plasmid, as in **A**). **(E)** Quantification of GFP-Bil2 colocalization with Bud6- and Sec4-positive secretory vesicles. Statistical significance in all panels calculated by 2-way student T-test (n.s., no significance, $^{*}p \leq 0.05$, $^{**}p \leq 0.01$, $^{***}p \leq 0.001$).

observed for GFP-Bil2. To further test the association of Bil2 with secretory vesicles, we performed a biochemical fractionation. Differential centrifugation was used to isolate secretory vesicles from cells co-expressing GFP-Bil2 with either Bud6-mCherry or mCherry-Sec4, and then colocalization was assessed by microscopy (**Figure 5D**). The majority of GFP-Bil2 puncta

(∼80%) colocalized with mCherry-Sec4, and approximately half of the GFP-Bil2 puncta colocalized with Bud6-mCherry (**Figure 5E**). These results more conclusively demonstrate that Bil2 associates with secretory vesicles, and suggest that approximately half of the Bil2-positive vesicles also harbor Bud6.

DISCUSSION

The initial goal of this study was to explore the cellular functions of a previously uncharacterized gene, YGL015c (*BIL2*), which was reported to interact with actin and the formin nucleation-promoting factor Bud6 (Ito et al., 2001; Yu et al., 2008). A previous proteomic screen had also identified this gene as being required for normal delivery of a marker protein to the cell surface via the secretory pathway, revealing that in *bil2*Δ cells the surface protein aberrantly accumulated in the *trans*-Golgi compartment (Proszynski et al., 2005). However, the specific role(s) of *BIL2* in this pathway were unclear. Given its suggested interactions with Bud6, which promotes formin-mediated actin cable nucleation, we decided to explore the possibility that Bil2 regulates formin-mediated actin cable assembly. Our *in vivo* observations showed that *bil2*Δ cells have defects in Bnr1-dependent actin cable architecture, including an increase in the total number of cable segments and a disorganization or entanglement of cable networks in mother cells. Consistent with these defects, the transport paths of secretory vesicles in *bil2*Δ cells were more circuitous compared to the paths of vesicles in wildtype cells. Further, purified Bil2 inhibited Bnr1-mediated actin nucleation but not filament elongation *in vitro*, both in bulk and TIRF microscopy assays. Based on these genetic and biochemical observations, we propose that Bil2 functions, at least in part, as a novel inhibitor of Bnr1-mediated actin cable nucleation required for proper secretory traffic.

Although a number of direct regulators of Bnr1 activity have been identified to date, the only other one with an activity profile similar to Bil2 is the F-BAR protein Hof1. Like Bil2, Hof1 inhibits Bnr1-mediated actin nucleation but not filament elongation (Graziano et al., 2014). In addition, both Bil2 and Hof1 inhibit the actin-nucleating FH2 domain of Bnr1. A low-resolution EM structure of the Hof1-FH2 complex revealed that the F-BAR domain of Hof1 binds to the FH2 domain near its actin-binding surfaces (Garabedian et al., 2018). It is possible that Bil2 uses a related mechanism to inhibit Bnr1. Alternatively, a Bil2-actin complex might directly interact with the Bnr1 FH2 domain to block nucleation. Indeed, it was recently shown that the mammalian formin INF2 is inhibited by binding of a cyclase-associated protein (CAP)-actin complex (Mu et al., 2019). Consistent with their related biochemical activities in suppressing Bnr1-mediated actin nucleation, we found that *bil2*Δ and *hof1*Δ mutations are synthetic lethal. These results suggest that Bil2 and Hof1 have overlapping, possibly complementary roles in controlling formin-mediated actin cable assembly *in vivo*. Nearly all of the *bil2*Δ*hof1*Δ double mutants were lethal, possibly due to a lethal level of disrupted secretory traffic and impaired polarized growth. The small percentage of *bil2*Δ*hof1*Δ double mutant cells that were viable grew very slowly and had enlarged cell morphologies.

Our observations raise the question of why yeast cells have so many different inhibitors for one formin (Bnr1). Bil2 and Hof1 inhibit Bnr1-mediated actin nucleation and genetically interact. Bud14 and Smy1 inhibit actin filament nucleation and elongation by Bnr1 and genetically interact (Chesarone et al., 2009; Chesarone-Cataldo et al., 2011). None of these four inhibitors of Bnr1 have any direct effects on Bni1 activity. Thus, cells appear to require tight spatiotemporal control over Bnr1 activity (nucleation and elongation) in order to build proper cable networks consisting of the appropriate number of cables with the appropriate length and architecture for optimal secretory traffic. It is also worth noting that no inhibitors of Bni1 activity have been identified to date. This may be related to Bnr1 having a

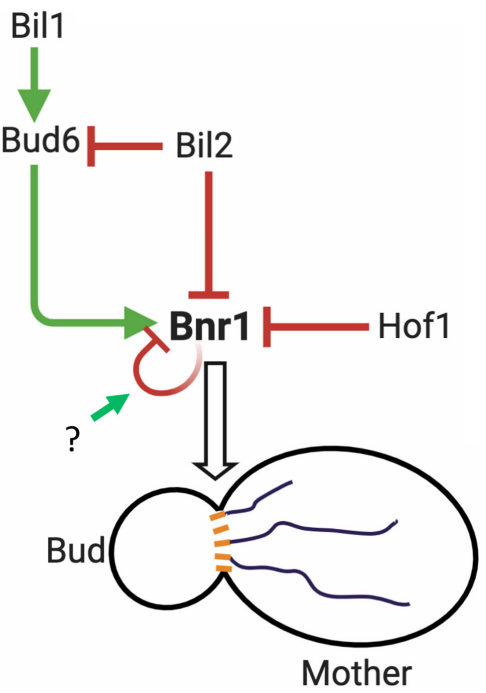

FIGURE 6 | Working model for the regulation of Bnr1-mediated actin cable nucleation. Bnr1 is anchored at the bud neck and assembles cables in the mother cell. Bud6 functions as an NPF, promoting actin nucleation by Bnr1. Bil2 and Hof1 specifically inhibit actin nucleation by Bnr1. Bud6 is delivered on secretory vesicles to the bud neck and overcomes Hof1 inhibition of Bnr1 as part of a positive feedback loop promoting cable assembly (Garabedian et al., 2018). Bud6 is not sufficient to overcome Bil2 inhibition of Bnr1. However, bud6 together with its binding partner Bil1 overcomes Bil2 inhibition to promote Bnr1-mediated actin nucleation. Bil2 and Bud6 are found together on many secretory vesicles, suggesting that Bil2 may help keep Bud6 inactive until it reaches the bud neck where Bil1 is found (Graziano et al., 2013). Bnr1 is also predicted to be autoinhibited via interactions of its N-terminal diaphanous inhibitory domain (DID) with its C-terminal diaphanous autoregulatory domain (DAD) (Li et al., 2003). However, it is not yet clear what mechanisms trigger the release of Bnr1 from autoinhibition. After a filament is nucleated, Bnr1 remains processively attached to the growing barbed end, where the duration and rate of filament elongation are controlled by other cellular factors, including Smy1 and Bud14 (Eskin et al., 2016). Model created using BioRender.com.

∼15-fold stronger nucleation activity compared to Bni1 (Moseley and Goode, 2005). In addition, it may be significant that Bnr1 is stably tethered to the bud neck, whereas Bni1 is dynamically recruited from the cytosol to the bud cortex, where it is transiently activated to nucleate cable assembly and then released (Buttery et al., 2007). These differences in the dynamics of the two formins may result in their activities requiring distinct regulatory mechanisms. Further, Bnr1 assembles cables that fill the mother cell, where cable overgrowth can be detrimental to secretory traffic. Thus, Bnr1 (but not Bni1) may require stronger inhibition to restrict its activity.

How do cells overcome Bil2 and Hof1 inhibition of Bnr1-mediated actin nucleation In the case of Hof1, its inhibitory effects on Bnr1 are overcome by the formin NPF Bud6, which depends on direct binding of Bud6 to Bnr1 (Garabedian et al., 2018). *In vivo*, Hof1 is anchored at the bud neck where Bnr1 also resides, and Bud6 is delivered on secretory vesicles to the bud neck. Genetic and biochemical evidence suggest that upon arrival Bud6 triggers Bnr1's release from Hof1 inhibition to promote actin cable assembly as part of a positive feedback loop. In contrast, we found that Bud6 alone is not sufficient to overcome the inhibitory effects of Bil2 on Bnr1. Instead, this requires Bud6 and its ligand Bil1. Thus, Bil1 appears to be specifically required for overcoming Bil2 inhibition of Bnr1, but not Hof1 inhibition of Bnr1. Similar to Bud6, we found that Bil2 associates with secretory vesicles. Thus, Bil2 may serve to inhibit Bud6's NPF activity while on vesicles until it arrives to the bud neck, where Bil1 relieves inhibition. Importantly, our results do not rule out the possibility that Bil2 has additional functions (beyond directly regulating Bnr1 activity) that influence cable architecture and/or the transport of vesicles along cables. Indeed, the yeast formin inhibitor Smy1 not only directly regulates Bnr1 activity but also plays an important role in recruiting myosin to secretory vesicles *in vivo*, and increases myosin processivity *in vitro* (Hodges et al., 2009; Lwin et al., 2016). Collectively, these observations lay a foundation for understanding the *in vivo* regulatory circuit controlling Bnr1-mediated actin nucleation (**Figure 6**). However, they also raise many new questions that need to be answered in future studies, including: (i) when and where each regulatory protein interacts with Bnr1, and with each other, *in vivo*, (ii) whether their effects on Bnr1 are regulated by post-translational modification, and (iii) what mechanism(s) trigger the release of Bnr1 from autoinhibition.

Finally, it will be important to determine if and how Bil2 (and Bil1) influence the other known cellular functions of Bud6, particularly its role in microtubule plus end capture and mitotic spindle orientation (Segal et al., 2002). Bud6 binds not only to formins but also the microtubule plus end-binding protein EB1 (Bim1), and is believed to coordinate actin and microtubule functions *in vivo* (Delgehyr et al., 2008; Ten Hoopen et al., 2012). Therefore, it will interesting to learn whether Bil1 and/or Bil2 contribute to this cytoskeletal crosstalk by Bud6. Further, what we learn from studying Bil1, Bil2, and Bud6 in yeast may provide valuable lessons for understanding the mechanisms coordinating actin and microtubule functions in other systems. While there are no clear homologs of Bil1, Bil2, or Bud6 outside of the fungal kingdom, mounting evidence suggests that adenomatous polyposis coli (APC) protein is a functional counterpart to Bud6 in animal cells. Similar to Bud6, APC binds to EB1 and serves as a formin NPF *in vitro* and *in vivo* (Okada et al., 2010; Breitsprecher et al., 2012; Juanes et al., 2017, 2019). Further, APC interacts with a large number of other cytoskeletal regulatory proteins. Some of these ligands may regulate APC's NPF activities in a manner related to how Bil1 and Bil2 regulate Bud6 NPF activity. Indeed, it was recently shown that EB1 directly inhibits the NPF activity of APC's Basic domain (Juanes et al., 2020). These findings, together with the results presented here, suggest that evolutionarily diverse organisms may have adapted to use distinct sets of proteins (lacking obvious sequence homology) to establish common regulatory schemes for controlling actin assembly.

DATA AVAILABILITY STATEMENT

The original contributions generated for this study are included in the article/**Supplementary Material**, further inquiries can be directed to the corresponding author.

AUTHOR CONTRIBUTIONS

TR and BG designed the research and wrote the manuscript. TR carried out all of the experiments and data analysis. BG obtained funding and supervised the project. Both authors contributed to the article and approved the submitted version.

FUNDING

This research was supported by a grant from the NIH to BG (R35 GM134895) and the Brandeis NSF Materials Research Science and Engineering Center (MRSEC) grant 142038.

ACKNOWLEDGMENTS

We are grateful to Julian Eskin, Brian Graziano, Mikael Garabedian, M. Angeles Juanes, and Alison Wirshing for useful project advice, help in generating key reagents, and/or editing of the manuscript. In addition, we thank Brianna Silverman, Malka Forman, and Yoni Israel for experimental assistance at different stages of the work.

SUPPLEMENTARY MATERIAL

The Supplementary Material for this article can be found online at: https://www.frontiersin.org/articles/10.3389/fcell.2021.634587/full#supplementary-material

REFERENCES

Bi, E., and Park, H.-O. (2012). Cell polarization and cytokinesis in budding yeast. *Genetics* 191, 347–387. doi: 10.1534/genetics.111.132886

Breitsprecher, D., and Goode, B. L. (2013). Formins at a glance. *J. Cell. Sci.* 126, 1–7. doi: 10.1242/jcs.107250

Breitsprecher, D., Jaiswal, R., Bombardier, J. P., Gould, C. J., Gelles, J., Goode, B. L., et al. (2012). Rocket launcher mechanism of collaborative actin assembly defined by single-molecule imaging. *Science* 336, 1164–1168. doi: 10.1126/science.1218062

Buttery, S. M., Kono, K., Stokasimov, E., and Pellman, D. (2012). Regulation of the formin Bnr1 by Septins and a MARK/Par1-family septin-associated kinase. *Mol. Biol. Cell.* 23, 4041–4053. doi: 10.1091/mbc.E12-05-0395

Buttery, S. M., Yoshida, S., and Pellman, D. (2007). Yeast formins Bni1 and Bnr1 utilize different modes of cortical interaction during the assembly of actin cables. *Mol. Biol. Cell.* 18, 1826–1838. doi: 10.1091/mbc.e06-09-0820

Calero, M., Chen, C. Z., Zhu, W., Winand, N., Havas, K. A., Gilbert, P. M., et al. (2003). Dual prenylation is required for rab protein localization and function. *Mol. Biol. Cell.* 14, 1852–1867. doi: 10.1091/mbc.e02-11-0707

Chesarone, M., Gould, C. J., Moseley, J. B., and Goode, B. L. (2009). Displacement of formins from growing barbed ends by bud14 is critical for actin cable architecture and function. *Dev. Cell.* 16, 292–302. doi: 10.1016/j.devcel.2008.12.001

Chesarone, M. A., DuPage, A. G., and Goode, B. L. (2010). Unleashing formins to remodel the actin and microtubule cytoskeletons. *Nat. Rev. Mol. Cell.* 11, 62–74. doi: 10.1038/nrm2816

Chesarone-Cataldo, M., Guérin, C., Yu, J. H., Wedlich-Soldner, R., Blanchoin, L., Goode, B. L., et al. (2011). The myosin passenger protein Smy1 controls actin cable structure and dynamics by acting as a formin damper. *Dev. Cell.* 21, 217–230. doi: 10.1016/j.devcel.2011.07.004

Chhabra, E. S., and Higgs, H. N. (2007). The many faces of actin: matching assembly factors with cellular structures. *Nat. Cell. Biol.* 9:1110. doi: 10.1038/ncb1007-1110

Cooper, J. A., Blum, J. D., and Pollard, T. D. (1984). Acanthamoeba castellanii capping protein: properties, mechanism of action, immunologic cross-reactivity, and localization. *J. Cell. Biol.* 99, 217–225. doi: 10.1083/jcb.99.1.217

Coué, M., Brenner, S. L., Spector, I., and Korn, E. D. (1987). Inhibition of actin polymerization by latrunculin A. *FEBS Lett.* 2, 316–318.

Delgehyr, N., Lopes, C. S., Moir, C. A., Huisman, S. M., and Segal, M. (2008). Dissecting the involvement of formins in Bud6p- mediated cortical capture of microtubules in S . Cerevisiae. *J. Cell. Sci.* 121, 3803–3814. doi: 10.1242/jcs.036269

Eskin, J. A., Rankova, A., Johnston, A. B., Alioto, S. L., and Goode, B. L. (2016). Common formin-regulating sequences in Smy1 and Bud14 are required for the control of actin cable assembly in vivo. *Mol. Biol. Cell.* 27, 828–837. doi: 10.1091/mbc.e15-09-0639

Evangelista, M., Blundell, K., Longtine, M. S., Chow, C. J., Adames, N., Pringle, J. R., et al. (1997). Bni1p, a yeast formin linking Cdc42p and the actin cytoskeleton during polarized morphogenesis. *Science* 276, 118–122. doi: 10.1126/science.276.5309.118

Evangelista, M., Pruyne, D., Amberg, D. C., Boone, C., and Bretscher, A. (2002). Formins direct Arp2/3-independent actin filament assembly to polarize cell growth in yeast. *Nat. Cell. Biol.* 4, 260–269. doi: 10.1038/ncb770

Faix, J., and Grosse, R. (2006). Staying in shape with formins. *Dev. Cell.* 10, 693–706. doi: 10.1016/j.devcel.2006.05.001

Gao, L., and Bretscher, A. (2008). Analysis of unregulated formin activity reveals how yeast can balance F-actin assembly between different microfilament-based organizations. *Mol. Biol. Cell.* 19, 1474–1484.

Gao, L., Liu, W., and Bretscher, A. (2010). The yeast formin Bnr1p has two localization regions that show spatially and temporally distinct association with septin structures. *Mol. Biol. Cell.* 21, 1253–1262. doi: 10.1091/mbc.e09-10-0861

Garabedian, M. V., Stanishneva-Konovalova, T., Lou, C., Rands, T. J., Pollard, L. W., Sokolova, O. S., et al. (2018). Integrated control of formin-mediated actin assembly by a stationary inhibitor and a mobile activator. *J. Cell Biol.* 217, 3512–3530. doi: 10.1083/jcb.201803164

Garabedian, M. V., Wirshing, A., Vakhrusheva, A., Turegun, B., Sokolova, O. S., Goode, B. L., et al. (2020). A septin-Hof1 scaffold at the yeast bud neck binds and organizes actin cables. *Mol. Biol. Cell.* 31, 1988–2001. doi: 10.1091/mbc.E19-12-0693

Ghose, D., and Lew, D. (2020). Mechanistic insights into actin-driven polarity site movement in yeast. *Mol. Biol. Cell.* 31, 1085–1102. doi: 10.1091/mbc.E20-01-0040

Glomb, O., Bareis, L., and Johnsson, N. (2019). YFR016c/aip5 is part of an actin nucleation complex in yeast. *Biol. Open* 8, 2–10. doi: 10.1242/bio.044024

Goode, B. L., and Eck, M. J. (2007). Mechanism and function of formins in the control of actin assembly. *Ann. Rev. Biochem.* 76, 593–627. doi: 10.1146/annurev.biochem.75.103004.142647

Govindan, B., Bowser, R., and Novick, P. (1995). The role of Myo2, a yeast class V myosin, in vesicular transport. *J. Cell. Biol.* 128, 1055–1068. doi: 10.1083/jcb.128.6.1055

Graziano, B. R., DuPage, A. G., Michelot, A., Breitsprecher, D., Moseley, J. B., Sagot, I., et al. (2011). Mechanism and cellular function of bud6 as an actin nucleation – promoting factor. *Mol. Biol. Cell.* 22, 4016–4028. doi: 10.1091/mbc.E11-05-0404

Graziano, B. R., Jonasson, E. M., Pullen, J. G., Gould, C. J., and Goode, B. L. (2013). Ligand-induced activation of a formin-NPF pair leads to collaborative actin nucleation. *J. Cell. Biol.* 201, 595–611. doi: 10.1083/jcb.201212059

Graziano, B. R., Yu, H. Y., Alioto, S. L., Eskin, J. A., Ydenberg, C. A., Waterman, D. P., et al. (2014). The F-BAR protein Hof1 tunes formin activity to sculpt actin cables during polarized growth. *Mol. Biol. Cell.* 25, 1730–1743. doi: 10.1091/mbc.E14-03-0850

Harsay, E., and Bretscher, A. (1995). Parallel secretory pathways to the cell surface in yeast. *J. Cell. Biol.* 131, 297–310. doi: 10.1083/jcb.131.2.297

Higgs, H. N., and Peterson, K. J. (2005). Phylogenetic analysis of the formin homology 2 domain. *Mol. Biol. Cell.* 16, 1–13. doi: 10.1091/mbc.E04

Higuchi, R., Vevea, J. D., Swayne, T. C., Chojnowski, R., Hill, V., Boldogh, I. R., et al. (2013). Actin dynamics affect mitochondrial quality control and aging in budding yeast. *Curr. Biol.* 23, 2417–2422. doi: 10.1016/j.cub.2013.10.022

Hodges, A. R., Bookwalter, C. S., Krementsova, E. B., and Trybus, K. M. (2009). A nonprocessive class V myosin drives cargo processively when a kinesin- related protein is a passenger. *Curr. Biol.* 19, 2121–2125. doi: 10.1016/j.cub.2009.10.069

Huxley, H. E., and Brown, W. (1967). The low-angle x-ray diagram of vertebrate striated muscle and its behaviour during contraction and rigor. *J. Mol. Biol.* 30, 383–434. doi: 10.1016/s0022-2836(67)80046-9

Imamura, H., Tanaka, K., Hihara, T., Umikawa, M., Kamei, T., Takahashi, K., et al. (1997). Bni1p and Bnr1p: downstream targets of the rho family small G-proteins which interact with profilin and regulate actin cytoskeleton in saccharomyces cerevisiae. *EMBO J.* 16, 2745–2755.

Ito, T., Chiba, T., Ozawa, R., Yoshida, M., Hattori, M., and Sakaki, Y. (2001). A Comprehensive Two-Hybrid analysis to explore the yeast protein interactome. *Proc. Natl. Acad. Sci. U S A.* 98, 4569–4574.

Jaiswal, R., Breitsprecher, D., Collins, A., Corrêa, I. R. Jr., Xu, M. Q., and Goode, B. L. (2013). The formin daam1 and fascin directly collaborate to promote filopodia formation. *Curr. Biol.* 23, 1373–1379. doi: 10.1016/j.cub.2013.06.013

Jin, H., and Amberg, D. C. (2000). The secretory pathway mediates localization of the cell polarity regulator Aip3p/Bud6p. *Mol. Biol. Cell.* 11, 647–661. doi: 10.1091/mbc.11.2.647

Juanes, M. A., Bouguenina, H., Eskin, J. A., Jaiswal, R., Badache, A., Goode, B. L. et al. (2017). Adenomatous polyposis coli nucleates actin assembly to drive cell migration and microtubule-induced focal adhesion turnover. *J. Cell. Biol.* 216, 2859–2875. doi: 10.1083/jcb.201702007

Juanes, M. A., Fees, C. P., Hoeprich, G. J., Jaiswal, R., and Goode, B. L. (2020). EB1 Directly regulates APC-mediated actin nucleation. *Curr. Biol.* 30, 4763–4772.

Juanes, M. A., Isnardon, D., Badache, A., Brasselet, S., Mavrakis, M., Goode, B. L. et al. (2019). The role of APC-mediated actin assembly in microtubule capture and focal adhesion turnover. *J. Cell. Biol.* 218, 3415–3435. doi: 10.1083/jcb.201904165

Kamei, T., Tanaka, K., Hihara, T., Umikawa, M., Imamura, H., Kikyo, M., et al. (1998). Interaction of Bnr1p with a novel Src homology 3 domain-containing Hof1p: implication in cytokinesis in saccharomyces cerevisiae. *J. Biol. Chem.* 273, 28341–28345. doi: 10.1074/jbc.273.43.28341

Kono, K., Saeki, Y., Yoshida, S., Tanaka, K., and Pellman, D. (2012). Proteasomal degradation resolves competition between cell polarization and cellular wound healing. *Cell* 150, 151–164. doi: 10.1016/j.cell.2012.05.030

Kovar, D. R. (2006). Molecular details of formin-mediated actin assembly. *Curr. Opin. Cell. Biol.* 18, 11–17. doi: 10.1016/J.CEB.2005.12.011

Li, F., Henry, N., and Higgs. (2003). The mouse formin MDia1 is a potent actin nucleation factor regulated by autoinhibition. *Curr. Biol.* 13, 1335–1340.

Longtine, M. S., McKenzie, A., Demarini, D. J., Shah, N. G., Wach, A., Brachat, A., et al. (1998). Additional modules for versatile and economical PCR-based gene deletion and modification in saccharomyces cerevisiae. *Yeast* 961, 953–961.

Lwin, K. M., Li, D., and Bretscher, A. (2016). Kinesin-related Smy1 enhances the Rab-dependent association of myosin-V with secretory cargo. *Mol. Biol. Cell.* 27, 2450–2462. doi: 10.1091/mbc.E16-03-0185

Moseley, B., and Goode, B. L. (2006). The yeast actin cytoskeleton: from cellular function to biochemical mechanism. *Microbiol. Mol. Biol. Rev.* 70, 605–645. doi: 10.1128/MMBR.00013-06

Moseley, J. B., and Goode, B. L. (2005). Differential activities and regulation of saccharomyces cerevisiae formin proteins Bni1 and Bnr1 by Bud6. *J. Biol. Chem.* 280, 28023–28033. doi: 10.1074/jbc.M503094200

Moseley, J. B., Sagot, I., Manning, A. L., Xu, Y., Eck, M. J., Pellman, D., et al. (2004). A conserved mechanism for Bni1- and MDia1-induced actin assembly and dual regulation of Bni1 by Bud6 and Profilin. *Mol. Biol. Cell.* 15, 896–907. doi: 10.1091/mbc.e03-08-0621

Mu, A., Fung, T. S., Kettenbach, A. N., Chakrabarti, R., and Higgs, H. N. (2019). A complex containing lysine-acetylated actin inhibits the formin INF2. *Nat. Cell Biol.* 21, 592–602. doi: 10.1038/s41556-019-0307-4

Okada, K., Bartolini, F., Deaconescu, A. M., Moseley, J. B., Dogic, Z., Grigorieff, N., et al. (2010). Adenomatous polyposis coli protein nucleates actin assembly and synergizes with the formin MDia1. *J. Cell. Biol.* 189, 1087–1096. doi: 10.1083/jcb.201001016

Okada, K., Ravi, H., Smith, E. M., and Goode, B. L. (2006). Aip1 and pofilin promote rapid turnover of yeast actin patches and cables: a coordinated mechanism for severing and capping filaments. *Mol. Biol. Cell.* 17, 2855–2868. doi: 10.1091/mbc.e06-02-0135

Ozaki-Kuroda, K., Yamamoto, Y., Nohara, H., Kinoshita, M., Fujiwara, T., Irie, K., et al. (2001). Dynamic localization and function of Bni1p at the sites of directed growth in saccharomyces cerevisiae. *Mol. Cell. Biol.* 21, 827–839. doi: 10.1128/MCB.21.3.827-839.2001

Proszynski, T. J., Klemm, R. W., Gravert, M., Hsu, P. P., Gloor, Y., Wagner, J., et al. (2005). A genome-wide visual screen reveals a role for sphingolipids and ergosterol in cell surface delivery in yeast. *Proc. Natl. Acad. Sci. U S A.* 102, 17981–17986.

Pruyne, D., Gao, L., Bi, E., and Bretscher, A. (2004). Stable and dynamic axes of polarity use distinct formin isoforms in budding yeast. *Mol. Biol. Cell* 15, 4971–4989. doi: 10.1091/mbc.e04-04-0296

Pruyne, D. W., Schott, D. H., and Bretscher, A. (1998). Tropomyosin-containing actin cables direct the Myo2p-dependent polarized delivery of secretory vesicles in budding yeast. *J. Cell Biol.* 143, 1931–1945. doi: 10.1083/jcb.143.7.1931

Sagot, I., Klee, S. K., and Pellman, D. (2002a). Yeast formins regulate cell polarity by controlling the assembly of actin cables. *Nat. Cell Biol.* 4, 42–50. doi: 10.1038/ncb719

Sagot, I., Rodal, A. A., Moseley, J., Goode, B. L., and Pellman, D. (2002b). An actin nucleation mechanism mediated by Bni1 and profilin. *Nat. Cell Biol.* 4, 626–631. doi: 10.1038/ncb834

Segal, M., Bloom, K., and Reed, S. I. (2000). Bud6 directs sequential microtubule interactions with the bud tip and bud neck during spindle morphogenesis in saccharomyces cerevisiae. *Mol. Biol. Cell.* 11, 3689–3702.

Segal, M., Bloom, K., and Reed, S. I. (2002). Kar9p-independent microtubule capture at Bud6p cortical sites primes spindle polarity before bud emergence in saccharomyces cerevisiae. *Mol. Biol. Cell* 13, 4141–4155.

Slubowski, C. J., Funk, A. D., Roesner, J. M., Paulissen, S. M., and Huang, L. S. (2015). Plasmids for C-terminal tagging in saccharomyces cerevisiae that contain improved GFP proteins, Envy and Ivy. *Yeast* 32, 379–387. doi: 10.1002/yea.3065

Spudich, J. A., and Watt, S. (1971). The regulation of rabbit skeletal muscle contraction. I. biochemical studies of the interaction of the tropomyosin-troponin complex with actin and the proteolytic fragments of myosin. *J. Biol. Chem.* 246, 4866–4871.

Ten Hoopen, R., Cepeda-García, C., Fernández-Arruti, R., Juanes, M. A., Delgehyr, N., Segal, M., et al. (2012). Mechanism for astral microtubule capture by cortical bud6p priming spindle polarity in S. Cerevisiae. *Curr. Biol.* 22, 1075–1083. doi: 10.1016/j.cub.2012.04.059

Vallen, E. A., Caviston, J., and Bi, E. (2000). Roles of Hof1p, Bni1p, Bnr1p, and Myo1p in cytokinesis in saccharomyces cerevisiae. *Mol. Biol. Cell.* 11, 593–611. doi: 10.1091/mbc.11.2.593

Xie, Y., Sun, J., Han, X., Turšić-Wunder, A., Toh, J. D. W., Hong, W., et al. (2019). Polarisome scaffolder Spa2-mediated macromolecular condensation of Aip5 for actin polymerization. *Nat. Commun.* 10, 1–18.

Xu, T., Vavylonis, D., Tsai, F. C., Koenderink, G. H., Nie, W., Yusuf, E., et al. (2015). SOAX: a software for quantification of 3D biopolymer networks. *Sci. Rep.* 5:9081. doi: 10.1038/srep09081

Yang, H.-C., and Pon, L. A. (2002). Actin cable dynamics in budding yeast. *Proc. Natl. Acad. Sci.* 99, 751–756. doi: 10.1073/pnas.022462899

Yu, H., Braun, P., Yildirim, M. A., Lemmens, I., Venkatesan, K., Sahalie, J., et al. (2008). High-quality binary protein interaction map of the yeast interactome network. *Science* 322, 104–110.

Yu, J. H., Crevenna, A. H., Bettenbühl, M., Freisinger, T., and Wedlich-Söldner, R. (2011). Cortical actin dynamics driven by formins and myosin V. *J. Cell. Sci.* 124, 1533–1541. doi: 10.1242/jcs.079038

Conflict of Interest: The authors declare that the research was conducted in the absence of any commercial or financial relationships that could be construed as a potential conflict of interest.

frontiers in Cell and Developmental Biology

REVIEW
published: 09 February 2021
doi: 10.3389/fcell.2021.635511

Dynamic Microtubule Arrays in Leukocytes and Their Role in Cell Migration and Immune Synapse Formation

Aglaja Kopf[1,2,3] *and Eva Kiermaier*[4]*

[1] CeMM Research Center for Molecular Medicine of the Austrian Academy of Sciences, Vienna, Austria, [2] Department of Dermatology, Medical University of Vienna, Vienna, Austria, [3] Ludwig Boltzmann Institute for Rare and Undiagnosed Diseases, Vienna, Austria, [4] Life and Medical Sciences Institute, Immune and Tumor Biology, University of Bonn, Bonn, Germany

The organization of microtubule arrays in immune cells is critically important for a properly operating immune system. Leukocytes are white blood cells of hematopoietic origin, which exert effector functions of innate and adaptive immune responses. During these processes the microtubule cytoskeleton plays a crucial role for establishing cell polarization and directed migration, targeted secretion of vesicles for T cell activation and cellular cytotoxicity as well as the maintenance of cell integrity. Considering this large spectrum of distinct effector functions, leukocytes require flexible microtubule arrays, which timely and spatially reorganize allowing the cells to accommodate their specific tasks. In contrast to other specialized cell types, which typically nucleate microtubule filaments from non-centrosomal microtubule organizing centers (MTOCs), leukocytes mainly utilize centrosomes for sites of microtubule nucleation. Yet, MTOC localization as well as microtubule organization and dynamics are highly plastic in leukocytes thus allowing the cells to adapt to different environmental constraints. Here we summarize our current knowledge on microtubule organization and dynamics during immune processes and how these microtubule arrays affect immune cell effector functions. We particularly highlight emerging concepts of microtubule involvement during maintenance of cell shape and physical coherence.

Keywords: microtubules, leukocytes, cell migration, immune synapse, cell coherence

OPEN ACCESS

Edited by:
Anne Straube,
University of Warwick,
United Kingdom

Reviewed by:
Martin Harterink,
Utrecht University, Netherlands
Irina Kaverina,
Vanderbilt University, United States
Pablo Vargas,
Institut Curie, France

***Correspondence:**
Eva Kiermaier
eva.kiermaier@uni-bonn.de

Specialty section:
This article was submitted to Cell Growth and Division, a section of the journal Frontiers in Cell and Developmental Biology

Received: *30 November 2020*
Accepted: *18 January 2021*
Published: *09 February 2021*

Citation:
Kopf A and Kiermaier E (2021) Dynamic Microtubule Arrays in Leukocytes and Their Role in Cell Migration and Immune Synapse Formation. Front. Cell Dev. Biol. 9:635511. doi: 10.3389/fcell.2021.635511

INTRODUCTION

The cytoskeleton plays a major role for accomplishing numerous immune cell effector functions. Microtubule filaments are crucially important for directing migratory cells to their final destination and for mediating specific cell-cell interactions between an antigen-presenting cell and a T cell. Microtubules are composed of α-/β-tubulin heterodimers which polymerize in a head-to-tail fashion to form a polar protofilament with the α-tubulin subunit exposed to one end – designated as minus-end – and β-tubulin exposed to the other end, which is commonly referred to as the plus-end (Nogales, 2000). In most eukaryotic cells, 13 protofilaments associate laterally to form long, hollow tubes, which are highly dynamic and stochastically oscillate between periods of growth and shrinkage, a property known as "dynamic instability" (Mitchison and Kirschner, 1984). Within

cells, microtubule minus-ends are mainly static and stably anchored to a variety of microtubule-organizing structures, from which individual filaments nucleate with their growing plus-ends projecting to the cell periphery (Wu and Akhmanova, 2017). The microtubule lattice as well as the microtubule plus-ends are decorated with microtubule associated proteins (MAPs) such as end-binding (EB) proteins, microtubule (de)-polymerases and regulatory kinesins, all of which modify the dynamics of microtubule filaments and their plus-ends and contribute to highly plastic and functionally specialized microtubule arrays (Bodakuntla et al., 2019). Besides the plethora of MAPs, distinct tubulin isoforms and posttranslational tubulin modifications (PTMs), which collectively make up the tubulin code, introduce additional diversity of microtubule networks (Gadadhar et al., 2017). Today it is well recognized that microtubule structure and dynamics are differentially regulated in a cell-type dependent manner thereby supporting specific morphologies and functions. Here we summarize our current understanding and recent advances of microtubule arrays and their functions in leukocytes.

LEUKOCYTES

Leukocytes are commonly known as white blood cells, which constitute the major component of the body's defensive unit against diseases. In contrast to erythrocytes, many types of leukocytes exist, which mainly originate from hematopoietic stem cells in the bone marrow. They are classified either by structure into granulocytes and agranulocytes or by cell lineage into myeloid or lymphoid cells. In contrast to other highly specialized cell types, which often reorganize microtubules into non-centrosomal arrays during differentiation, leukocytes primarily nucleate microtubules from the centrally located centrosome with individual filaments extending radially toward the cell periphery (Muroyama and Lechler, 2017; Meiring et al., 2020; **Figure 1**). One exception to this centrosome-derived microtubule array was described for T cells, in which microtubule nucleation can also proceed from non-centrosomal sites such as the Golgi apparatus (Ong et al., 2018).

One of the most characteristic features of all leukocytes is their highly motile behavior. Lymphocytes constantly patrol the body for foreign antigen by recirculating from blood, through tissue, into lymph and back into the blood stream. Myeloid cells such as neutrophils and monocytes emigrate from the blood stream into tissues when they detect changes on the surface of blood vessels that transmit signals of injury or infection (Springer, 1994). A critical link between innate and adaptive immunity constitute dendritic cells, which, in their resting state, patrol peripheral tissues in search for pathogens (Banchereau et al., 2000). Microbial encounter triggers a maturation process that enables these cells to ingest antigens and become responsive to lymph node homing guidance cues to initiate T cell priming (Steinman and Cohn, 1973). In their mature state, dendritic cells are highly migratory and move through the interstitial matrix to enter the draining lymph node via afferent lymphatic vessels (Worbs et al., 2017). Prior to migration, resting leukocytes respond to specific chemical signals by developing a defined polarized morphology with the formation of an actin-rich lamellipodium at the cell front and a contractile trailing edge at the back, which is referred to as the uropod (Sánchez-Madrid and del Pozo, 1999; Hind et al., 2016). Rearrangement of actin and microtubule filaments are critically involved in establishing this front-rear polarity. Newly synthesized actin polymers at the leading edge protrude the membrane in the forward direction, while myosin-mediated contraction of the trailing edge facilitates de-adhesion and propels the cell body forward. In contrast to stationary polarized cells such as neurons or epithelial cells, leukocytes change their polarity frequently and rapidly, in some cells on a time scale of seconds rather than minutes or hours. Here we focus on the spatial and temporal reorganization of the microtubule cytoskeleton during leukocyte migration in environments of different complexity. We refer the reader to an excellent recent review regarding actin-dependent remodeling of cell locomotion in three dimensional (3D) environments (Yamada and Sixt, 2019).

ADAPTIVE MIGRATION STRATEGIES DETERMINE THE DEPENDENCE ON MICROTUBULES

Leukocytes exhibit a remarkable repertoire of migratory plasticity, being able to instantaneously switch between adhesion-dependent and adhesion-independent migration. The latter is characterized by the absence of proteolytic degradation and requires frequent cell shape changes in combination with a highly polarized morphology, which bear parallels to the phenotypic behavior of migrating amoeba (Wilkinson, 1986). Due to these morphological similarities, leukocyte motility is commonly designated as being amoeboid, which refers to cell movement driven by frequent shape changes (*amoibe*; Greek for "change"). By contrast, adhesion-dependent migration occurs as a consecutive sequence of leading-edge protrusion, transmembrane force coupling by adhesion receptors and contraction of the cell rear to promote de-adhesion, closely resembling Abercrombie's three-step mesenchymal migration mode (Abercrombie et al., 1970, 1977).

Adaptive leukocyte migration strategies strongly depend on the environmental context: when moving along sheet like structures such as the endothelial lining of blood vessels or basement membranes, leukocytes exhibit a mesenchymal mode of migration. However, in most cases leukocytes reside in structurally complex microenvironments such as collagen-rich interstitial matrices or cell-rich compartments found in lymph nodes or granulomas. When embedded in such environments, leukocytes shift their mode of migration to an adhesion-independent amoeboid mode (Lämmermann et al., 2008; Renkawitz et al., 2009; Friedl and Wolf, 2010). This migration mode is powered by frequent cell shape changes that intercalate with any textured environment and thus propel a cell forward, thereby enabling leukocytes to move in an autonomous manner, irrespective of the chemical composition of their microenvironment (Reversat et al., 2020). Finally, leukocytes cross the endothelial cell barrier in a process called

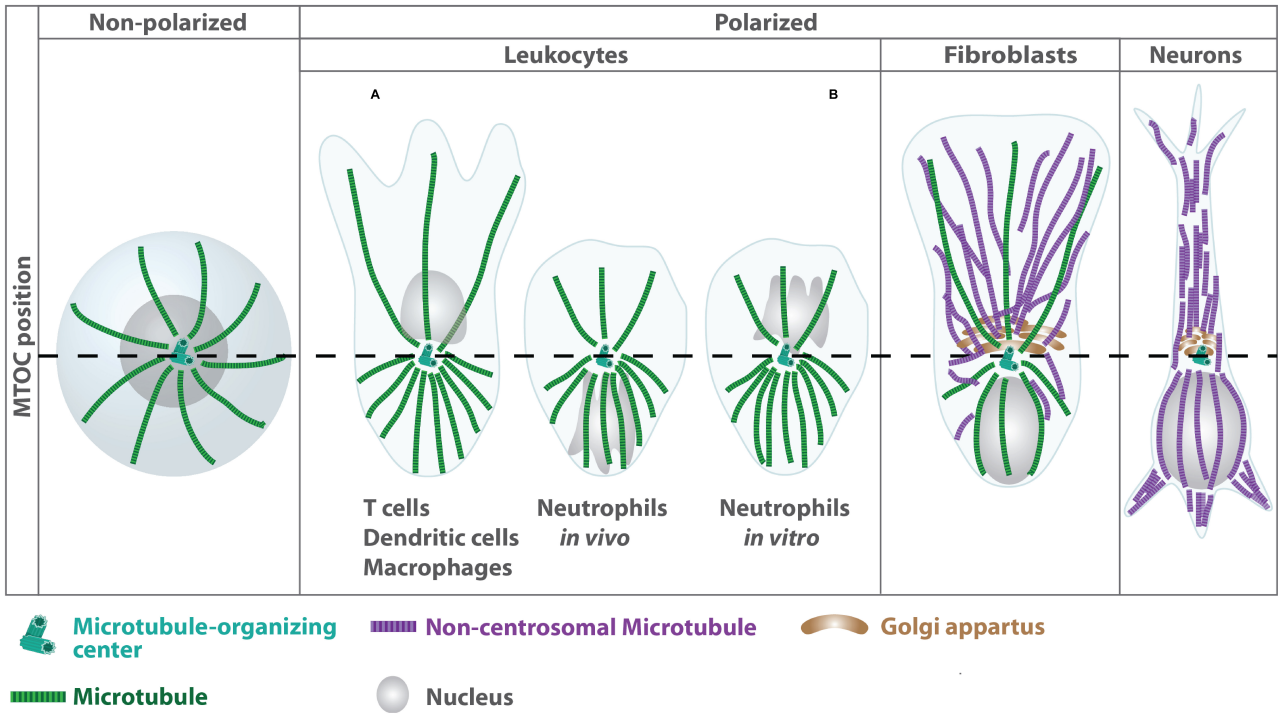

FIGURE 1 | Differential organization of microtubule arrays in distinct cell types. Terminal differentiation into effector cells such as neurons is associated with a reorganization of centrosomal microtubule filaments into non-centrosomal arrays (Muroyama and Lechler, 2017). In highly specialized leukocytes, the centrosome acts as single MTOC, from which a radial array of microtubule filaments project to the cell periphery. In unpolarized leukocytes, the centrosome is located centrally close to the nucleus (left panel). During polarization the MTOC reorients toward the uropod leading to higher densities of microtubule filaments at the cell's back (right panel). By contrast, fibroblasts exhibit an anterior MTOC localization relative to the nucleus. MTOC positioning is highly plastic in neutrophils and differs depending on the complexity of the environment (Yoo et al., 2013).

transendothelial migration (TEM) or diapedesis (Ley et al., 2007; Muller, 2011). While microtubule arrays in endothelial cells play an important role during TEM (Mamdouh et al., 2008), in leukocytes neither preexisting nor *de novo* generated microtubules seem to be essential for efficient transmigration (Fine et al., 2016; Yadav et al., 2019).

A unifying feature of both migration strategies is that, in order to fulfill their effector functions, migrating leukocytes need to integrate the entire imposed mechanochemical parameters of the microenvironment to successfully navigate to their destination site. While actin dynamics are essential for locomotion and cell contractility, dynamic microtubules are indispensable for cell shape and the establishment and maintenance of cell polarity. Much of the gained knowledge originates from studies of cells moving on 2D surfaces, but recent evidence suggests a differential role for microtubules during migration in complex 3D environments (**Figure 2**), where mesenchymal cells begin to depend on an intact microtubule network to move within soft matrices (Unemori and Werb, 1986; Doyle et al., 2009).

Microtubule Arrays in Simple Environments

The role of microtubules during leukocyte migration was initially assessed in neutrophils. In the absence of a chemotactic cue neutrophils rest or move without any preferred direction. This non-directed mode of locomotion is referred to as random migration. Uniform addition of a chemotactic factor increases random migration – a phenomenon termed stimulated random migration or chemokinesis. If the chemotactic factor is presented as a gradient, migration changes from a stimulated random mode to directional migration. Under these conditions, cells move toward the chemotactic source *en masse*, which is known as chemotaxis (Allan and Wilkinson, 1978; Zigmond et al., 1981). Various compounds have been identified to bind to tubulin and/or microtubules thereby altering microtubule polymerization and dynamics. Most of these agents originate from natural sources and were isolated from marine organisms, plants and bacteria (Amador et al., 2003). At high concentrations these compounds are often classified into either microtubule-stabilizing agents such as taxol and the epothilones or destabilizing agents, which include colchicine, vinblastine or nocodazole. Most microtubule-stabilizing agents bind to β-tubulin on the luminal side of microtubules and stabilize longitudinal and/or lateral tubulin contacts (Neuert et al., 2013; Alushin et al., 2014). Microtubule-destabilizing agents bind between the α- and β-tubulin subunit within the same dimer or between two different longitudinally aligned dimers. They act on microtubules by different mechanisms all of which de-stabilize the dynamic plus-ends of microtubules (Skoufias and Wilson, 1992; Ravelli et al., 2004; Gigant et al., 2005).

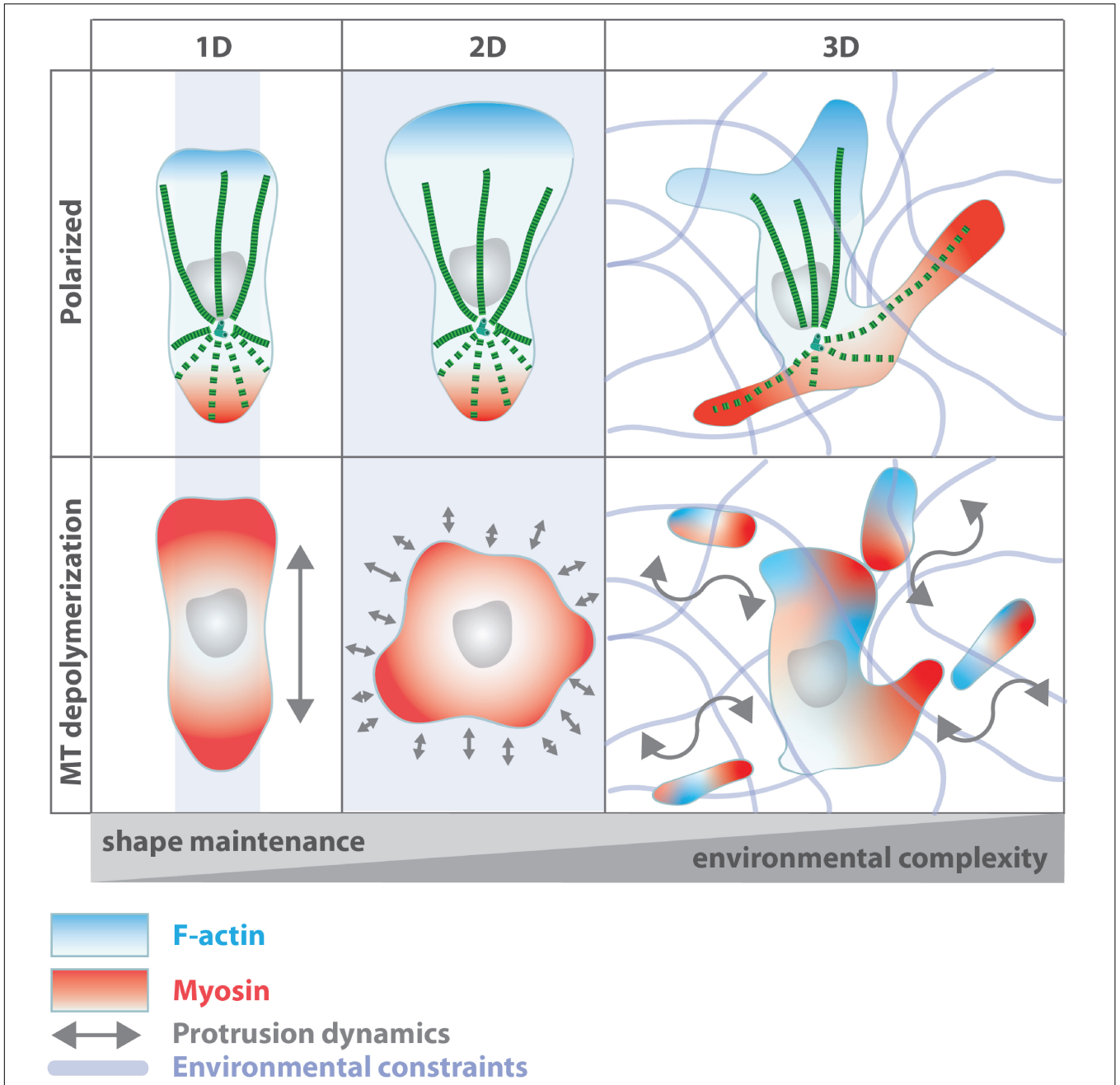

FIGURE 2 | Microtubule function during leukocyte migration in environments of different complexity. Microtubule depletion leads to uncoordinated actomyosin activation, yet with different consequences on cell shape and coherence depending on the geometry of the cell's surrounding. Oscillating myosin activation across the cortex yields in uncoordinated and unstable polarization in 2D while in linear channels (1D) leukocytes maintain their polarized shape. In complex 3D environments, microtubules mediate the coordination of multiple competing protrusions (Renkawitz et al., 2019; Kopf et al., 2020). Disruption of microtubule integrity impairs protrusion-retraction dynamics of competing extensions resulting in loss of cell shape and induction of cell fragmentation.

Probing neutrophils with microtubule destabilizing agents impairs direction-finding or directional movement during chemotaxis but not the mechanism of neutrophil locomotion *per se* (Bandmann et al., 1974; Gallin and Rosenthal, 1974; Keller et al., 1984; Niggli, 2003; Xu et al., 2005). A similar phenomenon of diminished persistent locomotion toward chemotactic cues upon disturbing microtubule integrity was also observed in macrophages, T cells and dendritic cells *in vitro* and *in vivo* (Ratner et al., 1997; Redd et al., 2006; Takesono et al., 2010; Yoo et al., 2013; Kopf et al., 2020). Stabilization of microtubules by taxol similarly disturbed the polarized distribution of F-actin and greatly reduced directional locomotion without affecting migration velocities of migrating T cells and neutrophils (Niggli, 2003; Yadav et al., 2019) indicating that dynamic microtubules

do not contribute to the force-generating mechanisms required for amoeboid migration but rather support the path of locomotion along the chemotactic gradient. Interestingly, in the absence of chemoattractant, microtubule depolymerization induces neutrophils to spontaneously polarize and migrate randomly suggesting that in resting neutrophils, microtubules rather suppress polarity instead of inducing it (Bandmann et al., 1974; Gallin and Rosenthal, 1974; Dziezanowski et al., 1980; Keller et al., 1984; Niggli, 2003; Xu et al., 2005).

How Do Microtubules Regulate Directional Locomotion in Simple Environments?

Leukocyte microtubules rapidly respond to chemotactic cues with increased filament polymerization (Gallin and Rosenthal, 1974; Robinson and Vandre, 1995). During cell polarization, the microtubule array reorients toward the uropod, which is maintained during locomotion and does not require microtubule disassembly or substrate attachment through integrin receptors (Malech et al., 1977; Anderson et al., 1982; Ratner et al., 1997; Eddy et al., 2002; Xu et al., 2005). Inhibition of myosin phosphorylation or actin polymerization causes an expansion of the microtubule array and penetration of microtubules into the lamellipodium indicating that F-actin- and myosin II-dependent forces lead to the development and maintenance of microtubule asymmetry (Eddy et al., 2002). During chemotaxis, the microtubule organizing center (MTOC) relocalizes behind the nucleus and microtubules align along the axis of migration with individual filaments orienting toward the uropod while the F-actin rich lamellipodium becomes populated with only few filaments extending to the leading edge cell membrane. One exception to the posterior localization of the MTOC is observed in neutrophils, which change MTOC orientation rapidly depending on the environmental conditions, yet, with individual filaments projecting to the back of the cell (Chiplonkar et al., 1992; Yoo et al., 2013). Relocalization of the microtubule array to the uropod increases microtubule density at the cells' back suggesting that microtubules promote back-directed processes rather than stabilization of the lamellipodium as reported for mesenchymal migration (Waterman-Storer et al., 1999). This is further supported by the fact that the MTOC follows the turning leading edge instead of guiding the direction of the lamellipodium indicating that the MTOC and microtubule filaments do not determine the cell's leading protrusion but rather act as a path finder by stabilizing a chosen direction of locomotion (Ueda et al., 1997; Xu et al., 2005).

How do Microtubules Stabilize the Path of Locomotion?

Recent studies in dendritic cells revealed that the dynamics of individual microtubule filaments are differentially regulated depending on their localization: while microtubules projecting to the leading edge are stable and long lived, microtubule dynamics at the trailing edge exhibit higher frequencies of shrinkage events compared to front-directed filaments. The high local microtubule depolymerization rate at the uropod is causally connected to retraction of the cell's back demonstrating that microtubules are able to regulate local cellular retraction events (Kopf et al., 2020). Two signaling modules have been identified, which act in concert to balance morphological frontness and backness in migrating cells: RhoA- and actomyosin dependent contractility stimulate cellular backness, while F actin-rich protrusions at the cell front are regulated by a trimeric G protein, the small GTPase Rac, and 3′ phosphoinositides such as PIP3 (Niggli, 2003; Xu et al., 2003; Yoo et al., 2010). Microtubules link RhoA and actomyosin activation by release of the RhoA-specific guanine nucleotide exchange factor (GEF)-H1 (Ren et al., 1998; Krendel et al., 2002; Chang et al., 2008). Microtubule depolymerization leads to untethering of GEF-H1 from the microtubule lattice, which in turn induces RhoA activation and downstream Rho-associated protein kinase (ROCK) signaling leading to myosin II phosphorylation and actomyosin contraction (Krendel et al., 2002; Nalbant et al., 2009). In migrating dendritic cells, microtubules projecting to the back of the cell stabilize the uropod by delivering GEF-H1, allowing for local activation of RhoA and myosin contraction (Kopf et al., 2020). Such subcellular microtubule-mediated activation processes, specifically lead to local contraction events via the RhoA-ROCK-myosin axis as demonstrated for the uropod. This local RhoA activation might explain the different behavior of neutrophils after microtubule depolymerization in the absence of chemotactic cues: while large and ramified dendritic cells allow local microtubule-mediated cell retraction events, in small cells such as neutrophils, microtubule depolymerization globally activates RhoA leading to oscillating cortical myosin activation and fluctuating cell polarization, which in turn induces random motility.

Microtubules in Complex Environments – Implications for Cell Coherence

The involvement of microtubules, specifically during leukocyte migration in complex environments, still remains an underexplored area of research. On top of that, not only environmental constraints but also cell intrinsic factors such as cell size and protrusion dynamics affect the level to which microtubules are required for migrating leukocytes.

To efficiently navigate through dense 3D microenvironments, leukocytes initially extend multiple protrusions into pores of their immediate vicinity to explore different potential paths for locomotion. Ultimately, they have to retract all but one protrusion thereby selecting one direction along which the cell further advances. The most critical part during migration in complex environments is translocation of the cell's nucleus, which constitutes the largest organelle within the cell. During path selection leukocytes position their nucleus to the cell front to act as a mechanical ruler allowing to detect pore size differences. Ultimately, cells bypass local hindrances within the extracellular matrix by choosing larger pore sizes thus favoring the path of least resistance (Renkawitz et al., 2019). The MTOC is positioned directly behind the nucleus and seems to push the nucleus forward (Zhao et al., 2012). Once the MTOC passes the junction point, competing cellular protrusions

become instable and retract in a microtubule dependent manner (Kopf et al., 2020). Due to their stiff nature, microtubule filaments grow in straight trajectories and fail to enter curved or buckled protrusions. Once protrusions bend beyond a critical point, microtubules start to depolymerize and – via release of GEF-H1 – locally activate RhoA and actomyosin contraction thereby inducing cellular retraction (**Figure 2**). This constitutes a remarkably simple mechanism of how multiple competing protrusions of ramified cells communicate with each other and establishes the microtubule cytoskeleton as an important mediator of cell integrity. Such subcellular microtubule-mediated actomyosin activation processes, which specifically lead to local retraction events of remote cell edges, seem to work primarily in large and ramified cells, while small cells such as neutrophils and T cells typically employ plasma membrane tension to communicate between multiple competing protrusions (Diz-Muñoz et al., 2016). In contrast to cells moving in geometrically simple environments, global microtubule depolymerization of cells embedded in complex 3D environments causes loss of cell coherence by uncoordinated protrusion dynamics, which ultimately leads to auto-fragmentation and cell death (Renkawitz et al., 2019; Kopf et al., 2020; **Figure 2**).

Similarly, microtubules also control cell shape in tissue-resident memory T (T_{RM}) cells. Skin T_{RM} cells exhibit highly dynamic shape changes when migrating within the constrained epidermal layer with extension of multiple competing protrusion similar to dendritic cells. Treatment of T_{RM} cells in the skin with microtubule destabilization agents induces cell elongation and fragmentation of extending dendrites suggesting that an intact microtubule network is also required to maintain cellular coherence of T_{RM} cells within the epidermis (Zaid et al., 2017). Besides GEF-H1, the atypical Cdc42-specific GEF dedicator of cytokinesis 8 (DOCK8) plays an important role for maintaining lymphocyte cell integrity. DOCK8-deficient T cells and natural killer cells develop an abnormally elongated shape and deformation of the nucleus in 3D collagen matrices and human skin tissues (Zhang Q. et al., 2014). Chemotaxis of DOCK8-deficient T cells is unaffected but cells fragmented frequently when moving in confined spaces, causing a distinct form of cell death and the inability to generate long-lived tissue resident T cells. These results establish a crucial role for DOCK8 in mediating cytoskeletal rearrangements during locomotion in 3D environments. Whether DOCK8 directly affects microtubule integrity is currently unknown.

In summary, there is mounting evidence that a dynamic microtubule cytoskeleton is essential for maintenance of cell shape and coherence by coordinating protrusion dynamics of leukocytes migrating in complex 3D environments.

Microtubules and the Formation of the Immune Synapse

The high specificity of immune responses largely depends on direct cell-cell interactions. Leukocytes are able to form tight contacts with other types of immune- or non-immune cells leading to the initiation of adaptive immune responses or activation of effector cells able to eliminate potentially dangerous cells. In analogy to the morphologically similar neuronal synapse, the contact area that is built between two adjacent cells is referred to as the immunological synapse. Two major types of immune synapses exist – helper T cell synapses forming between antigen-presenting cells and T helper cells and cytotoxic synapses, which are established between cytotoxic T cells or natural killer cells and a target cell. Both types of synapses share common features but also display cell type-specific differences. However, in both cases, the effector cells must distinguish foreign antigens from self-proteins, which poses a major challenge to this task in terms of specificity.

T Helper Cell and Cytotoxic Synapses

Efficient activation of T helper cells is mediated through the presentation of a specific antigen by an antigen-presenting cell. The T cell receptor first recognizes a cognate antigen, which is presented on major histocompatibility complexes on the surface of the antigen-presenting cell (Turley et al., 2000). Subsequently, this interaction leads to the formation of the immune synapse at the T cell-antigen-presenting cell junction. At the immune synapse, T cell receptors, integrins and co-stimulatory receptors engage with each other to form a series of supramolecular activation clusters (SMAC), which segregate into radial symmetric zones facing the antigen-presenting cell (Shaw and Dustin, 1997; Dustin and Choudhuri, 2016). Structurally, the T cell receptors and associated kinases cluster in the central area (central supramolecular activation cluster; central SMAC), while adhesion receptors and actin, as well as actin-interacting proteins, reorganize in surrounding external rings referred to as the peripheral and distal SMAC (peripheral SMAC and distal SMAC) (Monks et al., 1998; Grakoui et al., 1999; Krummel et al., 2000).

Cytotoxic lymphocytes play a crucial role in mediating innate and adaptive immune responses. Natural killer cells and cytotoxic T lymphocytes provide rapid responses to virally infected cells and tumor formation. They are able to directly eliminate cells by the release of large amounts of secretory lysosomes – termed lytic granules – leading to target cell lysis. Impaired functioning of cytotoxic T lymphocytes may lead to immune evasion of tumors and the emergence of chronic infections. Similar to T cell activation, the first step in cell-mediated cytolysis is binding of the cytotoxic T lymphocyte's T cell receptor to a foreign antigen presented on the surface of the target cell. Cytotoxic synapses structurally display a similar organization as T helper cell synapses with a ring of adhesion molecules surrounding an inner signaling domain. Secretion occurs into a specialized domain lying next to the central SMAC and within the peripheral SMAC. A secretory cleft, which appears as an indentation in the membrane of the target cell, lies opposite the secretory domain (Stinchcombe et al., 2001).

In both cases, T cell receptor-antigen ligation leads to repositioning of the centrosome from the uropod to the contact side: upon ligation of an antigen-loaded B cell with a T helper lymphocyte, the MTOC inside the T cell reorients toward the cell contact region with the antigen-presenting cell (Kupfer et al., 1986; Kupfer and Singer, 1989). α-/β-tubulin heterodimers polymerize from the MTOC and form

a network of microtubules at the T cell-antigen-presenting cell contact side. MTOC positioning toward the contact zone strictly depends on T cell receptor engagement with the cognate antigen and concomitantly drives the movement of other organelles such as the Golgi apparatus toward the immune synapse (Kupfer et al., 1986). The rapid repositioning of the T cell's MTOC allows microtubule plus-end directed transport of secretory vesicles containing effector molecules and polarized secretion of these molecules in the direction of the bound antigen-presenting cell (Kupfer et al., 1991). Similarly, Geiger and colleagues demonstrated relocalization of the MTOC and perinuclear Golgi apparatus toward the synapse upon cytotoxic T lymphocyte-target cell conjunction (Geiger et al., 1982). Disturbing microtubule integrity with nocodazole causes dispersion of the Golgi apparatus and reversibly inhibits target cell lysis indicating microtubule involvement in the delivery of lytic granules toward the immune synapse (Katz et al., 1982; Kupfer and Dennert, 1984).

Polarization of the microtubule cytoskeleton and directional secretion of soluble factors toward the immune synapse emerged as key events allowing for specific activation of effector cells and destruction of potentially dangerous cells. During the past 25 years, numerous studies shed light on the mechanisms and stimuli triggering MTOC repositioning in T cells. By contrast, much less is known about the antigen-presenting cell side of the immune synapse. Here we highlight the molecular basis of centrosome translocation and polarized vesicle secretion in T cells and antigen-presenting cells and the role of the microtubule cytoskeleton during these processes. We refer to excellent recent reviews, which discuss the signaling modules that regulate the repositioning of centrosomes toward the immune synapse (Martín-Cófreces and Sánchez-Madrid, 2018; Garcia and Ismail, 2020; Tittarelli et al., 2020).

Microtubule Dynamics at the Immune Synapse

In resting cytotoxic T lymphocytes, microtubules are highly dynamic switching constantly between growth and shrinkage. Microtubules contacting the cell cortex buckle, curl inward and slide laterally along the cell cortex or are prone to depolymerize (Kuhn and Poenie, 2002). Upon T cell receptor ligation, microtubule filaments are anchored to the peripheral SMAC, a ring-shaped structure which surrounds the central SMAC and colocalizes with clusters of the T cell's major integrin LFA-1. Subsequently to the attachment of microtubules to the cell cortex, the MTOC is recruited vectorially to the contact zone. Some microtubules bent at the contact site suggesting the presence of microtubule motor proteins anchored at the cell cortex, which act on microtubules to pull the MTOC toward the immune synapse (Kuhn and Poenie, 2002). Candidate molecules, which have been demonstrated to connect microtubules to the peripheral SMAC at the immune synapse are the cytoskeletal adaptor proteins IQGAP1 and Cdc42-interacting protein 4 (CIP4). IQGAP1 and actin are cleared away from the synapse via an expanding ring, which in turn exerts tension on the microtubule filaments that are anchored at the peripheral SMAC (Stinchcombe et al., 2006). CIP4 interacts with both, the actin and microtubule cytoskeleton and was proposed as functional link between the peripheral SMAC and MTOC polarization (Stinchcombe et al., 2006; Banerjee et al., 2007). MTOC translocation toward the immune synapse further requires precise regulation of microtubule dynamics. Overexpression of histone deacetylase 6, the enzyme that catalyzes the removal of acetylation at lysine 40 of α-tubulin and thus reduces microtubule stability, results in defective MTOC polarization toward the immune synapse (Serrador et al., 2004). Similarly, destabilization of microtubules by either depletion of formins or the microtubule-associated protein 4 (MAP4) impairs MTOC translocation in T cells (Andrés-Delgado et al., 2012; Bustos-Morán et al., 2017). After MTOC polarization, microtubules actively polymerize at the immune synapse. Altering microtubule plus-end dynamics by depletion of the microtubule catastrophe-inducing protein stathmin or the plus-end-binding protein 1 (EB1) as well as impairing EB1 phosphorylation delays MTOC reorientation and movement of vesicles at the immune synapse. Together, these findings highlight the importance of dynamic microtubules in the establishment of a functional immune synapse and T cell activation (Zyss et al., 2011; Filbert et al., 2012; Martin-Cofreces et al., 2012).

A prominent player to generate force for efficient MTOC relocalisation is the microtubule-based motor protein dynein. Dynein acts in concert with two other central components, dynactin and coiled coil containing activating adaptor proteins, which together with additional regulators form a high-molecular weight complex referred to as the cytoplasmic dynein complex (Reck-Peterson et al., 2018). Dynein is composed of six polypeptide chains, one single dynein heavy chain (DHC), two intermediate- and three light chains (dynein intermediate chain (DIC) and dynein light chain (DLC), respectively) all of which are present as two copies. The DHC contains the motor domain that associates with microtubules via a microtubule-binding domain (Kon et al., 2012; Schmidt et al., 2012). Through its direct interaction with the microtubule cytoskeleton, the dynein-dynactin machinery is able to move a variety of different cargoes toward the minus-end of microtubule filaments (Gill et al., 1991; Schroer and Sheetz, 1991).

In stimulated T helper cells, dynein and dynactin colocalize as rings with the adhesion and degranulation promoting adaptor protein (ADAP) at the peripheral SMAC. Similarly, microtubule filaments project to the immune synapse and associate with ADAP into a ring-like structure (Combs et al., 2006). Loss of ADAP diminishes recruitment of dynein and centrosome relocalization suggesting a causal link between ADAP, cytoplasmic dynein localization and MTOC reorientation toward the immune synapse. Accordingly, interference with dynein-dynactin activity by either overexpression of p50-dynamitin or silencing the DHC prevents MTOC relocalization after T cell receptor engagement supporting the notion that cytoplasmic dynein is functionally involved in centrosome polarization toward the immune synapse (Martin-Cofreces et al., 2008).

Provided that microtubule minus-ends are anchored at the MTOC these data support a model, in which the dynein-dynactin complex localizes to the plasma membrane at the immune

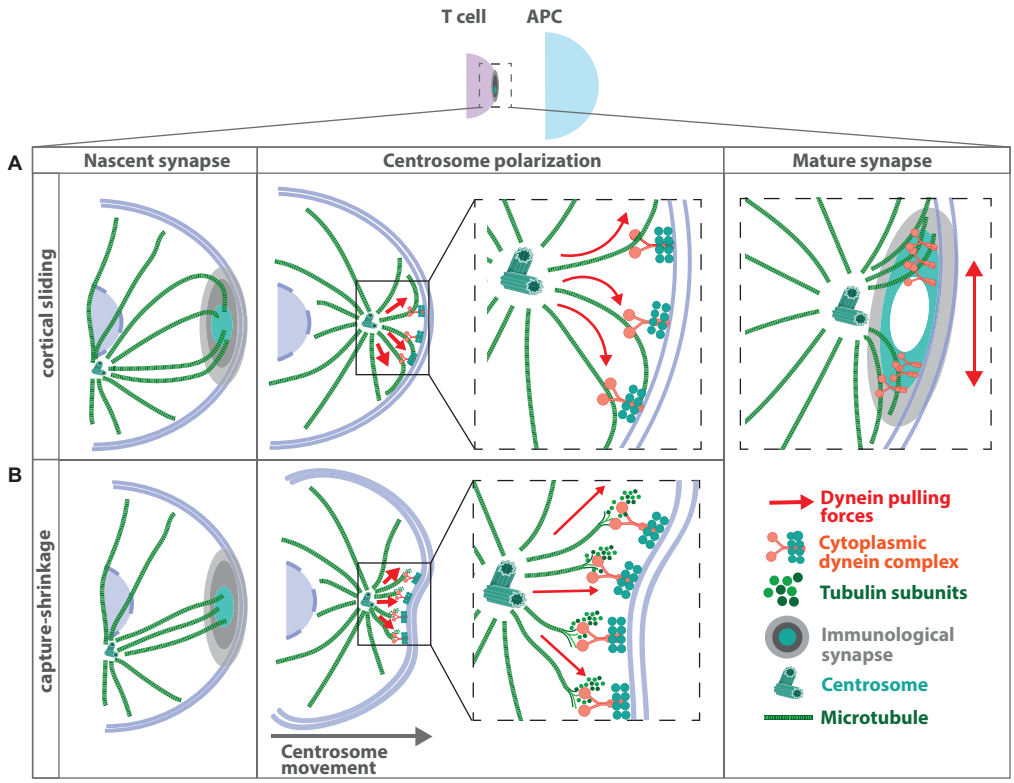

FIGURE 3 | Mechanisms of MTOC translocation during immune synapse formation. Antigen recognition on the surface of an antigen presenting cell by the T cell receptor leads to the formation of a tight contact zone between two adjacent cells. Microtubule filaments inside the T cell project toward the contact area and subsequently the MTOC gets recruited to the immune synapse. Two major models have been proposed how MTOC relocalization is achieved, both of which depend on the presence of the microtubule-associated motor protein dynein at the plasma membrane. **(A)** In the "cortical sliding model" dynein is held in place at the cell cortex and simultaneously walks toward the minus-end of the microtubule filaments. This leads to cortical sliding of microtubules and pulling of the MTOC toward the contact site (Martin-Cofreces et al., 2008). **(B)** The "capture-shrinkage model" suggests that the force, which is required for MTOC translocation is generated by the dynamic instability of microtubule filaments and transmitted via dynein (Yi et al., 2013). Here dynein couples microtubule depolymerization to the cell cortex to move the MTOC toward the synaptic membrane. Recently a revised model for MTOC translocation to the immune synapse was proposed, in which centrally localized dynein first pulls the centrosome straight toward the immune synapse. Afterward, dynein congresses at the peripheral SMAC, which leads to opposing forces acting laterally on the centrosome (Maskalenko et al., 2020). Such lateral pulling forces lead to oscillating movements of the centrosome at the immune synapse.

synapse and exerts the force, which is required to recruit the MTOC close to the contact site (**Figure 3A**). In this model, dynein is held in place at the cell cortex and simultaneously walks toward the minus-end of the microtubule filaments leading to cortical sliding of microtubules and pulling of the MTOC toward the plasma membrane (Martin-Cofreces et al., 2008). MTOC repositioning based on this cortical sliding mechanism has been assessed by quantitative biomechanical modeling (Kim and Maly, 2009). According to this model, a pulling mechanism is capable of MTOC reorientation and compatible with the vectorial description of MTOC translocation derived from earlier experiments (Kuhn and Poenie, 2002).

A second model based on experimental data suggests that the force, which is required for MTOC translocation is generated by microtubule depolymerization and coupled via dynein to move the MTOC toward the cortex (**Figure 3B**). In this model, dynein binds to microtubule plus-ends at the plasma membrane and drives MTOC repositioning via a capture-shrinkage mechanism (Yi et al., 2013). Optical tweezers were used to place the antigen-presenting cell to the opposite site of the T cell's MTOC allowing to image the process of MTOC repositioning and microtubule dynamics in T cells with high spatial and temporal resolution. MTOC repositioning follows two distinct kinetic phases: a fast polarization phase of ∼3.3 μm/min and a slower ∼0.9 μm/min docking phase. Similar to previous studies, microtubule plus-ends project from the MTOC toward the antigen-presenting cell but terminate at the center of the immune synapse in an end-on manner. Several microtubules center at the immune synapse and undergo simultaneous shortening thus bringing the immune synapse and the centrosome together. During microtubule shortening, the membrane underneath the immune synapse invaginates, suggesting force generation at the point of microtubule depolymerization. Similar to the cortical sliding mechanism, inhibition of dynein or microtubule integrity impairs MTOC repositioning (Yi et al., 2013). In support of this, *in vitro* reconstitution experiments showed that barrier-attached dynein is indeed able to trigger microtubule shrinkage and to generate

pulling forces, which are sufficient to center microtubule asters in confining geometries (Laan et al., 2012).

Differences in the underlying mechanism of centrosome repositioning most likely arise from the distinct experimental set-ups: T cell-antigen-presenting cell contacts were initially observed using polarization light microscopy in combination with end-stage fixed samples of cell-cell conjugates (Kuhn and Poenie, 2002; Martin-Cofreces et al., 2008). In order to observe the dynamics of centrosome reorientation toward the immune synapse, Yi and coworker established an optical trap, which allows precise control of cell positioning by placing the antigen-presenting cell opposite to the location of the T cell's centrosome. This allows real-time monitoring and quantitative analysis of MTOC relocalization.

However, in both models dynein anchored at the cell cortex is essential to generate or transmit the force required for MTOC polarization. It is well established that recruitment of dynein and subsequent MTOC translocation depends on the polarized accumulation of the lipid second messenger diacylglycerol (DAG) in the cell membrane (Quann et al., 2009). DAG is generated downstream of T cell receptor ligation by the hydrolysis of phosphatidylinositol-4,5-bisphosphate (PIP2) through Phospholipase C-γ (PLC-γ). Blocking DAG production or disrupting the localization of DAG impairs MTOC polarization in T helper cells and cytotoxic T lymphocytes. Mechanistically, DAG recruits and activates three distinct protein kinase C (PKC) isoforms to the synaptic membrane, which in turn control centrosome reorientation through the localization of dynein and non-muscle myosin II (Quann et al., 2011; Liu et al., 2013). The involvement of non-muscle myosin II suggests that there might be dynein-independent force-generating mechanisms operating to reorient the MTOC. In this regard, pharmacological dynein inhibition in Jurkat T cells, had no effect on MTOC translocation toward the immune synapse (Hashimoto-Tane et al., 2011). Yet, it is hard to estimate whether this might be due to incomplete dynein inhibition or dynein-independent mechanisms of MTOC reorientation. Dynein is further known to form a complex with either Lissencephaly 1 (LIS1) and NudE Neurodevelopment Protein 1 (NDE1), or with dynactin, a multisubunit complex whose largest subunit is $p150^{Glued}$ (Reck-Peterson et al., 2018). Both complexes form mutually exclusive with dynein and mediate distinct cellular activities during T cell activation (Nath et al., 2016). Knockdown of NDE1 or expression of a dominant negative form diminishes dynein localization at the immune synapse and translocation of the MTOC. By contrast, knockdown of $p150^{Glued}$ results in impaired recruitment of secretory vesicles toward the immune synapse whereas MTOC polarization is unaffected. These results suggest that dynein might play a dual role in activating T cells depending on the interacting partner protein (Nath et al., 2016). More recently, a study from the same group demonstrates that the NDE1–dynein complex first accumulates at the center of the immune synapse and then later becomes associated to the peripheral SMAC. The relocalization of dynein depends on the disrupted in schizophrenia 1 (DISC1)-girders of actin filaments (Girdin) complex (Maskalenko et al., 2020). Depletion of either DISC1 or Girdin results in loss of actin accumulation at the immune synapse, impaired recruitment of members of the dynein complex and a failure in MTOC translocation to the synapse. The authors propose a model for MTOC translocation, in which centrally located dynein first pulls the MTOC straight toward the immune synapse until it reaches the center of the dynein ring (**Figure 3**). When dynein relocates to the peripheral SMAC, opposing dynein forces would act to pull the MTOC laterally in an oscillating manner similar to what has been observed in experimental setups before (Kuhn and Poenie, 2002).

Independently of the mechanism of force generation and transmission, microtubules need to be anchored at the immune synapse to efficiently allow MTOC reorientation. Based on the "search and capture" model, which was first proposed in the context of microtubule-chromosome interaction during mitotic spindle assembly (Hill, 1985; Pavin and Toliæ-Nørrelykke, 2014), a mathematical model was established to determine the time of microtubule capture at the immune synapse (Sarkar et al., 2019). Here, microtubules grow and shrink from the MTOC thereby probing their vicinity for a proper anchor ("search"). Once they encounter dynein at the center of the immune synapse they bind to it in an end-on fashion ("capture"). This model incorporates the requirement of dynamic microtubule filaments for MTOC translocation and recapitulates efficient target capture with timescales comparable to experimental data. Search times largely depend on the relative size of the cell, the number of searching microtubules and the distance of the MTOC from the nuclear surface. They become minimal when the immune synapse forms at the nearest or at the farthest sites on the cell surface with respect to the perinuclear MTOC.

MTOC Translocation in Antigen-Presenting Cells

Microtubule organizing center polarization toward the immune synapse was also reported in antigen-presenting cells such as dendritic cells and B cells (Pulecio et al., 2010; Yuseff et al., 2011). In both cell types, reorientation depends on the small GTPase Cdc42 and its upstream activator DOCK8 (Randall et al., 2011). In dendritic cells, vesicles containing the pro-inflammatory cytokine IL-12 enrich around the MTOC immediately after T cell receptor ligation and become dragged toward the dendritic cell-T cell interface suggesting, that MTOC polarization in dendritic cells enables local priming of T cells (Pulecio et al., 2010). However, ultrastructural studies of T cell-dendritic cell conjugates and time-lapse videomicroscopy of plasmacytoid dendritic cell-T cell interactions did not reveal MTOC positioning close to the plasma membrane indicating that MTOC translocation in dendritic cells is dispensable for efficient T cell activation (Mittelbrunn et al., 2009; Ueda et al., 2011). In B cells, MTOC translocation is accompanied by repositioning of lysosomes, which rapidly move toward the B cell receptor-antigen interface and become locally released, allowing acidification of the B cell synapse and secretion of lysosomal proteases that promote the extraction of immobilized surface antigen. Inhibition of lysosome exocytosis results in compromised intracellular antigen processing and presentation to T cells (Duchez et al., 2011; Yuseff et al., 2011).

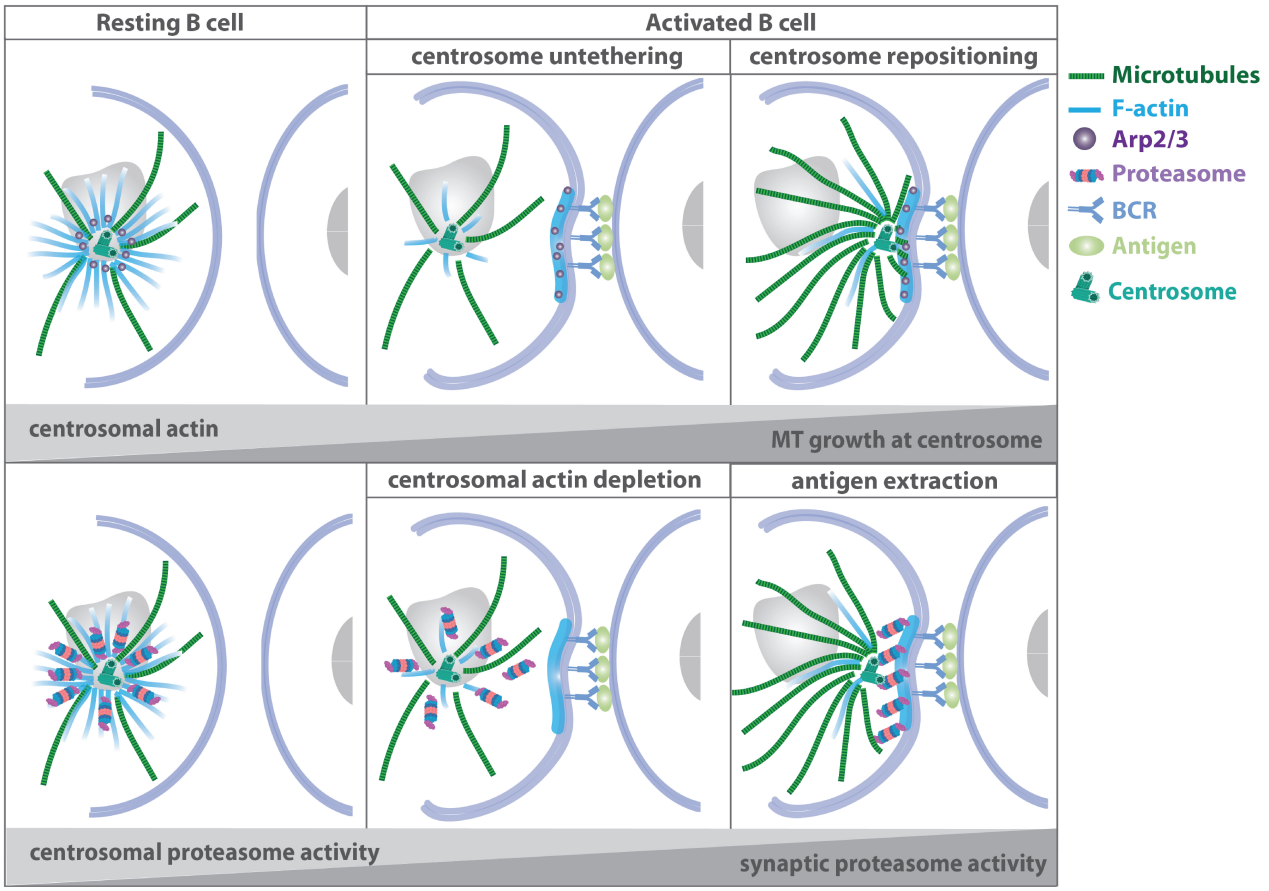

FIGURE 4 | Microtubule-actin crosstalk at the B cell synapse. Upper panel: in resting B cells, Arp2/3-mediated actin nucleation at the centrosome tethers the MTOC to the nucleus. Upon B cell receptor activation, Arp2/3 and F-actin are recruited to the immune synapse thus facilitating centrosome-nucleus separation and repositioning of the MTOC to the cell-cell contact side. Lower panel: proteasomal activity is required for centrosomal actin depletion and subsequent centrosome relocalization to the immune synapse (Obino et al., 2016; Ibañez-Vega et al., 2019).

The mechanisms of MTOC translocation in B cells rely on the interplay of actin and microtubule filaments at the centrosome: in addition to its role as MTOC, the centrosome functions as an organizer of a local network of actin filaments, which can impose physical constraints on the microtubule cytoskeleton, specifically affecting the growth and shape of microtubule filaments as well as the dynamics of the centrosome (Piel et al., 2000; Rodriguez et al., 2003; Huber et al., 2015; Colin et al., 2018; Dogterom and Koenderink, 2019). Centrosomal actin therefore directly regulates the amount and number of nucleating microtubule filaments, by acting as a physical barrier that restricts elongation of nascent microtubules (Farina et al., 2015; Inoue et al., 2019). In resting B lymphocytes, actin related protein 2/3 complex (Arp2/3)-mediated actin nucleation tethers the centrosome to the nucleus thus preventing cell polarization (**Figure 4**). Upon B cell receptor ligation, clearance of centrosomal Arp2/3 reduces F-actin nucleation at the centrosome and facilitates centrosome-nucleus separation allowing the repositioning of the MTOC to the immune synapse. Arp2/3 and F-actin reduction at the centrosome upon B cell activation results from their recruitment to the immune synapse and depends on the Cortactin homolog hematopoietic lineage cell-specific protein (HS1) (Obino et al., 2016). Moreover, proteasome activity is required for centrosomal actin depletion and subsequent centrosome relocalization to the immune synapse. B cells contain two pools of the 26S proteasome, which modulate actin dynamics at the centrosome and at the immune synapse. Proteasome inhibition results in elevated levels of ubiquitinylated proteins and actin at the centrosome, while less F-actin is found at the synaptic membrane. This suggests that upon B cell activation, centrosomal proteasome activity is required to degrade ubiquitylated proteins involved in actin polymerization thus enabling actin depletion and centrosome polarization toward the immune synapse (Ibañez-Vega et al., 2019).

Recently, the mechanistic link between local lysosome fusion at the B cell immune synapse and microtubule dynamics has been addressed (**Figure 5**): lysosome fusion at the synaptic membrane is supported by stabilization of centrosomal microtubules leading to the redistribution of the exocyst complex to the immune synapse (Sáez et al., 2019). B cell receptor engagement promotes the formation of a stable centrosomal microtubule network, which in turn releases Exo70, a component of the

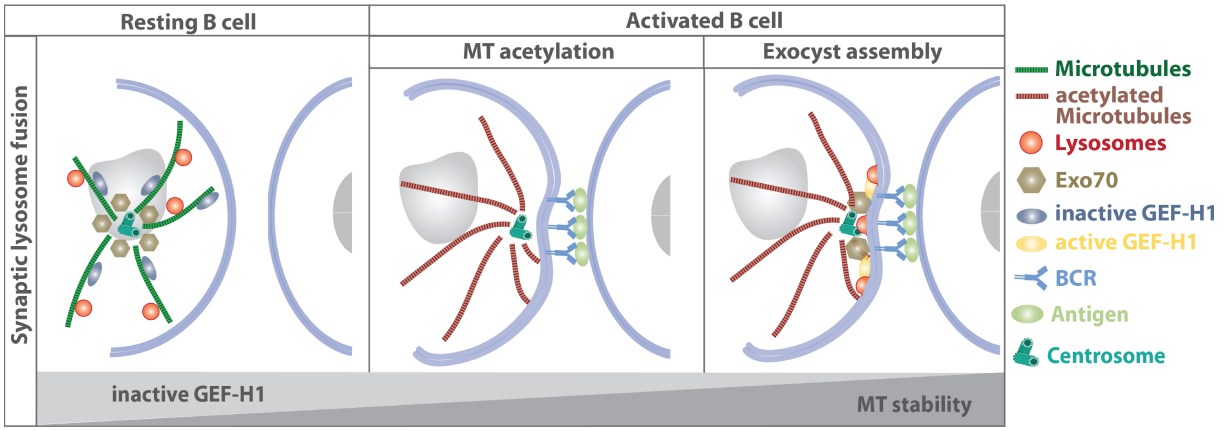

FIGURE 5 | Stabilization of centrosomal microtubules support lysosome fusion at the synaptic membrane by releasing Exo70 and GEF-H1. Concomitantly to the repositioning of the centrosome, lysosomes are recruited to the immune synapse and become locally released, allowing acidification of the B cell synapse and secretion of lysosomal proteases that promote the extraction of immobilized surface antigen. In resting B cells, GEF-H1 is bound to microtubule filaments and kept in its inactive state, while Exo70 is mainly associated to the centrosome. BCR engagement triggers microtubule acetylation, which results in the release of Exo70 and GEF-H1 and subsequent recruitment to the immune synapse. There, GEF-H1 promotes the assembly of the exocyst complex to enable local lysosome fusion at the synaptic membrane (Yuseff et al., 2011; Sáez et al., 2019).

exocyst complex, from the centrosome. Concomitantly, the GTP exchange factor GEF-H1 dissociates from microtubules and together with Exo70 promotes docking and fusion of lysosomes at the immune synapse.

Together, in antigen-presenting cells the direct actin-microtubule crosstalk determines the capacity of the MTOC to repolarize and nucleate microtubules in response to external stimuli and enables local lysosome delivery at the immune synapse.

Polarized Secretion of Effector Molecules at the Synapse

Initially, association of lytic granules with the MTOC and its repositioning toward the immune synapse have been identified as the only prerequisite for targeted secretion while plus-end directed motor transport along microtubule filaments was dispensable for specific killing (Stinchcombe et al., 2006). Lytic granules are delivered directly by the MTOC to an actin-depleted zone within the central SMAC. Yet, granules can also move from the periphery to the synapse using microtubule tracks that are oriented tangentially to the plasma membrane (Poenie et al., 2004). Later studies revealed that granules can take either path depending on the kinetics of downstream T cell receptor signaling (Beal et al., 2009). Lytic granule concentration around the MTOC prior to centrosome reorientation was proposed to increase the capacity of cytotoxic T lymphocytes to elicit a more effective cytolytic response against the next target cell (Stinchcombe and Griffiths, 2007). After leaving a target cell the granules often remain concentrated around the MTOC even when the MTOC repolarizes. This allows cytotoxic T lymphocytes to more rapidly release granules toward the next target cell. A causal link between lytic granule convergence and improved efficiency of target cell lysis was established by Hsu and colleagues demonstrating that concentration of lytic vesicles around the MTOC prevents bystander killing of healthy cells (Hsu et al., 2016; **Figure 6**). Granule convergence toward the MTOC was identified to occur rapidly (Wiedemann et al., 2006). Vesicles move toward microtubule minus-ends in a dynein-dependent manner but independently of microtubule and F-actin reorganization and commitment to cytotoxicity (Mentlik et al., 2010; Ritter et al., 2015). Dynein-mediated minus-end-directed movement of lytic granules is dependent on Src family kinase activity as well as downstream LFA-1 signaling (James et al., 2013; Zhang M. et al., 2014; Kabanova et al., 2018) and the adaptor Hook-related protein 3 (HkRP3) which links lytic granules to the dynein motor complex possibly via DOCK8 (Ham et al., 2015). More recently, vasodialator-stimulated phosphoprotein (VASP), an actin regulatory protein, was identified to regulate lytic granule convergence in natural killer cells. VASP depletion does not interfere with synapse formation and MTOC reorientation but is essential for efficient lytic granule concentration at the MTOC (Wilton and Billadeau, 2018). Once the MTOC and its associated vesicles polarized toward the plasma membrane, a complex between kinesin-1, Slp3, and Rab27 mediates plus-end directed transport of lytic granules along microtubule filaments and docking to the plasma membrane (Kurowska et al., 2012). Rab27a is also known to interact with Munc13-4 and is important for the final steps of lytic granule exocytosis (Ménager et al., 2007). Cells deficient in removing acetylation sites of α-tubulin due to depletion of histone deacetylase six fail to transport lytic granules to the target cell implying that microtubule dynamics and stability play an important role for terminal vesicle transport (Nunez-Andrade et al., 2016).

Whether centrosome polarization is a prerequisite for efficient cytotoxic T lymphocytes and natural killer cell-mediated killing is still a matter of debate. While in several studies impaired or delayed MTOC translocation as well as abrogation of

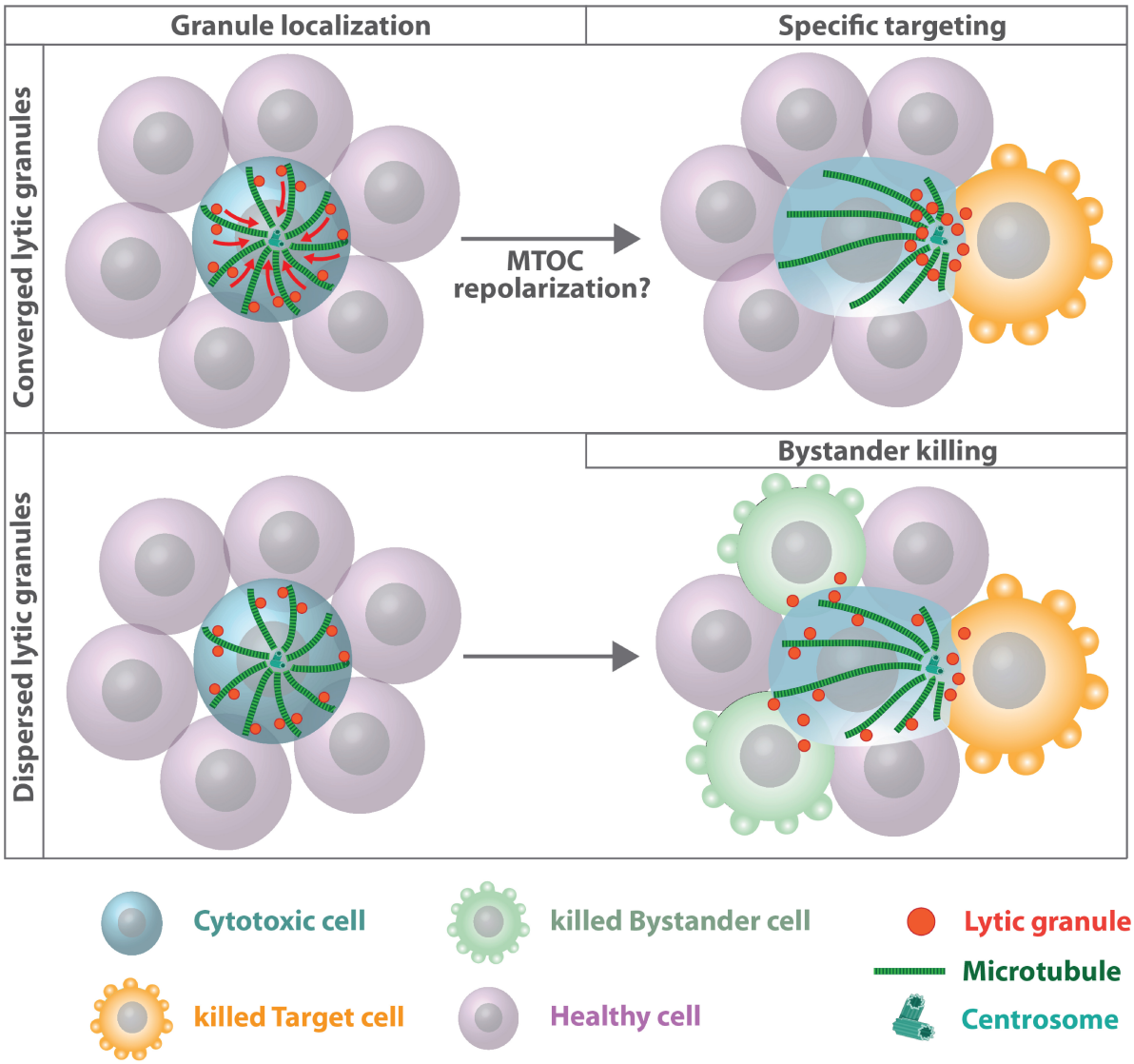

FIGURE 6 | Microtubules and lytic granule convergence. Cytotoxic cells assemble lytic granules around the MTOC, which improves the efficiency of targeted killing (upper panel). Impaired lytic granule convergence results in non-directed degranulation and bystander killing of healthy cells (Hsu et al., 2016). The role of centrosome polarization for efficient cytotoxic T lymphocytes and natural killer cell-mediated killing is still unclear. Under certain experimental conditions, MTOC relocalization toward the immune synapse is dispensable for polarized granule secretion and cytotoxicity (Bertrand et al., 2013; Tamzalit et al., 2020). Under these conditions plus-end directed transport along microtubule filaments might deliver lytic granules to the synapse.

transient centrosome docking with the plasma membrane is associated with reduced cytotoxicity (Quann et al., 2009; Tsun et al., 2011; Stinchcombe et al., 2015), other studies suggest efficient target cell killing prior to or in the absence of MTOC reorientation (Butler and Cooper, 2009; Bertrand et al., 2013). Recently, genetic depletion of centrioles was shown to have no measurable effect on lytic granule polarization, directionality of secretion and specificity of target killing, arguing for a centriole-independent way of lytic granule convergence and target cell specificity (Tamzalit et al., 2020). Nevertheless, centriole-deficient cytotoxic T lymphocytes exhibit reduced cytotoxic potential due to profound defects in lytic granule biogenesis and synaptic F-actin dynamics, resulting in reduced F-actin clearance at the center of the synapse and decreased synaptic force exertion. Centriole-depleted cytotoxic T lymphocytes still assemble components of the pericentriolar material into acentriolar MTOCs, which retain their ability to nucleate microtubule filaments, leading to a perturbed architecture of microtubule arrays in centriole-depleted cells. Depletion of microtubule filaments with nocodazole blocks centrosome reorientation and accumulation of lytic granules at the immune synapse but does not affect the directionality of granule release and bystander killing indicating that the microtubule cytoskeleton is important for facilitating transport of lytic granules to the immune synapse,

but centrosome polarization *per se* is not essential for the spatial specificity of fusion events (Tamzalit et al., 2020).

Concluding Remarks and Future Perspectives

Here we have summarized the multiple faces of microtubule involvement during immunological processes ranging from leukocyte migration to immune synapse formation and vesicle polarization. We have learned from recent studies that leukocyte microtubules are essential for the induction of tissue immunity by maintaining cell coherence of migrating leukocytes and regulating polarized secretion of granules and lysosomes. As such, microtubule arrays deserve precise attention and exact description in future studies of immunological processes.

Migrating dendritic cells exhibit differences in the dynamics of front- versus back-directed microtubule filaments. How this polarization is achieved and what are the key regulators of microtubule dynamics in migrating leukocytes still remain open questions. Advanced light sheet microscopy in combination with recently developed photo-switchable compounds and optogenetic constructs that target microtubule stability and dynamics are potent tools to investigate subcellular microtubule dynamics with high spatiotemporal resolution allowing to understand the functional principles of microtubule dynamics in tissue navigating cells (Borowiak et al., 2015; Müller-Deku et al., 2020; Van Geel et al., 2020). Similarly, the regulatory mechanisms of microtubule dynamics during immune synapse formation and polarized vesicle release are poorly understood. Plus-end binding proteins are essential regulators of polarized microtubule stability and density where EB1-dependent microtubule remodeling is crucial for vesicle trafficking and sustained T cell activation (Martin-Cofreces et al., 2012). Yet, how EBs are regulated at the plus-ends of microtubules and which factors regulate microtubule density during immune synapse formation is currently ill defined.

Adaptive immunity is to a large extent influenced by mechanical forces. Microtubules accumulate a great diversity of PTMs, which can alter microtubule dynamics and thus control the mechanical properties and function of microtubule filaments. Acetylation of α-tubulin at the luminal surface of microtubules affects filament stability and is associated with long lived microtubule subpopulations (Howes et al., 2014; Eshun-Wilson et al., 2019). Functionally, tubulin acetylation is required to protect microtubules from mechanical breakage indicating that acetylation increases mechanical resilience of microtubule filaments (Portran et al., 2017; Xu et al., 2017). Moreover, acetylation facilitates bundling of microtubules, which in turn enhances kinesin activity along microtubule tracks (Balabanian et al., 2017). In this regard, increased motor activities due to tubulin acetylation could promote sliding forces, which allow MTOC repositioning toward the immune synapse (Serrador et al., 2004).

During dendritic cell migration acetylation occurs predominantly on front directed microtubules (Serrador et al., 2004; Kopf et al., 2020). In particular microtubules reaching the base of the lamellipodium experience high forces from actin-based retrograde flow, which in mesenchymal cells influences microtubule dynamic instability and turnover (Waterman-Storer and Salmon, 1997). Stabilization of microtubules by acetylation could thus contribute to resist these forces and allow microtubules to grow into explorative protrusions.

In the future, it will be interesting to employ life cell sensors to analyze the role of PTMs in a detailed spatiotemporal manner during processes such as leukocyte migration and immune synapse formation. The tools are currently limited; however, recent advances now enable monitoring of tyrosinated microtubules in living cells (Kesarwani et al., 2020).

Moreover, T cell activation and effector function is a mechanosensitive process, in which force transduction across the T cell receptor complex generates significant traction stresses at the cell-cell interface (reviewed by Blumenthal and Burkhardt, 2020). These stresses are essential for enabling antigen recognition and T cell activation. Dynamic microtubules have recently been described as critical determinants of force generation during T cell activation by locally modulating actomyosin activation (Hui and Upadhyaya, 2017). However, whether and how a dynamic microtubule cytoskeleton also contributes to the force generating processes of antigen-presenting cells, and whether this is important for mounting an accurate immune response, is currently poorly understood. Therefore it will be crucial to decipher how mechanical coupling between the actomyosin system and the microtubule cytoskeleton affects immune synapse formation and activation of T cells.

Another interesting feature of leukocytes that has received limited attention during the past years is the centrosome-nucleus connection. It is well established that stationary or slow-moving cells such as neurons or cells of mesenchymal origin exhibit a stable front-back polarization (Meiring et al., 2020). However, highly motile leukocytes violate this paradigm and exhibit dynamic polarity configurations where the centrosome can be found in various positions with respect to the nucleus (Chiplonkar et al., 1992). Even more extreme is the flexible centrosomal-nuclear coupling distance of leukocytes. This is exemplified in migrating dendritic cells that reside in bifurcating channels, where in about 20% of the cases the MTOC uncouples transiently from the nucleus during path selection (Renkawitz et al., 2019). However, after path selection the centrosomal-nuclear distance decreases again. This behavior is to some extent similar to nucleokinesis in neurons in which the centrosome first changes its position into a leading process which is followed by nuclear movement toward the centrosome (Minegishi and Inagaki, 2020). The linker of nucleoskeleton and cytoskeleton (LINC) together with other molecular players such as Lissencephaly 1 (LIS1), myosin II activity and substrate topology contribute to centrosomal-nuclear axis orientation in many cell types (Luxton and Gundersen, 2011; Chang et al., 2015; Zhu et al., 2017) but the precise molecular mechanism of centrosome repositioning and centrosome-nucleus coupling remain largely unexplored in leukocytes.

The immune synapse is a well-known site of polarized membrane transport and localized vesicle release. While this process is fairly well understood in T cells and cytotoxic cells,

it is less clear how polarized secretion is regulated in antigen-presenting cells. MTOC relocalization in dendritic cells seems to be dispensable for the specific delivery of cytokines and T cell activation. As dendritic cells are able to interact and activate several T cells simultaneously (Miller et al., 2004) it seems favorable to nucleate microtubule filaments from the centrally located centrosome instead of a polarized MTOC. Computer simulations based on a general random velocity model predict efficient cargo delivery along microtubule filaments to specific target areas on the plasma membrane without MTOC translocation (Hafner and Rieger, 2016). Based on these simulations it is tempting to speculate that MTOC translocation constitutes an efficient strategy in favor of single cell-cell contacts while a centrally located MTOC promotes the formation of several active synapses. Future experiments yet have to clarify the role of MTOC polarization in antigen-presenting cells such as dendritic cells.

In contrast to mesenchymal cells, many of the core cell biological characteristics of the leukocyte microtubule cytoskeleton are currently poorly understood. Given that chemokines and other external factors, such as the mechanochemical composition of the microenvironment, act upstream of cytoskeletal regulation (Jin et al., 2019) it will not be surprising to discover new aspects and molecular mechanisms of microtubule regulatory functions in leukocytes. Since a large number of essential processes converge upon the microtubule cytoskeleton, understanding how microtubules support leukocyte functionality is critical to understanding the physiology and pathophysiology of immunological processes and will open up new strategies for targeted interventions.

AUTHOR CONTRIBUTIONS

Both authors contributed to the conceptual development of the work, literature research, and writing of the manuscript. AK composed the figures.

FUNDING

This work was funded by a fellowship of the Ministry of Innovation, Science, and Research of North-Rhine-Westphalia (AZ: 421-8.03.03.02-137069) to EK and the Deutsche Forschungsgesellschaft (DFG, German Research Foundation) under Germany's Excellence Strategy – EXC 2151 – 390873048.

REFERENCES

Abercrombie, M., Dunn, G. A., and Heath, J. P. (1977). The shape and movement of fibroblasts in culture. *Soc. Gen. Physiol. Ser.* 32, 57–70.

Abercrombie, M., Heaysman, J. E., and Pegrum, S. M. (1970). The locomotion of fibroblasts in culture. I. movements of the leading edge. *Exp. Cell Res.* 59, 393–398. doi: 10.1016/0014-4827(70)90646-90644

Allan, R. B., and Wilkinson, P. C. (1978). A visual analysis of chemotactic and chemokinetic locomotion of human neutrophil leucocytes. *Exp. Cell Res.* 111, 191–203. doi: 10.1016/0014-4827(78)90249-90245

Alushin, G. M., Lander, G. C., Kellogg, E. H., Zhang, R., Baker, D., and Nogales, E. (2014). High-resolution microtubule structures reveal the structural transitions in αβ-tubulin upon GTP hydrolysis. *Cell* 157, 1117–1129. doi: 10.1016/j.cell.2014.03.053

Amador, M. L., Jimeno, J., Paz-Ares, L., Cortes-Funes, H., and Hidalgo, M. (2003). Progress in the development and acquisition of anticancer agents from marine sources. *Ann. Oncol.* 14, 1607–1615. doi: 10.1093/annonc/mdg443

Anderson, D. C., Wible, L. J., Hughes, B. J., Smith, C. W., and Brinkley, B. R. (1982). Cytoplasmic microtubules in polymorphonuclear leukocytes: effects of chemotactic stimulation and colchicine. *Cell* 31, 719–729. doi: 10.1016/0092-8674(82)90326-90329

Andrés-Delgado, L., Antón, O. M., Bartolini, F., Ruiz-Sáenz, A., Correas, I., Gundersen, G. G., et al. (2012). INF2 promotes the formation of detyrosinated microtubules necessary for centrosome reorientation in T cells. *J. Cell Biol.* 198, 1025–1037. doi: 10.1083/jcb.201202137

Balabanian, L., Berger, C. L., and Hendricks, A. G. (2017). Acetylated microtubules are preferentially bundled leading to enhanced kinesin-1 motility. *Biophys. J.* 113, 1551–1560. doi: 10.1016/j.bpj.2017.08.009

Banchereau, J., Briere, F., Caux, C., Davoust, J., Lebecque, S., Liu, Y. J., et al. (2000). Immunobiology of dendritic cells. *Annu. Rev. Immunol.* 18, 767–811. doi: 10.1146/annurev.immunol.18.1.767

Bandmann, U., Rydgren, L., and Norberg, B. (1974). The difference between random movement and chemotaxis. effects of antitubulins on neutrophil granulocyte locomotion. *Exp. Cell Res.* 88, 63–73. doi: 10.1016/0014-4827(74)90618-90611

Banerjee, P. P., Pandey, R., Zheng, R., Suhoski, M. M., Monaco-Shawver, L., and Orange, J. S. (2007). Cdc42-interacting protein–4 functionally links actin and microtubule networks at the cytolytic NK cell immunological synapse. *J. Exp. Med.* 204, 2305–2320. doi: 10.1084/jem.20061893

Beal, A. M., Anikeeva, N., Varma, R., Cameron, T. O., Vasiliver-Shamis, G., Norris, P. J., et al. (2009). Kinetics of early T cell receptor signaling regulate the pathway of lytic granule delivery to the secretory domain. *Immunity* 31, 632–642. doi: 10.1016/j.immuni.2009.09.004

Bertrand, F., Müller, S., Roh, K.-H., Laurent, C., Dupré, L., and Valitutti, S. (2013). An initial and rapid step of lytic granule secretion precedes microtubule organizing center polarization at the cytotoxic T lymphocyte/target cell synapse. *Proc. Natl. Acad. Sci. U S A.* 110, 6073–6078. doi: 10.1073/pnas.1218640110

Blumenthal, D., and Burkhardt, J. K. (2020). Multiple actin networks coordinate mechanotransduction at the immunological synapse. *J. Cell Biol.* 219, 301–312. doi: 10.1083/jcb.201911058

Bodakuntla, S., Jijumon, A. S., Villablanca, C., Gonzalez-Billault, C., and Janke, C. (2019). Microtubule-Associated proteins: structuring the cytoskeleton. *Trends Cell Biol.* 29, 804–819. doi: 10.1016/j.tcb.2019.07.004

Borowiak, M., Nahaboo, W., Reynders, M., Nekolla, K., Jalinot, P., Hasserodt, J., et al. (2015). Photoswitchable inhibitors of microtubule dynamics optically control mitosis and cell death. *Cell* 162, 403–411. doi: 10.1016/j.cell.2015.06.049

Bustos-Morán, E., Blas-Rus, N., Beatriz Martin-Cofreces, N., and Sánchez-Madrid, F. (2017). Microtubule-associated protein-4 controls nanovesicle dynamics and T cell activation. *J. of Cell Sci.* 130, 1217–1223. doi: 10.1242/jcs.199042

Butler, B., and Cooper, J. A. (2009). Distinct roles for the actin nucleators Arp2/3 and hDia1 during NK-mediated cytotoxicity. *Curr. Biol.* 19, 1886–1896. doi: 10.1016/j.cub.2009.10.029

Chang, W., Antoku, S., Östlund, C., Worman, H. J., and Gundersen, G. G. (2015). Linker of nucleoskeleton and cytoskeleton (LINC) complex-mediated actin-dependent nuclear positioning orients centrosomes in migrating myoblasts. *Nucleus* 6, 77–88. doi: 10.1080/19491034.2015.1004947

Chang, Y.-C., Nalbant, P., Birkenfeld, J., Chang, Z.-F., and Bokoch, G. M. (2008). GEF-H1 couples nocodazole-induced microtubule disassembly to cell contractility via RhoA. *Mol. Biol. Cell* 19, 2147–2153. doi: 10.1091/mbc.e07-12-1269

Chiplonkar, J. M., Vandre, D. D., and Robinson, J. M. (1992). Stimulus-dependent relocation of the microtubule organizing center in human polymorphonuclear leukocytes. *J. Cell Sci.* 102(Pt 4), 723–728.

Colin, A., Singaravelu, P., Théry, M., Blanchoin, L., and Gueroui, Z. (2018). Actin-Network architecture regulates microtubule dynamics. *Curr. Biol.* 28, 2647–2656.e4. doi: 10.1016/j.cub.2018.06.028

Combs, J., Kim, S. J., Tan, S., Ligon, L. A., Holzbaur, E. L. F., Kuhn, J., et al. (2006). Recruitment of dynein to the Jurkat immunological synapse. *Proc. Natl. Acad. Sci. U.S.A.* 103, 14883–14888. doi: 10.1073/pnas.0600914103

Diz-Muñoz, A., Thurley, K., Chintamen, S., Altschuler, S. J., Wu, L. F., Fletcher, D. A., et al. (2016). Membrane tension acts through PLD2 and mTORC2 to limit actin network assembly during neutrophil migration. *PLoS Biol.* 14:e1002474. doi: 10.1371/journal.pbio.1002474

Dogterom, M., and Koenderink, G. H. (2019). Actin-microtubule crosstalk in cell biology. *Nat. Rev. Mol. Cell Biol.* 20, 38–54. doi: 10.1038/s41580-018-0067-61

Doyle, A. D., Wang, F. W., Matsumoto, K., and Yamada, K. M. (2009). One-dimensional topography underlies three-dimensional fibrillar cell migration. *J. Cell Biol.* 184, 481–490. doi: 10.1083/jcb.200810041

Duchez, S., Rodrigues, M., Bertrand, F., and Valitutti, S. (2011). Reciprocal polarization of T and B cells at the immunological synapse. *J. Immunol.* 187, 4571–4580. doi: 10.4049/jimmunol.1100600

Dustin, M. L., and Choudhuri, K. (2016). Signaling and polarized communication across the T Cell immunological synapse. *Annu. Rev. Cell Dev. Biol.* 32, 303–325. doi: 10.1146/annurev-cellbio-100814-125330

Dziezanowski, M. A., Destefano, M. J., and Rabinovitch, M. (1980). Effect of antitubulins on spontaneous and chemotactic migration of neutrophils under agarose. *J. Cell Sci.* 42, 379–388.

Eddy, R. J., Pierini, L. M., and Maxfield, F. R. (2002). Microtubule asymmetry during neutrophil polarization and migration. *Mol. Biol. Cell* 13, 4470–4483. doi: 10.1091/mbc.e02-04-0241

Eshun-Wilson, L., Zhang, R., Portran, D., Nachury, M. V., Toso, D. B., Löhr, T., et al. (2019). Effects of α-tubulin acetylation on microtubule structure and stability. *Proc. Natl. Acad. Sci.* 116, 10366–10371. doi: 10.1073/pnas.1900441116

Farina, F., Gaillard, J., Guérin, C., Couté, Y., Sillibourne, J., Blanchoin, L., et al. (2015). The centrosome is an actin-organizing centre. *Nat. Cell Biol.* 18, 65–75. doi: 10.1038/ncb3285

Filbert, E. L., Le Borgne, M., Lin, J., Heuser, J. E., and Shaw, A. S. (2012). Stathmin regulates microtubule dynamics and microtubule organizing center polarization in activated T cells. *J. Immunol.* 188, 5421–5427. doi: 10.4049/jimmunol.1200242

Fine, N., Dimitriou, I. D., Rullo, J., Sandí, M. J., Petri, B., Haitsma, J., et al. (2016). GEF-H1 is necessary for neutrophil shear stress-induced migration during inflammation. *J. Cell Biol.* 215, 107–119. doi: 10.1083/jcb.201603109

Friedl, P., and Wolf, K. (2010). Plasticity of cell migration: a multiscale tuning model. *J. Cell Biol.* 188, 11–19. doi: 10.1083/jcb.200909003

Gadadhar, S., Bodakuntla, S., Natarajan, K., and Janke, C. (2017). The tubulin code at a glance. *J. Cell Sci.* 130, 1347–1353. doi: 10.1242/jcs.199471

Gallin, J. I., and Rosenthal, A. S. (1974). The regulatory role of divalent cations in human granulocyte chemotaxis. evidence for an association between calcium exchanges and microtubule assembly. *J. Cell Biol.* 62, 594–609. doi: 10.1083/jcb.62.3.594

Garcia, E., and Ismail, S. (2020). Spatiotemporal regulation of signaling: focus on t cell activation and the immunological synapse. *IJMS* 21:3283. doi: 10.3390/ijms21093283

Geiger, B., Rosen, D., and Berke, G. (1982). Spatial relationships of microtubule-organizing centers and the contact area of cytotoxic T lymphocytes and target cells. *J. Cell Biol.* 95, 137–143. doi: 10.1083/jcb.95.1.137

Gigant, B., Wang, C., Ravelli, R. B. G., Roussi, F., Steinmetz, M. O., Curmi, P. A., et al. (2005). Structural basis for the regulation of tubulin by vinblastine. *Nature* 435, 519–522. doi: 10.1038/nature03566

Gill, S. R., Schroer, T. A., Szilak, I., Steuer, E. R., Sheetz, M. P., and Cleveland, D. W. (1991). Dynactin, a conserved, ubiquitously expressed component of an activator of vesicle motility mediated by cytoplasmic dynein. *J. Cell Biol.* 115, 1639–1650. doi: 10.1083/jcb.115.6.1639

Grakoui, A., Bromley, S. K., Sumen, C., Davis, M. M., Shaw, A. S., Allen, P. M., et al. (1999). The immunological synapse: a molecular machine controlling T cell activation. *Science* 285, 221–227. doi: 10.1126/science.285.5425.221

Hafner, A. E., and Rieger, H. (2016). Spatial organization of the cytoskeleton enhances cargo delivery to specific target areas on the plasma membrane of spherical cells. *Phys. Biol.* 13:066003. doi: 10.1088/1478-3975/13/6/066003

Ham, H., Huynh, W., Schoon, R. A., Vale, R. D., and Billadeau, D. D. (2015). HkRP3 is a microtubule-binding protein regulating lytic granule clustering and NK cell killing. *J. Immunol.* 194, 3984–3996. doi: 10.4049/jimmunol.1402897

Hashimoto-Tane, A., Yokosuka, T., Sakata-Sogawa, K., Sakuma, M., Ishihara, C., Tokunaga, M., et al. (2011). Dynein-Driven transport of T cell receptor microclusters regulates immune synapse formation and T cell activation. *Immunity* 34, 919–931. doi: 10.1016/j.immuni.2011.05.012

Hill, T. L. (1985). Theoretical problems related to the attachment of microtubules to kinetochores. *Proc. Natl. Acad. Sci. U S A.* 82, 4404–4408. doi: 10.1073/pnas.82.13.4404

Hind, L. E., Vincent, W. J. B., and Huttenlocher, A. (2016). Leading from the back: the role of the uropod in neutrophil polarization and migration. *Dev. Cell* 38, 161–169. doi: 10.1016/j.devcel.2016.06.031

Howes, S. C., Alushin, G. M., Shida, T., Nachury, M. V., and Nogales, E. (2014). Effects of tubulin acetylation and tubulin acetyltransferase binding on microtubule structure. *Mol. Biol. Cell* 25, 257–266. doi: 10.1091/mbc.E13-07-0387

Hsu, H.-T., Mace, E. M., Carisey, A. F., Viswanath, D. I., Christakou, A. E., Wiklund, M., et al. (2016). NK cells converge lytic granules to promote cytotoxicity and prevent bystander killing. *J. Cell Biol.* 215, 875–889. doi: 10.1083/jcb.201604136

Huber, F., Boire, A., López, M. P., and Koenderink, G. H. (2015). Cytoskeletal crosstalk: when three different personalities team up. *Curr. Opin. Cell Biol.* 32, 39–47. doi: 10.1016/j.ceb.2014.10.005

Hui, K. L., and Upadhyaya, A. (2017). Dynamic microtubules regulate cellular contractility during T-cell activation. *Proc. Natl. Acad. Sci. U S A.* 114, E4175–E4183. doi: 10.1073/pnas.1614291114

Ibañez-Vega, J., Del Valle, Batalla, F., Sáez, J. J., Soza, A., and Yuseff, M.-I. (2019). Proteasome dependent actin remodeling facilitates antigen extraction at the immune synapse of B cells. *Front. Immunol.* 10:225. doi: 10.3389/fimmu.2019.00225

Inoue, D., Obino, D., Pineau, J., Farina, F., Gaillard, J., Guérin, C., et al. (2019). Actin filaments regulate microtubule growth at the centrosome. *EMBO J.* 38:e99630. doi: 10.15252/embj.201899630

Liu, X., Kapoor, T. M., Chen, J. K., and Huse, M. (2013). Diacylglycerol promotes centrosome polarization in T cells via reciprocal localization of dynein and myosin II. *Proc. Natl. Acad. Sci.* 110, 11976–11981. doi: 10.1073/pnas.1306180110

James, A. M., Hsu, H.-T., Dongre, P., Uzel, G., Mace, E. M., Banerjee, P. P., et al. (2013). Rapid activation receptor- or IL-2-induced lytic granule convergence in human natural killer cells requires Src, but not downstream signaling. *Blood* 121, 2627–2637. doi: 10.1182/blood-2012-06-437012

Jin, W., Tamzalit, F., Kant Chaudhuri, P., Black, C. T., Huse, M., and Kam, L. C. (2019). T cell activation and immune synapse organization respond to the microscale mechanics of structured surfaces. *Proc Natl Acad Sci U S A.* 116, 19835–19840. doi: 10.1073/pnas.1906986116

Kabanova, A., Zurli, V., and Baldari, C. T. (2018). Signals controlling lytic granule polarization at the cytotoxic immune synapse. *Front. Immunol.* 9:307. doi: 10.3389/fimmu.2018.00307

Katz, P., Zaytoun, A. M., and Lee, J. H. (1982). Mechanisms of human cell-mediated cytotoxicity. III. dependence of natural killing on microtubule and microfilament integrity. *J. Immunol.* 129, 2816–2825.

Keller, H. U., Naef, A., and Zimmermann, A. (1984). Effects of colchicine, vinblastine and nocodazole on polarity, motility, chemotaxis and cAMP levels of human polymorphonuclear leukocytes. *Exp. Cell Res.* 153, 173–185. doi: 10.1016/0014-4827(84)90459-90452

Kesarwani, S., Lama, P., Chandra, A., Reddy, P. P., Jijumon, A. S., Bodakuntla, S., et al. (2020). Genetically encoded live-cell sensor for tyrosinated microtubules. *J. Cell Biol.* 219, 1448–1432. doi: 10.1083/jcb.201912107

Kim, M. J., and Maly, I. V. (2009). Deterministic mechanical model of T-Killer cell polarization reproduces the wandering of aim between simultaneously engaged targets. *PLoS Comput. Biol.* 5:e1000260. doi: 10.1371/journal.pcbi.1000260

Kon, T., Oyama, T., Shimo-Kon, R., Imamula, K., Shima, T., Sutoh, K., et al. (2012). The 2.8 A° crystal structure of the dynein motor domain. *Nature* 484, 345–350. doi: 10.1038/nature10955

Kopf, A., Renkawitz, J., Hauschild, R., Girkontaite, I., Tedford, K., Merrin, J., et al. (2020). Microtubules control cellular shape and coherence in amoeboid migrating cells. *J. Cell Biol.* 219:e201907154. doi: 10.1083/jcb.201907154

Krendel, M., Zenke, F. T., and Bokoch, G. M. (2002). Nucleotide exchange factor GEF-H1 mediates cross-talk between microtubules and the actin cytoskeleton. *Nat. Cell Biol.* 4, 294–301. doi: 10.1038/ncb773

Krummel, M. F., Sjaastad, M. D., Wülfing, C., and Davis, M. M. (2000). Differential clustering of CD4 and CD3zeta during T cell recognition. *Science* 289, 1349–1352. doi: 10.1126/science.289.5483.1349

Kuhn, J. R., and Poenie, M. (2002). Dynamic polarization of the microtubule cytoskeleton during CTL-mediated killing. *Immunity* 16, 111–121. doi: 10.1016/s1074-7613(02)00262-265

Kupfer, A., and Dennert, G. (1984). Reorientation of the microtubule-organizing center and the Golgi apparatus in cloned cytotoxic lymphocytes triggered by binding to lysable target cells. *J. Immunol.* 133, 2762–2766.

Kupfer, A., Mosmann, T. R., and Kupfer, H. (1991). Polarized expression of cytokines in cell conjugates of helper T cells and splenic B cells. *Proc. Natl. Acad. Sci. U.S.A.* 88, 775–779. doi: 10.1073/pnas.88.3.775

Kupfer, A., and Singer, S. J. (1989). The specific interaction of helper T cells and antigen-presenting B cells. IV. Membrane and cytoskeletal reorganizations in the bound T cell as a function of antigen dose. *J. Exp. Med.* 170, 1697–1713. doi: 10.1084/jem.170.5.1697

Kupfer, A., Swain, S. L., Janeway, C. A., and Singer, S. J. (1986). The specific direct interaction of helper T cells and antigen-presenting B cells. *Proc. Natl. Acad. Sci. U.S.A.* 83, 6080–6083. doi: 10.1073/pnas.83.16.6080

Kurowska, M., Goudin, N., Nehme, N. T., Court, M., Garin, J., Fischer, A., et al. (2012). Terminal transport of lytic granules to the immune synapse is mediated by the kinesin-1/Slp3/Rab27a complex. *Blood* 119, 3879–3889. doi: 10.1182/blood-2011-09-382556

Laan, L., Pavin, N., Husson, J., Romet-Lemonne, G., van Duijn, M., López, M. P., et al. (2012). Cortical dynein controls microtubule dynamics to generate pulling forces that position microtubule asters. *Cell* 148, 502–514. doi: 10.1016/j.cell.2012.01.007

Lämmermann, T., Bader, B. L., Monkley, S. J., Worbs, T., Wedlich-Söldner, R., Hirsch, K., et al. (2008). Rapid leukocyte migration by integrin-independent flowing and squeezing. *Nature* 453, 51–55. doi: 10.1038/nature06887

Ley, K., Laudanna, C., Cybulsky, M. I., and Nourshargh, S. (2007). Getting to the site of inflammation: the leukocyte adhesion cascade updated. *Nat. Rev. Immunol.* 7, 678–689. doi: 10.1038/nri2156

Luxton, G. G., and Gundersen, G. G. (2011). Orientation and function of the nuclear. *Curr. Opin. Cell Biol.* 23, 579–588. doi: 10.1016/j.ceb.2011.08.001

Malech, H. L., Root, R. K., and Gallin, J. I. (1977). Structural-Analysis of human neutrophil migration – centriole, microtubule, and microfilament orientation and function during chemotaxis. *J. Cell Biol.* 75, 666–693. doi: 10.1083/jcb.75.3.666

Mamdouh, Z., Kreitzer, G. E., and Muller, W. A. (2008). Leukocyte transmigration requires kinesin-mediated microtubule-dependent membrane trafficking from the lateral border recycling compartment. *J. Exp. Med.* 205, 951–966. doi: 10.1084/jem.20072328

Martin-Cofreces, N. B., Baixauli, F., López, M. J., Gil, D., Monjas, A., Alarcon, B., et al. (2012). End-binding protein 1 controls signal propagation from the T cell receptor. *EMBO J.* 31, 4140–4152. doi: 10.1038/emboj.2012.242

Martin-Cofreces, N. B., Robles-Valero, J., Cabrero, J. R., Mittelbrunn, M., Gordon-Alonso, M., Sung, C.-H., et al. (2008). MTOC translocation modulates is formation and controls sustained T cell signaling. *J. Cell Biol.* 182, 951–962. doi: 10.1083/jcb.200801014

Martín-Cófreces, N. B., and Sánchez-Madrid, F. (2018). Sailing to and docking at the immune synapse: role of tubulin dynamics and molecular motors. *Front. Immunol.* 9:1174. doi: 10.3389/fimmu.2018.01174

Maskalenko, N., Nath, S., Ramakrishnan, A., Anikeeva, N., Sykulev, Y., and Poenie, M. (2020). The DISC1-Girdin complex – a missing link in signaling to the T cell cytoskeleton. *J. Cell Sci.* 133:jcs242875. doi: 10.1242/jcs.242875

Meiring, J. C. M., Shneyer, B. I., and Akhmanova, A. (2020). Generation and regulation of microtubule network asymmetry to drive cell polarity. *Curr. Opin. Cell Biol.* 62, 86–95. doi: 10.1016/j.ceb.2019.10.004

Ménager, M. M., Ménasché, G., Romao, M., Knapnougel, P., Ho, C.-H., Garfa, M., et al. (2007). Secretory cytotoxic granule maturation and exocytosis require the effector protein hMunc13-4. *Nat. Immunol.* 8, 257–267. doi: 10.1038/ni1431

Mentlik, A. N., Sanborn, K. B., Holzbaur, E. L., and Orange, J. S. (2010). Rapid lytic granule convergence to the MTOC in natural killer cells is dependent on dynein but not cytolytic commitment. *Mol. Biol. Cell* 21, 2241–2256. doi: 10.1091/mbc.e09-11-0930

Miller, M. J., Safrina, O., Parker, I., and Cahalan, M. D. (2004). Imaging the single cell dynamics of CD4 +T cell activation by dendritic cells in lymph nodes. *J. Exp. Med.* 200, 847–856. doi: 10.1038/ni1058

Minegishi, T., and Inagaki, N. (2020). Forces to drive neuronal migration steps. *Front. Cell Dev. Biol.* 8:863. doi: 10.3389/fcell.2020.00863

Mitchison, T., and Kirschner, M. (1984). Dynamic instability of microtubule growth. *Nature* 312, 237–242. doi: 10.1038/312237a0

Mittelbrunn, M., Martínez, del Hoyo, G., López-Bravo, M., Martin-Cofreces, N. B., Scholer, A., et al. (2009). Imaging of plasmacytoid dendritic cell interactions with T cells. *Blood* 113, 75–84. doi: 10.1182/blood-2008-02-139865

Monks, C. R., Freiberg, B. A., Kupfer, H., Sciaky, N., and Kupfer, A. (1998). Three-dimensional segregation of supramolecular activation clusters in T cells. *Nature* 395, 82–86. doi: 10.1038/25764

Muller, W. A. (2011). Mechanisms of leukocyte transendothelial migration. *Annu. Rev. Pathol.* 6, 323–344. doi: 10.1146/annurev-pathol-011110-130224

Müller-Deku, A., Meiring, J. C. M., Loy, K., Kraus, Y., Heise, C., Bingham, R., et al. (2020). Photoswitchable paclitaxel-based microtubule stabilisers allow optical control over the microtubule cytoskeleton. *Nat. Commun.* 11:4640. doi: 10.1038/s41467-020-18389-18386

Muroyama, A., and Lechler, T. (2017). Microtubule organization, dynamics and functions in differentiated cells. *Development* 144, 3012–3021. doi: 10.1242/dev.153171

Nalbant, P., Chang, Y.-C., Birkenfeld, J., Chang, Z.-F., and Bokoch, G. M. (2009). Guanine nucleotide exchange factor-H1 regulates cell migration via localized activation of RhoA at the leading edge. *Mol. Biol. Cell* 20, 4070–4082. doi: 10.1091/mbc.e09-01-0041

Nath, S., Christian, L., Tan, S. Y., Ki, S., Ehrlich, L. I. R., and Poenie, M. (2016). Dynein separately partners with NDE1 and dynactin to orchestrate T cell focused secretion. *J. Immunol.* 197, 2090–2101. doi: 10.4049/jimmunol.1600180

Neuert, G., Munsky, B., Tan, R. Z., Teytelman, L., Khammash, M., and van Oudenaarden, A. (2013). Systematic identification of signal-activated stochastic gene regulation. *Science* 339, 584–587. doi: 10.1126/science.1231456

Niggli, V. (2003). Microtubule-disruption-induced and chemotactic-peptide-induced migration of human neutrophils: implications for differential sets of signalling pathways. *J. Cell Sci.* 116, 813–822. doi: 10.1242/jcs.00306

Nogales, E. (2000). Structural insights into microtubule function. *Annu. Rev. Biochem.* 69, 277–302. doi: 10.1146/annurev.biochem.69.1.277

Nunez-Andrade, N., Iborra, S., Trullo, A., Moreno-Gonzalo, O., Calvo, E., Catalan, E., et al. (2016). HDAC6 regulates the dynamics of lytic granules in cytotoxic T lymphocytes. *J. Cell Sci.* 129, 1305–1311. doi: 10.1242/jcs.180885

Obino, D., Farina, F., Malbec, O., Sáez, P. J., Maurin, M., Gaillard, J., et al. (2016). Actin nucleation at the centrosome controls lymphocyte polarity. *Nat. Commun.* 7:10969. doi: 10.1038/ncomms10969

Ong, S. T., Chalasani, M. L. S., Fazil, M. H. U. T., Prasannan, P., Kizhakeyil, A., Wright, G. D., et al. (2018). Centrosome- and golgi-localized protein kinase N-Associated protein serves as a docking platform for protein kinase A signaling and microtubule nucleation in migrating T-Cells. *Front. Immunol.* 9:397. doi: 10.3389/fimmu.2018.00397

Pavin, N., and Tolić-Nørrelykke, I. M. (2014). Swinging a sword: how microtubules search for their targets. *Syst. Synth. Biol.* 8, 179–186. doi: 10.1007/s11693-014-9134-x

Piel, M., Meyer, P., Khodjakov, A., Rieder, C. L., and Bornens, M. (2000). The respective contributions of the mother and daughter centrioles to centrosome activity and behavior in vertebrate cells. *J. Cell Biol.* 149, 317–329. doi: 10.1083/jcb.149.2.317

Poenie, M., Kuhn, J., and Combs, J. (2004). Real-time visualization of the cytoskeleton and effector functions in T cells. *Curr. Opin. Immunol.* 16, 428–438. doi: 10.1016/j.coi.2004.05.016

Portran, D., Schaedel, L., Xu, Z., Théry, M., and Nachury, M. V. (2017). Tubulin acetylation protects long-lived microtubules against mechanical ageing. *Nat. Cell Biol.* 19, 391–398. doi: 10.1038/ncb3481

Pulecio, J., Petrovic, J., Prete, F., Chiaruttini, G., Lennon-Dumenil, A.-M., Desdouets, C., et al. (2010). Cdc42-mediated MTOC polarization in dendritic cells controls targeted delivery of cytokines at the immune synapse. *J. Exp. Med.* 207, 2719–2732. doi: 10.1084/jem.20100007

Quann, E. J., Liu, X., Altan-Bonnet, G., and Huse, M. (2011). A cascade of protein kinase C isozymes promotes cytoskeletal polarization in T cells. *Nat. Immunol.* 12, 647–654. doi: 10.1038/ni.2033

Quann, E. J., Merino, E., Furuta, T., and Huse, M. (2009). Localized diacylglycerol drives the polarization of the microtubule-organizing center in T cells. *Nat. Immunol.* 10, 627–635. doi: 10.1038/ni.1734

Randall, K. L., Chan, S. S. Y., Ma, C. S., Fung, I., Mei, Y., Yabas, M., et al. (2011). DOCK8 deficiency impairs CD8 T cell survival and function in humans and mice. *J. Exp. Med.* 208, 2305–2320. doi: 10.1084/jem.20110345

Ratner, S., Sherrod, W. S., and Lichlyter, D. (1997). Microtubule retraction into the uropod and its role in T cell polarization and motility. *J. Immunol.* 159, 1063–1067.

Ravelli, R. B. G., Gigant, B., Curmi, P. A., Jourdain, I., Lachkar, S., Sobel, A., et al. (2004). Insight into tubulin regulation from a complex with colchicine and a stathmin-like domain. *Nature* 428, 198–202. doi: 10.1038/nature02393

Reck-Peterson, S. L., Redwine, W. B., Vale, R. D., and Carter, A. P. (2018). The cytoplasmic dynein transport machinery and its many cargoes. *Nat. Rev. Mol. Cell Biol.* 19, 382–398. doi: 10.1038/s41580-018-0004-3

Redd, M. J., Kelly, G., Dunn, G., Way, M., and Martin, P. (2006). Imaging macrophage chemotaxis in vivo: studies of microtubule function in zebrafish wound inflammation. *Cell Motil Cytoskeleton* 63, 415–422. doi: 10.1002/cm.20133

Ren, Y., Li, R., Zheng, Y., and Busch, H. (1998). Cloning and characterization of GEF-H1, a microtubule-associated guanine nucleotide exchange factor for Rac and Rho GTPases. *J. Biol. Chem.* 273, 34954–34960. doi: 10.1074/jbc.273.52.34954

Renkawitz, J., Kopf, A., Stopp, J., de Vries, I., Driscoll, M. K., Merrin, J., et al. (2019). Nuclear positioning facilitates amoeboid migration along the path of least resistance. *Nature* 568, 546–550. doi: 10.1038/s41586-019-1087-1085

Renkawitz, J., Schumann, K., Weber, M., Lämmermann, T., Pflicke, H., Piel, M., et al. (2009). Adaptive force transmission in amoeboid cell migration. *Nat. Biol.* 11, 1438–1443. doi: 10.1038/ncb1992

Reversat, A., Gaertner, F., Merrin, J., Stopp, J., Tasciyan, S., Aguilera, J., et al. (2020). Cellular locomotion using environmental topography. *Nature* 582, 582–585. doi: 10.1038/s41586-020-2283-z

Ritter, A. T., Asano, Y., Stinchcombe, J. C., Dieckmann, N. M. G., Chen, B.-C., Gawden-Bone, C., et al. (2015). Actin depletion initiates events leading to granule secretion at the immunological synapse. *Immunity* 42, 864–876. doi: 10.1016/j.immuni.2015.04.013

Robinson, J. M., and Vandre, D. D. (1995). Stimulus-Dependent alterations in macrophage microtubules – increased tubulin polymerization and detyrosination. *J. Cell Sci.* 108, 645–655.

Rodriguez, O. C., Schaefer, A. W., Mandato, C. A., Forscher, P., Bement, W. M., and Waterman-Storer, C. M. (2003). Conserved microtubule-actin interactions in cell movement and morphogenesis. *Nat. Cell Biol.* 5, 599–609. doi: 10.1038/ncb0703-599

Sáez, J. J., Diaz, J., Ibañez, J., Bozo, J. P., Cabrera Reyes, F., Alamo, M., et al. (2019). The exocyst controls lysosome secretion and antigen extraction at the immune synapse of B cells. *J. Cell Biol.* 218, 2247–2264. doi: 10.1083/jcb.201811131

Sánchez-Madrid, F., and del Pozo, M. A. (1999). Leukocyte polarization in cell migration and immune interactions. *EMBO J.* 18, 501–511. doi: 10.1093/emboj/18.3.501

Sarkar, A., Rieger, H., and Paul, R. (2019). Search and capture efficiency of dynamic microtubules for centrosome relocation during is formation. *Biophys. J.* 116, 2079–2091. doi: 10.1016/j.bpj.2019.04.008

Schmidt, H., Gleave, E. S., and Carter, A. P. (2012). Insights into dynein motor domain function from a 3.3-Å crystal structure. *Nat. Struct. Mol. Biol.* 19, 492–497. doi: 10.1038/nsmb.2272

Schroer, T. A., and Sheetz, M. P. (1991). Two activators of microtubule-based vesicle transport. *J. Cell Biol.* 115, 1309–1318. doi: 10.1083/jcb.115.5.1309

Serrador, J. M., Cabrero, J. R., Sancho, D., Mittelbrunn, M., Urzainqui, A., and Sánchez-Madrid, F. (2004). HDAC6 deacetylase activity links the tubulin cytoskeleton with immune synapse organization. *Immunity* 20, 417–428. doi: 10.1016/s1074-7613(04)00078-70

Shaw, A. S., and Dustin, M. L. (1997). Making the T Cell receptor go the distance: a topological view of T Cell activation. *Immunity* 6, 361–369. doi: 10.1016/S1074-7613(00)80279-4

Skoufias, D. A., and Wilson, L. (1992). Mechanism of inhibition of microtubule polymerization by colchicine: inhibitory potencies of unliganded colchicine and tubulin-colchicine complexes. *Biochemistry* 31, 738–746. doi: 10.1021/bi00118a015

Springer, T. A. (1994). Traffic signals for lymphocyte recirculation and leukocyte emigration – the multistep paradigm. *Cell* 76, 301–314. doi: 10.1016/0092-8674(94)90337-90339

Steinman, R. M., and Cohn, Z. A. (1973). Identification of a novel cell type in peripheral lymphoid organs of mice. I. morphology, quantitation, tissue distribution. *J. Exp. Med.* 137, 1142–1162. doi: 10.1084/jem.137.5.1142

Stinchcombe, J. C., Bossi, G., Booth, S., and Griffiths, G. M. (2001). The immunological synapse of CTL contains a secretory domain and membrane bridges. *Immunity* 15, 751–761. doi: 10.1016/s1074-7613(01)00234-235

Stinchcombe, J. C., and Griffiths, G. M. (2007). Secretory mechanisms in cell-mediated cytotoxicity. *Annu. Rev. Cell Dev. Biol.* 23, 495–517. doi: 10.1146/annurev.cellbio.23.090506.123521

Stinchcombe, J. C., Majorovits, E., Bossi, G., Fuller, S., and Griffiths, G. M. (2006). Centrosome polarization delivers secretory granules to the immunological synapse. *Nature* 443, 462–465. doi: 10.1038/nature05071

Stinchcombe, J. C., Randzavola, L. O., Angus, K. L., Mantell, J. M., Verkade, P., and Griffiths, G. M. (2015). Mother centriole distal appendages mediate centrosome docking at the immunological synapse and reveal mechanistic parallels with ciliogenesis. *Curr. Biol.* 25, 3239–3244. doi: 10.1016/j.cub.2015.10.028

Takesono, A., Heasman, S. J., Wojciak-Stothard, B., Garg, R., and Ridley, A. J. (2010). Microtubules regulate migratory polarity through Rho/ROCK signaling in T cells. *PLoS One* 5:e8774. doi: 10.1371/journal.pone.0008774

Tamzalit, F., Tran, D., Jin, W., Boyko, V., Bazzi, H., Kepecs, A., et al. (2020). Centrioles control the capacity, but not the specificity, of cytotoxic T cell killing. *Proc. Natl. Acad. Sci. U S A.* 117, 4310–4319. doi: 10.1073/pnas.1913220117

Tittarelli, A., Navarrete, M., Gleisner, M. A., Gebicke-Haerter, P., and Salazar-Onfray, F. (2020). Connexin-Mediated signaling at the immunological synapse. *IJMS* 21:3736. doi: 10.3390/ijms21103736

Tsun, A., Qureshi, I., Stinchcombe, J. C., Jenkins, M. R., la Roche de, M., Kleczkowska, J., et al. (2011). Centrosome docking at the immunological synapse is controlled by Lck signaling. *J. Cell Biol.* 192, 663–674. doi: 10.1083/jcb.201008140

Turley, S. J., Inaba, K., Garrett, W. S., Ebersold, M., Unternaehrer, J., Steinman, R. M., et al. (2000). Transport of peptide-MHC class II complexes in developing dendritic cells. *Science* 288, 522–527. doi: 10.1126/science.288.5465.522

Ueda, H., Morphew, M. K., McIntosh, J. R., and Davis, M. M. (2011). CD4+ T-cell synapses involve multiple distinct stages. *Proc. Natl. Acad. Sci. U S A.* 108, 17099–17104. doi: 10.1073/pnas.1113703108

Ueda, M., Gräf, R., MacWilliams, H. K., Schliwa, M., and Euteneuer, U. (1997). Centrosome positioning and directionality of cell movements. *Proc. Natl. Acad. Sci. U S A.* 94, 9674–9678.

Unemori, E. N., and Werb, Z. (1986). Reorganization of polymerized actin: a possible trigger for induction of procollagenase in fibroblasts cultured in and on collagen gels. *J. Cell Biol.* 103, 1021–1031. doi: 10.1083/jcb.103.3.1021

Van Geel, O., Cheung, S., and Gadella, T. W. J. (2020). Combining optogenetics with sensitive FRET imaging to monitor local microtubule manipulations. *Sci. Rep.* 10, 6034–6010. doi: 10.1038/s41598-020-62874-62873

Waterman-Storer, C. M., and Salmon, E. D. (1997). Actomyosin-based retrograde flow of microtubules in the lamella of migrating epithelial cells influences microtubule dynamic instability and turnover and is associated with microtubule breakage and treadmilling. *J. Cell Biol.* 139, 417–434. doi: 10.1083/jcb.139.2.417

Waterman-Storer, C. M., Worthylake, R. A., Liu, B. P., Burridge, K., and Salmon, E. D. (1999). Microtubule growth activates Rac1 to promote lamellipodial protrusion in fibroblasts. *Nat. Cell Biol.* 1, 45–50. doi: 10.1038/9018

Wiedemann, A., Depoil, D., Faroudi, M., and Valitutti, S. (2006). Cytotoxic T lymphocytes kill multiple targets simultaneously via spatiotemporal uncoupling of lytic and stimulatory synapses. *Proc. Natl. Acad. Sci. U S A.* 103, 10985–10990. doi: 10.1073/pnas.0600651103

Wilkinson, P. C. (1986). The locomotor capacity of human lymphocytes and its enhancement by cell growth. *Immunology* 57, 281–289.

Wilton, K. M., and Billadeau, D. D. (2018). VASP regulates NK cell lytic granule convergence. *J. Immunol.* 201, 2899–2909. doi: 10.4049/jimmunol.1800254

Worbs, T., Hammerschmidt, S. I., and Förster, R. (2017). Dendritic cell migration in health and disease. *Nat. Rev. Immunol.* 17, 30–48. doi: 10.1038/nri.2016.116

Wu, J., and Akhmanova, A. (2017). Microtubule-Organizing centers. *Annu. Rev. Cell Dev. Biol.* 33, 51–75. doi: 10.1146/annurev-cellbio-100616-160615

Xu, J., Wang, F., Van Keymeulen, A., Herzmark, P., Straight, A., Kelly, K., et al. (2003). Divergent signals and cytoskeletal assemblies regulate self-organizing polarity in neutrophils. *Cell* 114, 201–214.

Xu, J. S., Wang, F., Van Keymeulen, A., Rentel, M., and Bourne, H. R. (2005). Neutrophil microtubules suppress polarity and enhance directional migration. *Proc. Natl. Acad. Sci. U S A.* 102, 6884–6889. doi: 10.1073/pnas.0502106102

Xu, Z., Schaedel, L., Portran, D., Aguilar, A., Gaillard, J., Marinkovich, M. P., et al. (2017). Microtubules acquire resistance from mechanical breakage through intralumenal acetylation. *Science* 356, 328–332. doi: 10.1126/science.aai8764

Yadav, S. K., Stojkov, D., Feigelson, S. W., Roncato, F., Simon, H.-U., Yousefi, S., et al. (2019). Chemokine-triggered microtubule polymerization promotes neutrophil chemotaxis and invasion but not transendothelial migration. *J. Leukocyte Biol.* 105, 755–766. doi: 10.1002/JLB.3A1118-437RR

Yamada, K. M., and Sixt, M. (2019). Mechanisms of 3D cell migration. *Nat. Rev. Mol. Cell Biol.* 100, 353–315. doi: 10.1038/s41580-019-0172-179

Yi, J., Wu, X., Chung, A. H., Chen, J. K., Kapoor, T. M., and Hammer, J. A. (2013). Centrosome repositioning in T cells is biphasic and driven by microtubule end-on capture-shrinkage. *J. Cell Biol.* 202, 779–792. doi: 10.1083/jcb.201301004

Yoo, S. K., Deng, Q., Cavnar, P. J., Wu, Y. I., Hahn, K. M., and Huttenlocher, A. (2010). Differential regulation of protrusion and polarity by PI(3)K during neutrophil motility in live Zebrafish. *Devcel* 18, 226–236. doi: 10.1016/j.devcel.2009.11.015

Yoo, S. K., Lam, P. Y., Eichelberg, M. R., Zasadil, L., Bement, W. M., and Huttenlocher, A. (2013). The role of microtubules in neutrophil polarity and migration in live zebrafish. *J. Cell Sci.* 125, 5702–5710. doi: 10.1242/jcs.108324

Yuseff, M.-I., Reversat, A., Lankar, D., Diaz, J., Fanget, I., Pierobon, P., et al. (2011). Polarized secretion of lysosomesat the B cell synapse couples antigen extraction to processing and presentation. *Immunity* 35, 361–374. doi: 10.1016/j.immuni.2011.07.008

Zaid, A., Hor, J. L., Christo, S. N., Groom, J. R., Heath, W. R., Mackay, L. K., et al. (2017). Chemokine receptor-dependent control of skin tissue-resident memory T cell formation. *J. Immunol.* 199, 2451–2459. doi: 10.4049/jimmunol.1700571

Zhang, M., March, M. E., Lane, W. S., and Long, E. O. (2014). A signaling network stimulated by β2 integrin promotes the polarization of lytic granules in cytotoxic cells. *Sci. Signal.* 7:ra96. doi: 10.1126/scisignal.2005629

Zhang, Q., Dove, C. G., Hor, J. L., Murdock, H. M., Strauss-Albee, D. M., Garcia, J. A., et al. (2014). DOCK8 regulates lymphocyte shape integrity for skin antiviral immunity. *J. Exp. Med.* 211, 2549–2566. doi: 10.1084/jem.20141307

Zhao, T., Graham, O. S., Raposo, A., and St Johnston, D. (2012). Growing microtubules push the oocyte nucleus to polarize the Drosophila dorsal-ventral axis. *Science* 336, 999–1003. doi: 10.1126/science.1219147

Zhu, R., Antoku, S., and Gundersen, G. G. (2017). Centrifugal displacement of nuclei reveals multiple LINC complex mechanisms for homeostatic nuclear positioning. *Curr. Biol.* 27, 3097–3110.e5. doi: 10.1016/j.cub.2017.08.073

Zigmond, S. H., Levitsky, H. I., and Kreel, B. J. (1981). Cell polarity: an examination of its behavioral expression and its consequences for polymorphonuclear leukocyte chemotaxis. *J. Cell Biol.* 89, 585–592. doi: 10.1083/jcb.89.3.585

Zyss, D., Ebrahimi, H., and Gergely, F. (2011). Casein kinase I delta controls centrosome positioning during T cell activation. *J. Cell Biol.* 195, 781–797. doi: 10.1083/jcb.201106025

Conflict of Interest: The authors declare that the research was conducted in the absence of any commercial or financial relationships that could be construed as a potential conflict of interest.

frontiers in Cell and Developmental Biology

BRIEF RESEARCH REPORT
published: 09 February 2021
doi: 10.3389/fcell.2021.634218

Arabidopsis QWRF1 and QWRF2 Redundantly Modulate Cortical Microtubule Arrangement in Floral Organ Growth and Fertility

Huifang Ma, Liyuan Xu, Ying Fu and Lei Zhu**

State Key Laboratory of Plant Physiology and Biochemistry, College of Biological Sciences, China Agricultural University, Beijing, China

Floral organ development is fundamental to sexual reproduction in angiosperms. Many key floral regulators (most of which are transcription factors) have been identified and shown to modulate floral meristem determinacy and floral organ identity, but not much is known about the regulation of floral organ growth, which is a critical process by which organs to achieve appropriate morphologies and fulfill their functions. Spatial and temporal control of anisotropic cell expansion following initial cell proliferation is important for organ growth. Cortical microtubules are well known to have important roles in plant cell polar growth/expansion and have been reported to guide the growth and shape of sepals and petals. In this study, we identified two homolog proteins, QWRF1 and QWRF2, which are essential for floral organ growth and plant fertility. We found severely deformed morphologies and symmetries of various floral organs as well as a significant reduction in the seed setting rate in the *qwrf1qwrf2* double mutant, although few flower development defects were seen in *qwrf1* or *qwrf2* single mutants. QWRF1 and QWRF2 display similar expression patterns and are both localized to microtubules *in vitro* and *in vivo*. Furthermore, we found altered cortical microtubule organization and arrangements in *qwrf1qwrf2* cells, consistent with abnormal cell expansion in different floral organs, which eventually led to poor fertility. Our results suggest that QWRF1 and QWRF2 are likely microtubule-associated proteins with functional redundancy in fertility and floral organ development, which probably exert their effects *via* regulation of cortical microtubules and anisotropic cell expansion.

Keywords: floral organ development, microtubule associated protein, QWRF1, QWRF2, fertility

OPEN ACCESS

Edited by:
Yi Zhang,
Beijing Normal University, China

Reviewed by:
Jiejie Li,
Beijing Normal University, China
René Schneider,
Max Planck Institute of Molecular Plant Physiology, Germany

****Correspondence:***
Ying Fu
yingfu@cau.edu.cn
Lei Zhu
zhulei3369@cau.edu.cn

Specialty section:
This article was submitted to Cell Growth and Division, a section of the journal Frontiers in Cell and Developmental Biology

Received: *27 November 2020*
Accepted: *15 January 2021*
Published: *09 February 2021*

Citation:
Ma H, Xu L, Fu Y and Zhu L (2021) Arabidopsis QWRF1 and QWRF2 Redundantly Modulate Cortical Microtubule Arrangement in Floral Organ Growth and Fertility. Front. Cell Dev. Biol. 9:634218. doi: 10.3389/fcell.2021.634218

INTRODUCTION

Flower development is essential for sexual reproduction in flowering plants. Over the past three decades, complex gene regulatory networks have been shown to control the emergence of floral primordia and the formation of different types of floral organs in a stereotypical pattern (Denay et al., 2017). A classic "ABC" model in floral organ identity specification has been

raised (Bowman et al., 1991, 2012; Coen and Meyerowitz, 1991). Specification of floral organs (sepals, petals, stamens, and carpels) requires the combined activities of floral organ identity genes encoding MADS-domain transcription factors (Theißen et al., 2016). Following initiation, symmetrically arranged floral organs grow to their final shape and size; this is important for their reproductive function and for plant fertility. However, hormone deficiency, unfavorable environmental conditions, or genetic mutations leading to abnormal floral organ morphologies may eventually cause plant sterility (Reeves et al., 2012; Smith and Zhao, 2016).

Growth of floral organs relies on coordinated cell proliferation and expansion (Irish, 2010; Powell and Lenhard, 2012; Thomson and Wellmer, 2019). Transcription factors AINTEGUMENTA (ANT), JAGGED (JAG) and NUBBIN (NUB), cytochrome P450 KLUH, and E3 ubiquitin ligase BIG BROTHER (BB) have been reported to regulate cell proliferation in floral organs (Krizek, 1999; Zondlo and Irish, 1999; Krizek et al., 2000; Dinneny et al., 2004, 2006; Ohno et al., 2004; Disch et al., 2006; Anastasiou et al., 2007). However, the regulatory mechanism underlying cell expansion in the later phase of floral organ growth is largely unknown.

Cortical microtubules guide the orientation of cellulose microfibrils in the cell wall (Paredez et al., 2006; Gutierrez et al., 2009). Recently, Hervieux et al. (2016) reported that microtubules function as both stress sensors and growth regulators in *Arabidopsis thaliana*, *via* a mechanical feedback loop that regulates the growth and shape of the sepal. Signaling by rho GTPases of plants was also found to influence petal morphology in *Arabidopsis* by modulating cortical microtubules in both abaxial and adaxial epidermal cells of petals (Ren et al., 2016, 2017). Moreover, microtubule-associated proteins (MAPs) KATANIN 1 (KTN1) and INCREASED PETAL GROWTH ANISOTROPY 1 (IPGA1) were found to regulate microtubule organization, with important roles in cell expansion and petal shape (Ren et al., 2017; Yang et al., 2019a). Nevertheless, characterization of new regulators and their functions is needed to further understand the regulation of floral organ growth and flower development.

Arabidopsis QWRF family proteins share a highly conserved QWRF amino acid sequence and a DUF566 domain of unknown function (Pignocchi et al., 2009; Albrecht et al., 2010). One member of this family, ENDOSPERMDEFECTIVE1 (EDE1, also named QWRF5), has been shown to be an essential MAP for endosperm development (Pignocchi et al., 2009). QWRF1 (also named SNOWY COTYLEDON3, SCO3) is a peroxisome-associated protein required for plastid development. Its localization to the periphery of peroxisomes is dependent on microtubules (Albrecht et al., 2010). So far, there have been no reports about the function of QWRF2 in *Arabidopsis*.

In this study, we identified overlapping expression patterns of *QWRF1* and *QWRF2* in flowers. Severe fertility defects in the *qwrf1qwrf2* double mutant were attributed to abnormal development of floral organs. Further experiments demonstrated that both QWRF1 and QWRF2 are likely MAPs that are involved in the organization of cortical microtubule arrays, with essential roles in cell expansion, and that this regulatory mechanism is generally adopted for growth control in different floral organs.

MATERIALS AND METHODS

Plant Materials and Growth Conditions

Arabidopsis thaliana ecotype Col-0 was the background for all wild-type and mutant materials in this study. Seedlings were grown on half-strength Murashige and Skoog medium with 1% sucrose in a growth chamber before transfer to soil. Seedlings/plants were grown at 22°C with a photoperiod of 16 h light/8 h dark.

T-DNA insertion lines *qwrf1-1* (SALK_072931), *sco3-3* (SALK_089815), and *qwrf2-1* (SALK_119512) were obtained from the Arabidopsis Biological Resource Center. The insertion sites of *qwrf1-1* mutant and *sco3-3* mutants were 995 bp and 1,176 bp after the start codon, respectively, and the insertion site of *qwrf2-1* mutant was 1,325 bp after the start codon. Polymerase chain reaction (PCR)-based genotyping was performed using the primers listed in **Supplementary Table 1**.

Reverse-Transcription Quantitative PCR (RT-qPCR) Analysis

To quantify *QWRF1* and *QWRF2* transcripts in *qwrf1* and *qwrf2* mutants, total RNA was extracted from inflorescences and flowers using an RNA extraction kit (DP432, Tiangen, China) and reverse-transcribed with SuperScript^{TM} III (18080044, Thermo Scientific, United States). The primer pairs are listed in **Supplementary Table 1**. SYBR Premix Ex Taq (DRR081A, Takara Bio, Japan) was used for amplification.

CRISPR/Cas9 Method

The target sequence of *QWRF2* was selected by the CRISPR-P (Lei et al., 2014) technique. Guide RNAs were cloned from pCBC-DT1T2 and transformed into Col as previously described (Li et al., 2020). Briefly, we designed primers with two specific sites from target gene and pCBC-DT1T2 was used as PCR template. The PCR product was cloned into pHEE401 and transformed into Col-0 using the Agrobacterium-mediated flower-dipping method (Clough and Bent, 1998). We obtained a line with a 257-bp deletion in the first exon of *QWRF2* and named it *qwrf2cas9*. The CRISPR/Cas9 constructs were then removed to ensure genetic stability. Primers are listed in **Supplementary Table 1**.

Generation of Constructs and Transgenic Plants

A 2-kb region of the *QWRF1* and a 3-kb region of the *QWRF2* promoter were amplified from wild-type genomic DNA using the primers listed in **Supplementary Table 1**. The products were cloned into pCAMBIA1300 vectors (Cambia, Canberra, Australia), and *QWRF1/QWRF2* and GFP fusion sequences were inserted into the resulting pCAMBIA-*QWRF1pro* and pCAMBIA-*QWRF2pro* vectors, respectively, using a Clone Express II One Step cloning kit (C112-02, Vazyme, China). Sequence-verified constructs were transformed into wild-type

plants by the Agrobacterium-mediated flower dipping method (Clough and Bent, 1998).

GUS Staining and *in situ* Hybridization

For GUS staining, native promoters of *QWRF1* (*QWRF1pro*, 2057 bp fragment upstream of the start codon of *QWRF1*) and *QWRF2* (*QWRF2pro*, 3061 bp upstream of *QWRF2*) were inserted into the pCAMBIA1391 vector to drive the *GUS* reporter gene. GUS analysis was performed as previously described (He et al., 2018). Briefly, inflorescences were stained within solution containing 5-bromo-4-chloro-3-indolyl-b-D-glucuionode (X-Gluc) for 10 h at 37°C in the dark, and then destained in 70% ethanol and 30% ethanoic acid. Images were captured with an Olympus SZX16 microscope equipped with a color CCD camera (Olympus DP70) and ImagePro software (Media Cybernetics).

For *in situ* hybridization, primers (**Supplementary Table 1**) targeting the unique regions of *QWRF1* and *QWRF2* were used for PCR amplification to synthesize the sense and antisense probes using SP6 and T7 polymerases, respectively. Each PCR product was used as a template for *in vitro* transcription as described in the manufacturer's protocol (11175025910, Roche, Germany). *Arabidopsis* flowers were fixed in 3.7% formol-acetic-alcohol (FAA), and *in situ* hybridization was performed as described previously (Zhang et al., 2013). A DIG Nucleic Acid Detection Kit (Roche) was used to detect the hybridized probe, and images were captured with an Olympus BX51 digital camera equipped with a Cool SNAP HQ CCD camera (Photometrics), and MetaMorph software (Universal Imaging) was used for imaging analysis.

Agroinfiltration-Mediated Transient Expression

To generate the *35S:GFP-QWRF1* and *35S:GFP-QWRF2* constructs, we first cloned the coding sequences of *QWRF1* and *QWRF2* into the pDONR201 vector using Gateway BP Clonase II enzyme mix (11789020, Thermo Scientific), and subsequently cloned them into the pGWB506 vectors using Gateway LR Clonase enzyme mix (11791019, Thermo Scientific). *QWRF1-GFP* and *QWRF2-GFP* driven by the *pSUPER* promoter were cloned into transformed pCAMBIA1300. The resulting constructs were introduced into BY-2 tobacco (*Nicotiana tabacum*) suspension cells by a previously described *Agrobacterium* cocultivation method (An, 1985). Images were acquired with a Zeiss LSM 710 confocal microscope with a × 40 oil objective (1.3 NA).

Protein Expression and Microtubule-Binding Assays

To obtain QWRF1 and QWRF2 proteins, *QWRF1* and *QWRF2* cDNA were transferred from pDONR207 into pET30a (+) (Novagen) and used for *in vitro* translation with a $T_NT^®$T7 Quick Coupled Transcription/Translation System (L1170, Promega, United States). The resulting proteins were incubated with pre-polymerized microtubules, centrifuged at 100,000 × *g* for 30 min at 25°C, and then analyzed by 10% SDS-PAGE (Wang et al., 2007). The Transcend Chemiluminescent Non-Radioactive Translation Detection System (L5080, Promega) was used to detect biotin-labeled QWRF1 and QWRF2 proteins.

Light Microscopy and Scanning Electron Microscopy

To analyze fertilization rate, unfertilized ovules were counted in mature siliques to identify seed set frequency. Opened siliques were observed under an Olympus SZX16 microscope.

The flower stages were defined as reported by Smyth et al. (1990). Images of petals, sepals, stamen filaments, and stigma of stage 14 flowers from the wild type and *qwrf1qwrf2* double mutant were captured using a SZX16 microscope (Olympus). The lengths and width of petals, sepals, filaments, and stigma were measured using ImageJ software (National Institutes of Health[1]).

Clearing of stigma was performed as previously reported (Takeda et al., 2018). Briefly, inflorescences were fixed in 3.7% FAA, followed by dehydration through an ethanol series and cleared overnight in clearing solution (40 g chloral hydrate, 10 ml glycerol and 5 ml distilled water). Images were captured using an Olympus BX51 digital camera. All experiments were performed in triplicate, with 6–8 flowers measured in each experiment.

Cross-sections were cut to 2 μm thickness and stained with 0.1% (w/v) toluidine blue O in 0.1 M phosphate buffer, pH 7.0 (Ito et al., 2007). Images were captured using an Olympus BX51 digital camera.

Pollen grains on stigma were stained with aniline blue and then counted as described previously (Doucet et al., 2019). Samples were observed using an Olympus BX51 digital camera.

For staining of petal epidermal cells, stage 14 flowers were incubated in 50 μg/mL PI (propidium iodide, P4170, Sigma-Aldrich, United States) in half-strength MS liquid medium for 1 h, then observed under a Zeiss LSM 710 confocal microscope with a × 40 oil objective (1.3 NA).

The confocal analysis of ovules was performed as described previously (Cui et al., 2015). The pistils were fixed in 4% glutaraldehyde (12.5 mM cacodylate, pH6.9) and then dehydrated with ethanol gradient, clarified in benzyl benzoate: benzyl alcohol [2: 1(v/v)] overnight. Images were observed using a Zeiss LSM 710 microscope with a × 40 oil objective (1.3 NA).

Fresh material (stigma, anthers, or mature pollen grains) was spread onto the surface of adhesive tapes and observed using a scanning electron microscope (TM3000, Hitachi) at an accelerating voltage of 15 kV.

Cells expressing *35S:GFP-TUA6 (TUBULIN ALPHA-6*; Ueda et al., 1999) or *UBQ10:mCherry-MBD* (*microtubule binding domain*) were observed under a Zeiss LSM 710 confocal microscope with × 40 and × 60 oil objective (1.3 NA). Microtubule alignment was measured using fibriltool, an ImageJ plug-in, to calculate the anisotropy of the fibers (Boudaoud et al., 2014); a value close to 1 indicated strong anisotropy of the microtubules. Microtubule bundling was quantified as previously described (Higaki et al., 2010; Zhu et al., 2016). Samples were imaged with a Zeiss LSM 710 confocal laser scanning microscope. Z stacks of optical sections were taken and projected using

[1]http://rsb.info.nih.gov/ij

ZEN 2012 software. Images were skeletonized and masked by manually segmenting the cell region images with ImageJ. The intensity distribution of the microtubule pixels was determined using Skewness, an ImageJ plug-in, and used as an indicator of microtubule bundling. At least 100 cells were measured.

Cells were treated with a microtubule-specific depolymerizing drug, oryzalin (36182, Sigma-Aldrich), and an actin polymerization inhibitor, Lat B (latrunculin B, L5288, Sigma-Aldrich), as previously described (Kang et al., 2017). Cortical microtubule numbers in petal abaxial epidermal cells were quantified using ImageJ as previously reported (Liu et al., 2013; Sun et al., 2015). Briefly, a vertical line was drawn perpendicularly to the majority of the cortical microtubules, and the number of cortical microtubules across the line was counted manually as the density.

RESULTS

QWRF1 and QWRF2 Function Redundantly in Plant Fertility

To better understand the regulation of plant fertility and the role of modulating microtubules in this process, we searched for lower fertility phenotypes in mutants harboring a transfer (T)-DNA insertion in previously reported genes expressed in flowers, which are likely to encode microtubule-associated proteins (Pignocchi et al., 2009; Albrecht et al., 2010). We identified a mutant line (SALK_072931) with a mild seed setting rate phenotype (**Figure 1A**). This mutant harbored a T-DNA insertion in the first exon of the *AT3G19570.2* gene (**Supplementary Figure 1A**), which encodes a member of the QWRF protein family, QWRF1 (also named SCO3, Albrecht et al., 2010). RT-PCR analysis demonstrated that it was a null mutant (**Supplementary Figure 1B**), and we named it *qwrf1-1*. Fourteen days after pollination (DAP), a few unoccupied spaces containing small and white ovules that were probably unfertilized (Chen et al., 2014) could be seen in *qwrf1-1* siliques. This phenomenon was rarely found in wild-type siliques at this stage. In mature *qwrf1-1* siliques, about 7.1% of seeds were aborted, significantly different from the number in the wild type (1.6%) (**Figure 1B**), but the mean length of siliques was similar between the *qwrf1-1* mutant (15.1 $\pm$ 1.2 mm) and the wild type (15.3 $\pm$ 0.7 mm) (**Figure 1C**). Similar phenotypes were observed in *sco3-3* (**Figures 1A,B**), a previously reported *qwrf1* knockout line (Albrecht et al., 2010).

As the phenotypes of *qwrf1-1* mutants were relatively weak, we suspected a functional overlap among QWRF proteins. *QWRF2* (*AT1G49890*) is the closest homolog of *QWRF1* in *Arabidopsis* (Pignocchi et al., 2009). Therefore, we obtained a knockout T-DNA insertion line of *QWRF2* (named *qwrf2-1*, SALK_119512) from ABRC and generated another loss-of-function allele by CRISPR/Cas9 (named *qwrf2cas9*), which had a 257-nucleotide deletion after the 352th base pair, resulting in early termination of QWRF2 protein translation (**Supplementary Figure 1C**). There was no significant difference in seed setting rate or silique length between the wild-type and *qwrf2* mutant lines (**Figures 1B,C**). We then generated a *qwrf1qwrf2* double mutant by crossing *qwrf1-1* with *qwrf2-1* and analyzed the phenotypes (**Supplementary Figure 1B**). Unfertilized ovules were dramatically enhanced in the double mutant at 14 DAP, and the rate of seed setting was only 40% in the *qwrf1qwrf2* mutant (**Figures 1A,B**). The mean length of *qwrf1qwrf2* mature siliques was significantly shorter than that in the wild type (**Figure 1C**). We then introduced GFP-fused QWRF1 or QWRF2, driven by the respective native promoter, into the *qwrf1qwrf2* mutant (**Supplementary Figures 1D–G**). Expression of either one could rescue the seed setting rate and silique length phenotypes of the double mutant (**Figures 1A–C**). These results confirmed that the fertility defects in the double mutant could be attributed to the simultaneous loss of function of *QWRF1* and *QWRF2*, indicating their functional redundancy. Moreover, fusion with GFP (in the N- or the C-terminus) did not interfere with the proper function of QWRF1 or QWRF2 (**Figures 1A–C**).

QWRF1 and QWRF2 Have Important Roles in Floral Organ Growth

To understand how QWRF1 and QWRF2 influenced plant fertility, we first conducted reciprocal crosses between double mutant and wild-type plants. Pollination of wild-type stigma with *qwrf1qwrf2* pollens led to a mild but significant reduction in seed setting rate compared with self-pollinated wild-type plants (**Figure 1D**), indicating a defect in pollen development in the double mutant. Indeed, in stage 14 flowers, many *qwrf1qwrf2* mature anthers had far fewer pollen grains than wild-type anthers, and nearly 20% of *qwrf1qwrf2* pollen grains were aborted (**Supplementary Figure 2**). Moreover, pollinating *qwrf1qwrf2* plants with wild-type pollens caused a dramatic reduction in seed setting rate compared with either wild type self-pollinated or mutant pollen-pollinated wild-type plants (**Figures 1D,E**), indicating that defects in pistils contributed primarily to the fertility phenotypes of *qwrf1qwrf2* double mutants. We further analyzed the related developmental defects in pistils. Although we observed normal embryo sacs in unfertilized *qwrf1qwrf2* ovules (**Supplementary Figure 3**), we found abnormal stigma in the mutant: the *qwrf1qwrf2* papilla cells appeared shorter and more centralized compared with those of the wild type (**Figures 1F,G**). Moreover, when we used wild-type pollens to pollinate, much less pollen grain adhered on the mutant stigma than on wild-type stigma (**Figures 1H,I**), suggesting that the defect in papilla cells might perturb the adhesion of pollen grains on the stigma and subsequent fertilization. Furthermore, manual pollination of a *qwrf1qwrf2* plant with its own pollen grains resulted in significantly higher seed-setting rates compared with natural self-pollination (**Figures 1D,E**), suggesting physical barriers to self-pollination in the double mutant.

There were multiple developmental defects in *qwrf1qwrf2* flowers, including (1) shorter filaments such that the anthers hardly reached the stigma (**Figures 2A,B**); (2) a deformed floral organ arrangement lacking the cross-symmetry usually seen in the wild type, with bending petals sometimes forming an obstacle between anthers and stigma (**Figures 2C,D**); and (3) generally smaller and narrower petals and sepals compared with the wild type (**Figures 2E–J**). All these phenotypes were complemented

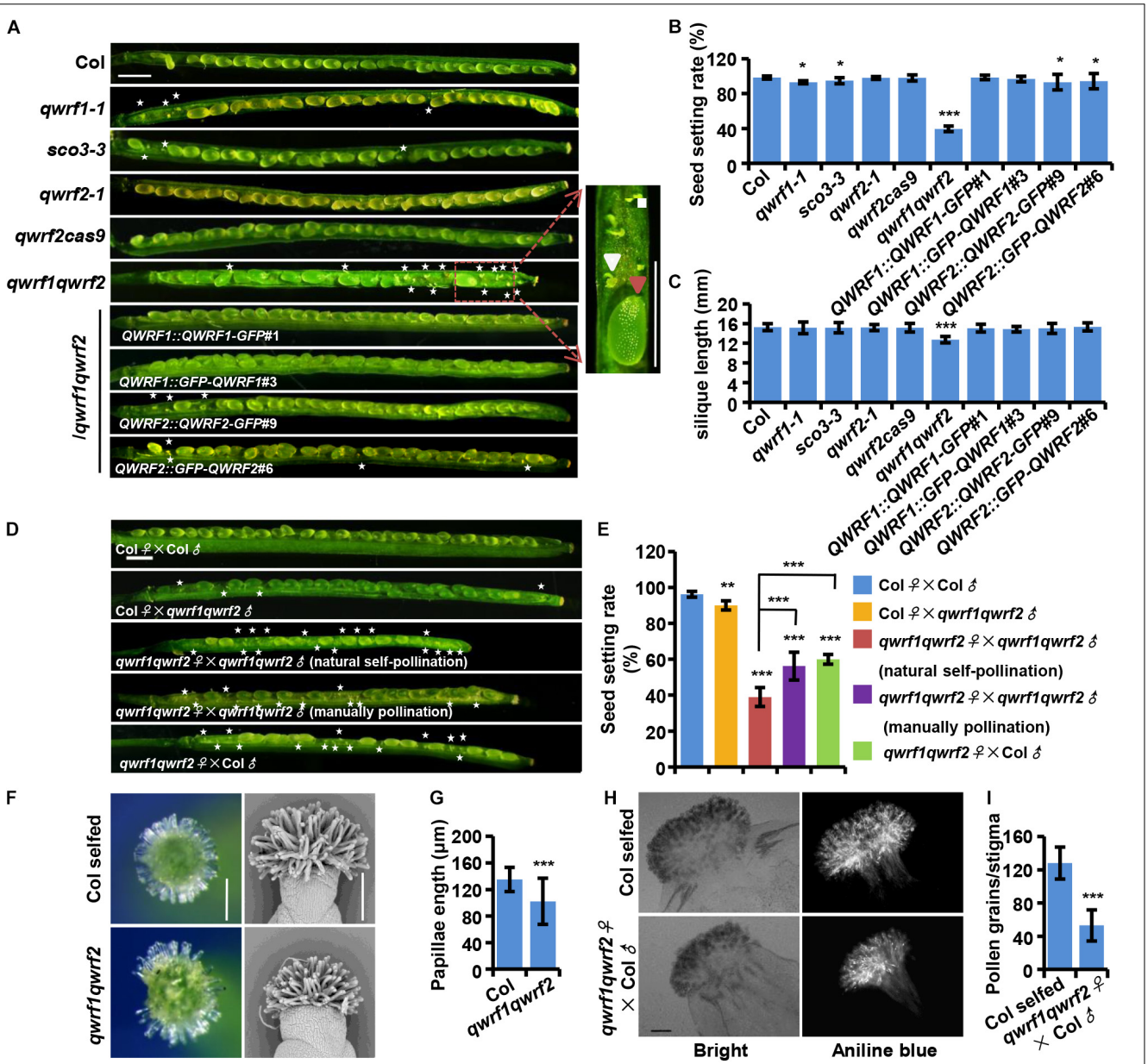

FIGURE 1 | QWRF1 and QWRF2 have functionally redundant roles in fertility. **(A)** Developing seeds on opened siliques, more unfertilized ovules were seen in *qwrf1* (*qwrf1-1* and *sco3-3*) single mutant and *qwrf1qwrf2* double mutant than in wild type. The siliques were shorter in *qwrf1qwrf2* compared to that in the wild type. There was no obvious difference between wild type and *qwrf2* (*qwrf2-1* and *qwrf2cass9*) single mutant. The defects in *qwrf1qwrf2* were rescued by the *qwrf1qwrf2* complementation lines (*QWRF1* or *QWRF2* cDNA constructs fused with a C-terminal GFP or N-terminal GFP). Asterisks indicate the unfertilized ovules. The close-up views shows the fertilized ovule (big and green, red arrowhead) and unfertilized ovule (small and white, white arrowhead) besides the panels. Scale bar, 1 mm. **(B)** and **(C)** Quantitative analysis of seed setting rate **(B)** and silique length **(C)** shown in panel **(A)**. The values are the mean ± SD of three independent experiments, each with at least nine siliques from three plants. $^{*}P < 0.05$, $^{***}P < 0.001$, Student's *t* test. **(D)** Fourteen days after pollination (DAP) siliques were derived from self-pollination or reciprocal crosses between the wild type and the *qwrf1qwrf2* double mutant plants. Compared with wild-type self-pollination siliques, unfertilized ovules were obviously existed no matter the *qwrf1qwrf2* was used as a male for pollen donors or as a female pollinated by the wild-type or the *qwrf1qwrf2* pollens. Manually pollination of *qwrf1qwrf2* plant can partially rescue the semi-sterile phenotype of *qwrf1qwrf2* when natural self-pollination. Asterisks indicate the unfertilized ovules. Scale bar, 1 mm. **(E)** Quantification of seed setting rate in panel **(D)**. The values are the mean ± SD of three independent experiments, each with at least nine siliques from three plants. $^{**}P < 0.01$, $^{***}P < 0.001$. **(F)** Compared to wild type, the *qwrf1qwrf2* stigmas papilla cells at stage 14 appeared shorter and more centralized when observed by stereoscope (left) and scanning electron microscopy (SEM, right). Scale bar, 200 μm. **(G)** Quantification of papillae length in panel **(F)**. Values are mean ± SD of 120 cells from 10 stigmas, $^{***}P < 0.001$, Student's *t* test. **(H)** Pollinated with wild-type pollens, much less pollen grains adhered on the *qwrf1qwrf2* stigma than on wild-type stigma. Pistils were collected at 2 h after-pollination (HAP) and pollen grains which adhered to the stigmatic papillae and stained by aniline blue were shown in the bright-field and fluorescent images, respectively. Scale bar, 100 μm. **(I)** Quantitative analysis of the adhered pollen grains numbers to each stigma from panel **(H)**. Values are mean ± SD of three independent experiments, each with 10 stigmas, $^{***}P < 0.001$, Student's *t* test.

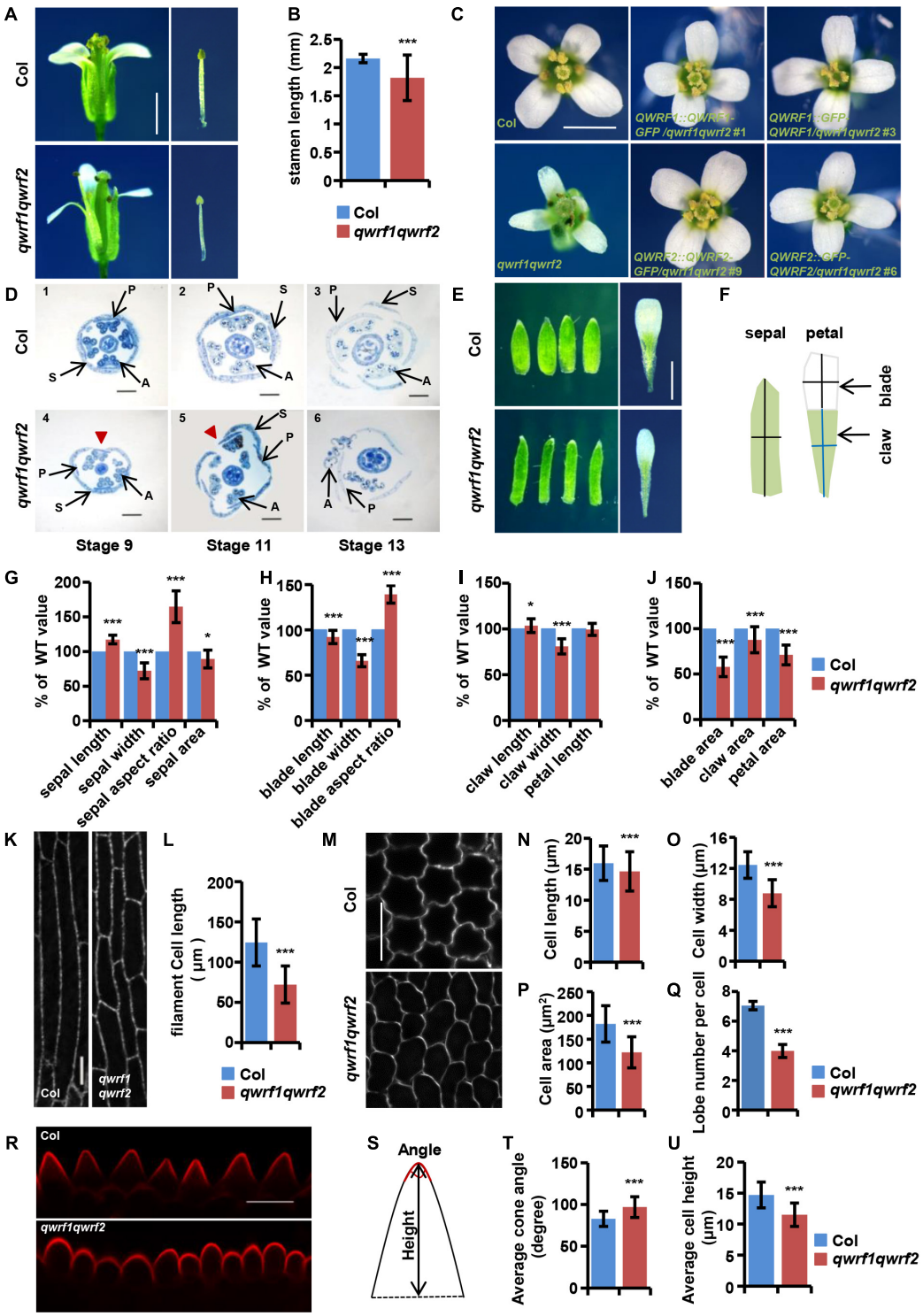

FIGURE 2 | The *qwrf1qwrf2* mutant displays severe developmental defects in floral organs. **(A)** Representative dissected flowers and stamens of wild type and *qwrf1qwrf2* at stage 14. The filament length of *qwrf1qwrf2* reduced than that of wild type. Scale bar, 1 mm. **(B)** Statistics of filament length in panel **(A)**. The values are the mean ± SD three independent assays, $n = 12$. $^{***}P < 0.001$, Student's t test. **(C)** Representative opened flowers of wild type, *qwrf1qwrf2* and various *qwrf1qwrf2* complementation lines. Compared with the wild-type cross-symmetrical floral organs, the floral organ morphology of the *qwrf1qwrf2* mutant was asymmetry clearly, which can be rescued by *qwrf1qwrf2* complementation lines. Scale bar, 1 mm. **(D)** Resin-embedded cross-sections of wild type (1–3) and *qwrf1qwrf2* mutant (4–6) flowers at different stages, flowers of *qwrf1qwrf2* show the disturbed sepals and petals organization. Red arrowheads indicate enlarged

(Continued)

FIGURE 2 | Continued
gap between adjacent sepals. P, petal; S, sepal; A, anther. Scale bar, 200 μm. **(E)** Compared to the wild type at stage 14, the sepals from *qwrf1qwrf2* were longer and narrower, and the petals were shorter and narrower, and both the sepal and petal area were reduced significantly. Scale bar, 1 mm. **(F)** Schematic diagram shows how the sepal and petal length and width were measured. **(G)** Quantification of sepal parameters in panel **(E)**. Values are mean ± SD of 20 sepals from different plants. $^{*}P < 0.05$, $^{***}P < 0.001$, Student's *t* test. **(H–J)** Quantification of petal parameters of wild type and *qwrf1qwrf2* in panel **(E)**. Values are mean ± SD of three independent assays, from at least 36 petals. $^{*}P < 0.05$, $^{***}P < 0.001$, Student's *t* test. **(K)** Epidermal cell in the middle region of stage 14 stamen filament from wild type and *qwrf1qwrf2* by transforming *UBQ10:mCherry-MBD* construct. Scale bar, 10 μm. **(L)** The stamen filament cells in wild type were longer than in *qwrf1qwrf2* mutant. Values are mean ± SD. $n = 120$ cells, $^{***}P < 0.001$, Student's *t* test. **(M)** Cells from the blade regions of petal abaxial epidermis of wild type and *qwrf1qwrf2* mutant at stages 14 by PI staining. The *qwrf1qwrf2* petal abaxial epidermis cell shape changed obviously compared with that in wild type. Scale bar, 10 μm. **(N–R)** Quantification of cell parameters from petal abaxial epidermis cells in panel **(M)**. **(N)** Reduced cell length in *qwrf1qwrf2*. **(O)** Reduced cell width in *qwrf1qwrf2*. **(P)** Reduced cell area in *qwrf1qwrf2*. **(Q)** Reduced number of lobes per cell in *qwrf1qwrf2*. Values are mean ± SD of more than 500 cells of 6–8 petals from different plants. $^{***}P < 0.001$, Student's *t* test. **(R)** Conical cells shape changed between wild type and *qwrf1qwrf2* mutant at stage 14 by PI staining. Scale bar, 10 μm. **(S)** The carton illustrating how the conical cell angles and heights were measured. **(T,U)** Quantitative analysis conical cell parameters from panel **(R)**. The angle of conical cell was increased **(T)** and conical cell heights decreased **(U)** in *qwrf1qwrf2* mutant than in wild type. Values are mean ± SD of more than 400 cells of 8 petals from different plants. $^{***}P < 0.001$, Student's *t* test.

by expression of GFP-fused QWRF1 or QWRF2 in *qwrf1qwrf2* mutant (**Figure 2C**).

Using RT-RCR we found that both *QWRF1* and *QWRF2* were constitutively expressed in plants, with high levels in flowers (**Supplementary Figure 4A**). The expression of *QWRF1* and *QWRF2* in sepals, petals, stamens, stamen filaments, and pistils was further confirmed by GUS activity assay and *in situ* hybridization analysis (**Supplementary Figures 4B,C**). These results were consistent with those previously reported by Albrecht et al. (2010) as well as those in the Genevestigator database[2].

The above evidence demonstrates the important and redundant roles of QWRF1 and QWRF2 in the development of the floral organ. Loss of function of both genes led to developmental defects in flowers, including shorter stamen filaments and abnormal arrangements in floral organs, which probably caused severe physical obstacles that hindered natural pollination and reduced the subsequent seed setting rate.

QWRF1 and QWRF2 Are Involved in Anisotropic Cell Expansion

In plants, growth of organs to their final size and shape depends on cell proliferation followed by cell expansion (Powell and Lenhard, 2012). Phenotypes such as shorter stamen filaments, and narrower and smaller petals and sepals in *qwrf1qwrf2* flowers suggest possible defects in polar cell expansion. To confirm this hypothesis, we analyzed cell morphology in various floral tissues. Besides shorter papilla cells (**Figures 1F,G**), the epidermal cells of the stamen filament were significantly shorter than those in the wild type (**Figures 2K,L**). Moreover, we observed adaxial and abaxial epidermal cells of petal blades from stage 14 flowers by PI staining. As shown in **Figures 2M–P**, *qwrf1qwrf2* abaxial petal epidermal cells had decreased average cell length, width, area, and reduced lobe numbers (**Figure 2Q**) compared with the wild type, indicating a reduction in cell expansion.

We also observed alterations of the shapes of conical cells in petal adaxial epidermis (using a method reported by Ren et al., 2017; **Figure 2R**). Quantitative analyses revealed a larger-than-wild-type cone angle in *qwrf1qwrf2* conical cells (**Figures 2S,T**), which lacked the pointed apex usually seen in the wild type, and a decrease in the average cell height (**Figure 2U**). These results suggest that QWRF1 and QWRF2 have a general role in the regulation of anisotropic cell expansion during floral organ growth.

QWRF1 and QWRF2 Associate With Microtubules *in vitro* and *in vivo*

To better understand the function of QWRF1 and QWRF2, we investigated the subcellular localization pattern of these two proteins. As barely any fluorescence was detected in complementary lines expressing GFP-fused QWRF1 or QWRF2 driven by their native promoter, we used the *pSUPER* promoter to drive GFP-fused QWRF proteins and transiently expressed them in tobacco BY-2 suspension cells. Regardless of which terminus was fused with GFP, QWRF1 were localized to a filament-like structure that could be disrupted by microtubule-disrupting drug oryzalin but not by microfilament-disrupting drug Lat B (**Figures 3A–D**). This suggested that QWRF1 co-localized with microtubules in BY-2 cells. QWRF2 showed a similar localization pattern (**Figures 3E–H**). To further verify whether QWRF1 and QWRF2 were MAPs, we performed an *in vitro* co-sedimentation assay. Owing to the difficulty of obtaining purified recombinant QWRF1 and QWRF2 proteins using a prokaryotic expression system, we used *in vitro* coupled transcription/translation to express QWRF proteins as previously described (Pignocchi et al., 2009). Biotinylated-lysine-labeled QWRF1 or QWRF2 protein was, respectively, incubated with or without paclitaxel-stabilized pre-polymerized microtubules before high-speed centrifugation. Both QWRF1 and QWRF2 were co-sedimented with pre-polymerized microtubules in the pellets, indicating their direct association with microtubules *in vitro* (**Figures 3I–J**, **Supplementary Figure 5**). These *in vivo* and *in vitro* results were consistent with our expectations, as previous studies have shown that QWRF1/SCO3 links the microtubule, and another QWRF family protein EDE1 is a MAP (Pignocchi et al., 2009; Albrecht et al., 2010).

QWRF1 and QWRF2 Modulate Cortical Microtubule Arrangement

In plant cells, cortical microtubule arrays influence anisotropic cell expansion by guiding the deposition and orientation of

[2]www.genevestigator.ethz.ch

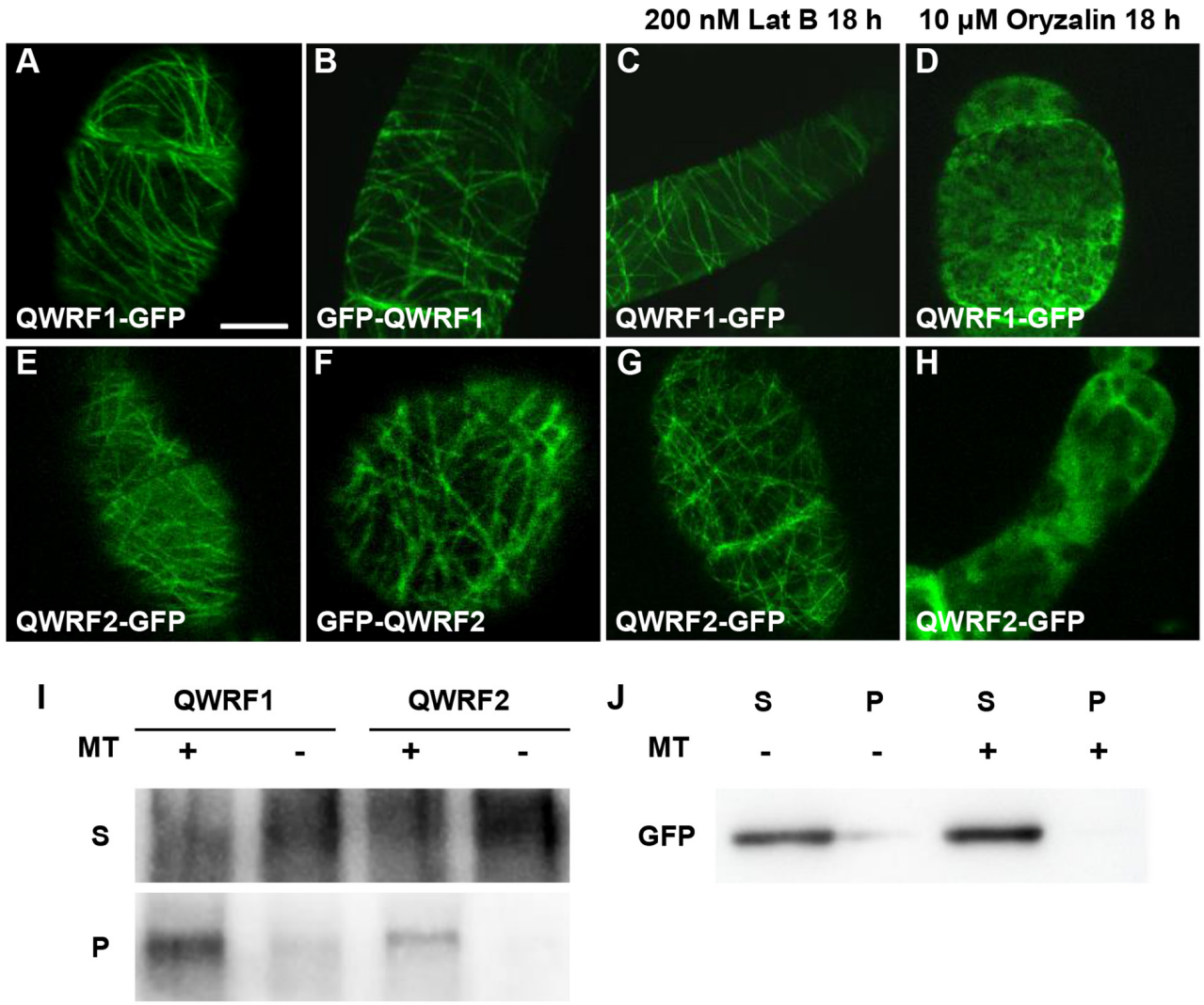

FIGURE 3 | QWRF1 and QWRF2 are associating with microtubule *in vitro* and *in vivo*. **(A–D)** Subcellular localization of QWRF1. **(E–H)** Subcellular localization of QWRF2. Confocal microscopy images of the tobacco BY-2 suspension cells transiently expressing *pSUPER:QWRF1-GFP* **(A,C,D)**, *35S:GFP-QWRF1* **(B)**, *pSUPER:QWRF2-GFP* **(E,G,H)** and *35S:GFP-QWRF2* **(F)**. All these construction exhibited filamentous structures in tobacco BY-2 suspension cells, when treated with various drugs for 18 h, filamentous structures visualized in this cell remained intact in the presence of 200 nM Lat B (actin polymerization inhibitor) treatment **(C,G)**, but these structures were disrupted by 10 μM oryzalin (microtubule-specific depolymerized drug) treatment **(D,H)**. Scale bar, 10 μm. **(I)** *In vitro*-biotinylated-lysine-labeled QWRF1 or QWRF2 protein expressed in a cell-free system was co-sedimented with (+) or without (–) taxol-stabilized microtubules. After high-speed centrifugation, QWRF1 and QWRF2 proteins could be detected in pellets with microtubules. **(J)** GFP was used as a negative control, which showed no preferential co-sedermentated with microtubules. MT, microtubules; S, supernatants; P, pellets.

cellulose microfibrils (Fujikura et al., 2014; Yang et al., 2019b). Therefore, regulation of the organization and dynamics of cortical microtubule arrays is important for the polar expansion of various cell types, and subsequently affects cell and organ morphogenesis. The above evidence showed obvious cell-expansion defects in various types of floral cells, and revealed the abnormal morphology of sepals, petals, and stamen filaments in the *qwrf1qwrf2* double mutant (**Figure 2**). Given that both QWRF1 and QWRF2 are suggested as MAPs, we proposed that they might exert their functions in anisotropic cell expansion and floral organ morphogenesis through modulation of cortical microtubule arrays. To test this hypothesis, we compared the cortical microtubule arrangements in epidermal cells of stamen filaments and petals between the *qwrf1qwrf2* double mutant and the wild type. As mentioned above, the *qwrf1qwrf2* mutant had shorter stamen filament epidermal cells than the wild type. To visualize the cortical microtubules in these cells, *UBQ10:mCherry-MBD* was introduced into the *qwrf1qwrf2* double mutant by crossing. As filament elongation starts at flower stage 12 and ends at stage 13 (Acosta and Przybyl, 2019), we observed stamen filaments at these two stages. At stage 12, most cortical microtubules were parallel and transversely oriented in the wild type, which is consistent with the fast cell elongation at this stage (**Figure 4A**). However, in *qwrf1qwrf2*

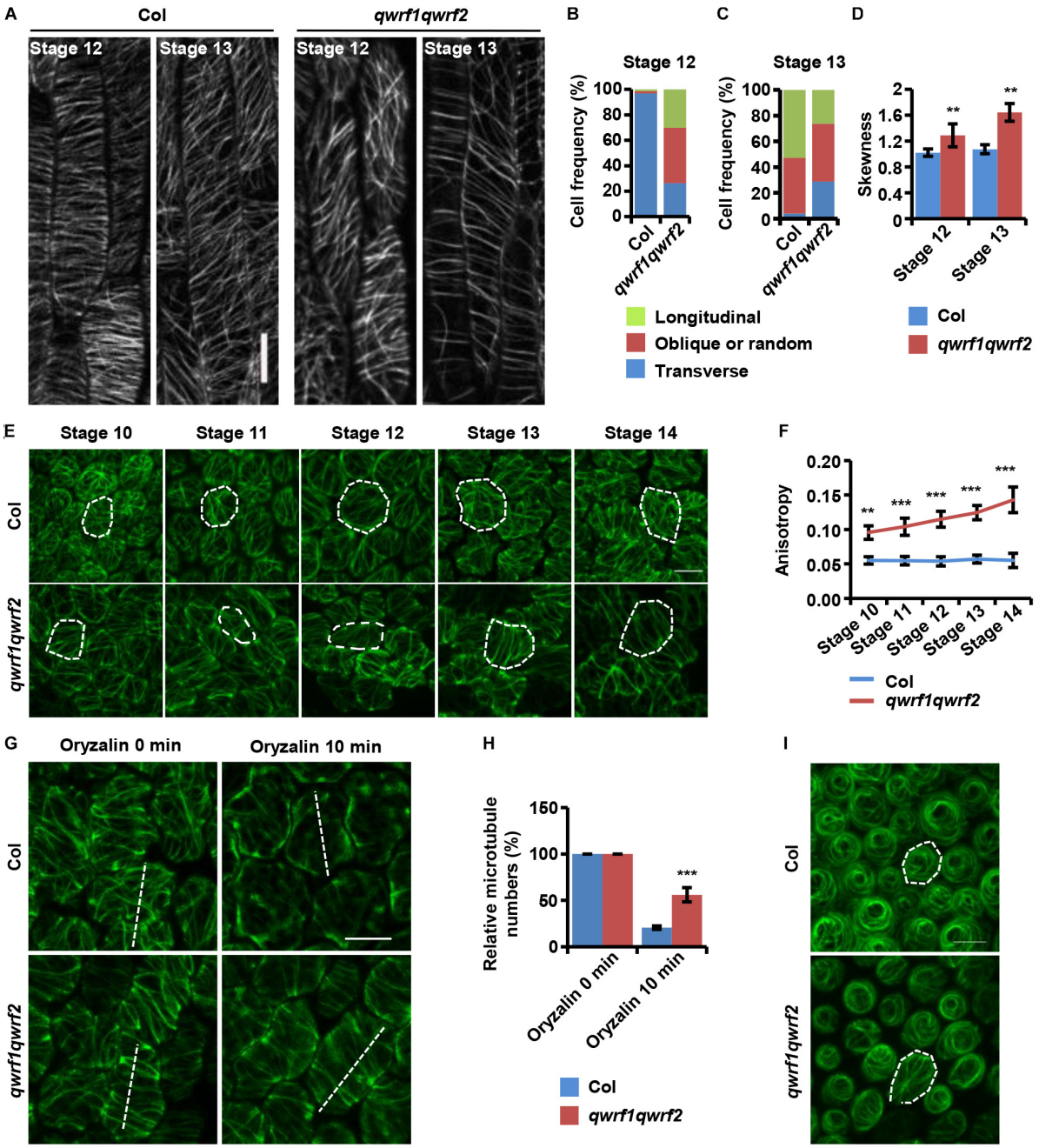

FIGURE 4 | QWRF1 and QWRF2 affect cortical microtubule organization and stability in floral organ cells. **(A)** *UBQ10:mCherry-MBD*-labelled cortical microtubules in wild-type and *qwrf1qwrf2* stamen filament epidermal cells. The cortical microtubules array in *qwrf1qwrf2* stamen filament epidermal cells is greatly altered compared with that in wild type. Scale bar, 20 μm. **(B,C)** Frequency of microtubule orientation patterns in wild-type and *qwrf1qwrf2* upper stamen filament epidermal cell at stage 12 and 13, measured by fibriltool, an Image J plug-in as described in the method. $n \geq 150$ cells. **(D)** Quantification of microtubule bundling (Skewness) from confocal optical images in panel **(A)**. The microtubule bundling was increased in *qwrf1qwrf2* stamen filament epidermal cells. Values are mean ± SD. $n \geq 100$ cells, $^{**}P < 0.01$, Student's *t* test. **(E)** Cortical microtubules of abaxial epidermal cells in petal blades of wild type and *qwrf1qwrf2* with a *35S:GFP-TUA6* background. The microtubule arrays in *qwrf1qwrf2* petal at stage 10–14 abaxial epidermal cells were more orderly. The white dotted lines depict cell outlines. Scale bar, 10 μm. **(F)** The microtubule alignment in panel **(E)** was measured by fibriltool, an Image J plug-in as described in the method. The anisotropy close to 1 represents contained more highly ordered cortical microtubule (CMT) arrays transversely oriented relative to the axis of cell elongation. Values are mean ± SD. $n \geq 200$ cells. $^{***}P < 0.001$, Student's *t* test. **(G)** The organization of cortical microtubules in *qwrf1qwrf2* cells is insensitive to treatment with 20 μM oryzalin for 10 min. Scale bar, 10 μm. **(H)** Fifteen-μm of white dashed lines cross the cortical microtubules **(G)**, and the number of cortical microtubules across the line was measured as the density. Three repeated measurements were performed and at least 100 cells were used. Values are mean ± SD of more than 100 cells. $^{***}P < 0.001$, Student's *t* test. **(I)** Cortical microtubules were observed in conical cells from opened flower petals of wild type and *qwrf1qwrf2* mutant stably expressing *35S:GFP-TUA6*, respectively. The white dotted lines depict cell outlines. Scale bar, 10 μm.

cells, far fewer microtubules were transversely oriented compared with the number in wild-type cells (**Figure 4B**). At stage 13, when cell elongation ends, cortical microtubules were arranged obliquely in both the wild type and *qwrf1qwrf2* double mutant (**Figure 4C**). Moreover, compared with wild-type cells, the bundling of microtubules in *qwrf1qwrf2* cells was significantly higher according to the skewness analysis (**Figure 4D**).

Next, we observed cortical microtubule arrays in petal epidermal cells by stably expressing *35S* promoter-driven *GFP-TUA6* in the wild type and *qwrf1qwrf2* double mutant. As shown in **Figure 2**, the *qwrf1qwrf2* mutant had shorter and narrower petal blades, and consistently shorter and narrower abaxial epidermal cells. Quantitative analyses also revealed that *qwrf1qwrf2* cells had much fewer lobes than wild-type cells (**Figure 2Q**), indicating a stronger restriction of lateral cell expansion. Consistently, we found sparser but more orderly cortical microtubules in *qwrf1qwrf2* abaxial petal epidermal cells than in wild-type cells throughout flower stages 10–14 (**Figures 4E,F**). After treatment with oryzalin, there were more intact microtubule filaments in mutant cells, indicating that microtubules were more stable when both QWRF1 and QWRF2 were absent (**Figures 4G,H**).

Given the change in cell shape of petal adaxial conical cells in the *qwrf1qwrf2* mutant (**Figure 2R**), we further investigated whether QWRF1 and QWRF2 affected microtubule organization in these cells. Similar to previous reports (Ren et al., 2017), microtubule arrays in wild-type cells displayed a well-ordered circumferential orientation. However, in *qwrf1qwrf2* mutant cells, microtubule arrays were randomly oriented (**Figure 4I**), consistent with the mutant conical cells having larger cone angle but shorter cell height (**Figures 2T,U**; Ren et al., 2017).

DISCUSSION

Organ growth is essential for floral organs to achieve their proper morphology and fulfill their functions. Spatial and temporal control of anisotropic expansion following initial cell proliferation is important for organ growth (Irish, 2010). However, the molecular mechanism underlying the regulation of floral organ growth is largely unknown. Recently, cortical microtubules have been reported to guide the growth and shape of sepals and petals by acting as both mechanical stress sensors and growth regulators (Hervieux et al., 2016; Yang et al., 2019b). In this study, we characterized a *qwrf1qwrf2* double mutant with defects in many aspects of flower development, including abnormal size and shape of sepals and petals, short stamen filaments and papilla cells, and an altered symmetric arrangement of floral organs (**Figure 2**). These defects represented physical barriers to successful sexual reproduction. However, both *qwrf1* and *qwrf2* single mutants showed few defects in flower development and sexual reproduction (although *qwrf1* showed a weak reduction in seed setting rate), indicating the redundant functions of QWRF1 and QWRF2 in floral organ growth and plant fertility. Nevertheless, the floral organs of *qwrf1qwrf2* double mutant are in four whorls, suggesting that QWRF1 and QWRF2 are not critical for floral meristem establishment and organ identity.

There were significant differences in the size and shape of epidermal cells in petals and stamen filaments between the wild type and the double mutant, indicating a role for QWRF1 and QWRF2 in anisotropic cell expansion. *In vitro* and *in vivo* analyses demonstrated that QWRF1 and QWRF2 were associated with microtubules. Moreover, epidermal cells of *qwrf1qwrf2* petals and stamen filaments had cortical microtubule arrays with sparse microtubule bundles in an altered orientation compared with the wild type. Overall, we concluded that QWRF1 and QWRF2 are required for proper growth and morphology of floral organs and thus for plant fertility, and probably function *via* modulating microtubule-dependent anisotropic cell expansion during organ growth.

QWRF1/SCO3 contains a C-terminal PTS1 (peroxisomal-targeting signal type 1) domain, tripeptide SRL, which targets the periphery of peroxisomes in *Arabidopsis* cultured cells. Interestingly, GFP:SCO3ΔSRL, which lacking the peroxisome location, was unable to complement the phenotype of *sco3-1* mutant as determined by chlorophyll content in cotyledons (Albrecht et al., 2010). However, in our study, we found that expressing QWRF1ΔSRL was able to rescue floral organ growth and fertility of *qwrf1qwrf2* plants (**Supplementary Figure 6**), suggesting that the effects of QWRF1 on floral organ growth and fertility are unrelated to its peroxisome association. Consistently, QWRF2 has no PTS1 domain but being associated with microtubules, and being functionally redundant with QWRF1.

We also observed incomplete anther dehiscence, and shriveled and shrunken pollen grains in *qwrf1qwrf2* opening flowers; how these two proteins regulate male gametophyte development needs further study. Given that EDE1/QWRF5, another QWRF family member, colocalizes with mitotic microtubules during endosperm development (Pignocchi et al., 2009), whether QWRF1 and QWRF2 participate in microsporogenesis *via* binding to and regulating mitotic microtubules is also worthy of further investigation. Notably, the *qwrf1qwrf2* ovules had normal embryo sacs (**Supplementary Figure 3**), indicating that they are not involved in megasporogenesis during flower development.

DATA AVAILABILITY STATEMENT

The datasets presented in this study can be found in online repositories. The names of the repository/repositories and accession number(s) can be found in the article/ **Supplementary Material**.

AUTHOR CONTRIBUTIONS

LZ, YF, and HM designed the project. HM and LX performed the experiments and analyzed the data. LZ and HM wrote the manuscript. YF revised the manuscript. All authors have contributed significantly to this work and all authors are in agreement with the contents of the manuscript.

FUNDING

This work was supported by the National Natural Science Foundation of China (Grant Nos. 31771489 and 32070311 to LZ; 32061143018, 91735305, and 91854119 to YF).

ACKNOWLEDGMENTS

We thank Tonglin Mao (China Agricultural University) for providing the tobacco (*Nicotiana tabacum*) BY-2 suspension cells. We also thank Qijun Chen (China Agricultural University) for providing the plasmid vectors pCBC-DT1T2 and pHEC401 to construct CRISPR-Cas9 mutant. We would like to thank Mengxiang Sun (Wuhan University) for his valuable comments on this study.

SUPPLEMENTARY MATERIAL

The Supplementary Material for this article can be found online at: https://www.frontiersin.org/articles/10.3389/fcell.2021.634218/full#supplementary-material

REFERENCES

Acosta, I. F., and Przybyl, M. (2019). Jasmonate signaling during *Arabidopsis* stamen maturation. *Plant Cell. Physiol.* 60, 2648–2659. doi: 10.1093/pcp/pcz201

Albrecht, V., Simkova, K., Carrie, C., Delannoy, E., Giraud, E., Whelan, J., et al. (2010). The cytoskeleton and the peroxisomal-targeted snowy cotyledon3 protein are required for chloroplast development in *Arabidopsis*. *Plant Cell* 22, 3423–3438. doi: 10.1105/tpc.110.074781

An, G. (1985). High efficiency transformation of cultured tobacco cells. *Plant Physiol.* 79, 568–570. doi: 10.1104/pp.79.2.568

Anastasiou, E., Kenz, S., Gerstung, M., MacLean, D., Timmer, J., Fleck, C., et al. (2007). Control of plant organ size by KLUH/CYP78A5-dependent intercellular signaling. *Dev. Cell* 13, 843–856. doi: 10.1016/j.devcel.2007.10.001

Boudaoud, A., Burian, A., Borowska-Wykret, D., Uyttewaal, M., Wrzalik, R., Kwiatkowska, D., et al. (2014). FibrilTool, an ImageJ plug-in to quantify fibrillar structures in raw microscopy images. *Nat. Protoc.* 9, 457–463. doi: 10.1038/nprot.2014.024

Bowman, J. L., Smyth, D. R., and Meyerowitz, E. M. (1991). Genetic interactions among floral homeotic genes of *Arabidopsis*. *Development* 112, 1–20.

Bowman, J. L., Smyth, D. R., and Meyerowitz, E. M. (2012). The ABC model of flower development: then and now. *Development* 139, 4095–4098. doi: 10.1242/dev.083972

Chen, Y. H., Shen, H. L., Hsu, P. J., Hwang, S. G., and Cheng, W. H. (2014). N-acetylglucosamine-1-P uridylyltransferase 1 and 2 are required for gametogenesis and embryo development in *Arabidopsis thaliana*. *Plant Cell Physiol.* 55, 1977–1993. doi: 10.1093/pcp/pcu127

Clough, S. J., and Bent, A. F. (1998). Floral dip: a simplified method for Agrobacterium-mediated transformation of *Arabidopsis thaliana*. *Plant J.* 16, 735–743. doi: 10.1046/j.1365-313x.1998.00343.x

Coen, E. S., and Meyerowitz, E. M. (1991). The war of the whorls: genetic interactions controlling flower development. *Nature* 353, 31–37. doi: 10.1038/353031a0

Cui, H. H., Liao, H. Z., Tang, Y., Du, X. Y., Chen, L. Q., Ye, D., et al. (2015). ABORTED GAMETOPHYTE 1 is required for gametogenesis in *Arabidopsis*. *J. Integr. Plant Biol.* 57, 1003–1016. doi: 10.1111/jipb.12341

Denay, G., Chahtane, H., Tichtinsky, G., and Parcy, F. (2017). A flower is born: an update on *Arabidopsis* floral meristem formation. *Curr. Opin. Plant Biol.* 35, 15–22. doi: 10.1016/j.pbi.2016.09.003

Dinneny, J. R., Weigel, D., and Yanofsky, M. F. (2006). NUBBIN and JAGGED define stamen and carpel shape in *Arabidopsis*. *Development* 133, 1645–1655. doi: 10.1242/dev.02335

Dinneny, J. R., Yadegari, R., Fischer, R. L., Yanofsky, M. F., and Weigel, D. (2004). The role of JAGGED in shaping lateral organs. *Development* 131, 1101–1110. doi: 10.1242/dev.00949

Disch, S., Anastasiou, E., Sharma, V. K., Laux, T., Fletcher, J. C., and Lenhard, M. (2006). The E3 ubiquitin ligase BIG BROTHER controls *Arabidopsis* organ size in a dosage-dependent manner. *Curr. Biol.* 16, 272–279. doi: 10.1016/j.cub.2005.12.026

Doucet, J., Truong, C., Frank-Webb, E., Lee, H. K., Daneva, A., Gao, Z., et al. (2019). Identification of a role for an E6-like 1 gene in early pollen–stigma interactions in *Arabidopsis thaliana*. *Plant Reprod.* 32, 307–322. doi: 10.1007/s00497-019-00372-x

Fujikura, U., Elsaesser, L., Breuninger, H., Sanchez-Rodriguez, C., Ivakov, A., Laux, T., et al. (2014). Atkinesin-13A modulates cell-wall synthesis and cell expansion in *Arabidopsis thaliana* via the THESEUS1 pathway. *PLoS Genet.* 10:e1004627. doi: 10.1371/journal.pgen.1004627

Gutierrez, R., Lindeboom, J. J., Paredez, A. R., Emons, A. M., and Ehrhardt, D. W. (2009). *Arabidopsis* cortical microtubules position cellulose synthase delivery to the plasma membrane and interact with cellulose synthase trafficking compartments. *Nat. Cell Biol.* 11, 797–806. doi: 10.1038/ncb1886

He, M., Lan, M., Zhang, B., Zhou, Y., Wang, Y., Zhu, L., et al. (2018). Rab-H1b is essential for trafficking of cellulose synthase and for hypocotyl growth in *Arabidopsis thaliana*. *J. Integr. Plant Biol.* 60, 1051–1069. doi: 10.1111/jipb.12694

Hervieux, N., Dumond, M., Sapala, A., Routier-Kierzkowska, A. L., Kierzkowski, D., Roeder, A. H., et al. (2016). A mechanical feedback restricts sepal growth and shape in *Arabidopsis*. *Curr. Biol.* 26, 1019–1028. doi: 10.1016/j.cub.2016.03.004

Higaki, T., Kutsuna, N., Sano, T., Kondo, N., and Hasezawa, S. (2010). Quantification and cluster analysis of actin cytoskeletal structures in plant cells: role of actin bundling in stomatal movement during diurnal cycles in *Arabidopsis* guard cells. *Plant J.* 61, 156–165. doi: 10.1111/j.1365-313x.2009.04032.x

Irish, V. F. (2010). The flowering of *Arabidopsis* flower development. *Plant J.* 61, 1014–1028. doi: 10.1111/j.1365-313X.2009.04065.x

Ito, T., Nagata, N., Yoshiba, Y., Ohme-Takagi, M., Ma, H., and Shinozaki, K. (2007). *Arabidopsis* MALE STERILITY1 encodes a PHD-type transcription factor and regulates pollen and tapetum development. *Plant Cell* 19, 3549–3562. doi: 10.1105/tpc.107.054536

Kang, E., Zheng, M., Zhang, Y., Yuan, M., Yalovsky, S., Zhu, L., et al. (2017). The microtubule-associated protein MAP18 affects ROP2 GTPase activity during root hair growth. *Plant Physiol.* 174, 202–222. doi: 10.1104/pp.16.01243

Krizek, B. A. (1999). Ectopic expression of AINTEGUMENTA in *Arabidopsis* plants results in increased growth of floral organs. *Dev. Genet.* 25, 224–236.

Krizek, B. A., Prost, V., and Macias, A. (2000). AINTEGUMENTA promotes petal identity and acts as a negative regulator of AGAMOUS. *Plant Cell* 12, 1357–1366. doi: 10.1105/tpc.12.8.1357

Lei, Y., Lu, L., Liu, H. Y., Li, S., Xing, F., and Chen, L. L. (2014). CRISPR-P: a web tool for synthetic single-guide RNA design of CRISPR-system in plants. *Mol. Plant* 7, 1494–1496. doi: 10.1093/mp/ssu044

Li, C., Shi, L., Wang, Y., Li, W., Chen, B., Zhu, L., et al. (2020). *Arabidopsis* ECAP is a new adaptor protein that connects JAZ repressors with the TPR2 Co-repressor to suppress jasmonate-responsive anthocyanin accumulation. *Mol. Plant* 13, 246–265. doi: 10.1016/j.molp.2019.10.014

Liu, X., Qin, T., Ma, Q., Sun, J., Liu, Z., Yuan, M., et al. (2013). Light-regulated hypocotyl elongation involves proteasome-dependent degradation of the microtubule regulatory protein WDL3 in *Arabidopsis*. *Plant Cell* 25, 1740–1755. doi: 10.1105/tpc.113.112789

Ohno, C. K., Reddy, G. V., Heisler, M. G., and Meyerowitz, E. M. (2004). The *Arabidopsis* JAGGED gene encodes a zinc finger protein that promotes leaf tissue development. *Development* 131, 1111–1122. doi: 10.1242/dev.00991

Paredez, A. R., Somerville, C. R., and Ehrhardt, D. W. (2006). Visualization of cellulose synthase demonstrates functional association with microtubules. *Science* 312, 1491–1495. doi: 10.1126/science.1126551

Pignocchi, C., Minns, G. E., Nesi, N., Koumproglou, R., Kitsios, G., Benning, C., et al. (2009). ENDOSPERM DEFECTIVE1 is a novel microtubule-associated protein essential for seed development in *Arabidopsis*. *Plant Cell* 21, 90–105. doi: 10.1105/tpc.108.061812

Powell, A. E., and Lenhard, M. (2012). Control of organ size in plants. *Curr. Biol.* 22, R360–R367. doi: 10.1016/j.cub.2012.02.010

Reeves, P. H., Ellis, C. M., Ploense, S. E., Wu, M. F., Yadav, V., Tholl, D., et al. (2012). A regulatory network for coordinated flower maturation. *PLoS Genet.* 8:e1002506. doi: 10.1371/journal.pgen.1002506

Ren, H., Dang, X., Cai, X., Yu, P., Li, Y., Zhang, S., et al. (2017). Spatio-temporal orientation of microtubules controls conical cell shape in *Arabidopsis thaliana* petals. *PLoS Genet.* 13:e1006851. doi: 10.1371/journal.pgen.1006851

Ren, H., Dang, X., Yang, Y., Huang, D., Liu, M., Gao, X., et al. (2016). SPIKE1 activates ROP GTPase to modulate petal growth and shape. *Plant Physiol.* 172, 358–371. doi: 10.1104/pp.16.00788

Smith, A. R., and Zhao, D. (2016). Sterility caused by floral organ degeneration and abiotic stresses in *Arabidopsis* and cereal grains. *Front. Plant Sci.* 7:1503. doi: 10.3389/fpls.2016.01503

Smyth, D. R., Bowman, J. L., and Meyerowitz, E. M. (1990). Early flower development in *Arabidopsis*. *Plant Cell* 2, 755–767. doi: 10.1105/tpc.2.8.755

Sun, J., Ma, Q., and Mao, T. (2015). Ethylene regulates the *Arabidopsis* microtubule-associated protein WAVE-DAMPENED2-LIKE5 in etiolated hypocotyl elongation. *Plant Physiol.* 169, 325–337. doi: 10.1104/pp.15.00609

Takeda, S., Ochiai, K., Kagaya, Y., Egusa, W., Morimoto, H., Sakazono, S., et al. (2018). Abscisic acid-mediated developmental flexibility of stigmatic papillae in response to ambient humidity in *Arabidopsis thaliana*. *Genes Genet. Syst.* 93, 209–220. doi: 10.1266/ggs.18-00025

Theißen, G., Melzer, R., and Rumpler, F. (2016). MADS-domain transcription factors and the floral quartet model of flower development: linking plant development and evolution. *Development* 143, 3259–3271. doi: 10.1242/dev.134080

Thomson, B., and Wellmer, F. (2019). Molecular regulation of flower development. *Curr. Top Dev. Biol.* 131, 185–210. doi: 10.1016/bs.ctdb.2018.11.007

Ueda, K., Matsuyama, T., and Hashimoto, T. (1999). Visualization of microtubules in living cells of transgenic *Arabidopsis thaliana*. *Protoplasma* 206, 201–206. doi: 10.1007/BF01279267

Wang, X., Zhu, L., Liu, B., Wang, C., Jin, L., Zhao, Q., et al. (2007). *Arabidopsis* MICROTUBULE-ASSOCIATED PROTEIN18 functions in directional cell growth by destabilizing cortical microtubules. *Plant Cell* 19, 877–889. doi: 10.1105/tpc.106.048579

Yang, Y., Chen, B., Dang, X., Zhu, L., Rao, J., Ren, H., et al. (2019a). *Arabidopsis* IPGA1 is a microtubule-associated protein essential for cell expansion during petal morphogenesis. *J. Integr. Plant Biol.* 70, 5231–5243. doi: 10.1093/jxb/erz284

Yang, Y., Huang, W., Wu, E., Lin, C., Chen, B., and Lin, D. (2019b). Cortical microtubule organization during petal morphogenesis in *Arabidopsis*. *Int. J. Mol. Sci.* 20:4913. doi: 10.3390/ijms20194913

Zhang, X., Zhou, Y., Ding, L., Wu, Z., Liu, R., and Meyerowitz, E. M. (2013). Transcription repressor HANABA TARANU controls flower development by integrating the actions of multiple hormones, floral organ specification genes, and GATA3 family genes in *Arabidopsis*. *Plant Cell* 25, 83–101. doi: 10.1105/tpc.112.107854

Zhu, J., Bailly, A., Zwiewka, M., Sovero, V., Di Donato, M., Ge, P., et al. (2016). TWISTED DWARF1 mediates the action of auxin transport inhibitors on actin cytoskeleton dynamics. *Plant Cell* 28, 930–948. doi: 10.1105/tpc.15.00726

Zondlo, S. C., and Irish, V. F. (1999). CYP78A5 encodes a cytochrome P450 that marks the shoot apical meristem boundary in *Arabidopsis*. *Plant J.* 19, 259–268. doi: 10.1046/j.1365-313x.1999.00523.x

Conflict of Interest: The authors declare that the research was conducted in the absence of any commercial or financial relationships that could be construed as a potential conflict of interest.

frontiers in Cell and Developmental Biology

REVIEW
published: 09 February 2021
doi: 10.3389/fcell.2021.632445

Multifaceted Function of Myosin-18, an Unconventional Class of the Myosin Superfamily

Zhaohui Ouyang[1†], Shuangshuang Zhao[2,3†], Su Yao[1†], Jing Wang[4,5], Yanqin Cui[2,3], Ke Wei[1] and Yaming Jiu[2,3,4,5*]*

[1] Institute for Regenerative Medicine, Shanghai East Hospital, Shanghai Key Laboratory of Signaling and Disease Research, Frontier Science Center for Stem Cell Research, Ministry of Education of China, School of Life Sciences and Technology, Tongji University, Shanghai, China, [2] The Joint Program in Infection and Immunity, Guangzhou Women and Children's Medical Center, Guangzhou Medical University, Guangzhou, China, [3] Institut Pasteur of Shanghai, Chinese Academy of Sciences, Shanghai, China, [4] Unit of Cell Biology and Imaging Study of Pathogen Host Interaction, The Center for Microbes, Development and Health, Key Laboratory of Molecular Virology and Immunology, Institut Pasteur of Shanghai, Chinese Academy of Sciences, Shanghai, China, [5] University of Chinese Academy of Sciences, Beijing, China

OPEN ACCESS

Edited by:
Ting Gang Chew, Zhejiang University-University of Edinburgh Institute, China

Reviewed by:
Saravanan Palani, Indian Institute of Science (IISc), India
Junqi Huang, Jinan University, China

***Correspondence:**
Ke Wei
kewei@tongji.edu.cn
Yaming Jiu
ymjiu@ips.ac.cn

[†] These authors have contributed equally to this work

Specialty section:
This article was submitted to Cell Growth and Division, a section of the journal Frontiers in Cell and Developmental Biology

Received: *23 November 2020*
Accepted: *04 January 2021*
Published: *09 February 2021*

Citation:
Ouyang Z, Zhao S, Yao S, Wang J, Cui Y, Wei K and Jiu Y (2021) Multifaceted Function of Myosin-18, an Unconventional Class of the Myosin Superfamily. Front. Cell Dev. Biol. 9:632445. doi: 10.3389/fcell.2021.632445

Myosin is a diverse superfamily of motor proteins responsible for actin-based motility and contractility in eukaryotic cells. Myosin-18 family, including myosin-18A and myosin-18B, belongs to an unconventional class of myosin, which lacks ATPase motor activity, and the investigations on their functions and molecular mechanisms in vertebrate development and diseases have just been initiated in recent years. Myosin-18A is ubiquitously expressed in mammalian cells, whereas myosin-18B shows strong enrichment in striated muscles. Myosin-18 family is important for cell motility, sarcomere formation, and mechanosensing, mostly by interacting with other cytoskeletal proteins and cellular apparatus. Myosin-18A participates in several intracellular transport processes, such as Golgi trafficking, and has multiple roles in focal adhesions, stress fibers, and lamellipodia formation. Myosin-18B, on the other hand, participates in actomyosin alignment and sarcomere assembly, thus relating to cell migration and muscle contractility. Mutations of either *Myo18a* or *Myo18b* cause cardiac developmental defects in mouse, emphasizing their crucial role in muscle development and cardiac diseases. In this review, we revisit the discovery history of myosin-18s and summarize the evolving understanding of the molecular functions of myosin-18A and myosin-18B, with an emphasis on their separate yet closely related functions in cell motility and contraction. Moreover, we discuss the diseases tightly associated with myosin-18s, especially cardiovascular defects and cancer, as well as highlight the unanswered questions and potential future research perspectives on myosin-18s.

Keywords: myosin-18A, myosin-18B, biomechanics, muscle development, cancer

INTRODUCTION

Myosins are a large superfamily of proteins that are responsible for providing motility of various components in the cells and motility of cells, tissues, and organs. Following the discovery of the major motor proteins in striated muscles, namely, the class II myosins, more and more different subfamilies of myosins have been identified in animals. All myosins contain a motor domain, which in most cases is an ATPase, and can hydrolyze an ATP to create conformational changes,

underlining the motor function of the myosins. However, not all myosin motors possess the ATPase-driven motor activity, exemplified by the recently discovered myosin-18 family consisting of myosin-18A and myosin-18B. This unconventional family of myosin has been found to be associated with multiple cellular processes and implicated in a wide range of diseases, including cancer and myopathy (Taft et al., 2014).

Gene Structure and Expression of Myosin-18s

In 2000, the first member of myosin-18s, myosin-18A, was identified in bone marrow stromal cells through a differential display screen (Furusawa et al., 2000). MYO18A, the founding member of the class XVIII myosins, was initially named as MysPDZ (myosin-containing PDZ domain) (Furusawa et al., 2000) and later renamed myosin-18A because of discovery of other closely related genes. The *MYO18B* gene was annotated in 2002 (Nishioka et al., 2002) and was found to be present in vertebrates only (Salamon et al., 2003). Myosin-18A was found in a much broader range of animals, implying that myosin-18B could be derived from myosin-18A *via* a duplication event during evolution (Salamon et al., 2003).

In mouse, *MYO18A* is located on chromosome 11 and encodes for three major splice isoforms, a long myosin-18Aα, a short myosin-18Aβ, and myosin-18Aγ, which is specifically expressed in striated muscle (Horsthemke et al., 2019; **Figure 1**). Myosin-18Aα consists of 2,035-amino-acid residues (∼230 kDa), myosin-18Aβ has 1,719-amino-acid residues (∼196 kDa), and myosin-18Aγ has 2,409-amino-acid residues (267 kDa), respectively. The human *MYO18A* gene is on chromosome 17, and human myosin-18Aα comprises 2,054-amino-acid residues (∼233 kDa), and myosin-18Aβ has 1,723-amino-acid residues (∼196 kDa). Mouse *Myo18B* is located on chromosome 5 and produces myosin-18B with 2,605-amino-acid residues (∼288 kDa), whereas human *MYO18B* gene is on chromosome 22, and it encoded a 2567-amino-acid residues (∼285 kDa) myosin-18B. The alternative splicing of myosin-18B was poorly understood; it is possible that various isoforms of myosin-18B similar to myosin-18A exist.

The central region of all isoforms of myosin-18A and myosin-18B contains a motor domain, followed by a short light chain–binding domain and a coiled-coil tail domain. These are the core features of most myosins and exhibit the highest similarity with the conventional muscle myosin-2 (Taft and Latham, 2020; **Figure 1**). The fundamental function of the motor domain of classic myosins is the ATPase activity, which causes conformational changes after hydrolyzing an ATP, thus providing traction between myosin and actin filaments and ultimately movement in cells and tissues (Preller and Manstein, 2013). And the coiled-coil domain allows dimerization of myosins (Preller and Manstein, 2013). Importantly, a few key amino acid residues highly conserved in the motor domain of classic myosins are mutated in both members of myosin-18 family (Taft and Latham, 2020). Particularly, two highly conserved serine residues known for facilitating efficient catalysis of the ATPase are mutated to alanine and threonine in both myosin-18A and myosin-18B (Taft and Latham, 2020). This finding prompted researchers to examine whether myosin-18s have motor functions. This important biochemical activity is thoroughly examined in myosin-18A from *Drosophila* (Guzik-Lendrum et al., 2011), mouse (Guzik-Lendrum et al., 2013), and human (Taft et al., 2013). No ATPase activity was found in any of the isoforms of myosin-18A, while actin binding was evident in all forms (Guzik-Lendrum et al., 2011, 2013; Taft et al., 2013), suggesting myosin-18A lacks motor activity and thus is an unconventional myosin. Although such detailed biochemical characterization of myosin-18B was not available, it does have the same mutations in the core motor domain as myosin-18A (**Figure 1**), and subsequent research assumes myosin-18B also lacks motor activity (Jiu et al., 2019). Following the motor domain, both myosin-18s have a short light chain–binding domain, which binds to the essential light chain (ELC) and regulatory light chain (RLC) in conventional class II muscle myosins (Preller and Manstein, 2013). The light chain–binding domain of all isoforms of myosin-18A and myosin-18B has two IQ motifs, which are known for interacting with calmodulin (CaM) or CaM-like light chains (Odronitz and Kollmar, 2007). Direct interaction of myosin-18A with ELC and RLC was experimentally confirmed (Guzik-Lendrum et al., 2013), whereas myosin-18B is expected to be capable of similar interactions due to sequence similarity. The coiled-coil domain is important for dimerization and incorporation into non-muscle myosin 2 (NM2) filaments. Both myosin-18A and myosin-18B do exhibit such activities (Ajima et al., 2008; Billington et al., 2015; Jiu et al., 2019), which is not different from conventional myosins. Flanking the generic motor domain and coiled-coil domain of myosin-18A and myosin-18B are long N-terminal and C-terminal domains, which are distinctive features of myosin-18 family proteins. The N-terminal domain of myosin-18Aα contains a KE motif rich in lysine and glutamate residues, as well as a PDZ domain, which was the reason myosin-18A was initially named as MysPDZ for "myosin-containing PDZ domain" (Furusawa et al., 2000). While myosin-18Aβ lacks an N-terminal domain, myosin-18Aγ has a long N-terminal domain with a unique sequence of unknown function except a short polyproline II (PPII) helix (Horsthemke et al., 2019; **Figure 1**). Myosin-18B also has large N-terminal and C-terminal domains. These domains are less studied, and they exhibit little similarity to known sequences, except a putative nuclear localization sequence (NLS) in its C-terminal domain (Salamon et al., 2003).

Myosin-18Aα is ubiquitously expressed in all tissues, and the shorter myosin-18Aβ is detected in hematopoietic cells (Mori et al., 2003), whereas the longer myosin-18Aγ has been found to be enriched in striated muscles (Horsthemke et al., 2019). Unlike the myosin-18Aα or myosin-18Aβ, the expression pattern of myosin-18B resembles that of myosin-18Aγ, which is highly enriched in cardiac and

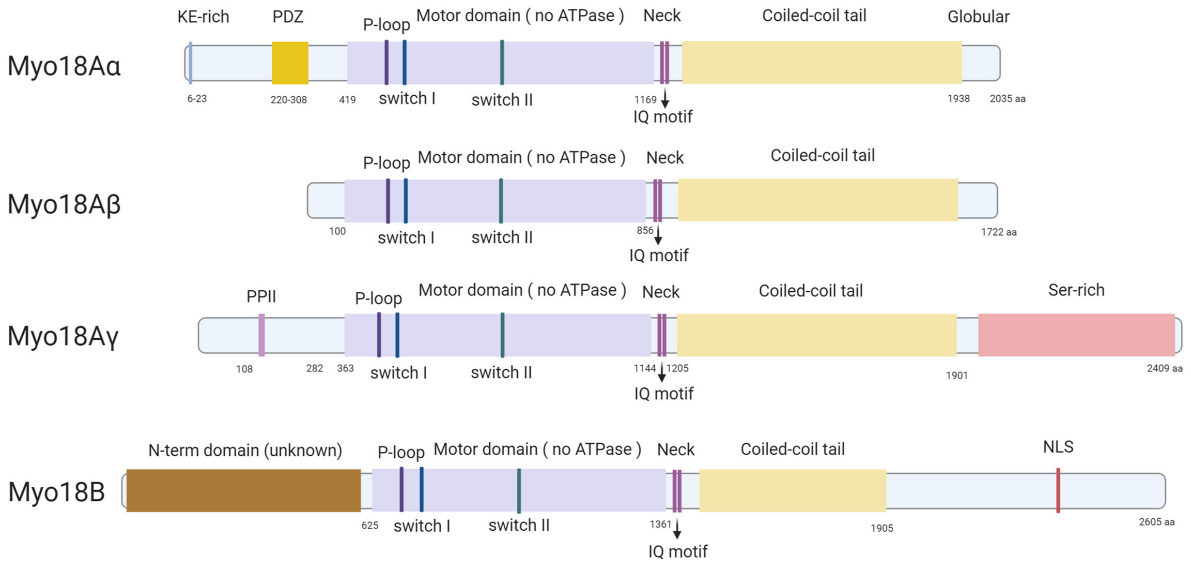

FIGURE 1 | Protein structures of all known isoforms of myosin-18A and myosin-18B. All known isoforms of myosin-18A and myosin-18B contain a central motor domain and a coiled-coil tail domain linked by a short neck domain with two IQ motifs, whereas different isoforms are different in their distinct N-terminal and C-terminal extensions. Myosin-18Aα has a KE-rich region and a PDZ domain in its N-terminal extension, and myosin-18Aγ contains a proline-rich PPII domain in the N-terminal and a long serine-rich C-terminal. Myosin-18B has both long N- and C-terminals, and an NLS domain in the C-terminal extension is the only domain with a predicted function.

skeletal muscles and is detected at low level in other tissues (Salamon et al., 2003).

Biochemical and Cellular Functions of Myosin-18s

Myosin-18A

Like many other myosins, myosin-18A can bind to actin and plays important roles in different actin structures (Taft and Latham, 2020). In 2005, Isogawa and colleagues used GFP-tagged fragments of human myosin-18A to test their actin-binding activity, and it was found that the N-terminal domain has a strong interaction with actin, which does not involve ATPase activity (Isogawa et al., 2005). Mori and colleagues reached similar conclusions at the same year with coimmunoprecipitation analysis showing that myosin-18A can self-associate through its coiled-coil domain and interact with actin under the mediation of the KE-rich domain (Mori et al., 2005). Later studies showed that both N-terminal and the motor domain of myosin-18A possess actin-binding activity (Guzik-Lendrum et al., 2013; Taft et al., 2013). However, because of its lack of motor activity, the molecular and cellular function of the interaction between myosin-18A and actin could not be the conventional actomyosin contraction, thus attracting attention of researchers on its specific roles on cytoskeleton. In a search for regulators of actomyosin retrograde flow essential for cell motility, Tan and colleagues found that myosin-18A interacted with Rac/Cdc42-binding kinase MRCK, a Rho GTPase effector kinase crucial for actomyosin retrograde flow (Tan et al., 2008). This interaction was found to be facilitated by the adaptor protein LRAP35a, and the tripartite complex formed by MRCK/myosin-18A/LRAP35a was responsible for the assembly of lamellar actomyosin bundles and of a subnuclear actomyosin network (Tan et al., 2008; **Figure 2**). The association between myosin-18A and lamellipodia and lamella was further demonstrated by the interaction between myosin-18A and PAK2/βPIX/GIT1 (p21-activated kinase2/PAK-interacting exchange factor-β/G protein–coupled receptor kinase interactor-1) complex, which is localized at lamellipodia and membrane ruffles (Hsu et al., 2010, 2014; **Figure 2**). Both MRCK and PAK2 are downstream effectors of small GTPase; however, the role of small GTPases in regulating the myosin-18A/PAK2/βPIX/GIT1 complex formation and function is still a puzzle. Furthermore, myosin-18A can coassemble with NM2 filaments and regulate the assembly of actomyosin bundles and stress fibers (Billington et al., 2015). Knocking down myosin-18A in prostate cancer cells increased circumferential NM2-associated actin filament arrays in the lamella (Makowska et al., 2015), different from phenotypes of knockdown of other myosins, suggesting its role in actomyosin is different from other myosins.

As mentioned above, myosin-18A can bind to F-actin, and it was found that this interaction can be further enhanced by binding of GOLPH3, a phosphoprotein of the Golgi membrane (Taft et al., 2013; **Figure 2**). GOLPH3 is known for its Golgi localization through interaction with phosphatidylinositol-4-phosphate (PI4P), a phospholipid enriched in Golgi membranes (Dippold et al., 2009). Moreover, in search for binding partners of GOLPH3, myosin-18A was identified to be interacting with GOLPH3 with its N-terminal extension and motor domains (Dippold et al., 2009). Recently, Rahajeng et al. (2019) demonstrate that GOLPH3 can drive PI4P-dependent membrane curvature of the Golgi. In this study, overexpression of amino-terminally tagged GOLPH3 unable to interact with myosin-18A

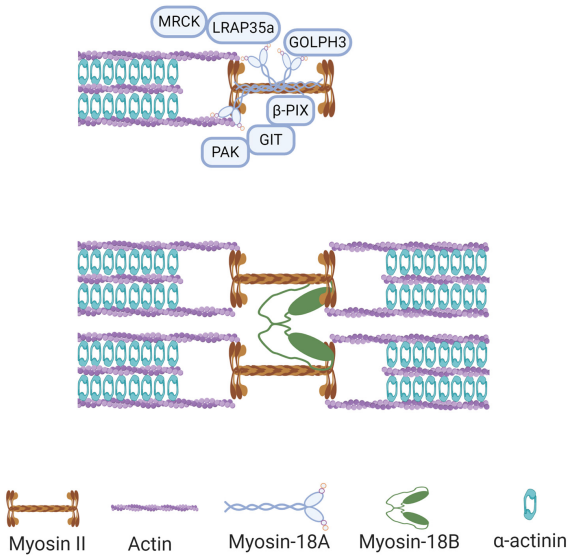

FIGURE 2 | Functions of myosin-18s in non-muscle cells. Myosin-18A binds to actin filaments and bundled with myosin II in non-muscle cells, and it can interact with multiple proteins in this context, including MRCK, GOLPH3, and PAK2/βPIX/GIT1 complex. Myosin-18B assembles with myosin II filaments and facilitates fusion of adjacent myosin stacks during actomyosin bundle maturation.

results in both excessive tubulation of the Golgi and ineffective trafficking (Rahajeng et al., 2019). In addition, knockdown of myosin-18A showed similar phenotype, suggesting both GOLPH3-induced Golgi membrane curvature and recruiting of myosin-18A are required for forward trafficking from the Golgi to the plasma membrane (Rahajeng et al., 2019).

Except for being a GOLPH3 binding partner, myosin-18A was also identified as a receptor for lung surfactant protein A (SP-A). Yang et al. demonstrated that myosin-18A physically interacts with SP-A and proposed that a cryptic transmembrane domain in myosin-18A is responsible for the extracellular localization of its motor and C-terminal domains (Yang et al., 2005). Additionally, the interaction between myosin-18A and SP-A was also found to be important for macrophage activation (Yang et al., 2015). Besides, CD245, a highly conserved motor enzyme reported as a receptor for SP-A, has also been identified as myosin-18A (De Masson et al., 2016). Certainly, these studies shed light on the new feature of myosin-18A function. However, the obvious question raised is that how a protein that is generally observed to be cytosolic without transmembrane domain in most studies (9, 10) could act as a receptor for molecules found in the extracellular space. To understand this intriguing role of myosin-18A, additional studies will be needed.

Myosin-18B

Although myosin-18B is highly enriched in striated muscle cells, it is also present in non-muscle cells at low levels (Salamon et al., 2003). In the initial characterization, myosin-18B protein was found to have a special expression pattern during muscle differentiation: it is totally cytoplasmic in undifferentiated myoblast cells, but a fraction of this protein will translocate into the nucleus in differentiated muscle cells (Salamon et al., 2003). In addition, myosin-18B was found to be located on the Z-lines of striated muscle myofibrils, despite that conventional myosin is located in the A-bands and acts as a molecular motor for muscle contraction (Salamon et al., 2003; Ajima et al., 2008). However, recent studies have observed a different, if not totally opposite, localization of myosin-18B in muscular sarcomere, which appears to be localized to the A-bands, similar to the conventional myosins (Berger et al., 2017; Latham et al., 2020). Moreover, its localization during human embryonic stem cells (hESCs) to cardiomyocytes was also found to be opposite to the initial finding, which showed they localize in the nucleus of hESCs and become sarcomeric during cardiomyocyte differentiation (Latham et al., 2020). These obvious discrepancies may be due to different methods of detection, as multiple antibodies and GFP labels were used to examine the expression of myosin-18B, and some of these methods may not accurately reflect the endogenous expression pattern of myosin-18B. In non-muscle cells, myosin-18B has been reported to be expressed in punctate pattern throughout the cytoplasm, in membrane protrusions, and within stress fibers (Inoue et al., 2006; Ajima et al., 2008; Jiu et al., 2019).

Although the cellular localization of myosin-18B is not clear, some of its cellular functions have recently been discovered. In non-muscle cells, myosin-18B was found to promote the assembly of myosin II stacks, which are important for a variety of vital processes in cells (Jiu et al., 2019). Specifically, myosin-18B assembles with NM2 filaments and facilitates fusion of adjacent myosin stacks, which in turn promotes actomyosin bundle maturation (Jiu et al., 2019; **Figure 2**). In addition, *MYO18B* gene knockout cells display thin stress fibers, which can be rescued by AMPK activation, whereas myosin-18B overexpression leads to strong actin network, which can be abolished by CaMKK2 inhibition (Zhao et al., 2020), suggesting myosin-18B plays an important role in the actin stress fibers of the mechanically sensitive CaMKK2-AMPK-VASP signaling cascade (Zhao et al., 2020). In striated muscle cells, recent studies found that myosin-18B is an essential sarcomeric accessory protein, which can bind actin thin filaments in the forming sarcomere and be incorporated in the thick filaments, coinciding with striation onset of cardiomyocyte differentiation (Latham et al., 2020). Therefore, it was suggested that myosin-18B regulates higher-order organization of the cardiac sarcomere from within the thick filament (Latham et al., 2020).

Myosin-18s in Muscle Development and Physiology

Because of the enriched expression of myosin-18B in cardiac and skeletal muscle, its role in striated muscle cells has been of particular interest to researchers. Its expression was found to be elevated during differentiation of C2C12 myoblast to myotubes (Salamon et al., 2003), and robust expression of myosin-18B was also observed as early as E9.5 mouse heart and E13.5 skeletal muscle precursors (Ajima et al., 2008), suggesting it has an important role in muscle development. Indeed, *MYO18B*

gene knockout mice showed early embryonic lethality at E10.5 with severe cardiac defects (Ajima et al., 2008), suggesting cardiomyocyte development and function require myosin-18B. Electron microscopy analysis uncovered disrupted sarcomere structure in *MYO18B* knockout cardiomyocytes with defective alignment of thick and thin myofibril filaments (Ajima et al., 2008), indicating that myosin-18B functions in the process of myofibril organization. Two independent *MYO18B* mutants in zebrafish revealed additional role of myosin-18B in skeletal muscle integrity (Berger et al., 2017; Gurung et al., 2017). Zebrafish development can proceed to some extent without proper heart function, allowing examination of skeletal muscle defect of zebrafish *MYO18B* mutants with cardiac defects similar to the mouse mutant (Gurung et al., 2017). It was evident that sarcomeres of skeletal muscle were disorganized, and force could not be generated from the fast-twitch muscles of *MYO18B* mutant zebrafish (Berger et al., 2017; Gurung et al., 2017). Two independent findings of *MYO18B* mutations linked in human myopathies further confirmed the conserved function of myosin-18B in striated muscle development (Alazami et al., 2015; Malfatti et al., 2015). A homozygous missense mutation (c.6496G > T, p.Glu2166*), which produced a truncated myosin-18B missing parts of the C-terminal domain, was found in patients with nemaline myopathy (Malfatti et al., 2015), characterized by dysmorphism, clinodactyly, hypotonia, muscle weakness, and cardiomyopathy. Another homozygous mutation (c.6905C > A) was identified in two patients with Klippel–Feil anomaly, presenting myopathy and distinct facial features (Alazami et al., 2015). This mutation results in a premature stop codon and induces nonsense-mediated decay of the mutant *MYO18B* mRNA, leading to a null phenotype. Interestingly, similar to the sarcomere defects in mouse and zebrafish *MYO18B* mutants, a failed assembly of mature sarcomere in striated muscles is found in all these patients, confirming myosin-18B functions in sarcomere assembly across different species. In addition, research associating *MYO18B* mutation with infant death accompanied by muscular defect was also reported recently (Armes et al., 2018). Possibly, the underlying mechanism is similar to the other reports, that myosin-18B is required for muscle development and function.

Altogether, these similar loss-of-function phenotypes of myosin-18B in different organisms highlight the importance of myosin-18B in sarcomere assembly and striated muscle development. However, the phenotypic description did not provide sufficient evidence illuminating how myosin-18B regulates sarcomere assembly, given that it does not possess a motor activity, which is crucial to sarcomere function. It is possible that myosin-18B serves as a structural glue that ties newly synthesized actomyosin bundles into well-organized sarcomeric structures, similar to its function in facilitating stress fiber assembly in non-muscle cells (Jiu et al., 2019). A recent study in the differentiation from hESCs to cardiomyocytes revealed that myosin-18B binds actin thin filaments and is incorporated in the thick filaments during the onset of striation (Latham et al., 2020; **Figure 3**). Loss-of-function studies are warranted to further illuminate the function of human myosin-18B in cardiomyocytes.

Myosin-18A was thought to be absent in the muscle; thus, its involvement in striated muscle was revealed later than myosin-18B. In 2013, Bonn and colleagues found the sole myosin-18 in *Drosophila* is localized to the fusion pore between fusing myoblasts and around the Z-line of mature muscle cells (Bonn et al., 2013). However, the deficiency of myosin-18 did not affect muscle development because of possible compensation of other myosins (Bonn et al., 2013). Because it is the only myosin-18 in *Drosophila*, this observation did not provide a clear clue whether myosin-18A is functioning in muscle in vertebrates. There were two consecutive studies in zebrafish that revealed the role of myosin-18A in striated muscle development and function (Cao et al., 2014, 2016). Two myosin-18A genes *MYO18A*α and *MYO18A*β exist in zebrafish, and both of them were expressed in somites during muscle development, and knockdown of *MYO18A*, as well as overexpression of the PDZ domain disrupted myofiber integrity (Cao et al., 2014). Subsequently, a few binding partners of myosin-18A in zebrafish was identified, including p190Rho-guanine nucleotide exchange factor (p190RhoGEF) and Golgin45, and their interaction was suggested to be required for extracellular matrix adhesion, Golgi apparatus formation, F-actin bundle organization, and eventually muscle integrity (Cao et al., 2016). A recently study in mouse confirmed that myosin-18A is essential for cardiac development and sarcomere organization (Horsthemke et al., 2019), as global knockout and cardiomyocyte-specific conditional knockout of *MYO18A* cause early embryonic lethality due to cardiac defect accompanied with sarcomere disruption in cardiomyocytes (Horsthemke et al., 2019). It also revealed that there is actually a cardiomyocyte-specific isoform of myosin-18A, myosin-18Aγ, which plays a key role in cardiac development (Horsthemke et al., 2019). Characterization of myosin-18Aγ showed that it has a long N-terminal domain containing a short PPII helix (**Figure 1**) and is localized within the A-band of sarcomeres (Horsthemke et al., 2019; **Figure 3**). However, the molecular function of myosin-18Aγ is largely unknown (**Figure 3**).

Knockout of either *MYO18A* and *MYO18B* in mouse led to embryonic lethality around E13.5 with similar sarcomere defects in cardiomyocytes, suggesting that they both may have essential role in sarcomere assembly with little overlapping functions or compensation. Currently, plenty *in vivo* evidence suggested that myosin-18s are important in cytoskeletal development of cardiomyocytes (Ajima et al., 2008; Berger et al., 2017; Gurung et al., 2017; Horsthemke et al., 2019), mainly through phenotypical description of loss-of-function mutants. However, *in vitro* or cellular functional studies are largely missing in cardiac or striated muscles, with the subcellular localizations of myosin-18s remaining unclear (Salamon et al., 2003; Latham et al., 2020). Therefore, extensive study on the molecular mechanisms of myosin-18s in sarcomere formation and maintenance is guaranteed.

Myosin-18s in Cancer and Other Diseases

Both myosin-18A and myosin-18B have been implicated in cancers (Taft and Latham, 2020). Interestingly, apart from

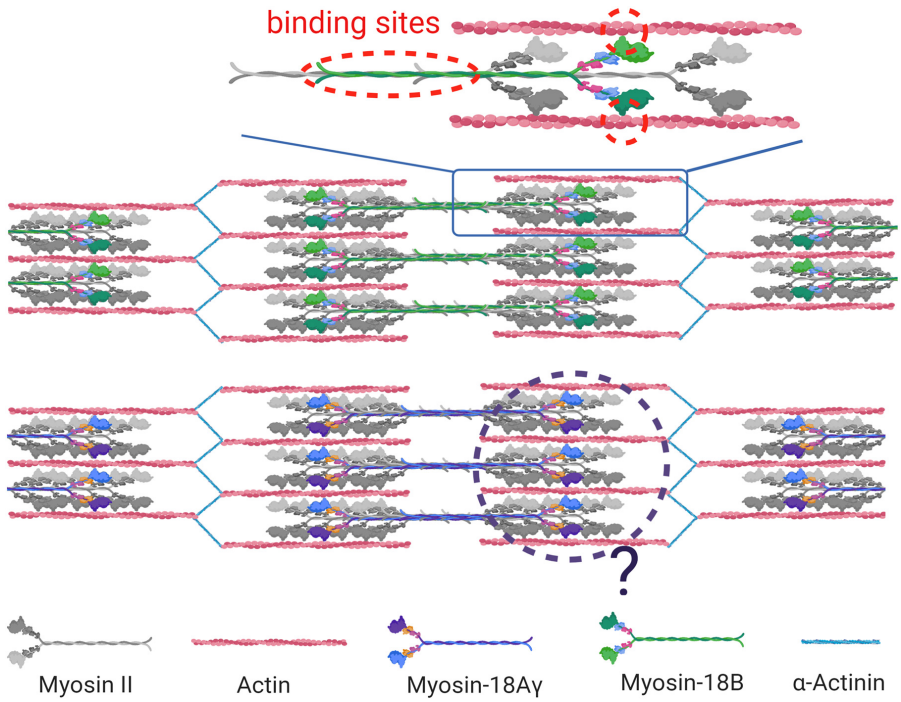

FIGURE 3 | Function of myosin-18s in striated muscle cells. Myosin-18B and myosin-18 Aγ are localized in the sarcomere in striated muscle cells. Myosin-18B binds actin thin filaments and is incorporated in the thick myosin filaments *via* its coiled-coiled domain in sarcomeres of cardiomyocytes (molecular binding highlighted in red dotted circle). Whether mψοσιν-18Aγ possesses a similar function is yet to be discovered (black dotted circle).

gene fusion and translocation events that link myosin-18s with cancer, their expression levels seem to be positively or negatively associated with different types of cancers, suggesting that their roles in cancer is also context dependent.

The first line of evidence showing the involvement of myosin-18s in cancer came from a report that *MYO18B* was found to be frequently deleted, mutated, and hypermethylated in lung cancers (Nishioka et al., 2002). And overexpression of *MYO18B* suppressed proliferation and anchorage-independent growth of lung cancer cells (Nishioka et al., 2002), suggesting myosin-18B serves as a tumor suppressor. Mutations or silenced expression of *MYO18B* was subsequently found in ovarian cancers (Yanaihara et al., 2004), colorectal cancers (Nakano et al., 2005), melanoma and pancreatic ductal adenocarcinoma (Bleeker et al., 2009), and neuroendocrine cancer (Bhatla et al., 2016). And in line with the initial discovery that *MYO18B* is silenced by hypermethylation of its promoter in lung cancers (Nishioka et al., 2002), hypermethylation of *MYO18B* promoter was found to be associated with weaker response to chemotherapies in ovarian cancers (Tomar et al., 2017), whereas hypomethylation of its promoter is associated with high *MYO18B* expression and favorable outcomes of T-cell acute leukemia cases (Haider et al., 2019). Although most studies on *MYO18B* in cancer support its role as a tumor suppressor, one report in hepatocellular carcinoma found that high *MYO18B* expression was associated with worse survival of this type of cancer, and knocking down *MYO18B* reduced proliferation and migration (Zhang et al., 2018).

Unlike the findings in *MYO18B*, *MYO18A* was mostly associated with cancers through gene fusion events, with *MYO18A* frequently found to be fused with other oncogenes such as FGFR1 (Walz et al., 2005), PDGFRB (Walz et al., 2009), and MLL (Ussowicz et al., 2012). In terms of its own function in cancer, it has been found that myosin-18A expression was increased in prostate cancer cells (Makowska et al., 2015), and its knockdown reorganized long NM2A-rich stress fibers and affected the cells' ability to migrate (Makowska et al., 2015), suggesting a role of myosin-18A in prostate cancer metastasis (Peckham, 2016).

Other than myopathies and cancer, myosin-18s have also been implicated in other diseases. Myosin-18A was found to be localized to plasma membrane in human fibroblasts and translocate to viral assembly complex after human cytomegalovirus (HCMV) infection and plays a role in virus production (Jean Beltran et al., 2016). It was proposed that myosin-18A facilitates connections between vesicles loaded with virus and myosin filament containing NM2-binding domains (Billington et al., 2015), thus regulating the movement of the virus-loaded vesicles (Jean Beltran et al., 2016). In line with this study, myosin-18A was found to be required for the hepatitis C virus secretion (Bishe et al., 2012), possibly through regulating Golgi budding process *via* interaction with GOLPH3 (Dippold et al., 2009; Bishe et al., 2012). Myosin-18B was reported

to be associated with schizophrenia (Takata et al., 2013) and mathematical ability (Ludwig et al., 2013), as single-nucleotide polymorphisms in myosin-18B were found to be linked to depth of intraparietal sulcus in the brain, which is responsible for mathematical abilities (Ludwig et al., 2013). However, the latter association was not supported by subsequent studies (Pettigrew et al., 2015).

CONCLUSION AND PERSPECTIVES

At the beginning of the 21st century, myosin-18A and myosin-18B were identified respectively, which together form the myosin-18 family. Unlike the conventional myosin family, myosin-18s lacks active ATPase-driven motor activity and is characterized by the presence of large N- and C-terminal extensions flanking a generic myosin core structure (**Figure 1**).

Myosin-18A plays multiple roles in different actin structures, including focal adhesions, actin stress fibers, lamellar actomyosin bundles, and Golgi apparatus (**Figure 2**). However, which splice isoform of myosin-18A localizes to Golgi or plays a role in Golgi morphology remains unknown. A recent study observed neither the colocalization nor any impact of reduced myosin-18Aα levels on Golgi morphology by immunofluorescence assay (Bruun et al., 2017). It was considered an unknown splice variant of myosin-18A, which may take part in this function, and further studies are needed to verify the speculation.

At present, three myosin-18A splice isoforms have been identified, namely, myosin-18Aα, myosin-18Aβ, and myosin-18Aγ (Horsthemke et al., 2019). Myosin-18Aα contains two distinct functional regions: a KE motif and a PDZ domain in its N-terminal extension, whereas myosin-18Aγ has a single PPII helix in its N-terminal extension (**Figure 1**). Myosin-18Aβ completely lacks these domains with a short N-terminal extension (**Figure 1**). Several studies showed a strong ATP-independent interaction of myosin-18A N-terminal extension with actin (Isogawa et al., 2005; Mori et al., 2005; Billington et al., 2015). But the precise structural and functional properties of the N-terminus, for example, the role of PPII, remain to be resolved. As for C-terminal extension, it is the least characterized domain of myosin-18A. So far, the Rho GTPase activator βPIX (PAK-interacting exchange factor-β) is the only one that was identified as a direct binding partner of the C-terminal domain (Hsu et al., 2010). Besides the common functions as a myosin family member, myosin-18A has a unique feature of binding to SPA at the cell surface, as SPA-receptor 210 (Yang et al., 2005). But myosin-18A has no predicted transmembrane domains. How is myosin18A transported to the cell membrane? Does the PDZ domain, which mediates membrane association, participate in this function? Further research may shed light on this unique role of myosin-18A.

The second XVIII myosin family member, myosin-18B, expresses highly in cardiac and skeletal striated muscles and is also widely distributed at a low level in organs and tissues. Except for the generic myosin configuration, myosin-18B comprises several unique domains, such as ERM domain in the tail region and a putative NLS in the C-term extension (Salamon et al., 2003; **Figure 1**). And the functional capabilities of these proposed domains remain to be assessed. Recently, several researches on the cellular localization and biochemical function of myosin-18B shed light on the understanding of this unique protein. Jiu et al. observed that myosin-18B plays as a "glue" molecule for assembling myosin II stacks and promotes the maturation of contractile actomyosin bundles (Jiu et al., 2019; **Figure 2**). Moreover, a follow-up study found myosin-18B also plays a critical role in the mechanosensitive regulation *via* CaMKK2-AMPK-VASP pathway (Zhao et al., 2020). Another controversial aspect of myosin-18B is its localization in striated muscle cells. While most conventional myosins are localized to the A-bands, myosin-18B was reported to be localized to the Z-lines (Salamon et al., 2003; Ajima et al., 2008), as well as A-bands (Berger et al., 2017; Latham et al., 2020), of striated muscle myofibrils. More precise and well-defined methods will be needed to explain the differences and confirm the localization of myosin-18B in sarcomere, which is critical to its function in muscle cells.

Myosin-18A and myosin-18B share ∼40% identity at the protein level and display unique roles at specific subcellular localities. The common localization myosin-18A and myosin-18B, such as stress fibers in non-muscle cells and sarcomeric structures in striated muscle, raises the question of whether they have distinct or overlapping functions within these shared sites. Both *MYO18A* and *MYO18B* knockout mice have sarcomere defects in cardiomyocytes and early embryonic lethality (Ajima et al., 2008; Horsthemke et al., 2019), suggesting that they have essential role in cardiac sarcomere assembly, whereas only MYO18B has been indicated in human congenital cardiac defects (Alazami et al., 2015; Malfatti et al., 2015). The detailed molecular function of myosin-18s in sarcomeres and whether they have distinct functions in cardiomyocytes require further research.

In terms of disease, both myosin-18A and myosin-18B have predominantly been investigated in cancers, including lung, prostate, and ovarian cancers (Nishioka et al., 2002; Yanaihara et al., 2004; Nakano et al., 2005; Walz et al., 2005, 2009; Bleeker et al., 2009; Ussowicz et al., 2012; Bhatla et al., 2016; Tomar et al., 2017; Zhang et al., 2018; Haider et al., 2019). Myosin-18A also participates in HCMV infection (Jean Beltran et al., 2016) and hepatitis C virus (HCV) secretion (Bishe et al., 2012). However, the molecular mechanisms of myosin-18A's involvement in cancer and virus transport are still not known. Moreover, *MYO18B* gene, identified as a tumor suppressor, recently was reported as a tumor promoter in hepatocellular carcinoma progression (Zhang et al., 2018).

From all above, although functions of myosin-18 family at the molecular and cellular level have been greatly resolved during the recent 20 years, it is not hard to see that there is still a long way to go before completely unraveling the mysteries of members of this new branch within the myosin family.

AUTHOR CONTRIBUTIONS

YJ and KW initiated and made the outline of the manuscript. ZO, SZ, and YS drafted the manuscript with contributions from all other authors.

FUNDING

This work was supported by CAS-VPST Silk Road Science Fund 2021 (GJHZ2021138), Key Research and Development Program, Ministry of Science and Technology of China (2017YFA0105601 and 2018YFA0800104), National Natural Science Foundation of China (92054104, 31970660, 31771613, and 32070823), Fundamental Research Funds for the Central Universities (22120200411), National Key Research and Development Program (2019YF1200103), Shanghai Municipal Science and Technology Major Project (2019SHZDZX02), Natural Science Foundation of Shanghai (19ZR1463000), Chemical Reagent & Instrumental Development Foundation of Shanghai (1914200700), and Key Laboratory of Molecular Virology & Immunology, Institut Pasteur of Shanghai (KLMVI-OP-202001).

ACKNOWLEDGMENTS

The authors thank the Peak Disciplines (Type IV) of Institutions of Higher Learning in Shanghai, and the Frontier Science Research Center for Stem Cells, Ministry of Education for their support. The proteins in **Figures 2** and **3** were created with BioRender.com.

REFERENCES

Ajima, R., Akazawa, H., Kodama, M., Takeshita, F., Otsuka, A., Kohno, T., et al. (2008). Deficiency of Myo18B in mice results in embryonic lethality with cardiac myofibrillar aberrations. *Genes Cells* 13, 987–999.

Alazami, A. M., Kentab, A. Y., Faqeih, E., Mohamed, J. Y., Alkhalidi, H., Hijazi, H., et al. (2015). A novel syndrome of Klippel-Feil anomaly, myopathy, and characteristic facies is linked to a null mutation in MYO18B. *J. Med. Genet.* 52, 400–404.

Armes, J. E., Williams, M., Price, G., Wallis, T., Gallagher, R., Matsika, A., et al. (2018). Application of whole genome sequencing technology in the investigation of genetic causes of fetal, perinatal, and early infant death. *Pediatr. Dev. Pathol.* 21, 54–67.

Berger, J., Berger, S., Li, M., and Currie, P. D. (2017). Myo18b is essential for sarcomere assembly in fast skeletal muscle. *Hum. Mol. Genet.* 26, 1146–1156.

Bhatla, T., Dandekar, S., Lu, B. Y., Wang, J., Han, E., Bitterman, D., et al. (2016). Genomic Characterization Of Poorly Differentiated Neuroendocrine Carcinoma In A Pediatric Patient. *J. Pediatr. Hematol. Oncol.* 38, e21–e25.

Billington, N., Beach, J. R., Heissler, S. M., Remmert, K., Guzik-Lendrum, S., Nagy, A., et al. (2015). Myosin 18A coassembles with nonmuscle myosin 2 to form mixed bipolar filaments. *Curr. Biol.* 25, 942–948.

Bishe, B., Syed, G. H., Field, S. J., and Siddiqui, A. (2012). Role of phosphatidylinositol 4-phosphate (PI4P) and its binding protein GOLPH3 in hepatitis C virus secretion. *J. Biol. Chem.* 287, 27637–27647.

Bleeker, F. E., Lamba, S., Rodolfo, M., Scarpa, A., Leenstra, S., Vandertop, W. P., et al. (2009). Mutational profiling of cancer candidate genes in glioblastoma, melanoma and pancreatic carcinoma reveals a snapshot of their genomic landscapes. *Hum. Mutat.* 30, E451–E459.

Bonn, B. R., Rudolf, A., Hornbruch-Freitag, C., Daum, G., Kuckwa, J., Kastl, L., et al. (2013). Myosin heavy chain-like localizes at cell contact sites during *Drosophila* myoblast fusion and interacts in vitro with Rolling pebbles 7. *Exp. Cell Res.* 319, 402–416.

Bruun, K., Beach, J. R., Heissler, S. M., Remmert, K., Sellers, J. R., and Hammer, J. A. (2017). Re-evaluating the roles of myosin 18Aalpha and F-actin in determining Golgi morphology. *Cytoskeleton (Hoboken)* 74, 205–218.

Cao, J., Li, S., Shao, M., Cheng, X., Xu, Z., and Shi, D. (2014). The PDZ-containing unconventional myosin XVIIIA regulates embryonic muscle integrity in zebrafish. *J. Genet. Genom.* 41, 417–428.

Cao, J. M., Cheng, X. N., Li, S. Q., Heller, S., Xu, Z. G., and Shi, D. L. (2016). Identification of novel MYO18A interaction partners required for myoblast adhesion and muscle integrity. *Sci. Rep.* 6:36768.

De Masson, A., Giustiniani, J., Marie-Cardine, A., Bouaziz, J. D., Dulphy, N., Gossot, D., et al. (2016). Identification of CD245 as myosin 18A, a receptor for surfactant A: a novel pathway for activating human NK lymphocytes. *Oncoimmunology* 5:e1127493.

Dippold, H. C., Ng, M. M., Farber-Katz, S. E., Lee, S. K., Kerr, M. L., Peterman, M. C., et al. (2009). GOLPH3 bridges phosphatidylinositol-4- phosphate and actomyosin to stretch and shape the Golgi to promote budding. *Cell* 139, 337–351.

Furusawa, T., Ikawa, S., Yanai, N., and Obinata, M. (2000). Isolation of a novel PDZ-containing myosin from hematopoietic supportive bone marrow stromal cell lines. *Biochem. Biophys. Res. Commun.* 270, 67–75.

Gurung, R., Ono, Y., Baxendale, S., Lee, S. L., Moore, S., Calvert, M., et al. (2017). A zebrafish model for a human myopathy associated with mutation of the unconventional myosin MYO18B. *Genetics* 205, 725–735.

Guzik-Lendrum, S., Heissler, S. M., Billington, N., Takagi, Y., Yang, Y., Knight, P. J., et al. (2013). Mammalian myosin-18A, a highly divergent myosin. *J. Biol. Chem.* 288, 9532–9548.

Guzik-Lendrum, S., Nagy, A., Takagi, Y., Houdusse, A., and Sellers, J. R. (2011). Drosophila melanogaster myosin-18 represents a highly divergent motor with actin tethering properties. *J. Biol. Chem.* 286, 21755–21766.

Haider, Z., Larsson, P., Landfors, M., Kohn, L., Schmiegelow, K., Flaegstad, T., et al. (2019). An integrated transcriptome analysis in T-cell acute lymphoblastic leukemia links DNA methylation subgroups to dysregulated TAL1 and ANTP homeobox gene expression. *Cancer Med.* 8, 311–324.

Horsthemke, M., Nutter, L. M. J., Bachg, A. C., Skryabin, B. V., Honnert, U., Zobel, T., et al. (2019). A novel isoform of myosin 18A (Myo18Agamma) is an essential sarcomeric protein in mouse heart. *J. Biol. Chem.* 294, 7202–7218.

Hsu, R. M., Hsieh, Y. J., Yang, T. H., Chiang, Y. C., Kan, C. Y., Lin, Y. T., et al. (2014). Binding of the extreme carboxyl-terminus of PAK-interacting exchange factor beta (betaPIX) to myosin 18A (MYO18A) is required for epithelial cell migration. *Biochim. Biophys. Acta* 1843, 2513–2527.

Hsu, R. M., Tsai, M. H., Hsieh, Y. J., Lyu, P. C., and Yu, J. S. (2010). Identification of MYO18A as a novel interacting partner of the PAK2/betaPIX/GIT1 complex and its potential function in modulating epithelial cell migration. *Mol. Biol. Cell* 21, 287–301.

Inoue, T., Kon, T., Ajima, R., Ohkura, R., Tani, M., Yokota, J., et al. (2006). MYO18B interacts with the proteasomal subunit Sug1 and is degraded by the ubiquitin-proteasome pathway. *Biochem. Biophys. Res. Commun.* 342, 829–834.

Isogawa, Y., Kon, T., Inoue, T., Ohkura, R., Yamakawa, H., Ohara, O., et al. (2005). The N-terminal domain of MYO18A has an ATP-insensitive actin-binding site. *Biochemistry* 44, 6190–6196.

Jean Beltran, P. M., Mathias, R. A., and Cristea, I. M. (2016). A portrait of the human organelle proteome in space and time during cytomegalovirus infection. *Cell Syst.* 3:e366.

Jiu, Y., Kumari, R., Fenix, A. M., Schaible, N., Liu, X., Varjosalo, M., et al. (2019). Myosin-18B promotes the assembly of myosin ii stacks for maturation of contractile actomyosin bundles. *Curr. Biol.* 29:e85.

Latham, S. L., Weiss, N., Schwanke, K., Thiel, C., Croucher, D. R., Zweigerdt, R., et al. (2020). Myosin-18B regulates higher-order organization of the cardiac sarcomere through thin filament cross-linking and thick filament dynamics. *Cell Rep.* 32:108090.

Ludwig, K. U., Samann, P., Alexander, M., Becker, J., Bruder, J., Moll, K., et al. (2013). A common variant in myosin-18B contributes to mathematical abilities in children with dyslexia and intraparietal sulcus variability in adults. *Transl. Psychiatry* 3:e229.

Makowska, K. A., Hughes, R. E., White, K. J., Wells, C. M., and Peckham, M. (2015). Specific myosins control actin organization. cell morphology, and migration in prostate cancer cells. *Cell Rep.* 13, 2118–2125.

Malfatti, E., Bohm, J., Lacene, E., Beuvin, M., Romero, N. B., and Laporte, J. (2015). A premature stop codon in MYO18B is associated with severe nemaline myopathy with cardiomyopathy. *J. Neuromuscul. Dis.* 2, 219–227.

Mori, K., Furusawa, T., Okubo, T., Inoue, T., Ikawa, S., Yanai, N., et al. (2003). Genome structure and differential expression of two isoforms of a novel PDZ-containing myosin (MysPDZ) (Myo18A). *J. Biochem.* 133, 405–413.

Mori, K., Matsuda, K., Furusawa, T., Kawata, M., Inoue, T., and Obinata, M. (2005). Subcellular localization and dynamics of MysPDZ (Myo18A) in live mammalian cells. *Biochem. Biophys. Res. Commun.* 326, 491–498.

Nakano, T., Tani, M., Nishioka, M., Kohno, T., Otsuka, A., Ohwada, S., et al. (2005). Genetic and epigenetic alterations of the candidate tumor-suppressor gene MYO18B, on chromosome arm 22q, in colorectal cancer. *Genes Chromosomes Cancer* 43, 162–171.

Nishioka, M., Kohno, T., Tani, M., Yanaihara, N., Tomizawa, Y., Otsuka, A., et al. (2002). MYO18B, a candidate tumor suppressor gene at chromosome 22q12.1, deleted, mutated, and methylated in human lung cancer. *Proc. Natl. Acad. Sci. U S A.* 99, 12269–12274.

Odronitz, F., and Kollmar, M. (2007). Drawing the tree of eukaryotic life based on the analysis of 2,269 manually annotated myosins from 328 species. *Genome Biol.* 8:R196.

Peckham, M. (2016). How myosin organization of the actin cytoskeleton contributes to the cancer phenotype. *Biochem. Soc. Trans.* 44, 1026–1034.

Pettigrew, K. A., Fajutrao Valles, S. F., Moll, K., Northstone, K., Ring, S., Pennell, C., et al. (2015). Lack of replication for the myosin-18B association with mathematical ability in independent cohorts. *Genes Brain Behav.* 14, 369–376.

Preller, M., and Manstein, D. J. (2013). Myosin structure, allostery, and mechano-chemistry. *Structure* 21, 1911–1922.

Rahajeng, J., Kuna, R. S., Makowski, S. L., Tran, T. T. T., Buschman, M. D., Li, S., et al. (2019). Efficient golgi forward trafficking requires GOLPH3-Driven. PI4P-Dependent membrane curvature. *Dev. Cell* 50, 573–585.e5.

Salamon, M., Millino, C., Raffaello, A., Mongillo, M., Sandri, C., Bean, C., et al. (2003). Human MYO18B, a novel unconventional myosin heavy chain expressed in striated muscles moves into the myonuclei upon differentiation. *J. Mol. Biol.* 326, 137–149.

Taft, M. H., Behrmann, E., Munske-Weidemann, L. C., Thiel, C., Raunser, S., and Manstein, D. J. (2013). Functional characterization of human myosin-18A and its interaction with F-actin and GOLPH3. *J. Biol. Chem.* 288, 30029–30041.

Taft, M. H., and Latham, S. L. (2020). Myosin XVIII. *Adv. Exp. Med. Biol.* 1239, 421–438.

Taft, M. H., Radke, M. B., Stanczak, M., Thiel, C., and Manstein, D. J. (2014). Human Myosin-18B - A versatile actin binding protein. *Biophys. J.* 106, 179a–180a.

Takata, A., Iwayama, Y., Fukuo, Y., Ikeda, M., Okochi, T., Maekawa, M., et al. (2013). A population-specific uncommon variant in GRIN3A associated with schizophrenia. *Biol. Psychiatry* 73, 532–539.

Tan, I., Yong, J., Dong, J. M., Lim, L., and Leung, T. (2008). A tripartite complex containing MRCK modulates lamellar actomyosin retrograde flow. *Cell* 135, 123–136.

Tomar, T., Alkema, N. G., Schreuder, L., Meersma, G. J., de Meyer, T., van Criekinge, W., et al. (2017). Methylome analysis of extreme chemoresponsive patients identifies novel markers of platinum sensitivity in high-grade serous ovarian cancer. *BMC Med.* 15:116. doi: 10.1186/s12916-017-0870-0

Ussowicz, M., Jaskowiec, A., Meyer, C., Marschalek, R., Chybicka, A., Szczepanski, T., et al. (2012). A three-way translocation of MLL, MLLT11, and the novel reciprocal partner gene MYO18A in a child with acute myeloid leukemia. *Cancer Genet.* 205, 261–265.

Walz, C., Chase, A., Schoch, C., Weisser, A., Schlegel, F., Hochhaus, A., et al. (2005). The t(8;17)(p11;q23) in the 8p11 myeloproliferative syndrome fuses MYO18A to FGFR1. *Leukemia* 19, 1005–1009.

Walz, C., Haferlach, C., Hanel, A., Metzgeroth, G., Erben, P., Gosenca, D., et al. (2009). Identification of a MYO18A-PDGFRB fusion gene in an eosinophilia-associated atypical myeloproliferative neoplasm with a t(5;17)(q33-34;q11.2). *Genes Chromosomes Cancer* 48, 179–183.

Yanaihara, N., Nishioka, M., Kohno, T., Otsuka, A., Okamoto, A., Ochiai, K., et al. (2004). Reduced expression of MYO18B, a candidate tumor-suppressor gene on chromosome arm 22q, in ovarian cancer. *Int. J. Cancer* 112, 150–154.

Yang, C. H., Szeliga, J., Jordan, J., Faske, S., Sever-Chroneos, Z., Dorsett, B., et al. (2005). Identification of the surfactant protein A receptor 210 as the unconventional myosin 18A. *J. Biol. Chem.* 280, 34447–34457.

Yang, L., Carrillo, M., Wu, Y. M., DiAngelo, S. L., Silveyra, P., Umstead, T. M., et al. (2015). SP-R210 (Myo18A) isoforms as intrinsic modulators of macrophage priming and activation. *PLoS One* 10:e0126576. doi: 10.1371/journal.pone.0126576

Zhang, Z., Zhu, J., Huang, Y., Li, W., and Cheng, H. (2018). MYO18B promotes hepatocellular carcinoma progression by activating PI3K/AKT/mTOR signaling pathway. *Diagn Pathol.* 13:85.

Zhao, S., Shi, X., Zhang, Y., Wen, Z., Cai, J., Gao, W., et al. (2020). Myosin-18B promotes mechanosensitive CaMKK2-AMPK-VASP regulation of contractile actin stress fibers. *iScience* 23:100975.

Conflict of Interest: The authors declare that the research was conducted in the absence of any commercial or financial relationships that could be construed as a potential conflict of interest.

frontiers in Cell and Developmental Biology

MINI REVIEW
published: 18 March 2021
doi: 10.3389/fcell.2021.649899

Nucleus-Cytoskeleton Crosstalk During Mitotic Entry

Margarida Dantas[1,2,3†], *Joana T. Lima*[1,4†] *and Jorge G. Ferreira*[1,4*]

[1] *Instituto de Investigação e Inovação em Saúde – i3S, University of Porto, Porto, Portugal,* [2] *BiotechHealth Ph.D. Programme, University of Porto, Porto, Portugal,* [3] *Instituto de Ciências Biomédicas Abel Salazar (ICBAS), University of Porto, Porto, Portugal,* [4] *Departamento de Biomedicina, Faculdade de Medicina, University of Porto, Porto, Portugal*

In preparation for mitosis, cells undergo extensive reorganization of the cytoskeleton and nucleus, so that chromosomes can be efficiently segregated into two daughter cells. Coordination of these cytoskeletal and nuclear events occurs through biochemical regulatory pathways, orchestrated by Cyclin-CDK activity. However, recent studies provide evidence that physical forces are also involved in the early steps of spindle assembly. Here, we will review how the crosstalk of physical forces and biochemical signals coordinates nuclear and cytoplasmic events during the G2-M transition, to ensure efficient spindle assembly and faithful chromosome segregation.

Keywords: mitosis, nucleus, cytoskeleton, centrosome, mechanotransduction, chromosome, nuclear lamina

OPEN ACCESS

Edited by:
Anne Straube,
University of Warwick,
United Kingdom

Reviewed by:
Paola Vagnarelli,
Brunel University London,
United Kingdom
Manuel Mendoza,
INSERM U964 Institut de Génétique et de Biologie Moléculaire et Cellulaire (IGBMC), France
Ulrike Kutay,
ETH Zürich, Switzerland

****Correspondence:***
Jorge G. Ferreira
jferreir@ibmc.up.pt

† These authors have contributed equally to this work

Specialty section:
This article was submitted to Cell Growth and Division, a section of the journal Frontiers in Cell and Developmental Biology

Received: *05 January 2021*
Accepted: *26 February 2021*
Published: *18 March 2021*

Citation:
Dantas M, Lima JT and Ferreira JG (2021) Nucleus-Cytoskeleton Crosstalk During Mitotic Entry. Front. Cell Dev. Biol. 9:649899. doi: 10.3389/fcell.2021.649899

INTRODUCTION

An efficient mitosis is required to maintain genomic stability and ensure correct tissue development and homeostasis. While nuclear envelope breakdown (NEB) marks the irreversible step of mitotic commitment, the process starts well before, as chromosomes condense (Antonin and Neumann, 2016) and centrosomes separate (Whitehead et al., 1996). This occurs simultaneously with a global reorganization of the microtubule and actin cytoskeletons. Accordingly, the interphase microtubule cytoskeleton disassembles (Mchedlishvili et al., 2018) and overall microtubule dynamics change (Zhai et al., 1996), which allows the formation of a bipolar spindle (Heald and Khodjakov, 2015) required for accurate chromosome capture (**Figure 1**). At the same time, the interphase actin cytoskeleton is replaced with a mitotic actomyosin network that is connected with the plasma membrane (Chugh and Paluch, 2018) and drives mitotic rounding (Rosa et al., 2015). Importantly, timely progression through these steps requires the activity of mitotic kinases such as CDK1 and PLK1 (Gavet and Pines, 2010b; Ramanathan et al., 2015; Gheghiani et al., 2017). Simultaneously, within the nucleus, a cascade of events regulated by the same mitotic kinases initiate chromosome condensation (Abe et al., 2011) and trigger disassembly of the nuclear pore complex (NPC; Linder et al., 2017) and nuclear lamina (NL; Heald and McKeon, 1990; Peter et al., 1990).

Here, we will discuss how the interactions between the cytoskeleton and nucleus set the stage for spindle assembly and how the prophase nucleus acts as more than a passive player to ensure a successful mitosis.

MITOTIC CELL ROUNDING

Mitotic cell rounding is a feature of a large number of eukaryotic cells that lack a cell wall (Mitchison, 1992; Gibson et al., 2006; Thery and Bornens, 2008). However, this is not a universal characteristic, as some metazoan cells such as Ptk1 or newt pneumocytes are still

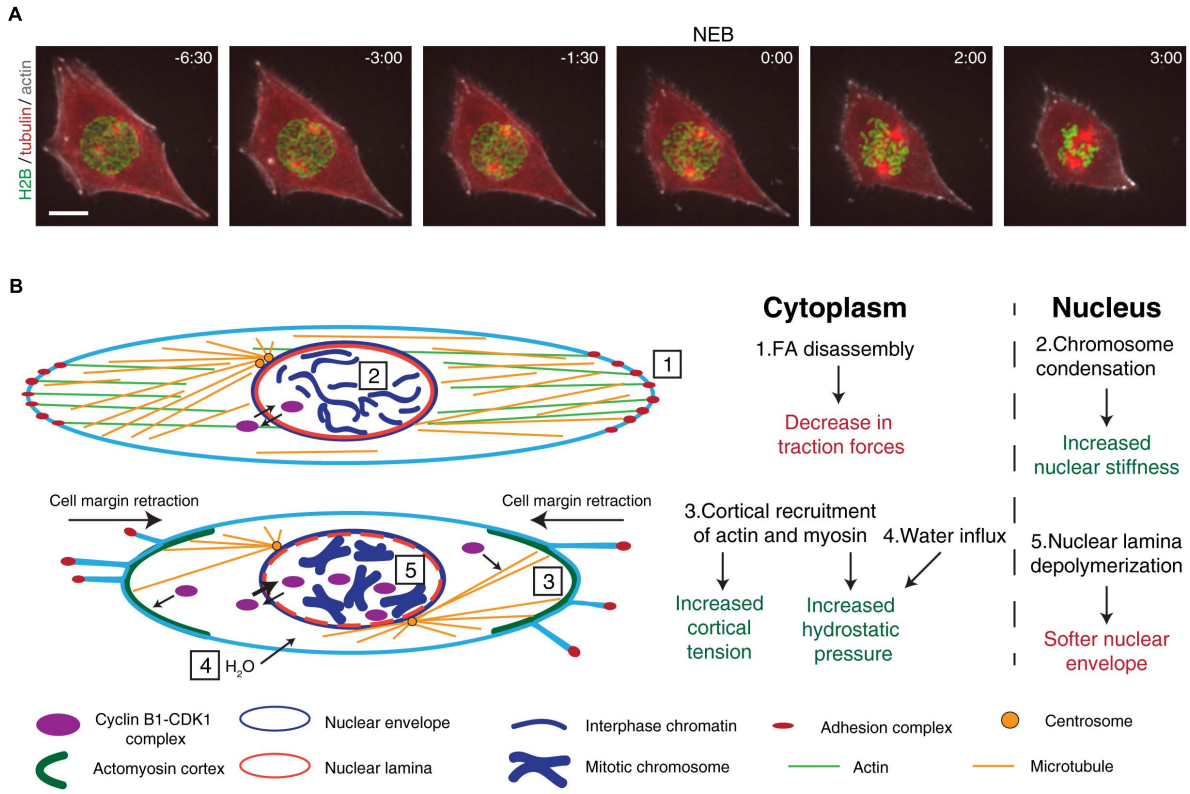

FIGURE 1 | Overview of the cytoskeletal and nuclear reorganization that occur during mitotic entry. **(A)** Representative frames from a movie of a RPE-1 cell expressing H2B-GFP/tubulin-RFP/SiR-actin during mitotic entry. It is possible to observe the main events that occur during mitotic entry, such as cell rounding, chromosome condensation, and centrosome separation. After NEB, mitotic rounding continues as the spindle assembles. Time is in min:sec. Scale bar, 10 μm. Time zero corresponds to NEB. **(B)** Main events that occur during the G2-M transition. Cyclin B1-CDK1 complexes shuttle between the cytoplasm and the nucleus. At this stage, the cell is attached to the extracellular matrix through membrane-bound adhesion complexes (1) and the microtubule and actin cytoskeletons are in their interphase configuration. Inside the nucleus, chromatin is decondensed and the nuclear envelope and nuclear lamina are intact (2). As cells prepare to enter mitosis, adhesion complexes disassemble, leading to cell membrane retraction and mitotic cortex assembly (3). Together with osmotic swelling (4), this leads to increased intracellular pressure. At the same time, active cyclin B1-CDK1 complexes accumulate in the nucleus, triggering chromosome condensation, nuclear lamina depolymerization (5), and nuclear envelope permeabilization. These events trigger changes global changes in the forces during the G2-M transition.

capable of progressing through mitosis without rounding (Roos, 1973; Hayden et al., 1990; Rieder and Alexander, 1990). The rounding process is regulated by CDK1 activity (Jones et al., 2018) and starts in the early stages of mitosis (Matthews et al., 2012) with the loss of Arp2/3-dependent lamellipodia (Bovellan et al., 2014) and disassembly of focal adhesions (FAs; Dao et al., 2009). This loss of FAs leads to the decrease in cell traction forces observed during G2 (Uroz et al., 2018; Vianay et al., 2018) and prophase (Nunes et al., 2020) and allows cell margin retraction (Mitchison, 1992; Maddox and Burridge, 2003) (**Figure 1**). In turn, this change in cell shape enables the formation of a stiff actomyosin cortex (Maddox and Burridge, 2003; Kunda et al., 2008; Fischer-Friedrich et al., 2016), through the CDK1-mediated phosphorylation of Myosin II (Ramanathan et al., 2015) and Ect2, a RhoGEF that activates the RhoA GTPase (Matthews et al., 2012). In combination with an increase in hydrostatic pressure (Stewart et al., 2011) and cell volume (Zlotek-Zlotkiewicz et al., 2015), likely driven by water influx (Son et al., 2015), these changes provide the necessary space for mitotic spindle assembly and accurate chromosome capture (Kunda et al., 2008; Lancaster et al., 2013). Consequently, a failure in mitotic cell rounding triggered by either blocking FA disassembly or mechanical compression leads to defects in spindle assembly and mitotic progression (Lancaster et al., 2013; Nunes et al., 2020) and increases chromosome missegregation (Tse et al., 2012; Lancaster et al., 2013; Cattin et al., 2015; Matthews et al., 2020). The need for cell rounding was further emphasized with the proposal of an "adhesion-dependent checkpoint," which acts through DEPDC1B to inhibit RhoA activation and allow FA dismantling during the G2-M transition (Marchesi et al., 2014), required for normal proliferation and development of zebrafish embryos.

CENTROSOME SEPARATION AND SPINDLE ASSEMBLY

In animal cells, spindle assembly originates mainly from the centrosomes. For this reason, many studies have focused on centrosome behavior during the early stages of mitosis.

Initial centrosome separation requires the combined action of microtubule-associated molecular motors such as kinesin-5 and dynein (for review, see Tanenbaum and Medema, 2010). The plus-end directed kinesin-5 has a homo-tetrameric structure that can crosslink and slide anti-parallel microtubules apart (Kashina et al., 1996). This generates pushing forces on microtubules that lead to centrosome separation (Whitehead et al., 1996). For this reason, kinesin-5 has been involved in spindle assembly in nearly all model systems analyzed (Sawin et al., 1992; Heck et al., 1993; Blangy et al., 1995), with the exception of *C. elegans* (Bishop et al., 2005). Dynein, on the other hand is a microtubule minus-end directed motor (Roberts et al., 2013). To generate the pulling forces necessary for centrosome separation, dynein needs to be tethered to sub-cellular structures such as the nuclear envelope (NE; Splinter et al., 2010; Bolhy et al., 2011; Nunes et al., 2020) or the cell cortex (Kotak et al., 2012). The combined activity of these motors is sufficient to drive centrosome separation, but it does not explain the biased movement of centrosomes to the shortest axis of the nucleus (Magidson et al., 2011; Nunes et al., 2020). Such a bias would require additional cues (either external or internal) or an asymmetry in the forces exerted on the centrosomes, to direct centrosome movement. Notwithstanding, the extent of centrosome separation, as well as their positioning at the moment of NEB, remain major contributors to chromosome missegregation events. Failure to fully separate centrosomes during mitotic entry can contribute to deviant spindle morphologies (Silkworth et al., 2012; Nam et al., 2015), increasing the likelihood of generating erroneous kinetochore-microtubule attachments. Most of these attachments are sensed by the Spindle Assembly Checkpoint (SAC), which generates a "wait-anaphase" signal until all chromosomes are correctly attached (Lara-Gonzalez et al., 2012). However, merotelic attachments, which occur when one kinetochore is bound to microtubules emanating from different poles, are usually invisible to the SAC (Gregan et al., 2011). Consequently, cells with incompletely separated centrosomes at NEB tend to have a higher rate of chromosome missegregation (Kaseda et al., 2012; Silkworth et al., 2012; Nunes et al., 2020).

During metaphase, cortical force generators dictate spindle orientation (Thery et al., 2007; Kotak et al., 2012) by sensing external cues (Thery et al., 2005; Toyoshima and Nishida, 2007; Fink et al., 2011). However, during the initial stages of mitosis, as cells round up and the actomyosin cortex is yet to be assembled, these cortical force generators are not present (Kiyomitsu and Cheeseman, 2012; Kotak et al., 2012). Therefore, it is likely that the cues required for centrosome positioning during early mitosis are not provided by external signals, but rather derive from an internal input. One such signal could be provided by the NE-specific pool of dynein, that is dependent on association with the RanBP2-BicD2 (Splinter et al., 2010) or Nup133/CENP-F/NudE-NudEL (Bolhy et al., 2011) pathways, in a CDK1-dependent manner (Baffet et al., 2015). Accordingly, preventing dynein loading on the NE results in a failure to separate (van Heesbeen et al., 2013; De Simone et al., 2016; Boudreau et al., 2019) and correctly position centrosomes (Splinter et al., 2010; Bolhy et al., 2011; Nunes et al., 2020). The manner in which the properties of the prophase nucleus dictate dynein localization and activity to ensure positioning of centrosomes on the shortest nuclear axis and avert chromosome missegregation remains an open question.

THE NUCLEUS AND NUCLEO-CYTOSKELETAL COUPLING

The cell nucleus is encased by a NE that acts as a barrier between cytoplasmic and nuclear components. The NE is composed of and inner (INM) and an outer (ONM) nuclear membrane, NPCs and a dense NL. The NL consists mainly of A-type and B-type Lamins, which are type V intermediate filaments that provide structural support to the nucleus (Dechat et al., 2010). Lamins can interact with chromatin and with NE membrane proteins, such as Emerin, LAP2, or nuclear soluble factors such as barrier-to-autointegration factor (BAF) (Ungricht and Kutay, 2017).

The nucleus is continuously under the influence of external forces. When physical forces are applied to the cell, they are decoded into biochemical signals in a process known as mechanotransduction. This process starts at the cell membrane, where adhesion complexes sense external cues (Sun et al., 2016). The cytoskeleton then relays these signals to the nucleus through the linker of nucleoskeleton and cytoskeleton (LINC) complex (Lombardi and Lammerding, 2011), which triggers a nuclear mechanical response that depends on the NL (Stephens et al., 2017), chromatin condensation (Schreiner et al., 2015; Stephens et al., 2017) and nucleo-cytoskeletal coupling (Lombardi and Lammerding, 2011). This ultimately leads to changes in nuclear structure and organization (Lammerding, 2011; Maurer and Lammerding, 2019) and regulates cell cycle progression (Uroz et al., 2018; Vitiello et al., 2019).

As mentioned above, a series of well-coordinated events ensure timely mitotic entry, starting with chromosome condensation (Antonin and Neumann, 2016) and cytoskeletal reorganization (Ramkumar and Baum, 2016; Champion et al., 2017), and culminating in nuclear permeabilization (Beaudouin et al., 2002; Salina et al., 2002). In higher eukaryotes, nuclear permeabilization starts with the removal of nucleoporins from NPCs (Dultz et al., 2008; Katsani et al., 2008), which triggers a loss of the nucleo-cytoplasmic boundary. The process continues with the contribution of dynein-driven, microtubule-dependent pulling forces, which generate holes in the nucleus and assist in membrane clearing from chromosomes (Beaudouin et al., 2002; Salina et al., 2002; Muhlhausser and Kutay, 2007). Finally, the NL depolymerizes, due to Lamin phosphorylation and consequent nucleoplasmic release (Heald and McKeon, 1990; Peter et al., 1990; Georgatos et al., 1997). These steps are essential to allow the interaction of microtubules with kinetochores on mitotic chromosomes. In interphase, the mechanical response of the nucleus is dictated by the chromatin condensation state (Stephens et al., 2017), the levels of Lamin A (Buxboim et al., 2017) and the interaction of heterochromatin with the nuclear membrane (Schreiner et al., 2015). Remarkably, as cells transition from G2 to mitosis, all the above components are extensively modified. Phosphorylation of Lamin A by

CDK1 (Heald and McKeon, 1990; Peter et al., 1990), triggers its disassembly from the NL and consequent release into the nucleoplasm (Georgatos et al., 1997). Although direct measurements of nuclear stiffness at this stage have not been made, it is possible to assume that NL depolymerization significantly changes the mechanical response of the nucleus, facilitating NEB. Accordingly, MEFs with Lamin A/C deficiency show impaired nuclear stiffness and mechanics (Lammerding et al., 2004, 2006). This is in line with observations in human cells, showing that loss of Lamin A renders nuclei softer (Pajerowski et al., 2007) and prone to rupture (Earle et al., 2020). Taken together, these observations implicate the NL in the mechanical stability of the nucleus and highlight the need for its depolymerization during prophase (Georgatos et al., 1997), to facilitate microtubule-dependent nuclear permeabilization (Beaudouin et al., 2002; Salina et al., 2002). At the same time, mitotic chromosomes condense, altering their structure and stiffness (Stephens et al., 2017; Sun et al., 2018; Biggs et al., 2019). Evidence from metaphase chromosomes isolated from HeLa cells showed this process to be largely dependent on condensins (Sun et al., 2018), although histone post-translational modifications also play an important role (Biggs et al., 2019). Finally, the actin cytoskeleton, which is connected to the nucleus through the LINC complex (Versaevel et al., 2014), is remodeled to assemble a mitotic cortex (Ramkumar and Baum, 2016). This remodeling might modify the connections between the cytoskeleton and the nucleus, contributing to changes in nuclear mechanics. Accordingly, disrupting the actin cytoskeleton in NIH3T3 cells was sufficient to modify the compressive forces exerted on the nucleus and induce changes in chromatin organization (Li et al., 2014). Taken together, these studies suggest that the mechanical properties of the nucleus change during the G2-M transition and warrant further investigation on the functional relevance of nuclear mechanics for mitotic fidelity.

While measurements of the mechanical properties of the nucleus during the G2-M transition are still missing, there is already significant evidence to support a role for the nucleus and nucleus-associated components in other steps of mitosis, namely in determining chromosome segregation fidelity. One key component in nuclear mechanotransduction is the aforementioned LINC complex (**Figure 2**). This complex consists of SUN (Sad1, UNC84) proteins in the INM and KASH (Klarsicht, ANC-1, and Syne Homology)-containing proteins in the ONM (Starr and Fridolfsson, 2010). Importantly, studies in MEFs using a microneedle assay to apply controlled cytoskeletal strains, in combination with dominant-negative forms of SUN and KASH proteins, showed that an intact LINC complex is essential for force transmission to the nucleus (Lombardi et al., 2011). Similarly, in cultured human cells, depletion of both SUN1 and SUN2 delayed NE disassembly (**Figure 2**), similarly to what is observed after microtubule depolymerization with nocodazole (Turgay et al., 2014). Consequently, centrosome separation is disrupted (Stiff et al., 2020) and mitotic progression affected (Turgay et al., 2014). Moreover, an intact LINC complex is essential during early mitosis for decreasing chromosome scattering (Booth et al., 2019), likely facilitating their capture and congression (Booth et al., 2019; Stiff et al., 2020). Importantly, the LINC complex also directly associates with dynein on the NE to control nuclear migration (Malone et al., 2003; Zhang et al., 2009; Fridolfsson and Starr, 2010; Yu et al., 2011) and meiotic chromosome movement (Chikashige et al., 2006; Sato et al., 2009). Given that an intact LINC complex is required for force transmission to the nucleus (Lombardi et al., 2011) and NE dynein is essential for centrosome positioning (Nunes et al., 2020), it is possible that LINC-mediated mechanical forces could play an important part in determining correct centrosome positioning by ensuring timely dynein loading. Accordingly, depletion of SUN1 and SUN2 is sufficient to abolish NE dynein localization (Turgay et al., 2014; Nunes et al., 2019). Whether this is directly due to a defect in nuclear mechanotransduction triggered by loss of the LINC complex remains unknown (**Figure 2**).

Other nuclear components have also been implicated in spindle assembly and chromosome segregation. Blocking the removal of NE membranes at mitotic onset leads to defects in spindle assembly and chromosome segregation (Turgay et al., 2014; Champion et al., 2019). Similar defects in membranes removal could also be triggered by expression of a mutant version of Lamin A that is observed in progeria patients (Dechat et al., 2007). However, Lamin A, together with BAF and LAP2α, is also directly involved in spindle assembly and orientation by targeting dynein to the cell cortex (Qi et al., 2015). Moreover, chromosome distribution is altered in LMNA mutant fibroblasts (Meaburn et al., 2007). Such alterations could directly affect chromosome distribution during early mitosis, disrupting the disk-like prometaphase chromosome organization, essential for spindle assembly (Magidson et al., 2011). Taken together, these defects could explain why Lamin A/C deficiency leads to aneuploidy and chromosomal instability (Dechat et al., 2007; Capo-chichi et al., 2011; Capo-Chichi et al., 2016; Smith et al., 2018). Interestingly, mitotic problems are not exclusive to Lamin A. In *C. elegans,* it was shown that reduced levels of MAN1 and Emerin, INM proteins which interact with Lamins and the LINC complex (Piccus and Brayson, 2020), trigger "anaphase-bridged chromatin" (Liu et al., 2003), a phenotype also observed in a mouse model of laminopathy (Pratt et al., 2011), and in human cells with reduced Lamin A levels (Cao et al., 2007). Moreover, loss of Lamin B2 in human cells was also shown to trigger chromosomal instability, by interfering with the spatial organization of chromosomes (Ranade et al., 2017) and affecting spindle assembly (Kuga et al., 2014).

Although these reports are compelling, there are alternative hypotheses to explain how alterations in Lamins could indirectly trigger mitotic defects. Chromatin is thought to associate with the NL through specific sequences known as lamina-associated domains (LADs) (van Steensel and Belmont, 2017) that are considered to be transcriptionally repressive regions (Guelen et al., 2008) and help organize chromosomes within the nuclear volume (Mewborn et al., 2010). Notably, Lamin A phosphorylation on Ser22, essential for NL depolymerization during mitotic entry (Heald and McKeon, 1990), was recently shown to act as a transcriptional regulator (Ikegami et al., 2020),

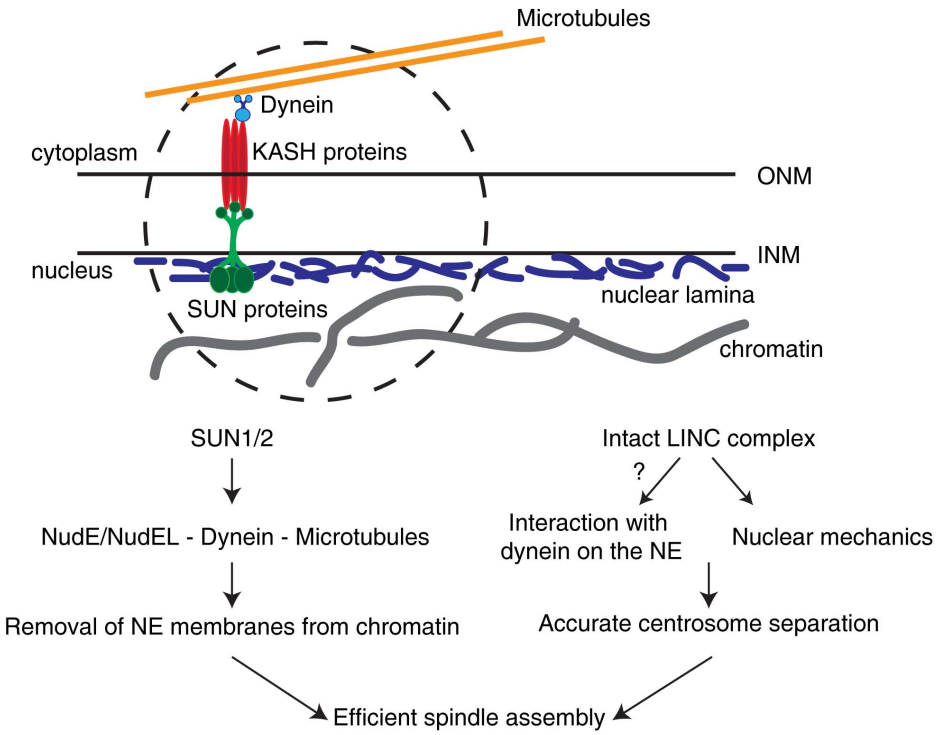

FIGURE 2 | The LINC complex in early spindle assembly and chromosome segregation. The LINC complex consists of SUN1/2 trimers on the inner nuclear membrane (INM) and KASH proteins on the outer nuclear membrane (ONM). In somatic cells, different KASH proteins differentially bind to specific motors (e.g., dynein) or to distinct cytoskeletal components. These complexes are able to sense forces relayed by the cytoskeleton and transmit them to the nuclear interior. During the G2-M transition, SUN proteins are required to remove NE membranes from chromatin and position centrosomes. In addition, an intact LINC complex is necessary for correct centrosome separation. Whether this is due to LINC complex-dependent loading of dynein on the NE or to nuclear mechanotransduction remains unclear.

which could explain why LMNA mutants show altered gene expression patterns (Mewborn et al., 2010). Whether the mitotic defects triggered by Lamin A loss could be due to changes in its transcriptional program remains to be determined.

MECHANICAL FORCES IN CELL CYCLE PROGRESSION

The link between mechanical forces and the cell cycle has long been recognized (Chen et al., 1997; Huang et al., 1998). In capillary endothelial cells, tractional forces are sufficient to trigger the G1-S transition by increasing Cyclin D1 levels and down-regulating the cell cycle inhibitor $p27^{Kip}$ (Huang et al., 1998). This likely occurs by force-mediated nuclear deformation that triggers the activation of transcription factors such as TEAD and AP1, leading to the induction of genes that promote the G1-S transition (Aureille et al., 2019). In agreement with these observations, recent data obtained in MDCK monolayers showed that both tension and mechanical energy are good predictors of G1 duration (Uroz et al., 2018).

Other stages of the cell cycle are also mechanically regulated. In fact, the organization pattern of actomyosin forces sets the duration of the S and G2 phases, by modulating centriole duplication and Plk4 recruitment (Vitiello et al., 2019). In addition, there is evidence from MDCK monolayers and isolated cells, for a decrease in cell traction forces during G2 and early mitosis (Uroz et al., 2018; Vianay et al., 2018; Nunes et al., 2020), which occurs in tandem with the disassembly of FAs (Dao et al., 2009) and an increased expression of DEPDC1B (Marchesi et al., 2014). How these events are coordinated is still unclear. It is possible that, during the G2-M transition, a FA-generated mechanical signal is relayed from the cell membrane to the nucleus, triggering DEPDC1B expression, which would then act as a RhoA inhibitor to regulate adhesion dynamics (Marchesi et al., 2014). This, together with increased CDK1 activity (Jones et al., 2018), would set the timing for FA disassembly and mitotic entry (Gavet and Pines, 2010a,b; Marchesi et al., 2014).

CONCLUSION

Efficient assembly of a mitotic spindle requires accurate coordination between cytoplasmic and nuclear events. This is achieved, at least partly, by the activity and localization of the Cyclin B1-CDK1 complex (Gavet and Pines, 2010a,b). In the cytoplasm, CDK1 enables centrosome separation (Smith et al., 2011) and induces global changes in microtubule dynamics by directly phosphorylating microtubule-associated

proteins (MAPs) and modifying their microtubule binding capacity (Lamb et al., 1990; Verde et al., 1990; Verde et al., 1992). On the other hand, inside the nucleus, CDK1 contributes to NPC disassembly (Linder et al., 2017) and NL depolymerization (Heald and McKeon, 1990; Peter et al., 1990). These biochemical events trigger a global cellular reorganization that allows the assembly of an actomyosin cortex and a microtubule-based mitotic spindle.

In addition to the biochemical pathways controlling mitotic entry, it has long been proposed that mechanical forces also regulate the cell cycle (Huang et al., 1998; Lancaster et al., 2013; Uroz et al., 2018; Vianay et al., 2018; Aureille et al., 2019). High cellular tension triggers a transition from G1 to S phase (Huang et al., 1998; Uroz et al., 2018; Aureille et al., 2019) and also regulates the length of the S-G2 phases of the cell cycle (Vitiello et al., 2019). In part, this could be due to tension-generated NE deformation that is sufficient to trigger mechanically-activated transcriptional programs (Aureille et al., 2019) and affect cell proliferation (Versaevel et al., 2012). As cells progress toward mitosis, tension decreases (Uroz et al., 2018; Vianay et al., 2018; Nunes et al., 2020), likely reflecting adhesion complex disassembly (Dao et al., 2009), mediated by increased levels of Cyclin B1 (Gavet and Pines, 2010b; Jones et al., 2018). Overall, these observations highlight the interactions between physical forces and the cell cycle machinery and raise the interesting possibility that mechanical forces could directly influence the biochemical signals that control mitotic entry, contributing to the fidelity of chromosome segregation. As new tools emerge that allow us to probe the physical properties of cells, we will gain further insight on how the spatiotemporal dynamics of nuclear mechanics and nucleus-cytoskeleton coupling contribute to spindle assembly efficiency and chromosome segregation fidelity.

AUTHOR CONTRIBUTIONS

MD, JL, and JF jointly wrote the manuscript. JF provided the conceptual framework. All authors contributed to the article and approved the submission.

FUNDING

Work in the Biophysics of Cell Division Laboratory was supported by Portuguese funds through FCT—Fundação para a Ciência e a Tecnologia/Ministério da Ciência, Tecnologia e Ensino Superior in the framework of the project PTDC/BIA-CEL/6740/2020. MD was supported by the grant PD/BD/135548/2018 from the BiotechHealth FCT-funded Ph.D. program. JL was supported by the grant SFRH/BD/147169/2019 from FCT.

ACKNOWLEDGMENTS

We would like to thank all the members of the Biophysics of Cell Division Laboratory for their critical reading of the manuscript. We would like to apologize to all colleagues whose work contributed for our current knowledge on the mechanisms of mitotic entry, but which could not be cited due to space limitations.

REFERENCES

Abe, S., Nagasaka, K., Hirayama, Y., Kozuka-Hata, H., Oyama, M., Aoyagi, Y., et al. (2011). The initial phase of chromosome condensation requires Cdk1-mediated phosphorylation of the CAP-D3 subunit of condensin II. *Genes Dev.* 25, 863–874. doi: 10.1101/gad.2016411

Antonin, W., and Neumann, H. (2016). Chromosome condensation and decondensation during mitosis. *Curr. Opin. Cell Biol.* 40, 15–22. doi: 10.1016/j.ceb.2016.01.013

Aureille, J., Buffière-Ribot, V., Harvey, B. E., Boyault, C., Pernet, L., Andersen, T., et al. (2019). Nuclear envelope deformation controls cell cycle progression in response to mechanical force. *EMBO Rep.* 20, e48084.

Baffet, A. D., Hu, D. J., and Vallee, R. B. (2015). Cdk1 activates pre-mitotic nuclear envelope dynein recruitment and apical nuclear migration in neural stem cells. *Dev. Cell* 33, 703–716. doi: 10.1016/j.devcel.2015.04.022

Beaudouin, J., Gerlich, D., Daigle, N., Eils, R., and Ellenberg, J. (2002). Nuclear envelope breakdown proceeds by microtubule-induced tearing of the lamina. *Cell* 108, 83–96. doi: 10.1016/s0092-8674(01)00627-4

Biggs, R., Liu, P. Z., Stephens, A. D., and Marko, J. F. (2019). Effects of altering histone posttranslational modifications on mitotic chromosome structure and mechanics. *Mol. Biol. Cell* 30, 820–827. doi: 10.1091/mbc.e18-09-0592

Bishop, J. D., Han, Z., and Schumacher, J. M. (2005). The *Caenorhabditis elegans* Aurora B kinase AIR-2 phosphorylates and is required for the localization of a BimC kinesin to meiotic and mitotic spindles. *Mol. Biol. Cell* 16, 742–756. doi: 10.1091/mbc.e04-08-0682

Blangy, A., Lane, H. A., D'herin, P., Harper, M., Kress, M., and Nigg, E. A. (1995). Phosphorylation by p34cdc2 regulates spindle association of human Eg5, a kinesin-related motor essential for bipolar spindle formation in vivo. *Cell* 83, 1159–1169. doi: 10.1016/0092-8674(95)90142-6

Bolhy, S., Bouhlel, I., Dultz, E., Nayak, T., Zuccolo, M., Gatti, X., et al. (2011). A Nup133-dependent NPC-anchored network tethers centrosomes to the nuclear envelope in prophase. *J. Cell Biol.* 192, 855–871. doi: 10.1083/jcb.201007118

Booth, A. J. R., Yue, Z., Eykelenboom, J. K., Stiff, T., Luxton, G. W. G., Hochegger, H., et al. (2019). Contractile acto-myosin network on nuclear envelope remnants positions human chromosomes for mitosis. *Elife* 8:e46902.

Boudreau, V., Chen, R., Edwards, A., Sulaimain, M., and Maddox, P. S. (2019). PP2A-B55/SUR-6 collaborates with the nuclear lamina for centrosome separation during mitotic entry. *Mol. Biol. Cell* 30, 876–886.

Bovellan, M., Romeo, Y., Biro, M., Boden, A., Chugh, P., Yonis, A., et al. (2014). Cellular control of cortical actin nucleation. *Curr. Biol.* 24, 1628–1635. doi: 10.1016/j.cub.2014.05.069

Buxboim, A., Irianto, J., Swift, J., Athirasala, A., Shin, J. W., Rehfeldt, F., et al. (2017). Coordinated increase of nuclear tension and lamin-A with matrix stiffness outcompetes lamin-B receptor that favors soft tissue phenotypes. *Mol. Biol. Cell* 28, 3333–3348. doi: 10.1091/mbc.e17-06-0393

Cao, K., Capell, B. C., Erdos, M. R., Djabali, K., and Collins, F. S. (2007). A lamin A protein isoform overexpressed in Hutchinson-Gilford progeria syndrome interferes with mitosis in progeria and normal cells. *Proc. Natl. Acad. Sci. U.S.A.* 104, 4949–4954. doi: 10.1073/pnas.0611640104

Capo-chichi, C. D., Cai, K. Q., Simpkins, F., Ganjei-Azar, P., Godwin, A. K., and Xu, X. X. (2011). Nuclear envelope structural defects cause chromosomal numerical instability and aneuploidy in ovarian cancer. *BMC Med.* 9:28. doi: 10.1186/1741-7015-9-28

Capo-Chichi, C. D., Yeasky, T. M., Smith, E. R., and Xu, X. X. (2016). Nuclear envelope structural defect underlies the main cause of aneuploidy in ovarian carcinogenesis. *BMC Cell Biol.* 17:37. doi: 10.1186/s12860-016-0114-8

Cattin, C. J., Duggelin, M., Martinez-Martin, D., Gerber, C., Muller, D. J., and Stewart, M. P. (2015). Mechanical control of mitotic progression in single animal cells. *Proc. Natl. Acad. Sci. U.S.A.* 112, 11258–11263. doi: 10.1073/pnas.1502029112

Champion, L., Linder, M. I., and Kutay, U. (2017). Cellular reorganization during mitotic entry. *Trends Cell Biol.* 27, 26–41. doi: 10.1016/j.tcb.2016.07.004

Champion, L., Pawar, S., Luithle, N., Ungricht, R., and Kutay, U. (2019). Dissociation of membrane-chromatin contacts is required for proper chromosome segregation in mitosis. *Mol. Biol. Cell* 30, 427–440. doi: 10.1091/mbc.e18-10-0609

Chen, C. S., Mrksich, M., Huang, S., Whitesides, G. M., and Ingber, D. E. (1997). Geometric control of cell life and death. *Science* 276, 1425–1428. doi: 10.1126/science.276.5317.1425

Chikashige, Y., Tsutsumi, C., Yamane, M., Okamasa, K., Haraguchi, T., and Hiraoka, Y. (2006). Meiotic proteins bqt1 and bqt2 tether telomeres to form the bouquet arrangement of chromosomes. *Cell* 125, 59–69.

Chugh, P., and Paluch, E. K. (2018). The actin cortex at a glance. *J. Cell Sci.* 131:jcs186254. doi: 10.1242/jcs.186254

Dao, V. T., Dupuy, A. G., Gavet, O., Caron, E., and De Gunzburg, J. (2009). Dynamic changes in Rap1 activity are required for cell retraction and spreading during mitosis. *J. Cell Sci.* 122, 2996–3004. doi: 10.1242/jcs.041301

De Simone, A., Nedelec, F., and Gonczy, P. (2016). Dynein transmits polarized actomyosin cortical flows to promote centrosome separation. *Cell Rep.* 14, 2250–2262. doi: 10.1016/j.celrep.2016.01.077

Dechat, T., Adam, S. A., Taimen, P., Shimi, T., and Goldman, R. D. (2010). Nuclear lamins. *Cold Spring Harb. Perspect. Biol.* 2:a000547.

Dechat, T., Shimi, T., Adam, S. A., Rusinol, A. E., Andres, D. A., Spielmann, H. P., et al. (2007). Alterations in mitosis and cell cycle progression caused by a mutant lamin A known to accelerate human aging. *Proc. Natl. Acad. Sci. U.S.A.* 104, 4955–4960. doi: 10.1073/pnas.0700854104

Dultz, E., Zanin, E., Wurzenberger, C., Braun, M., Rabut, G., Sironi, L., et al. (2008). Systematic kinetic analysis of mitotic dis- and reassembly of the nuclear pore in living cells. *J. Cell Biol.* 180, 857–865. doi: 10.1083/jcb.200707026

Earle, A. J., Kirby, T. J., Fedorchak, G. R., Isermann, P., Patel, J., Iruvanti, S., et al. (2020). Mutant lamins cause nuclear envelope rupture and DNA damage in skeletal muscle cells. *Nat. Mater.* 19, 464–473.

Fink, J., Carpi, N., Betz, T., Betard, A., Chebah, M., Azioune, A., et al. (2011). External forces control mitotic spindle positioning. *Nat. Cell Biol.* 13, 771–778. doi: 10.1038/ncb2269

Fischer-Friedrich, E., Toyoda, Y., Cattin, C. J., Müller, D. J., Hyman, A. A., and Jülicher, F. (2016). Rheology of the active cell cortex in mitosis. *Biophys. J.* 111, 589–600. doi: 10.1016/j.bpj.2016.06.008

Fridolfsson, H. N., and Starr, D. A. (2010). Kinesin-1 and dynein at the nuclear envelope mediate the bidirectional migrations of nuclei. *J. Cell Biol.* 191, 115–128. doi: 10.1083/jcb.201004118

Gavet, O., and Pines, J. (2010a). Activation of cyclin B1–Cdk1 synchronizes events in the nucleus and the cytoplasm at mitosis. *J. Cell Biol.* 189, 247–259. doi: 10.1083/jcb.200909144

Gavet, O., and Pines, J. (2010b). Progressive activation of CyclinB1-Cdk1 coordinates entry to mitosis. *Dev. Cell* 18, 533–543. doi: 10.1016/j.devcel.2010.02.013

Georgatos, S. D., Pyrpasopoulou, A., and Theodoropoulos, P. A. (1997). Nuclear envelope breakdown in mammalian cells involves stepwise lamina disassembly and microtubule-drive deformation of the nuclear membrane. *J. Cell Sci.* 110(Pt 17), 2129–2140.

Gheghiani, L., Loew, D., Lombard, B., Mansfeld, J., and Gavet, O. (2017). PLK1 activation in Late G2 Sets up commitment to mitosis. *Cell Rep.* 19, 2060–2073. doi: 10.1016/j.celrep.2017.05.031

Gibson, M. C., Patel, A. B., Nagpal, R., and Perrimon, N. (2006). The emergence of geometric order in proliferating metazoan epithelia. *Nature* 442, 1038–1041. doi: 10.1038/nature05014

Gregan, J., Polakova, S., Zhang, L., Tolic-Norrelykke, I. M., and Cimini, D. (2011). Merotelic kinetochore attachment: causes and effects. *Trends Cell Biol.* 21, 374–381. doi: 10.1016/j.tcb.2011.01.003

Guelen, L., Pagie, L., Brasset, E., Meuleman, W., Faza, M. B., Talhout, W., et al. (2008). Domain organization of human chromosomes revealed by mapping of nuclear lamina interactions. *Nature* 453, 948–951. doi: 10.1038/nature06947

Hayden, J. H., Bowser, S. S., and Rieder, C. L. (1990). Kinetochores capture astral microtubules during chromosome attachment to the mitotic spindle: direct visualization in live newt lung cells. *J. Cell Biol.* 111, 1039–1045. doi: 10.1083/jcb.111.3.1039

Heald, R., and Khodjakov, A. (2015). Thirty years of search and capture: the complex simplicity of mitotic spindle assembly. *J. Cell Biol.* 211, 1103–1111. doi: 10.1083/jcb.201510015

Heald, R., and McKeon, F. (1990). Mutations of phosphorylation sites in lamin A that prevent nuclear lamina disassembly in mitosis. *Cell* 61, 579–589. doi: 10.1016/0092-8674(90)90470-y

Heck, M. M., Pereira, A., Pesavento, P., Yannoni, Y., Spradling, A. C., and Goldstein, L. S. (1993). The kinesin-like protein KLP61F is essential for mitosis in *Drosophila*. *J. Cell Biol.* 123, 665–679. doi: 10.1083/jcb.123.3.665

Huang, S., Chen, C. S., and Ingber, D. E. (1998). Control of cyclin D1, p27(Kip1), and cell cycle progression in human capillary endothelial cells by cell shape and cytoskeletal tension. *Mol. Biol. Cell* 9, 3179–3193. doi: 10.1091/mbc.9.11.3179

Ikegami, K., Secchia, S., Almakki, O., Lieb, J. D., and Moskowitz, I. P. (2020). Phosphorylated Lamin A/C in the nuclear interior binds active enhancers associated with abnormal transcription in progeria. *Dev. Cell* 52, 699–713.e11.

Jones, M. C., Askari, J. A., Humphries, J. D., and Humphries, M. J. (2018). Cell adhesion is regulated by CDK1 during the cell cycle. *J. Cell Biol.* 217, 3203–3218. doi: 10.1083/jcb.201802088

Kaseda, K., Mcainsh, A. D., and Cross, R. A. (2012). Dual pathway spindle assembly increases both the speed and the fidelity of mitosis. *Biol. Open* 1, 12–18. doi: 10.1242/bio.2011012

Kashina, A. S., Scholey, J. M., Leszyk, J. D., and Saxton, W. M. (1996). An essential bipolar mitotic motor. *Nature* 384:225. doi: 10.1038/384225a0

Katsani, K. R., Karess, R. E., Dostatni, N., and Doye, V. (2008). In vivo dynamics of *Drosophila* nuclear envelope components. *Mol. Biol. Cell* 19, 3652–3666. doi: 10.1091/mbc.e07-11-1162

Kiyomitsu, T., and Cheeseman, I. M. (2012). Chromosome- and spindle-pole-derived signals generate an intrinsic code for spindle position and orientation. *Nat. Cell Biol.* 14, 311–317. doi: 10.1038/ncb2440

Kotak, S., Busso, C., and Gonczy, P. (2012). Cortical dynein is critical for proper spindle positioning in human cells. *J. Cell Biol.* 199, 97–110. doi: 10.1083/jcb.201203166

Kuga, T., Nie, H., Kazami, T., Satoh, M., Matsushita, K., Nomura, F., et al. (2014). Lamin B2 prevents chromosome instability by ensuring proper mitotic chromosome segregation. *Oncogenesis* 3:e94. doi: 10.1038/oncsis.2014.6

Kunda, P., Pelling, A. E., Liu, T., and Baum, B. (2008). Moesin controls cortical rigidity, cell rounding, and spindle morphogenesis during mitosis. *Curr. Biol.* 18, 91–101. doi: 10.1016/j.cub.2007.12.051

Lamb, N. J., Fernandez, A., Watrin, A., Labbe, J. C., and Cavadore, J. C. (1990). Microinjection of p34cdc2 kinase induces marked changes in cell shape, cytoskeletal organization, and chromatin structure in mammalian fibroblasts. *Cell* 60, 151–165. doi: 10.1016/0092-8674(90)90725-t

Lammerding, J. (2011). Mechanics of the nucleus. *Compr. Physiol.* 1, 783–807.

Lammerding, J., Fong, L. G., Ji, J. Y., Reue, K., Stewart, C. L., Young, S. G., et al. (2006). Lamins A and C but not lamin B1 regulate nuclear mechanics. *J. Biol. Chem.* 281, 25768–25780. doi: 10.1074/jbc.m513511200

Lammerding, J., Schulze, P. C., Takahashi, T., Kozlov, S., Sullivan, T., Kamm, R. D., et al. (2004). Lamin A/C deficiency causes defective nuclear mechanics and mechanotransduction. *J. Clin. Invest.* 113, 370–378. doi: 10.1172/jci200419670

Lancaster, O. M., Le Berre, M., Dimitracopoulos, A., Bonazzi, D., Zlotek-Zlotkiewicz, E., Picone, R., et al. (2013). Mitotic rounding alters cell geometry to ensure efficient bipolar spindle formation. *Dev. Cell* 25, 270–283. doi: 10.1016/j.devcel.2013.03.014

Lara-Gonzalez, P., Westhorpe, F. G., and Taylor, S. S. (2012). The spindle assembly checkpoint. *Curr. Biol.* 22, R966–R980.

Li, Q., Kumar, A., Makhija, E., and Shivashankar, G. V. (2014). The regulation of dynamic mechanical coupling between actin cytoskeleton and nucleus by matrix geometry. *Biomaterials* 35, 961–969. doi: 10.1016/j.biomaterials.2013.10.037

Linder, M. I., Kohler, M., Boersema, P., Weberruss, M., Wandke, C., Marino, J., et al. (2017). Mitotic Disassembly of nuclear pore complexes involves CDK1- and PLK1-mediated phosphorylation of key interconnecting nucleoporins. *Dev. Cell* 43, 141–156.e7.

Liu, J., Lee, K. K., Segura-Totten, M., Neufeld, E., Wilson, K. L., and Gruenbaum, Y. (2003). MAN1 and emerin have overlapping function(s) essential for chromosome segregation and cell division in *Caenorhabditis elegans*. *Proc. Natl. Acad. Sci. U.S.A.* 100, 4598–4603. doi: 10.1073/pnas.0730821100

Lombardi, M. L., Jaalouk, D. E., Shanahan, C. M., Burke, B., Roux, K. J., and Lammerding, J. (2011). The interaction between nesprins and sun proteins at the nuclear envelope is critical for force transmission between the nucleus and cytoskeleton. *J. Biol. Chem.* 286, 26743–26753. doi: 10.1074/jbc.m111.233700

Lombardi, M. L., and Lammerding, J. (2011). Keeping the LINC: the importance of nucleocytoskeletal coupling in intracellular force transmission and cellular function. *Biochem. Soc. Trans.* 39, 1729–1734. doi: 10.1042/bst20110686

Maddox, A. S., and Burridge, K. (2003). RhoA is required for cortical retraction and rigidity during mitotic cell rounding. *J. Cell Biol.* 160, 255–265. doi: 10.1083/jcb.200207130

Magidson, V., O'connell, C. B., Loncarek, J., Paul, R., Mogilner, A., and Khodjakov, A. (2011). The spatial arrangement of chromosomes during prometaphase facilitates spindle assembly. *Cell* 146, 555–567. doi: 10.1016/j.cell.2011.07.012

Malone, C. J., Misner, L., Le Bot, N., Tsai, M. C., Campbell, J. M., Ahringer, J., et al. (2003). The C. elegans hook protein, ZYG-12, mediates the essential attachment between the centrosome and nucleus. *Cell* 115, 825–836. doi: 10.1016/s0092-8674(03)00985-1

Marchesi, S., Montani, F., Deflorian, G., D'antuono, R., Cuomo, A., Bologna, S., et al. (2014). DEPDC1B coordinates de-adhesion events and cell-cycle progression at mitosis. *Dev. Cell* 31, 420–433. doi: 10.1016/j.devcel.2014.09.009

Matthews, H. K., Delabre, U., Rohn, J. L., Guck, J., Kunda, P., and Baum, B. (2012). Changes in Ect2 localization couple actomyosin-dependent cell shape changes to mitotic progression. *Dev. Cell* 23, 371–383. doi: 10.1016/j.devcel.2012.06.003

Matthews, H. K., Ganguli, S., Plak, K., Taubenberger, A. V., Win, Z., Williamson, M., et al. (2020). Oncogenic signaling alters cell shape and mechanics to facilitate cell division under confinement. *Dev. Cell* 52, 563–573.e3.

Maurer, M., and Lammerding, J. (2019). The driving force: nuclear mechanotransduction in cellular function, fate, and disease. *Annu. Rev. Biomed. Eng.* 21, 443–468. doi: 10.1146/annurev-bioeng-060418-052139

Mchedlishvili, N., Matthews, H. K., Corrigan, A., and Baum, B. (2018). Two-step interphase microtubule disassembly aids spindle morphogenesis. *BMC Biol.* 16:14. doi: 10.1186/s12915-017-0478-z

Meaburn, K. J., Cabuy, E., Bonne, G., Levy, N., Morris, G. E., Novelli, G., et al. (2007). Primary laminopathy fibroblasts display altered genome organization and apoptosis. *Aging Cell* 6, 139–153. doi: 10.1111/j.1474-9726.2007.00270.x

Mewborn, S. K., Puckelwartz, M. J., Abuisneineh, F., Fahrenbach, J. P., Zhang, Y., Macleod, H., et al. (2010). Altered chromosomal positioning, compaction, and gene expression with a lamin A/C gene mutation. *PLoS One* 5:e14342. doi: 10.1371/journal.pone.0014342

Mitchison, T. J. (1992). Actin based motility on retraction fibers in mitotic PtK2 cells. *Cell Motil. Cytoskeleton* 22, 135–151. doi: 10.1002/cm.970220207

Muhlhausser, P., and Kutay, U. (2007). An in vitro nuclear disassembly system reveals a role for the RanGTPase system and microtubule-dependent steps in nuclear envelope breakdown. *J. Cell Biol.* 178, 595–610. doi: 10.1083/jcb.200703002

Nam, H. J., Naylor, R. M., and Van Deursen, J. M. (2015). Centrosome dynamics as a source of chromosomal instability. *Trends Cell Biol.* 25, 65–73. doi: 10.1016/j.tcb.2014.10.002

Nunes, V., Dantas, M., Vitiello, E., Wang, E., Carpi, N., Balland, M., et al. (2019). Mechanosensitive nuclear asymmetries define a bipolar spindle scaffold to ensure mitotic fidelity. *bioRxiv*. [Preprint]. doi: 10.1101/526939

Nunes, V., Dantas, M., Vitiello, E., Wang, I., Carpi, N., Balland, M., et al. (2020). Centrosome-nuclear axis repositioning drives the assembly of a bipolar spindle scaffold to ensure mitotic fidelity. *Mol. Biol. Cell* 31, 1675–1690. doi: 10.1091/mbc.e20-01-0047

Pajerowski, J. D., Dahl, K. N., Zhong, F. L., Sammak, P. J., and Discher, D. E. (2007). Physical plasticity of the nucleus in stem cell differentiation. *Proc. Natl. Acad. Sci. U.S.A.* 104, 15619–15624. doi: 10.1073/pnas.0702576104

Peter, M., Nakagawa, J., Doree, M., Labbe, J. C., and Nigg, E. A. (1990). In vitro disassembly of the nuclear lamina and M phase-specific phosphorylation of lamins by cdc2 kinase. *Cell* 61, 591–602. doi: 10.1016/0092-8674(90)90471-p

Piccus, R., and Brayson, D. (2020). The nuclear envelope: LINCing tissue mechanics to genome regulation in cardiac and skeletal muscle. *Biol. Lett.* 16:20200302. doi: 10.1098/rsbl.2020.0302

Pratt, C. H., Curtain, M., Donahue, L. R., and Shopland, L. S. (2011). Mitotic defects lead to pervasive aneuploidy and accompany loss of RB1 activity in mouse *LmnaDhe* dermal fibroblasts. *PLoS One* 6:e18065. doi: 10.1371/journal.pone.0018065

Qi, R., Xu, N., Wang, G., Ren, H., Li, S., Lei, J., et al. (2015). The lamin-A/C-LAP2alpha-BAF1 protein complex regulates mitotic spindle assembly and positioning. *J. Cell Sci.* 128, 2830–2841. doi: 10.1242/jcs.164566

Ramanathan, S. P., Helenius, J., Stewart, M. P., Cattin, C. J., Hyman, A. A., and Muller, D. J. (2015). Cdk1-dependent mitotic enrichment of cortical myosin II promotes cell rounding against confinement. *Nat. Cell Biol.* 17, 148–159. doi: 10.1038/ncb3098

Ramkumar, N., and Baum, B. (2016). Coupling changes in cell shape to chromosome segregation. *Nat. Rev. Mol. Cell Biol.* 17, 511–521. doi: 10.1038/nrm.2016.75

Ranade, D., Koul, S., Thompson, J., Prasad, K. B., and Sengupta, K. (2017). Chromosomal aneuploidies induced upon Lamin B2 depletion are mislocalized in the interphase nucleus. *Chromosoma* 126, 223–244. doi: 10.1007/s00412-016-0580-y

Rieder, C. L., and Alexander, S. P. (1990). Kinetochores are transported poleward along a single astral microtubule during chromosome attachment to the spindle in newt lung cells. *J. Cell Biol.* 110, 81–95. doi: 10.1083/jcb.110.1.81

Roberts, A. J., Kon, T., Knight, P. J., Sutoh, K., and Burgess, S. A. (2013). Functions and mechanics of dynein motor proteins. *Nat. Rev. Mol. Cell Biol.* 14, 713–726. doi: 10.1038/nrm3667

Roos, U. P. (1973). Light and electron microscopy of rat kangaroo cells in mitosis. I. Formation and breakdown of the mitotic apparatus. *Chromosoma* 40, 43–82. doi: 10.1007/bf00319836

Rosa, A., Vlassaks, E., Pichaud, F., and Baum, B. (2015). Ect2/Pbl acts via Rho and polarity proteins to direct the assembly of an isotropic actomyosin cortex upon mitotic entry. *Dev. Cell* 32, 604–616. doi: 10.1016/j.devcel.2015.01.012

Salina, D., Bodoor, K., Eckley, D. M., Schroer, T. A., Rattner, J. B., and Burke, B. (2002). Cytoplasmic dynein as a facilitator of nuclear envelope breakdown. *Cell* 108, 97–107. doi: 10.1016/s0092-8674(01)00628-6

Sato, A., Isaac, B., Phillips, C. M., Rillo, R., Carlton, P. M., Wynne, D. J., et al. (2009). Cytoskeletal forces span the nuclear envelope to coordinate meiotic chromosome pairing and synapsis. *Cell* 139, 907–919. doi: 10.1016/j.cell.2009.10.039

Sawin, K. E., Leguellec, K., Philippe, M., and Mitchison, T. J. (1992). Mitotic spindle organization by a plus-end-directed microtubule motor. *Nature* 359, 540–543. doi: 10.1038/359540a0

Schreiner, S. M., Koo, P. K., Zhao, Y., Mochrie, S. G., and King, M. C. (2015). The tethering of chromatin to the nuclear envelope supports nuclear mechanics. *Nat. Commun.* 6:7159.

Silkworth, W. T., Nardi, I. K., Paul, R., Mogilner, A., and Cimini, D. (2012). Timing of centrosome separation is important for accurate chromosome segregation. *Mol. Biol. Cell* 23, 401–411. doi: 10.1091/mbc.e11-02-0095

Smith, E., Hegarat, N., Vesely, C., Roseboom, I., Larch, C., Streicher, H., et al. (2011). Differential control of Eg5-dependent centrosome separation by Plk1 and Cdk1. *EMBO J.* 30, 2233–2245. doi: 10.1038/emboj.2011.120

Smith, E. R., Capo-Chichi, C. D., and Xu, X. X. (2018). Defective nuclear lamina in aneuploidy and carcinogenesis. *Front. Oncol.* 8:529. doi: 10.3389/fonc.2018.00529

Son, S., Kang, J. H., Oh, S., Kirschner, M. W., Mitchison, T. J., and Manalis, S. (2015). Resonant microchannel volume and mass measurements show that suspended cells swell during mitosis. *J. Cell Biol.* 211, 757–763. doi: 10.1083/jcb.201505058

Splinter, D., Tanenbaum, M. E., Lindqvist, A., Jaarsma, D., Flotho, A., Yu, K. L., et al. (2010). Bicaudal D2, dynein, and kinesin-1 associate with nuclear pore complexes and regulate centrosome and nuclear positioning during mitotic entry. *PLoS Biol.* 8:e1000350. doi: 10.1371/journal.pbio.1000350

Starr, D. A., and Fridolfsson, H. N. (2010). Interactions between nuclei and the cytoskeleton are mediated by SUN-KASH nuclear-envelope bridges. *Annu. Rev. Cell Dev. Biol.* 26, 421–444. doi: 10.1146/annurev-cellbio-100109-104037

Stephens, A. D., Banigan, E. J., Adam, S. A., Goldman, R. D., and Marko, J. F. (2017). Chromatin and lamin A determine two different mechanical response regimes of the cell nucleus. *Mol. Biol. Cell* 28, 1984–1996. doi: 10.1091/mbc.e16-09-0653

Stewart, M. P., Helenius, J., Toyoda, Y., Ramanathan, S. P., Muller, D. J., and Hyman, A. A. (2011). Hydrostatic pressure and the actomyosin cortex drive mitotic cell rounding. *Nature* 469, 226–230. doi: 10.1038/nature09642

Stiff, T., Echegaray-Iturra, F. R., Pink, H. J., Herbert, A., Reyes-Aldasoro, C. C., and Hochegger, H. (2020). Prophase-specific perinuclear actin coordinates centrosome separation and positioning to ensure accurate chromosome segregation. *Cell Rep.* 31:107681. doi: 10.1016/j.celrep.2020.107681

Sun, M., Biggs, R., Hornick, J., and Marko, J. F. (2018). Condensin controls mitotic chromosome stiffness and stability without forming a structurally contiguous scaffold. *Chromosome Res.* 26, 277–295. doi: 10.1007/s10577-018-9584-1

Sun, Z., Guo, S. S., and Fassler, R. (2016). Integrin-mediated mechanotransduction. *J. Cell Biol.* 215, 445–456. doi: 10.1083/jcb.201609037

Tanenbaum, M. E., and Medema, R. H. (2010). Mechanisms of centrosome separation and bipolar spindle assembly. *Dev. Cell* 19, 797–806. doi: 10.1016/j.devcel.2010.11.011

Thery, M., and Bornens, M. (2008). Get round and stiff for mitosis. *HFSP J.* 2, 65–71. doi: 10.2976/1.2895661

Thery, M., Jimenez-Dalmaroni, A., Racine, V., Bornens, M., and Julicher, F. (2007). Experimental and theoretical study of mitotic spindle orientation. *Nature* 447, 493–496. doi: 10.1038/nature05786

Thery, M., Racine, V., Pepin, A., Piel, M., Chen, Y., Sibarita, J. B., et al. (2005). The extracellular matrix guides the orientation of the cell division axis. *Nat. Cell Biol.* 7, 947–953. doi: 10.1038/ncb1307

Toyoshima, F., and Nishida, E. (2007). Integrin-mediated adhesion orients the spindle parallel to the substratum in an EB1- and myosin X-dependent manner. *EMBO J.* 26, 1487–1498. doi: 10.1038/sj.emboj.7601599

Tse, H. T., Weaver, W. M., and Di Carlo, D. (2012). Increased asymmetric and multi-daughter cell division in mechanically confined microenvironments. *PLoS One* 7:e38986. doi: 10.1371/journal.pone.0038986

Turgay, Y., Champion, L., Balazs, C., Held, M., Toso, A., Gerlich, D. W., et al. (2014). SUN proteins facilitate the removal of membranes from chromatin during nuclear envelope breakdown. *J. Cell Biol.* 204, 1099–1109. doi: 10.1083/jcb.201310116

Ungricht, R., and Kutay, U. (2017). Mechanisms and functions of nuclear envelope remodelling. *Nat. Rev. Mol. Cell Biol.* 18, 229–245. doi: 10.1038/nrm.2016.153

Uroz, M., Wistorf, S., Serra-Picamal, X., Conte, V., Sales-Pardo, M., Roca-Cusachs, P., et al. (2018). Regulation of cell cycle progression by cell-cell and cell-matrix forces. *Nat. Cell Biol.* 20, 646–654. doi: 10.1038/s41556-018-0107-2

van Heesbeen, R. G., Raaijmakers, J. A., Tanenbaum, M. E., and Medema, R. H. (2013). Nuclear envelope-associated dynein cooperates with Eg5 to drive prophase centrosome separation. *Commun. Integr. Biol.* 6:e23841. doi: 10.4161/cib.23841

van Steensel, B., and Belmont, A. S. (2017). Lamina-associated domains: links with chromosome architecture, heterochromatin, and gene repression. *Cell* 169, 780–791. doi: 10.1016/j.cell.2017.04.022

Verde, F., Dogterom, M., Stelzer, E., Karsenti, E., and Leibler, S. (1992). Control of microtubule dynamics and length by cyclin A- and cyclin B-dependent kinases in Xenopus egg extracts. *J. Cell Biol.* 118, 1097–1108. doi: 10.1083/jcb.118.5.1097

Verde, F., Labbe, J. C., Doree, M., and Karsenti, E. (1990). Regulation of microtubule dynamics by cdc2 protein kinase in cell-free extracts of Xenopus eggs. *Nature* 343, 233–238. doi: 10.1038/343233a0

Versaevel, M., Braquenier, J. B., Riaz, M., Grevesse, T., Lantoine, J., and Gabriele, S. (2014). Super-resolution microscopy reveals LINC complex recruitment at nuclear indentation sites. *Sci. Rep.* 4:7362.

Versaevel, M., Grevesse, T., and Gabriele, S. (2012). Spatial coordination between cell and nuclear shape within micropatterned endothelial cells. *Nat. Commun.* 3:671.

Vianay, B., Senger, F., Alamos, S., Anjur-Dietrich, M., Bearce, E., Cheeseman, B., et al. (2018). Variation in traction forces during cell cycle progression. *Biol. Cell* 110, 91–96. doi: 10.1111/boc.201800006

Vitiello, E., Moreau, P., Nunes, V., Mettouchi, A., Maiato, H., Ferreira, J. G., et al. (2019). Acto-myosin force organization modulates centriole separation and PLK4 recruitment to ensure centriole fidelity. *Nat. Commun.* 10:52.

Whitehead, C. M., Winkfein, R. J., and Rattner, J. B. (1996). The relationship of HsEg5 and the actin cytoskeleton to centrosome separation. *Cell Motil. Cytoskeleton* 35, 298–308. doi: 10.1002/(sici)1097-0169(1996)35:4<298::aid-cm3>3.0.co;2-3

Yu, J., Lei, K., Zhou, M., Craft, C. M., Xu, G., Xu, T., et al. (2011). KASH protein Syne-2/Nesprin-2 and SUN proteins SUN1/2 mediate nuclear migration during mammalian retinal development. *Hum. Mol. Genet.* 20, 1061–1073. doi: 10.1093/hmg/ddq549

Zhai, Y., Kronebusch, P. J., Simon, P. M., and Borisy, G. G. (1996). Microtubule dynamics at the G2/M transition: abrupt breakdown of cytoplasmic microtubules at nuclear envelope breakdown and implications for spindle morphogenesis. *J. Cell Biol.* 135, 201–214. doi: 10.1083/jcb.135.1.201

Zhang, X., Lei, K., Yuan, X., Wu, X., Zhuang, Y., Xu, T., et al. (2009). SUN1/2 and Syne/Nesprin-1/2 complexes connect centrosome to the nucleus during neurogenesis and neuronal migration in mice. *Neuron* 64, 173–187. doi: 10.1016/j.neuron.2009.08.018

Zlotek-Zlotkiewicz, E., Monnier, S., Cappello, G., Le Berre, M., and Piel, M. (2015). Optical volume and mass measurements show that mammalian cells swell during mitosis. *J. Cell Biol.* 211, 765–774. doi: 10.1083/jcb.201505056

Conflict of Interest: The authors declare that the research was conducted in the absence of any commercial or financial relationships that could be construed as a potential conflict of interest.

frontiers in Cell and Developmental Biology

OPINION
published: 26 March 2021
doi: 10.3389/fcell.2021.649626

The Morphological Diversity of Plant Organs: Manipulating the Organization of Microtubules May Do the Trick

Zhiru Bao [1,2,3], Zhijing Xu [1,2,3], Jingze Zang [1,2,3], Katharina Bürstenbinder [4†] and Pengwei Wang [1,2,3]*

[1] Key Laboratory of Horticultural Plant Biology (MOE), College of Horticulture and Forestry Sciences, Huazhong Agricultural University, Wuhan, China, [2] Interdisciplinary Sciences Research Institute, Huazhong Agricultural University, Wuhan, China, [3] National R&D Centre for Citrus Preservation, Huazhong Agricultural University, Wuhan, China, [4] Department of Molecular Signal Processing, Leibniz Institute of Plant Biochemistry, Halle (Saale), Germany

Keywords: cytoskeleton, microtubules, cell morphogenesis, organ shape, IQD, ROP

OPEN ACCESS

Edited by:
Ting Gang Chew,
Zhejiang University-University of Edinburgh Institute, China

Reviewed by:
Deshu Lin,
Fujian Agriculture and Forestry University, China
Andrei Smertenko,
Washington State University, United States

***Correspondence:**
Pengwei Wang
wangpengwei@mail.hzau.edu.cn

†ORCID:
Katharina Bürstenbinder
orcid.org/000-0002-3493-4800

Specialty section:
This article was submitted to Cell Growth and Division, a section of the journal Frontiers in Cell and Developmental Biology

Received: 05 January 2021
Accepted: 08 March 2021
Published: 26 March 2021

Citation:
Bao Z, Xu Z, Zang J, Bürstenbinder K and Wang P (2021) The Morphological Diversity of Plant Organs: Manipulating the Organization of Microtubules May Do the Trick. Front. Cell Dev. Biol. 9:649626. doi: 10.3389/fcell.2021.649626

PLANT MICROTUBULES AND MICROTUBULE-ASSOCIATED PROTEINS

The plant cytoskeleton is a highly dynamic filamentous system and plays important roles in various intracellular processes including cell division, intracellular trafficking, immune responses, and stress tolerance (Li and Staiger, 2018; Livanos and Müller, 2019). Although both actin and microtubules are essential in the determination of cell morphology and organ shape, in this article we will mainly focus on microtubules, which are regulated by various microtubule-associated proteins (MAPs). Aberrant expression of MAPs affects microtubule organization and consequently cell function and morphogenesis (Ruan et al., 2018). Microtubules are essential in cell wall formation by guiding the directional movement of cellulose synthase complexes in the plasma membrane (PM) (Paredez et al., 2006). Perturbation of microtubule functions often leads to changes in cell wall composition and cell stiffness, ultimately affecting cell expansion and plant architecture. Loss- or gain-of-function in several MAPs and MT-related proteins, e.g., IQ67-Domain proteins (IQD) and Rho of plant GTPases (ROPs), leads to anisotropic or helical growth phenotypes in petals, cotyledons and hypocotyls, which are attributed to the alteration of microtubule organization (Yang et al., 2019; Zang et al., 2021). In dividing plant cells, microtubules form unique structures such as the preprophase band, the acentrosomal mitotic spindle, and the phragmoplast, essential for cell plate directional expansion (**Figure 1A**).

Although the structure and function of microtubules is similar across kingdoms, plants have evolved specific regulatory mechanisms to coordinate cytoskeletal functions in response to incoming signals. Within these diverse signaling pathways, calcium ions (Ca^{2+}) serve as universal second messengers and several studies implicate roles of Ca^{2+} in regulation of the cytoskeleton (Hepler, 2016). Ca^{2+} signals may be integrated at microtubules via differential binding of calmodulin (CaM)-Ca^{2+} sensors to several MAPs (Kölling et al., 2019). One class of CaM targets are IQDs, which are plant-specific microtubule binding proteins that may recruit CaM to microtubules and other specific subcellular compartments in response to Ca^{2+} signals to coordinate plant development and cell shape formation (Bürstenbinder et al., 2013, 2017; Zang et al., 2021).

THE REGULATION OF CORTICAL MICROTUBULES IN LEAF PAVEMENT CELL SHAPE

Leaf pavement cells emerged as a popular model system to study the formation of complex cell shapes. In several species, including *Arabidopsis*, pavement cells display an interlocking jigsaw puzzle-shape appearance, whose development relies on polarity establishment and is influenced by the cytoskeleton, hormonal signals, and mechanical stress (Bidhendi et al., 2019; Pan et al., 2020). The removal of actin filaments or actin regulating proteins (e.g., ARP2/3; SCAR/WAVE) leads to smaller lobes (Cifrová et al., 2020) suggesting that cortical actin filaments that localize to the growing lobe tips may regulate lobe outgrowth. In pavement cells, cortical microtubules are persistently enriched in periclinal walls at the convex side of lobes and mutants defective in MAPs often display defects in lobe formation and/or growth (Armour et al., 2015; Wong et al., 2019). Microtubules thus may generate a patch of anisotropic strain or guide a local thickening of the cell wall to restrict growth and promote lobe formation (**Figure 1B**) (Altartouri et al., 2019; Wong et al., 2019).

A recent study proposed the role of auxin gradient in regulating the pavement cell pattern through transmembrane kinase 1 (TMK1)-dependent ROP6 nanoclustering at the PM (Grones et al., 2020). The activated ROP6 nanoclusters recruit RIC1 (ROP-interactive CRIB motif-containing protein 1) effector proteins, which localize at cortical microtubules and interact with Katanin1 (KTN1) to promote microtubule ordering and lead to the formation of indentations (**Figures 1B,C**) (Ren et al., 2017; Pan et al., 2020). Interestingly, IQD13, a protein that interacts with cortical microtubules and the PM, regulates the distribution of active ROP domains on the PM in differentiating metaxylem cells (Sugiyama et al., 2017). Therefore, it is likely that IQD proteins may interact with other MAPs and regulate ROP activity in non-xylem cells in a similar way, such as IQD5 that is also enriched at indentation sites (**Figure 1C**) (Liang et al., 2018; Mitra et al., 2019; Li et al., 2020).

In contrast, other work supports a turgor-driven mechanical model for the regulation of interlocking patterns. The localized mechano-stress asymmetry could trigger the local MT rearrangement and subsequent local cellulose deposition coupled with de-esterified pectin, collectively contributing to local cell wall reinforcement, outgrowth restriction, and the formation of indentation regions (Majda et al., 2017; Bidhendi et al., 2019). Therefore, the interplay among plant hormones, microtubule regulators and mechano-sensing are complicated but exciting stories for future studies.

In addition, it is known that the structure of microtubules or actin can be influenced by each other. Cells with dysfunctional actin networks also exhibit alternations in microtubule organization (Cifrová et al., 2020). Our recent study has revealed a plant specific actin-microtubule bridging complex, consisting of Networked protein 3C (NET3C), Kinesin Light Chain-Related/Cellulose Microtubule Uncoupling1 (KLCR1/CMU1) and IQDs. These proteins localize to membrane interfaces, and cross link the ER network, PM, actin cytoskeleton, and microtubules (Zang et al., 2021). Their respective mutants all exhibit defects in pavement cell morphogenesis, implicating a function of membrane contact sites and the cytoskeleton-membrane interface in microtubule regulation (**Figure 1B**). Therefore, as the ER, PM, and cytoskeleton are closely associated, affecting membrane lipid or protein composition may also affect cytoskeleton organization, producing a net effect on cell morphologies.

MICROTUBULE REGULATING PROTEINS ARE COMMON GENETIC TRAITS FOR MORPHOLOGICAL DIVERSITY OF CROP PLANTS

Likewise, the shape determination of other plant organs is likely conserved, and fruit (or seed) shape establishment is a good example. Fruits exhibit a great diversity, from simple spherical and cylindrical structures to more complex shapes. Their morphogenesis is tightly controlled by cell expansion and cell division (**Figure 1D**). In agreement with this hypothesis, recent discoveries indicate that genes encoding microtubule related proteins are regularly identified to affect fruit shape from independent genetic mapping studies (Wu et al., 2018; Yang et al., 2020). A prominent example are IQD proteins, which emerged as key regulators of organ morphogenesis during domestication. In tomato, watermelon, cucumber, and rice, the expression level of IQDs is positively associated with elongated fruit/seed shape (Wu et al., 2011; Pan et al., 2017; Dou et al., 2018; Yang et al., 2020).

In rice, the expression level of OsIQD14 or OsIQD26 proteins, which act in auxin and brassinosteroid signaling pathways respectively, are directly related to the weight and length of grains, possibly by regulating cell proliferation in spikelet hulls through a microtubule dependent pathway (**Figure 1C**, Duan et al., 2017; Yang et al., 2020). Similarly, the tomato *sun* mutant, which exhibits higher expression of *SlIQD12*, has longer fruits than the wild type, producing excessive longitudinal cell divisions and decreased cell division in the transverse direction. This suggests that changes in the cell division patterns and rearranging directional cell expansion contribute significantly to fruit elongation (Wu et al., 2011). A recent study found that OsRac1, a member of ROP-GTPases, controls rice grain size and yield by promoting cell division (Zhang et al., 2019). In maize, *rop* mutants show asymmetric cell division in guard cells, due to the disruption of cortical division zone positioning (Humphries et al., 2011). Intriguingly, several IQD proteins identified to date localize to interphase microtubules and mitotic microtubules, including the preprophase band, mitotic spindle, or phragmoplast (Bürstenbinder et al., 2017; Liang et al., 2018). Therefore, ROP and IQD proteins may be involved in determination of cell division patterns in crop fruits and other plant organs (**Figure 1E**).

IQD proteins share hallmarks of scaffold proteins that interact with multiple MAPs, likely providing a platform for macromolecular complex assemblies that regulate the microtubule structure (Bürstenbinder et al., 2013, 2017). A recent study showed that the *Arabidopsis* MAP, Spiral2 (SPR2) physically interacts with IQD18, and this interaction is reduced

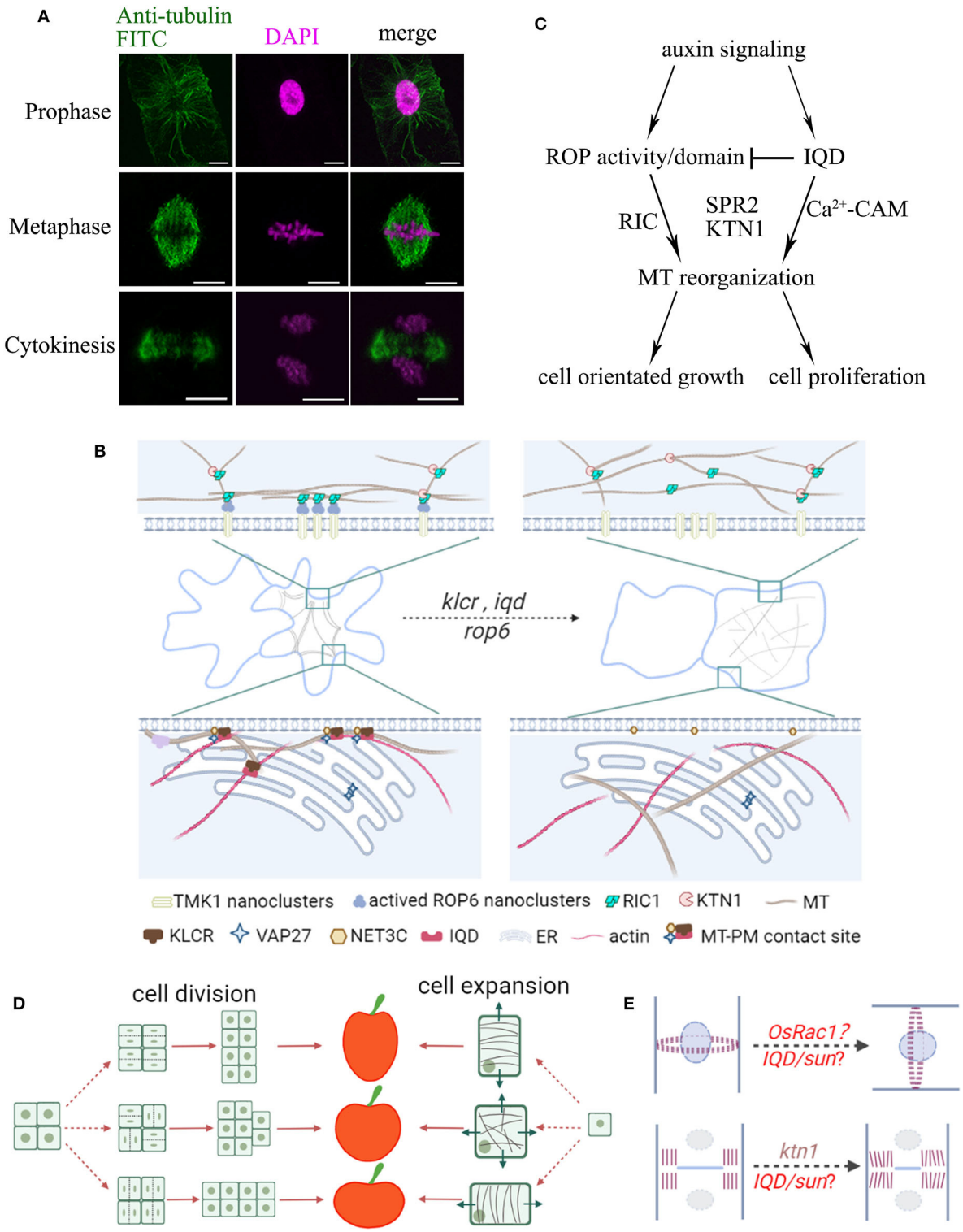

FIGURE 1 | Schematic summary of the organization of plant organ shape regulated by microtubules. **(A)** Localization of microtubules during cell division. BY-2 cells were immuno-labeled with anti-tubulin (microtubules, green) and DAPI (magenta, DNA). Microtubules rearrange throughout prophase, metaphase, and telophase to form the preprophase band (PPB), spindle apparatus, and phragmoplast, respectively. Bars, 10 μm. **(B)** Leaf pavement cells display a typical jigsaw puzzle-shape appearance. During lobe formation, cortical microtubules are enriched at convex neck regions. MT-PM contact sites may take part in reorganization of microtubule arrays through IQDs-KLCR and ROP6-RIC1 proteins, whose mutants show more circular pavement cells and disorganized cytoskeletal networks. **(C)** Model of ROP and IQD pathways and their (proposed) role in regulating cell growth and division. Auxin signals activate ROPs, and recruit RIC1, KTN1 or other MAPs to promote microtubule ordering. On the other hand, auxin signals also activate IQDs, which regulate the distribution of ROPs on the PM and the organization of microtubules,

(Continued)

FIGURE 1 | and direct the orientation of cell growth and division. **(D)** Fruit shapes are controlled by the direction of cell division and cell expansion. During anisotropic growth, the orientation of cortical microtubules is perpendicular to the direction of cell expansion. For example, in elongated fruits, cell expansion is likely oriented longitudinally and microtubules are aligned transversely. **(E)** The position of the PPB marks the site of cell division. The positional information is maintained by a polarized membrane domain, termed CDZ. The new cell wall is inserted at the cell center by the phragmoplast, which guides the growing cell plate toward the CDZ. The direction of cell division will greatly influence organ shape. Altered expression of ROPs may affect division plane positioning. Mutants in *KTN1* display delayed phragmoplast growth. Division plane determination may further be controlled by other shape regulators such as IQDs or other MAPs.

in the presence of Ca^{2+} (Wendrich et al., 2018). KTN1 severs microtubules at crossovers and promotes microtubule bundle formation. Free SPR2 may bind to microtubule minus ends and promote KTN1-dependent severing, resulting in increased microtubule dynamics (Nakamura et al., 2018; Wendrich et al., 2018). Similarly, IQDs may control cell division orientation by coordinating the severing activity of KTN1 during cytokinesis (Komis et al., 2017; Li et al., 2020). Moreover, phenotypic studies of *ktn1* mutants showed defective organization of mitotic microtubule arrays, delayed cytokinetic progression, and unstable PPB organization, all of which lead to excessive longitudinal cell divisions at ectopic positions (**Figures 1C,D**), similar to those observed in the fruit organ of *sun* mutant (Panteris et al., 2011; Komis et al., 2017; Ovečka et al., 2020).

In *Arabidopsis*, IQD5 stabilizes microtubules and regulates pavement cell morphogenesis, possibly by controlling the rates of cellulose deposition in anticlinal cell walls (Liang et al., 2018; Mitra et al., 2019). Similarly, IQD16, also termed Abnormal Shoot 6 (ABS6), mediates cortical microtubule organization, and pavement cell expansion (Bürstenbinder et al., 2017), which may involve physical interaction with the microtubule severing factor KTN1 (Li et al., 2020). Interestingly, aberrant expression of many IQD proteins changes pavement cell shape. IQDs may affect anisotropic cell expansion by recruiting CaMs and CaM-Likes (CMLs) and/or KLCR/CMUs, and rearrange the microtubule cytoskeleton topology and cellulose deposition not only during pavement cell development (**Figure 1C**) (Bürstenbinder et al., 2013; Mitra et al., 2019). Altered abundance of IQDs thus may override stress-derived growth patterns and manipulating *IQD* expression levels may provide a promising strategy in *de novo* domestication approaches to generate fruit organs with altered shape. Additionally, fruit shape is also partially regulated by proteins of the TRM (TONNEAU1 Recruiting Motif) family, which are subunits of a TTP (TON1-TRM-PP2A) complex (Spinner et al., 2013). Overexpression or loss-of-function of *TRMs* in rice and tomato changes cell elongation and cell division, producing elongated or shortened grains and fruits (Wang et al., 2015; Wu et al., 2018).

CONCLUSION AND FUTURE PERSPECTIVE

The regulation of microtubule organization is affected by multiple signals, such as plant hormones (e.g., ethylene, brassinosteroids), mechanical forces, and light (Ma et al., 2018; Ruan et al., 2018), which we have not discussed here in detail because of length constrains. It is noteworthy that plant hormones are commonly applied in agriculture. Thus, manipulating microtubule function precisely through exogenous application of these hormones may provide an alternative approach for crop cultivation, fruit shape and quality establishment. On the other hand, current studies on the function of microtubules in cell morphogenesis mainly rely on simple experimental systems, such as root and leaf pavement cells (a two-dimensional system). The real situation in fruits and other complex-shaped organs might be different. As each individual cell can sense the pressure and stereo-hinderance generated by neighboring cells, such feed-back mechanisms also affect cellular heterogeneity and microtubule organization (Long et al., 2020). Therefore, further studies of cytoskeleton structure and dynamics in more complex tissues, although challenging, will certainly advance our knowledge in the field.

AUTHOR CONTRIBUTIONS

ZB, ZX, and PW wrote the manuscript. ZB and JZ drew the schematic diagram. ZX arranged the references. KB and PW proposed some suggestions and modification opinions. All authors contributed to the article and approved the submitted version.

FUNDING

This work was supported by the National Key Research and Development Program (2018YFD1000200), NSFC grant (nos. 91854102 and 31772281), Fundamental Research Funds for the Central Universities (no. 2662018PY036) to PW and by core-funding of the Leibniz Society and grants of the Deutsche Forschungsgemeinschaft (DFG, BU2955/1-1 and BU2955/2-1), and the German-Israeli Foundation for Scientific Research and Development (GIF) to KB.

ACKNOWLEDGMENTS

We greatly acknowledge the work conducted in the field of cytoskeleton research and apologize to all authors whose primary research could not be cited due to space limitations.

REFERENCES

Altartouri, B., Bidhendi, A. J., Tani, T., Suzuki, J., Conrad, C., Chebli, Y., et al. (2019). Pectin chemistry and cellulose crystallinity govern pavement cell morphogenesis in a multi-step mechanism. *Plant Physiol.* 181, 127–141. doi: 10.1104/pp.19.00303

Armour, W. J., Barton, D. A., Law, A. M., and Overall, R. L. (2015). Differential growth in periclinal and anticlinal walls during lobe formation in *Arabidopsis* cotyledon pavement cells. *Plant Cell* 27, 2484–2500. doi: 10.1105/tpc.114.126664

Bidhendi, A. J., Altartouri, B., Gosselin, F. P., and Geitmann, A. (2019). Mechanical stress initiates and sustains the morphogenesis of wavy leaf epidermal cells. *Cell Rep.* 28, 1237–1250. doi: 10.1016/j.celrep.2019.07.006

Bürstenbinder, K., Möller, B., Plötner, R., Stamm, G., Hause, G., Mitra, D., et al. (2017). The IQD family of calmodulin-binding proteins links calcium signaling to microtubules, membrane subdomains, and the nucleus. *Plant Physiol.* 173, 1692–1708. doi: 10.1104/pp.16.01743

Bürstenbinder, K., Savchenko, T., Müller, J., Adamson, A. W., Stamm, G., Kwong, R., et al. (2013). *Arabidopsis* calmodulin-binding protein IQ67-domain 1 localizes to microtubules and interacts with kinesin light chain-related protein-1. *J. Biol. Chem.* 288, 1871–1882. doi: 10.1074/jbc.M112.396200

Cifrová, P., Oulehlová, D., Kollárová, E., Martinek, J., Rosero, A., Žárský, V., et al. (2020). Division of labor between two actin nucleators-the Formin FH1 and the ARP2/3 complex-in *Arabidopsis* epidermal cell morphogenesis. *Front. Plant Sci.* 11:148. doi: 10.3389/fpls.2020.00148

Dou, J., Zhao, S., Lu, X., He, N., Zhang, L., Ali, A., et al. (2018). Genetic mapping reveals a candidate gene (ClFS1) for fruit shape in watermelon (*Citrullus lanatus* L.). *Theor. Appl. Genet.* 131, 947–958. doi: 10.1007/s00122-018-3050-5

Duan, P., Xu, J., Zeng, D., Zhang, B., Geng, M., Zhang, G., et al. (2017). Natural variation in the promoter of GSE5 contributes to grain size diversity in rice. *Mol. Plant.* 10, 685–694. doi: 10.1016/j.molp.2017.03.009

Grones, P., Majda, M., Doyle, S. M., Van Damme, D., and Robert, S. (2020). Fluctuating auxin response gradients determine pavement cell-shape acquisition. *Proc. Natl. Acad. Sci. U.S.A.* 117, 16027–16034. doi: 10.1073/pnas.2007400117

Hepler, P. K. (2016). The cytoskeleton and its regulation by calcium and protons. *Plant Physiol.* 170, 3–22. doi: 10.1104/pp.15.01506

Humphries, J. A., Vejlupkova, Z., Luo, A., Meeley, R. B., Sylvester, A. W., Fowler, J. E., et al. (2011). ROP GTPases act with the receptor-like protein PAN1 to polarize asymmetric cell division in maize. *Plant Cell* 23, 2273–2284. doi: 10.1105/tpc.111.085597

Kölling, M., Kumari, P., and Bürstenbinder, K. (2019). Calcium- and calmodulin-regulated microtubule-associated proteins as signal-integration hubs at the plasma membrane-cytoskeleton nexus. *J. Exp. Bot.* 70, 387–396. doi: 10.1093/jxb/ery397

Komis, G., Luptovčiak, I., Ovečka, M., Samakovli, D., Šamajová, O., and Šamaj, J. (2017). Katanin effects on dynamics of cortical microtubules and mitotic arrays in *Arabidopsis thaliana* revealed by advanced live-cell imaging. *Front. Plant Sci.* 8:866. doi: 10.3389/fpls.2017.00866

Li, J., and Staiger, C. J. (2018). Understanding cytoskeletal dynamics during the plant immune response. *Annu. Rev. Phytopathol.* 56, 513–533. doi: 10.1146/annurev-phyto-080516-035632

Li, Y., Deng, M., Liu, H., Li, Y., Chen, Y., Jia, M., et al. (2020). ABNORMAL SHOOT 6 interacts with KATANIN 1 and SHADE AVOIDANCE 4 to promote cortical microtubule severing and ordering in *Arabidopsis*. *J. Integr. Plant Biol.* doi: 10.1111/jipb.13003. [Epub ahead of print].

Liang, H., Zhang, Y., Martinez, P., Rasmussen, C. G., Xu, T., and Yang, Z. (2018). The microtubule-associated protein IQ67 DOMAIN5 modulates microtubule dynamics and pavement cell shape. *Plant Physiol.* 177, 1555–1568. doi: 10.1104/pp.18.00558

Livanos, P., and Müller, S. (2019). Division plane establishment and cytokinesis. *Annu. Rev. Plant Biol.* 70, 239–267. doi: 10.1146/annurev-arplant-050718-100444

Long, Y., Cheddadi, I., Mosca, G., Mirabet, V., Dumond, M., Kiss, A., et al. (2020). Cellular heterogeneity in pressure and growth emerges from tissue topology and geometry. *Curr. Biol.* 30, 1504–1516. doi: 10.1016/j.cub.2020.02.027

Ma, Q., Wang, X., Sun, J., and Mao, T. (2018). Coordinated regulation of hypocotyl cell elongation by light and ethylene through a microtubule destabilizing protein. *Plant Physiol.* 176, 678–690. doi: 10.1104/pp.17.01109

Majda, M., Grones, P., Sintorn, I. M., Vain, T., Milani, P., Krupinski, P., et al. (2017). Mechanochemical polarization of contiguous cell walls shapes plant pavement cells. *Dev. Cell* 43, 290-304.e4. doi: 10.1016/j.devcel.2017.10.017

Mitra, D., Klemm, S., Kumari, P., Quegwer, J., Möller, B., Poeschl, Y., et al. (2019). Microtubule-associated protein IQ67 DOMAIN5 regulates morphogenesis of leaf pavement cells in *Arabidopsis thaliana*. *J. Exp. Bot.* 70, 529–543. doi: 10.1093/jxb/ery395

Nakamura, M., Lindeboom, J. J., Saltini, M., Mulder, B. M., and Ehrhardt, D. W. (2018). SPR2 protects minus ends to promote severing and reorientation of plant cortical microtubule arrays. *J. Cell Biol.* 217, 915–927. doi: 10.1083/jcb.201708130

Ovečka, M., Luptovčiak, I., Komis, G., Šamajová, O., Samakovli, D., and Šamaj, J. (2020). Spatiotemporal pattern of ectopic cell divisions contribute to mis-shaped phenotype of primary and lateral roots of katanin1 mutant. *Front. Plant Sci.* 11:734. doi: 10.3389/fpls.2020.00734

Pan, X., Fang, L., Liu, J., Senay-Aras, B., Lin, W., Zheng, S., et al. (2020). Auxin-induced signaling protein nanoclustering contributes to cell polarity formation. *Nat. Commun.* 11:3914. doi: 10.1038/s41467-020-17602-w

Pan, Y., Liang, X., Gao, M., Liu, H., Meng, H., Weng, Y., et al. (2017). Round fruit shape in WI7239 cucumber is controlled by two interacting quantitative trait loci with one putatively encoding a tomato SUN homolog. *Theor. Appl. Genet.* 130, 573–586. doi: 10.1007/s00122-016-2836-6

Panteris, E., Adamakis, I. D., Voulgari, G., and Papadopoulou, G. (2011). A role for katanin in plant cell division: microtubule organization in dividing root cells of fra2 and lue1 *Arabidopsis thaliana* mutants. *Cytoskeleton* 68, 401–413. doi: 10.1002/cm.20522

Paredez, A. R., Somerville, C. R., and Ehrhardt, D. W. (2006). Visualization of cellulose synthase demonstrates functional association with microtubules. *Science* 312, 1491–1495. doi: 10.1126/science.1126551

Ren, H., Dang, X., Cai, X., Yu, P., Li, Y., Zhang, S., et al. (2017). Spatio-temporal orientation of microtubules controls conical cell shape in *Arabidopsis thaliana* petals. *PLoS Genet.* 13:e1006851. doi: 10.1371/journal.pgen.1006851

Ruan, Y., Halat, L. S., Khan, D., Jancowski, S., Ambrose, C., Belmonte, M. F., et al. (2018). The microtubule-associated protein CLASP sustains cell proliferation through a brassinosteroid signaling negative feedback loop. *Curr. Biol.* 28, 2718–2729. doi: 10.1016/j.cub.2018.06.048

Spinner, L., Gadeyne, A., Belcram, K., Goussot, M., Moison, M., Duroc, Y., et al. (2013). A protein phosphatase 2A complex spatially controls plant cell division. *Nat. Commun.* 4:1863. doi: 10.1038/ncomms2831

Sugiyama, Y., Wakazaki, M., Toyooka, K., Fukuda, H., and Oda, Y. (2017). A novel plasma membrane-anchored protein regulates xylem cell-wall deposition through microtubule-dependent lateral inhibition of Rho GTPase domains. *Curr. Biol.* 27, 2522–2528. doi: 10.1016/j.cub.2017.06.059

Wang, Y., Xiong, G., Hu, J., Jiang, L., Yu, H., Xu, J., et al. (2015). Copy number variation at the GL7 locus contributes to grain size diversity in rice. *Nat. Genet.* 47, 944–948. doi: 10.1038/ng.3346

Wendrich, J., Yang, B. J., Mijnhout, P., Xue, H. W., De Rybel, B., and Weijers, D. (2018). IQD proteins integrate auxin and calcium signaling to regulate microtubule dynamics during *Arabidopsis* development. *bioRxiv* [Preprint] 275560. doi: 10.1101/275560

Wong, J. H., Kato, T., Belteton, S. A., Shimizu, R., Kinoshita, N., Higaki, T., et al. (2019). Basic Proline-Rich Protein-mediated microtubules are essential for lobe growth and flattened cell geometry. *Plant Physiol.* 181, 1535–1551. doi: 10.1104/pp.19.00811

Wu, S., Xiao, H., Cabrera, A., Meulia, T., and van der Knaap, E. (2011). SUN regulates vegetative and reproductive organ shape by changing cell division patterns. *Plant Physiol.* 157, 1175–1186. doi: 10.1104/pp.111.181065

Wu, S., Zhang, B., Keyhaninejad, N., Rodríguez, G. R., Kim, H. J., Chakrabarti, M., et al. (2018). A common genetic mechanism underlies morphological diversity in fruits and other plant organs. *Nat. Commun.* 9:4734. doi: 10.1038/s41467-018-07216-8

Yang, B., Wendrich, J. R., De, Rybel B., Weijers, D., and Xue, H. W. (2020). Rice microtubule-associated protein IQ67-DOMAIN14 regulates grain shape by modulating microtubule cytoskeleton dynamics. *Plant Biotechnol. J.* 18, 1141–1152. doi: 10.1111/pbi.13279

Yang, Y., Huang, W., Wu, E., Lin, C., Chen, B., and Lin, D. (2019). Cortical microtubule organization during petal morphogenesis in *Arabidopsis*. *Int. J. Mol. Sci.* 20:4913. doi: 10.3390/ijms 20194913

Zang, J., Klemm, S., Pain, C., Duckney, P., Bao, Z., Stamm, G., et al. (2021). A novel plant actin-microtubule bridging complex regulates cytoskeletal and ER structure at ER-plasma membrane contact sites. *Curr. Biol.* 31, 1–10. doi: 10.1016/j.cub.2020.12.009

Zhang, Y., Xiong, Y., Liu, R., Xue, H. W., and Yang, Z. (2019). The Rho-family GTPase OsRac1 controls rice grain size and yield by regulating cell division. *Proc. Natl. Acad. Sci. U.S.A.* 116, 16121–16126. doi: 10.1073/pnas. 1902321116

Conflict of Interest: The authors declare that the research was conducted in the absence of any commercial or financial relationships that could be construed as a potential conflict of interest.

frontiers in Cell and Developmental Biology

REVIEW
published: 01 April 2021
doi: 10.3389/fcell.2021.653801

The Nuclear Mitotic Apparatus (NuMA) Protein: A Key Player for Nuclear Formation, Spindle Assembly, and Spindle Positioning

Tomomi Kiyomitsu and Susan Boerner*

Cell Division Dynamics Unit, Okinawa Institute of Science and Technology Graduate University, Onna-son, Japan

The nuclear mitotic apparatus (NuMA) protein is well conserved in vertebrates, and dynamically changes its subcellular localization from the interphase nucleus to the mitotic/meiotic spindle poles and the mitotic cell cortex. At these locations, NuMA acts as a key structural hub in nuclear formation, spindle assembly, and mitotic spindle positioning, respectively. To achieve its variable functions, NuMA interacts with multiple factors, including DNA, microtubules, the plasma membrane, importins, and cytoplasmic dynein. The binding of NuMA to dynein via its N-terminal domain drives spindle pole focusing and spindle positioning, while multiple interactions through its C-terminal region define its subcellular localizations and functions. In addition, NuMA can self-assemble into high-ordered structures which likely contribute to spindle positioning and nuclear formation. In this review, we summarize recent advances in NuMA's domains, functions and regulations, with a focus on human NuMA, to understand how and why vertebrate NuMA participates in these functions in comparison with invertebrate NuMA-related proteins.

Keywords: NuMA, spindle, nuclear formation, dynein, Ran-GTP

OPEN ACCESS

Edited by:
Anne Straube,
University of Warwick,
United Kingdom

Reviewed by:
Andreas Merdes,
Centre de Biologie Intégrative (CBI),
France
Sachin Kotak,
Indian Institute of Science (IISc), India
Sander Van Den Heuvel,
Utrecht University, Netherlands

****Correspondence:***
Tomomi Kiyomitsu
tomomi.kiyomitsu@oist.jp

Specialty section:
This article was submitted to Cell Growth and Division, a section of the journal Frontiers in Cell and Developmental Biology

Received: *15 January 2021*
Accepted: *10 March 2021*
Published: *01 April 2021*

Citation:
Kiyomitsu T and Boerner S (2021) The Nuclear Mitotic Apparatus (NuMA) Protein: A Key Player for Nuclear Formation, Spindle Assembly, and Spindle Positioning. Front. Cell Dev. Biol. 9:653801. doi: 10.3389/fcell.2021.653801

INTRODUCTION

The nuclear mitotic apparatus (NuMA) protein was initially identified as a non-histone chromatin protein in human cell lines (Lydersen et al., 1980) and named after its localization pattern to both the interphase nucleus and mitotic spindle poles (Lydersen and Pettijohn, 1980; **Figure 1A**). Since NuMA's dynamic translocation from the nucleus to the spindle poles was different from previously characterized nuclear components, NuMA was regarded as a novel class of nuclear protein, involved in both mitosis and nuclear reformation (Compton and Cleveland, 1994). Over the last 40 years, NuMA has been extensively studied in mammalian cultured cells, *Xenopus* egg extracts, and other vertebrate models (Cleveland, 1995; Sun and Schatten, 2006; Radulescu and Cleveland, 2010). One of the key findings early on was that NuMA interacts with cytoplasmic dynein to tether microtubules to spindle poles (Merdes et al., 1996). Later studies confirmed and expanded upon this result, positioning NuMA as a mitotic dynein adaptor, as described below.

Another important finding was that NuMA interacts with leucine/glycine/asparagine-repeat-containing protein (LGN) to form the evolutionarily conserved NuMA/LGN/Gαi complex at the mitotic cell cortex (Du and Macara, 2004). This study led to the discovery that NuMA plays a conserved role at the mitotic cell cortex for spindle positioning like *C. elegans* LIN-5

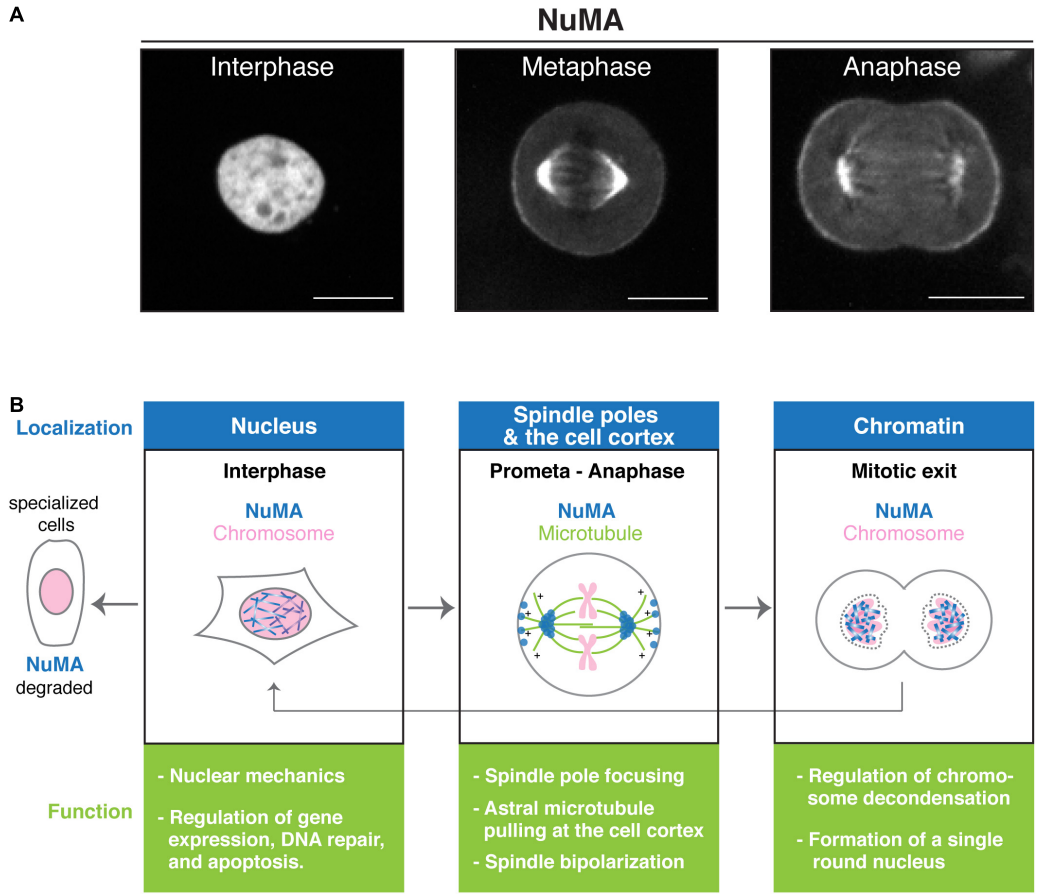

FIGURE 1 | Nuclear mitotic apparatus (NuMA's) functions during the cell cycle. **(A)** Images of endogenous NuMA fused with mClover in human HCT116 cells (Okumura et al., 2018). NuMA accumulates in the nucleus in interphase, but mainly localizes at the spindle poles in metaphase. NuMA is also targeted to the cell cortex near the spindle poles during metaphase, and the level increases during anaphase (Collins et al., 2012; Kiyomitsu and Cheeseman, 2013; Kotak et al., 2013; Seldin et al., 2013; Zheng et al., 2014). Scale bars = 10 μm. **(B)** Schematic showing how NuMA (blue) dynamically changes its subcellular localization during the cell cycle. Chromosomes and microtubules are shown in pink and green, respectively. Key functions of NuMA at these locations are summarized.

(Lorson et al., 2000; Srinivasan et al., 2003) and *Drosophila* Mud [Bowman et al., 2006; Izumi et al., 2006; Siller et al., 2006; The first publication is Lorson et al. (2000)]. Building on this, and other pioneering work on asymmetric cell division in *C. elegans* and *Drosophila* (Galli and van den Heuvel, 2008; Gonczy, 2008; Siller and Doe, 2009), further studies have established the conceptual framework that cortical cues converge on a conserved ternary complex, NuMA/LGN/Gαi in vertebrates, Lin-5/GPR-1/2/Gα in *C. elegans*, and Mud/Pins/Gα in *Drosophila*, that recruits and activates dynein to position the spindle in asymmetric division (Lechler and Fuchs, 2005; Poulson and Lechler, 2010; Morin and Bellaiche, 2011; Williams et al., 2011). In symmetrically-dividing vertebrate cells, the NuMA/LGN/Gαi complex is also involved in recruiting dynein and controlling spindle position and orientation (**Figure 1A**; Woodard et al., 2010; Peyre et al., 2011; Collins et al., 2012; Kiyomitsu and Cheeseman, 2012; Kotak et al., 2012; Kiyomitsu, 2019).

Interestingly, the cortical function seems to be most conserved in NuMA-related proteins. For example, LIN-5 and Mud localize at both spindle poles and the cell cortex, but only serve an essential function at the cell cortex for spindle positioning and are non-essential for bipolar spindle assembly (Lorson et al., 2000; Bowman et al., 2006; Izumi et al., 2006; Siller et al., 2006). In addition, yeast Num1 was recently proposed as a functional homolog of NuMA based on its functional similarities at the cell cortex (Greenberg et al., 2018). Intriguingly, plants lack a homolog of NuMA, as well as cytoplasmic dynein (Yamada and Goshima, 2017), suggesting that plants have developed alternative mechanisms to control nuclear formation, spindle assembly and positioning.

In the last 10 years, many functional domains of human NuMA were identified, providing useful information to understand NuMA's functions and regulations at the molecular level. In this review, we focus on vertebrate NuMA because several features, such as nuclear localization, appear to be specific to this group. We begin with an overview of the localization and the structural domains of the human NuMA protein, and then discuss how vertebrate NuMA participates in spindle assembly, spindle positioning and nuclear formation.

LOCALIZATION AND AN OVERALL STRUCTURE OF NuMA

In cultured human cells, NuMA accumulates in the nucleus in interphase and at the spindle poles and cell cortex during mitosis (**Figure 1A**). NuMA's spindle-pole localization is most likely conserved in all cell types, including meiotic cells (Taimen et al., 2004; Alvarez Sedo et al., 2011; Kolano et al., 2012), but its nuclear and cortical localization may vary in different developmental contexts: nuclear NuMA is degraded in some specialized cells, such as smooth and skeletal muscle fibers (Merdes and Cleveland, 1998; **Figure 1B** left). Furthermore, cortical NuMA targeting is differentially regulated between symmetric and asymmetric division in mouse epidermal cells (Poulson and Lechler, 2010).

Human NuMA is a large (∼238 kDa) protein that consists of N-terminal and C-terminal globular domains and a central long coiled-coil domain (Compton et al., 1992; Yang et al., 1992; **Figure 2A**). Full length NuMA expressed in *E. coli* forms a homo-dimer using the coiled-coil region (Harborth et al., 1995; Forth et al., 2014). Purified NuMA shows a long rod-shaped structure that has globular ends and a central long (∼210 nm) α-helical domain that appears more or less flexible (Harborth et al., 1995, 1999; **Figure 2A**). The globular domains interact with many factors, whereas the central region has structural and likely intramolecular regulatory roles as described below.

DYNEIN-BINDING DOMAINS IN THE N-TERMINAL REGION OF NuMA

The N-terminal region is required to interact with cytoplasmic dynein and dynactin complexes during mitosis (Kotak et al., 2012). A recent structural study revealed that NuMA$^{1-153}$ contains a Hook domain that directly interacts with dynein light intermediate chain (LIC) 1 and 2 (Renna et al., 2020; **Figure 2B**; all domains are listed in **Table 1**). The authors also identified a CC1-box like motif, NuMA$^{360-385}$, adjacent to the Hook domain which forms part of the binding interface between NuMA and LIC (Renna et al., 2020; **Figure 2B**). In addition, NuMA$^{417-422}$ contains a Spindly-like motif which is well conserved in vertebrates (Okumura et al., 2018; Tsuchiya et al., 2021), and may interact with the dynactin point-end complex (Gama et al., 2017; Lee et al., 2020). As NuMA$^{1-505}$, but not NuMA$^{1-413}$ and NuMA$^{214-705}$, is sufficient for dynein recruitment to the cell cortex (Okumura et al., 2018), multiple interaction sites in the N-terminal region appear to be important to stably interact with the dynein-dynactin complex during mitosis. These studies indicate that NuMA acts as a dynein activating adaptor (Lee et al., 2020), but in contrast to other established dynein adaptors such as BICD2 (McKenney et al., 2014; Schlager et al., 2014), its ability to form a ternary complex with purified dynein and dynactin and activate dynein motility *in vitro* has not been shown; post translational modifications may be required to form dynein–dynactin–NuMA complexes during mitosis.

On the other hand, the interphase role of the N-terminal region of NuMA is not clear. Although both N-terminal and C-terminal globular domains contain several S/TPXX motifs which are supposed to contribute to DNA binding (Suzuki, 1989), the N-terminal NuMA fragments do not show clear DNA or chromatin binding compared to NuMA's C-terminal (Serra-Marques et al., 2020). However, the N-terminal domain may contribute to the lattice formation of NuMA oligomers in the nucleus (Gueth-Hallonet et al., 1998; Harborth et al., 1999), as described below.

THE CENTRAL LONG COILED-COIL DOMAIN OF NuMA

Electron micrographs of recombinant human NuMA indicate that the central region forms a long flexible rod-shaped structure (Harborth et al., 1995; **Figure 2A**). One of most important functions of the central region is homo-dimerization. *In vitro* studies suggest that either the N-terminal (199–432 or 1–400 a.a) or C-terminal part (670–1700 a.a.) of the central coiled-coil is sufficient to form a homo-dimer (Harborth et al., 1995; Forth et al., 2014). Dimerization is most likely critical for most NuMA functions, including dynein binding via its N-terminal Hook domain (Renna et al., 2020) and microtubule cross-linking activities via the C-terminal domain (Forth et al., 2014).

The predicted long coiled-coil region of vertebrate NuMA proteins, which exceeds 1,000 a.a. in length, is likely to perform other important functions. Transient overexpression of wild type NuMA in HeLa cells induced a regular nuclear lattice structure which has quasi-hexagonal organization (Gueth-Hallonet et al., 1998). Interestingly, an addition or deletion in the coiled-coil domain changed the spacing of the hexagons, suggesting that the central coiled-coil defines the length of the nuclear lattice structure (Gueth-Hallonet et al., 1998; Harborth et al., 1999).

Recently, Serra-Marques et al. (2020) found that the long coiled-coil is also required for the formation of a single, round nucleus, and that this role is independent from NuMA's role in spindle formation. In addition, the authors revealed that a small portion of the coiled-coil$^{213-705}$ is sufficient to prevent NuMA's C-terminal region from binding chromosomes during late metaphase and anaphase (Serra-Marques et al., 2020).

At the mitotic cell cortex, the coiled-coil region of NuMA$^{706-1699}$ is required to generate proper spindle pulling forces when NuMA constructs are targeted to the membrane during mitosis (Okumura et al., 2018). However, the coiled-coil region is dispensable for bipolar spindle formation (Hueschen et al., 2017). At the cell cortex, the long coiled-coil may be used to separate dynein from the actin-rich cell cortex and/or to increase the efficiency of astral microtubule capture by cortical NuMA-dynein complexes during mitosis (Kiyomitsu, 2019).

MICROTUBULE-BINDING DOMAINS IN NuMA'S C-TERMINAL REGION

The C-terminal globular region of NuMA$^{1700-2115}$ contains several important domains that determine its localization and function (**Figure 2C**). First, this region contains two

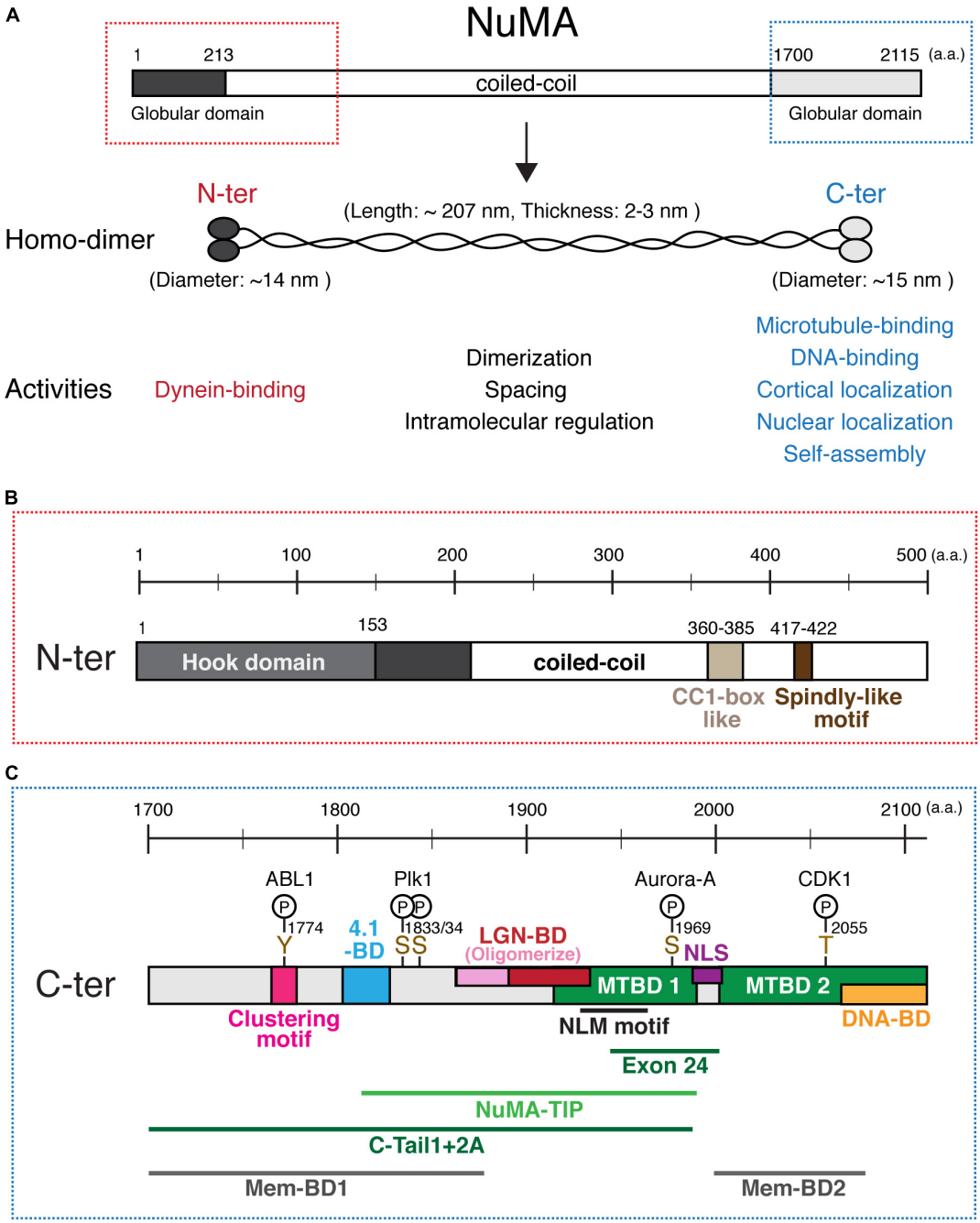

FIGURE 2 | NuMA's domain structure. **(A)** Diagrams of full length NuMA. Human NuMA isoform 1 (NP_006176) consists of 2,115 amino acids (a.a.) (Yang et al., 1992), whereas NuMA isoform 2 (NP_001273490) is lacking 14 a.a. at the 1,539–1,552 region (Compton et al., 1992). In this review, we refer to isoform 1. NuMA forms a homodimer through its central coiled-coil region. The central rod-shaped structure has an average length of ~207 nm and a thickness of ~2–3 nm, while N-terminal and C-terminal globular structures show a diameter of ~14 and ~15 nm, respectively (Harborth et al., 1995). **(B)** Domains in the N-terminal region. **(C)** Domains, motifs, phosphorylation sites, and functional regions in the C-terminal region of NuMA. See the text and **Table 1** for details. NuMA$^{1944-2003}$, corresponding to either exon 22 for mice or exon 24 for human, was deleted in Silk et al. (2009); Kolano et al. (2012), and Tsuchiya et al. (2021), instead of depleting the complete MTBD1.

microtubule binding domains (MTBDs); here we refer to them as MTBD1$^{1914-1985}$ (Du et al., 2002) and MTBD2$^{2002-2115}$ (Gallini et al., 2016; Chang et al., 2017; **Figure 2C**). Although MTBD1 has weaker microtubule-binding affinity than MTBD2 *in vitro* (Chang et al., 2017), MTBD1 contains the conserved NuMA–LIN-5–Mud (NLM) motif$^{1922-1957}$ (Siller et al., 2006) and acts to establish and maintain spindle-pole focusing (**Figure 3A**) in mouse fibroblasts (Silk et al., 2009), mouse

TABLE 1 | A summary of NuMA's domain and modifications.

Region (a.a.)	Domain and modification	References
1–153	Hook domain that interacts with LIC 1 and 2	Renna et al., 2020
1–213	Globular domain	Radulescu and Cleveland, 2010
1–505	Sufficient for cortical dynein recruitment	Okumura et al., 2018
360–385	CC1-box like motif	Renna et al., 2020
417–422	Spindly-like motif	Okumura et al., 2018; Tsuchiya et al., 2021
199–432	Dimerization	Harborth et al., 1995
670–1700	Dimerization	Harborth et al., 1995
1–400	Dimerization	Forth et al., 2014
Coiled-coil region (706–1699)	Required for spindle pulling force generation. Inhibits chromatin binding during anaphase and promotes the formation of a single round nucleus	Okumura et al., 2018; Serra-Marques et al., 2020
1699–1876	Membrane binding region (Mem-BD) 1	Kotak et al., 2014
1701–1725	Cleavage site during apoptosis	Gueth-Hallonet et al., 1997
1701–1981	C-tail1 + 2A: sufficient for minus-end targeting	Hueschen et al., 2017
1768–1777	Clustering domain	Okumura et al., 2018
1788–1925	Sufficient for metaphase cortical localization	Seldin et al., 2013
1802–1824	4.1 protein binding region	Mattagajasingh et al., 2009
1811–1985	NuMA-TIP	Seldin et al., 2016
1861–1928	Longer binding region of LGN^{7-367}	Pirovano et al., 2019
1900–1926	Minimal binding region of LGN	Zhu et al., 2011b
1914–1985	Microtubule binding domain (MTBD) 1	Du et al., 2002
1922–1957	NLM motif	Siller et al., 2006
1944–2003	Human exon 24 (=mouse exon 22)	Silk et al., 2009; Gallini et al., 2016
1996–2074	Membrane binding region (Mem-BD) 2	Zheng et al., 2014
1988–2005	NLS sequence	Tang et al., 1994; Chang et al., 2017
2002–2115	Microtubule binding domain (MTBD) 2	Gallini et al., 2016; Chang et al., 2017
2058–2115	DNA binding domain	Rajeevan et al., 2020
Y1774	Phosphorylation residue by ABL1	Matsumura et al., 2012
SS1833/34	Phosphorylation residues by Plk1	Kettenbach et al., 2011
S1969	Phosphorylation residue by Aurora-A kinase (at spindle pole)	Gallini et al., 2016; Kotak et al., 2016
T2055	Phosphorylation residue by CDK (during metaphase)	Compton and Luo, 1995; Kotak et al., 2013
Full length NuMA	MARs (DNA sequence) binding	Luderus et al., 1994

meiosis I spindle (Kolano et al., 2012), and human HCT116 cells (Tsuchiya et al., 2021).

In some cells, such as mouse keratinocytes, MTBD1 is not required for spindle pole focusing, but is required for spindle orientation (Seldin et al., 2016). Full length NuMA accumulates at the minus-end of microtubules, and the $NuMA^{1701-1981}$ fragment, called C-Tail1 + 2A, is sufficient for minus-end recognition (Hueschen et al., 2017). In addition, NuMA's dimerized C-terminal fragment that crosslinks two parallel microtubules tends to move in the minus-end direction under forces (Forth et al., 2014). However, intriguingly, the $NuMA^{1811-1985}$ fragment, called NuMA-TIP, appears to preferentially accumulate at the curling microtubule ends, and can remain attached to the depolymerizing microtubule plus-end (Seldin et al., 2016). The authors propose that this unique property of MTBD1 may be important to facilitate the interaction of astral microtubule plus-ends with NuMA at the cell cortex during spindle orientation (Seldin et al., 2016). However, in human cells, MTBD2, but not MTBD1, is required for spindle pulling activity when NuMA constructs are targeted to the cell cortex (Okumura et al., 2018). Interestingly, MTBD2 can bind both the microtubule lattice and tubulin dimers (Pirovano et al., 2019), indicating that MTBD2 may act not only for astral microtubule binding, but also for regulating plus-end dynamics of astral microtubules during the cortical pulling-force generation. How and when the MTBDs come into play during spindle pole focusing and orientation likely depends on the cellular context (Borgal and Wakefield, 2018).

CORTICAL TARGETING DOMAINS IN NuMA'S C-TERMINAL REGION

NuMA's C-terminal domain also defines its cortical localization during mitosis by binding to LGN, band 4.1 proteins and the plasma membrane. Whereas LGN is targeted to the cell cortex by binding to GDP-bound Gαi through its C-terminal GoLoco motif, LGN binds and links NuMA to the cell cortex using its N-terminal TPR motif (**Figure 3B**). LGN and Gαi are indispensable for cortical localization of NuMA in metaphase (Du and Macara, 2004; Woodard et al., 2010; Kiyomitsu and Cheeseman, 2012; Kotak et al., 2012). Zhu et al. (2011b) identified the $NuMA^{1900-1926}$ peptide as the minimal region required to bind to the inner groove of LGN^{TPR}. This LGN-binding domain partially overlaps with MTBD1 (**Figure 2C**), and LGN binding thus inhibits the microtubule binding activity of NuMA *in vitro* (Du et al., 2002; **Figure 3**, green asterisk). Recently, Pirovano et al. (2019) revealed that a longer $NuMA^{1861-1928}$ region forms a hetero-hexamer with LGN^{7-367}, in which an extended $NuMA^{1861-1880}$ region hooks onto an adjacent LGN to form oligomers. Consistently, expression of a longer $NuMA^{1788-1925}$ fragment is targeted to the LGN-localizing metaphase cell cortex, whereas a shorter one, $NuMA^{1892-1925}$, is not (Seldin et al., 2013).

However, given the complicated cortical protein network, additional mechanisms might contribute to cortical NuMA–LGN targeting and stability. In fact, it has been shown that

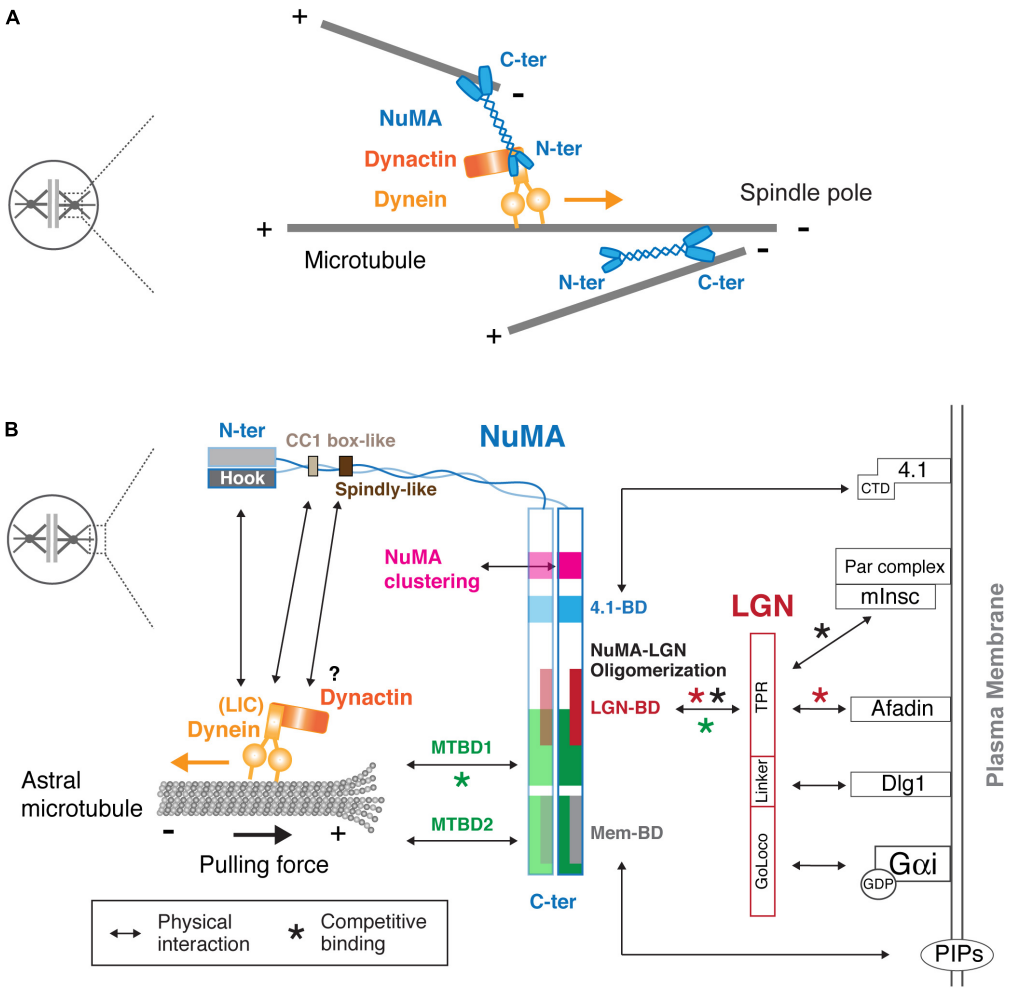

FIGURE 3 | Physical interaction map of NuMA at the spindle pole and the mitotic cell cortex. **(A)** Models of the spindle pole focusing function of NuMA. Using two microtubule-binding C-terminal globular domains, the NuMA homodimer bundles and crosslinks microtubules around the spindle pole region (Radulescu and Cleveland, 2010; Forth et al., 2014). In addition, NuMA recognizes the minus-ends of spindle microtubules and recruits the dynein-dynactin complex, which transports NuMA-bound spindle microtubules toward poles, resulting in microtubule focusing at the poles (Hueschen et al., 2017). See text for details. **(B)** NuMA interacts with the cortical proteins and plasma membrane through its C-terminal region, whereas it binds to dynein and dynactin via its N-terminal region. Arrows indicate physical interactions. As indicated by red asterisks, NuMA competes with Afadin for LGN binding. In addition, NuMA competes with mInsc for LGN binding during asymmetric cell division (black asterisks). The MTBD1 overlaps LGN–BD, and thus LGN binding to NuMA inhibits the microtubule binding activity of MTBD1 (green asterisks). LGN consists of TPR, Linker and GoLoco motifs, and each motif interacts with Afadin (Carminati et al., 2016), Dlg1 (Saadaoui et al., 2014), and the GDP-bound form of Gαi (Jia et al., 2012), respectively. NuMA/LGN/Gαi constitutes a conserved core pathway for cortical dynein recruitment. The C-terminal domain (CTD) of band 4.1 proteins interacts with the NuMA C-terminal domain, and is sufficient to rescue cortical NuMA enrichment in anaphase in LGN and 4.1 co-depleted cells (Kiyomitsu and Cheeseman, 2013). See text for details.

cortical NuMA–LGN is affected by disrupting cortical actin networks (Kaji et al., 2008; Carminati et al., 2016) or their regulators (Machicoane et al., 2014; Kschonsak and Hoffmann, 2018). Recently, Carminati et al. (2016) demonstrated that F-actin binding protein Afadin, which also binds LGN competitively with NuMA, is required to facilitate NuMA–LGN complex formation at the metaphase cell cortex (**Figure 3B**). On the other hand, Dlg1, that directly interacts with the phosphorylated LGN linker region (Zhu et al., 2011a) is also required for cortical LGN and NuMA localization (Saadaoui et al., 2014).

In asymmetrically dividing epithelial or mammary stem cells, the situation is more complex. Par3-binding mInsc (mammalian homolog of Inscuteable) and NuMA compete for binding to LGN^{TPR}, with mInsc showing a more than fivefold higher affinity (Culurgioni et al., 2011; Yuzawa et al., 2011; Zhu et al., 2011b). Previously, mInsc-bound LGN-Gαi was supposed to be transferred to NuMA, but Cukurgioni et al. recently reported that the Inscuteable-LGN tetramer is so stable that LGN cannot be dissociated from Inscuteable by NuMA (Culurgioni et al., 2018). The authors proposed that the Inscuteable-LGN tetramer generates a localized pool of Gαi-GTP molecules, which upon GTP-hydrolysis recruits a distinct population of LGN that subsequently recruits NuMA and dynein to orient the spindle (Culurgioni et al., 2018).

Although the LGN pathways are critical for cortical NuMA localization during metaphase in both symmetric and asymmetric divisions (Morin and Bellaiche, 2011), recent studies revealed that NuMA can be targeted to the anaphase cell cortex independently of LGN in symmetrically dividing mammalian cells (Collins et al., 2012; Kiyomitsu and Cheeseman, 2013; Kotak et al., 2013; Seldin et al., 2013; Zheng et al., 2014). Band 4.1 proteins link the plasma membrane to the actin cytoskeleton (Baines et al., 2014), and interact with NuMA via their C-terminal domain (CTD) and NuMA's 4.1-binding domain (1802–1824) (Mattagajasingh et al., 2009; **Figure 3B**). This NuMA-4.1 interaction appears to be important for the cortical stability of NuMA in metaphase keratinocytes (Seldin et al., 2013), but also has an important role for anaphase NuMA localization: double depletion of LGN and 4.1 proteins eliminates cortical NuMA in anaphase human cells (Kiyomitsu and Cheeseman, 2013). Importantly, this phenotype was rescued by the expression of the membrane-targeted C-terminal domain (CTD) of band 4.1 (Kiyomitsu and Cheeseman, 2013), which does not bind to actin, suggesting that 4.1 proteins contribute to anaphase NuMA localization independently of LGN and cortical actin structures. How 4.1 proteins regulate NuMA remains unclear; one possibility is that they increase cortical NuMA retention by linking it with the cell cortex and/or transferring NuMA to the plasma membrane (as described below). In addition to these cortical proteins, other proteins may be involved in cortical NuMA recruitment in developmental contexts. For example, NuMA's C-terminal region interacts with Disheveled, which controls spindle orientation during Zebrafish gastrulation (Segalen et al., 2010).

Importantly, NuMA can directly interact with the plasma membrane. The C-terminal region contains two membrane-binding domains, NuMA$^{1699-1876}$ (Kotak et al., 2014) and NuMA$^{1996-2074}$ (Zheng et al., 2014), which overlap with 4.1-BD and MTBD2, respectively, (**Figure 2C**) and are referred to as Mem-BD1 and 2 in this review (**Figure 2C**). Both membrane-binding domains preferentially bind to phosphorylated forms of phosphatidylinositol (PIPs) and are required for efficient cortical accumulation of NuMA (Kotak et al., 2014; Zheng et al., 2014). Mem-BD2, which partially overlaps with the DNA-binding domain (**Figure 2C**), is required for proper chromosome separation during anaphase (Zheng et al., 2014).

DNA-BINDING DOMAIN IN NuMA'S C-TERMINAL REGION

In contrast to invertebrate NuMA-related proteins, vertebrate NuMA proteins analyzed so far localize in the nucleus (Lydersen and Pettijohn, 1980; Compton et al., 1992; Yang et al., 1992; Merdes et al., 1996). Previously, human NuMA was reported to interact with defined DNA sequences called matrix attached regions (MARs) *in vitro* (Luderus et al., 1994). Recently, two studies demonstrated that the C-terminal region of human NuMA interacts with DNA *in vitro* and chromatin in cells (Rajeevan et al., 2020; Serra-Marques et al., 2020). Rajeevan et al. (2020) showed that the C-terminus NuMA$^{2058-2115}$ fragment is sufficient to bind DNA *in vitro*, and the basic amino acids within the region are critical for its interaction with chromatin in cells (**Figure 2C**). When endogenous NuMA was replaced with mutated versions lacking its DNA-binding ability, cells showed improper chromosome decondensation during mitotic exit and an abnormal nuclear shape (Rajeevan et al., 2020), suggesting that NuMA–DNA interactions are critical for proper regulation of chromosome decondensation during nuclear reformation.

NUCLEAR LOCALIZATION SEQUENCE/SIGNAL IN NuMA'S C-TERMINAL REGION

NuMA has a nuclear localization signal/sequence (NLS) between the MTBDs in its C-terminal region (Tang et al., 1994; **Figure 2C**). When Chang et al. (2017) solved the crystal structure of the importin-α-NuMA-C-terminus complex, they found that NuMA–NLS exhibits a novel, non-classic interaction mode with importin-α, and that importin-β sterically inhibits NuMA's MTBD2 *in vitro*. The NLS sequence is well conserved from *H. sapiens* to *X. laevis* (Chang et al., 2017), but not in *C. elegans* LIN-5, or *drosphila* Mud (Lorson et al., 2000; Siller et al., 2006). In fish, the highly conserved KR, H and KK residues of the NLS, which interact with the minor-, linker and the major-NLS-binding site on importin-α, respectively (Chang et al., 2017), are not identical and several amino acids are inserted between the H and KK residues (Tsuchiya et al., 2021); yet the Zebrafish NuMA C-terminal region can be targeted to the nucleus (Segalen et al., 2010). It would be interesting to understand whether NuMA localizes to the nucleus in other fish species, and why the NLS was acquired in vertebrates.

THE CLUSTERING DOMAIN IN NuMA'S C-TERMINAL REGION

The C-terminal globular domain has another key feature that facilitates NuMA's self-assembly into oligomers (Harborth et al., 1999). *In vitro*, 10–12 NuMA homo-dimers assemble through its C-terminal region to form multi-arm oligomers. Each oligomer has a central clustered core with projected arms, and may be connected to create 3D nuclear architecture during interphase (Harborth et al., 1999). NuMA's punctate signals at the cell cortex are most likely a result of its oligomerization/clustering. This clustering activity is attributed to a well-conserved 10 a.a sequence of NuMA$^{1768-1777}$ (Okumura et al., 2018). Mutant analyses indicated that NuMA's clustering is required for spindle pulling and spindle orientation at metaphase (Okumura et al., 2018), and for spindle bipolarization during prometaphase in acentrosomal human cells (Chinen et al., 2020), but is dispensable for spindle pole focusing (Okumura et al., 2018). It will be exciting to see what kind of structures are actually generated in cells by NuMA's clustering activity both in mitosis and interphase. Especially, it is important to understand how this clustering activity synergetically functions with NuMA–LGN oligomer formation to organize high-ordered functional structures that

capture and pull on astral microtubules at the mitotic cell cortex (Pirovano et al., 2019; **Figure 3**).

MITOTIC AND MEIOTIC REGULATION OF NuMA

Since NuMA's C-terminal domain binds to microtubules, the plasma membrane, and chromatin (**Figure 2C**), these interactions must be regulated throughout the cell cycle. In fact, the well conserved threonine at 2055 (T2055) is phosphorylated by CDK during metaphase (Compton and Luo, 1995; Kotak et al., 2013; Seldin et al., 2013), which inhibits NuMA's cortical association and thus promotes microtubule-binding. CDK-based phosphorylation of NuMA is also critical for releasing NuMA from the chromosomes at mitotic entry (Rajeevan et al., 2020). During anaphase, NuMA is dephosphorylated by the PPP2CA–B55gamma–PPP2R1B complex (Keshri et al., 2020), which dissociates NuMA from the spindle poles (Gehmlich et al., 2004) and promotes its cortical association.

The microtubule binding activity of NuMA is vital for its mitotic and meiotic functions (Silk et al., 2009; Kolano et al., 2012; Tsuchiya et al., 2021). Thus, importins that sterically inhibit C-terminal microtubule-binding (Chang et al., 2017) must be released during mitosis. Previously, it was demonstrated that the NuMA-importin interaction is disrupted by Ran-GTP binding to importin-β in *Xenopus* egg extracts (Nachury et al., 2001; Wiese et al., 2001), and that Ran-GTP is essential for acentrosomal spindle assembly in female meiosis (Dumont et al., 2007; Holubcova et al., 2015; Drutovic et al., 2020). However, recent evidence suggests that Ran-GTP is not essential for mitotic spindle assembly and mitotic progression in chicken DT40 (Furuta et al., 2016) and human HCT116 cells (Tsuchiya et al., 2021). In addition, Ran-GTP is not required to activate NuMA and TPX2 in HCT116 cells (Tsuchiya et al., 2021), suggesting that additional parallel pathways exist to activate these proteins at a distance from chromosomes (Wei et al., 2015; Eibes et al., 2018; Brownlee and Heald, 2019). As cellular concentrations of Ran-GTP are variable across cell types and organisms (Kalab et al., 2006; Hasegawa et al., 2013), and the size of spindles and cells change dramatically during early embryonic divisions (Courtois et al., 2012; Levy and Heald, 2012), it would be important to determine how NuMA is spatiotemporally activated by Ran and other factors during mitosis and meiosis.

MITOTIC REGULATION OF NuMA AT THE SPINDLE POLES AND THE CELL CORTEX

Once activated, the NuMA homo-dimer binds to microtubules independently of dynein (Heald et al., 1997; Hueschen et al., 2017) and cross-links two microtubules using its two C-terminal globular domains (**Figure 3A**; Forth et al., 2014). This microtubule crosslinking function may be facilitated at the spindle poles by binding to other microtubule associated proteins such as Rae1 (Wong et al., 2006), Eg5 (Iwakiri et al., 2013), and dynein/dynactin complexes (Merdes et al., 1996, 2000). On the other hand, when new microtubules are created in the spindle, NuMA is targeted to their minus-ends and subsequently forms a complex with dynein and dynactin; when this complex binds adjacent microtubules and moves toward their minus end, it pulls the NuMA-bound microtubules along, resulting in a focused spindle pole (Hueschen et al., 2017; **Figure 3A**).

At the poles, NuMA is phosphorylated by Aurora-A kinase at S1969, which leads to its dynamic mobility from the spindle poles to the cell cortex during metaphase (Gallini et al., 2016; Kotak et al., 2016; **Figure 2C**). NuMA is also phosphorylated by Polo-like kinase 1 (Plk1) at SS1833/34 (Kettenbach et al., 2011), which promotes NuMA's turnover rate at both spindle poles and the cell cortex, and when inhibited results in NuMA's accumulation at both locations (Sana et al., 2018). Plk1 localizes at the spindle poles, but also accumulates at kinetochores of misaligned chromosomes which locally diminish cortical LGN when they are located near the cell cortex (Tame et al., 2016). Since NuMA and LGN are inter-dependent (Du and Macara, 2004), the kinetochore-localized Plk1 may also target NuMA, which in turn reduces LGN. However, artificial membrane tethering of Plk1 dissociated dynein, but not LGN, from the cell cortex (Kiyomitsu and Cheeseman, 2012). In addition, when the immunoprecipitated GFP–LGN complexes were incubated with Plk1, Plk1 dissociated dynein and dynactin, but not NuMA, from LGN (Kiyomitsu and Cheeseman, 2012). Therefore, kinetochore- or centrosome-localized Plk1 may down-regulate the NuMA–LGN interaction synergetically in cooperation with other factors derived from chromosomes or centrosomes. Another kinase, ABL1, phosphorylates the well-conserved Y1774 residue of NuMA to control spindle orientation (Matsumura et al., 2012). Y1774 is located in the clustering motif (Okumura et al., 2018), but it remains unknown whether ABL1 regulates NuMA's clustering activity.

In addition to these kinases, Ran-GTP gradients negatively regulate cortical NuMA–LGN localization near chromosomes in a distance dependent manner (Kiyomitsu and Cheeseman, 2012). Although molecular mechanisms by which Ran-GTP eliminates the NuMA–LGN complex from the cell cortex remain unclear, the cortical patterning created by chromosome-derived Ran-GTP is sufficient to explain why the mitotic spindle orients along its interphase cell axis (Dimitracopoulos et al., 2020). NuMA's continuous exclusion from the equatorial region of the cell cortex during anaphase is dependent on the signals downstream of the centralspindlin complexes (Kotak et al., 2014).

INTERPHASE FUNCTION OF NuMA

Several lines of evidence indicate that NuMA acts as a non-essential nucleoskeletal element in interphase (Zeng et al., 1994; Merdes and Cleveland, 1998; Harborth et al., 1999), which is nicely reviewed by Radulescu and Cleveland (2010). However, it is difficult to understand this role separately from the several roles it plays during mitosis since mitotic errors cause abnormal nuclei. Recently, Serra-Marques et al. (2020) nicely demonstrated that NuMA's contribution to building a single, round nucleus

is independent from its mitotic functions by inducing mitotic exit in NuMA KO Rpe1 cells without spindles (**Figure 1B**). Furthermore, they showed that NuMA keeps the decondensing chromosome mass compact during mitotic exit (Serra-Marques et al., 2020). Although the precise mechanisms are still unclear, evidence suggests that NuMA, like barrier-to-auto integration factor (BAF) at the chromosome ensemble surface (Samwer et al., 2017), may offer structural support throughout the nucleus by cross-linking chromosomes and preventing the nuclear envelop from penetrating into the chromosome mass, which results in a decrease of multinucleation and abnormally shaped nuclei during mitotic exit (Serra-Marques et al., 2020). Alternatively, NuMA may coordinate chromosome compaction and nuclear envelop assembly using its binding abilities to both chromosomes and membrane (Serra-Marques et al., 2020), as well as its binding to importins which can recruit membrane vesicles and nucleoporins (Lu et al., 2012).

In addition to its roles during mitotic exit, NuMA promotes the nucleus' mechanical robustness (Serra-Marques et al., 2020) and could contribute to several interphase events, including chromatin organization (Abad et al., 2007), gene expression (Harborth et al., 2000; Ohata et al., 2013), DNA repair (Vidi et al., 2014; Moreno et al., 2019), and apoptosis (Gueth-Hallonet et al., 1997; Kivinen et al., 2005; Lin et al., 2007). Since chromatin architecture is highly dynamic during different phases of the cell cycle (Shoaib et al., 2020), acute protein depletion technologies, such as auxin-inducible degron (AID) (Natsume et al., 2016; Yesbolatova et al., 2020; Tsuchiya et al., 2021), would be useful to precisely understand the interphase functions of NuMA in future studies.

DISCUSSION

Vertebrate NuMA, and its related proteins in invertebrates, have been extensively studied using many techniques and model organisms. Over the past 10 years, much light has been shed on this multi-functional protein, revealing key domains, modifications and binding partners. However, we still do not know how NuMA contributes to spindle pole focusing, spindle positioning or nuclear formation at the molecular and structural level. In the next 10 years, it would be especially important to visualize the functional structures of NuMA and its complexes using biochemical reconstitution, high-resolution imaging and *in situ* structural analyses. In addition, most reported interactions and functions are not sufficiently validated in a physiological condition. Since many functions discussed in this review appear to be specific in vertebrates, vertebrate developmental models would be useful to obtain a comprehensive understanding of the diverse functions of NuMA. Furthermore, optogenetic manipulation of NuMA, or its related proteins, would serve as a powerful tool to control spindle position and orientation (Fielmich et al., 2018; Okumura et al., 2018), and could reveal physiological roles of division orientation and daughter cell size during development (Jankele et al., 2021).

Many key questions about NuMA remain to be answered. (1) How does NuMA recognize microtubule minus-ends and depolymerizing microtubule plus-ends? (2) How are dynein–dynactin–NuMA complexes formed during mitosis and meiosis and regulated at the spindle poles? (3) How are different cortical NuMA complexes assembled at the mitotic cell cortex and spatiotemporally regulated by intrinsic and extrinsic signals? (4) When does NuMA start to localize at the mitotic cell cortex to control spindle positioning during early vertebrate development? (5) What kinds of high-ordered structures are created by NuMA at the cell cortex and interphase nucleus to generate cortical spindle pulling forces and a mechanically robust nucleus, respectively? (6) How is NuMA dissociated from importins in a Ran-independent manner? (7) Why did NuMA acquire an NLS in vertebrates? (8) How has the NuMA gene evolved to achieve different functions in different organisms? Addressing these questions must provide new, exciting insights not only to advance our knowledge about nucleus formation, spindle assembly and spindle positioning, but also to understand how complex human cell architecture evolved.

AUTHOR CONTRIBUTIONS

TK wrote the first draft, acquired the fund. TK and SB revised manuscript, figures, and Table. SB got the images of **Figure 1A**. Both authors contributed to the article and approved the submitted version.

FUNDING

This work was supported by a grant from the Okinawa Institute of Science and Technology Graduate University, Japan.

ACKNOWLEDGMENTS

We thank Euikyung Yu for assistance in preparing the Table. We also thank the reviewers for their critical and constructive comments.

REFERENCES

Abad, P. C., Lewis, J. I, Mian, S., Knowles, D. W., Sturgis, J., Badve, S., et al. (2007). NuMA influences higher order chromatin organization in human mammary epithelium. *Mol. Biol. Cell* 18, 348–361. doi: 10.1091/mbc.e06-06-0551

Alvarez Sedo, C., Schatten, H., Combelles, C. M., and Rawe, V. Y. (2011). The nuclear mitotic apparatus (NuMA) protein: localization and dynamics in human oocytes, fertilization and early embryos. *Mol. Hum. Reprod.* 17, 392–398. doi: 10.1093/molehr/gar009

Baines, A. J., Lu, H. C., and Bennett, P. M. (2014). The Protein 4.1 family: hub proteins in animals for organizing membrane proteins. *Biochim. Biophys. Acta* 1838, 605–619. doi: 10.1016/j.bbamem.2013.05.030

Borgal, L., and Wakefield, J. G. (2018). Context-dependent spindle pole focusing. *Essays Biochem.* 62, 803–813. doi: 10.1042/ebc20180034

Bowman, S. K., Neumuller, R. A., Novatchkova, M., Du, Q., and Knoblich, J. A. (2006). The *Drosophila* NuMA homolog mud regulates spindle orientation in asymmetric cell division. *Dev. Cell* 10, 731–742. doi: 10.1016/j.devcel.2006.05.005

Brownlee, C., and Heald, R. (2019). Importin alpha partitioning to the plasma membrane regulates intracellular scaling. *Cell* 176, 805–815.e808.

Carminati, M., Gallini, S., Pirovano, L., Alfieri, A., Bisi, S., and Mapelli, M. (2016). Concomitant binding of Afadin to LGN and F-actin directs planar spindle orientation. *Nat. Struct. Mol. Biol.* 23, 155–163. doi: 10.1038/nsmb.3152

Chang, C. C., Huang, T. L., Shimamoto, Y., Tsai, S. Y., and Hsia, K. C. (2017). Regulation of mitotic spindle assembly factor NuMA by Importin-beta. *J. Cell Biol.* 216, 3453–3462. doi: 10.1083/jcb.201705168

Chinen, T., Yamamoto, S., Takeda, Y., Watanabe, K., Kuroki, K., Hashimoto, K., et al. (2020). NuMA assemblies organize microtubule asters to establish spindle bipolarity in acentrosomal human cells. *EMBO J.* 39:e102378.

Cleveland, D. W. (1995). NuMA: a protein involved in nuclear structure, spindle assembly, and nuclear re-formation. *Trends Cell Biol.* 5, 60–64. doi: 10.1016/s0962-8924(00)88947-3

Collins, E. S., Balchand, S. K., Faraci, J. L., Wadsworth, P., and Lee, W. L. (2012). Cell cycle-regulated cortical dynein/dynactin promotes symmetric cell division by differential pole motion in anaphase. *Mol. Biol. Cell* 23, 3380–3390. doi: 10.1091/mbc.e12-02-0109

Compton, D. A., and Cleveland, D. W. (1994). NuMA, a nuclear protein involved in mitosis and nuclear reformation. *Curr. Opin. Cell Biol.* 6, 343–346. doi: 10.1016/0955-0674(94)90024-8

Compton, D. A., and Luo, C. (1995). Mutation of the predicted p34cdc2 phosphorylation sites in NuMA impair the assembly of the mitotic spindle and block mitosis. *J. Cell Sci.* 108(Pt 2), 621–633.

Compton, D. A., Szilak, I., and Cleveland, D. W. (1992). Primary structure of NuMA, an intranuclear protein that defines a novel pathway for segregation of proteins at mitosis. *J. Cell Biol.* 116, 1395–1408. doi: 10.1083/jcb.116.6.1395

Courtois, A., Schuh, M., Ellenberg, J., and Hiiragi, T. (2012). The transition from meiotic to mitotic spindle assembly is gradual during early mammalian development. *J. Cell Biol.* 198, 357–370. doi: 10.1083/jcb.201202135

Culurgioni, S., Alfieri, A., Pendolino, V., Laddomada, F., and Mapelli, M. (2011). Inscuteable and NuMA proteins bind competitively to Leu-Gly-Asn repeat-enriched protein (LGN) during asymmetric cell divisions. *Proc. Natl. Acad. Sci. U.S.A.* 108, 20998–21003. doi: 10.1073/pnas.1113077108

Culurgioni, S., Mari, S., Bonetti, P., Gallini, S., Bonetto, G., Brennich, M., et al. (2018). Insc:LGN tetramers promote asymmetric divisions of mammary stem cells. *Nat. Commun.* 9:1025.

Dimitracopoulos, A., Srivastava, P., Chaigne, A., Win, Z., Shlomovitz, R., Lancaster, O. M., et al. (2020). Mechanochemical crosstalk produces cell-intrinsic patterning of the cortex to orient the mitotic spindle. *Curr. Biol.* 30, 3687–3696.e3684.

Drutovic, D., Duan, X., Li, R., Kalab, P., and Solc, P. (2020). RanGTP and importin beta regulate meiosis I spindle assembly and function in mouse oocytes. *EMBO J.* 39:e101689.

Du, Q., and Macara, I. G. (2004). Mammalian Pins is a conformational switch that links NuMA to heterotrimeric G proteins. *Cell* 119, 503–516. doi: 10.1016/j.cell.2004.10.028

Du, Q., Taylor, L., Compton, D. A., and Macara, I. G. (2002). LGN blocks the ability of NuMA to bind and stabilize microtubules. A mechanism for mitotic spindle assembly regulation. *Curr. Biol.* 12, 1928–1933. doi: 10.1016/s0960-9822(02)01298-8

Dumont, J., Petri, S., Pellegrin, F., Terret, M. E., Bohnsack, M. T., Rassinier, P., et al. (2007). A centriole- and RanGTP-independent spindle assembly pathway in meiosis I of vertebrate oocytes. *J. Cell Biol.* 176, 295–305. doi: 10.1083/jcb.200605199

Eibes, S., Gallisa-Sune, N., Rosas-Salvans, M., Martinez-Delgado, P., Vernos, I., and Roig, J. (2018). Nek9 phosphorylation defines a new role for TPX2 in Eg5-dependent centrosome separation before nuclear envelope breakdown. *Curr. Biol.* 28, 121–129.e124.

Fielmich, L. E., Schmidt, R., Dickinson, D. J., Goldstein, B., Akhmanova, A., and van den Heuvel, S. (2018). Optogenetic dissection of mitotic spindle positioning in vivo. *Elife* 7:e38198.

Forth, S., Hsia, K. C., Shimamoto, Y., and Kapoor, T. M. (2014). Asymmetric friction of nonmotor MAPs can lead to their directional motion in active microtubule networks. *Cell* 157, 420–432. doi: 10.1016/j.cell.2014.02.018

Furuta, M., Hori, T., and Fukagawa, T. (2016). Chromatin binding of RCC1 during mitosis is important for its nuclear localization in interphase. *Mol. Biol. Cell* 27, 371–381. doi: 10.1091/mbc.e15-07-0497

Galli, M., and van den Heuvel, S. (2008). Determination of the cleavage plane in early C. elegans embryos. *Annu. Rev. Genet.* 42, 389–411. doi: 10.1146/annurev.genet.40.110405.090523

Gallini, S., Carminati, M., De Mattia, F., Pirovano, L., Martini, E., Oldani, A. I, et al. (2016). NuMA phosphorylation by aurora-A orchestrates spindle orientation. *Curr. Biol.* 26, 458–469. doi: 10.1016/j.cub.2015.12.051

Gama, J. B., Pereira, C., Simoes, P. A., Celestino, R., Reis, R. M., Barbosa, D. J., et al. (2017). Molecular mechanism of dynein recruitment to kinetochores by the Rod-Zw10-Zwilch complex and Spindly. *J. Cell Biol.* 216, 943–960. doi: 10.1083/jcb.201610108

Gehmlich, K., Haren, L., and Merdes, A. (2004). Cyclin B degradation leads to NuMA release from dynein/dynactin and from spindle poles. *EMBO Rep.* 5, 97–103. doi: 10.1038/sj.embor.7400046

Gonczy, P. (2008). Mechanisms of asymmetric cell division: flies and worms pave the way. *Nat. Rev. Mol. Cell Biol.* 9, 355–366. doi: 10.1038/nrm2388

Greenberg, S. R., Tan, W., and Lee, W. L. (2018). Num1 versus NuMA: insights from two functionally homologous proteins. *Biophys. Rev.* 10, 1631–1636. doi: 10.1007/s12551-018-0472-x

Gueth-Hallonet, C., Wang, J., Harborth, J., Weber, K., and Osborn, M. (1998). Induction of a regular nuclear lattice by overexpression of NuMA. *Exp. Cell Res.* 243, 434–452. doi: 10.1006/excr.1998.4178

Gueth-Hallonet, C., Weber, K., and Osborn, M. (1997). Cleavage of the nuclear matrix protein NuMA during apoptosis. *Exp. Cell Res.* 233, 21–24. doi: 10.1006/excr.1997.3557

Harborth, J., Wang, J., Gueth-Hallonet, C., Weber, K., and Osborn, M. (1999). Self assembly of NuMA: multiarm oligomers as structural units of a nuclear lattice. *EMBO J.* 18, 1689–1700. doi: 10.1093/emboj/18.6.1689

Harborth, J., Weber, K., and Osborn, M. (1995). Epitope mapping and direct visualization of the parallel, in-register arrangement of the double-stranded coiled-coil in the NuMA protein. *EMBO J.* 14, 2447–2460. doi: 10.1002/j.1460-2075.1995.tb07242.x

Harborth, J., Weber, K., and Osborn, M. (2000). GAS41, a highly conserved protein in eukaryotic nuclei, binds to NuMA. *J. Biol. Chem.* 275, 31979–31985. doi: 10.1074/jbc.m000994200

Hasegawa, K., Ryu, S. J., and Kalab, P. (2013). Chromosomal gain promotes formation of a steep RanGTP gradient that drives mitosis in aneuploid cells. *J. Cell Biol.* 200, 151–161. doi: 10.1083/jcb.201206142

Heald, R., Tournebize, R., Habermann, A., Karsenti, E., and Hyman, A. (1997). Spindle assembly in Xenopus egg extracts: respective roles of centrosomes and microtubule self-organization. *J. Cell Biol.* 138, 615–628. doi: 10.1083/jcb.138.3.615

Holubcova, Z., Blayney, M., Elder, K., and Schuh, M. (2015). Human oocytes. Error-prone chromosome-mediated spindle assembly favors chromosome segregation defects in human oocytes. *Science* 348, 1143–1147. doi: 10.1126/science.aaa9529

Hueschen, C. L., Kenny, S. J., Xu, K., and Dumont, S. (2017). NuMA recruits dynein activity to microtubule minus-ends at mitosis. *Elife* 6:e29328.

Iwakiri, Y., Kamakura, S., Hayase, J., and Sumimoto, H. (2013). Interaction of NuMA protein with the kinesin Eg5: its possible role in bipolar spindle assembly and chromosome alignment. *Biochem. J.* 451, 195–204. doi: 10.1042/bj20121447

Izumi, Y., Ohta, N., Hisata, K., Raabe, T., and Matsuzaki, F. (2006). *Drosophila* Pins-binding protein Mud regulates spindle-polarity coupling and centrosome organization. *Nat. Cell Biol.* 8, 586–593. doi: 10.1038/ncb1409

Jankele, R., Jelier, R., and Gonczy, P. (2021). Physically asymmetric division of the C. elegans zygote ensures invariably successful embryogenesis. *Elife* 10:e61714.

Jia, M., Li, J., Zhu, J., Wen, W., Zhang, M., and Wang, W. (2012). Crystal structures of the scaffolding protein LGN reveal the general mechanism by which GoLoco binding motifs inhibit the release of GDP from Galphai. *J. Biol. Chem.* 287, 36766–36776. doi: 10.1074/jbc.m112.391607

Kaji, N., Muramoto, A., and Mizuno, K. (2008). LIM kinase-mediated cofilin phosphorylation during mitosis is required for precise spindle positioning. *J. Biol. Chem.* 283, 4983–4992. doi: 10.1074/jbc.m708644200

Kalab, P., Pralle, A., Isacoff, E. Y., Heald, R., and Weis, K. (2006). Analysis of a RanGTP-regulated gradient in mitotic somatic cells. *Nature* 440, 697–701. doi: 10.1038/nature04589

Keshri, R., Rajeevan, A., and Kotak, S. (2020). PP2A–B55gamma counteracts Cdk1 and regulates proper spindle orientation through the cortical dynein adaptor NuMA. *J. Cell Sci.* 133:jcs243857. doi: 10.1242/jcs.243857

Kettenbach, A. N., Schweppe, D. K., Faherty, B. K., Pechenick, D., Pletnev, A. A., and Gerber, S. A. (2011). Quantitative phosphoproteomics identifies substrates and functional modules of Aurora and Polo-like kinase activities in mitotic cells. *Sci. Signal.* 4:rs5. doi: 10.1126/scisignal.2001497

Kivinen, K., Kallajoki, M., and Taimen, P. (2005). Caspase-3 is required in the apoptotic disintegration of the nuclear matrix. *Exp. Cell Res.* 311, 62–73. doi: 10.1016/j.yexcr.2005.08.006

Kiyomitsu, T. (2019). The cortical force-generating machinery: how cortical spindle-pulling forces are generated. *Curr. Opin. Cell Biol.* 60, 1–8. doi: 10.1016/j.ceb.2019.03.001

Kiyomitsu, T., and Cheeseman, I. M. (2012). Chromosome- and spindle-pole-derived signals generate an intrinsic code for spindle position and orientation. *Nat. Cell Biol.* 14, 311–317. doi: 10.1038/ncb2440

Kiyomitsu, T., and Cheeseman, I. M. (2013). Cortical dynein and asymmetric membrane elongation coordinately position the spindle in anaphase. *Cell* 154, 391–402. doi: 10.1016/j.cell.2013.06.010

Kolano, A., Brunet, S., Silk, A. D., Cleveland, D. W., and Verlhac, M. H. (2012). Error-prone mammalian female meiosis from silencing the spindle assembly checkpoint without normal interkinetochore tension. *Proc. Natl. Acad. Sci. U.S.A.* 109, E1858–E1867.

Kotak, S., Afshar, K., Busso, C., and Gonczy, P. (2016). Aurora A kinase regulates proper spindle positioning in C. elegans and in human cells. *J. Cell Sci.* 129, 3015–3025. doi: 10.1242/jcs.184416

Kotak, S., Busso, C., and Gonczy, P. (2012). Cortical dynein is critical for proper spindle positioning in human cells. *J. Cell Biol.* 199, 97–110. doi: 10.1083/jcb.201203166

Kotak, S., Busso, C., and Gonczy, P. (2013). NuMA phosphorylation by CDK1 couples mitotic progression with cortical dynein function. *EMBO J.* 32, 2517–2529. doi: 10.1038/emboj.2013.172

Kotak, S., Busso, C., and Gonczy, P. (2014). NuMA interacts with phosphoinositides and links the mitotic spindle with the plasma membrane. *EMBO J.* 33, 1815–1830. doi: 10.15252/embj.201488147

Kschonsak, Y. T., and Hoffmann, I. (2018). Activated ezrin controls MISP levels to ensure correct NuMA polarization and spindle orientation. *J. Cell Sci.* 131:jcs214544. doi: 10.1242/jcs.214544

Lechler, T., and Fuchs, E. (2005). Asymmetric cell divisions promote stratification and differentiation of mammalian skin. *Nature* 437, 275–280. doi: 10.1038/nature03922

Lee, I. G., Cason, S. E., Alqassim, S. S., Holzbaur, E. L. F., and Dominguez, R. (2020). A tunable LIC1-adaptor interaction modulates dynein activity in a cargo-specific manner. *Nat. Commun.* 11:5695.

Levy, D. L., and Heald, R. (2012). Mechanisms of intracellular scaling. *Annu. Rev. Cell Dev. Biol.* 28, 113–135. doi: 10.1146/annurev-cellbio-092910-154158

Lin, H. H., Hsu, H. L., and Yeh, N. H. (2007). Apoptotic cleavage of NuMA at the C-terminal end is related to nuclear disruption and death amplification. *J. Biomed. Sci.* 14, 681–694. doi: 10.1007/s11373-007-9165-3

Lorson, M. A., Horvitz, H. R., and van den Heuvel, S. (2000). LIN-5 is a novel component of the spindle apparatus required for chromosome segregation and cleavage plane specification in Caenorhabditis elegans. *J. Cell Biol.* 148, 73–86. doi: 10.1083/jcb.148.1.73

Lu, Q., Lu, Z., Liu, Q., Guo, L., Ren, H., Fu, J., et al. (2012). Chromatin-bound NLS proteins recruit membrane vesicles and nucleoporins for nuclear envelope assembly via importin-alpha/beta. *Cell Res.* 22, 1562–1575. doi: 10.1038/cr.2012.113

Luderus, M. E., den Blaauwen, J. L., de Smit, O. J., Compton, D. A., and van Driel, R. (1994). Binding of matrix attachment regions to lamin polymers involves single-stranded regions and the minor groove. *Mol. Cell. Biol.* 14, 6297–6305. doi: 10.1128/mcb.14.9.6297

Lydersen, B. K., Kao, F. T., and Pettijohn, D. (1980). Expression of genes coding for non-histone chromosomal proteins in human-Chinese hamster cell hybrids. An electrophoretic analysis. *J. Biol. Chem.* 255, 3002–3007. doi: 10.1016/s0021-9258(19)85842-8

Lydersen, B. K., and Pettijohn, D. E. (1980). Human-specific nuclear protein that associates with the polar region of the mitotic apparatus: distribution in a human/hamster hybrid cell. *Cell* 22, 489–499. doi: 10.1016/0092-8674(80)90359-1

Machicoane, M., de Frutos, C. A., Fink, J., Rocancourt, M., Lombardi, Y., Garel, S., et al. (2014). SLK-dependent activation of ERMs controls LGN-NuMA localization and spindle orientation. *J. Cell Biol.* 205, 791–799. doi: 10.1083/jcb.201401049

Matsumura, S., Hamasaki, M., Yamamoto, T., Ebisuya, M., Sato, M., Nishida, E., et al. (2012). ABL1 regulates spindle orientation in adherent cells and mammalian skin. *Nat. Commun.* 3:626.

Mattagajasingh, S. N., Huang, S. C., and Benz, E. J. Jr. (2009). Inhibition of protein 4.1 R and NuMA interaction by mutagenization of their binding-sites abrogates nuclear localization of 4.1 R. *Clin. Transl. Sci.* 2, 102–111. doi: 10.1111/j.1752-8062.2008.00087.x

McKenney, R. J., Huynh, W., Tanenbaum, M. E., Bhabha, G., and Vale, R. D. (2014). Activation of cytoplasmic dynein motility by dynactin-cargo adapter complexes. *Science* 345, 337–341. doi: 10.1126/science.1254198

Merdes, A., and Cleveland, D. W. (1998). The role of NuMA in the interphase nucleus. *J. Cell Sci.* 111(Pt 1), 71–79.

Merdes, A., Heald, R., Samejima, K., Earnshaw, W. C., and Cleveland, D. W. (2000). Formation of spindle poles by dynein/dynactin-dependent transport of NuMA. *J. Cell Biol.* 149, 851–862. doi: 10.1083/jcb.149.4.851

Merdes, A., Ramyar, K., Vechio, J. D., and Cleveland, D. W. (1996). A complex of NuMA and cytoplasmic dynein is essential for mitotic spindle assembly. *Cell* 87, 447–458. doi: 10.1016/s0092-8674(00)81365-3

Moreno, N. S., Liu, J., Haas, K. M., Parker, L. L., Chakraborty, C., Kron, S. J., et al. (2019). The nuclear structural protein NuMA is a negative regulator of 53BP1 in DNA double-strand break repair. *Nucleic Acids Res.* 47, 10475. doi: 10.1093/nar/gkz802

Morin, X., and Bellaiche, Y. (2011). Mitotic spindle orientation in asymmetric and symmetric cell divisions during animal development. *Dev. Cell* 21, 102–119. doi: 10.1016/j.devcel.2011.06.012

Nachury, M. V., Maresca, T. J., Salmon, W. C., Waterman-Storer, C. M., Heald, R., and Weis, K. (2001). Importin beta is a mitotic target of the small GTPase Ran in spindle assembly. *Cell* 104, 95–106. doi: 10.1016/s0092-8674(01)00194-5

Natsume, T., Kiyomitsu, T., Saga, Y., and Kanemaki, M. T. (2016). Rapid protein depletion in human cells by auxin-inducible degron tagging with short homology donors. *Cell Rep.* 15, 210–218. doi: 10.1016/j.celrep.2016.03.001

Ohata, H., Miyazaki, M., Otomo, R., Matsushima-Hibiya, Y., Otsubo, C., Nagase, T., et al. (2013). NuMA is required for the selective induction of p53 target genes. *Mol. Cell. Biol.* 33, 2447–2457. doi: 10.1128/mcb.01221-12

Okumura, M., Natsume, T., Kanemaki, M. T., and Kiyomitsu, T. (2018). Dynein-Dynactin-NuMA clusters generate cortical spindle-pulling forces as a multi-arm ensemble. *Elife* 7:e36559.

Peyre, E., Jaouen, F., Saadaoui, M., Haren, L., Merdes, A., Durbec, P., et al. (2011). A lateral belt of cortical LGN and NuMA guides mitotic spindle movements and planar division in neuroepithelial cells. *J. Cell Biol.* 193, 141–154. doi: 10.1083/jcb.201101039

Pirovano, L., Culurgioni, S., Carminati, M., Alfieri, A., Monzani, S., Cecatiello, V., et al. (2019). Hexameric NuMA:LGN structures promote multivalent interactions required for planar epithelial divisions. *Nat. Commun.* 10:2208.

Poulson, N. D., and Lechler, T. (2010). Robust control of mitotic spindle orientation in the developing epidermis. *J. Cell Biol.* 191, 915–922. doi: 10.1083/jcb.201008001

Radulescu, A. E., and Cleveland, D. W. (2010). NuMA after 30 years: the matrix revisited. *Trends Cell Biol.* 20, 214–222. doi: 10.1016/j.tcb.2010.01.003

Rajeevan, A., Keshri, R., Kapoor, S., and Kotak, S. (2020). NuMA interaction with chromatin is vital for proper chromosome decondensation at the mitotic exit. *Mol. Biol. Cell* 31, 2437–2451. doi: 10.1091/mbc.e20-06-0415

Renna, C., Rizzelli, F., Carminati, M., Gaddoni, C., Pirovano, L., Cecatiello, V., et al. (2020). Organizational principles of the NuMA-dynein interaction interface and implications for mitotic spindle functions. *Structure* 28, 820–829.e826.

Saadaoui, M., Machicoane, M., di Pietro, F., Etoc, F., Echard, A., and Morin, X. (2014). Dlg1 controls planar spindle orientation in the neuroepithelium through direct interaction with LGN. *J. Cell Biol.* 206, 707–717. doi: 10.1083/jcb.201405060

Samwer, M., Schneider, M. W. G., Hoefler, R., Schmalhorst, P. S., Jude, J. G., Zuber, J., et al. (2017). DNA cross-bridging shapes a single nucleus from a set of mitotic chromosomes. *Cell* 170, 956–972.e923.

Sana, S., Keshri, R., Rajeevan, A., Kapoor, S., and Kotak, S. (2018). Plk1 regulates spindle orientation by phosphorylating NuMA in human cells. *Life Sci. Alliance* 1:e201800223. doi: 10.26508/lsa.201800223

Schlager, M. A., Hoang, H. T., Urnavicius, L., Bullock, S. L., and Carter, A. P. (2014). In vitro reconstitution of a highly processive recombinant human dynein complex. *EMBO J.* 33, 1855–1868. doi: 10.15252/embj.201488792

Segalen, M., Johnston, C. A., Martin, C. A., Dumortier, J. G., Prehoda, K. E., David, N. B., et al. (2010). The Fz-Dsh planar cell polarity pathway induces oriented cell division via Mud/NuMA in *Drosophila* and zebrafish. *Dev. Cell* 19, 740–752. doi: 10.1016/j.devcel.2010.10.004

Seldin, L., Muroyama, A., and Lechler, T. (2016). NuMA-microtubule interactions are critical for spindle orientation and the morphogenesis of diverse epidermal structures. *Elife* 5:e12504.

Seldin, L., Poulson, N. D., Foote, H. P., and Lechler, T. (2013). NuMA localization, stability, and function in spindle orientation involve 4.1 and Cdk1 interactions. *Mol. Biol. Cell* 24, 3651–3662. doi: 10.1091/mbc.e13-05-0277

Serra-Marques, A., Houtekamer, R., Hintzen, D., Canty, J. T., Yildiz, A., and Dumont, S. (2020). The mitotic protein NuMA plays a spindle-independent role in nuclear formation and mechanics. *J. Cell Biol.* 219:e202004202.

Shoaib, M., Nair, N., and Sorensen, C. S. (2020). Chromatin landscaping at mitotic exit orchestrates genome function. *Front. Genet.* 11:103. doi: 10.3389/fgene.2020.00103

Silk, A. D., Holland, A. J., and Cleveland, D. W. (2009). Requirements for NuMA in maintenance and establishment of mammalian spindle poles. *J. Cell Biol.* 184, 677–690. doi: 10.1083/jcb.200810091

Siller, K. H., Cabernard, C., and Doe, C. Q. (2006). The NuMA-related Mud protein binds Pins and regulates spindle orientation in *Drosophila* neuroblasts. *Nat. Cell Biol.* 8, 594–600. doi: 10.1038/ncb1412

Siller, K. H., and Doe, C. Q. (2009). Spindle orientation during asymmetric cell division. *Nat. Cell Biol.* 11, 365–374. doi: 10.1038/ncb0409-365

Srinivasan, D. G., Fisk, R. M., Xu, H., and van den Heuvel, S. (2003). A complex of LIN-5 and GPR proteins regulates G protein signaling and spindle function in C elegans. *Genes Dev.* 17, 1225–1239. doi: 10.1101/gad.1081203

Sun, Q. Y., and Schatten, H. (2006). Role of NuMA in vertebrate cells: review of an intriguing multifunctional protein. *Front. Biosci.* 11:1137–1146. doi: 10.2741/1868

Suzuki, M. (1989). SPXX, a frequent sequence motif in gene regulatory proteins. *J. Mol. Biol.* 207, 61–84. doi: 10.1016/0022-2836(89)90441-5

Taimen, P., Parvinen, M., Osborn, M., and Kallajoki, M. (2004). NuMA in rat testis–evidence for roles in proliferative activity and meiotic cell division. *Exp. Cell Res.* 298, 512–520. doi: 10.1016/j.yexcr.2004.05.002

Tame, M. A., Raaijmakers, J. A., Afanasyev, P., and Medema, R. H. (2016). Chromosome misalignments induce spindle-positioning defects. *EMBO Rep.* 17, 317–325. doi: 10.15252/embr.201541143

Tang, T. K., Tang, C. J., Chao, Y. J., and Wu, C. W. (1994). Nuclear mitotic apparatus protein (NuMA): spindle association, nuclear targeting and differential subcellular localization of various NuMA isoforms. *J. Cell Sci.* 107(Pt 6), 1389–1402.

Tsuchiya, K., Hayashi, H., Nishina, M., Okumura, M., Sato, Y., Kanemaki, M. T., et al. (2021). Ran-GTP is non-essential to activate NuMA for mitotic spindle-pole focusing but dynamically polarizes HURP near chromosomes. *Curr. Biol.* 31, 115–127.e113.

Vidi, P. A., Liu, J., Salles, D., Jayaraman, S., Dorfman, G., Gray, M., et al. (2014). NuMA promotes homologous recombination repair by regulating the accumulation of the ISWI ATPase SNF2h at DNA breaks. *Nucleic Acids Res.* 42, 6365–6379. doi: 10.1093/nar/gku296

Wei, J. H., Zhang, Z. C., Wynn, R. M., and Seemann, J. (2015). GM130 regulates golgi-derived spindle assembly by activating TPX2 and capturing microtubules. *Cell* 162, 287–299. doi: 10.1016/j.cell.2015.06.014

Wiese, C., Wilde, A., Moore, M. S., Adam, S. A., Merdes, A., and Zheng, Y. (2001). Role of importin-beta in coupling Ran to downstream targets in microtubule assembly. *Science* 291, 653–656. doi: 10.1126/science.1057661

Williams, S. E., Beronja, S., Pasolli, H. A., and Fuchs, E. (2011). Asymmetric cell divisions promote Notch-dependent epidermal differentiation. *Nature* 470, 353–358. doi: 10.1038/nature09793

Wong, R. W., Blobel, G., and Coutavas, E. (2006). Rae1 interaction with NuMA is required for bipolar spindle formation. *Proc. Natl. Acad. Sci. U.S.A.* 103, 19783–19787. doi: 10.1073/pnas.0609582104

Woodard, G. E., Huang, N. N., Cho, H., Miki, T., Tall, G. G., and Kehrl, J. H. (2010). Ric-8A and Gi alpha recruit LGN, NuMA, and dynein to the cell cortex to help orient the mitotic spindle. *Mol. Cell. Biol.* 30, 3519–3530. doi: 10.1128/mcb.00394-10

Yamada, M., and Goshima, G. (2017). Mitotic spindle assembly in land plants: molecules and mechanisms. *Biology (Basel)* 6:6. doi: 10.3390/biology6010006

Yang, C. H., Lambie, E. J., and Snyder, M. (1992). NuMA: an unusually long coiled-coil related protein in the mammalian nucleus. *J. Cell Biol.* 116, 1303–1317. doi: 10.1083/jcb.116.6.1303

Yesbolatova, A., Saito, Y., Kitamoto, N., Makino-Itou, H., Ajima, R., Nakano, R., et al. (2020). The auxin-inducible degron 2 technology provides sharp degradation control in yeast, mammalian cells, and mice. *Nat. Commun.* 11:5701.

Yuzawa, S., Kamakura, S., Iwakiri, Y., Hayase, J., and Sumimoto, H. (2011). Structural basis for interaction between the conserved cell polarity proteins Inscuteable and Leu-Gly-Asn repeat-enriched protein (LGN). *Proc. Natl. Acad. Sci. U.S.A.* 108, 19210–19215. doi: 10.1073/pnas.1110951108

Zeng, C., He, D., and Brinkley, B. R. (1994). Localization of NuMA protein isoforms in the nuclear matrix of mammalian cells. *Cell Motil. Cytoskeleton* 29, 167–176. doi: 10.1002/cm.970290208

Zheng, Z., Wan, Q., Meixiong, G., and Du, Q. (2014). Cell cycle-regulated membrane binding of NuMA contributes to efficient anaphase chromosome separation. *Mol. Biol. Cell* 25, 606–619. doi: 10.1091/mbc.e13-08-0474

Zhu, J., Shang, Y., Xia, C., Wang, W., Wen, W., and Zhang, M. (2011a). Guanylate kinase domains of the MAGUK family scaffold proteins as specific phospho-protein-binding modules. *EMBO J.* 30, 4986–4997. doi: 10.1038/emboj.2011.428

Zhu, J., Wen, W., Zheng, Z., Shang, Y., Wei, Z., Xiao, Z., et al. (2011b). LGN/mInsc and LGN/NuMA complex structures suggest distinct functions in asymmetric cell division for the Par3/mInsc/LGN and Galphai/LGN/NuMA pathways. *Mol. Cell* 43, 418–431. doi: 10.1016/j.molcel.2011.07.011

Conflict of Interest: The authors declare that the research was conducted in the absence of any commercial or financial relationships that could be construed as a potential conflict of interest.

frontiers in Cell and Developmental Biology

ORIGINAL RESEARCH
published: 12 April 2021
doi: 10.3389/fcell.2021.665919

Feedback-Driven Mechanisms Between Phosphorylated Caveolin-1 and Contractile Actin Assemblies Instruct Persistent Cell Migration

*Xuemeng Shi[1,2], Zeyu Wen[3,4], Yajun Wang[5], Yan-Jun Liu[5], Kun Shi[1,2] and Yaming Jiu[1,2,3,4]**

[1] The Joint Program in Infection and Immunity, Guangzhou Women and Children's Medical Center, Guangzhou Medical University, Guangzhou, China, [2] The Joint Program in Infection and Immunity, Institut Pasteur of Shanghai, Chinese Academy of Sciences, Shanghai, China, [3] Key Laboratory of Molecular Virology and Immunology, The Center for Microbes, Development and Health, Institut Pasteur of Shanghai, Chinese Academy of Sciences, Shanghai, China, [4] University of Chinese Academy of Sciences, Beijing, China, [5] Shanghai Institute of Cardiovascular Diseases, and Institutes of Biomedical Sciences, Zhongshan Hospital, Fudan University, Shanghai, China

OPEN ACCESS

Edited by:
Ting Gang Chew,
Zhejiang University-University of Edinburgh Institute, China

Reviewed by:
Shiro Suetsugu,
Nara Institute of Science and Technology (NAIST), Japan
Da Jia,
Sichuan University, China

***Correspondence:**
Yaming Jiu
ymjiu@ips.ac.cn

Specialty section:
This article was submitted to Cell Growth and Division, a section of the journal Frontiers in Cell and Developmental Biology

Received: 09 February 2021
Accepted: 22 March 2021
Published: 12 April 2021

Citation:
Shi X, Wen Z, Wang Y, Liu Y-J, Shi K and Jiu Y (2021) Feedback-Driven Mechanisms Between Phosphorylated Caveolin-1 and Contractile Actin Assemblies Instruct Persistent Cell Migration. Front. Cell Dev. Biol. 9:665919. doi: 10.3389/fcell.2021.665919

The actin cytoskeleton and membrane-associated caveolae contribute to active processes, such as cell morphogenesis and motility. How these two systems interact and control directional cell migration is an outstanding question but remains understudied. Here we identified a negative feedback between contractile actin assemblies and phosphorylated caveolin-1 (CAV-1) in migrating cells. Cytoplasmic CAV-1 vesicles display actin-associated motilities by sliding along actin filaments or/and coupling to do retrograde flow with actomyosin bundles. Inhibition of contractile stress fibers, but not Arp2/3-dependent branched actin filaments, diminished the phosphorylation of CAV-1 on site Tyr14, and resulted in substantially increased size and decreased motility of cytoplasmic CAV-1 vesicles. Reciprocally, both the CAV-1 phospho-deficient mutation on site Tyr14 and CAV-1 knockout resulted in dramatic AMPK phosphorylation, further causing reduced active level of RhoA-myosin II and increased active level of Rac1-PAK1-Cofilin, consequently led to disordered contractile stress fibers and prominent lamellipodia. As a result, cells displayed depolarized morphology and compromised directional migration. Collectively, we propose a model in which feedback-driven regulation between actin and CAV-1 instructs persistent cell migration.

Keywords: actin filaments, actomyosin bundles, Arp2/3 complex-dependent lamellipodia, directional cell migration, caveolin-1

INTRODUCTION

The actin cytoskeleton and caveolae are important players in regulating cell morphology and directional migration. Early electron microscopy studies revealed the association of caveolae with filamentous actin (Rohlich and Allison, 1976; Rothberg et al., 1992; Valentich et al., 1997), and later the actin-binding protein filamin A was found to be important for caveolae co-alignment with actin stress fibers (Muriel et al., 2011). However, aside from membrane-located caveolae which has been extensively studied as tension sensor and intimately interact with cortical actin

(Sinha et al., 2011), the interactive mechanisms between actin and cytoplasmic caveolin-1 (CAV-1), principal structural component of caveolae (Navarro et al., 2004), have remained elusive. For example, how specific actin assemblies control the cytoplasmic CAV-1, and reciprocally, how CAV-1 protein *per se* regulate signaling cascades to control dynamic actin assemblies and subsequent cell behavior.

Cytoplasmic CAV-1 could either form pivotal structural component for caveolae, or form non-caveolae CAV-1 vesicles/foci (Razani et al., 2002b; Pol et al., 2020). It is speculated, but no direct evidence yet, that the organization and trafficking of both CAV-1 forms are tightly associated with distinct intracellular actin assemblies and critical actin-binding proteins. Global disruption of the actin network by cytochalasin D treatment was found to form strong clustering of CAV-1 (Fujimoto et al., 1995; Mundy et al., 2002). Patches of non-polymerized actin are concentrated around rapidly moving CAV-1 spots (Echarri et al., 2012; Stoeber et al., 2012). Depletion of myosin-1c, one actin associated motor protein, induces a perinuclear accumulation of CAV-1 and a decrease in caveolar density (Hernandez et al., 2013). Knockdown of actin nucleator mDia1 and Abl kinase induces caveolae clustering, whereas active mDia1 increases stress fiber formation, and reduces the numbers of clustered "caveolar rosettes" superstructures (Echarri et al., 2012). Nevertheless, silencing the Arp2/3 complex or its activators N-WASP and cortactin does not affect the endocytic process of CAV-1 vesicles from the plasma membrane (Echarri et al., 2012), but how their roles during the dynamic regulation of intracellular CAV-1 remain less examined.

Actin assemblies require the spatial and temporal integration of different signaling components (Ridley et al., 2003; Vicente-Manzanares et al., 2005). By coordinating the active levels of Rho family of small GTPases and ultimately, actin polymerization, Rac1 regulates lamellipodia protrusion and membrane ruffles and Cdc42 triggers filopodia, whereas RhoA regulates the formation of actomyosin-formed stress fibers and cell contractility (Ridley et al., 2003; Raftopoulou and Hall, 2004; Vicente-Manzanares et al., 2005).

Previous reports suggest that CAV-1 promotes cell migration (Zhang et al., 2000; Gonzalez et al., 2004; Grande-Garcia et al., 2007; Joshi et al., 2008; Hill et al., 2012). For example, CAV-1 depletion in mouse embryonic fibroblasts has been shown to elevate the active level of Rac1 and Cdc42 while decrease the RhoA activity, thus lead to defects in actin remolding associated cell motility (Grande-Garcia et al., 2007). However, other studies indicate that CAV-1 could be a negative regulator in the context of cell migration. For instance, restoration of CAV-1 expression in MTLn3 cells reduces the chemotactic directed cell migration (Zhang et al., 2000). Likewise, CAV-1 knockdown increased the persistent migration toward sphingosine-1 phosphate in bovine aortic endothelial cells (Gonzalez et al., 2004). Although some of these discrepancies could be ascribed to technical or cell type specificity issues, it appears important to ascertain what kind of role, if any, CAV-1 plays in the coordinated processes of directional migration through controlling of actin assembly and remodeling.

In this study we identified that the cytoplasmic CAV-1 vesicles move concurrently with the retrograde flow of actin filaments toward the deep cytoplasmic perinuclei region, and meanwhile are also able to laterally slide along the actin filaments. Moreover, contractile actomyosin bundles determine the organization and dynamics of intracellular CAV-1 by disturbing its phosphorylation level, whereas branched actin structures are dispensable. Importantly, CAV-1 depletion leads to compromised intrinsic persistent migration through remolding the active level of AMPK, which in turn regulates the activity of Rac1 and downstream PAK1 and Cofilin for protrusive lamellipodia, and correspondingly the activity of RhoA and subsequent changes in stress fibers formation and contraction. Furthermore, the phosphorylation of CAV-1 on site Tyr14 plays an essential role in regulating these kinase-GTPase signaling axis governed actin remodeling. Taken together, our study comprehensively investigates and hence provides new insights into the interactive feedback mechanisms between actin assemblies and cytoplasmic CAV-1 in the context of cell migration.

RESULTS

Cytoplasmic CAV-1 Interacts With Actin Filaments in Human Osteosarcoma Cells

To identify novel actin filament interactions, we performed a proximity-dependent biotin identification (BioID) analysis (Roux et al., 2012) on human osteosarcoma cells (U2OS) using a biotin ligase fused to Tropomyosin-3.1 (Tpm3.1), a central actin filaments component (**Supplementary Figure 1A**; Parreno et al., 2020). Among the high-confidence interactors, CAV-1, which has been used as a measure of cytoplasmic trafficking of both individual and clustered forms of caveolae (Mundy et al., 2002; Echarri et al., 2012), was chosen for further investigation (**Figure 1A**).

Previous studies have demonstrated co-alignment of CAV-1 with filamentous actin in a number of cell types, such as NIH3T3 cells, epithelial cells, fibroblasts, myofibroblasts and muscle cells (Rohlich and Allison, 1976; Rothberg et al., 1992; Valentich et al., 1997). Immunofluorescence imaging on U2OS cells, which are much adherent and show clear endogenous staining of cytoskeleton (Jiu et al., 2015, 2019), revealed an extensive actin network and readily recognizable CAV-1 vesicles, and the cytoplasmic CAV-1 vesicles were found aligned with actin filaments occasionally (**Figure 1B**), indicating the enability to determine the association between these structures in U2OS cells.

We next assess the actin associated intracellular movement of CAV-1, using expression of fluorescent protein fusion constructs. This revealed a punctate pattern that colocalized with endogenous CAV-1 but showed no co-distribution with Rab8-labeled endosomes, indicating a proper distribution with respect to the endogenous protein (**Supplementary Figure 1B**). By using wheat germ agglutinin (WGA), a small-molecule marked the plasma membrane, we showed that the actin filaments-associated CAV-1 signals were mainly localized in the cytoplasm

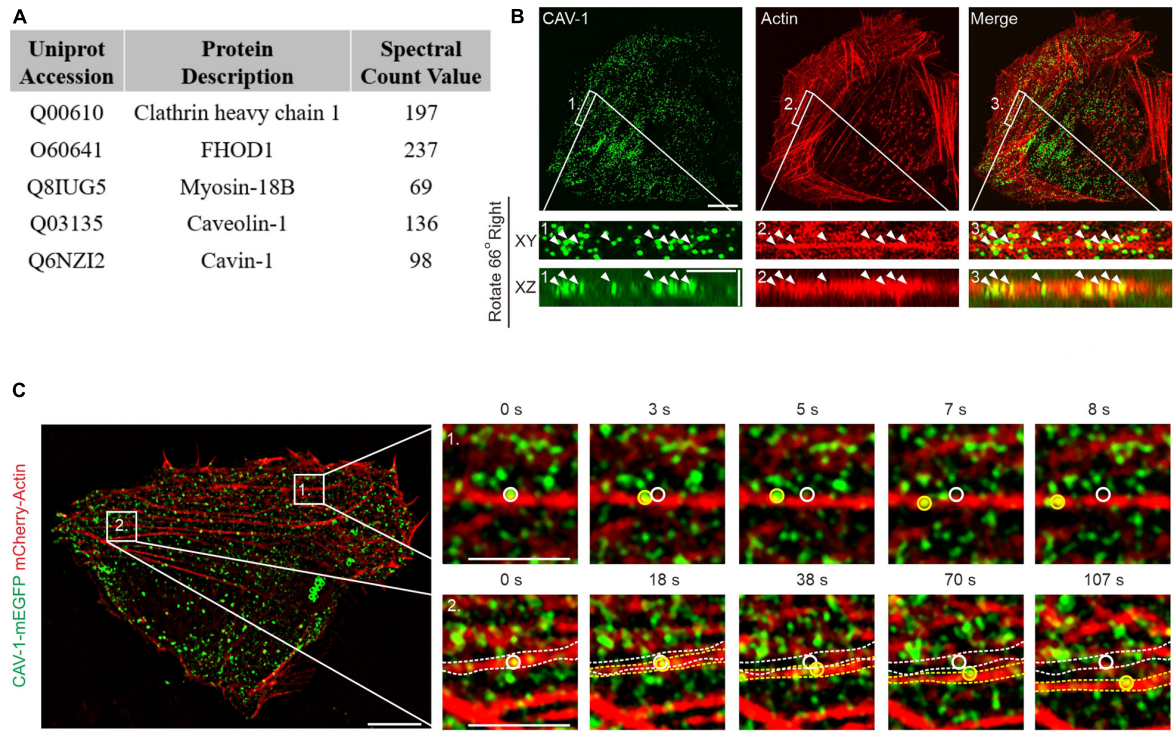

FIGURE 1 | The association of actin filaments with cytoplasmic CAV-1 in human osteosarcoma cells. **(A)** Top protein hits from the BioID screen for identification of Tpm3.1-associated proteins in U2OS cells. **(B)** Localization of endogenous CAV-1 and actin filaments in U2OS cells detected by CAV-1 antibody and fluorescent phalloidin, respectively. Magnified regions from the area indicated by white boxes demonstrate that cytoplasmic CAV-1 aligns with actin filaments (white arrowheads). The bottom panels show the orthographic view of the enlarged region, where "XY" and "XZ" indicated different cross-sections. Bars, 10 μm (in cell images), 2 μm (in magnified images and orthographic views). **(C)** Time-lapse imaging of U2OS cells co-expressing CAV-1-mEGFP and mCherry-actin revealing that actin-associated cytoplasmic CAV-1 vesicles move along actin filaments (Box 1) and do retrograde flow with contractile arcs (Box 2). The magnified regions of Box 1 and 2 in different time point are shown on the right panels, respectively. White and yellow circles and dotted lines in the magnified regions indicate the starting and ending position of discrete CAV-1 tagged vesicles and contractile arcs, respectively. The recording was set as every 1 s for 200 s. Bars, 10 μm (in cell image) and 5 μm (in Box 1 and Box 2).

(**Supplementary Figure 1C**). To record the cytoplasmic CAV-1 vesicles, we optimized the imaging focal plane based on the clear and sharp appearance of DAPI-labeled nucleus in the following experiments, which demarcated the cytoplasmic (middle layer) rather than the plasma membrane (bottom layer) field (**Supplementary Figure 1D**).

Live cell imaging enabled us to identify that while the CAV-1 vesicles at the perinuclear area did not exhibit regular movements, others which close to cell periphery associated with contractile actin transverse arcs and displayed retrograde flow toward the cell center, accompanying with cases of sliding along actin filaments (**Figure 1C** and **Supplementary Videos 1, 2**). Together, these data provide direct evidences that CAV-1 vesicles interact with actin network in human osteosarcoma cells.

Contractile Actin Assemblies Are Critical for the Organization and Dynamics of CAV-1 Vesicles by Disturbing Its Phosphorylation Level

Global pharmacological disruption of actin cytoskeleton in U2OS cells leads to an increase of cytoplasmic CAV-1 clustering (**Supplementary Figures 2A,B**). In migrating cells actin filaments are able to assemble into distinct three-dimensional structures. To further elucidate the underlying regulation by these specific actin arrangements to cytoplasmic CAV-1 vesicles, we employed different actin-directed drugs with specific targets (**Figure 2A**). Blebbistatin and CK666 inhibiting myosin II ATPase activity and Arp2/3 complex were applied, and thereby interfering with the formation of contractile and branched filament assemblies, respectively (Kovacs et al., 2004; Chanez-Paredes et al., 2019). Neither of the drugs affected the transcription and expression level of CAV-1 (**Supplementary Figures 2C,D**), while fluorescence imaging witnessed their expected effects on actin organization with extensive loss of prominent contractile bundles after exposure to blebbistatin and of lamellipodia after CK666 treatment, respectively (**Figure 2A**). Enlarged CAV-1 vesicles appeared upon blebbistatin addition, but remain similar size as in wild-type under CK666 circumstance (**Figure 2B**). Moreover, the motility of cytoplasmic CAV-1 vesicles was significantly compromised when myosin II activity, but not Arp2/3, was inhibited (**Figure 2C**). Having identified that actomyosin dependent contractility is important for cytoplasmic CAV-1, prompted us to confirm this influence by using

alternative approach. Myosin-18B depletion cells are reluctant to form large myosin II stack and subsequent result in less contractile actin stress fibers (Jiu et al., 2019), while elimination of ARPC2, component of Arp2/3 complex (Goley and Welch, 2006), leads to less branched actin formed lamellipodia. Consistent with the results by pharmacological inhibitors, increased size and decreased motility of CAV-1 vesicles were observed in myosin-18B knockout cells, but not ARPC2 knockdown cells (**Supplementary Figures 2E–H**). Fluorescence recovery after photobleaching (FRAP) measurement was also applied to validate the relatively slow kinetics of cytoplasmic CAV-1 molecules lacking of contractile actomyosin bundles (**Figures 2D,E**).

Tyr14 is an important phosphorylation site to modulate CAV-1 activity and subsequent focal adhesion dynamics, cell migration and mechanical stimuli (Navarro et al., 2004; Zimnicka et al., 2016; Wong et al., 2020). The phospho-deficient (Y14F) and phospho-mimic (Y14D) mutants were exogenously expressed in CAV-1 knockout (CAV-1 KO) cells, respectively, to eliminate the interference of endogenous CAV-1. With tracking of real-time imaging, we revealed that the CAV-1 (Y14D) vesicles represented faster motility while the CAV-1 (Y14F) vesicles are overall slower than wild-type (**Figures 2F,G**), suggesting that CAV-1 phosphorylation is intimately correlates with its cytoplasmic dynamics.

Notably in this context, we examined the effects of above drugs on the phosphorylation state of CAV-1. Western blot indicated that the phosphorylated CAV-1 level on site Tyr14 was apparently decreased in actomyosin inhibition vs. wild-type, but was not significantly altered upon Arp2/3 inhibition (**Figures 2H,I**). Taken together, these data demonstrate that contractile actin assemblies are critical for the organization and dynamics of cytoplasmic CAV-1, most likely by regulating its phospho-related active level.

Phospho-Deficient and Depletion of CAV-1 Compromises the Assembly of Contractile Stress Fibers by Deactivating RhoA-Dependent Myosin Phosphorylation

To explore the cellular function of CAV-1, we generated CAV-1 knockout (KO) U2OS cells by CRISPR/Cas9 approach with two different target sites, and one of the CAV-1 KO cell lines was chosen for further analysis (**Supplementary Figure 3A**), and the rest cells were used for verification in some of the experiments (data not shown). Phalloidin staining was shown that wild-type cells contained prominent stress fibers, whereas both CAV-1 KO and RNA silencing induced CAV-1 knockdown (CAV-1 KD) cells contained a disorganized meshwork of actin filaments, characterized by thinner contractile stress fibers (**Figure 3A** and **Supplementary Figures 3B,C**). The quantification by using Ridge Detection plugin in ImageJ (Kumari et al., 2020; Zhao et al., 2020) confirmed that there was significant decrease in levels of thick actin filament bundles in CAV-1 KO/KD cells, whereas the total amount of filaments remained comparable (**Figure 3B** and **Supplementary Figure 3C**). To allow more precise analysis, cells were plated on crossbow shaped fibronectin micropatterns, where they obtain nearly identical shapes and display characteristic organization of stress-fiber network (Jiu et al., 2015). The contractile actomyosin bundles were typically thinner in CAV-1 KO cells compared to wild-type cells on micropatterns (**Figure 3C**). Moreover, CAV-1 KO cells displayed wider lamella which is a phenotype associated with defects in the assembly and contractility of stress fibers (Burnette et al., 2014; Jiu et al., 2015). Corresponding with the reduced amounts of thick stress fibers, the average sizes of vinculin-positive focal adhesions and phosphorylation level of focal adhesion kinase (FAK) were decreased in CAV-1 KO cells (**Figure 3C** and **Supplementary Figure 2D**). Importantly, exogenously expression of the full-length CAV-1-mEGFP completely restore the stress fiber and focal adhesion phenotypes, but not the phospho-deficient CAV-1(Y14F)-mEGFP (**Figures 3A–C**), indicating that Tyr14 is a critical site for CAV-1 and expression this single point mutation of CAV-1 recapitulates the CAV-1 KO phenotype of compromised stress fiber assemblies. Furthermore, CAV-1 deficient cells exhibited weaker contractile forces and an unbalanced tension distribution to the substrate (**Figure 3D**), which is the consequences from actomyosin defects.

Small GTPase RhoA regulates the phosphorylation of myosin light chain (MLC) to promote stress fiber contractility and assembly (Guilluy et al., 2011a,b; Lessey et al., 2012). By using pull-down assay and RhoA-GTP biosensor GFP-AHPH (Piekny and Glotzer, 2008; Rong et al., 2021), we revealed that the active level of GTP bound RhoA significantly decreased in CAV-1 KO cells, exogenously expression of CAV-1-mEGFP restore the active level of RhoA (**Figure 3E** and **Supplementary Figure 3E**). To confirm these observations, we tested the consequences downstream of RhoA. Phosphorylation of MLC and the level of tropomyosin (isoform Tpm4.2) which required for myosin II filament formation and integrity (Umemoto et al., 1989; Burgess et al., 2007; Geeves et al., 2015), also displayed significant reduction in CAV-1 KO cells (**Figure 3F** and **Supplementary Figures 3F,G**). p190RhoGAP is a major upstream negative regulator of Rho GTPases (Jaffe and Hall, 2005), knockdown of which restores the decreased RhoA-GTP level and the weaker stress fibers in CAV-1 depletion cells (**Figures 3G,H**). Collectively, these results reveal that CAV-1 is critical for the contractile stress fibers formation.

Phospho-Deficient and Depletion of CAV-1 Leads to AMPK Activation Followed by Rac1-Dependent PAK1 and Cofilin Phosphorylation, and Subsequent Lamellipodia Formation

It is important to note that in addition to disorganized stress fiber network, both CAV-1 KO and phospho-deficient CAV-1(Y14F) cells appear more pronounced lamellipodia in the cell edge visualized by actin and ARPC2 staining (**Figures 3A**, **4A**). The actin distribution was further checked by interference reflection microscopy (IRM), which is applied to visualize molecules near the cell-substrate interactions (Verschueren, 1985). Consistent with aforementioned phalloidin staining, strong stress fibers were

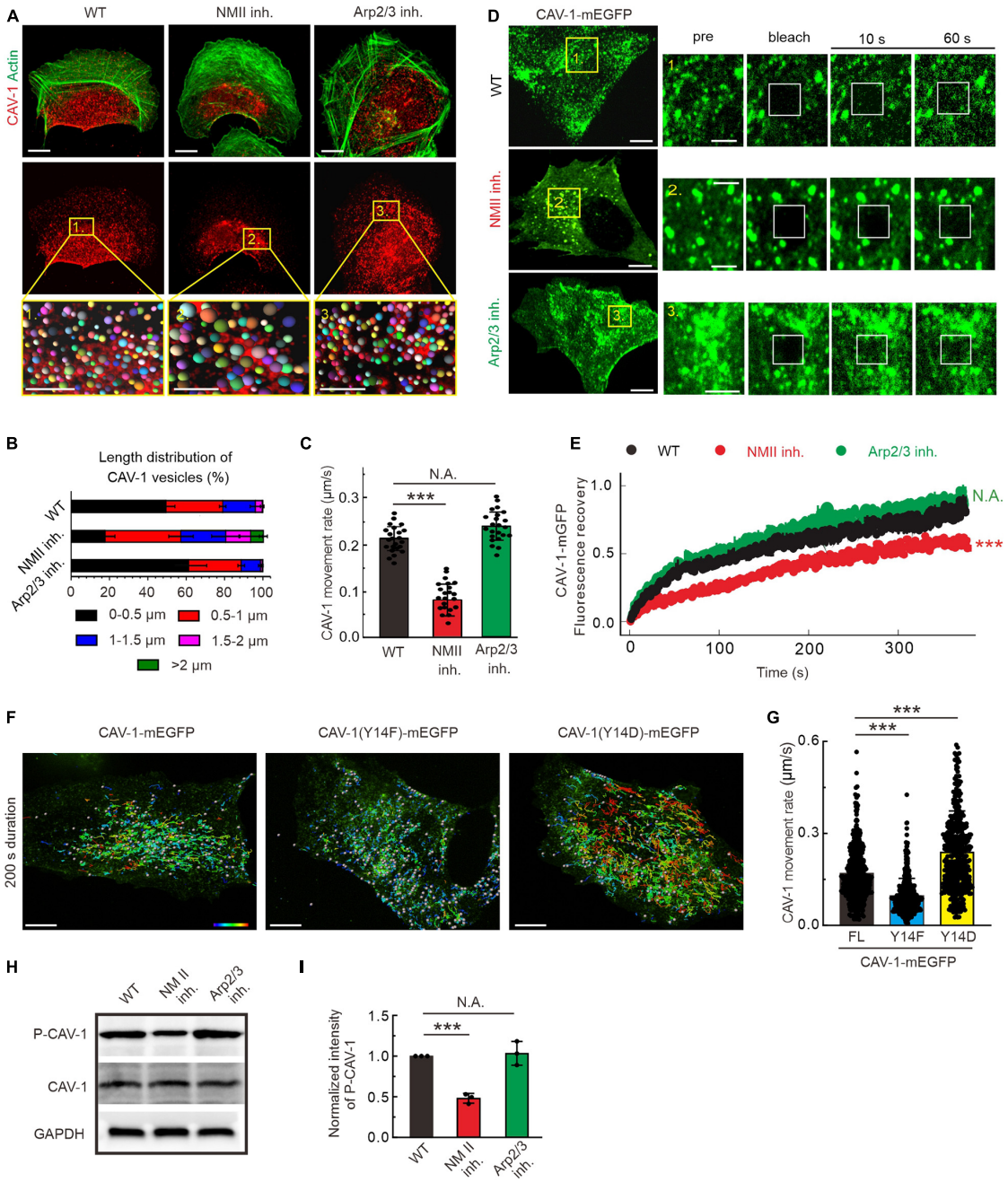

FIGURE 2 | The organization, dynamics and phosphorylation of CAV-1 are regulated by contractile actin assemblies. **(A)** Immunofluorescence staining of endogenous F-actin and CAV-1 vesicles in wild type (WT), myosin II inhibition (NMII inh.) and Arp2/3 complex inhibition (Arp2/3 inh.) cells, respectively. The representative analysis of CAV-1 positive dots detected by Imaris of magnified yellow boxes 1, 2, and 3 on the top panels are marked as balls which are randomly colored on the lower panels. The size of the color balls indicates the calculated sizes of CAV-1 vesicles. Bars, 10 μm (in cell images) and 5 μm (in the magnified box). **(B)** The length distribution of CAV-1 vesicles. The number of vesicles in each group of size is divided by the total CAV-1 number of the same cell. n = 25,602 vesicles from 32 WT cells, 13,456 vesicles from 31 myosin II inhibition cells, and 26,103 vesicles from 29 Arp2/3 complex inhibition cells. **(C)** Quantification of the movement rate of CAV-1 vesicles in wild-type (n = 26), myosin II inhibition (n = 22), and Arp2/3 complex inhibition (n = 23) cells. **(D)** FRAP analysis of CAV-1-mGFP dynamics in WT, NM II inh. and Arp2/3 inh. cells. Magnified regions represent time-lapse images of the bleached regions. Bars, 10 μm (in cell images) and 5 μm (in the magnified time-lapse image). **(E)** Normalized average FRAP recovery curves of CAV-1-mEGFP in WT (n = 23), NM II inh. (n = 22), and Arp2/3 inh. (n = 22) cells. **(F)** The representative 200 s duration dot tracking analysis of mEGFP tagged CAV-1, CAV-1(Y14F) and CAV-1(Y14D) vesicles in CAV-1 KO cells by Imaris. Color-coded bar from blue to red indicates the tracked mean speeds ranging from 0 to 0.4 μm/s. Bars, 10 μm. **(G)** Quantification of the movement rate of CAV-1 positive vesicles. n = 419/496/432 vesicles from 10 CAV-1/CAV-1(Y14F)/CAV-1(Y14D)-mEGFP expressing cells. **(H,I)** Western blot analysis **(H)** and quantifications **(I)** of phosphorylated CAV-1 (Tyr14) (compared to total CAV-1) in WT, NM II inh. and Arp2/3 inh. cell lysates. The obtained intensity value from wild-type cells was set to 1. n = 3. Data in panel **(C,G,I)** are presented as mean ± SD. ***$P \leq 0.001$; N.A., not significant (one-way ANOVA). All the data are from three independent experiments.

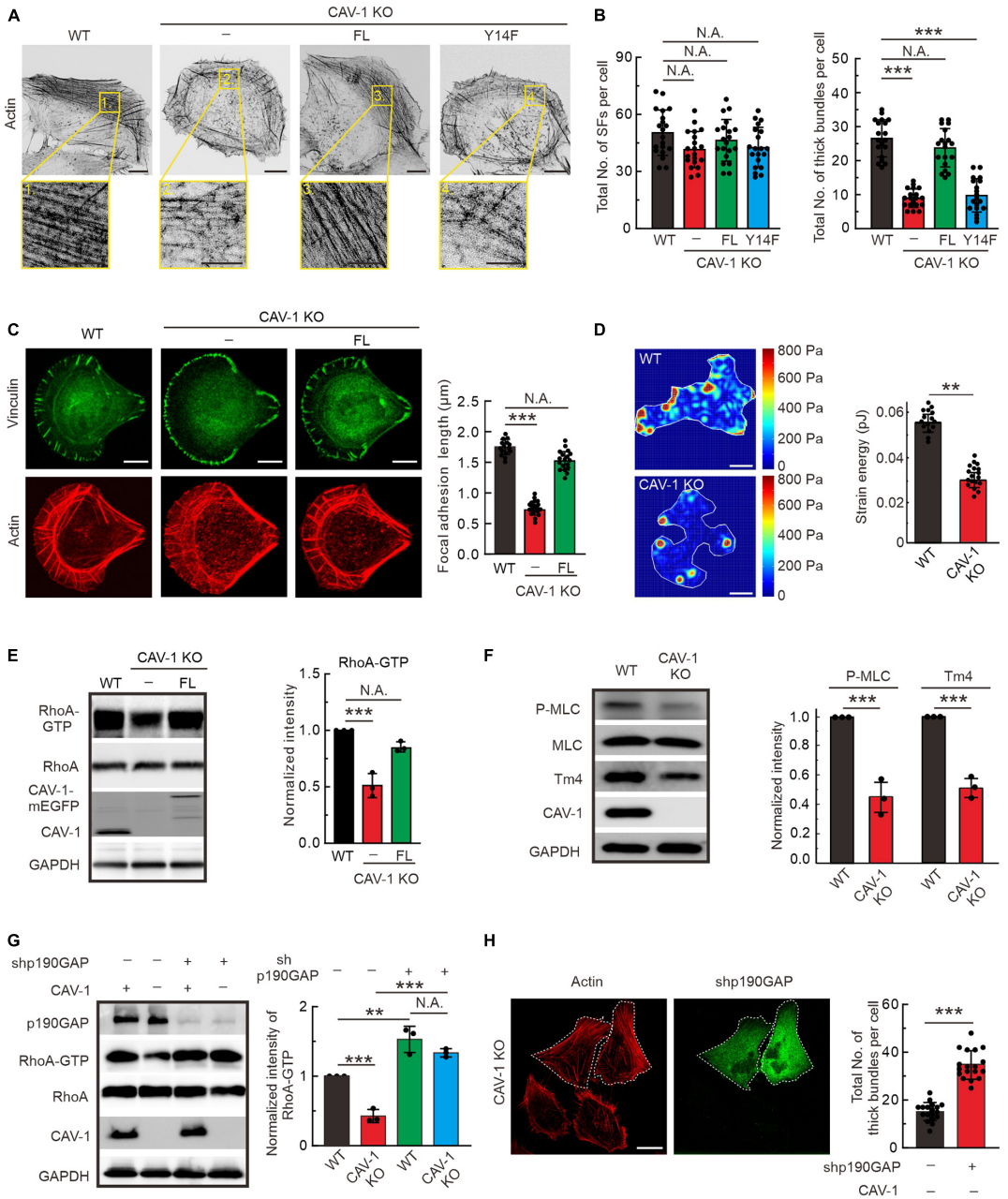

FIGURE 3 | RhoA-Myosin II regulated assembly of contractile stress fibers is inhibited in CAV-1 KO cells. **(A)** Representative images of actin filaments visualized by phalloidin in WT, CAV-1 knockout (CAV-1 KO), full-length CAV-1(FL), and phospho-deficient CAV-1(Y14F) expressing cells. Magnified regions represent the contractile stress fiber. Bars, 10 μm (in cell images) and 5 μm (in the magnified box). **(B)** The average numbers of total and thick filaments were calculated for cells depicted in panel A. n = 20 cells from each group. **(C)** Representative images of actin filaments and focal adhesions visualized by phalloidin and vinculin antibody staining, respectively, in WT, CAV-1 KO cells, and CAV-1(FL)-mEGFP expressing cells cultured on crossbow shaped fibronectin coated micropatterns. Bars, 10 μm. Quantifications of focal adhesion lengths of each group are shown on the left. n = 15/17/18 from WT/CAV-1 KO/CAV-1(FL)-rescue cells. **(D)** Representative force maps of WT and CAV-1 KO U2OS cells grown on 25 kPa polyacrylamide dishes with fluorescent nanobeads. Bars, 10 μm. Quantification of contractile strain energy in WT (n = 15) and CAV-1 KO (n = 17) cells are shown on the right. **(E)** Pull-down assays were performed for WT, CAV-1 KO, and CAV-1(FL)-rescue cells. Proteins bound to GST-Rhotekin binding domain were analyzed by western blots and further quantified (compared to total RhoA) based on the band's intensity. n = 3. **(F)** Western blot analysis and quantifications of phosphorylated MLC (Thr18/Ser19) (compared to total MLC) and Tpm4.2 in WT and CAV-1 KO cell lysates. n = 3. **(G)** WT and CAV-1 KO cells were transfected with Control shRNA and p190RhoGAP shRNA for 72 h, respectively. Cell lysis from each group were analyzed by western blots and further quantified based on the band's intensity. n = 3. In panel **(E–G)**, the obtained intensity value from WT cells was set to 1. **(H)** CAV-1 knockout cells transfected with p190RhoGAP shRNA were stained by Alexa 568 phalloidin. The p190RhoGAP knockdown cells are marked by dotted lines. The average numbers of thick filaments were calculated on the right. n = 18 cells from each group. Data in panel **(B–H)** are presented as mean ± SD. In **(B,C,G)**, $^{***}P < 0.001$; $^{**}P < 0.01$; N.A., not significant (one-way ANOVA). In **(D–F,H)**, $^{***}P < 0.001$; $^{**}P < 0.01$; N.A., not significant (unpaired t-test). All the data are from three independent experiments.

hardly observed in CAV-1 KO cells, while more prominent lamellipodia were localized around the leading edge in response to CAV-1 depletion (**Supplementary Figure 4A**). To test whether strong lamellipodia has consequences in membrane ruffling, we performed time-lapse analysis focusing on the cell edges and revealed that ruffling is much faster and broader, yet concomitantly not able to push membrane forward in CAV-1 KO cells, whereas the protrusive ruffling activity in wild-type cells display less frequency and occurs only in the direction of movement (**Figure 4B** and **Supplementary Video 3**).

AMP-activated protein kinase (AMPK) is a phylogenetically conserved intracellular energy sensor that has been shown to regulate small GTPases (Salani et al., 2012; Luo et al., 2018). By western blots, we noticed that the phosphorylation level of AMPK was significantly increased in CAV-1 KO cells, which could be rescued by full-length but not Y14F phospho-deficient CAV-1, furthering indicating the essential role of site Tyr14 of CAV-1 and confirming the actin associated phenocopy of CAV-1 KO with CAV-1 (Y14F) mutation (**Figure 4C**). In addition to RhoA, we also measured the GTP bound active levels of Rac1 and Cdc42, and found that CAV-1 depletion led to more active Rac1 and Cdc42 while their total protein levels remained unaffected (**Figure 4D** and **Supplementary Figure 4B**). It has been already known that Rac1 induce the formation of lamellipodia and surface protrusions generated by actin-remodeling reactions (Ridley et al., 1992, 2003). In this regard, the thicker lamellipodia and active membrane ruffling observed in CAV-1 KO cells fit well as a consequence of the active AMPK and Rac1.

Furthermore, we evaluated and found an increase in the basal activation of lamellipodia related PAK1 and Cofilin (**Figure 4E**). Importantly, the phosphorylated AMPK, PAK1 and Cofilin in CAV-1 KO cells prefer to localize more to the cell edges where lamellipodia form (**Figure 4F** and **Supplementary Figures 4C–F**). By treating with AMPK inhibitor compound C (Dasgupta and Seibel, 2018), both the distribution of phosphorylated Cofilin and lamellipodia width were restored to wild-type level in CAV-1 KO cells (**Figure 4G**), supporting the hypothesis that changes of actin protrusive network in the absence of CAV-1 is regulated by AMPK-Rac1-PAK1-Cofilin signaling cascade.

To test whether AMPK is the original cause for the actin network rearrangement in CAV-1 depletion cells, we blocked AMPK activation and revealed the clear recovery of increased Rac1-GTP and decreased RhoA-GTP, as well as elevated levels of phosphorylated PAK1 and Cofilin in CAV-1 KO background (**Figure 4H**). Taken together, we identified that sensitize AMPK mediated activities of GTPases in CAV-1 depletion cells play essential roles for actin cytoskeleton remolding.

Cell Morphology and Directional Migration Are Impaired by Depletion of CAV-1

In order to explore whether the dysbiosis of actin assemblies in CAV-1 depletion cells affects cell shape and behavior, we recorded and measured cell morphology and directional cell migration. Most of wild-type U2OS cells exhibited a polarized morphology, with an elongated, polygonal shape. However, CAV-1 depletion cells adopted a rounded, non-polarized shape with lamellipodia encircling the entire cell (**Figures 5A,B**). Moreover, both the migration velocity and persistence were significantly reduced in CAV-1 KO cells quantified from cells on the custom-designed micro-channels and wound healing settings (**Figures 5C–E**, **Supplementary Figures 5A,B**, and **Supplementary Video 4**). Hepatocarcinoma Huh7 cells have no endogenous CAV-1 (Moreno-Caceres et al., 2017) (**Supplementary Figures 5C,D**) and stable exogenously expression of CAV-1-mEGFP led to increased would healing ability (**Supplementary Figures 5E,F**), further validating the role of CAV-1 in cell migration. Collectively, our results demonstrate that CAV-1 is required for the integrity and hemostasis of actin assemblies, and subsequent cell polarized morphology establishment and directional cell migration.

DISCUSSION

Despite accumulated information regarding the association between cortical actin filaments and membrane-located mechanosensitive caveolae with tension reservoir function (Sinha et al., 2011), here we propose a feedback-driven model which demonstrate that the interplay between cytoplasmic actin assemblies and phosphorylated CAV-1 coordinates cell migration (**Figure 5F**). Aside from plasma membrane bounded CAV-1, we observed that the cellular CAV-1 display actin associated motility by sliding along or/and undergoing retrograde flow with actin filaments. Adequate contractility of actin filaments is essential for the phosphorylation of CAV-1 on its critical site Tyr14, and the subsequent distribution and motility of the intracellular CAV-1 vesicles. Importantly, both CAV-1 depletion and CAV-1 phosphorylation on Tyr14 are able to affect the active levels of AMPK, RhoA/Rac1 GTPase, and further disrupt the homostasis of contractile and protrusive structures of cytoplasmic actin, which lead to significant changes in cell morphology and directional migration.

In view of live cell imaging findings that cytoplasmic CAV-1 vesicles not only move along actin filaments but also accompany with actomyosin transverse arcs for centripetal flow, it is tempting to speculate that these "tracking" and "anchoring" function of elongated actin filament bundles to CAV-1 vesicles perhaps requires molecular motor related contraction and consumes adenosine triphosphate (ATP) to implement these dynamic association. This speculation is coincided with our results that inhibiting the motor activity of myosin II significantly weakens the movement of the cytoplasmic CAV-1 vesicles (**Figures 2C–E**). Previous work by us reveals that vimentin intermediate filaments (IFs) function as physical barriers to restrain the intracellular trafficking of CAV-1 vesicles (Jiu, 2018; Shi et al., 2020). It is thus possible that the overall integrity and motility pattern of the cytoplasmic CAV-1 are comprehensively regulated by both actin and IFs cytoskeletal networks. Moreover, trafficking of CAV-1 from plasma membrane to perinuclear area has been reported by far dependent on microtubules (Conrad et al., 1995; Mundy et al., 2002; Echarri et al., 2012; Echarri and Del Pozo, 2015). Therefore, our finding which associates contractile actin

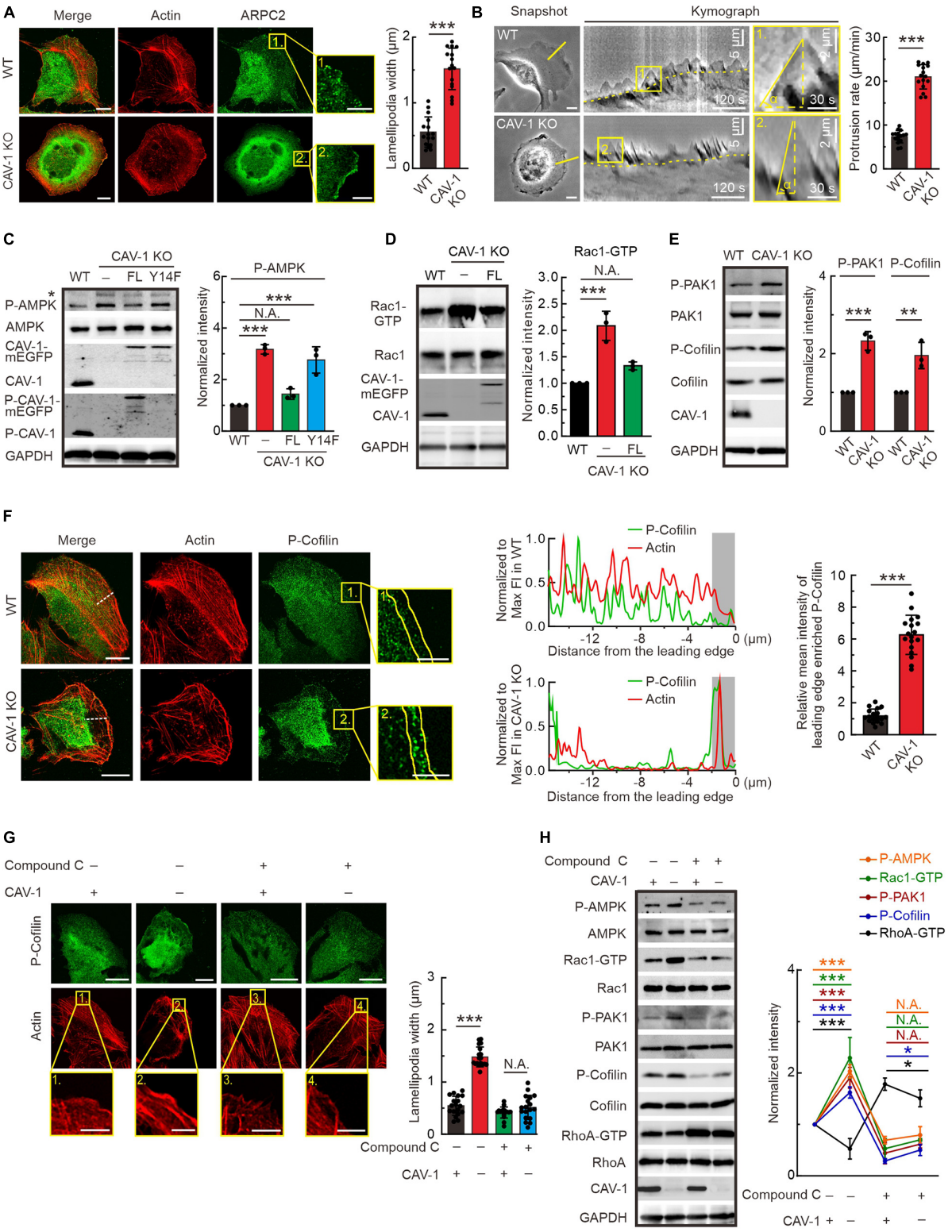

FIGURE 4 | Actin protrusive network is upregulated by AMPK-Rac1-PAK1-Cofilin signaling cascade in cells lacking CAV-1. **(A)** Immunofluorescence microscopy analysis demonstrating that more pronounced endogenous ARPC2 colocalizes with F-actin (visualized by Alexa 568 phalloidin) on the lamellipodia protrusions in CAV-1 deficient cells. Magnified regions of cell edges on the right show the distribution of ARPC2 in WT and CAV-1 KO cells. Bars, 10 μm (in cell images) and 5 μm (in the magnified box). Quantification of width of lamellipodial protrusions are shown on the right. *n* = 16 regions from 16 cells for each group. **(B)** Representative images of membrane ruffling by time-lapse microscope. 1-pixel-wide areas were cut out to generate a 300 frame 2 s interval kymograph. Yellow dashed lines

(Continued)

FIGURE 4 | Continued
indicate the track of cell movement. An enlarged region is displayed on the right, vertical dashed lines show the membrane protrusion distance, while horizontal dashed lines mark the duration of protrusion. Bars, 10 μm (in cell images) and 2 μm (in the magnified box). Quantification of protrusion rate are shown on the right. $n = 16$ regions from 16 cells for each group. **(C)** P-AMPK (Thr172) and total AMPK were detected from the lysates of each group by western blotting. Please note that CAV-1(Y14F)-mEGFP can't be detected by using phospho-CAV-1(Tyr14) antibody. Asterisk denotes the non-specific band. Quantification of P-AMPK (Thr172) levels (compared to total AMPK) from each group was shown on the right panel. $n = 3$. **(D)** Pull-down assays were performed for WT, CAV-1 KO, and CAV-1 KO; CAV-1-mEGFP re-expressed cells. Proteins bound to GST-PAK binding domain were analyzed by western blots and further quantified (compared to total Rac1) based on the band's intensity. $n = 3$. **(E)** Western blot analysis and quantification (compared to total PAK1 and Cofilin) of the levels of phosphorylated PAK1 (Thr423) and Cofilin (Ser3) in WT and CAV-1 KO cell lysates. $n = 3$. **(F)** Immunostaining and quantification of endogenous P-Cofilin (Ser3) and F-actin distribution in WT and CAV-1 KO cells. A 16 μm length line was used to generate a line profile to illustrate the co-localization of P-Cofilin (Ser3) and F-actin. The lamellipodia region was enlarged on the right, and 2 μm width region was chosen to analyze the mean intensity of P-Cofilin (Ser3) on the leading edge. Bars, 10 μm (in cell images) and 5 μm (in the magnified box). $n = 18$ regions from 18 cells for each group. **(G)** Immunostaining and quantification of endogenous P-cofilin (Ser3) distribution upon compound C treatment in WT and CAV-1 KO cells. Magnified regions represent the lamellipodia region. Bars, 10 μm (in cell images) and 5 μm (in the magnified box). $n = 18$ regions from 18 cells for each group. **(H)** Western blot analysis and quantification of the phosphorylated levels of AMPK (Thr172), PAK1 (Thr423), Cofilin (Ser3) and activity of Rac1 and RhoA upon compound C treatment. $n = 3$. In panel **(C–E,H)**, the obtained intensity value from wild-type cells was set to 1. All the data are presented as mean ± SD. In **(C,G,H)**, $^{***}P < 0.001$; $^{*}P < 0.05$; N.A., not significant (one-way ANOVA). In **(D–F)**, $^{***}P < 0.001$; $^{**}P < 0.01$ (unpaired *t*-test). All the data are from three independent experiments.

filaments with dynamics of cellular CAV-1 vesicles appears as a novel and complementary observation and will contribute to characterize the integrated cycling of caveolae. In addition, early studies have shown that the motility of CAV-1 is bound to depolymerized actin fibers by cytochalasin D application (Mundy et al., 2002; Thomsen et al., 2002; Stoeber et al., 2012). Combined with our results, we argue that the cytoplasmic distribution and dynamics of caveolae are mostly dependent on the contractile and filamentous status of actin, which representing the abundant and stiff of actin structures.

We assume that CAV-1 depleted U2OS cells which used in this study are considered to be deprivation of all three caveolin genes, because (1) CAV-2 has been shown to be degraded in the absence of CAV-1 through the proteasomal pathway (Razani et al., 2002a), and (2) CAV-3 is a muscle specific caveolin which showed no endogenous expression in U2OS cells (Galbiati et al., 2001; Razani et al., 2002b). In line with our finding, activation of AMPK by CAV-1 depletion has been also detected in other human colon tumor cells (Ha et al., 2012), indicating the activity control of CAV-1 to AMPK is a broad regulation in cancer cells. Moreover, depletion of CAV1 led to AMPK activation followed by a p53-dependent G1 cell-cycle arrest and autophagy, suggesting that elevated CAV1 may contribute to the ATP generation (Ha et al., 2012).

This is already a common view that there is mutual inhibition between the lamellipodia formation in cell frontness and the contractile stress fiber formation in cell backness (Li et al., 2003; Meili and Firtel, 2003; Xu et al., 2003) during persistent migration. Thus, we propose that CAV-1 depletion disequilibrates the balance between RhoA-mediated actomyosin bundles and Rac1-mediated lamellipodia formation, which potentiates the interpretation of the cell migration defects. Furthermore, here we identify a previously unexpected role for CAV-1 phosphorylation on site Tyr14 in inhibition of AMPK, and also disrupt the GTPase homeostasis and eventually cell migration.

Other plasma membrane domains, such as clathrin-coated pits are functionally linked to actin-regulatory factors (Girao et al., 2008; Grassart et al., 2014; Tweten et al., 2017), but an alignment with actin filaments is not apparent in those invaginations, suggesting that the association of caveolae with actin filaments fulfills a particular function, and that differentiates them from clathrin-coated pits. It will be interesting to explore in the future why caveolae associate with certain actin filament structures but not with others, when and how this association is stimulated and regulate various cell behavior.

MATERIALS AND METHODS

Cell Culture and Transfections

Human osteosarcoma (U2OS) cells and human hepatocarcinoma (Huh7) cells were maintained in high glucose (4.5 g/L) Dulbecco's modified Eagle's medium (DMEM) (#06-1055-57-1A, Biological Industries, Kibbutz Beit-Haemek, Israel) supplemented with 10% fetal bovine serum (FBS, #10270-106, Gibco, Waltham, MA, United States), 100 U/ml Penicillin, 100 μg/ml Streptomycin, and 4 mM L-Glutamine (later referred as complete DMEM) at 37°C in humidified atmosphere with 5% CO_2. Transient transfections were performed with Fugene HD (Promega, Madison, WI, United States) according to manufacturer's instructions using a Fugene HD: DNA ratio of 3.5:1 and 24 h incubation prior assay. siRNA experiments were performed with Lipofectamine RNAiMAX (Invitrogen, Carlsbad, CA, United States) using 40 nM On-target plus human siRNA of CAV-1 (target sequence 5′ CCCUAAACACCUCAACGAU 3′), and ARPC2 (target sequence 5′ CCAUGUAUGUUGAGUCUAA 3′) (Dharmacon, Lafayette, CO, United States) for 72 h, respectively. AllStars Neg. Control siRNA (Qiagen, Hilden, Germany) was used as a control siRNA.

CAV-1 CRISPR Knockout Cell Line Generation

CAV-1 knockout U2OS cell line was generated based on pSpCas9 (BB)-2A-GFP vector (a gift from Feng Zhang, #48138, Addgene, Cambridge, MA, United States). Briefly, two guide sequence targeting of human CAV-1 were selected based on CRISPR Design Tool[1] with the primer: 5′ AGTGTACGACGCGCACACCA 3′ and 5′

[1] crispr.mit.edu

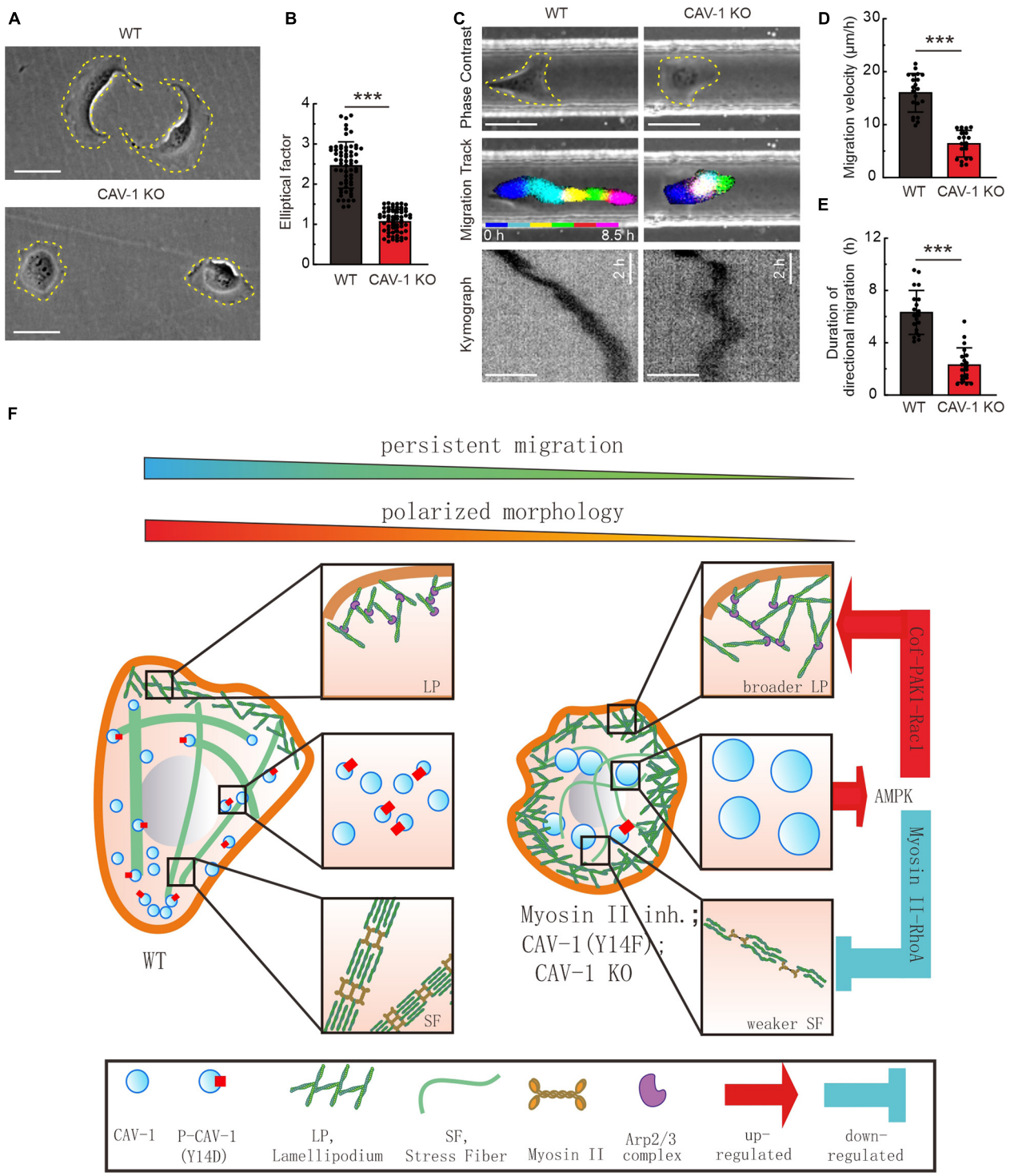

FIGURE 5 | CAV-1 is required for the cell polarized morphology establishment and directional cell migration. **(A)** Phase contrast imaging reveals the morphology of WT and CAV-1 KO cells. Bars, 50 μm. **(B)** The elliptical factor (length/breadth) were calculated for WT (n = 63) and CAV-1 KO (n = 63) cells. **(C)** Representative images form time-lapse videos of WT and CAV-1 KO cells migrating in 50 μm width and 50 μm height channels with fibronectin-coated surface. Color lines indicate the trajectory of each single cell nucleus stained by Hoechst and the kymograph are shown in the lower panel. Bars, 50 μm. **(D,E)** Migration velocities **(D)** and directionalities **(E)** of WT and CAV-1 KO cells. Quantification is based on tracking of the displacement of nuclei. The data are presented as average velocity obtained from a 10 h cell tracking. n = 21 cells for each group in panel **(D)** and 20 cells in panel E. In **(B,D)**, ***$P < 0.001$ (Mann-Whitney test); In **(E)**, ***$P < 0.001$ (unpaired t-test). All the data are from three independent experiments. **(F)** A working model illustrates the negative feedback loop between actin assemblies and cytoplasmic CAV-1.

TGGGGGCAAATACGTAGACT 3′ for CAV-1-knockout. Transfected cells were detached at 24 h post-transfection and sorted with FACS Aria II (BD Biosciences, Bedford, MA, United States), using low intensity GFP-expression pass gating, as single cell onto 96-well plate supplemented DMEM containing 20% FBS and 10 mM HEPES. CRISPR clones were cultivated for 2 weeks prior selecting clones with no discernible CAV-1 protein expression using western blotting.

Immunofluorescence Microscopy

Immunofluorescence (IF) experiments were performed as previously described (Jiu et al., 2019). Briefly, cells were fixed with 4% PFA in PBS for 15 min at room temperature (RT), washed three times with PBS, and permeabilized with 0.1% Triton X-100 in PBS for 5 min. Cells were then blocked in PBS supplemented with 5% BSA. Both primary and secondary antibodies were applied onto cells and incubated at RT for 2 h. Alexa-conjugated phalloidin was added together with secondary antibody solutions onto cells. Alexa 647-wheat germ agglutinin (WGA) (#W32466, Thermo Fisher Scientific) was used to visualize the plasma membrane. All IF data were obtained with Olympus SpinSR10 Ixplore spinning disk confocal microscope with UplanApo 100×/1.5 Oil objective (Olympus Corporation, Tokyo, Japan). The pixel size was optimized properly to achieve the maximum resolution which was calculated to be 65 nm. For detection and measure of the cytoplasmic CAV-1 tagged vesicles, the "Spots" tool of Imaris 9.2 (Bitplane, Zurich, Switzerland) was used with the configuration defined as 2 μm for estimated XY diameter. The numbers and sizes of spots were calculated subsequently. For detection and measure of the lamellipodia width, a plot profile perpendicular to the plasma membrane was made by using imageJ, and the peak zone was defined as the width.

Live Cell Imaging

For live cell imaging, 35 mm glass-bottomed dishes (MatTek Corporation, Ashland, MA, United States) were coated with 10 μg/ml fibronectin (#F2006, Sigma Corp., St. Louis, MO, United States) in PBS for at least 3 h at 37°C, washed with PBS twice and immersed in complete DMEM medium without phenol red (#01-053-1A, Biological Industries, Kibbutz Beit-Haemek, Israel) before seeding of cells. The time-lapse images of cells with transient transfection of CAV-1-mEGFP and mCherry-actin were acquired with Olympus cellSens Dimension system, consisting of an Olympus SpinSR10 Ixplore spinning disk confocal and a Yokogawa CSU-W1 confocal scanner. Appropriate filters, heated sample environment (+37°C), controlled 5% CO_2 and UplanApo 100×/1.5 Oil objective (Olympus Corporation, Tokyo, Japan) was used. The recording was set as every 1 s for 200 s and one focal plane was recorded for all live cell videos. For tracking and speed measurement of CAV-1 vesicles, the Imaris 9.2 (Bitplane, Zurich, Switzerland) "Track" module with globular-objects over time was used as in previous study (Jiu, 2018). Two micrometers estimated XY diameter, 5 μm max distance and 3 max gap size were set for analyzing.

Interference Reflection Microscopy (IRM)

In order to image cells using IRM, we added a 50/50 beam splitter (which reflects 50% and transmits 50% of the chosen wavelength) in an empty filter cube of the Olympus IX73 inverted widefield fluorescence microscopy (Olympus Corporation, Tokyo, Japan). The 50/50 beam splitter partially reflects the 488 nm light to the sample, and then the light reflected from the sample is collected by the camera. The light reflected from the glass/medium interface (I1) and the light reflected from the medium/cell plasma membrane interface (I2) can interference, the optical path difference between I1 and I2 will result in a constructive bright signal or a destructive dark signal (Verschueren, 1985; Mahamdeh and Howard, 2019).

Western Blotting (WB)

All cell lysates were prepared by washing the cells once with PBS and scraping them into RIPA lysis buffer (50 mM Tris pH 7.4, 150 mM NaCl, 1% Triton X-100, 1% sodium deoxycholate and 0.1% SDS) supplemented with 1 mM PMSF, 10 mM DTT, 40 μg/ml DNase I and 1 μg/ml of leupeptin, pepstatin, and aprotinin. All preparations were conducted at 4°C. Protein concentrations were determined with BCA Protein Assay kit (#23227, Thermo Fisher Scientific, Waltham, MA, United States) and equal amounts of the total cell lysates were mixed with Laemmli Sample Buffer (LSB), boiled, and ran on 12.5% SDS-PAGE gels. Proteins were transferred to nitrocellulose membrane with Trans-Blot Turbo transfer system (Bio-Rad, Hercules, CA, United States) using Mini TGX gel transfer protocol. Membrane was blocked in 5% BSA for 1 h at RT. Primary and secondary antibodies were diluted into fresh blocking buffer for overnight at 4°C and 1 h at RT, respectively. Proteins were detected from the membranes with SuperSigna West Femto Maximum Sensitivity Substrate (Thermo Fisher Scientific, Waltham, MA, United States).

Plasmids

mCherry-actin was a kind gift from Pekka Lappalainen (University of Helsinki, Finland). CAV-1-mCherry (#27705), CAV-1-mEGFP (#27704) and GFP-AHPH (#Cat68026) were from Addgene (Watertown, MA, United States). All plasmids were sequenced for verification. CAV-1(Y14D)-mEGFP and CAV-1 (Y14F)-mEGFP was constructed by the overlap extension method, respectively (Horton et al., 1989). To knockdown p190RhoGAP in U2OS cells, human p190RhoGAP (GenBank NM_004491.4) targeting sequence (5′ CCGGCGGTTGGTTCATGGGTACATTCTCGAGAATGTAC CCATGAACCAACCGTTTTTT 3′) and control, non-targeting sequence (5′ CCGGGGTTCTCCGAACGTGTCACGTCTCGA GACGTGACACGTTCGGAGAACCTTTTTG 3′) were cloned into pLKO.1-TRC-copGFP-T2A-Puro vector, respectively.

Drug Treatment

The following drugs were used at a defined dose and time: blebbistatin (#b0560; Sigma, St. Louis, MO, United States) with 10 μM for 30 min, CK666 (#sml0006, Sigma, St. Louis, MO,

United States) with 40 μM for 1 h, Latrunculin B (LatB, #sc-203318, Santa Cruz, Dallas, TX, United States) with 0.5 μM for 0.5 h and Compound C (#S7306, Selleck Chemicals, Houston, TX, United States) with 5 μM for 24 h.

Antibodies

The following antibodies were used in this study: CAV-1 (D46G3) rabbit antibody (1:1,000 dilution for WB, 1:200 for IF; #3267, Cell Signaling, Beverly, MO, United States); Phospho-CAV-1 (Tyr14) rabbit antibody (dilution 1:1,000 for WB; #3251, Cell signaling); AMPK rabbit antibody (dilution 1:500 for WB; #SAB4502329, Sigma, St. Louis, MO, United States); P-AMPK (Thr172) rabbit antibody (dilution 1:500 for WB, 1:100 for IF; #2531S, Cell Signaling); Cofilin (E-8) mouse antibody (dilution 1:1,000 for WB; #sc-376476, Santa Cruz, Dallas, TX, United States); Phospho-Cofilin (Ser3) rabbit antibody (dilution 1:1,000 for WB, 1:200 for IF; #3313, Cell signaling); p190RhoGAP rabbit antibody (dilution 1:2,000 for WB; #26789, Proteintech, Rosemont, IL, United States); FAK rabbit antibody (dilution 1:1,000 for WB; #3285, Cell Signaling); Phospho-FAK (Tyr397) rabbit antibody (dilution 1:1,000 for WB; #3283, Cell Signaling); PAK1 rabbit antibody (dilution 1:1,000; #2602, Cell Signaling); Phospho-PAK1 (Thr423)/PAK2 (Thr402) rabbit antibody (dilution 1:1,000 for WB, 1:200 for IF; #2601, Cell Signaling); Tpm4.2 (LC24) mouse antibody (dilution 1:500 for WB and IF; a kind gift from Peter W. Gunning, UNSW Australia); Phospho-myosin light chain 2 (Thr18/Ser19) rabbit antibody (dilution 1:500 for WB, 1:200 for IF; #3674, Cell Signaling); Myosin light chain mouse antibody (dilution 1:1,000 for WB; #M4401, Sigma); Vinculin mouse antibody (dilution 1:100 for IF; #V9131, Sigma); ARPC2 rabbit antibody (dilution 1:1,000 for WB and IF; #15058, Proteintech, Rosemont, IL, United States); Myosin-18B rabbit antibody (dilution 1:500 for WB; #HPA000953, Sigma); Rab8 rabbit antibody (dilution 1:100 for IF; #R5530, Sigma); and GAPDH mouse polyclonal antibody (dilution 1:1,000 for WB; #G8795, Sigma).

FRAP

Cells were transfected with CAV-1-mEGFP and incubated for 24 h. Confocal images were acquired with a 3I Marianas imaging system (3I Intelligent Imaging Innovations, Denver, CO, United States), consisting of an inverted spinning disk confocal microscope Zeiss Axio Observer Z1 (Zeiss, Oberkochen, Germany), a Yokogawa CSU-X1 M1 confocal scanner and 63 × /1.2 WC-Apochromat Corr WD = 0.28 M27 objective (Zeiss). Heated sample environment (+37°C) and 5% CO_2 control were used. SlideBook 6.0 software (3I Intelligent Imaging Innovations) was used for the image acquirement. Five pre-bleach images were acquired followed by bleaching scans with 100% intensity laser lines over the region of interest. Recovery of fluorescence was monitored 50 times every 200 ms and 300 times every 1 s. The intensity of the bleached area was normalized to a neighboring non-bleached area. Mean scatter plots were calculated from different FRAP experiments and the means and standard deviations were calculated.

Filament Analysis

The total number of stress fibers and the number of thick actin filament bundles in U2OS cells were quantified with ridge detection plugin (v1.4.0) from Fiji ImageJ (1.53c, Wayne Rasband, National Institutes of Health NIH). The parameters used for detecting the total number of stress fibers are: line width 20.0, high contrast 230, low contrast 100, sigma 6.57, low threshold 0.0, and upper threshold 0.34. The parameters used for quantifying the thick bundles are: line width 29.0, high contrast 230, low contrast 87, sigma 8.87, low threshold 0.0, and upper threshold 0.17. The dorsal stress fibers in cells on petri dishes and the ventral stress fibers in cells on micropattern chips are manually outlined, and subsequently measured the lengths for quantification.

BioID Screen

BirA-Tpm3.1 was transfected into U2OS cells, which induced biotinylation of transverse arcs and ventral stress fibers (**Supplementary Figure 1A**). Backbone vector pmycBioID-C1 was transfected as control. Cells were grown for 24 h in complete DMEM and another 24 h in the presence of 50 μM biotin. Single-step affinity purifications of the biotinylated proteins, liquid chromatography mass spectrometry sample preparation, and mass spectrometry were performed as in Jiu et al. (2015). To obtain a list of high-confidence protein interactions for Tpm3.1 the data was filtered against our in-house BioID contaminant database.

Real-Time Quantitative PCR

Total mRNA was extracted with GeneJET RNA purification kit (#K0731, Thermo Fisher Scientific, Madison, WI, United States) and single stranded cDNA was synthetized (#K1671, Thermo Fisher Scientific) from 500 ng of extracted mRNA. The following primers were used: forward CAV-1 5′ AACCTCCTCACAGTTTTCATCC 3′, reverse CAV-1 5′ CTTGTTGTTGGGCTTGTAGATG 3′, forward GAPDH 5′ GAAGGTGAAGGTCGGAGTC 3′, reverse GAPDH 5′ GAAGATGGTGATGGGATTTC 3′. Quantitative PCR reactions were carried out with Maxima SYBR Green/ROX (#K0221, Thermo Fisher Scientific) in Bio-Rad CFX96 (Bio-Rad). Changes in expression were calculated with $2^{-\Delta\Delta Ct}$ method, and normalized to GAPDH and WT expression levels, respectively.

Cell Migration Assay

The microfluidic device is made of PDMS (RTV615, NY, United States) by soft lithography from a patterned SU-8 silicon wafer. Glass coverslips were plasma bounded to PDMS layer. Each device consists of 10 channels of 50 μm in wide and height, 3 mm in length. In migration assay, all channels were coated with 10 μg/ml fibronectin for 1 h at 37°C. Cells were incubated with Hoechst 33342 for 10 min and subsequently washed twice with PBS and replaced with complete DMEM.

Cells were collected from culture dishes using trypsin-EDTA, and resuspended in complete DMEM to a concentration of 2×10^7 cells/ml. Twenty microliters of cell suspension was added to the device inlet. Cells were allowed to adhere and spread overnight. All wells of the device were then filled with 120 ml of complete DMEM. Devices were incubated at 37°C and 5% CO_2 before imaging by Olympus IX73 inverted microscopy with the UplanFL 10 × /0.3 objective (Olympus, Tokyo, Japan). Average migration velocity and directional migration duration were quantified by tracking the nucleus movement in between 5 min imaging cycles for 10 h. Only cells that did not collide with one another were selected for measurements.

Wound Healing Assay

Cells were seeded in a 6-well cell culture plate with a cell density of 25,000/cm^2 and cultivated at 37°C in 5% CO_2 overnight. Subsequently, the cell monolayers were scratched with a sterile 0.2 mL pipette tip to create linear wounds and washed with PBS to remove detached cells. Cells were incubated in a serum-free DMEM medium to eliminate cell proliferation and then observed by Olympus IX73 inverted microscopy with the UplanFL 10×/0.3 objective (Olympus, Tokyo, Japan). The migration rates were measured using ImageJ.

Small GTPase Activity Assay

Active RhoA, Rac1 and Cdc42 Detection Kit (#8820, #8815 and #8819, Cell Signaling, Beverly, MO, United States) were used to measure the activity of these small GTPases. Briefly, cell lysates were prepared by washing cells once with ice-cold PBS and scraping them into lysis buffer plus 1 mM PMSF. Next, transfer the cell lysate to the spin cup which contains 100 μl agarose beads and 400 μg GST-Rhotekin-RBD (for binding to RhoA-GTP) or GST-PAK1-PBD (for binding to Rac1/Cdc42-GTP). Incubate the reaction mixture at 4°C for 1 h with gentle rocking. Then wash the beads three times with washing buffer and incubated with reducing sample buffer for 2 min at RT. Centrifuge the tube at 6,000 g for 2 min and heat the eluted samples for 5 min at 100°C. Anti-Rho, anti-Rac1 and anti Cdc42 antibodies (#8789, #8631 and #8747, Cell Signaling) were used to test active RhoA, Rac1, and Cdc42 by western blot, respectively.

Traction Force Microscopy

Traction force microscopy was used to measure the contractile forces that cells exerted upon their substrate as previously described (Jiu et al., 2017). Briefly, cells were cultured for 3–8 h on custom-made 35-mm dishes (Matrigen Life Technologies, CA, United States) with fibronectin-coated PAA gel with either 25 or 0.5 kPa stiffness. The diameter of 200 nm yellow-green fluorescent (505/515) microspheres was immobilized to the surface of the gel. Images of the cells and the fluorescent microspheres directly underneath the cells were acquired during the experiments and after cell detachment with trypsin. By comparing the reference image with the experimental image, we computed the cell-exerted displacement field. From the displacement fields, and manual traces of the cell contours, together with knowledge of substrate stiffness, we computed the traction force fields using the approach of constrained Fourier-transform traction cytometry. From the traction fields, we calculated the strain energy by equation

$$U = \frac{1}{2}\int \mathbf{T}(r)\,.\mathbf{u}(r)dA$$

It was the total deformation energy produced by the cells through applying the traction on the surface of the substrate, which suggested an integrated measure of cell traction.

Statistical Analysis

Statistical data analyses were performed with Excel (Microsoft, Redmond, WA, United States) and Graphpad Prism 8 (GraphPad Software, La Jolla, CA). Normality of the data was examined with the Shapiro-Wilk test and a quantile-quantile plot. For the data following normal distribution, Student's two-sample unpaired *t*-test was used. If data did not follow normal distribution, Mann-Whitney *u*-test for two independent samples was conducted. One-way ANOVA followed by a Tukey's *post-hoc* test was used to evaluate differences between three or more groups. For analyzing the CAV-1 movement rate, the mean speed of each vesicle within 200 s live cell video was measured by Imaris "Track" module and pooled together to calculate the average rate with color bars indicating the tracked mean speed ranging from 0 to 0.4 μm/s (**Figure 2F**).

DATA AVAILABILITY STATEMENT

All datasets generated for this study are included in the article/**Supplementary Material**, further inquiries can be directed to the corresponding author/s.

AUTHOR CONTRIBUTIONS

XS carried out the majority of the experiments and interpretation of the data. ZW performed part of the data analysis. XS and KS participated in designing of the study. YW and Y-JL fabricated the micro-channel for cell migration assay. YJ conceived the study and wrote the manuscript with contributions from all other authors. All authors contributed to the article and approved the submitted version.

FUNDING

This study was supported by National Natural Science Foundation of China (92054104 and 31970660); CAS-VPST Silk Road Science Fund (GJHZ2021138); Shanghai Municipal Science and Technology Major Project (2019SHZDZX02); Natural Science Foundation of Shanghai (19ZR1463000); and Key Laboratory of

Molecular Virology & Immunology, Institut Pasteur of Shanghai (KLMVI-OP-202001).

ACKNOWLEDGMENTS

We thank Pekka Lappalainen (University of Helsinki) and Roger Karlsson (Stockholm University) for critical reading and discussion of the manuscript, and Baohua Ji (Zhejiang University) for helping with the traction force analysis.

SUPPLEMENTARY MATERIAL

The Supplementary Material for this article can be found online at: https://www.frontiersin.org/articles/10.3389/fcell.2021.665919/full#supplementary-material

Supplementary Figure 1 | The expression and motility of CAV-1 vesicles in U2OS cells. **(A)** A schematic cartoon demonstrates that tropomyosin is a tightly actin associated components. Immunofluorescence staining of Biotin fused Tpm3.1 and streptavidin localized to actin filaments to verify the screen are shown in the lower panel. Bars, 10 μm. **(B)** Representative immunofluorescence images of overexpressing CAV-1-mCherry paired with endogenous CAV-1 and Rab8 antibodies, respectively. The yellow box in the merged images show magnified images. Bars, 10 μm (in cell images) and 5 μm (in the magnified box). **(C)** Localization of endogenous CAV-1 and actin filaments in U2OS cells detected by CAV-1 antibody and fluorescent phalloidin, respectively. WGA was used to label the plasma membrane. Magnified regions from the area indicated by white boxes demonstrate that cytoplasmic CAV-1 aligns with actin filaments. The orthogonal view shows the view of the enlarged region, where "XY" and "XZ" indicated different cross-sections. **(D)** Representative images of actin filaments and endogenous CAV-1. DAPI was used to mark the nucleus. "Middle" refers to the cytoplasmic field of the cell, and "Bottom" indicates the ventral plasma membrane area. Bars, 10 μm (in cell images), 5 μm (in magnified images and orthographic views).

Supplementary Figure 2 | Actin assemblies regulate the size and dynamics of CAV-1 vesicles. **(A)** Immunofluorescence staining of endogenous F-actin and CAV-1 positive vesicles in U2OS cells treated with 0.2 μM LatB for 30 min. Magnified regions represent the cytoplasmic CAV-1. Bars, 10 μm (in cell images) and 5 μm (in the magnified box). **(B)** The length distribution of CAV-1 vesicles. The number of vesicles in each group of size is divided by the total CAV-1 number of the same cell. n = 6,432 vesicles from 12 WT cells, and 9,543 vesicles from 18 LatB treatment cells. **(C,D)** The transcriptional and translational level of CAV-1 is examined by RT-PCR **(C)** and western blot **(D)** in total cell lysates of WT, NMII inh. and Arp2/3 inh. cells. **(E)** Western blot analysis of endogenous Myosin-18B (Myo18B) level in total cell lysates of WT and Myo18B KO cells by CRISPR/Cas9 methods. **(F)** Western blot analysis of endogenous ARPC2 level in total cell lysates of WT and ARPC2 knockdown (ARPC2 siRNA) cells. **(G)** The length distribution of CAV-1 vesicles. The number of vesicles in each size group is divided by the total CAV-1 number of the same cell. n = 17,902 vesicles from 27 cells (WT), 15,434 vesicles from 33 cells (Myo18B KO), and 14,434 vesicles from 23 cells (ARPC2 siRNA). **(H)** Quantification of the movement rate of CAV-1 vesicles in the whole WT (n = 31), Myo18B KO (n = 28) cells, and ARPC2 siRNA (n = 28) cells. All the data are presented as mean ± SD. In **(E,G)**, $^{***}P < 0.001$; N.A., not significant (one-way ANOVA). All the data are from three independent experiments.

Supplementary Figure 3 | CAV-1 is critical for the contractile stress fiber formation by regulating RhoA-Myosin II. **(A)** Western blot analysis of endogenous CAV-1 levels in total cell lysates of WT and CAV-1 CRISPR/Cas9 knockout cells. **(B)** Western blot analysis of endogenous CAV-1 levels in total cell lysates upon RNA silencing. **(C)** Representative images of actin filaments visualized by phalloidin in WT and CAV-1 knockdown cells. Magnified regions represent the contractile stress fibers and protrusive lamellipodia. Bars, 10 μm (in cell images) and 5 μm (in the magnified box). Quantification of the average numbers of total and thick filaments, and lamellipodia width in 20 WT and 20 CAV-1 knockdown cells. **(D)** P-FAK (Tyr397) and total FAK were detected from the lysates of each group by western blotting. Quantification of P-FAK (Tyr397) levels (compared to total FAK) from each group was shown on the right panel. n = 3. **(E)** WT and CAV-1 KO cells transfected with active RhoA sensor GFP-AHGP were stained by Alexa 568 phalloidin. Bars, 10 μm. The average intensity of GFP-AHPH were calculated on the right. n = 20 for WT and CAV-1 KO cells. **(F)** WT and CAV-1 KO cells stained with phalloidin and P-MLC (Thr18/Ser19) antibody demonstrate decreased phosphorylation of P-MLC in cells lacking CAV-1. Bars, 10 μm (in cell images) and 5 μm (in the magnified box). The average intensity of P-MLC was calculated on the right. n = 19 for groups depicted on the left. **(G)** Representative images and quantification of Tm4 in WT and CAV-1 KO cells. n = 21 for each group. All the data are presented as mean ± SD. In **(C–E,G)**, $^{***}P < 0.001$; $^{**}P < 0.01$; N.A., not significant (unpaired t-test). In **(F)**, $^{***}P < 0.001$ (Mann-Whitney test); All the data are from three independent experiments.

Supplementary Figure 4 | Changes of actin protrusive network in the absence of CAV-1 is regulated by AMPK-Rac1-PAK1-Cofilin signaling cascade. **(A)** Representative images of actin filaments visualized by Interference Reflection Microscopy (IRM). Magnified regions represent the contractile stress fibers and protrusive lamellipodia. Bars, 10 μm (in cell images) and 5 μm (in the magnified box). **(B)** Pull-down assays were performed for WT and CAV-1 KO cells. Proteins bound to GST-PAK binding domain were analyzed by western blots and further quantified (compared to total Cdc42) based on the band's intensity. n = 3. **(C,D)** Immunostaining **(C)** and quantification **(D)** of endogenous P-AMPK (Thr172) and F-actin distribution in WT and CAV-1 KO cells. A 16 μm length line was used to generate a line profile to illustrate the co-localization of P-AMPK (Thr172) and F-actin. The lamellipodia region was enlarged on the right, and 2 μm width region was chosen to analyze the mean intensity of P-AMPK (Thr172) on the leading edge. Bars, 10 μm (in cell images) and 5 μm (in the magnified box). n = 20 regions from each group. **(E,F)** Immunostaining **(E)** and quantification **(F)** of endogenous P-PAK1 (Thr423) and F-actin distribution in WT and CAV-1 KO cells. A 16 μm length line was used to generate a line profile to illustrate the co-localization of P-PAK1 (Thr423) and F-actin. The lamellipodia region was enlarged on the right, and 2 μm width region was chosen to analyze the mean intensity of P-PAK1 (Thr423) on the leading edge. Bars, 10 μm (in cell images) and 5 μm (in the magnified box). n = 20 regions from each group. All the data are presented as mean ± SD. In **(B,D,F)**, $^{***}P < 0.001$ (unpaired t-test). All the data are from three independent experiments.

Supplementary Figure 5 | Cell morphology and directional migration are impaired in response to CAV-1 deficiency. **(A)** Wound healing assay was performed in WT and CAV-1 KO cells. The representative images in different time point during wound healing were shown. Bars, 100 μm. **(B)** Quantitation of the averaged wound healing rate. **(C)** Western blot analysis of endogenous CAV-1 and stable expressed CAV-mEGFP in Huh7 cells. **(D)** Representative images of CAV-1-mEGFP in non-transfected WT and CAV-1-mEGFP stable expressed Huh7 cells. Bars, 10 μm. **(E,F)** Representative images **(E)** and measurement of the wound healing rate **(F)** of WT and CAV-1-mEGFP stable expressed Huh7 cells. Bars, 100 μm. All the data are presented as mean ± SD. $^{**}P < 0.01$ (unpaired t-test). All the data are from three independent experiments.

Supplementary Video 1 | Related to **Figure 1C** (Box 1). Time-lapse video of CAV-1-mEGFP sliding along actin filaments in U2OS Cells. White and yellow arrows indicate the starting and ending position of discrete CAV-1 tagged vesicles, respectively. The display rate is 3 frames per second. Bar, 5 μm.

Supplementary Video 2 | Related to **Figure 1C** (Box 2). Time-lapse video of CAV-1-mEGFP associated with contractile actin transverse arcs and displayed retrograde flow toward the cell center in U2OS Cells. White and yellow arrows indicate the starting and ending position of discrete CAV-1 tagged vesicles, respectively. The display rate is 15 frames per second. Bar, 5 μm.

Supplementary Video 3 | Related to **Figure 4B**. Live cell phase contrast imaging of WT (left) and CAV-1 KO (right) cells membrane ruffling for 10 min with the time interval of 2 s. The display rate is 15 frames per second. Bar, 10 μm.

Supplementary Video 4 | Related to **Figure 5C**. Live cell phase contrast imaging of WT (upper) and CAV-1 KO (lower) cells migrating in 50 μm height and width channel for 10 h with the time interval of 5 min. Nucleus were stained by Hoechst. The display rate is 15 frames per second. Bar, 50 μm.

REFERENCES

Burgess, S. A., Yu, S., Walker, M. L., Hawkins, R. J., Chalovich, J. M., and Knight, P. J. (2007). Structures of smooth muscle myosin and heavy meromyosin in the folded, shutdown state. *J. Mol. Biol.* 372, 1165–1178. doi: 10.1016/j.jmb.2007.07.014

Burnette, D. T., Shao, L., Ott, C., Pasapera, A. M., Fischer, R. S., Baird, M. A., et al. (2014). A contractile and counterbalancing adhesion system controls the 3D shape of crawling cells. *J. Cell Biol.* 205, 83–96. doi: 10.1083/jcb.201311104

Chanez-Paredes, S., Montoya-Garcia, A., and Schnoor, M. (2019). Cellular and pathophysiological consequences of Arp2/3 complex inhibition: role of inhibitory proteins and pharmacological compounds. *Cell Mol. Life Sci.* 76, 3349–3361. doi: 10.1007/s00018-019-03128-y

Conrad, P. A., Smart, E. J., Ying, Y. S., Anderson, R. G., and Bloom, G. S. (1995). Caveolin cycles between plasma membrane caveolae and the Golgi complex by microtubule-dependent and microtubule-independent steps. *J. Cell Biol.* 131(Pt 1), 1421–1433. doi: 10.1083/jcb.131.6.1421

Dasgupta, B., and Seibel, W. (2018). Compound C/Dorsomorphin: Its Use and Misuse as an AMPK Inhibitor. *Methods Mol. Biol.* 1732, 195–202. doi: 10.1007/978-1-4939-7598-3_12

Echarri, A., and Del Pozo, M. A. (2015). Caveolae - mechanosensitive membrane invaginations linked to actin filaments. *J. Cell Sci.* 128, 2747–2758. doi: 10.1242/jcs.153940

Echarri, A., Muriel, O., Pavon, D. M., Azegrouz, H., Escolar, F., Terron, M. C., et al. (2012). Caveolar domain organization and trafficking is regulated by Abl kinases and mDia1. *J. Cell Sci.* 125(Pt 13), 3097–3113. doi: 10.1242/jcs.090134

Fujimoto, T., Miyawaki, A., and Mikoshiba, K. (1995). Inositol 1,4,5-trisphosphate receptor-like protein in plasmalemmal caveolae is linked to actin filaments. *J. Cell Sci.* 108(Pt 1), 7–15.

Galbiati, F., Razani, B., and Lisanti, M. P. (2001). Caveolae and caveolin-3 in muscular dystrophy. *Trends Mol. Med.* 7, 435–441. doi: 10.1016/s1471-4914(01)02105-0

Geeves, M. A., Hitchcock-DeGregori, S. E., and Gunning, P. W. (2015). A systematic nomenclature for mammalian tropomyosin isoforms. *J. Muscle Res. Cell Motil.* 36, 147–153. doi: 10.1007/s10974-014-9389-6

Girao, H., Geli, M. I., and Idrissi, F. Z. (2008). Actin in the endocytic pathway: from yeast to mammals. *FEBS Lett.* 582, 2112–2119. doi: 10.1016/j.febslet.2008.04.011

Goley, E. D., and Welch, M. D. (2006). The ARP2/3 complex: an actin nucleator comes of age. *Nat. Rev. Mol. Cell Biol.* 7, 713–726. doi: 10.1038/nrm2026

Gonzalez, E., Nagiel, A., Lin, A. J., Golan, D. E., and Michel, T. (2004). Small interfering RNA-mediated down-regulation of caveolin-1 differentially modulates signaling pathways in endothelial cells. *J. Biol. Chem.* 279, 40659–40669. doi: 10.1074/jbc.M407051200

Grande-Garcia, A., Echarri, A., de Rooij, J., Alderson, N. B., Waterman-Storer, C. M., Valdivielso, J. M., et al. (2007). Caveolin-1 regulates cell polarization and directional migration through Src kinase and Rho GTPases. *J. Cell Biol.* 177, 683–694. doi: 10.1083/jcb.200701006

Grassart, A., Cheng, A. T., Hong, S. H., Zhang, F., Zenzer, N., Feng, Y., et al. (2014). Actin and dynamin2 dynamics and interplay during clathrin-mediated endocytosis. *J. Cell Biol.* 205, 721–735. doi: 10.1083/jcb.201403041

Guilluy, C., Dubash, A. D., and Garcia-Mata, R. (2011a). Analysis of RhoA and Rho GEF activity in whole cells and the cell nucleus. *Nat. Protoc.* 6, 2050–2060. doi: 10.1038/nprot.2011.411

Guilluy, C., Swaminathan, V., Garcia-Mata, R., O'Brien, E. T., Superfine, R., and Burridge, K. (2011b). The Rho GEFs LARG and GEF-H1 regulate the mechanical response to force on integrins. *Nat. Cell Biol.* 13, 722–727. doi: 10.1038/ncb2254

Ha, T. K., Her, N. G., Lee, M. G., Ryu, B. K., Lee, J. H., Han, J., et al. (2012). Caveolin-1 increases aerobic glycolysis in colorectal cancers by stimulating HMGA1-mediated GLUT3 transcription. *Cancer Res.* 72, 4097–4109. doi: 10.1158/0008-5472.CAN-12-0448

Hernandez, V. J., Weng, J., Ly, P., Pompey, S., Dong, H., Mishra, L., et al. (2013). Cavin-3 dictates the balance between ERK and Akt signaling. *eLife* 2:e00905. doi: 10.7554/eLife.00905

Hill, M. M., Daud, N. H., Aung, C. S., Loo, D., Martin, S., Murphy, S., et al. (2012). Co-regulation of cell polarization and migration by caveolar proteins PTRF/Cavin-1 and caveolin-1. *PLoS One* 7:e43041. doi: 10.1371/journal.pone.0043041

Horton, R. M., Hunt, H. D., Ho, S. N., Pullen, J. K., and Pease, L. R. (1989). Engineering hybrid genes without the use of restriction enzymes: gene splicing by overlap extension. *Gene* 77, 61–68. doi: 10.1016/0378-1119(89)90359-4

Jaffe, A. B., and Hall, A. (2005). Rho GTPases: biochemistry and biology. *Annu. Rev. Cell Dev. Biol.* 21, 247–269. doi: 10.1146/annurev.cellbio.21.020604.150721

Jiu, Y. (2018). Vimentin intermediate filaments function as a physical barrier during intracellular trafficking of caveolin-1. *Biochem. Biophys. Res. Commun.* 507, 161–167. doi: 10.1016/j.bbrc.2018.10.199

Jiu, Y., Kumari, R., Fenix, A. M., Schaible, N., Liu, X., Varjosalo, M., et al. (2019). Myosin-18B promotes the assembly of Myosin II stacks for maturation of contractile actomyosin bundles. *Curr Biol* 29, 81–92.e5. doi: 10.1016/j.cub.2018.11.045

Jiu, Y., Lehtimaki, J., Tojkander, S., Cheng, F., Jaalinoja, H., Liu, X., et al. (2015). Bidirectional interplay between vimentin intermediate filaments and contractile actin stress fibers. *Cell Rep.* 11, 1511–1518. doi: 10.1016/j.celrep.2015.05.008

Jiu, Y., Peranen, J., Schaible, N., Cheng, F., Eriksson, J. E., Krishnan, R., et al. (2017). Vimentin intermediate filaments control actin stress fiber assembly through GEF-H1 and RhoA. *J. Cell Sci.* 130, 892–902. doi: 10.1242/jcs.196881

Joshi, B., Strugnell, S. S., Goetz, J. G., Kojic, L. D., Cox, M. E., Griffith, O. L., et al. (2008). Phosphorylated caveolin-1 regulates Rho/ROCK-dependent focal adhesion dynamics and tumor cell migration and invasion. *Cancer Res.* 68, 8210–8220. doi: 10.1158/0008-5472.CAN-08-0343

Kovacs, M., Toth, J., Hetenyi, C., Malnasi-Csizmadia, A., and Sellers, J. R. (2004). Mechanism of blebbistatin inhibition of myosin II. *J. Biol. Chem.* 279, 35557–35563. doi: 10.1074/jbc.M405319200

Kumari, R., Jiu, Y., Carman, P. J., Tojkander, S., Kogan, K., Varjosalo, M., et al. (2020). Tropomodulins control the balance between protrusive and contractile structures by stabilizing Actin-Tropomyosin filaments. *Curr. Biol.* 30, 767–778.e5. doi: 10.1016/j.cub.2019.12.049

Lessey, E. C., Guilluy, C., and Burridge, K. (2012). From mechanical force to RhoA activation. *Biochemistry* 51, 7420–7432. doi: 10.1021/bi300758e

Li, Z., Hannigan, M., Mo, Z., Liu, B., Lu, W., Wu, Y., et al. (2003). Directional sensing requires G beta gamma-mediated PAK1 and PIX alpha-dependent activation of Cdc42. *Cell* 114, 215–227. doi: 10.1016/s0092-8674(03)00559-2

Luo, X., Wang, D., Zhu, X., Wang, G., You, Y., Ning, Z., et al. (2018). Autophagic degradation of caveolin-1 promotes liver sinusoidal endothelial cells defenestration. *Cell Death Dis.* 9:576. doi: 10.1038/s41419-018-0567-0

Mahamdeh, M., and Howard, J. (2019). Implementation of interference reflection microscopy for label-free, high-speed imaging of microtubules. *J. Vis. Exp.* doi: 10.3791/59520

Meili, R., and Firtel, R. A. (2003). Two poles and a compass. *Cell* 114, 153–156. doi: 10.1016/s0092-8674(03)00553-1

Moreno-Caceres, J., Caballero-Diaz, D., Nwosu, Z. C., Meyer, C., Lopez-Luque, J., Malfettone, A., et al. (2017). The level of caveolin-1 expression determines response to TGF-beta as a tumour suppressor in hepatocellular carcinoma cells. *Cell Death Dis.* 8:e3098. doi: 10.1038/cddis.2017.469

Mundy, D. I., Machleidt, T., Ying, Y. S., Anderson, R. G., and Bloom, G. S. (2002). Dual control of caveolar membrane traffic by microtubules and the actin cytoskeleton. *J. Cell Sci.* 115(Pt 22), 4327–4339. doi: 10.1242/jcs.00117

Muriel, O., Echarri, A., Hellriegel, C., Pavon, D. M., Beccari, L., and Del Pozo, M. A. (2011). Phosphorylated filamin A regulates actin-linked caveolae dynamics. *J. Cell Sci.* 124(Pt 16), 2763–2776. doi: 10.1242/jcs.080804

Navarro, A., Anand-Apte, B., and Parat, M. O. (2004). A role for caveolae in cell migration. *FASEB J.* 18, 1801–1811. doi: 10.1096/fj.04-2516rev

Parreno, J., Amadeo, M. B., Kwon, E. H., and Fowler, V. M. (2020). Tropomyosin 3.1 association with actin stress fibers is required for lens epithelial to mesenchymal transition. *Invest. Ophthalmol. Vis. Sci.* 61:2. doi: 10.1167/iovs.61.6.2

Piekny, A. J., and Glotzer, M. (2008). Anillin is a scaffold protein that links RhoA, actin, and myosin during cytokinesis. *Curr. Biol.* 18, 30–36. doi: 10.1016/j.cub.2007.11.068

Pol, A., Morales-Paytuvi, F., Bosch, M., and Parton, R. G. (2020). Non-caveolar caveolins - duties outside the caves. *J. Cell Sci.* 133:jcs241562. doi: 10.1242/jcs.241562

Raftopoulou, M., and Hall, A. (2004). Cell migration: Rho GTPases lead the way. *Dev. Biol.* 265, 23–32. doi: 10.1016/j.ydbio.2003.06.003

Razani, B., Wang, X. B., Engelman, J. A., Battista, M., Lagaud, G., Zhang, X. L., et al. (2002a). Caveolin-2-deficient mice show evidence of severe pulmonary dysfunction without disruption of caveolae. *Mol. Cell Biol.* 22, 2329–2344. doi: 10.1128/mcb.22.7.2329-2344.2002

Razani, B., Woodman, S. E., and Lisanti, M. P. (2002b). Caveolae: from cell biology to animal physiology. *Pharmacol. Rev.* 54, 431–467. doi: 10.1124/pr.54.3.431

Ridley, A. J., Paterson, H. F., Johnston, C. L., Diekmann, D., and Hall, A. (1992). The small GTP-binding protein rac regulates growth factor-induced membrane ruffling. *Cell* 70, 401–410. doi: 10.1016/0092-8674(92)90164-8

Ridley, A. J., Schwartz, M. A., Burridge, K., Firtel, R. A., Ginsberg, M. H., Borisy, G., et al. (2003). Cell migration: integrating signals from front to back. *Science* 302, 1704–1709. doi: 10.1126/science.1092053

Rohlich, P., and Allison, A. C. (1976). Oriented pattern of membrane-associated vesicles in fibroblasts. *J. Ultrastruct. Res.* 57, 94–103. doi: 10.1016/s0022-5320(76)80059-7

Rong, Y., Yang, W., Hao, H., Wang, W., Lin, S., Shi, P., et al. (2021). The Golgi microtubules regulate single cell durotaxis. *EMBO Rep.* 22:e51094. doi: 10.15252/embr.202051094

Rothberg, K. G., Heuser, J. E., Donzell, W. C., Ying, Y. S., Glenney, J. R., and Anderson, R. G. (1992). Caveolin, a protein component of caveolae membrane coats. *Cell* 68, 673–682. doi: 10.1016/0092-8674(92)90143-z

Roux, K. J., Kim, D. I., Raida, M., and Burke, B. (2012). A promiscuous biotin ligase fusion protein identifies proximal and interacting proteins in mammalian cells. *J. Cell Biol.* 196, 801–810. doi: 10.1083/jcb.201112098

Salani, B., Maffioli, S., Hamoudane, M., Parodi, A., Ravera, S., Passalacqua, M., et al. (2012). Caveolin-1 is essential for metformin inhibitory effect on IGF1 action in non-small-cell lung cancer cells. *FASEB J.* 26, 788–798. doi: 10.1096/fj.11-192088

Shi, X., Fan, C., and Jiu, Y. (2020). Unidirectional regulation of vimentin intermediate filaments to Caveolin-1. *Int. J. Mol. Sci.* 21:7436. doi: 10.3390/ijms21207436

Sinha, B., Koster, D., Ruez, R., Gonnord, P., Bastiani, M., Abankwa, D., et al. (2011). Cells respond to mechanical stress by rapid disassembly of caveolae. *Cell* 144, 402–413. doi: 10.1016/j.cell.2010.12.031

Stoeber, M., Stoeck, I. K., Hanni, C., Bleck, C. K., Balistreri, G., and Helenius, A. (2012). Oligomers of the ATPase EHD2 confine caveolae to the plasma membrane through association with actin. *EMBO J.* 31, 2350–2364. doi: 10.1038/emboj.2012.98

Thomsen, P., Roepstorff, K., Stahlhut, M., and van Deurs, B. (2002). Caveolae are highly immobile plasma membrane microdomains, which are not involved in constitutive endocytic trafficking. *Mol. Biol. Cell* 13, 238–250. doi: 10.1091/mbc.01-06-0317

Tweten, D. J., Bayly, P. V., and Carlsson, A. E. (2017). Actin growth profile in clathrin-mediated endocytosis. *Phys. Rev. E* 95, 052414. doi: 10.1103/PhysRevE.95.052414

Umemoto, S., Bengur, A. R., and Sellers, J. R. (1989). Effect of multiple phosphorylations of smooth muscle and cytoplasmic myosins on movement in an in vitro motility assay. *J. Biol. Chem.* 264, 1431–1436.

Valentich, J. D., Popov, V., Saada, J. I., and Powell, D. W. (1997). Phenotypic characterization of an intestinal subepithelial myofibroblast cell line. *Am. J. Physiol.* 272(Pt 1), C1513–C1524. doi: 10.1152/ajpcell.1997.272.5.C1513

Verschueren, H. (1985). Interference reflection microscopy in cell biology: methodology and applications. *J. Cell Sci.* 75, 279–301.

Vicente-Manzanares, M., Webb, D. J., and Horwitz, A. R. (2005). Cell migration at a glance. *J. Cell Sci.* 118(Pt 21), 4917–4919. doi: 10.1242/jcs.02662

Wong, T. H., Dickson, F. H., Timmins, L. R., and Nabi, I. R. (2020). Tyrosine phosphorylation of tumor cell caveolin-1: impact on cancer progression. *Cancer Metastasis Rev.* 39, 455–469. doi: 10.1007/s10555-020-09892-9

Xu, J., Wang, F., Van Keymeulen, A., Herzmark, P., Straight, A., Kelly, K., et al. (2003). Divergent signals and cytoskeletal assemblies regulate self-organizing polarity in neutrophils. *Cell* 114, 201–214. doi: 10.1016/s0092-8674(03)00555-5

Zhang, W., Razani, B., Altschuler, Y., Bouzahzah, B., Mostov, K. E., Pestell, R. G., et al. (2000). Caveolin-1 inhibits epidermal growth factor-stimulated lamellipod extension and cell migration in metastatic mammary adenocarcinoma cells (MTLn3). Transformation suppressor effects of adenovirus-mediated gene delivery of caveolin-1. *J. Biol. Chem.* 275, 20717–20725. doi: 10.1074/jbc.M909895199

Zhao, S., Shi, X., Zhang, Y., Wen, Z., Cai, J., Gao, W., et al. (2020). Myosin-18B promotes mechanosensitive CaMKK2-AMPK-VASP regulation of contractile actin stress fibers. *iScience* 23:100975. doi: 10.1016/j.isci.2020.100975

Zimnicka, A. M., Husain, Y. S., Shajahan, A. N., Sverdlov, M., Chaga, O., Chen, Z., et al. (2016). Src-dependent phosphorylation of caveolin-1 Tyr-14 promotes swelling and release of caveolae. *Mol. Biol. Cell* 27, 2090–2106. doi: 10.1091/mbc.E15-11-0756

Conflict of Interest: The authors declare that the research was conducted in the absence of any commercial or financial relationships that could be construed as a potential conflict of interest.

frontiers in Cell and Developmental Biology

REVIEW
published: 21 April 2021
doi: 10.3389/fcell.2021.649082

The Role of Cell Adhesion and Cytoskeleton Dynamics in the Pathogenesis of the Ehlers-Danlos Syndromes and Hypermobility Spectrum Disorders

Sabeeha Malek and Darius V. Köster*

Division of Biomedical Sciences, Centre for Mechanochemical Cell Biology, Warwick Medical School, University of Warwick, Coventry, United Kingdom

OPEN ACCESS

Edited by:
Ting Gang Chew, Zhejiang University-University of Edinburgh Institute, China

Reviewed by:
Yaming Jiu, Institut Pasteur of Shanghai (CAS), China
Peng Xia, Life Sciences Institute Zhejiang University, China

***Correspondence:**
Sabeeha Malek
s.malek@warwick.ac.uk
Darius V. Köster
d.koester@warwick.ac.uk

Specialty section:
This article was submitted to Cell Growth and Division, a section of the journal Frontiers in Cell and Developmental Biology

Received: *03 January 2021*
Accepted: *22 March 2021*
Published: *21 April 2021*

Citation:
Malek S and Köster DV (2021) The Role of Cell Adhesion and Cytoskeleton Dynamics in the Pathogenesis of the Ehlers-Danlos Syndromes and Hypermobility Spectrum Disorders. Front. Cell Dev. Biol. 9:649082. doi: 10.3389/fcell.2021.649082

The Ehlers-Danlos syndromes (EDS) are a group of 13 disorders, clinically defined through features of joint hypermobility, skin hyperextensibility, and tissue fragility. Most subtypes are caused by mutations in genes affecting the structure or processing of the extracellular matrix (ECM) protein collagen. The Hypermobility Spectrum Disorders (HSDs) are clinically indistinguishable disorders, but are considered to lack a genetic basis. The pathogenesis of all these disorders, however, remains poorly understood. Genotype-phenotype correlations are limited, and findings of aberrant collagen fibrils are inconsistent and associate poorly with the subtype and severity of the disorder. The defective ECM, however, also has consequences for cellular processes. EDS/HSD fibroblasts exhibit a dysfunctional phenotype including impairments in cell adhesion and cytoskeleton organization, though the pathological significance of this has remained unclear. Recent advances in our understanding of fibroblast mechanobiology suggest these changes may actually reflect features of a pathomechanism we herein define. This review departs from the traditional view of EDS/HSD, where pathogenesis is mediated by the structurally defective ECM. Instead, we propose EDS/HSD may be a disorder of membrane-bound collagen, and consider how aberrations in cell adhesion and cytoskeleton dynamics could drive the abnormal properties of the connective tissue, and be responsible for the pathogenesis of EDS/HSD.

Keywords: Ehlers-Danlos syndrome, hypermobility spectrum disorder, fibroblasts, integrins, cytoskeleton, mechanobiology

INTRODUCTION

The Ehlers-Danlos syndromes (EDS) are a group of heritable connective tissue disorders defined by the presence of three clinical features: joint hypermobility, skin hyperextensibility, and tissue fragility (Malfait et al., 2017). The condition is named after two dermatologists, Edvard Lauritz Ehlers and Henri-Alexandre Danlos both of whom independently characterized some of the first clinical descriptions of EDS in the early 20th Century (Parapia and Jackson, 2008). The formal categorization of the EDS subtypes began in the 1960s, and there have since been several

reclassifications following advances in our understanding of the molecular and genetic basis of these disorders (**Table 1**). Most subtypes have now been shown to be caused by mutations in genes affecting the structure or processing of collagen (Malfait et al., 2017). Most recently, the International Consortium on the ehlers-danlos syndromes proposed updated diagnostic criteria in 2017, which recognizes 13 different EDS subtypes (Malfait et al., 2017). Since its publication, a 14th subtype of EDS has been identified (Blackburn et al., 2018). While provisional diagnoses can be made based on clinical major and minor criteria, a definitive diagnosis now relies on the molecular identification of the causative variant(s) in the respective gene. The exception lies with the hypermobile form of EDS (hEDS; formerly EDS type III) which, despite being the most common form, remains as the only subtype without an identified distinct genetic variation, and whose diagnosis remains clinical alone. In addition, it is important to recognize the related Hypermobility Spectrum Disorders (HSD) which are clinically indistinguishable from hEDS, and both diagnoses are often termed together as hEDS/HSD. HSD is a diagnosis the EDS consortium had intended to reflect patients who demonstrate the characteristic feature of hEDS, i.e., joint hypermobility, but lack sufficient clinical evidence to demonstrate a genetic aetiology to their presentation. The segregation of these diagnoses was intended to produce a more homogenous cohort to further aid research efforts to identify the genetic markers of hEDS, but does not differentiate patients in terms of severity of symptoms or disability (Tinkle et al., 2009; Copetti et al., 2019). Collectively, EDS/HSD has a diagnosed prevalence of 1 in 500 (Demmler et al., 2019).

Our current understanding of EDS/HSD pathogenesis is informed by the two best characterized subtypes, the classical (cEDS) and vascular (vEDS) forms, which are consequent to mutations in genes encoding the minor collagen proteins, type V (Symoens et al., 2012), and type III (Pepin et al., 2000), respectively. Mutations either cause haploinsufficiency, which is a 50% reduction in protein expression caused by a nonsense-mediated decay of the non-viable RNA transcript (Leistritz et al., 2011; Symoens et al., 2012), or the production of a structurally defective procollagen molecule which is retained within the endoplasmic reticulum (Smith et al., 1997; Symoens et al., 2012). Consequently, in both scenarios, the absence of sufficient functional minor collagen proteins in the extracellular matrix (ECM) then impedes with their role in regulating the formation and organization of the major type I collagen into fibrils (**Figure 1**; Liu et al., 1997; Wenstrup et al., 2004a,b; D'hondt et al., 2018; Wang et al., 2020). This disrupts the integrity of the ECM and is assumed to be the underlying cause of connective tissue weakness.

However, this notion is not truly reflected in transmission electron microscopy (TEM) analyses of collagen fibril structure and organization in EDS/HSD skin biopsies, though general abnormalities can be found. These abnormalities include reduced and disorganized collagen bundles with abnormal orientations, or non-circular cross-sections of collagen fibrils that are described as "flower-like," or with variable diameters both larger and smaller than would be typically expected (Holbrook and Byers, 1982; Hausser and Anton-Lamprecht, 1994; Hermanns-Lê and Piérard, 2006). vEDS patients have been characterized as having collagen fibrils that are smaller and more variable, and with an overall reduced density (Smith et al., 1997), while cEDS is associated with the presence of flower-like collagen fibrils (Vogel et al., 1979; de Moraes et al., 2000; Bowen et al., 2017; Angwin et al., 2020).

Yet, these findings are not consistent and this should be considered significant. It has long been noted that the degree of ultrastructural changes observed do not correlate with clinical severity (Proske et al., 2006), or presentation (Kobayasi, 2004; Hermanns-Lê et al., 2012). Further studies have shown that patients can present with no significant collagen abnormalities, despite a clinical presentation and/or confirmation of genetic disorder. In 2019, one study reported two individuals with a likely pathogenic variant of the COL5A1 gene that did not present with the typical collagen flowers expected (Angwin et al., 2019), contradicting a consensus previously reached by the EDS committee in 2017 (Bowen et al., 2017). Another study in vEDS patients found that the size of collagen fibers and bundle characteristics did not discriminate between vEDS and control participants, nor did all vEDS participants present with abnormal fibril diameters (Ong et al., 2012). More recently, a larger study of 177 EDS patients found that no specific TEM finding could be associated with any specific EDS subtype (Angwin et al., 2020). Remarkably, from the 177 patients with a clinical diagnosis, 147 (83%) had a normal TEM report, and from the 24 patients with a genetic confirmation of their subtype, 7 (29%) also had a normal biopsy report (Angwin et al., 2020). Conversely, it has been demonstrated that clinically unaffected family members and control participants can also present with the same EDS-associated ultrastructural abnormalities without displaying features of a connective tissue disorder (Kobayasi, 2004; Hermanns-Lê et al., 2012). As such, the only conclusion that can be derived from these collective TEM studies is that an abnormal biopsy finding is more frequently found in EDS/HSD patients (Angwin et al., 2020).

These findings demonstrate that despite the categorization of EDS/HSD as a disorder of collagen, the reported ultrastructural collagen abnormalities do not appear to be the principal mediators of abnormal connective tissue properties in these disorders. It is therefore plausible to assume that other related factors heavily influence connective tissue properties and mediate the EDS/HSD phenotype. One such factor may be the cellular mechanics of fibroblasts, the predominant cell type that populates the connective tissue.

THE ROLE OF FIBROBLASTS IN MEDIATING THE PROPERTIES OF THE CONNECTIVE TISSUE

The ability of fibroblasts to directly exert force and influence the tension in the surrounding environment is significant, as it directly affects the viscoelastic properties of the connective

TABLE 1 | Past and present classifications of EDS subtypes and their molecular basis.

2017 International Classification of EDS (2017-present) (Malfait et al., 2017)	Villefranche criteria (1998–2016) (Beighton et al., 1998)	Berlin Nosology (1988–1998) (Beighton et al., 1988)	Genetic basis	Protein	OMIM condition
Classical EDS (cEDS)	EDS Classical Type	Gravis (EDS type I)	COL5A1	Type V collagen	130000
		Mitis (EDS type II)	COL5A2		130010
	**	**	COL1A1	Type I collagen	–
Classical-like EDS (clEDS) type 1	**	**	TNXB	Tenascin XB	606408
**Classical-like EDS type 2	**	**	AEBP1	Aortic Aarboxypeptidase-Like Protein	618000
Cardiac-valvular (cvEDS)	**	**	COL1A2	Type I collagen	225320
Vascular EDS (vEDS)	EDS Vascular Type	Arterial-ecchymotic (EDS type IV)	COL3A1	Type III collagen	130050
	**	**	COL1A1	Type I collagen	–
Hypermobile EDS (hEDS)	EDS Hypermobility Type	Hypermobile (EDS type III)	Unknown	Unknown	130020
Arthrochalasia (aEDS)	EDS Arthrochalasia Type	Arthrochalasis multiplex congenita (EDS type VIIA)	COL1A1	Type I collagen	130060
	**	Arthrochalasis multiplex congenita (EDS type VIIB)	COL1A2	Type I collagen	617821
Dermatosparaxis EDS (dEDS)	EDS Dermatosparaxis Type	Human Dermatosparaxis (EDS type VIIC)	ADAMTS2	Procollagen I N-proteinase	225410
Kyphoscoliotic EDS (kEDS)	EDS Kyphoscoliosis Type	Ocular-Scoliotic (EDS type VIA)	PLOD1	Lysyl hydroxylase 1	225400
	**	**	FKBP14	FK506 Binding Protein 22kDa	614557
Brittle Cornea syndrome (BCS)	**	Ocular-Scoliotic (EDS type VIB)	ZNF469	Zinc finger protein 469	229200
	**	**	PRDM5	PR domain-containing protein 5	614170
Spondylodysplastic EDS (spEDS)	Other forms (Progeroid EDS)	**	B4GALT7	β-1,4-galactosyltransferase 7	130070
	**	**	B3GALT6	β3GalT6	615349
	**	**	SLC39A13	ZIP13	612350
Musculocontractural EDS (mcEDS)	**	**	CHST14	Dermatan-4 sulfotransferase-1	601776
	**	**	DSE	Dermatan sulfate epimerase-1	615539
Myopathic EDS (mEDS)	**	**	COL12A1	Type XII collagen	616471
Periodontal EDS (pEDS)	Other forms (Periodontal type)	Periodontitis type (EDS type VIII)	C1R	C1r	130080
			C1S	C1s	617174
(X-linked cardiac valvular dysplasia)*	Other forms (X-linked EDS)	X-linked type (EDS type V)	FLNA	Filamin-A	314400
Occipital horn syndrome (OHS)*	Occipital horn syndrome (OHS)*	X-linked cutis laxa (EDS type IX)	ATP7A	ATPase, Cu (2++)-transporting, alpha polypeptide	304150
*	Other forms (Fibronectin-deficient EDS)	Fibronectin-deficient (EDS type X)	–	–	225310
Familial hypermobility syndrome (FHS)*	Other forms (Familial hypermobility syndrome)	Familial articular hypermobility syndrome (EDS type XI)	–	–	147900

**Removed as an EDS subtype from the criteria.*
***Unidentified or unrecognized EDS subtype at time of criteria formation.*

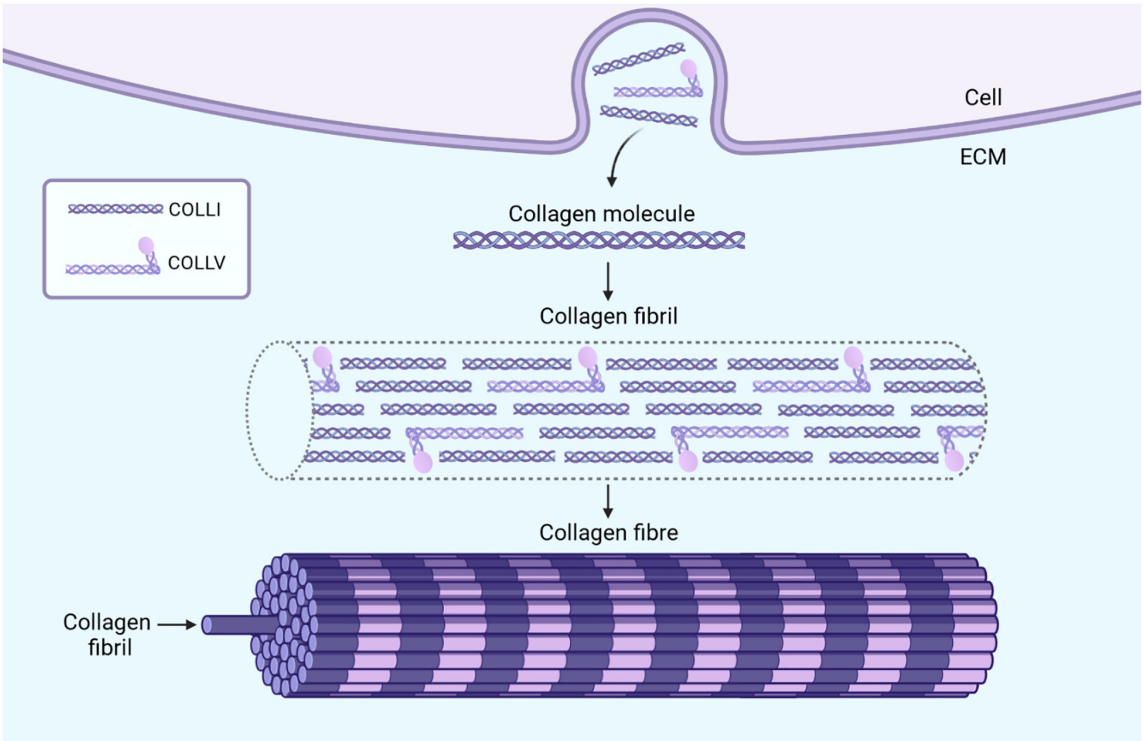

FIGURE 1 | The formation and function of collagen fibrils in connective tissue. Fibroblasts secrete collagen molecules into the ECM which associate in a staggered pattern to form collagen fibrils. These collagen fibrils consist mostly of the major collagen protein, type I, while the minor collagen proteins, such as type III and type V constitute only a fraction of fibril mass (Theocharidis and Connelly, 2019). The importance of these minor collagens, however, lies in their role in regulating the diameter and organization of collagen fibrils. In the example of type V collagen molecules, the presence of a non-collagenous domain which projects outwards introduces steric hindrances when incorporated within collagen fibrils (Wenstrup et al., 2004a). This limits the lateral growth of the fibrils and may also play a role in regulating their diameter (Wenstrup et al., 2004a). Multiple collagen fibrils together form collagen fibers which provide tensile strength to the connective tissue. The absence of sufficient amounts of minor collagen proteins, like in EDS, can result in poorly formed collagen fibrils, and in turn, collagen fibers (Theocharidis and Connelly, 2019). The tissue specific expression and roles of the minor collagen proteins presumably accounts for the characteristic presentation of each specific EDS subtype, all of which differ in the varying presence, manifestation, and degrees of joint hypermobility, skin hyperextensibility, and tissue fragility. *Image created with BioRender.com*.

tissue. This has been demonstrated through gel contraction assays (**Figure 2**) (Dallon and Ehrlich, 2008). Fibroblasts seeded into isolated and recombinant collagen gels generate tractional forces by cytoskeleton contractility which propagate throughout the gel matrix. This compacts the collagen fibrils, eliminating water from between the fibrils which decreases the gel volume. The contraction of this gel is proposed to reflect the ability of fibroblasts to contract an open wound, hence this is used as the typical model assay for the study of cell-ECM interactions in the context of wound healing.

Such gel contraction assays have provided several relevant findings of note. Firstly, the ability of fibroblasts to contract the gel significantly, demonstrates how the cellular mechanics of fibroblasts can directly influence the material properties of their environment, e.g. the connective tissue (Delvoye et al., 1991; Eastwood et al., 1994, 1996). These assays have also demonstrated the key cellular features enabling gel contraction. One is cell adhesion to collagen via integrins, as blocking integrin-mediated adhesion with antibodies prevented gel contraction (Klein et al., 1991; Schiro et al., 1991; Kelynack et al., 2000). Equally important is an active cytoskeleton, as using molecular inhibitors that interfere with actin filament and microtubule polymerization abrogates tractional force generation and reduces tension within the gel (Kolodney and Wysolmerski, 1992; Swierczewski et al., 2016; Giannopoulos et al., 2018). The involvement of intermediate filaments has also been indicated in this process, as vimentin-null fibroblasts show a reduced ability to contract the gel (Ridge et al., 2016).

However, the significance of these findings is not just/limited to the context of wound healing, but reflect important processes involved in the ongoing maintenance of connective tissue function. It has been shown that fibroblasts do not simply contract the gel when seeded, but they alter their cytoskeletal contractility to adapt to any external loads applied in order to maintain an overall resting tension in the environment (Delvoye et al., 1991; Brown et al., 1998; Mizutani et al., 2004; Giannopoulos et al., 2018; Zollinger et al., 2018). Indeed, the specific level of resting tension established by fibroblasts has been described as a "tensile setpoint", and their tendency to

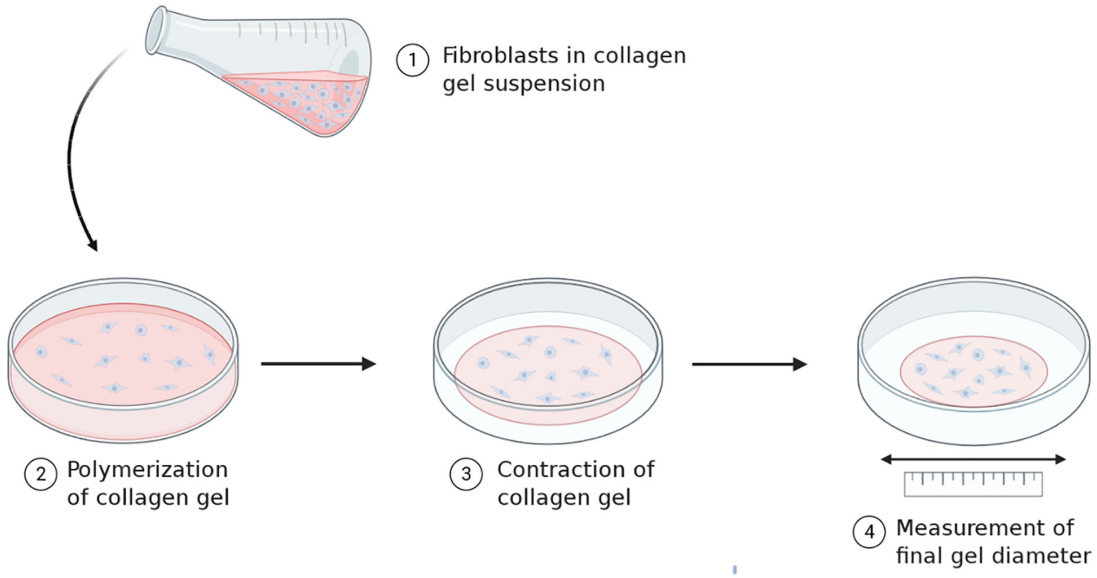

FIGURE 2 | Principles underlying collagen gel contraction assays. Standard gel contraction assays involve seeding fibroblasts into a collagen gel solution and allowing the suspension to polymerize. The freshly polymerized gel is placed in media for a set time period and allowed to contract. Changes in the diameter of the gel are measured before and after and can be used as a parameter to quantify cell contractility. *Image created with BioRender.com.*

actively maintain this equilibrium as "tensional homeostasis" (Brown et al., 1998). Furthermore, it has been shown that the ability to maintain tensional homeostasis is not dependent on the stiffness of the environment, and is only limited by the load force not the displacement (Freyman et al., 2002). This suggests that healthy fibroblasts are also capable of compensating for a materially weak ECM by adjusting the level of contractile force needed to maintain overall normal levels of resting tension (Tomasek et al., 2002). Experiments on mouse subcutaneous connective tissue have also reproduce these findings in a more physiological setting. Stretching connective tissue samples caused a disproportionate change in fibroblast morphology, which could not be explained by simple passive spreading of cells, but indicated an active response (Langevin et al., 2005, 2011). The importance of active processes in mediating tensional homeostasis was shown when inducing cell death or inhibiting cytoskeleton dynamics increased the tension within the connective tissue by 60-80% upon stretch (Langevin et al., 2011).

These findings indicate that fibroblast mechanics play a significant role in mediating the properties of the connective tissue beyond the context of wound healing. Fibroblasts actively alter their contractile forces in response to everyday mechanical strains and loads for the purposes of maintaining appropriate tension, hence, also determining the viscoelastic properties of the connective tissue. Furthermore, these processes are dependent on the key processes of cell adhesion and cytoskeleton dynamics. Impairments in any of these processes, therefore, may affect connective tissue integrity and viscoelasticity, and contribute to the pathogenesis of EDS/HSD.

Indeed, fibroblast dysfunction has been implicated in the pathogenesis of several other connective tissue disorders. Fibroblasts from patients with floppy eyelid syndrome, a hyperelasticity disorder affecting the upper eyelid, demonstrate a significantly higher tensile setpoint compared to control (Ezra et al., 2010). In Dupuytren's contracture, a condition affecting the facia of the hand, fibroblasts are unable to respond appropriately to mechanical loading, and exert an opposite response and of a greater magnitude compared to control fibroblasts, something which also disturbed the attainment of tensional homeostasis (Bisson et al., 2004, 2009). Of particular significance are findings from Pelvic Organ Prolapse (POP) patients, a condition of weakened connective tissue highly associated with EDS/HSD (Carley and Schaffer, 2000; Lammers et al., 2012). Under static conditions, POP fibroblasts in cell culture demonstrate a significantly higher expression of the cytoskeleton proteins actin, α-tubulin, and vimentin compared to control cells, indicating an increased mechano-response to the stiff substrate of a culture dish (Wang et al., 2015). In response to mechanical strain, however, POP fibroblasts exhibit a significant decrease in the expression of actin, in contrast to control cells that increased actin expression under the same conditions (Wang et al., 2015). Another study also found that POP fibroblasts delayed the alignment of their actin cytoskeleton in the direction of the force in response to mechanical strain compared to control cells (Ruiz-Zapata et al., 2013). These findings indicate that POP fibroblasts are unable to efficiently respond to mechanical forces, which may even overload and impair the integrity of cytoskeletal system. In the context of a whole tissue environment, such a

failure would contribute to the weakening of the connective tissue, and similar mechanisms may exist and contribute to the pathogenesis of EDS/HSD.

EDS/HSD FIBROBLASTS EXHIBIT RELEVANT INTEGRIN-MEDIATED CHANGES IN CELL ADHESION AND CYTOSKELETON ORGANIZATION

The culturing of fibroblasts derived from the dermal biopsies of EDS/HSD patients have revealed several relevant molecular changes (Zoppi et al., 2018b; Chiarelli et al., 2019), including an altered integrin expression profile that is shared amongst the main EDS/HSD subtypes (Zoppi et al., 2018b). Integrins are cell surface receptors composed of one α and one β subunit, giving rise to 24 unique integrins which play a central role in cell adhesion, cell signaling, and cell survival (Barczyk et al., 2010). Integrins mediate the attachment between the cell and specific ECM proteins like collagen or fibronectin (**Figure 3**). Binding of the ECM ligand exposes the cytoplasmic tail of the integrin, which provides a scaffold to allow recruitment of paxilin, vinculin, talin, and other proteins during the formation of multi-protein complexes called focal adhesions constituting signaling complexes (Kanchanawong et al., 2010; Parsons et al., 2010). These in turn, regulate the activity of the Rho family of GTPases, which act as molecular switches to regulate downstream signaling processes and cytoskeleton organization (Kanchanawong et al., 2010; Parsons et al., 2010). These adhesion sites act as a strong anchoring point for the actin cytoskeleton, important for the mechanical feedback between cell and ECM.

The integrin profile demonstrated in EDS/HSD involves the downregulation of the collagen receptor, $\alpha_2\beta_1$ integrin, as well as the fibronectin receptor, $\alpha_5\beta_1$ integrin, while the vitronectin receptor, $\alpha_v\beta_3$ integrin, is upregulated instead. In EDS/HSD, this $\alpha_v\beta_3$ integrin functions as an alternative receptor for fibronectin (Zoppi et al., 2018b). The expression of this specific integrin profile is termed the "integrin switch" (Zoppi et al., 2004, 2018b), which can be recreated in control cells with a functional blocking of the $\alpha_2\beta_1$ receptor (Zoppi et al., 2004). This demonstrates that the absence of a structurally organized collagen in the ECM failing to engage with its receptor $\alpha_2\beta_1$ leads to the altered integrin expression profile. This, in turn, will influence other cellular processes that may be critical in the pathogenesis EDS/HSD.

The first of these is mechano-sensitivity, which is an ability of fibroblasts to sense the compliance of their environment and the strain present within it (Schwartz, 2010). This process would be essential to produce the appropriate cytoskeletal response to mechanical strain and requires the cooperative actions of various integrins. A study demonstrating such cooperation of integrins with different mechanosensitive roles showed the $\alpha_5\beta_1$ integrins to be implicated in force generation, whereas α_v-class integrins mediated the structural adaptations to forces (Schiller et al., 2013). Fibroblasts in which the interaction between the $\alpha_v\beta_3$ integrin and fibronectin is blocked, also failed to sense the rigidity of a fibronectin matrix (Jiang et al., 2006). This would suggest that the integrin switch would alter the mechano-sensing ability of EDS/HSD fibroblasts. Indeed, there is already some indication that this process is perturbed in hEDS/HSD. When hEDS/HSD fibroblasts were cultured on a stiff culture substrate, excessive actin stress fibers could be observed compared to control (Zoppi et al., 2018a), however, these were absent in hEDS/HSD fibroblasts that were directly observed within tissue samples (Celli et al., 2020). This demonstrates that excessive stress fiber formation is not a persistent feature of hEDS/HSD fibroblasts, but instead, could be reflective of mechano-sensitivity aberrations. It is possible that this abnormal cytoskeletal response only occurred when fibroblasts adhered to stiff substrates *in vitro*, but not when they remained within their native soft tissue environment. Such mechano-sensitivity aberrations are physiologically relevant, as conditions of mechanical strain can temporarily stiffen the environment of fibroblasts *in vivo*, and, similarly, produce an abnormal cytoskeletal response which contributes to abnormal connective tissue properties.

The integrin switch may also impair cell-ECM adhesion, which may be crucial for tissue integrity. Indeed, aberrant adhesion has already been demonstrated in EDS/HSD. In cEDS and vEDS fibroblasts, cell-ECM adhesion has been shown to be mediated specifically between the $\alpha_v\beta_3$ integrin and fibronectin, whereas control cells show no such critical dependency (Zoppi et al., 2008). The fibronectin organization itself is impaired in EDS/HSD, present only as rare fibrils in the ECM (Zoppi et al., 2018b), further indicating a compromised cell-ECM interaction. The strength of the cell-ECM adhesions themselves, may also be limited. A single bond between the $\alpha_2\beta_1$ integrin and collagen can withstand a mechanical force of 160 pN (Niland et al., 2011), whereas bonds between $\alpha_5\beta_1$ and fibronectin begin to break at 30 pN (Kong et al., 2009). Bonds between $\alpha_v\beta_3$ and fibronectin break at even lower forces (Roca-Cusachs et al., 2009). This was demonstrated in a study where adhesion between cells and fibronectin-coated beads was mediated either by the $\alpha_v\beta_3$ integrin or $\alpha_5\beta_1$. Following application of a 1 nN force for 100 s, cells adhering via $\alpha_v\beta_3$ completely detached from the beads, whereas cells adhering via the $\alpha_5\beta_1$ integrin maintained adhesion (Roca-Cusachs et al., 2009). The same differences in adhesion strength were also observed when clustering of the integrins was promoted (Roca-Cusachs et al., 2009). It is suggested that these weaker $\alpha_v\beta_3$ bonds facilitate force detection by breaking more easily, and hence, their role is to enable mechano-transduction rather than adhesion. Consequently, these collective findings suggest that the integrin switch, alongside the defective fibronectin organization observed in EDS/HSD, may produce far weaker connections between the cell and ECM. These may break more easily under conditions of mechanical strain, and contribute to the weakening of the integrity of the connective tissue (Roca-Cusachs et al., 2009).

Some impairments in the cytoskeleton of EDS/HSD fibroblasts have also been observed *in vitro*. cEDS and vEDS fibroblasts demonstrate a disorganized actin cytoskeleton (Zoppi et al., 2008), whereas in hEDS and HSD, the actin cytoskeleton is organized into stress fibers (Zoppi et al., 2018a). Furthermore,

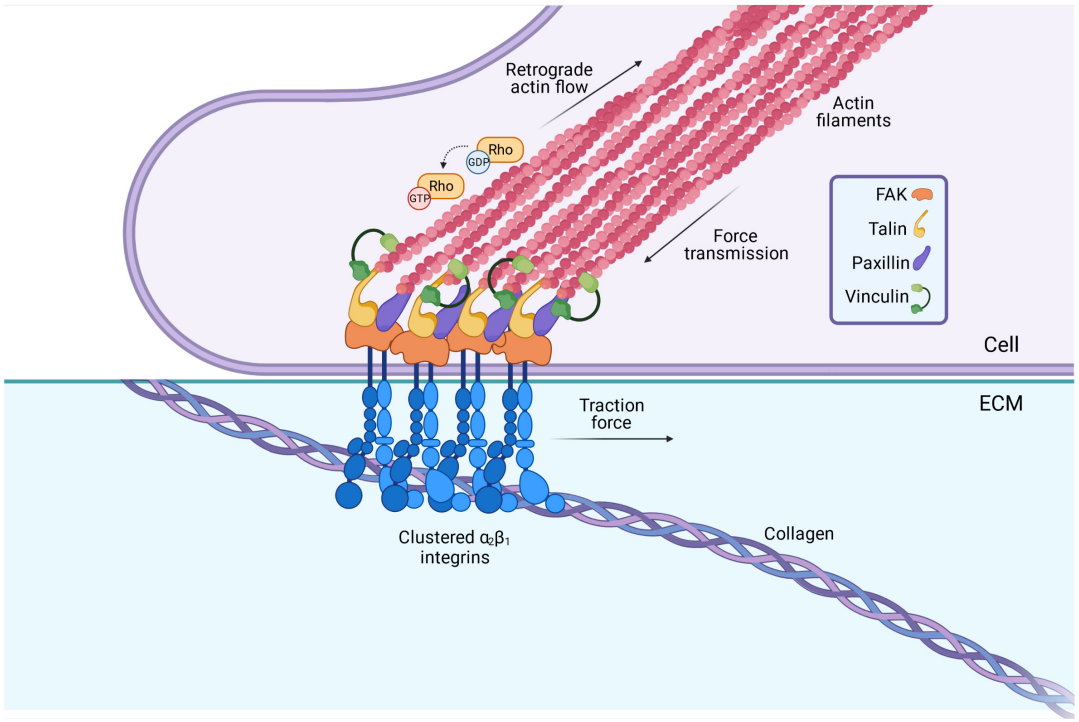

FIGURE 3 | Integrins serve as a vital connection between the cells' internal cytoskeleton and the ECM. Integrins span the membrane of fibroblasts, with vital intracellular and extracellular domains. Binding of the ECM ligand (collagen, fibronectin etc.) to the extracellular domain leads to the activation of the integrin, and a conformational change in its cytoplasmic tail. This triggers a rapid recruitment of adaptor proteins such as talin and paxillin to the cytoplasmic tail, which in turn, triggers a signaling cascade involving the Rho GTPases. These act as molecular switches to regulate the polymerization of actin, and hence, play an important role in determining the cytoskeletons contractility. The lateral assembly or "clustering" of integrins also occurs upon ligand binding, to form multi-protein complexes termed "focal adhesions" at the cell surface. These act as strong anchoring points and mediate the specific attachment between the cell cytoskeleton and the ECM. *Image created with BioRender.com.*

cEDS and vEDS fibroblasts show a decreased migratory capacity (Viglio et al., 2008; Zoppi et al., 2018a), whereas cell migration is significantly increased in hEDS and HSD fibroblasts (Zoppi et al., 2018a). This migratory capacity is relevant, as it involves the same mechanical machinery that generates the tractional forces implicated in mediating tensional homeostasis (Pollard and Borisy, 2003; Webster et al., 2014). These findings indicate that this aspect of EDS/HSD fibroblast function may also be aberrant and contribute to abnormal connective tissue properties.

The integrin switch itself may also have further implications for cytoskeleton dynamics. Integrins are also known to influence the activities of the Rho-GTPases, RhoA, Rac1, and Cdc42, which are crucial to cell protrusion formation (Lawson and Burridge, 2014), which in turn, is involved in the tensional homeostasis mechanism (Webster et al., 2014). During this process, the initial extension of the plasma membrane is driven predominantly through Rac-mediated actin polymerization, while RhoA and Cdc42 activity contributes to extension of cell protrusions at later stages of cell spreading (Ridley, 2015). It has been demonstrated that β1 integrin subunit in particular, is required to support RhoA activation at later stages of cell spreading (Danen et al., 2002). Overexpression of the β3 subunit has also been shown to enhance the activity of RhoA and promote stress fiber formation, whereas overexpression of the β1 subunit enhanced Rac activity and cell protrusion formation (Miao et al., 2002). In another study examining cell migration in epithelial cells, adhesion via $\alpha_v\beta_3$ was shown to support extensive actin cytoskeletal reorganization and the formation of a single broad protrusion at the leading edge, whereas cell adhesion via $\alpha_5\beta_1$ caused the extension of thinner protrusions (Danen et al., 2005). These findings indicate that the integrin profile demonstrated in EDS/HSD cells, may also have direct consequences on the ability of fibroblasts to form and/or maintain cell protrusions under conditions of mechanical strain and maintain connective tissue tension.

ASSESSING DERMATOSPARAXIS AND EDS FIBROBLAST DYSFUNCTION THROUGH GEL CONTRACTION ASSAYS

It is clear from the molecular changes described that fibroblast dysfunction is to be expected in EDS/HSD, involving aberrations in both cell adhesion and cytoskeleton dynamics. This has been directly examined in gel contraction studies performed with fibroblasts from animals with dermatosparaxis, which

is equivalent to the human form of dermatosparaxis EDS (dEDS; formerly EDS type VIIC) (Colige et al., 1999). This disorder is caused by mutations in the ADAMTS2 gene, which encodes the procollagen N-proteinase enzyme, and consequently results in poorly structured and loosely arranged collagen fibrils in the ECM (Bavinton et al., 1985). However, similarly, to the ongoing discrepancies in human EDS/HSD studies, the TEM findings of aberrant collagen fibrils in dermatosparaxis animals do not appear to reflect severity of presentation, and therefore, fail to fully account for and explain the abnormal properties of the connective tissue (Bavinton et al., 1985). The gel contraction abilities, however, do more accurately reflect clinical presentation. Dermal fibroblasts from mildly affected sheep demonstrate a gel contraction profile approaching that of control dermal fibroblasts (Ramshaw et al., 1991), while those from severely affected calf and sheep failed to contract the gel (Delvoye et al., 1983, 1986, 1991; Ramshaw et al., 1991). Furthermore, fibroblasts obtained from the less affected tissues in the severely presenting calf, like the tendons, vena cava, and aorta, also reflect this tissue specific presentation, and contracted the gel, similarly, to control fibroblasts (Delvoye et al., 1983). These finding are highly significant, as the correlation of fibroblast dysfunction with severity of manifestation, both between differently presenting animals, and between tissues within the same animal, likely demonstrates one of the main pathomechanisms mediating the observed connective tissue abnormalities. This provides confirmation that dysfunction of the fibroblast does indeed, constitute a relevant pathomechanism for EDS/HSD, and one that has now been demonstrated in a relevant animal model.

The nature of the fibroblasts inability to contract the gel was later shown to be due to the cell surface absence of a 34 kDa collagen binding protein related to anchorin CII (Mauch et al., 1988), which prevented effective cell adhesion of dermatosparatic fibroblasts to collagens type I and IV (Mauch et al., 1986). Consequently, it appears these fibroblasts were unable to attach to the type I collagen in the gel and effectively mediate the cytoskeletal forces needed to contract the collagen gel, as well as maintain homeostatic levels of tension within a restrained gel (Delvoye et al., 1991). These findings, therefore, confirm that impaired cell adhesion is a significant feature of fibroblast dysfunction, reducing integrity of the connective tissue integrity.

These findings highlight the complexity that underlies monogenic disorders. Pathogenesis of dermatosparaxis in this case, may not have been principally mediated by the aberrant collagen molecule itself, but mediated by a reduced cell surface expression of a cell adhesion molecule, that initially appears unrelated to the underlying ADAMTS2 mutation. This demonstrates that far more complex cellular and molecular processes underlie the pathway from initial mutated gene to final pathogenic phenotype and is likely to involve the interplay of various independent environmental and related factors. These independent factors could influence critical pathogenic features, and either promote a less or more severe phenotype in the affected individuals, which may help to explain the vast heterogeneity seen in the presentation of these disorders.

The same gel contraction studies were also performed with human EDS samples at the time, however, they demonstrated unexpected results. Fibroblasts from patients of several EDS subtypes showed no gel contraction abnormalities and behaved similar to control fibroblasts (Delvoye et al., 1986, 1991). Remarkably, this also included dEDS, which has an identical genetic basis to dermatosparaxis. It was concluded from these studies that fibroblast dysfunction did not contribute to the pathogenesis of human EDS/HSD, and research into this pathomechanism discontinued as focus turned toward identifying further EDS-related genes.

However, this conclusion now appears contradictory to our molecular understanding of EDS/HSD. The $\alpha_2\beta_1$ integrin is the main collagen receptor in humans and plays the equivalent role to the anchorin CII-related protein in mediating the attachment between the cell and collagen. The $\alpha_2\beta_1$ integrin is also downregulated in EDS/HSD fibroblasts as part of the integrin switch (Zoppi et al., 2018b). Furthermore, several gel contraction studies performed in control cells while blocking the collagen-$\alpha_2\beta_1$ interaction, prevented contraction of the gel (Klein et al., 1991; Schiro et al., 1991; Kelynack et al., 2000). These findings all highly indicate that the integrin switch seen in EDS/HSD fibroblasts should result in similar impairments in cell-ECM adhesion and prevent gel contraction, while also reflecting their pathological behavior *in vivo*.

Our understanding of the mechanisms regulating these molecular processes has also progressed. It is now apparent that these gel contraction assays do not truly reflect the EDS/HSD scenario in humans specifically, and hence, the drawn conclusions may not be valid. It has since been demonstrated that adding relevant collagen to the media of cultured human EDS fibroblasts promotes phenotypic correction, which reverses the integrin switch and restores the expression of $\alpha_2\beta_1$ to the cell surface (Zoppi et al., 2004). As such, the collagen supplied in these gel contraction assays may have corrected the phenotype of human EDS fibroblasts, and restored the cell surface expression of $\alpha_2\beta_1$. This would have promoted normal gel contraction, yet not reflect the true *in vivo* behavior of EDS/HSD fibroblasts. Hence, the human equivalent of this pathomechanism cannot be demonstrated through standard gel contraction assays. The existence of this pathomechanism therefore, has not been excluded in human patients, nor has it yet been truly examined.

DISCUSSION

This review had the aim to highlight a potential pathomechanism in EDS/HSD involving fibroblast dysfunction. Three principal stages of this pathomechanism can be described (**Figure 4**).

The first is a failed interaction between collagen and its receptor, the $\alpha_2\beta_1$ integrin (Zoppi et al., 2018b). The underlying cause of this failed interaction is specific for

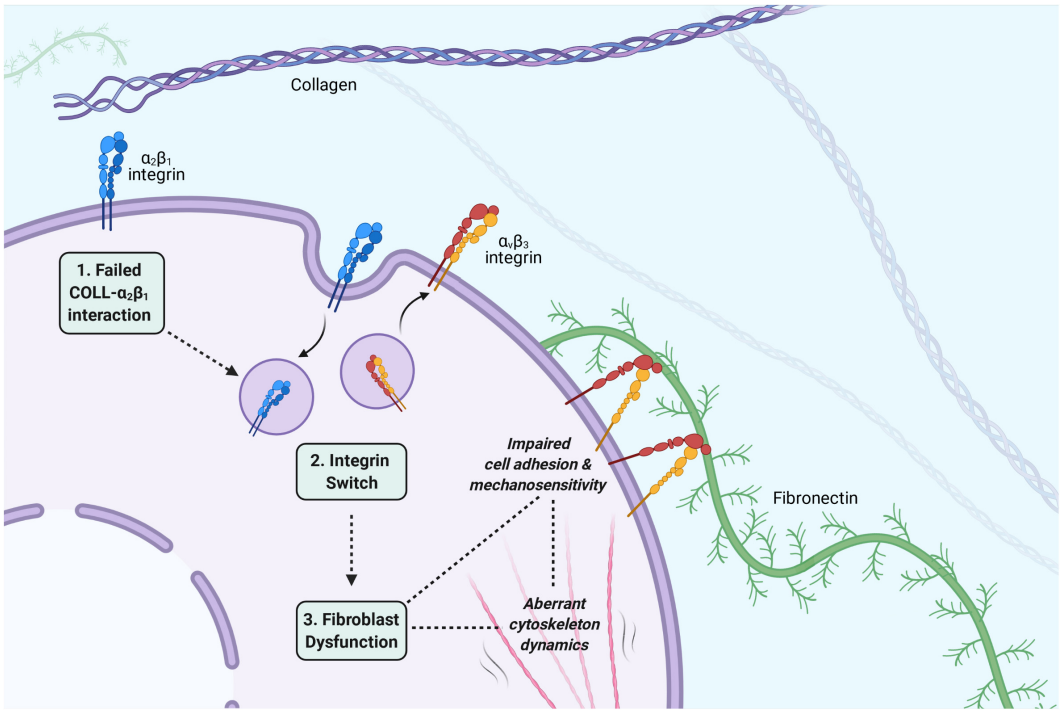

FIGURE 4 | The three principal stages of the proposed pathomechanism for EDS/HSD. (1) A failed interaction between collagen and $\alpha_2\beta_1$: A disorganized or defective collagen-ECM prevents engagement of the collagen ligand with its receptor, the $\alpha_2\beta_1$ integrin, and triggers the integrin switch. (2) The integrin switch: Fibroblasts respond to the defective collagen-ECM by switching their cell adhesion profile to promote adhesion to other ECM ligands. The $\alpha_2\beta_1$ and $\alpha_5\beta_1$ integrins are downregulated, and $\alpha_v\beta_3$ is upregulated, which then mediates the attachment between cell and ECM via fibronectin. (3) Fibroblast dysfunction: The altered integrin profile also has various consequences for the fibroblasts phenotype, which affects its ability to implement the tensional homeostasis mechanism and maintain integrity of the connective tissue. Impaired cell-ECM adhesion may promote fragility of the connective tissue. Impairments in mechanosensitivity may cause an incorrect interpretation of tension within the connective tissue and facilitate an abnormal cytoskeleton response. Aberrations in the dynamic cytoskeleton response itself, may also facilitate abnormalities in the viscoelastic properties of the connective tissue. All such aspects may contribute to the EDS/HSD phenotype. *Image created with BioRender.com*.

each EDS subtype, and can easily be accounted for in the genetically characterized subtypes of EDS. In cEDS and vEDS for example, mutations in the minor collagen genes prevent the organization of type I collagen into fibrils, which prevents its engagement with $\alpha_2\beta_1$ (Zoppi et al., 2018b). In hEDS and HSD, though the principle underlying molecular defect is unknown, an enhanced expression of the matrix metalloproteinase (MMP), MMP-9, has been observed (Zoppi et al., 2018a). The proteolytic activity of MMP-9 could promote a general disassembly of the ECM, and in turn, prevent the engagement of collagen with $\alpha_2\beta_1$. This stage of the pathomechanism, however, also allows the possibility of an acquired EDS phenotype, consequent to any other disease processes that interferes with collagen-$\alpha_2\beta_1$ binding. Speculatively, any autoimmune or inflammatory condition that promotes a general disassembly of collagen in the ECM could initiate the same pathomechanism and promote connective tissue abnormalities, which then manifest through features of joint hypermobility, skin hyperextensibility, and tissue fragility.

The second stage of the pathomechanism involves the integrin switch itself, which is a shared feature of the main EDS/HSD subtypes (Zoppi et al., 2018b). Following the failed collagen-$\alpha_2\beta_1$ interaction, a downregulation of the $\alpha_2\beta_1$ integrin itself occurs, which is accompanied by a downregulation of the fibronectin receptor $\alpha_5\beta_1$, and an upregulation of the alternative fibronectin receptor $\alpha_v\beta_3$. It is possible that fibroblasts are able to sense the compromised collagen-ECM via the $\alpha_2\beta_1$ integrin, and recognize a potential risk of *anoikis*, a specific form of cell death that occurs upon cell detachment from the ECM. To avoid such a fate, it is possible that fibroblasts respond by switching their integrin profile to promote cell adhesion to other ECM ligands, such as fibronectin, in order to maintain some form of attachment to the ECM and survive. Indeed, this notion is supported by apoptosis assays performed in cEDS and vEDS fibroblasts, where the $\alpha_v\beta_3$ integrin was specifically shown to rescue EDS cells from *anoikis* (Zoppi et al., 2008), indicating that this integrin switch is indeed, a critical cell survival response. The importance of cell-ECM adhesion, however, extends beyond the transmission of cell survival signals, and we have described in this review its importance in maintaining connective tissue integrity. The integrin switch, therefore, may form a key stage of this

pathomechanism, due to the consistent nature of this finding across all of the main EDS/HSD subtypes, as well as the critical consequences in weakening cell-ECM adhesion and its contribution to overall fibroblast dysfunction.

The final stage of this pathomechanism is fibroblast dysfunction itself, which ultimately mediates the abnormal properties of the connective tissue. The critical features of this dysfunction are impairments in cell adhesion and cytoskeleton dynamics. As already described, impaired cell-ECM adhesion weakens the integrity of the connective tissue, however, it also prevents fibroblasts from mediating their cytoskeletal forces to the surrounding environment and implement the tensional homeostasis mechanism. The integrin switch itself, has also been shown to directly affect cytoskeleton dynamics, impairing the cytoskeletal forces that are transferred through the weakened cell-ECM adhesions. The integrin switch may also cause abnormalities in the mechanosensitivity of fibroblasts, which may prevent accurate interpretations of the surrounding ECM properties, and hence, may produce an inappropriate response by fibroblasts. As such, key connective tissue properties such as viscoelasticity and integrity are all affected consequent the integrin switch and may contribute to the pathogenesis of EDS/HSD.

The contribution of this specific pathomechanism to the overall EDS/HSD phenotype could potentially be significant. It has to be highlighted that the current TEM analyses of collagen fibril structure and organization in EDS/HSD are highly inconsistent, and fail to associate with any EDS subtype, specific connective tissue abnormality, or severity of the manifestation (Angwin et al., 2020). Indeed, even the most significant abnormality associated with EDS/HSD, in the form of collagen flowers in cEDS, is one that cannot explain the disproportionate changes in skin viscoelasticity seen in this subtype, and is also one that is found in unaffected individuals (Hermanns-Lê et al., 2012). To our knowledge, the studies into fibroblast mechanics in dermatosparaxis animals, are the only non-genetic findings to have correlated with severity of connective tissue manifestation (Delvoye et al., 1983; Ramshaw et al., 1991), yet the possible significance of this appears to have been overlooked.

These findings suggest that what unites and defines the EDS/HSD subtypes may not be defects in the structure and/or organization of collagen itself, but in cell adhesion to collagen. If such a notion is correct, this may provide an ideal basis for the development of a universal or non-specific diagnostic test that truly captures all EDS/HSD subtypes, irrespective of the principal underlying defect. An assessment for membrane-bound collagen for example, would highly indicate that cell-ECM adhesion has switched *in vivo* from collagen to other ECM ligands, reflecting the occurrence of the initial stages of this pathomechanism in patients presenting with connective tissue ailments. This is of importance, since the most common forms of hEDS and HSD, are currently without any diagnostic biomarker, and it is likely that further unidentified subtypes remain. This may also have implications for other related disorders such as fibromyalgia, and Myalgic Encephalomyelitis/Chronic Fatigue Syndrome (ME/CFS), which demonstrate significant overlaps with hypermobility and connective tissue abnormalities, though the association is poorly understood (Bragée et al., 2020; Eccles et al., 2020). It is plausible therefore, that similar pathomechanisms involving fibroblast dysfunction may be contributing to the pathogenesis of these related disorders, which could be explored through their associations with membrane-bound collagen.

Of additional importance is to determine if this pathomechanism contributes to arterial fragility in vEDS, a lethal subtype of EDS with a median life expectancy of 40 years (Eagleton, 2016). Death commonly occurs due to complications associated with spontaneous vascular or hollow organ ruptures, however, the development of these are also poorly understood (Eagleton, 2016). If such a pathomechanism demonstrates itself to be significant, the development of a therapeutic agent that promotes arterial integrity via these processes could provide hope for a number of patients.

AUTHOR CONTRIBUTIONS

SM and DK conceived this manuscript. SM wrote the initial draft of the manuscript. DK reviewed, added, and edited the content of the manuscript. Both authors contributed to and approved the final manuscript for submission.

FUNDING

SM was supported by the Biotechnology and Biological Sciences Research Council (BBSRC) and University of Warwick funded Midlands Integrative Biosciences Training Partnership (MIBTP) (grant number BB/M01116X/1). DK was supported by the Wellcome-Warwick Quantitative Biomedical Program (RMRCB0058).

ACKNOWLEDGMENTS

The authors would like to thank the Midlands Integrative Biosciences Training Partnership (MIBTP), Biotechnology and Biological Sciences Research Council (BBSRC), Dr. Emma Reinhold, and Dr. Gemma Pearce for supporting our EDS/HSD research.

REFERENCES

Angwin, C., Brady, A. F., Colombi, M., Ferguson, D. J. P., Pollitt, R., Pope, F. M., et al. (2019). Absence of Collagen Flowers on Electron Microscopy and Identification of (Likely) Pathogenic COL5A1 Variants in Two Patients. *Genes* 10, 762. doi: 10.3390/genes10100762

Angwin, C., Ghali, N., Baker, D., Brady, A. F., Pope, F. M., Vandersteen, A., et al. (2020). Electron microscopy in the diagnosis of Ehlers-Danlos syndromes: correlation with clinical and genetic investigations. *The British journal of dermatology* 182, 698–707. doi: 10.1111/bjd.18165

Barczyk, M., Carracedo, S., and Gullberg, D. (2010). Integrins. *Cell and tissue research* 339, 269–280.

Bavinton, J. H., Peters, D. E., and Ramshaw, J. A. (1985). A morphologic study of a mild form of ovine dermatosparaxis. *The Journal of investigative dermatology* 84, 391–395. doi: 10.1111/1523-1747.ep12265475

Beighton, P., de Paepe, A., Danks, D., Finidori, G., Gedde-Dahl, T., Goodman, R., et al. (1988). 'International Nosology of Heritable Disorders of Connective Tissue, Berlin, 1986. *American Journal of Medical Genetics* 29, 581–594.

Beighton, P., De Paepe, A., Steinmann, B., Tsipouras, P., and Wenstrup, R. J. (1998). Ehlers-Danlos syndromes: revised nosology, Villefranche, 1997. Ehlers-Danlos National Foundation (USA) and Ehlers-Danlos Support Group (UK). *American Journal of Medical Genetics* 77, 31–37. doi: 10.1002/(sici)1096-8628(19980428)77:1<31::aid-ajmg8>3.0.co;2-o

Bisson, M. A., Beckett, K. S., McGrouther, D. A., Grobbelaar, A. O., and Mudera, V. (2009). Transforming growth factor-beta1 stimulation enhances Dupuytren's fibroblast contraction in response to uniaxial mechanical load within a 3-dimensional collagen gel. *The Journal of hand surgery* 34, 1102–1110. doi: 10.1016/j.jhsa.2009.02.008

Bisson, M. A., Mudera, V., McGrouther, D. A., and Grobbelaar, A. O. (2004). The contractile properties and responses to tensional loading of Dupuytren's disease–derived fibroblasts are altered: a cause of the contracture? *Plastic and reconstructive surgery* 113, 611–621. doi: 10.1097/01.prs.0000101527.76293.f1

Blackburn, P., Xu, Z., Tumelty, K., Zhao, R., Monis, W., Harris, K., et al. (2018). Bi-allelic Alterations in AEBP1 Lead to Defective Collagen Assembly and Connective Tissue Structure Resulting in a Variant of Ehlers-Danlos Syndrome. *American journal of human genetics* 102, 696–705. doi: 10.1016/j.ajhg.2018.02.018

Bowen, J. M., Glenda, J. S., Nigel, P. B., Marina, C., Mark, E. L., Fransiska, M., et al. (2017). 'Ehlers–Danlos syndrome, classical type'. *American Journal of Medical Genetics Part C: Seminars in Medical Genetics* 175, 27–39.

Bragée, B., Michos, A., Drum, B., Fahlgren, M., Szulkin, R., and Bertilson, B. C. (2020). Signs of Intracranial Hypertension, Hypermobility, and Craniocervical Obstructions in Patients With Myalgic Encephalomyelitis/Chronic Fatigue Syndrome. *Frontiers in neurology* 11:828. doi: 10.3389/fneur.2020.00828

Brown, R. A., Prajapati, R., McGrouther, D. A., Yannas, I. V., and Eastwood, M. (1998). Tensional homeostasis in dermal fibroblasts: mechanical responses to mechanical loading in three-dimensional substrates. *Journal of cellular physiology* 175, 323–332. doi: 10.1002/(sici)1097-4652(199806)175:3<323::aid-jcp10>3.0.co;2-6

Carley, M. E., and Schaffer, J. (2000). Urinary incontinence and pelvic organ prolapse in women with Marfan or Ehlers Danlos syndrome. *American journal of obstetrics and gynecology* 182, 1021–1023. doi: 10.1067/mob.2000.105410

Celli, M., Iacovino, C., Febbo, A., Lotti, L. V., Miraglia, E., Celli, L., et al. (2020). Ultrastructure study of skin fibroblasts in patients with Ehlers-Danlos Syndrome (EDS): preliminary results. *La Clinica terapeutica* 171, e431–e436.

Chiarelli, N., Ritelli, M., Zoppi, N., and Colombi, M. (2019). Cellular and Molecular Mechanisms in the Pathogenesis of Classical, Vascular, and Hypermobile Ehlers-Danlos Syndromes. *Genes* 10, 609. doi: 10.3390/genes10080609

Colige, A., Al Sieron, S. W., Li, U., Schwarze, E., Petty, W., Wertelecki, W., et al. (1999). Human Ehlers-Danlos syndrome type VII C and bovine dermatosparaxis are caused by mutations in the procollagen I N-proteinase gene. *American Journal of Human Genetics* 65, 308–317. doi: 10.1086/302504

Copetti, M., Morlino, S., Colombi, M., Grammatico, P., Fontana, A., and Castori, M. (2019). Severity classes in adults with hypermobile Ehlers-Danlos syndrome/hypermobility spectrum disorders: a pilot study of 105 Italian patients. *Rheumatology* 58, 1722–1730.

Dallon, J., and Ehrlich, H. (2008). A review of fibroblast-populated collagen lattices. *Wound repair and regeneration : official publication of the Wound Healing Society [and] the European Tissue Repair Society* 16, 472–479. doi: 10.1111/j.1524-475x.2008.00392.x

Danen, E. H., Sonneveld, P., Brakebusch, C., Fassler, R., and Sonnenberg, A. (2002). The fibronectin-binding integrins alpha5beta1 and alphavbeta3 differentially modulate RhoA-GTP loading, organization of cell matrix adhesions, and fibronectin fibrillogenesis. *The Journal of cell biology* 159, 1071–1086. doi: 10.1083/jcb.200205014

Danen, E. H., van Rheenen, J., Franken, W., Huveneers, S., Sonneveld, P., Jalink, K., et al. (2005). Integrins control motile strategy through a Rho-cofilin pathway. *The Journal of cell biology* 169, 515–526. doi: 10.1083/jcb.200412081

de Moraes, A. M., Cintra, M. L., Sampaio, A., de, S., Sotto, M. N., and Sesso, A. (2000). The ultrastructural and histophotometric study of elastic and collagen fibers in type II Ehlers-Danlos syndrome and subclinical forms. *Ultrastructural pathology* 24, 129–134. doi: 10.1080/01913120050132859

Delvoye, P., Mauch, C., Krieg, T., and Lapiere, C. M. (1986). Contraction of collagen lattices by fibroblasts from patients and animals with heritable disorders of connective tissue. *The British journal of dermatology* 115, 139–146. doi: 10.1111/j.1365-2133.1986.tb05709.x

Delvoye, P., Nusgens, B., and Lapière, C. M. (1983). The capacity of retracting a collagen matrix is lost by dermatosparactic skin fibroblasts. *The Journal of investigative dermatology* 81, 267–270. doi: 10.1111/1523-1747.ep12518288

Delvoye, P., Wiliquet, P., Levêque, J. L., Nusgens, B. V., and Lapière, C. M. (1991). Measurement of mechanical forces generated by skin fibroblasts embedded in a three-dimensional collagen gel. *The Journal of investigative dermatology* 97, 898–902. doi: 10.1111/1523-1747.ep12491651

Demmler, J. C., Mark, D. A., Reinhold, E. J., Choy, E., Lyons, R. A., and Brophy, S. T. (2019). Diagnosed prevalence of Ehlers-Danlos syndrome and hypermobility spectrum disorder in Wales, UK: a national electronic cohort study and case–control comparison. *BMJ* 9, 58961.

D'hondt, S., Guillemyn, B., Syx, D., Symoens, S., De Rycke, R., Vanhoutte, L., et al. (2018). Type III collagen affects dermal and vascular collagen fibrillogenesis and tissue integrity in a mutant Col3a1 transgenic mouse model. *Matrix biology : journal of the International Society for Matrix Biology* 70, 72–83. doi: 10.1016/j.matbio.2018.03.008

Eagleton, M. J. (2016). Arterial complications of vascular Ehlers-Danlos syndrome. *Journal of vascular surgery* 64, 1869–1880. doi: 10.1016/j.jvs.2016.06.120

Eastwood, M., McGrouther, D. A., and Brown, R. A. (1994). A culture force monitor for measurement of contraction forces generated in human dermal fibroblast cultures: evidence for cell-matrix mechanical signalling. *Biochimica et biophysica acta* 1201, 186–192. doi: 10.1016/0304-4165(94)90040-x

Eastwood, M., Porter, R., Khan, U., McGrouther, G., and Brown, R. (1996). Quantitative analysis of collagen gel contractile forces generated by dermal fibroblasts and the relationship to cell morphology. *Journal of cellular physiology* 166, 33–42. doi: 10.1002/(sici)1097-4652(199601)166:1<33::aid-jcp4>3.0.co;2-h

Eccles, J. A., Thompson, B., Themelis, K., Amato, M., Stocks, R., Pound, A., et al. (2020). Beyond Bones - The Relevance of Variants of Connective Tissue (Hypermobility) to Fibromyalgia, ME/CFS and Controversies Surrounding Diagnostic Classification: An Observational Study. *Clin Med (Lond)* 21, 53–58. doi: 10.7861/clinmed.2020-0743

Ezra, D. G., Ellis, J. S., Beaconsfield, M., Collin, R., and Bailly, M. (2010). Changes in fibroblast mechanostat set point and mechanosensitivity: an adaptive response to mechanical stress in floppy eyelid syndrome. *Investigative ophthalmology & visual science* 51, 3853–3863. doi: 10.1167/iovs.09-4724

Freyman, T. M., Yannas, I. V., Yokoo, R., and Gibson, L. J. (2002). Fibroblast contractile force is independent of the stiffness which resists the contraction. *Experimental cell research* 272, 153–162. doi: 10.1006/excr.2001.5408

Giannopoulos, A., Svensson, R. B., Heinemeier, K. M., Schjerling, P., Kadler, K. E., Holmes, D. F., et al. (2018). Cellular homeostatic tension and force transmission measured in human engineered tendon. *Journal of Biomechanics* 78, 161–165. doi: 10.1016/j.jbiomech.2018.07.032

Hausser, I., and Anton-Lamprecht, I. (1994). Differential ultrastructural aberrations of collagen fibrils in Ehlers-Danlos syndrome types I-IV as a means of diagnostics and classification. *Human genetics* 93, 394–407.

Hermanns-Lê, T., and Piérard, G. E. (2006). Collagen fibril arabesques in connective tissue disorders. *American Journal of Clinical Dermatology* 7, 323–326. doi: 10.2165/00128071-200607050-00006

Hermanns-Lê, T., Reginster, M.-A., Piérard-Franchimont, C., Delvenne, P., Piérard, G. E., and Manicourt, D. (2012). Dermal ultrastructure in low Beighton score members of 17 families with hypermobile-type Ehlers-Danlos syndrome. *Journal of Biomedicine & Biotechnology* 2012, 878107.

Holbrook, K. A., and Byers, P. H. (1982). 'Structural abnormalities in the dermal collagen and elastic matrix from the skin of patients with inherited connective tissue disorders'. *The Journal of investigative dermatology* 79 (Suppl.), 1.

Jiang, G., Huang, A. H., Cai, Y., Tanase, M., and Sheetz, M. P. (2006). Rigidity sensing at the leading edge through alphavbeta3 integrins and RPTPalpha. *Biophysical Journal* 90, 1804–1809. doi: 10.1529/biophysj.105.072462

Kanchanawong, P., Shtengel, G., Pasapera, A. M., Ramko, E. B., Davidson, M. W., Hess, H. F., et al. (2010). 'Nanoscale architecture of integrin-based cell adhesions'. *Nature* 468, 580–584. doi: 10.1038/nature09621

Kelynack, K. J., Hewitson, T. D., Nicholls, K. M., Darby, I. A., and Becker, G. J. (2000). Human renal fibroblast contraction of collagen I lattices is an integrin-mediated process. *Nephrology, dialysis, transplantation* 15, 1766–1772. doi: 10.1093/ndt/15.11.1766

Klein, C. E., Dressel, D., Steinmayer, T., Mauch, C., Eckes, B., Krieg, T., et al. (1991). Integrin alpha 2 beta 1 is upregulated in fibroblasts and highly aggressive melanoma cells in three-dimensional collagen lattices and mediates the reorganization of collagen I fibrils. *The Journal of cell biology* 115, 1427–1436. doi: 10.1083/jcb.115.5.1427

Kobayasi, T. (2004). Abnormality of dermal collagen fibrils in Ehlers Danlos syndrome. Anticipation of the abnormality for the inherited hypermobile disorders. *European journal of dermatology : EJD* 14, 221–229.

Kolodney, M. S., and Wysolmerski, R. B. (1992). Isometric contraction by fibroblasts and endothelial cells in tissue culture: a quantitative study. *The Journal of cell biology* 117, 73–82. doi: 10.1083/jcb.117.1.73

Kong, F., García, A. J., Mould, A. P., Humphries, M. J., and Zhu, C. (2009). Demonstration of catch bonds between an integrin and its ligand. *The Journal of cell biology* 185, 1275–1284. doi: 10.1083/jcb.200810002

Lammers, K., Lince, S. L., Spath, M. A., van Kempen, L. C., Hendriks, J. C., Vierhout, M. E., et al. (2012). Pelvic organ prolapse and collagen-associated disorders. *International urogynecology journal* 23, 313–319.

Langevin, H. M., Bouffard, N. A., Badger, G. J., Iatridis, J. C., and Howe, A. K. (2005). Dynamic fibroblast cytoskeletal response to subcutaneous tissue stretch ex vivo and in vivo. *American journal of physiology. Cell physiology* 288, C747–C756.

Langevin, H. M., Bouffard, N. A., Fox, J. R., Palmer, B. M., Wu, J., Iatridis, J. C., et al. (2011). 'Fibroblast Cytoskeletal Remodeling Contributes to Connective Tissue Tension'. *J Cell Physiol* 226, 1166–1175. doi: 10.1002/jcp.22442

Lawson, C. D., and Burridge, K. (2014). The on-off relationship of Rho and Rac during integrin-mediated adhesion and cell migration. *Small GTPases* 5, e27958. doi: 10.4161/sgtp.27958

Leistritz, D. F., Pepin, M. G., Schwarze, U., and Byers, P. H. (2011). COL3A1 haploinsufficiency results in a variety of Ehlers-Danlos syndrome type IV with delayed onset of complications and longer life expectancy. *Genetics in medicine : official journal of the American College of Medical Genetics* 13, 717–722. doi: 10.1097/gim.0b013e3182180c89

Liu, X., Wu, H., Byrne, M., Krane, S., and Jaenisch, R. (1997). Type III collagen is crucial for collagen I fibrillogenesis and for normal cardiovascular development. *Proceedings of the National Academy of Sciences of the United States of America* 94, 1852–1856. doi: 10.1073/pnas.94.5.1852

Malfait, F., Francomano, C., Byers, P., Belmont, J., Berglund, B., Black, J., et al. (2017). 'The 2017 international classification of the Ehlers-Danlos syndromes'. *American Journal of Medical Genetics. Part C, Seminars in Medical Genetics* 175, 8–26.

Mauch, C., Aumailley, M., Paye, M., Lapière, C. M., Timpl, R., and Krieg, T. (1986). Defective attachment of dermatosparactic fibroblasts to collagens I and IV. *Experimental cell research* 163, 294–300. doi: 10.1016/0014-4827(86)90060-1

Mauch, C., van der Mark, K., Helle, O., Mollenhauer, J., Pfäffle, M., and Krieg, T. (1988). A defective cell surface collagen-binding protein in dermatosparactic sheep fibroblasts. *The Journal of cell biology* 106, 205–211. doi: 10.1083/jcb.106.1.205

Miao, H., Li, S., Hu, Y. L., Yuan, S., Zhao, Y., Chen, B. P., et al. (2002). Differential regulation of Rho GTPases by beta1 and beta3 integrins: the role of an extracellular domain of integrin in intracellular signaling. *Journal of cell science* 115, 2199–2206.

Mizutani, T., Haga, H., and Kawabata, K. (2004). Cellular stiffness response to external deformation: tensional homeostasis in a single fibroblast. *Cell motility and the cytoskeleton* 59, 242–248. doi: 10.1002/cm.20037

Niland, S., Westerhausen, C., Schneider, S. W., Eckes, B., Schneider, M. F., and Eble, J. A. (2011). Biofunctionalization of a generic collagenous triple helix with the α2β1 integrin binding site allows molecular force measurements. *The international journal of biochemistry & cell biology* 43, 721–731. doi: 10.1016/j.biocel.2011.01.013

Ong, K. T., Plauchu, H., Peyrol, S., Roux, E., Errazuriz, E., Khau Van Kien, P., et al. (2012). Ultrastructural scoring of skin biopsies for diagnosis of vascular Ehlers-Danlos syndrome. *Virchows Archiv : an international journal of pathology* 460, 637–649. doi: 10.1007/s00428-012-1233-z

Parapia, L. A., and Jackson, C. (2008). Ehlers-Danlos syndrome–a historical review. *British Journal of Haematology* 141, 32–35.

Parsons, J. T., Horwitz, A. R., and Schwartz, M. A. (2010). Cell adhesion: integrating cytoskeletal dynamics and cellular tension. *Nature Reviews. Molecular Cell Biology* 11, 633–643. doi: 10.1038/nrm2957

Pepin, M., Schwarze, U., Superti-Furga, A., and Byers, P. H. (2000). Clinical and genetic features of Ehlers-Danlos syndrome type IV, the vascular type. *The New England Journal of Medicine* 342, 673–680.

Pollard, T. D., and Borisy, G. G. (2003). Cellular motility driven by assembly and disassembly of actin filaments. *Cell* 112, 453–465.

Proske, S., Hartschuh, W., Enk, A., and Hausser, I. (2006). Ehlers-Danlos syndrome - 20 years experience with diagnosis and classification at the university skin clinic of Heidelberg. *Journal der Deutschen Dermatologischen Gesellschaft = Journal of the German Society of Dermatology : JDDG* 4, 308–318.

Ramshaw, J. A., Mitrangas, K., and Bateman, J. F. (1991). Heterogeneity in dermatosparaxis is shown by contraction of collagen gels. *Connective tissue research* 25, 295–300.

Ridge, K., Shumaker, D., Robert, A., Hookway, C., Gelfand, V., Janmey, P., et al. (2016). Methods for Determining the Cellular Functions of Vimentin Intermediate Filaments. *Methods in enzymology* 568, 389–426.

Ridley, A. J. (2015). Rho GTPase signalling in cell migration. *Current opinion in cell biology* 36, 103–112.

Roca-Cusachs, P., Gauthier, N. C., Del Rio, A., and Sheetz, M. P. (2009). Clustering of alpha(5)beta(1) integrins determines adhesion strength whereas alpha(v)beta(3) and talin enable mechanotransduction. *Proceedings of the National Academy of Sciences of the United States of America* 106, 16245–16250.

Ruiz-Zapata, A. M., Kerkhof, M. H., Zandieh-Doulabi, B., Brölmann, H. A., Smit, T. H., and Helder, M. N. (2013). Fibroblasts from women with pelvic organ prolapse show differential mechanoresponses depending on surface substrates. *International urogynecology journal* 24, 1567–1575.

Schiller, H. B., Hermann, M. R., Polleux, J., Vignaud, T., Zanivan, S., Friedel, C. C., et al. (2013). β1- and αv-class integrins cooperate to regulate myosin II during rigidity sensing of fibronectin-based microenvironments. *Nature cell biology* 15, 625–636.

Schiro, J. A., Chan, B. M., Roswit, W. T., Kassner, P. D., Pentland, A. P., Hemler, M. E., et al. (1991). Integrin alpha 2 beta 1 (VLA-2) mediates reorganization and contraction of collagen matrices by human cells. *Cell* 67, 403–410.

Schwartz, M. A. (2010). Integrins and extracellular matrix in mechanotransduction. *Cold Spring Harbor perspectives in biology* 2, 5264.

Smith, L. T., Schwarze, U., Goldstein, J., and Byers, P. H. (1997). Mutations in the COL3A1 gene result in the Ehlers-Danlos syndrome type IV and alterations in the size and distribution of the major collagen fibrils of the dermis. *The Journal of investigative dermatology* 108, 241–247.

Swierczewski, R., Hedley, J., and Redfern, C. P. (2016). High-resolution micromechanical measurement in real time of forces exerted by living cells. *Cell adhesion & migration* 10, 322–330.

Symoens, S., Syx, D., Malfait, F., Callewaert, B., De Backer, J., Vanakker, O., et al. (2012). Comprehensive molecular analysis demonstrates type V collagen mutations in over 90% of patients with classic EDS and allows to refine diagnostic criteria. *Human mutation* 33, 1485–1493.

Theocharidis, G., and Connelly, J. (2019). Minor collagens of the skin with not so minor functions. *Journal of anatomy* 235, 418–429.

Tinkle, B. T., Bird, H. A., Grahame, R., Lavallee, M., Levy, H. P., and Sillence, D. (2009). The lack of clinical distinction between the hypermobility type of Ehlers-Danlos syndrome and the joint hypermobility syndrome (a.k.a. hypermobility syndrome). *American Journal of Medical Genetics. Part A* 149A, 2368–2370.

Tomasek, J. J., Gabbiani, G., Hinz, B., Chaponnier, C., and Brown, R. A. (2002). Myofibroblasts and mechano-regulation of connective tissue remodelling. *Nature Reviews. Molecular Cell Biology* 3, 349–363.

Viglio, S., Zoppi, N., Sangalli, A., Gallanti, A., Barlati, S., Mottes, M., et al. (2008). Rescue of Migratory Defects of Ehlers-Danlos Syndrome Fibroblasts in Vitro by Type V Collagen but Not Insulin-Like Binding protein-1. *The Journal of investigative dermatology* 128, 1915–1919.

Vogel, A., Holbrook, K. A., Steinmann, B., Gitzelmann, R., and Byers, P. H. (1979). Abnormal collagen fibril structure in the gravis form (type I) of Ehlers-Danlos syndrome. *Laboratory Investigation; a Journal of Technical Methods and Pathology* 40, 201–206.

Wang, C., Brisson, B. K., Terajima, M., Li, Q., Hoxha, K., Han, B., et al. (2020). Type III collagen is a key regulator of the collagen fibrillar structure and biomechanics of articular cartilage and meniscus. *Matrix biology : journal of the International Society for Matrix Biology* 20, 85–86.

Wang, S., Zhang, Z., Lü, D., and Xu, Q. (2015). Effects of mechanical stretching on the morphology and cytoskeleton of vaginal fibroblasts from women with pelvic organ prolapse. *International journal of molecular sciences* 16, 9406–9419.

Webster, K. D., Ng, W. P., and Fletcher, D. A. (2014). Tensional homeostasis in single fibroblasts. *Biophysical Journal* 107, 146–155.

Wenstrup, R. J., Florer, J. B., Brunskill, E. W., Bell, S. M., Chervoneva, I., and Birk, D. E. (2004a). Type V collagen controls the initiation of collagen fibril assembly. *The Journal of biological chemistry* 279, 53331–53337.

Wenstrup, R. J., Florer, J. B., Cole, W. G., Willing, M. C., and Birk, D. E. (2004b). Reduced type I collagen utilization: a pathogenic mechanism in COL5A1 haplo-insufficient Ehlers-Danlos syndrome. *Journal of cellular biochemistry* 92, 113–124.

Zollinger, A. J., Xu, H., Figueiredo, J., Paredes, J., Seruca, R., Stamenović, D., et al. (2018). Dependence of Tensional Homeostasis on Cell Type and on Cell-Cell Interactions. *Cellular and molecular bioengineering* 11, 175–184.

Zoppi, N., Barlati, S., and Colombi, M. (2008). FAK-independent alphavbeta3 integrin-EGFR Complexes Rescue From Anoikis Matrix-Defective Fibroblasts. *Biochimica et biophysica acta* 1783, 1177–1188.

Zoppi, N., Chiarelli, N., Binetti, S., Ritelli, M., and Colombi, M. (2018a). 'Dermal fibroblast-to-myofibroblast transition sustained by αvß3 integrin-ILK-Snail1/Slug signaling is a common feature for hypermobile Ehlers-Danlos syndrome and hypermobility spectrum disorders'. *Biochimica Et Biophysica Acta. Molecular Basis of Disease* 1864, 1010–1023.

Zoppi, N., Chiarelli, N., Ritelli, M., and Colombi, M. (2018b). Multifaced Roles of the αvβ3 Integrin in Ehlers-Danlos and Arterial Tortuosity Syndromes' Dermal Fibroblasts. *International journal of molecular sciences* 19, 982.

Zoppi, N., Gardella, R., De Paepe, A., Barlati, S., and Colombi, M. (2004). Human Fibroblasts With Mutations in COL5A1 and COL3A1 Genes Do Not Organize Collagens and Fibronectin in the Extracellular Matrix, Down-Regulate alpha2beta1 Integrin, and Recruit alphavbeta3 Instead of alpha5beta1 Integrin. *The Journal of biological chemistry* 279, 18157–18168.

Conflict of Interest: The authors declare that the research was conducted in the absence of any commercial or financial relationships that could be construed as a potential conflict of interest.

frontiers in Cell and Developmental Biology

ORIGINAL RESEARCH
published: 17 September 2021
doi: 10.3389/fcell.2021.702741

Wnt Signaling Induces Asymmetric Dynamics in the Actomyosin Cortex of the *C. elegans* Endomesodermal Precursor Cell

*Francesca Caroti, Wim Thiels, Michiel Vanslambrouck and Rob Jelier**

Predictive Genetics and Multicellular Systems, CMPG, University of Leuven, Leuven, Belgium

OPEN ACCESS

Edited by:
Ana Xavier De Carvalho, Universidade Do Porto, Portugal

Reviewed by:
Anne-Cécile Reymann, INSERM U964 Institut de Génétique et de Biologie Moléculaire et Cellulaire (IGBMC), France
François Robin, Institut National de la Santé et de la Recherche Médicale (INSERM), France
Grégoire Michaux, UMR6290 Institut de Genetique et Developpement de Rennes (IGDR), France

***Correspondence:**
Rob Jelier
rob.jelier@kuleuven.be

Specialty section:
This article was submitted to Cell Growth and Division, a section of the journal Frontiers in Cell and Developmental Biology

Received: *29 April 2021*
Accepted: *23 August 2021*
Published: *17 September 2021*

Citation:
Caroti F, Thiels W, Vanslambrouck M and Jelier R (2021) Wnt Signaling Induces Asymmetric Dynamics in the Actomyosin Cortex of the C. elegans *Endomesodermal Precursor Cell. Front. Cell Dev. Biol. 9:702741. doi: 10.3389/fcell.2021.702741*

During asymmetrical division of the endomesodermal precursor cell EMS, a cortical flow arises, and the daughter cells, endodermal precursor E and mesodermal precursor MS, have an enduring difference in the levels of F-actin and non-muscular myosin. Ablation of the cell cortex suggests that these observed differences lead to differences in cortical tension. The higher F-actin and myosin levels in the MS daughter coincide with cell shape changes and relatively lower tension, indicating a soft, actively moving cell, whereas the lower signal in the E daughter cell is associated with higher tension and a more rigid, spherical shape. The cortical flow is under control of the Wnt signaling pathway. Perturbing the pathway removes the asymmetry arising during EMS division and induces subtle defects in the cellular movements at the eight-cell stage. The perturbed cellular movement appears to be associated with an asymmetric distribution of E-cadherin across the EMS cytokinesis groove. ABpl forms a lamellipodium which preferentially adheres to MS by the E-cadherin HMR-1. The HMR-1 asymmetry across the groove is complete just at the moment cytokinesis completes. Perturbing Wnt signaling equalizes the HMR-1 distribution across the lamellipodium. We conclude that Wnt signaling induces a cortical flow during EMS division, which results in a transition in the cortical contractile network for the daughter cells, as well as an asymmetric distribution of E-cadherin.

Keywords: cell shape, asymmetric division, E-cadherin, Wnt signaling, *Caenorhabditis elegans*, nonmuscle myosin, F-actin (filamentous actin), cellular cortex

INTRODUCTION

Understanding how cells self-organize during development into multicellular systems is a fundamental challenge in biology. One formative process during self-organization is the breaking of symmetry, particularly by polarization of cells and asymmetric divisions. A central role is played by the cellular cortex, a thin, highly dynamic actomyosin mesh just underneath the membrane of eukaryotic cells. Non-muscular myosin acts on the actin fibers, generates forces, and creates tension in the cortical network. Uneven tension in the cortex drives cell shape changes, for example during morphogenesis (Lecuit and Lenne, 2007). The cortex further contributes to shape changes during mitosis, and plays an important role in cell polarization and asymmetrical divisions.

The first asymmetric stem cell–like division of the *Caenorhabditis elegans* embryo has been extensively used as a model for polarized divisions. Directed contractility of the actomyosin cortex and the PAR system work together to establish the polarity of the zygote (Lang and Munro, 2017). Following a polarizing signal, in the form of the microtubule organizing center introduced by the sperm cell, an actomyosin cortical flow is initialized. This flow segregates a subset of PAR proteins into the nascent anterior, which facilitates the establishment of a posterior domain with a different set of PAR proteins (Dickinson et al., 2017; Lang and Munro, 2017; Wang et al., 2017). In other cells cortical flows were shown to have a surprising role in cellular positioning. Chiral counter rotating flows participate in the orientation of the mitotic spindle in several cells during early embryogenesis, which is important for left-right asymmetry breaking during early embryogenesis (Pimpale et al., 2020).

Here we aimed to identify further asymmetrical cortical processes by observing non-muscular myosin (NMY-2) and filamentous actin (F-actin) during the divisions of the early *C. elegans* embryo. We found a striking asymmetrical pattern in the EMS division at the four-cell stage. The EMS division is asymmetric, with the daughter E giving rise to endoderm and MS to muscle cells, among other cell types (Rose and Gönczy, 2014). The EMS cell is polarized along the A/P axis, not by the PAR system, but by a partially redundant Wnt and MES-1 signal from the neighboring P2 cell (Bei et al., 2002). In this paper, we characterize the cortical behavior of EMS and its descendants and study how it is affected by perturbation of the Wnt pathway.

MATERIALS AND METHODS

C. elegans Strains and Maintenance

Caenorhabditis elegans strains were grown on NGM plates at 20°C as previously described (Brenner, 1974). The strains used in this study are listed in **Table 1**.

RNAi Experiments

RNAi was performed by feeding as described (Kamath et al., 2000). Briefly, L4 hermaphrodites were placed on NGM plates containing 25 μg/ml carbenicilline, 1 mM IPTG and seeded with bacteria expressing dsRNA. The induction was performed at 37°C for 4 h. The clones for *mom-2, dsh-2,* and *mig-5* RNAi were from the Vidal library. For all experiments a negative control (empty vector pL4440) was included to avoid scoring phenotypes not linked to the gene-specific RNAi. Phenotypes were scored after 48 h incubation at 20°C by *in vivo* imaging.

Microscopy

Long term imaging of the embryos was performed with a Zeiss LSM880 microscope using the fast-super resolution AiryScan mode and a Plan-Apochromat 63x/1.4 DIC M27 oil immersion objective. Z-stacks were acquired every 0.5 μm. The embryos were mounted on slides with M9 and Polybead Microspheres 20 μm (Polysciences) were used as spacer. The embryos were imaged every 2 min, except for the cell shape analysis (1.5 min) and cortical flows (5 s).

Ablation of the Cell Cortex

Ablations were performed with a 355 nm pulsed laser UGA-42 Caliburn from Rapp OptoElectronic mounted on a Zeiss LSM880. The cell cortex of a single cell was ablated in the anterior-posterior direction for 300 ms along a line of 4 μm at 11.3% laser strength. Ablations were performed after divisions were fully completed, several minutes after completion of cytokinesis. For E and MS this implied P2 division was at least underway, but more often P2 cytokinesis had already completed. Experiments were only included if the cell showed rapid healing of the cut, and proceeded to divide at least once. To detect the cytoskeleton dynamics, the time lapses were recorded as a single plane imaged at a rate of $\pm$1 fps. The RJ012 strain was used for the ablation experiments, using the Airyscan detector in R/S mode for imaging the cortex and exciting NMY-2::GFP and the Lifeact peptide by 488 and 561 nm laser light, respectively. The two fluorophores were either excited together, or in separate frames.

Analysis of Cortical Mechanical Characteristics

The physical properties typically measured through a cortical ablation experiment are cortical tension and cortical stiffness. As laid out in Mayer et al. (2010), cortical tension is proportional to the velocity away from the ablation line immediately after the ablation ($v_{\perp,0}$), and the stiffness is inversely proportional to the relaxation time of the velocity (τ). The relaxation time is given by $\tau = \zeta/k$, where k is the elastic stiffness of the cortex and ζ characterizes frictional interactions between the cortex and the surrounding fluid. Because the fluid in which the cortex is embedded is likely to be relatively uniform throughout the embryo, differences in this parameter are expected to reflect differences in stiffness.

To quantify cortical velocities after ablation we used a custom-made Particle Image Velocimetry (PIV) analysis pipeline, based on manually annotated markers. These markers were placed on either the NMY-2 or F-actin channel using an in-house lineaging tool over a 7 s time frame (**Supplementary Figures**, **Table 1**). All markers were placed within 2.5 microns distance orthogonal to the cut and at every time interval within the time frame. Three ABpl cells displayed noticeable cortical flow, which was separately annotated using markers in close vicinity, but sufficiently distant from the cut as to not be affected by the ablation retraction. We subsequently corrected for flow by averaging the flow velocities per time step and subtracting the resulting mean flow velocity vector from the velocity field.

As in Mayer et al. (2010), the dynamics of the velocity component orthogonal to the cut line were modeled as a simple viscoelastic response, with the characteristic exponential decay over time: $v_\perp(t) = v_{\perp,0}e^{-t/\tau}$. Given markers were only tracked for 6 s post-cut, cortical resealing dynamics were not taken up in the model. A non-linear least squares method from the SciPy package was used to fit the model.

To obtain overall fits and confidence intervals fits for $v_{\perp,0}$ and τ a bootstrap was performed ($n = 1{,}000$) on the total data set of outward velocities, weighted to ensure sampling from each experiment with equal probability. The significance for

TABLE 1 | *C. elegans* strains used in this work.

Strain	Genotype	Resources
SWG001	gesIs001[Pmex-5::Lifeact::mKate2::nmy-2UTR, unc-119+]	Reymann et al., 2016
LP306	cpIs53 [mex-5p::GFP-C1::PLC(delta)-PH::tbb-2 3'UTR + unc-119 (+)] II	Heppert et al., 2016
LP172	hmr-1(cp21[hmr-1::GFP + LoxP]) I	Marston et al., 2016
RW10029	zuIs178 [his-72(5' UTR)::his-72::SRPVAT::GFP::his-72 (3' UTR) + unc-119(+)].	Bao et al., 2006
stIs10024 [pie-1::H2B::GFP::pie-1 3' UTR + unc-119(+)]		
LP162	nmy-2(cp13[nmy-2::GFP + LoxP]) I.	Dickinson et al., 2013
RJ001	Cross between LP172 and SWG001	This work
RJ006	Cross between RW10029 and SWG001	This work
RJ012	Cross between LP162 and SWG001	This work
RJ013	Cross between LP306 and SWG001	This work

contrasts between cells was also derived via a weighted bootstrap approach ($n = 1{,}000$) for every cell pair that was compared. A null distribution was simulated based on a sampling from the total set of outward velocities for that cell pair. Cell labels were randomly shuffled within this bootstrap dataset. The absolute value of the difference between the parameter inference for the compared cells was subsequently compared to the actual observed parameter difference for that cell pair. The *p*-value is then defined as the proportion of bootstraps that resulted in an equal or higher difference.

Image Analysis and Quantification

The confocal images were processed using the free software Fiji (https://imagej.net/Fiji). To quantify the Lifeact::MKATE-2 and NMY-2::GFP intensity at the cell cortex a maximum intensity projection was made for the z-planes containing the cell cortex specific signal. For every cell at each time point, a cell outline was drawn manually before measuring the cortical signal intensity.

Statistical Analyses and Visualization

Analyses and plots were made using R (version 3.6.3) and via the packages *gam*, *nlme, lme4*, and *emmeans*, unless indicated otherwise. For **Figures 1B,C**, the intensity signal was corrected in several steps. First, background signal (areas surrounding the cortices) was measured and subtracted from the cortical signal for every embryo, timepoint, and plane. Second, the signal I is corrected for systematic intensity differences between embryos were corrected by measuring the average intensity across the cells of the signal per embryo, and calculating a scaling factor s_e for every embryo e: $s_e = \frac{\frac{1}{mn}\sum_i^n \sum_j^m I_{i,j}}{\frac{1}{m}\sum_j^m I_{i,j}}$, with n the number of embryos, m the measurements per embryo. Measurements for an embryo are then multiplied by this value to yield corrected values $I^*_{c,e}$. Third, effects on signal due to time of imaging (bleaching) and depth of the imaging plane (signal degradation), were corrected by fitting a GAM regression model $f(t, z)$ on the data for all embryos with a linear effect for bleaching (t time of imaging) and a smoothing spline to the log of the plane (z). The correction for an observation was calculated and scaled as $I^+_{c,e} = \frac{I^*_{c,e} - f(t,z) + \bar{I^*}}{\bar{I^*}}$. Finally, a model is fit on the corrected $I^+_{c,e}$ to estimate relative intensity values for individual cells using the *gls* function, taking into account time correlation between intensity measures using a first order autocorrelation structure (*corAR1* in *gls*). For **Figure 1B**, least square means and their standard errors are estimated on the model by *emmeans* with the Satterthwaite method and sampling to estimate variance components (mode *appx-satterthwaite*). For **Figure 1C**, a quadratic function is plotted which was fitted over time per cell using the *gls* function, again with a corAR1 correlation model. The plotted standard error over the fit is estimated based on the model's covariance matrix calculated by the *vcov* function.

When comparing volume and sphericity over time (**Figure 3**, **Supplementary Figures 1**, **2**), mixed effect models were fitted with *lmer,* with random effects capturing embryo specific effects and evaluating temporal correlations. Volume ratios were modeled as described in the paper describing the segmentation methodology (Thiels et al., 2021). The model for sphericity of the E-cell using the *lmer*-package syntax is expressed as:

$$sphericity \backsim 1 + time + category + (1|embryo)$$

The fixed effects are given by a time component and a categorical variable "*category*" (wild-type or *dsh-2/mig-5* mutant), while the random effect accommodates the variation between embryos. This model was arrived at after model simplifications. A random effect per embryo on the time coefficient was considered, but was removed as it was not significant (χ^2-test, $p = 0.2$).

The **Figures 1D,E** and the graphs in **Figure 4** where made with Python (version 3.7). **Figure 1D** was made by fitting a 2D tensor spline (package *pygam*, function *LinearGAM*) on the intensity data. Data was standardized per embryo (subtracting mean, division by standard deviation). The fitted spline was plotted using *contourf* from the package *matplotlib*.

Figure 1E was made based on manually tracking cortical features using the same custom tool as described for the PIV analysis above. The velocities of the features were next averaged and plotted using Python and the *quiver* function from package *matplotlib*.

Figure 4B is made by fitting a natural spline to normalized intensity data using Python and the package *statsmodels*.

For **Figure 4C**, the signal intensity was corrected by subtracting background (cytosolic) signal and scaled to the observed range of values across the contact area. The figure was made with the visualization package *seaborn* and the used test is the mixed two way anova test using Python and the *pingouin* package, with correction for repeated measures within embryos.

Analysis of Cellular Positioning

To follow cellular positioning over time, we imaged, tracked and analyzed histone labeled nuclei in embryos of the RW10029 as described before (Dzyubachyk et al., 2009; Krüger et al., 2015; Jelier et al., 2016), for both wildtype and RNAi treated embryos. To precisely establish differences in cellular positioning, a stringent alignment protocol was used. Time alignment was done by taking the last timepoint of the eight cell stage, which was the timepoint before division of either ABpl, ABpr, ABar, or ABal. Next, embryos were aligned in space by Procrustes analysis, which scales, centers and rotates the embryos to minimize the overall distance between nuclei. A Generalized Procrustes Analysis was performed to make a reference embryo for the wild-type embryos. Next all embryos were aligned by Procrustes Analysis to this reference. Finally, the distances across the different axes of the embryo (anterior-posterior, dorsal-ventral, left-right), were measured for every cell between all embryos and the reference embryo. The non-parametric two-sided Wilcoxon test was used to compare wild-type to the RNAi treated embryos.

Figure 3D was made with a custom tool (Java FX) to visualize and explore lineages, and shows a single RNAi embryo compared to the reference. **Figure 3E** is a scatter plot made in R and shows the positioning of ABpl in the aligned embryos relative to the reference along the anterior-posterior and dorsal-ventral axes.

RESULTS

To observe dynamical cortical behavior in the early embryo we used a strain (RJ012) expressing the F-actin binding peptide Lifeact tagged by the fluorophore mKate2 and non-muscular myosin (NMY-2) tagged with GFP, through modification of the endogenous *nmy-2* locus. As previously described (Reymann et al., 2016), we observed asymmetric levels of F-actin and NMY-2 in the cellular cortex during the zygotic division (**Figure 1A**), with P1 having lower levels for both markers. The lower level for both markers is maintained for both P1 descendants at the 4-cell stage, the endomesodermal precursor cell EMS and P2 (**Figure 1A**, **Supplementary Movie 1**), though the effect is more pronounced for the F-actin marker. The pattern propagates into the eight-cell stage, where three of the four P1 descendants have lower signal. However, the MS cell breaks with the pattern and has a relatively high level for both markers (**Figure 1B**). By monitoring the F-actin signal in the cortex of EMS and its daughters over time (**Figure 1C**), it becomes clear that the differences between E and MS arise during the division. To better characterize the phenomenon, we proceeded to follow the intensity of cortical F-actin during the EMS division with high temporal and spatial resolution (**Figure 1D**). Starting about 5 min prior to completion of cytokinesis, a gradient of F-actin signal arises across the EMS cell, with a rapid signal decrease on the posterior side and signal peaking just anterior to the cytokinesis cleft. After cytokinesis completes, the cortex of MS maintains a higher signal compared to E. We also observed highly dynamic cortical flow changes during cell division. In **Figure 1E** we represent the cortical flow based on manually tracked features of F-actin visualized by Lifeact. Nine hundred and sixty cortical features were traced, totaling 2,596 datapoints across three embryos. Until 4.5 min before completion of cytokinesis, EMS has a homogeneous flow to the dorsal side. Then the flow redirects to a posterior to anterior flow and a slight asymmetry in speed arises between the anterior and posterior halves of the cell (270–180 s before cytokinesis). Finally, a marked asymmetry arises between the anterior and posterior of the cell (from −180 s till completion of cytokinesis). The flow speeds up in the posterior, whereas it comes to a near standstill in the anterior. Further, we observed differences in duration at which distinct features (F-actin fragments) are visible in the cortex, with a much shorter feature life time for the posterior side of the EMS cell (E side). During the last 3 min before cytokinesis completes, features are visible during ∼25 s for the anterior side, vs. ∼13 s for the posterior side (H0 of no difference rejected at $p << 0.001$, oneway ANOVA), which indicates a more dynamic F-actin network in the posterior cortex.

Cortical flows are associated with anisotropies in cortical tension across the cell (Mayer et al., 2010). However, the observed differences in F-actin and NMY-2 in the daughter cells also point to a durable restructuring of the cellular cortex after division. We should interpret Lifeact intensity results with caution as we can not exclude that the Lifeact peptide is an imperfect indicator of actual quantities of F-actin in the descending cells (Hirani et al., 2019). Perhaps the asymmetric inheritance of bound peptide during the division severely reduces the concentration in the E cell, or maybe the Lifeact peptide has relatively slow F-actin binding dynamics in the apparently highly dynamic cortex of the E cell. Nonetheless, the NMY-2 marker is a fusion to the endogenous gene, which can be expected to be accurate, and it shows the same trend although with smaller changes. To test whether the observed changes in marker abundance after division of EMS translate into differences in mechanical properties of the cortex of E and MS. We performed ablation experiments of the cortex of these cells at the eight-cell stage, and followed the opening and closing of the ablation cut over time (**Figure 2A**). Typically, the cortex's response to ablation is modeled by assuming that it behaves as a 2D active viscoelastic gel (Saha et al., 2016). A typical cortical ablation analysis aims to quantify the evolving opening speed of the cut, with an expected exponential decay (**Figure 2B**). The initial recoil speed orthogonal to the cortical cut upon ablation is proportional to the stress across the cut (Mayer et al., 2010; Saha et al., 2016). Further, the speed decay over time is related to the stiffness of the cortex, with a lower relaxation time indicating a stiffer cortex (Mayer et al., 2010). As shown in **Figures 2C–E** has a higher initial outwards velocity than MS, indicating a considerably higher cortical tension, approximately twice that of MS. The ABpl cell, which is F-actin rich and is a relatively spread out cell at this stage, has an even lower velocity and cortical tension. The E cell also appears to have a stiffer cortex than MS and ABpl as

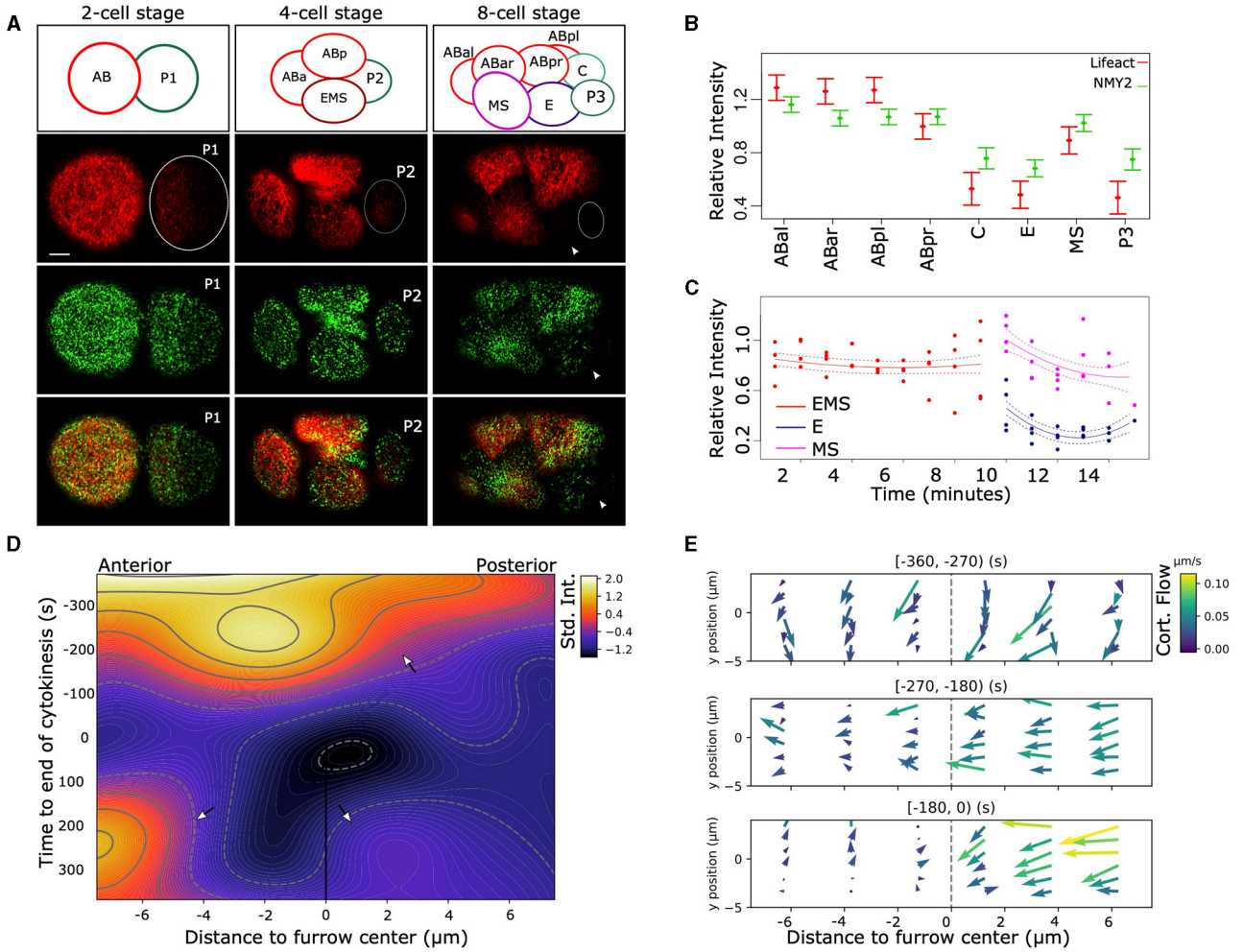

FIGURE 1 | Asymmetric distribution of F-actin and NMY-2 in the early *C. elegans* embryo. **(A)** Asymmetrical distribution in the amount of F-actin (Lifeact, red) and non-muscular myosin (NMY-2::eGFP, green) can be observed after the first, second, and third round of divisions. At the two-cell stage, AB (left) has higher signal than P1 (dotted circle), and the P1 descendants EMS and P2 (dotted circle) have lower signal than the AB descendants (left and top). The top row of figures indicates the positions and names of the cells. At the eight-cell stage, the P2 descendants P3 (right, very dim, dotted circle) and C (not visible), as well as EMS descendant E (arrowhead) have lower signal than the AB descendants (ABal bottom-left, ABar top-left, and ABpr top-right). Bar indicates 5 μm (first image at the bottom). **(B)** Quantification of the cortical signal of NMY-2 and F-actin in the cells at the eight-cell stage. Data represent four embryos measured over time and are normalized for differences in intensity between dyes, embryos, background signal, imaging depth, the effect of bleaching due to imaging, and corrected for repeated measures (see section 2). F-actin and NMY-2 behave roughly similar, though NMY-2 differences are smaller. Both signals are asymmetrically distributed in the EMS daughters E and MS, with markedly lower signal in E ($p < 0.005$). Error bars represent standard error around the mean. **(C)** The relative F-actin signal changes abruptly during the EMS division. EMS, E, and MS cortex for four embryos are measured over time; signal is corrected for several confounders and repeated measures. **(D)** Heatmap representing the intensity of F-actin signal in the cortex during the EMS division to MS (anterior) and E (posterior). The heatmap represents a 2D spline fit to intensity data taken from image stacks with 5 s intervals from three embryos, corrected for systematic signal intensity differences between embryos. The furrow center (at the origin) is defined by the location of the membrane at the center of the cell at the moment of membrane closure. During cytokinesis the strong curvature of the membrane induces a temporary loss of signal from the focal planes (around t = 0). The contour lines indicated lines with identical intensity values. The top arrow highlights rapid signal loss on the posterior side of the cell. The lower left arrow points to the signal in MS, lower right the much lower signal in the E cell. **(E)** The cortex of EMS shows large differences in cortical flow between the anterior and posterior sides relative to the cytokinetic furrow. The data is based on manual tracking of cortical features of three embryos. Image stacks are 5 s apart.

manifested through the lower relaxation time, though the effect only has a marginal significance level ($p < 0.1$, **Figure 2D**). To obtain more information on the nature of these differences we also considered the shape of the cells. The motivation is that high overall cortical tension makes cells more rigid and spherical, similar to when cells round up prior to mitosis by increasing cortical stiffness and tension (Stewart et al., 2011), whereas lower cortical tension allows more flexible and irregular shapes. We employed a novel cellular segmentation pipeline to retrieve the shapes of the cells from confocal microscopy images of embryos with fluorescently membranes (strain RJ013) (Thiels et al., 2021). Over time, E retains a mostly spherical

shape, whereas MS develops a more irregular shape, and in some embryos forms a lamellipodium structure 4.5 min after EMS division (**Figure 2E**, MS lamellipodium in embryos 1 and 2, see **Supplementary Figure 1** for sphericity measures). Both observations, combined with the assumption that the friction experienced by the cortex is relatively stable in the short time frame, point to a higher cortical tension in E.

As the EMS cell is polarized by the Wnt and MES-1 signaling pathways, which induces the E fate in the posterior daughter born next to P2 (Goldstein, 1992; Bei et al., 2002), we asked if the Wnt signaling induces the cortical flows and reorganization of the cortex. **Figure 3A** shows the results of Wnt pathway knockdown by RNAi for the Wnt ligand *mom-2* and RNAi for *dsh-2* and *mig-5*, two genes coding for the disheveled proteins active during early embryogenesis. The disheveled proteins relay the signal coming from the Frizzled receptors upon binding the Wnt ligand (e.g., MOM-2) to distinct cellular responses. Both RNAi experiments resulted in the near equalization of F-actin signal during, and after the EMS division (**Figure 3B**) with high penetrance (*mom-2* RNAi: 7/8; *dsh-2/mig-5* RNAi: 24/34). Though both RNAi experiments perturb Wnt signaling and equalize the division with respect to F-actin, we found they varied in the extent that they affect the fate induction of the E cell. RNAi of *mom-2* invariantly inhibited E fate induction, perturbing the ingression of the cells during gastrulation. RNAi of the *dsh-2/mig-5* did not have the same effect, with gastrulation of Ea and Ep proceeding normally, including the fate-specific delayed division of these cells (Sulston et al., 1983). This indicates therefore that the F-actin distribution in EMS is not essential for the fate induction of the E cell.

To evaluate whether Wnt signaling has an effect on the cell shape, we segmented cells following EMS division in five *dsh-2/mig-5* RNAi embryos, and compared to seven wildtype embryos. The perturbation does not remove the volume asymmetry in the EMS division (**Supplementary Figure 2A**), but instead increases it slightly. However the perturbation does make the E-cell shape more irregular, and decreases sphericity ($p < 0.05$, mixed effects model with χ^2-test, **Figure 3C**, **Supplementary Figures 2B**, **3**), which points to a drop in cortical tension.

We next asked if there is a direct contribution of the asymmetry in EMS to the cellular movements occurring around, and after EMS division. We therefore precisely tracked cellular movements, division timings and division angles during the four and eight-cell stage by lineaging wildtype and RNAi treated embryos (Bao et al., 2006; Krüger et al., 2015; Jelier et al., 2016). By comparing eight RNAi to ten wildtype embryos, we found very limited phenotypes in these early stages, but we did observe a modest mispositioning of the ABpl and ABar cell, with the former ending up positioned posterior to their normal location at the end of the eight-cell stage (**Figure 3C**). The ABpl cell moves a long way across the embryo during the seven to eight-cell stage as part of the formation of a cellular arrangement that is important for left-right asymmetry in the embryo (Pohl and Bao, 2010). ABpl forms a lamellipodium into the cytokinesis groove of the dividing EMS cell preceding this movement, and specifically associates with MS. In our hands, the formation of the lamellipodium or the size of the movement of the ABpl cell is not reduced due to the RNAi perturbation of Wnt signaling. However, ABpl is modestly and consistently misdirected to the posterior side for both *mom-2* and *dsh-2/mig-5* RNAi treatments (**Figures 3D,E**, $p < 0.001$, Wilcoxon rank sum test).

As the ABpl cell moves over MS and E, it most likely exerts a force on either or both of these cells. To exert such a force, cell adhesions are required. As the E-cadherin HMR-1 is known to play a role in cell adhesion in early embryogenesis, we decided to image the localization of HMR-1 during EMS division. For this purpose we used a strain expressing the endogenous HMR-1 fused to GFP as well as the tagged F-actin marker Lifeact::mKate-2 (strain RJ001). We observed that HMR-1 distribution across the EMS-ABp(l) contact is highly dynamic (**Figure 4A**). Initially the distribution is homogeneous across the cell contact. As the EMS division approaches, the HMR-1 distribution becomes polarized and accumulates more on the anterior side of the interface. Just before cytokinesis of EMS completes, the HMR-1 signal abruptly disappears along the future E-ABpl interface. In **Figure 4B**, the distribution of HMR-1 across the ABpl/EMS interface is characterized over three embryos. We next asked if this distribution also depends on Wnt signaling. **Figures 4C,D** show the effect of *dsh-2/mig-5* RNAi on the distribution of HMR-1. The asymmetry in the distribution across the ABpl-EMS interface is completely removed and thus depends on the polarization driven by Wnt signaling. The phenotype was seen in six out of seven observed *dsh-2/mig-5* RNAi treated embryos. Concluding, Wnt signaling drives asymmetric distribution of E-cadherin across E and MS, which plays a role in ABpl specifically interacting with MS.

DISCUSSION

During EMS division, the cellular cortex undergoes active reorganization prior to cytokinesis, with cortical flows and a shift in apparent F-actin and NMY-2 distribution. This behavior appears similar in nature to the cortical flow during the pseudo-cleavage furrow phase of first zygotic division where the cell polarity of the cell is established (Reymann et al., 2016). Like the zygotic division, the EMS division is asymmetric in the fate and volume of the daughter cells, and the spindle orientation and spindle location are tightly regulated. The way polarization is induced differs, with the zygote being polarized by the centrioles donated by the sperm, whereas the EMS cell is polarized by signaling from the posterior P2 cell (reviewed in Rose and Gönczy, 2014). Also, during the zygotic division, the cortical flow is associated with the displacement of PAR proteins, the subsequent establishment of asymmetric AP cortical domains and the unequal segregation of cell fate determinants (Rose and Gönczy, 2014). This system plays no similar role in the EMS cell given that the PAR proteins are not distributed along the EMS polarization axis (Nance and Priess, 2002). Instead the polarization and fate change are induced by Wnt and Src signaling from P2. The signaling induces an asymmetrical distribution of several Wnt pathway proteins in the so-called Wnt/β-Catenin asymmetry pathway, specifically APC (APR-1) and the β-Catenin WRM-1 to the anterior (MS) side, and

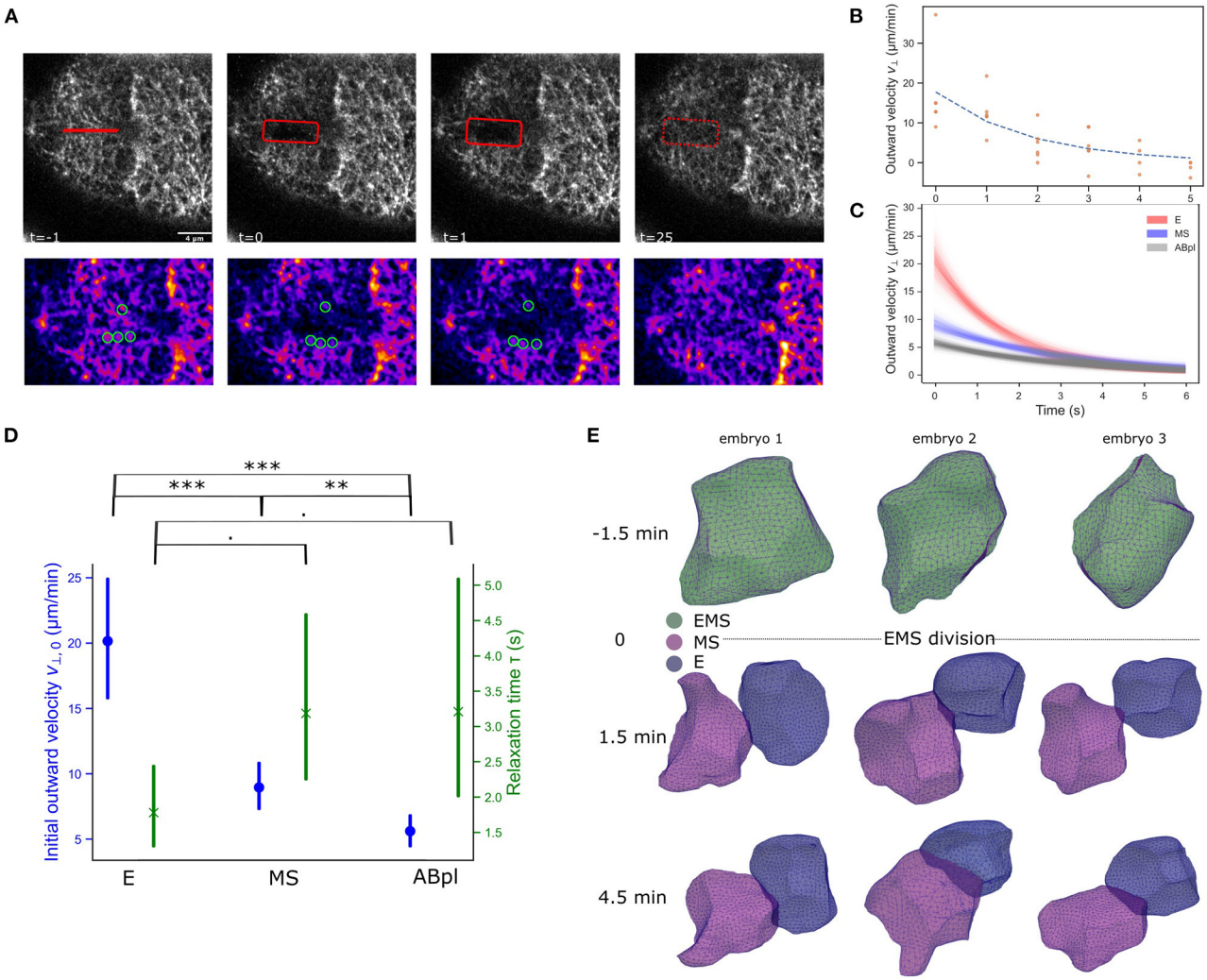

FIGURE 2 | The differences in the NMY-2 and F-actin markers across E and MS coincide with cortical tension differences and cell shape changes. **(A)** Illustration of cortical ablation experiments on an E cell. A 4 μm cut is made by a pulsed 355 nm laser (UGA-42 Caliburn). In the sequence the opening of the cut, highlighted with the rectangle can be observed, followed by repair of the cortical disruption. The second row shows the manual PIV measurement for this experiment. The image is processed (blurring and background subtraction), and a color LUT is used to better see intensity contrasts. Cortical features are marked with green circles. A modest recoil is noted, and after ±25 s the cut is repaired. Scale bar is 4 νm. **(B)** Output of the PIV analysis. An example of outward velocities for an E cell are shown with an exponential trend fit. The movement is quickly reduced to low levels and the maximal gap opening is achieved after 3–5 s. **(C)** Exponential fit for the ablations of E, MS, and ABpl cells, with confidence interval. The analysis is based on 4, 7, and 7 experiments respectively. The E and MS cells show different initial velocities, which indicates E has larger initial tension than MS. For reference, also the ABpl cell was ablated, which has still higher F-actin/NMY-2 than MS (cf. **Figure 1B**), and this cells shows very little cortical tension. **(D)** Statistical analysis of the cortical ablation experiment, showing both the initial outward velocity estimate and the relaxation time. Bars represent 95% confidence level and test results are based on a permutation test (weighted bootstrap, see section 2). $\cdot\ p < 0.1$, $^{**}p < 0.01$, $^{***}p < 0.001$. **(E)** E and MS take different cellular shapes after division. Cells were reconstructed from images of embryos with membranes tagged by a membrane binding domain fused to GFP.

Frizzled and Disheveled homologs remain to the posterior (E) side (reviewed in Sawa and Korswagen, 2013; Lam and Phillips, 2017). Interestingly, the anterior polarizing movement of APR-1 coincides with the cortical flow (Heppert et al., 2018), and transport of this protein may be one particular role of the flow. We show here that perturbation of the Wnt ligand (*mom-2* RNAi) or the disheveled proteins (*dsh-2/mig-5* RNAi) nearly abolishes the cortical flow and NMY-2 and F-actin distribution asymmetries. A similar observation on the cortical asymmetry has been reported following RNAi for Wnt signaling genes for the zygotic division (Naganathan et al., 2014). The disheveled proteins can modulate the F-actin network indirectly, for example by activating the small GTPases RHO and RAC in the context of the planar-cell-polarity cascade, which then activate downstream targets to modulate the actin cytoskeleton, or through interactions with formins that can induce actin nucleation and elongation of actin fibers (reviewed in Wallingford and Habas, 2005). The cortical asymmetry is not

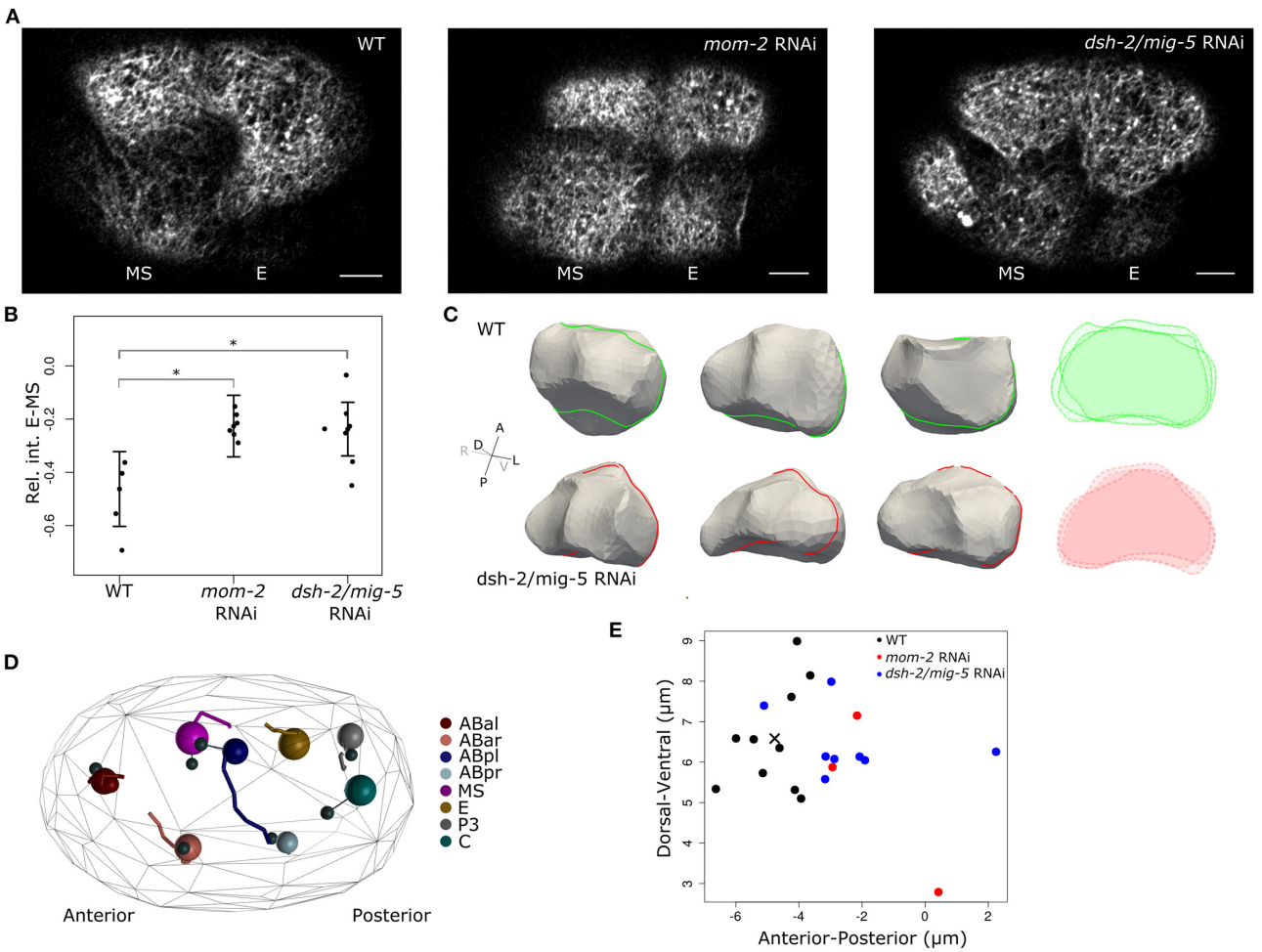

FIGURE 3 | Wnt signaling drives asymmetric cortical behavior during and after EMS division. **(A)** Cortical images showing effect on F-actin distribution when Wnt signaling is disrupted. F-actin shows nearly symmetric distribution between the E and MS daughters when either the Wnt ligand (*mom-2*) or the disheveled proteins (*dsh-2, mig-5*) are knocked down. Images are taken 3–5 min after completion of cytokinesis. Scale bars indicate 5 μm. **(B)** Quantification of the effect of disruption of Wnt signaling on F-actin asymmetry between E and MS. Cortical intensity is measured and corrected as before, the shown values are the difference in intensity between E and MS (E-MS). Error bars represent the standard error and are centered around the mean. **(C)** Shape reconstruction of the E cell in both wildtype and *dsh-2/mig-5* RNAi embryos 3' after EMS division, with overlaid intersections shown in the right panel. At the shown moment, the perturbed embryos have more irregularly shaped E cells, with in some embryos a marked indentation at the posterior side by P2 as it is going through division. **(D)** Disrupting Wnt signaling induces a minor positional phenotype at the eight-cell stage. Systematic analysis of cellular positioning by lineaging 8 embryos treated with *dsh-2/mig-5* RNAi showed a slightly more posterior positioning of the ABpl cell. The large spheres represent the cells in a perturbed embryo. The positioning in the reference embryos is shown by connecting the cells to small black spheres that represent the cells' average position in reference embryos. The movements of the cells are shown by traces in the same color. **(E)** Position of ABpl in wild type and RNAi embryos. ABpl is consistently positioned more to the posterior when the Wnt signal is disrupted by RNAi for either the Wnt ligand (*mom-2*) or the Dsh proteins (*dsh-2/mig-5*) (cross indicates the average WT position). The cross marks the average position of ABpl in the reference embryos. *indicates significance at the 0.05 level

essential for the fate induction in EMS as the knockdown of the disheveled proteins left E-fate associated properties, such as delayed division of Ea/p and gastrulation time, in place. This matches earlier reports of low penetrance (∼3%) for *dsh-2/mig-5* RNAi causing defects in the endoderm fate induction (Liu et al., 2010). This limited effect has been attributed to simultaneous MES-1 signaling from P2, which provides a redundant pathway to induce the E-fate (Bei et al., 2002).

We verified by ablation that the properties of the cortex in the daughter cells remain different after the division, with higher cortical tension in the E cell. These changes are supported by observations of the cell shape of E and MS, where the former remains spherical after division and the latter rapidly changes shape and repositions. The higher cortical tension in the E cell is reduced upon *dsh-2/mig-5* RNAi, with the E cell showing more deformation upon pressures from neighboring cells. It is interesting to consider that the differences in the cortical behavior and physical properties between E and MS play a role in the robust cellular positioning in the early embryo, with the lower effective tension

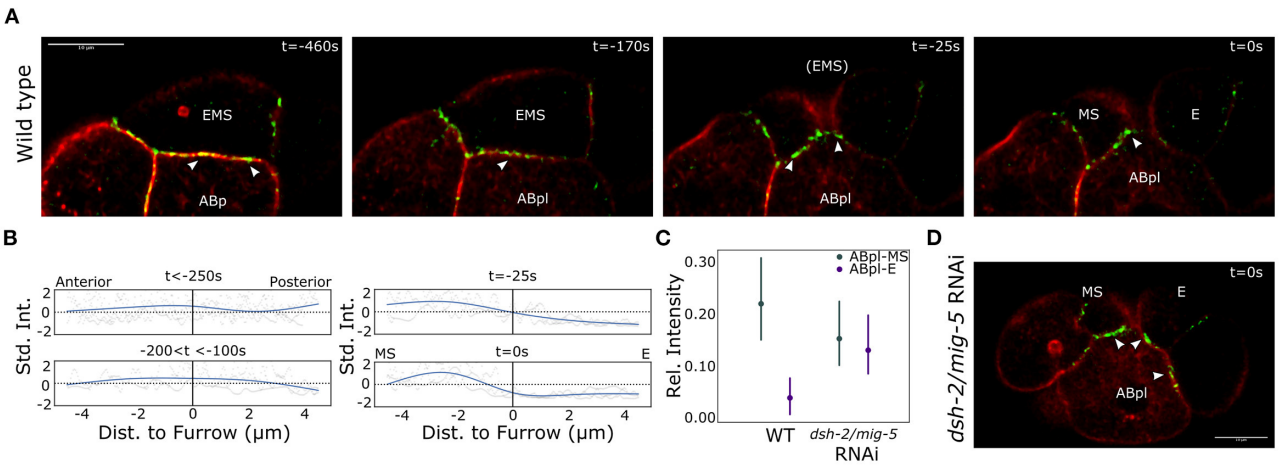

FIGURE 4 | Asymmetric E-cadherin distribution coincides with the asymmetric cortical dynamics in EMS. **(A)** Distribution of the E-cadherin HMR-1 across the interface between EMS and ABp/ABpl. Note that ABpl forms a lamellipodium that precedes the ABpl movement following EMS division. Life act marking F-actin in red, the E-cadherin HMR-1 in green. Arrow heads indicate HMR-1 foci as mentioned in the text. Scale bar indicates 10 μm. **(B)** Quantification of the HMR-1 distribution over the ABpl/EMS interface. A natural spline is fit on the normalized data from three wildtype embryos. **(C)** The HMR-1 asymmetry is controlled by the Wnt signal. The RNAi effect on the distribution across the two cells is significant ($p < 0.005$) in a mixed 2-way ANOVA test. Data from seven wildtype embryos and three *dsh-2/mig-5* RNAi treated embryos. The signal is corrected for background, normalized for differences in signal range, and the model includes a random effect to capture embryo specific effects. Bars indicate 95% confidence interval. **(D)** Illustration of the HMR-1 signal in E and MS after completion of cytokinesis upon RNAi treatment for the disheveled genes *dsh-2/mig-5*. Colors are as for **(A)**.

of MS facilitating the changes in shape and movement of the cell.

We found that perturbing the Wnt signaling with RNAi induces only a modest positional phenotype at the eight-cell stage, with a small displacement of ABpl to the posterior, while maintaining the overall movement of the cell. This led us to postulate that the way ABpl exerts forces on the E and MS cells has changed, for instance by having a stronger adhesion to the E-cell. By following E-cadherin on the cortex of EMS and descendants we indeed observed that cytokinesis is associated with a marked displacement of E-cadherin toward the anterior descendant MS. In the wildtype embryo, ABpl moves over and associates with MS, with foci of the E-cadherin HMR-1 at the interface. Whereas upon perturbation of the Wnt signaling by *dsh-2/mig-5* RNAi, the HMR-1 distribution shifted to the posterior E cell. The cortical dynamics and flow are likely directly associated with the distribution of E-cadherin between E and MS, as cortical flows can transport E-cadherin. An example is the basal-to-apical flow of cadherin at cell junctions (Kametani and Takeichi, 2007), where E-cadherin latches on to F-actin through α-catenin, which itself binds to E-cadherin by mediation of β-catenin. Further, local contractility can lead to accumulation of cortical F-actin and aggregation of cortical proteins (Munjal et al., 2015). During the EMS division the cortical flow could transport HMR-1 to the anterior side of the cytokinetic furrow, and the transient F-actin accumulation on the anterior may play a role in aggregating HMR-1 at this location. HMR-1 can also modify the cortical contractility and flow, as in the *C. elegans* zygote, where HMR-1 has been reported to slow down cortical flows by drag and negatively regulate RHO-1 activity, a GTPase associated with recruitment and activation of myosin II (Padmanabhan et al., 2017). The accumulation of HMR-1 to the anterior side of the cytokinesis cleft may therefore also play a role in slowing down the cortical flow.

It is interesting that a lower apparent amount of F-actin and NMY-2 in E vs. MS appears to be associated with a higher cortical tension in the former. This is in contrast to the zygotic division, a higher tension is generated by the anterior part of the cell, which has higher F-actin and NMY-2 signal than the posterior side (Mayer et al., 2010). However, there are many facets that modulate the activity of the cortex, and the mechanisms of the observed difference remain to be elucidated. It is possible that the active ATP-driven force generation is upregulated in E, e.g., by local NMY-2 phosphorylation (Wei et al., 2020), which could drive up the tension, irrespective of the lower density. The difference may also be caused by differences in crosslinking in the cortex, as crosslinking is a key regulator of actomyosin contractility (Inoue et al., 2011; Krueger et al., 2019). Further, cortical tension is hypothesized to be maximal for an intermediate level of connectivity in the actomyosin network (Chugh et al., 2017; Ding et al., 2017). When connectivity is too high or too low, the generated tension in the network will be low (Ennomani et al., 2016), and a high level of connectivity has been suggested to make the network incapable of transmitting tensions over larger distances (Ennomani et al., 2016). This line of reasoning aligns with the dense F-actin networks we observe in MS and the AB descendants.

We conclude that during EMS division a cortical flow arises, as well as a dynamic transition in the cortical contractile network and E-cadherin distribution. The abrupt

change in cortical dynamics, during and after EMS division, is driven by Wnt signaling, and the observed cell state transition is associated with changes in cortical tensions, cell shape and actomyosin organization of the descendant cells. The mechanisms underlying such transitions are an active research area, and further study of this asymmetric division could unveil new insight into the determinants of actin network architecture.

DATA AVAILABILITY STATEMENT

The original contributions presented in the study are included in the article and **Supplementary Material**, further inquiries can be directed to the corresponding author.

AUTHOR CONTRIBUTIONS

FC made the initial observation and performed the experiments. MV performed part of the ablation experiments. WT performed the cell shape analyses. RJ supervised, performed image analyses, lineage tracking and the statistical analyses, and wrote the paper. All authors contributed to the article and approved the submitted version.

ACKNOWLEDGMENTS

We thank the Stephan Grill lab for kindly sharing the strain SWG001. The other strains were provided by the CGC, which was funded by NIH Office of Research Infrastructure Programs (P40 OD010440). Experiment expenses and FC were supported by FWO research grant G055017N, WT was supported by FWO Aspirant grant 11I2921N. We thank Liesbet Temmerman, Ellen Geens, Bart Smeets, and Jef Vangheel for discussions.

SUPPLEMENTARY MATERIAL

The Supplementary Material for this article can be found online at: https://www.frontiersin.org/articles/10.3389/fcell.2021.702741/full#supplementary-material

REFERENCES

Bao, Z., Murray, J. I., Boyle, T., Ooi, S. L., Sandel, M. J., and Waterston, R. H. (2006). Automated cell lineage tracing in *Caenorhabditis elegans*. *Proc. Natl. Acad. Sci. U.S.A.* 103, 2707–2712. doi: 10.1073/pnas.0511111103

Bei, Y., Hogan, J., Berkowitz, L. A., Soto, M., Rocheleau, C. E., Pang, K. M., et al. (2002). SRC-1 and Wnt signaling act together to specify endoderm and to control cleavage orientation in early *C. elegans* embryos. *Dev. Cell* 3, 113–125. doi: 10.1016/S1534-5807(02)00185-5

Brenner, S. (1974). The genetics of *Caenorhabditis elegans*. *Genetics* 77, 71–94. doi: 10.1093/genetics/77.1.71

Chugh, P., Clark, A. G., Smith, M. B., Cassani, D. A. D., Dierkes, K., Ragab, A., et al. (2017). Actin cortex architecture regulates cell surface tension. *Nat. Cell Biol.* 19, 689–697. doi: 10.1038/ncb3525

Dickinson, D. J., Schwager, F., Pintard, L., Gotta, M., and Goldstein, B. (2017). A single-cell biochemistry approach reveals par complex dynamics during cell polarization. *Dev. Cell* 42, 416–434.e11. doi: 10.1016/j.devcel.2017.07.024

Dickinson, D. J., Ward, J. D., Reiner, D. J., and Goldstein, B. (2013). Engineering the *Caenorhabditis elegans* genome using cas9-triggered homologous recombination. *Nat. Methods* 10, 1028–1034. doi: 10.1038/nmeth.2641

Ding, W. Y., Ong, H. T., Hara, Y., Wongsantichon, J., Toyama, Y., Robinson, R. C., et al. (2017). Plastin increases cortical connectivity to facilitate robust polarization and timely cytokinesis. *J. Cell Biol.* 216, 1371–1386. doi: 10.1083/jcb.201603070

Dzyubachyk, O., Jelier, R., Lehner, B., Niessen, W., and Meijering, E. (2009). Model-based approach for tracking embryogenesis in *Caenorhabditis elegans* fluorescence microscopy data. *Conf. Proc. IEEE Eng. Med. Biol. Soc.* 2009, 5356–5359. doi: 10.1109/IEMBS.2009.5334046

Ennomani, H., Letort, G., Gurin, C., Martiel, J.-L., Cao, W., Nédélec, F., et al. (2016). Architecture and connectivity govern actin network contractility. *Curr. Biol.* 26, 616–626. doi: 10.1016/j.cub.2015.12.069

Goldstein, B. (1992). Induction of gut in *Caenorhabditis elegans* embryos. *Nature* 357, 255–257. doi: 10.1038/357255a0

Heppert, J. K., Dickinson, D. J., Pani, A. M., Higgins, C. D., Steward, A., Ahringer, J., et al. (2016). Comparative assessment of fluorescent proteins for *in vivo* imaging in an animal model system. *Mol. Biol. Cell* 27, 3385–3394. doi: 10.1091/mbc.e16-01-0063

Heppert, J. K., Pani, A. M., Roberts, A. M., Dickinson, D. J., and Goldstein, B. (2018). A CRISPR tagging-based screen reveals localized players in WNT-directed asymmetric cell division. *Genetics* 208, 1147–1164. doi: 10.1534/genetics.117.300487

Hirani, N., Illukkumbura, R., Bland, T., Mathonnet, G., Suhner, D., Reymann, A.-C., et al. (2019). Anterior-enriched filopodia create the appearance of asymmetric membrane microdomains in polarizing *C. elegans* zygotes. *J. Cell Sci.* 132:jcs230714. doi: 10.1242/jcs.230714

Inoue, Y., Tsuda, S., Nakagawa, K., Hojo, M., and Adachi, T. (2011). Modeling myosin-dependent rearrangement and force generation in an actomyosin network. *J. Theor. Biol.* 281, 65–73. doi: 10.1016/j.jtbi.2011.04.004

Jelier, R., Kruger, A., Swoger, J., Zimmermann, T., and Lehner, B. (2016). Compensatory cell movements confer robustness to mechanical deformation during embryonic development. *Cell Syst.* 3, 160–171. doi: 10.1016/j.cels.2016.07.005

Kamath, R. S., Martinez-Campos, M., Zipperlen, P., Fraser, A. G., and Ahringer, J. (2000). Effectiveness of specific RNA-mediated interference through ingested double-stranded RNA in *Caenorhabditis elegans*. *Genome Biol.* 2:RESEARCH0002. doi: 10.1186/gb-2000-2-1-research0002

Kametani, Y., and Takeichi, M. (2007). Basal-to-apical cadherin flow at cell junctions. *Nat. Cell Biol.* 9, 92–98. doi: 10.1038/ncb1520

Krueger, D., Quinkler, T., Mortensen, S. A., Sachse, C., and De Renzis, S. (2019). Cross-linker-mediated regulation of actin network organization controls tissue morphogenesis. *J. Cell Biol.* 218, 2743–2761. doi: 10.1083/jcb.201811127

Krüger, A. V., Jelier, R., Dzyubachyk, O., Zimmerman, T., Meijering, E., and Lehner, B. (2015). Comprehensive single cell-resolution analysis of the role of chromatin regulators in early *C. elegans* embryogenesis. *Dev. Biol.* 398, 153–162. doi: 10.1016/j.ydbio.2014.10.014

Lam, A. K., and Phillips, B. T. (2017). WNT signaling polarizes *C. elegans* asymmetric cell divisions during development. *Results Probl. Cell Differ.* 61, 83–114. doi: 10.1007/978-3-319-53150-2_4

Lang, C. F., and Munro, E. (2017). The par proteins: from molecular circuits to dynamic self-stabilizing cell polarity. *Development* 144, 3405–3416. doi: 10.1242/dev.139063

Lecuit, T., and Lenne, P.-F. (2007). Cell surface mechanics and the control of cell shape, tissue patterns and morphogenesis. *Nat. Rev. Mol. Cell Biol.* 8, 633–644. doi: 10.1038/nrm2222

Liu, J., Maduzia, L. L., Shirayama, M., and Mello, C. C. (2010). NMY-2 maintains cellular asymmetry and cell boundaries, and promotes a src-dependent asymmetric cell division. *Dev. Biol.* 339, 366–373. doi: 10.1016/j.ydbio.2009.12.041

Marston, D. J., Higgins, C. D., Peters, K. A., Cupp, T. D., Dickinson, D. J., Pani, A. M., et al. (2016). Mrck-1 drives apical constriction in *C. elegans* by linking developmental patterning to force generation. *Curr. Biol.* 26, 2079–2089. doi: 10.1016/j.cub.2016.06.010

Mayer, M., Depken, M., Bois, J. S., Jülicher, F., and Grill, S. W. (2010). Anisotropies in cortical tension reveal the physical basis of polarizing cortical flows. *Nature* 467, 617–621. doi: 10.1038/nature09376

Munjal, A., Philippe, J.-M., Munro, E., and Lecuit, T. (2015). A self-organized biomechanical network drives shape changes during tissue morphogenesis. *Nature* 524, 351–355. doi: 10.1038/nature14603

Naganathan, S. R., Fürthauer, S., Nishikawa, M., Jülicher, F., and Grill, S. W. (2014). Active torque generation by the actomyosin cell cortex drives left-right symmetry breaking. *eLife* 3:e04165. doi: 10.7554/eLife.04165

Nance, J., and Priess, J. R. (2002). Cell polarity and gastrulation in *C. elegans*. *Development* 129, 387–397. doi: 10.1242/dev.129.2.387

Padmanabhan, A., Ong, H. T., and Zaidel-Bar, R. (2017). Non-junctional e-cadherin clusters regulate the actomyosin cortex in the *C. elegans* zygote. *Curr. Biol.* 27, 103–112. doi: 10.1016/j.cub.2016.10.032

Pimpale, L. G., Middelkoop, T. C., Mietke, A., and Grill, S. W. (2020). Cell lineage-dependent chiral actomyosin flows drive cellular rearrangements in early development. *eLife* 9:54930. doi: 10.7554/eLife.54930

Pohl, C., and Bao, Z. (2010). Chiral forces organize left-right patterning in *C. elegans* by uncoupling midline and anteroposterior axis. *Dev. Cell* 19, 402–412. doi: 10.1016/j.devcel.2010.08.014

Reymann, A.-C., Staniscia, F., Erzberger, A., Salbreux, G., and Grill, S. W. (2016). Cortical flow aligns actin filaments to form a furrow. *eLife* 5:e17807. doi: 10.7554/eLife.17807.031

Rose, L., and Gönczy, P. (2014). Polarity establishment, asymmetric division and segregation of fate determinants in early *C. elegans* embryos. *WormBook* 1–43. doi: 10.1895/wormbook.1.30.2

Saha, A., Nishikawa, M., Behrndt, M., Heisenberg, C.-P., Jülicher, F., and Grill, S. W. (2016). Determining physical properties of the cell cortex. *Biophys. J.* 110, 1421–1429. doi: 10.1016/j.bpj.2016.02.013

Sawa, H., and Korswagen, H. C. (2013). WNT signaling in *C. elegans*. *WormBook* 1–30. doi: 10.1895/wormbook.1.7.2

Stewart, M. P., Helenius, J., Toyoda, Y., Ramanathan, S. P., Muller, D. J., and Hyman, A. A. (2011). Hydrostatic pressure and the actomyosin cortex drive mitotic cell rounding. *Nature* 469, 226–230. doi: 10.1038/nature09642

Sulston, J. E., Schierenberg, E., White, J. G., and Thomson, J. N. (1983). The embryonic cell lineage of the nematode *Caenorhabditis elegans*. *Dev. Biol.* 100, 64–119. doi: 10.1016/0012-1606(83)90201-4

Thiels, W., Smeets, B., Cuvelier, M., Caroti, F., and Jelier, R. (2021). spheresDT/Mpacts-PiCS: cell tracking and shape retrieval in membrane-labeled embryos. *Bioinformatics*. 2021:btab557. doi: 10.1093/bioinformatics/btab557

Wallingford, J. B., and Habas, R. (2005). The developmental biology of dishevelled: an enigmatic protein governing cell fate and cell polarity. *Development* 132, 4421–4436. doi: 10.1242/dev.02068

Wang, S.-C., Low, T. Y. F., Nishimura, Y., Gole, L., Yu, W., and Motegi, F. (2017). Cortical forces and CDC-42 control clustering of PAR proteins for *Caenorhabditis elegans* embryonic polarization. *Nat. Cell Biol.* 19, 988–995. doi: 10.1038/ncb3577

Wei, H., Lambie, E. J., Osório, D. S., Carvalho, A. X., and Conradt, B. (2020). Pig-1 melk-dependent phosphorylation of nonmuscle myosin ii promotes apoptosis through ces-1 snail partitioning. *PLoS Genet.* 16:e1008912. doi: 10.1371/journal.pgen.1008912

Conflict of Interest: The authors declare that the research was conducted in the absence of any commercial or financial relationships that could be construed as a potential conflict of interest.

Publisher's Note: All claims expressed in this article are solely those of the authors and do not necessarily represent those of their affiliated organizations, or those of the publisher, the editors and the reviewers. Any product that may be evaluated in this article, or claim that may be made by its manufacturer, is not guaranteed or endorsed by the publisher.

Advantages of publishing in Frontiers

OPEN ACCESS
Articles are free to read for greatest visibility and readership

FAST PUBLICATION
Around 90 days from submission to decision

HIGH QUALITY PEER-REVIEW
Rigorous, collaborative, and constructive peer-review

TRANSPARENT PEER-REVIEW
Editors and reviewers acknowledged by name on published articles

Frontiers
Avenue du Tribunal-Fédéral 34
1005 Lausanne | Switzerland

Visit us: www.frontiersin.org
Contact us: frontiersin.org/about/contact

REPRODUCIBILITY OF RESEARCH
Support open data and methods to enhance research reproducibility

DIGITAL PUBLISHING
Articles designed for optimal readership across devices

FOLLOW US
@frontiersin

IMPACT METRICS
Advanced article metrics track visibility across digital media

EXTENSIVE PROMOTION
Marketing and promotion of impactful research

LOOP RESEARCH NETWORK
Our network increases your article's readership